

University of Manchester



The University of Manchester

**Sedimentary processes and deposits around
the Azores volcanic islands and implications
for hazard assessment**

A thesis submitted to the University of Manchester for the degree of
Doctor of Philosophy in the Faculty of Science and Engineering

2022

Yu-Chun Chang

Faculty of Science and Engineering
School of Natural Sciences
Department of Earth and Environmental Sciences

Lead supervisor:

Dr. Neil Mitchell (The University of Manchester)

Co-supervisor:

Dr. Bart van Dongen (The University of Manchester)

External supervisors:

Dr. Rui Quartau (Hydrographic Institute of Portugal)

Dr. Thor H. Hansteen (GEOMAR, Helmholtz-Zentrum für Ozeanforschung Kiel, Kiel, Germany)

Internal examiner:

Dr. Ian Kane (The University of Manchester)

External examiner:

Dr. Sebastian Watt (University of Birmingham)

Table of contents

Table of contents	2
List of tables	7
List of figures	8
Abstract	11
Declaration	12
Copyright statement	12
Acknowledgement	13
Preface	15
List of publications	16
Chapter 1. Introduction	17
1.1 Motivation	17
1.2 Rationale.....	19
1.3 Aims and objectives	26
1.4 Thesis structure.....	27
Chapter 2. Geological background and general review of processes and hazards around insular volcanic islands	30
2.1 Geological background.....	30
2.2 Geological processes affecting volcanic ocean islands	32
2.2.1 Volcanism.....	32
2.2.2 Tectonics	33
2.2.3 Mass wasting	33
2.2.4 Biogenic production	34
2.2.5 Erosion.....	34
2.2.6 Eustatic sea-level change.....	37
2.3 Hazards at/around volcanic islands	37
2.3.1 Hazards related to eruptive activities.....	37
2.3.2 Earthquakes	40
2.3.3 Submarine landslides.....	41
2.3.4 Tsunamis	42
2.3.5 Hazards within the Azores Islands	44
Chapter 3. Landslides in the upper submarine slopes of volcanic islands: the central Azores	45
Abstract	46
3.1 Introduction	47
3.2 Geological setting.....	50
3.3 Materials and methods.....	53

3.3.1 Research materials.....	53
3.3.2 Landslide identification and calculations of area and volume.....	53
3.3.3 Landslide size-frequency analysis	57
3.3.4 Estimates of peak horizontal accelerations during earthquakes	57
3.3.5 Sediment cohesion estimates	58
3.3.6 Estimates of tsunami height.....	59
3.4 Results	60
3.4.1 Seismic ground shaking.....	60
3.4.2 Submarine landslide inventory and volume-frequency distribution.....	62
3.4.3 Assessment of cohesions of steep deposits.....	64
3.4.4 Assessment of tsunami wave heights at source	66
3.5 Discussion	67
3.5.1 Assessing varied submarine landslide features in the central Azores	67
3.5.2 Comparing the Azores landslide area-volume relationship with those of other settings.....	71
3.5.3 Comparing cumulative volume distributions with those of other areas	72
3.5.4 Lessons for assessing geohazards of volcanic islands.....	73
3.6 Conclusions	74
Data availability	75
Acknowledgement.....	76
Chapter 4. Volcaniclastic deposits and sedimentation processes around volcanic ocean islands: the central Azores	77
Abstract	78
4.1 Introduction	79
4.2 Geological setting.....	82
4.3 Materials and methods.....	85
4.3.1 Visual core descriptions and sample selection	85
4.3.2 Volcanic glass geochemical analysis.....	87
4.3.3 Morphometric analyses of volcanic grains	88
4.3.4 Bulk mineral assemblage analysis.....	89
4.3.5 Organic carbon and nitrogen and carbon isotope analyses.....	89
4.3.6 Discriminating pyroclastic fallout, primary turbidite and secondary turbidite.....	90
4.4 Results	91
4.4.1 Facies visual descriptions	93
4.4.2 Volcanic glass geochemistry	95
4.4.3 Morphologies of volcanic grains	96
4.4.4 Bulk mineral assemblage.....	98

4.4.5 Total organic carbon, total nitrogen, and carbon isotopes.....	100
4.5 Discussion	102
4.5.1 Origins of volcanoclastic turbidites.....	103
4.5.2 Applicability of morphological analysis of volcanic grains in other volcanic settings.....	104
4.5.3 Lateral correlation of pyroclastic fallout beds	105
4.6 Conclusions	108
Acknowledgement.....	110
Chapter 5. Asymmetric abundances of submarine sediment waves around the Azores volcanic islands	111
Abstract	112
5.1 Introduction	113
5.2 Regional Setting	114
5.2.1 Turbidite census.....	116
5.2.2 Flank collapses, pyroclastic and lava flows as submarine sedimentary flow sources	116
5.2.3 Potential sources of other kinds of sedimentary flows	118
5.2.4 Oceanographic conditions	118
5.3 Materials and Methods	120
5.3.1 Bathymetric, seismic reflection and backscatter data.....	120
5.3.2 Shelf sediment sampling and characterization	121
5.3.3 Wave conditions	121
5.3.4 Sediment wave train identification and density map.....	122
5.3.5 Sediment threshold of motion modelling	126
5.3.6 Internal tidal waves.....	128
5.4 Results	129
5.4.1 Sediment wave characteristics.....	129
5.4.2 Evidence of shelf sediment mobility	136
5.4.3 Internal wave effects.....	142
5.5 Discussion	143
5.5.1 Evidence of shelf sediment mobility over the Holocene and at present.....	143
5.5.2 Processes forming sediment waves:	144
5.5.3 Other processes modifying the morphologies of sediment waves.....	148
5.6 Conclusions	149
Data availability	150
Acknowledgement.....	150

Chapter 6. Emplacement history of volcanoclastic turbidites around the central Azores volcanic islands: frequencies of slope landslides and eruptions	152
Abstract	153
6.1 Introduction	154
6.2 Regional Setting	155
6.2.1 Explosive eruptions on the central Azores islands	155
6.2.2 Volcanism-associated sediment gravity flows as turbidite sources.....	158
6.2.3 Other sources of sediment gravity flows	159
6.3 Materials and Methods	161
6.3.1 Sediment cores and sample collections	161
6.3.2 Marine geophysical data.....	164
6.3.3 Turbidite volume modelling.....	165
6.4 Results	167
6.4.1 Stratigraphy of the sediment cores	167
6.4.2 Turbidite volume modelling results.....	173
6.5 Discussion	177
6.5.1 Implications of the turbidite volume estimates.....	177
6.5.2 Has sediment deposition history been affected by climatic changes?.....	181
6.6 Conclusions	184
Acknowledgement.....	185
Chapter 7. Discussion and suggestion	187
7.1 Synthesis and broader discussion	187
7.2 Future work	192
7.2.1 Landslides in the upper submarine slopes of volcanic islands	192
7.2.2 Volcanoclastic deposits and sedimentation processes around volcanic ocean islands	193
7.2.3 Asymmetric abundances of submarine sediment waves around volcanic islands	193
7.2.4 Emplacement history of volcanoclastic turbidites around volcanic islands	194
Chapter 8. Concluding remarks	195
References	199
Appendix	245
Appendix 3.1 Detailed submarine landslide mapping results for individual islands.....	245
Appendix 3.2 Morphometric parameters of the landslide valleys used to compute the tsunami amplitude above them.	247
Appendix 4.1 Characteristics and interpretations of volcanoclastic-rich layers.....	249
Appendix 4.2 Geochemical composition of full glass data	255
Appendix 4.3 Morphometric measurements of volcanic grains	276

Appendix 4.4 Total organic carbon, total nitrogen, and carbon isotopes 306
Appendix 5.1 Validation of wave property simulation 307
Appendix 5.2 Computed wave-induced stresses and the used parameters..... 309
Appendix 6.1 Geochemical composition of full glass data for core 1230 at depth 180-250
cm. 313

Total word count: 93714

List of tables

Table 1.1. Compiled list of datasets used in the study.....	22
Table 3.1. Synthesis of volume-area relationships.	72
Table 4.1. Characteristics and interpretations of facies identified in sediment cores around the central Azores islands.....	92
Table 6.1. Information on microfossil samples and radiocarbon dating results	170
Table 6.2. Modelled ages and volumes of volcanoclastic turbidites	173

List of figures

Figure 1.1. Maps of regional tectonic settings and distributions of historical natural hazards of the (a) Azores Islands, (b) central Azores group and (c) São Miguel Island.....	18
Figure 1.2. Processes affecting the evolution of volcanic ocean islands	20
Figure 1.3. Two conceptual models of internal structures of volcanic ocean islands.	20
Figure 1.4. Features of seafloor topography on high-resolution bathymetric data on the submarine slopes of the (a) Faial, (b) Pico, (c) São Jorge, (d) Terceira and (e) São Miguel Islands.....	23
Figure 1.5. Photoscans of sediment gravity cores collected around the Azores Islands.	25
Figure 2.1. Neotectonic maps of the five studied Azores islands.....	30
Figure 2.3. Natural hazards that are associated with volcanic activities.	40
Figure 2.4. Complexity of interacting processes at volcanic islands that may precondition and trigger submarine landslides and turbidity currents	42
Figure 2.5. Volume-frequency plot illustrating the submarine landslide scales and recurrence periods.	43
Figure 3.1. (a) Distribution of high-resolution bathymetry data in the central Azores available to this study (outlined by black-dashed lines).	48
Figure 3.2. Distributions of earthquakes.	52
Figure 3.3. Illustration of different classes and types of valley polygons.	56
Figure 3.4. Shallow slope failure parameters used in the static limit-equilibrium calculation and estimates of tsunami height at source.	59
Figure 3.5. Peak horizontal accelerations (PHA) derived from the International Seismological Centre catalog for 1964–2019 earthquakes..	61
Figure 3.6. Histograms of slope valleys..	63
Figure 3.7. Summaries of total areas and volumes of slope valleys of each island	63
Figure 3.8. Empirical relationship between area (A_i) and volume (V) for the central Azores valleys of type 2 and classes A-C.....	64
Figure 3.9. Complementary cumulative distribution functions (CCDF) of (a) area and (b) volume for valleys most likely to be landslide scars (type 2 and classes A-C).....	64
Figure 3.10. Estimates of sediment cohesion with varied slope angles from the pseudo-static analysis with no seismic accelerations..	65
Figure 3.11. Cumulative frequency of tsunami amplitudes (A) at source	67
Figure 3.12. Cumulative volumes of slope valley per unit slope area for subdivisions of Pico and São Jorge islands (all valley classes and types).....	69
Figure 3.13. CCDFs of landslide volumes	73

Figure 4.1. Locations of the four investigated gravity cores between the five central Azores Islands and enlarged map of local gradients on the north flank of Terceira.....	84
Figure 4.2. Photographic scans, interpreted lithological columns, grain size with locations of analysed samples, sedimentary structures, and facies interpretations of the cores.....	86
Figure 4.3. Selected photos of volcanic particles and bioclasts from different core samples.	89
Figure 4.4. Enlargements of core sections illustrating sedimentary structures in each facies..	93
Figure 4.5. Geochemical and morphometric characteristics of volcanic particles from selected beds representing the three deposit types	95
Figure 4.6. Average values and one standard deviations of (a) normalised perimeter length and (b) aspect ratios of samples	97
Figure 4.7. Mineral assemblages from XRD analyses of bulk sediment samples.....	99
Figure 4.8. Organic carbon contents of the samples sorted by facies.....	100
Figure 4.9. $\delta^{13}\text{C}$ and ratios of total organic carbon and total nitrogen for the samples.	101
Figure 4.10. Average values and one standard deviations of (a) normalised perimeter length and (b) aspect ratios of volcanoclastic particles from the data of Cassidy et al. (2014).	105
Figure 4.11. Geochemical variations of volcanic glasses in selected samples interpreted as fallout.....	106
Figure 4.12. Thickness frequency distributions of volcanoclastic beds preserved in comparatively proximal drilling sites of different volcanic settings.	107
Figure 5.1. Bathymetry of the central and eastern Azores Islands with depth contours every 1000 m.....	115
Figure 5.2. Photographic scans of four gravity cores (1215, 1219, 1226 and 1230) and interpreted deposit emplacement mechanisms simplified from Chang et al. (2021b).....	117
Figure 5.3. Bathymetric profiles along sediment wave trains.....	123
Figure 5.4. Maps of local maximum gradient along with interpreted trains of sediment waves	124
Figure 5.5. Enlarged maps of local maximum gradient to the north of the Azores Islands .	130
Figure 5.6. Dimensions of selected sediment waves in the Azores and comparison with those of other volcanic islands.....	132
Figure 5.7. Seismic reflection sections from north (a-b) and south (c-d) of São Miguel Island.	134
Figure 5.8. Densities of sediment wave trains measured along the contour segments shown between the dashed arrows.....	135

Figure 5.9. Acoustic backscatter mosaics for the (a) northeast, (b) northwest and (c) southwest shelves of Faial Island.	137
Figure 5.10. Dropdown camera images extracted from a transect of video footage for ground-truthing backscattering areas.	138
Figure 5.11. Characteristics of surface sediments on the shelves of Faial and Pico.....	139
Figure 5.12. Rose diagrams of wave directions and significant wave heights for windward locations of islands in the central Azores and eastern Azores.....	141
Figure 5.13. Assessment of surface sediment mobility on the shelves of Faial and Pico	141
Figure 5.14. Assessment of critical gradients for breaking of internal tidal waves.....	143
Figure 6.1. Bathymetry of the central Azores Islands contoured every 50 m from 500 to 3200 m.....	157
Figure 6.2. Summary of cores taken from the sites	160
Figure 6.3. Selected photos of planktonic foraminifera species from the samples used for radiocarbon dating.	162
Figure 6.4. Conceptual elements of geometry used in calculation of turbidite volume, which attempts to account for varied degrees of deposit confinement and lateral thinning rate.. ...	166
Figure 6.5. Data from samples of primary volcanoclastic beds in core 1230 from core depths 168–262 cm to 262–368 cm bsf.	168
Figure 6.6. Comparison of major element compositions of two well-dated ignimbrites on land with those of volcanic glass shards in the sediment cores.....	169
Figure 6.7. Sediment deposition history in the cores based on the ¹⁴ C dating and two correlated ignimbrites.....	171
Figure 6.8. Seismic reflection data over core sites.	175
Figure 6.9. Turbidite volume modelling results	176
Figure 6.10. Basin-floor volumes of turbidites predicted with 30.75%/km thinning rates for cores 1230, 1219 and 1215 compared with volumes of landslide valleys in their adjacent upper submarine slopes turbidites.	178
Figure 6.11. Temporal variations in (a) turbidite thicknesses and (b) best-estimated turbidite volumes.	183
Figure 7.1. Synthesis of key findings of Chapters 3 to 6.....	187
Figure 7.2. Results from other volcanic settings that can be compared with results of this project.....	188

Abstract

In this project, interdisciplinary methods are applied to study abundant submarine landslide valleys, sediment wave trains and volcanoclastic deposits in submarine parts of Azores volcanic islands to assess the sedimentary processes, characteristics of deposits and their hazard implications. Marine geophysical data help to characterise geomorphological features of submarine topography. Sedimentary structures, morphometric parameters, geochemical compositions of volcanic particles and bulk sediments, and chronostratigraphy are derived from marine sediments. Statistical methods are used to find relationships between data sets. Numerical calculations help to assess the sedimentary processes induced by external forces (e.g., ground motion, wave-induced stress and oceanic current).

Four key findings are found. 1. More than 1200 submarine slope valleys have been found around the central Azores, mostly caused by landslides. Thirteen landslides would likely have generated tsunamis with heights of 1–7 m at source, hence potentially hazardous. Higher landslide volumes of submarine slopes in Terceira and São Jorge Islands compared to Faial and Pico Islands may result from more frequent large earthquakes beneath Faial and Pico. 2. Sediment wave trains are twice as abundant on northern island slopes compared with their southern slopes. This asymmetry is associated with greater wave energy arising from the northwest, leading to greater coastal erosion and wave-induced bed stress, encouraging sediment suspension and redeposition on the slopes and eventually initiating sediment gravity flows. (3) A wide range of information is integrated to discriminate tephra fallout and primary and secondary volcanoclastic turbidites in four gravity cores collected nearby the Azores islands. Sediment type discrimination suggests that two-thirds of volcanoclastic beds originate from eruptions and only one-third are from submarine landslides. (4) Modelling of turbidite volumes in the basins suggests only sediments from the largest landslides and eruptions have been deposited in the basins. Age-depth models built from ^{14}C dates of foraminifera from hemipelagic intervals and tephra bed correlation suggest the emplacement ages and the frequencies of large submarine landslides and volcanic eruptions are both > 1 ky.

Declaration

I hereby declare, that no portion of the work referred to in the thesis has been submitted in support of an application for another degree or qualification of this or any other university or other institute of learning.

Yu-Chun Chang

Copyright statement

- i. The author of this thesis (including any appendices and/or schedules to this thesis) owns certain copyright or related rights in it (the “Copyright”) and s/he has given The University of Manchester certain rights to use such Copyright, including for administrative purposes.
- ii. Copies of this thesis, either in full or in extracts and whether in hard or electronic copy, may be made only in accordance with the Copyright, Designs and Patents Act 1988 (as amended) and regulations issued under it or, where appropriate, in accordance with licensing agreements which the University has from time to time. This page must form part of any such copies made.
- iii. The ownership of certain Copyright, patents, designs, trademarks and other intellectual property (the “Intellectual Property”) and any reproductions of copyright works in the thesis, for example graphs and tables (“Reproductions”), which may be described in this thesis, may not be owned by the author and may be owned by third parties. Such Intellectual Property and Reproductions cannot and must not be made available for use without the prior written permission of the owner(s) of the relevant Intellectual Property and/or Reproductions.
- iv. Further information on the conditions under which disclosure, publication and commercialisation of this thesis, the Copyright and any Intellectual Property University IP Policy (see <http://documents.manchester.ac.uk/display.aspx?DocID=24420>), in any relevant thesis restriction declarations deposited in the University Library, The University Library’s regulations (see <http://www.library.manchester.ac.uk/about/regulations/>) and in The University’s policy on Presentation of Theses.

Acknowledgement

I want to thank my lead supervisor Neil Mitchell deeply. PhD degree is such a long journey with endless struggles, challenges, arguments and self-doubt. However, Neil's patience, encouragement, support, and advice are never absent throughout the entire journey. I am sincerely grateful that I had this opportunity to work with Neil. I have learned a lot from his experience and wisdom, which helped me with grant applications, article publications, presentations at academic conferences and (under)graduate supervision. His systematic training has nourished and cultivated me to be ready for challenges in the future. It is about to end my journey in the UK, but I hope we can sit in a bar for a glass of beer or paddle the boat on the lake together for his lovely kid someday soon.

I thank my co-supervisor Bart van Dongen, for his care and help during my PhD journey. I would like to thank Bart and other geochemistry teammates (Sharon Fraser, Emily Flud, Milton Babajide Macaulay, Rakiya Muhammad, Elsa-Marie Portányi, Emma Burns, Katrina Cullen, Oliver Moore and Yusuf Aubakar) to help and accompany me to process my marine sediment samples and varied geochemical analyses. I also had great fun with the geochemistry family in the weekly meeting at the bar and the Christmas party at Bart's home. The joyful atmosphere and time make me feel a sense of belonging.

I thank my two excellent external supervisors Thor Hansteen and Rui Quartau. They are all kind and supportive. Thor has hosted me twice in Kiel. He well-arranged the accommodation place and the laboratory access for me to prepare the samples for volcanic geochemical analysis. I am quite missing the time when we had the daily afternoon coffee break and a small field trip to a gravel beach. Rui is always highly engaged in my research project and provides constructive opinions on the difficulties we met. Thor and Rui are both very supportive and inspire me a lot throughout my entire PhD.

I would like to thank my co-authors, Julie Schindlbeck-Belo, Armin Freundt, Fernando Tempera, Christian Hübscher, and Liliana Rusu, for their critical data support and constructive suggestions for the paper. I am also grateful for the helpful comments from my PhD viva examiners and paper reviewers, which significantly improved this study.

I would also like to thank every research staff and technician who assisted me in running the analyses at the University of Manchester, GEOMAR Helmholtz Centre for Ocean Research Kiel, University of Liverpool, Scottish Universities Environment Research Centre (SUERC), British Ocean Sediment Core Research Facility (BOSCORF) and the University of Rhode Island. Those critical analyses cannot be properly done without their full support. I would also like to honourably mention my intelligent Taiwanese friends. Their valuable research

experience and expertise had helped me better design my geochemical analyses when I had little clue about the geochemical field.

Special thanks are given to the technical and administration support from staff of the Department of Earth and Environmental Sciences. They are computing officer Kofi Owusu, education officer Mike Turner, PGR administrators Claire Erskine, fieldwork administrator Dave Norwood, administrative assistant Annette Barker, experimental officer, deputy health and safety advisor John Waters and deputy school operations manager Helena Gittins.

I had the privilege of being a member of the Basin's lab in the department, where I served as a treasury of the AAPG student chapter at the Manchester with great helps from great partners, Connor Doyle and Jingyue Hao. Many thanks to all my other friends in the Basin group for making my stay in Manchester unforgettable. I especially thank Zhongwei Zhao, Wen Shi and Karina Hernandez of our marine geology and geophysics group for their accompanies during the time at Manchester and oversea trips to conferences.

I appreciate the financial support from the Taiwan Government and a series of funding agencies supporting me with data credit, research and travel grants, which are given in the acknowledgements of the individual chapters. I would like to thank everyone who has helped me to complete this project in the past four years.

I genuinely thank Sung-Ping Chang, Ssu-Ting Lai, An-Sheng Lee and Kuan-Yu Ke, the committee of Taiwanese Geoscientists in Europe (TaiGe). I am so proud of us for funding the first-ever official Taiwanese-based geoscience group in the European area that is supported by the associations and institutions in Taiwan.

Finally, I would like to thank my dear family and partner Yi-Chen Huang for their full support. Life is too short to be wasted. I hope I can enjoy the rest moment with dear you.

Preface

I, Yu-Chun Chang, obtained my BSc and MSc in Earth Sciences at National Cheng Kung University (Taiwan) in 2012 and 2014. In September 2018, I was funded by the Taiwan Government and started my PhD project, sedimentary processes and deposits around the Azores volcanic islands and implications for hazard assessment, at the University of Manchester, UK. The project involved three trips to Kiel and Rhode Islands to sample marine sediments from gravity cores collected around the central Azores islands. Laboratory analytical works have been conducted in Manchester, Liverpool, Kiel and Glasgow for sample preparation and physical and chemical analyses (microscope observations, volcanic glass compositions, bulk mineral assemblage, total organic carbon, total nitrogen, carbon isotopes and radiocarbon analysis). Travels and analyses were mostly funded by varied research grants (AAPG grants-in-aid, International Exchanges grant from the Royal Society and NERC-funded radiocarbon analysis).

The results of this PhD thesis have been presented seven times in oral and poster presentations at national and international conferences, workshops and seminars with three travel grant support from varied associations (IAS, ECORD MagellanPlus Workshop, BGA Gray-Milne and Royal Society). I have been awarded one outstanding student poster in BSRG 2019 and the Blue Marble Geographics academic scholarship in 2022. I was invited five times to share my research results at different institutions, organizations and student chapters. This thesis has resulted in four first author scientific manuscripts. Three of the manuscripts (Chapters 3 to 5) have been published in SCI journals and the last one in the stage of review.

List of publications

Chang, Y.-C., Mitchell*, N. C., Schindlbeck, J. C., Hansteen, T. H., Freundt, A., Hübscher C., Quartau, R., Emplacement history of volcanoclastic turbidites around the central Azores volcanic islands: frequencies of slope landslides and eruption. *Geosphere* (in revision).

Chang*, Y.-C., Mitchell, N. C., Quartau, R., F., Rusu, L., Hübscher C., Tempera. F., 2022, Asymmetric abundances of submarine sediment waves around the Azores volcanic islands, *Marine Geology*, <https://doi.org/10.1016/j.margeo.2022.106837>

Chang*, Y.-C., Mitchell, N., Quartau, R., 2021. Landslides in the Upper Submarine Slopes of Volcanic Islands: the Central Azores. *Geochemistry, Geophysics, Geosystems*. <https://doi.org/10.1029/2021GC009833>

Chang*, Y.-C., Mitchell, N. C., Hansteen, T. H., Schindlbeck, J. C., Freundt, A., 2021, Volcanoclastic deposits and sedimentation processes around volcanic ocean islands: the central Azores. Geological Society, London, Special Publications, 520, SP520-2021-62. <https://doi.org/10.1144/SP520-2021-62>

Published Abstracts

Chang*, Y.-C., Mitchell, N., Quartau, R., Hansteen, T., Schindlbeck-Belo, J., and Freundt, A.: Geological hazard assessment of volcanic islands: Insights from seafloor geomorphology and turbidites in sediment cores, central Azores Islands, EGU General Assembly 2022, Vienna, Austria, 23–27 May 2022, EGU22-1025, <https://doi.org/10.5194/egusphere-egu22-1025>, 2022

Chang*, Y.-C., Mitchell, N. C., Quartau, R., Hansteen. T.H., *Size Distribution and Causes of Submarine Landslides, Azores Islands*. EGU General Assembly 2019, Vienna, Austria 7–12 April 2019, EGU2019-1332

(*: Corresponding author)

Chapter 1. Introduction

1.1 Motivation

Millions of people live close to volcanoes around the world. Many of them are located around the Pacific Rim, and some are close to spreading centres like the Mid-Atlantic Ridge. Volcanic ocean islands are volcanoes lying in the oceans away from the subducting plate boundaries. Their glamorous scenery and unique environment always attract thousands of tourists visiting there every year. However, travelling or living close to an active volcanic island is not without risks. It is maybe the thrill experience of the lifetime—or a fatal destination. Illustrating the potential for future catastrophes, in June 1783, the Laki volcanic fissure vent in Iceland erupted for eight months. This eruption produced the largest lava flow in historical times and damaged tens of farms (Thorarinsson, 1979). Nonetheless, the most significant impact caused by this eruption was the emission of voluminous toxic SO₂ volcanic gases from the 25-km-long fissure, resulting in a severe haze famine and the loss of 75% of livestock and 24% of citizens in Iceland (Hammer, 1977). This eruption even profoundly affected the global temperature in the subsequent years as an abnormal temperature drop found in the eastern US between 1783 and 1784 (Sigurdsson, 1982) due to the effects of significant gas emissions on the backscattering of solar radiation and cooling of the earth (Hansen et al., 1981). Though more locally important, similar damages have occurred in the other volcanic ocean islands, such as the Capelinhos eruption of Faial island in 1957–1958 (Machado et al., 1962) and the eruption on Tristan da Cunha in 1962 (Baker et al., 1964).

The damage caused by the volcanic activities on volcanic ocean islands and the subsequent influences on broader issues highlight the necessity of understanding the role of volcano-sedimentary processes and how they vary over time. Developing the knowledge of the geological processes allows the preconditions, triggering mechanisms and their hazards to be better revealed. It is particularly critical for volcanic ocean islands, such as the Azores archipelago (Fig. 1), because of their remote locations and the difficulty of evacuation and support when severely interrupted by volcanic ash clouds. The lack of understanding may lead

to underestimating the consequences of hazards occurring there. This project, therefore, contributes towards the effort to comprehensively investigate the interplay between different geological processes (sedimentary deposition and transportation, biogenic production, tectonic movements and volcanic activity) and hazards (earthquakes, volcanic eruptions, submarine landslides and landslide-induced tsunamis) affecting the Azores volcanic ocean islands. The preconditions, event magnitudes, frequencies and temporal-spatial changes of these processes and comparisons between other volcanic settings can be explored by integrating marine geophysical and geochemical, sedimentary, physical oceanographic and chronostratigraphic data.

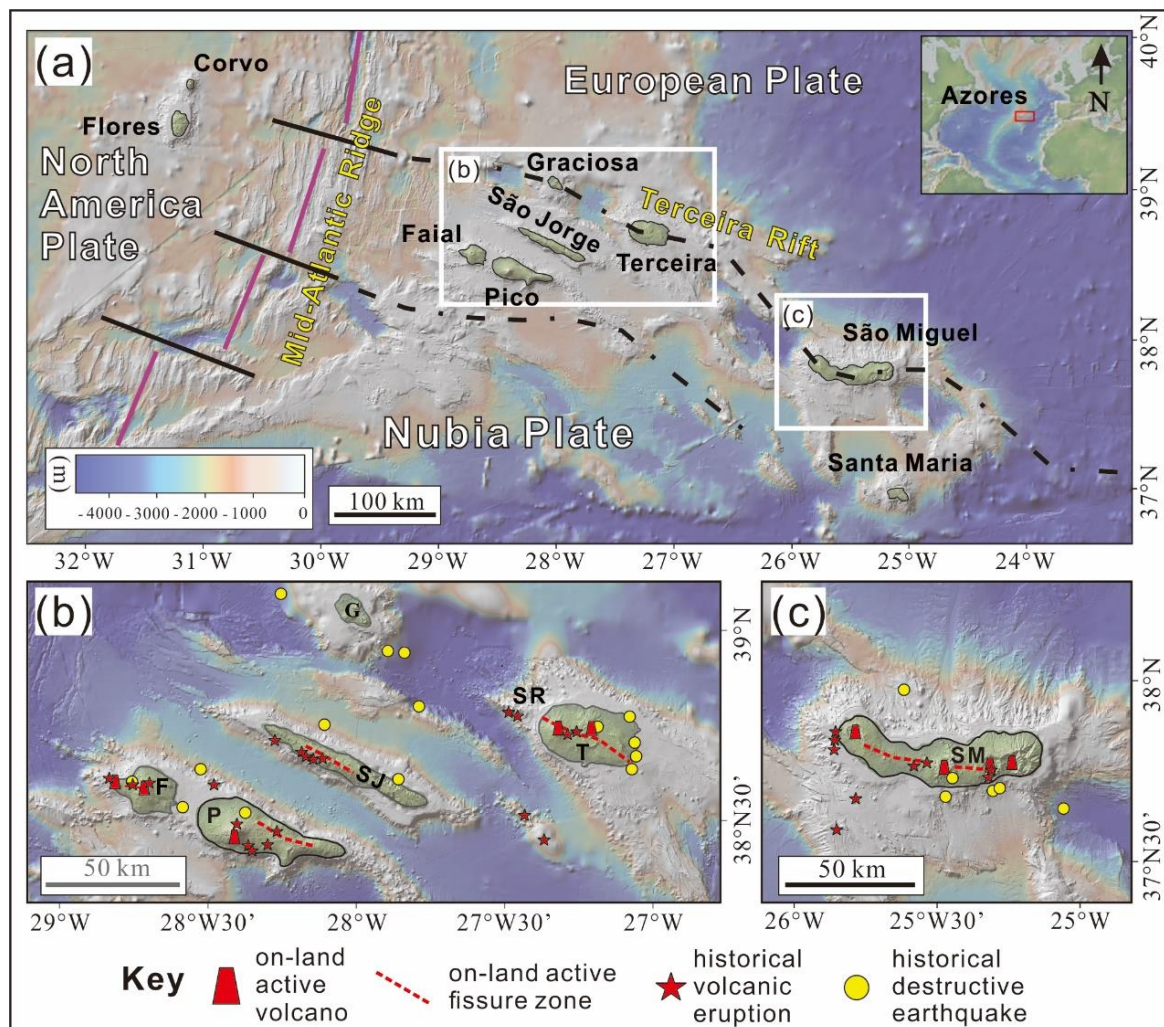


Figure 1.1. Maps of regional tectonic settings and distributions of historical natural hazards of the (a) Azores Islands, (b) central Azores group and (c) São Miguel Island. Bathymetric data are derived from Global Multi-Resolution Topography Data Synthesis (GMRT) of GeoMapApp (Ryan et al., 2009).

1.2 Rationale

The present-day geomorphology of insular volcanic islands is a combined result of volcanic, tectonic, mass-wasting, sedimentary, and oceanographic processes (Fig. 1.2; Ramalho et al., 2013). Volcaniclastic and sedimentary materials denuded from the islands through volcanic, tectonic, and sedimentary processes are transferred to their surrounding seafloor (Menard, 1983). Therefore, they can help to assess the magnitudes of volcanic eruptions and submarine slope failures and their variance over time, as has been done for Gran Canaria (Carey et al., 1998; Schmincke and Sumita, 1998), Reunion (Ollier et al., 1998; Saint-Ange et al., 2013) and Cape Verde (Eisele et al., 2015b). Understanding the geological processes that affect volcanic ocean islands helps to explore the submarine and internal structure of volcanic ocean islands and guyots, where high-quality data able to reveal internal structure is limited. For example, scientific drilling has been attempted at only a few islands and seamounts (e.g., Hawaiian Islands (Moore et al., 1996), Sao Miguel (Muecke et al., 1974), the Louisville Seamounts (Buchs et al., 2018) and the Walvis Ridge (Sager et al., 2022)). However, these have been almost exclusively in their centres or in the deep sedimentary basins around them rather than on their steeply dipping flanks.

Two contrasting models of internal structures of volcanic ocean islands were originally proposed based on marine geophysical data, ocean-bottom photographs, and dredge samples (Moore and Fiske, 1969). Accordingly, submarine flanks could be either composed of volcaniclastics with occasional lavas extruded from submarine vents (Fig. 1.3a; Moore et al., 1995) or substantial quenched pillow lavas fed by lava tubes from land vents (Fig. 1.3b; Moore and Fiske, 1969; Fornari et al., 1979). The first compositional model was inferred from the observations of widespread thick fragmental debris layers (7.5 km) on the submarine slopes of Kilauea, Hawaiian Islands (Moore and Chadwick, 1995). The pillow-lava model served as the structural prototype for interpreting other ocean island volcanoes where coherent pillow lavas formed dominantly on the submarine flank surface, transitioning to volcaniclastic only when vents approached sea-level (e.g., La Palma, Canary Islands; Staudigel and Schmincke, 1984). Although individual chapters of this thesis mainly focus on the sedimentary processes,

characteristics of deposits and hazards around the Azores volcanic ocean islands, that work in combination also addresses a broader need to reveal the structure under the submarine flanks of the Azores volcanic islands, contributing to the above debates.

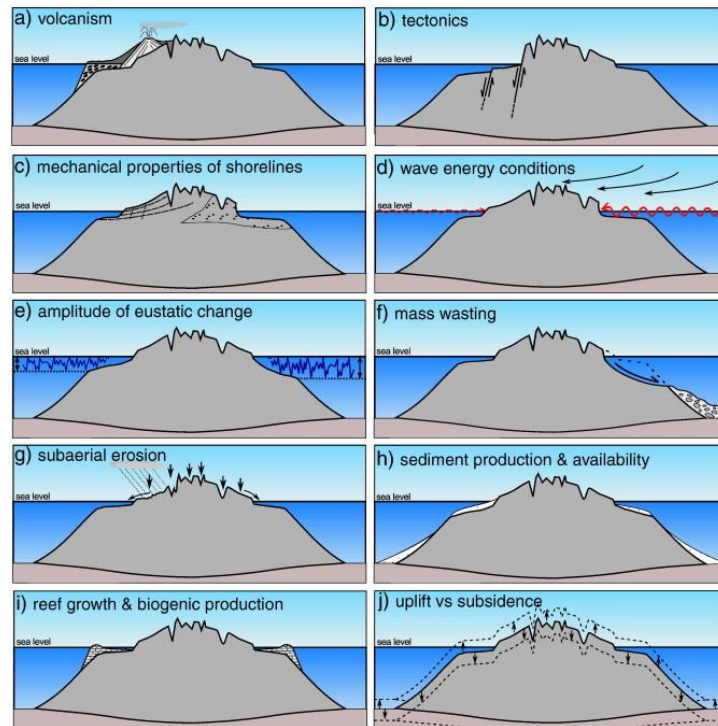


Figure 1.2. Processes affecting the evolution of volcanic ocean islands (Ramalho et al., 2013).

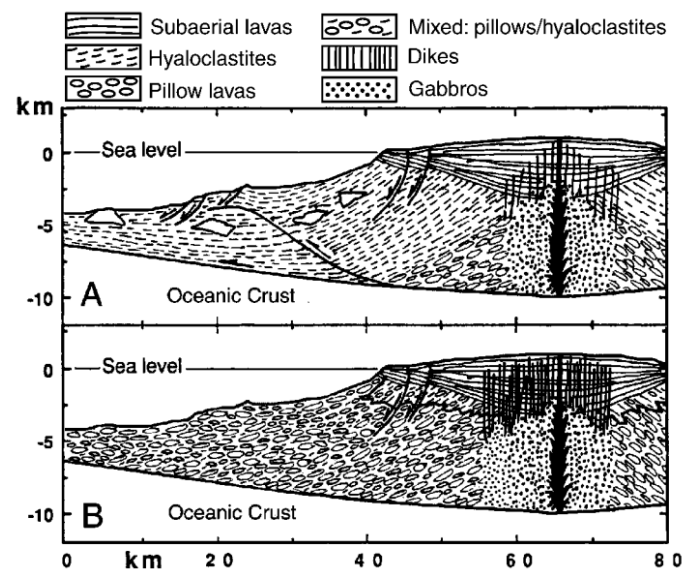


Figure 1.3. Two conceptual models of internal structures of volcanic ocean islands (Garcia and Davis, 2001). (a) Fragmental debris model. (b) Pillow-lava model. Note in (b) that hyaloclastites and pillow lavas are dominant in the upper 1 km and the rest of submarine section, respectively.

The first systematic marine geophysical survey in the Azores occurred in 1978 (Searle 1980), focusing mainly on the central and eastern Azores islands and the adjacent Mid-Atlantic Ridge. In the past two decades, increasing marine surveys with more advanced survey systems have been carried out for extensively imaging and collecting sediment samples to better reveal marine tectonic and volcanic structures (Mitchell et al., 2018 and references therein). In this study, six types of data have been compiled from different marine research cruises and data repositories (Table 1.1), including one set of instrumental earthquake records, three sets of high-resolution multibeam bathymetry, two sets of seismic reflection sections, one set of sediment profiler records, one set of backscatter images, two sets of sediment cores, and three sets of oceanographic properties. High-resolution bathymetric data have revealed rugged submarine slopes and widespread sediment wave trains on the seafloor of the central and eastern Azores area (Fig. 1.4), likely resulting from frequent submarine geological processes such as mass wasting (Mitchell et al., 2012; Quartau et al., 2014; 2015) and sedimentary flows (Weiß et al., 2015 and 2016). Coarse dark volcanoclastic beds and fine pale clay-rich beds are interspersed in the sediment cores collected adjacent to the central Azores islands (Fig. 1.5), suggesting frequent supply of sediment from eruptions and landslides. The many flat-floored basins lying close to the eruptive centres and island slopes of the Azores islands (Fig. 1.1.b and 1.1.c) provide a great chance to study the sediments originating from large geological events and potentially also allow more products of smaller events to be captured because of their locations proximal (within 10–30 km) to potential sources on or near the islands. The observed features in submarine geomorphology and sediments cores were investigated by combining all types of available data (Table 1-1) with numerical and statistical analyses to answer questions related to magnitudes and frequencies of volcanic and submarine sedimentary processes, induced hazards, and mechanisms behind them.

Table 1.1. Compiled list of datasets used in the study

Dataset	Data contents and coverage/location	Collected years	Chapter
Earthquake events	30 largest earthquakes with $M_w > 4.5$ for the central Azores from 1964 to 2019.	International Seismological Centre catalog, downloaded 2019	Chapter 3
High-resolution multibeam bathymetry A	Resolution ranging 0.26–26 m from 10 to 1000 m depth. A combined dataset of grid node spacing of 10–25 m ² for the submarine slopes and basin floors around Faial, Pico and São Jorge islands.	<i>RV Arquipélago</i> 2003	Chapters 3, 5 and 6
High-resolution multibeam bathymetry B	Resolution ranging 0.5–1 m in the shallowest 100 m water depth to 20–50 m at 2000 m water depth for the submarine shelves, slopes and basin floors around Terceira island and Serreta Ridge.	<i>RV l'Atalante</i> in 2011	Chapters 3, 4, 5 and 6
High-resolution multibeam bathymetry C	Resolution ranging from 5 m in the shallowest 200 m water depth to 50 m at 2000 m water depth for the submarine slopes and basin floors around São Miguel island and partly on the central group islands. A combined dataset of grid node spacing of 26–50 m ² .	<i>RV Meteor</i> in 2009, 2015 and 2016	Chapter 5
Seismic reflection dataset A	Four 2D multichannel seismic reflection sections located on the northern and southern slopes of São Miguel island. Signals were recorded with a 600 m long streamer comprising 144 channels.	<i>RV Meteor</i> in 2009	Chapter 5
Seismic reflection dataset B	Four 2D multichannel seismic reflection sections located on the submarine slopes and seafloors of Faial, Pico and São Jorge islands and Serreta Ridge. Signals were recorded with a 600 m long streamer comprising 144 channels.	<i>RV Meteor</i> in 2015	Chapter 6
Sediment profiler records	Three sediment profiler sections were collected on the submarine slopes around Pico and São Jorge islands and Serreta Ridge using a hull-mounted Parasound system emitting two pulses of high primary frequencies (18 kHz and 22 kHz) which generate lower frequency narrow beam signals by the parametric effect.	<i>RV Meteor</i> in 2015	Chapter 6
Backscatter mosaic images	Combined dataset of backscatter for the shelf of Faial island derived from beam-forming sonar (50 kHz) and phase-measuring sonar (117 kHz) systems. Backscatter mosaics were produced at a resolution of 1 m and grid node spacing of 5–20 m ² .	<i>RV Arquipélago</i> in 2003 and <i>RV Águas Vivas</i> in 2004	Chapter 5
Sediment core dataset A	Four gravity sediment cores of ~ 2.5, 4.9, 2.1 and 3.7 m length collected from basin floors around the central Azores islands	<i>RV Meteor</i> in 2017	Chapters 4 and 6
Sediment core dataset B	Eighty-eight sites on the shelves of Faial and Pico islands were box-cored in water depths of 20–80 m.	<i>RV Arquipélago</i> in 2003	Chapter 5
Wave property dataset A	A two-year interval of wave properties extracted from a SWAN model for the central (29°W, 39°N) and eastern (26°W, 38°N) Azores areas.	January 2013 to December 2014	Chapter 5
Wave property dataset B	A three-month interval of wave properties extracted from a SWAN model for the central (29°W, 39°N) and eastern (26°W, 38°N) Azores areas.	January 2001 to March 2001	Chapter 5
Ocean density profiles	Seven ocean density profiles derived from conductivity-temperature-depth (CTD) measurements crossing the central Azores islands.	Unknown	Chapter 5

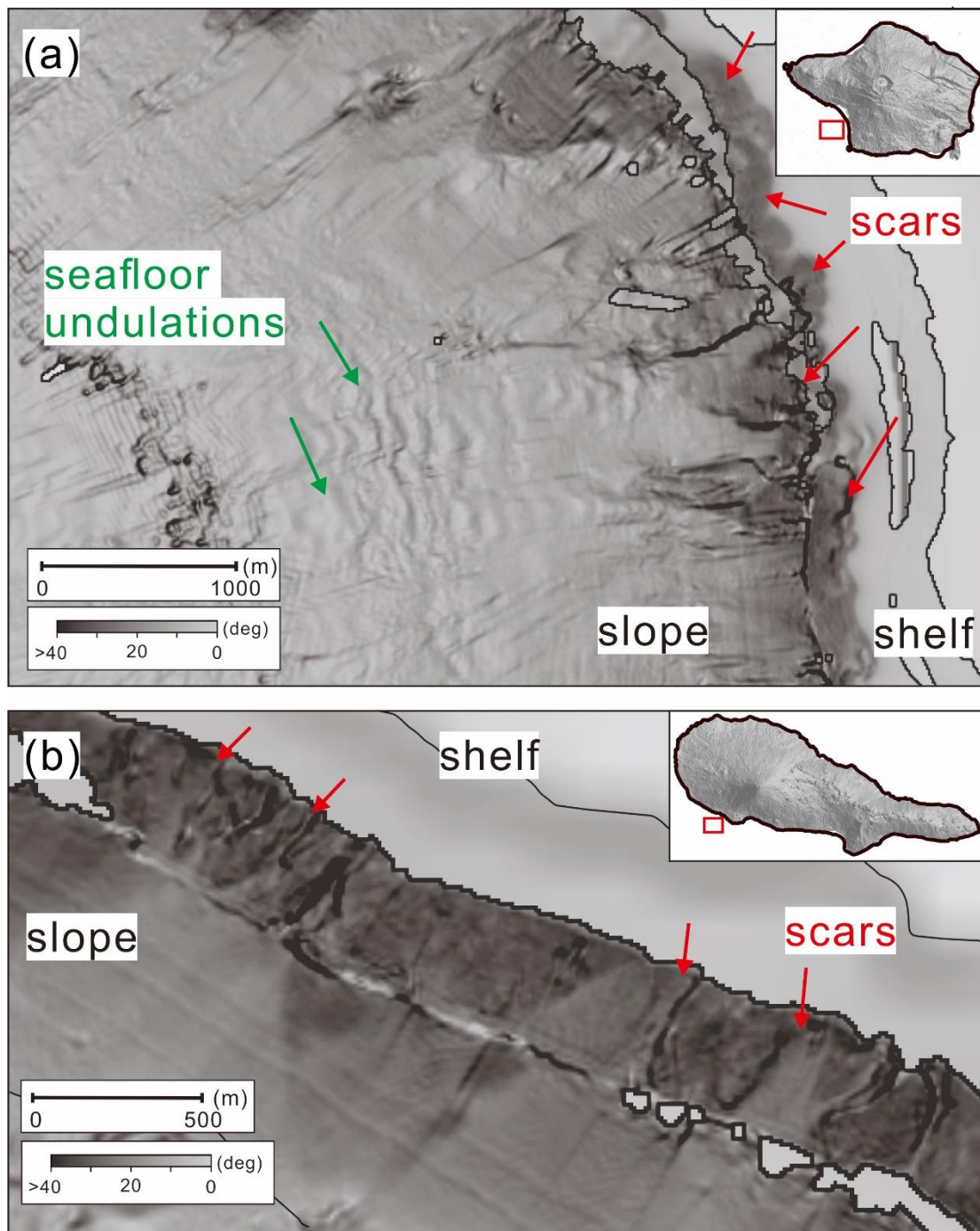


Figure 1.4. Features of seafloor topography on high-resolution bathymetric data on the submarine slopes of the (a) Faial, (b) Pico, (c) São Jorge, (d) Terceira and (e) São Miguel Islands. Steep head scars along the submarine island slopes and widespread sediment trains are distributed on the seafloor.

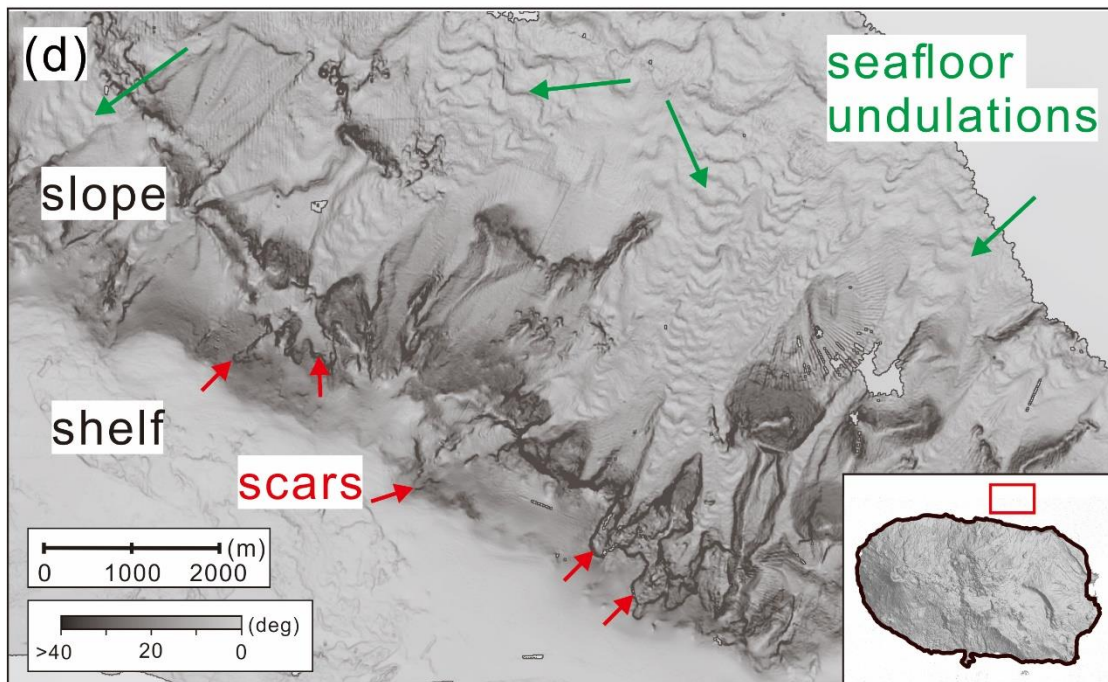
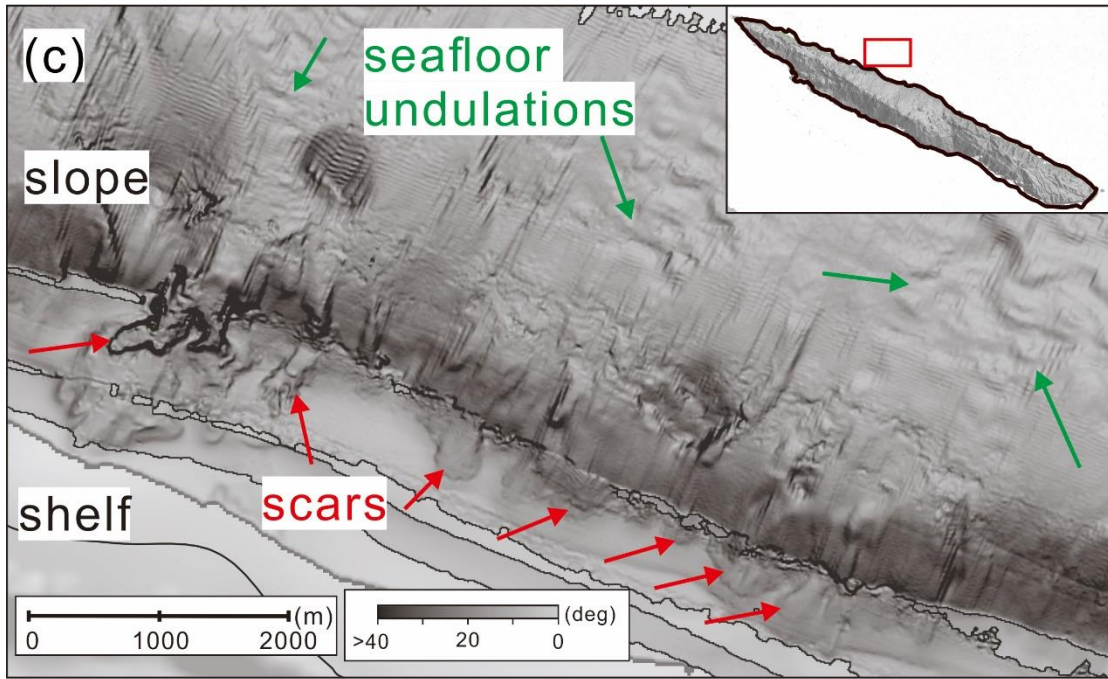


Figure 1.4 continued

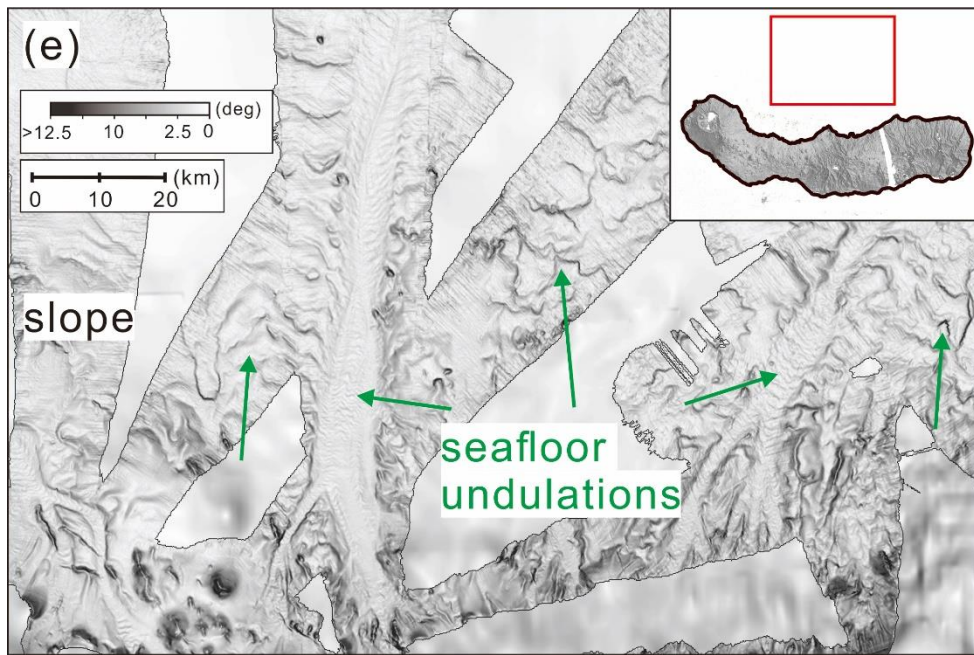


Figure 1.4 continued

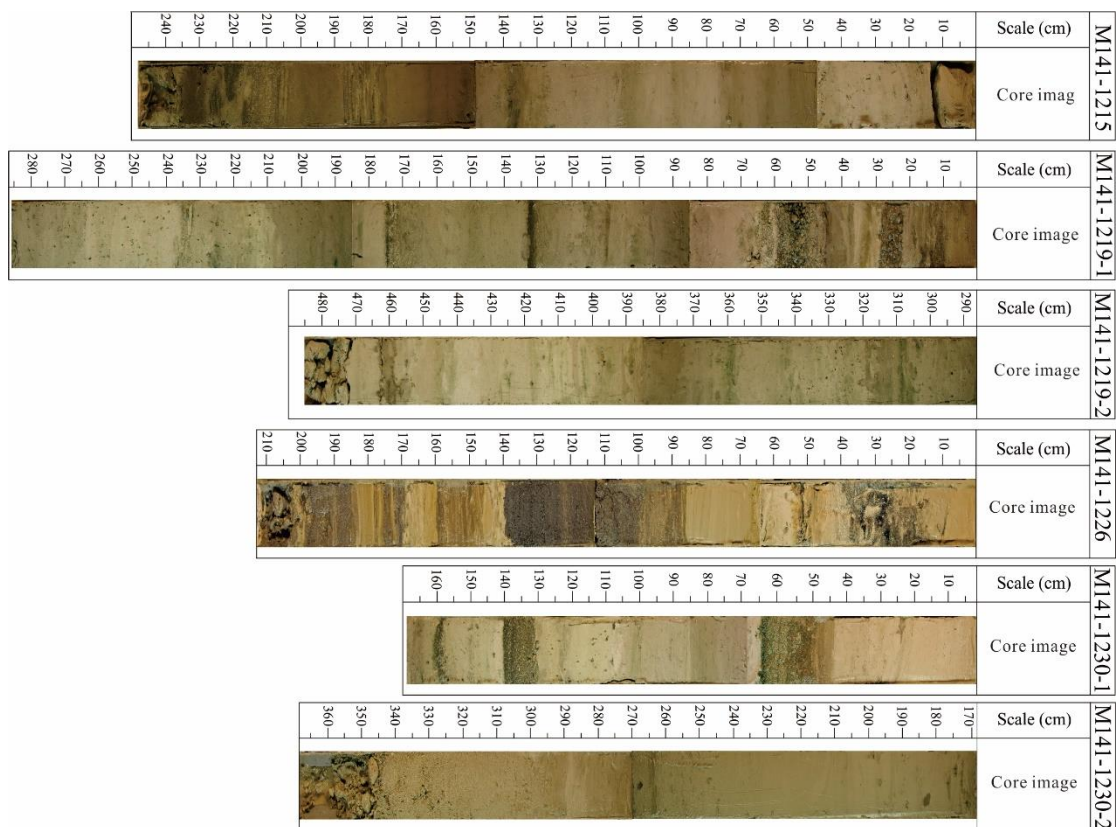


Figure 1.5. Photoscans of sediment gravity cores collected around the Azores Islands. Dark volcaniclastic-rich sediments are frequently found in the cores.

1.3 Aims and objectives

Aims

Aim 1: How is sediment created by volcanism, erosion and biological activity transferred to the archaepelagic aprons of volcanic islands?

Aim 2: What processes are responsible for the high abundances and varied characteristics of slope valleys around the submarine flanks of the central Azores volcanic islands?

Aim 3: What are the implications of slope valleys for assessing hazards associated with submarine landslides?

Aim 4: What processes are responsible for creating trains of submarine sediment waves around the Azores volcanic islands?

Aim 5: What are the characteristics and emplacement frequencies of volcanoclastic deposits in sediment cores originating from eruptions and landslides?

Aim 6: How do the records in sediment cores near to the Azores islands compare with potential sources on the islands and with sediment records in other volcanic settings?

In order to address these aims, a series of objectives have been tackled as outlined below.

Aim 1 is essentially addressed by all the following objectives.

Addressing aim 2, the objectives of Chapter 3 are to:

- Identify and classify submarine landslide valleys by adopting different classification schemes based on marine geophysical data.
- Assess different factors that may cause variations in submarine landslide features amongst the Central Azores.

Addressing aim 3, the objectives of Chapters 3 are to:

- Carry out landslide volume-frequency statistical analysis to represent the relative probability that a landslide greater than a particular size occurs.

- Use empirical equations to estimate tsunami heights at source.
- Generate measures of landslide abundances and size, and interpret them from varied long-term earthquake risk and other factors among the islands.

Addressing aim 4, the objectives of Chapter 5 are to:

- Use morphological evidence from marine geophysical data and logic in explaining the asymmetric abundances of sediment waves to determine the main process forming the wave trains.
- Assess shelf sediment mobility from sidescan sonar data, sedimentary grain size texture and the threshold of movement under wave-induced stresses.

Addressing aim 5, the objectives of Chapters 4 and 6 are to:

- Discriminate different types of emplaced volcanoclastic beds based on multiple lines of evidence, including sedimentary structures, and morphometric and geochemical analyses.
- Build age-depth models based on ^{14}C dates of foraminifera from hemipelagic intervals and tephra-bed correlation to find the frequencies of submarine landslides and eruptions.

Addressing aim 6, the objectives of Chapters 4 and 6 are to:

- Compare volumes of secondary volcanoclastic turbidites derived by geometric modelling with volumes of their adjacent upper slope submarine landslide valleys.
- Model the volumes of pyroclastic turbidites in the basins to adjust the known total volumes of explosive erupted materials based on land deposits.
- Correlate pyroclastic beds between cores and their adjacent islands.
- Compare volcanoclastic bed thickness-frequency distributions of the Azorean cores with those near other oceanic islands

1.4 Thesis structure

The thesis is written in a journal format and structured into eight chapters.

Chapter 1 is general introduction. This chapter brief the motivation, rationale, and research aims and objectives of this thesis.

Chapter 2 is general literature review. This chapter describes the most relevant background knowledge of the processes and natural hazards around the volcanic ocean islands.

Chapter 3 is a scientific manuscript entitled “Landslides in the upper submarine slopes of volcanic islands: the central Azores”. In the work for this manuscript, >1200 slope valleys in high-resolution multibeam sonar data are identified and the implications for tsunami and long-term seismic hazards are assessed. Differences in landslide size distributions between islands have been found, which suggest potential differences in triggering or conditioning by earthquakes amongst them. The landslide abundances and geometrical properties also allow tsunami hazards to be assessed.

Chapter 4 is a scientific manuscript entitled “Volcaniclastic deposits and sedimentation processes around volcanic ocean islands: the central Azores”. This manuscript discriminates tephra fallout, and primary and secondary volcaniclastic turbidites around the islands using a range of information (e.g., sedimentary structures, volcanic glass composition and morphometric parameters, bulk mineralogy and organic geochemistry) to resolve volcaniclastic bed type ambiguities. Volcanic glass composition and their morphometric parameters and existence of shelf-origin biogenic material are found to be the most critical clues. The results suggest that volcaniclastic turbidites originate mainly from pyroclastic flows and only one third from submarine landslides.

Chapter 5 is a scientific manuscript entitled “Asymmetric abundances of submarine sediment waves around the Azores volcanic islands”. Sediment waves are shown to be more abundant on the northern submarine flanks of the islands than on their southern flanks. This observation favours explanations for their formation involving sedimentary gravity flows. Arguments involving greater coastal erosion and shelf sediment mobilisation suggest that flows should be more common from the northwest arising from the prevailing direction of wind and waves. A

field of giant sediment waves on the northern flank of São Miguel Island, in contrast, is suggested to have been the result of pyroclastic flows from one or more giant eruptions.

Chapter 6 is a scientific manuscript entitled “Emplacement history of volcaniclastic turbidites around the central Azores volcanic islands: frequencies of slope landslides and eruptions”. In this manuscript, four age-depth models were created based on tephra bed correlation and ¹⁴C dates of foraminifera from hemipelagic intervals. This work has revealed hemipelagic sediment fluxes and frequencies of eruptions and landslides and their changes over time, hence allowing an independent assessment of the sedimentary history of the Azores islands. Turbidite volume modelling suggests that the deposits preserved in the cores originate from only the largest landslides, whereas smaller landslides generate flows that deposit on the slopes.

Chapter 7 is a synthesis and broader discussion. This chapter discusses the insights into the research project in general and recommends future work.

Chapter 8 is concluding remarks. This chapter briefs the principal results of each scientific manuscript and the progress overall towards Aim 1.

Chapter 2. Geological background and general review of processes and hazards around insular volcanic islands

2.1 Geological background

The Azores archipelago consists of nine volcanic islands lying close to the slow-spreading Mid-Atlantic Ridge (Fig. 1.1). They can be divided into the western group (Flores and Corvo), the central group (Faial, Pico, São Jorge, Terceira and Graciosa) and the eastern group (São Miguel and Santa Maria). They rise above a broad oceanic plateau of thick crust, developed at a hyper-slow oblique spreading hotspot-dominated plate boundary or formed by intense volcanism or mantle melting from other sources (White et al., 1976; Bonatti, 1990; Gente et al., 2003; Vogt and Jung, 2004). Nine Azores islands are generally aligned NW–SE and their volcanic alignments and tectonic structures on the islands mainly align in two directions (i.e., N150°E and N110°E–N120°E; Fig. 2.1), likely resulting from a regional dextral transtensional deformation (Lourenço et al., 1998; Miranda et al., 2015).

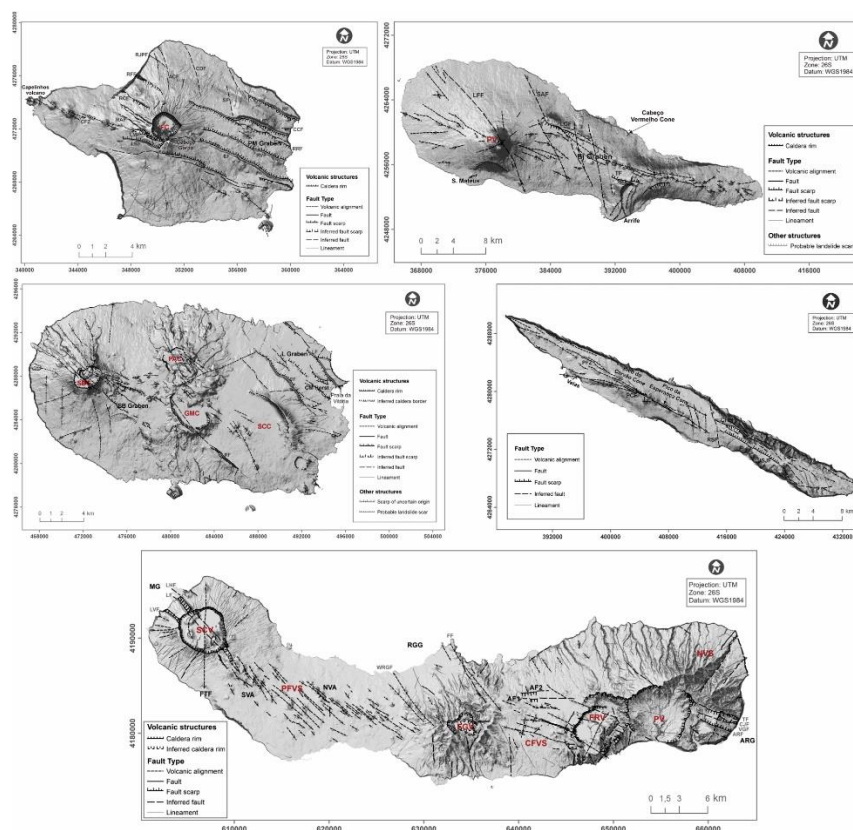


Figure 2.1. Neotectonic maps of the five studied Azores islands derived from Maderia et al. (2015).

Many of the Azores Islands are geologically young, with tectonic and volcanic activities during at least the late Quaternary (Féraud et al., 1980) and continuing toward the present (Gaspar et al., 2015). For instance, cinder cones on São Jorge and Pico islands and basaltic Holocene lava flows on the fissure zones of Terceira island have been sheared or displaced by active faults (Madeira and Brum da Silveira, 2003; Madeira et al., 2015), evidence of pre-historic seismic activity. The recent $^{40}\text{Ar}/^{39}\text{Ar}$ and K/Ar dating results suggests that the oldest edifice on Terceira is younger than 0.4 Ma and the most recent-formed edifice is ~ 50 ka (Calvert et al., 2006; Hildenbrand et al., 2014). São Jorge Island can be subdivided into old and young volcanic complexes according to the results of $^{40}\text{Ar}/^{39}\text{Ar}$ and K/Ar dating (Hildenbrand et al., 2008; Pinto Ribeiro et al., 2010; Marques et al., 2018). The oldest subdivision in the southeast is of age 1.2–1.85 Ma, and the intermediate to young volcanic subdivisions in the northwest is younger than 0.75 Ma. Two historical eruptions occurred in the northwest of São Jorge in 1580 and 1808 (Madeira, 1998). The oldest part of Faial Island is of age ~ 850 ka (Hildenbrand et al., 2012), but most parts of the island are widely blanketed by a younger volcanic complex of 10–440 ka age (Pacheco, 2001; Pimentel et al., 2015). The Capelo fissure system in the west is younger than 10 ka and its youngest unit (i.e., Volcano Capelinhos) arose from the sea during the historical basaltic eruption of 1957/58 (Machado et al., 1962). K/Ar dates suggest that Pico Island has developed since 0.19 Ma (Costa et al., 2015) and has had three historical eruptions since 1562. Although radio-isotopic dating has been extensively carried out on samples from São Miguel Island, the geological history of the Azores island remains poorly constrained as some obtained ages of the same volcanic unit vary by a factor of 4. Despite lacking an unambiguous evolutionary history, recent works generally agree that São Miguel Island was built since at least 1 Ma with a westward developing trend (Féraud et al., 1980; Gandino et al., 1985; Johnson et al., 1998).

Eruptions in the Azores are usually moderate (e.g., effusive Hawaiian eruption), but more explosive eruptive styles can also occur, with mildly explosive Strombolian, phreatomagmatic to Plinian eruptions (Machado, 1959; Cole et al., 2001; Calvert et al., 2006; Pimentel, 2007;

Larrea et al., 2014; Sibrant et al., 2014). Mild basaltic eruptions were usually related to fissure volcanic systems, generating lava flows with directions following the regional NW–SE tectonic trend. The explosive ignimbrite-forming eruptions instead were associated with caldera development that is capable of generating dispersed pyroclastic fallout and pyroclastic density current deposits (e.g., Pimentel et al., 2015; 2021). Such ignimbrite sequences have been frequently identified on Terceira, Faial and São Miguel Islands.

2.2 Geological processes affecting volcanic ocean islands

There are relatively few detailed studies of insular volcanic islands or of the Azores islands in particular. Therefore, in this section, knowledge and examples from other islands and continental shelves or slopes with comparable geomorphology are drawn upon to suggest the types of processes and structures that may occur in the Azores.

2.2.1 Volcanism

Volcanism is the foremost factor of insular volcanic island growth and is also an important sediment source. Although volcanism is often associated with rising juvenile magma from the mantle or lower crust, other near-surface activities can also induce volcanism due to surface mass unloading resulting from multistage retrogressive landslides (Hunt et al., 2018) and hydrothermal depressurisation (Reid, 2004). Depending on magma viscosity and gas content, eruptive styles can be divided into effusive and explosive eruptions. Effusive volcanism generally generates large tracts of low viscosity lava flows (Peterson, 1976), expanding the shorelines of insular islands. Opening of linear fissure vents, lava flows and domes extruding onto the surface are usually associated with effusive or mildly explosive eruptions (e.g., Pedrazzi et al., 2015). Explosive eruptions instead involve a sudden exsolution and expansion of gas during depressurisation of viscous magma, resulting in gas and tephra particles (a collective term used to describe all ejected volcanic particle irrespective of size, shape and composition of erupted clasts (e.g., Fisher, 1961; White and Houghton, 2006)) ejected out of the volcano. Explosive eruptions are subdivided into different types from mildly-moderately explosive styles (e.g., Strombolian, phreatomagmatic and Vulcanian) to fiercely explosive

styles (e.g., Peléan and Plinian eruptions). Significant explosive volcanism can greatly reshape island landscapes by destructing or constructing calderas (e.g., Gertisser et al., 2010) or by inducing volcanic island flank collapse and landslides. Such explosive activities are usually responsible for life and property loss. Illustrating their potential, explosive eruptions in volcanic arcs can be even more significant and inject voluminous sulfate aerosols into the stratosphere, eventually causing a decrease in global surface temperatures for the following several years (e.g., Rampino and Self, 1982).

2.2.2 Tectonics

Tectonic structures can be formed associated with magma intrusion (e.g., dyke swarms; Walker, 1960), regional plate deformation (e.g., fault scarps; Carmo et al., 2015) and deep-seated slumping (Moore et al., 1989). Tectonic activities, when they occur, are typically accompanied by earthquakes. Besides creating new tectonic structures, vertical movements (either uplift or subsidence) can affect sedimentary processes (subaerial erosion and biogenic production; Quartau et al., 2014) and trigger mass wasting (e.g., destabilizing volcanic flanks and the unconsolidated deposits on them; Masson et al., 2006). For instance, modelling the 1975 Kalapana, Hawaii, earthquake ($M_s = 7.1$) revealed that it was caused by large-scale slumping occurring in the south flank of Kilauea Island (Eissler and Kanamori, 1987).

2.2.3 Mass wasting

Mass movement (either small, gradual, or catastrophic) is one of the most effective mechanisms for transporting coarse sediments to the sea (Trenhaile, 2011). Triggering of mass wasting can be either directly, indirectly or non-directly associated with volcanic activities. For instance, an explosive eruption can directly deconstruct volcanic edifices (e.g., Gertisser et al., 2010; Paris et al., 2017). Volcanic flank slope failures can be indirectly associated with volcanic activities because of volcano-tectonic earthquakes (Carracedo, 1994) and excess deposition of magmatic material (lava flow and unconsolidated pyroclastic material; Di Traglia et al., 2018), which can overload the submarine slopes or lead to slope over-steepening. Other non-volcanic processes involve cyclic loading originating from earthquakes (Keefer, 1994) and storm-waves (Zhang et

al., 2016), and reduced slope strength due to excess sedimentation, erosion and gas pressure (Hampton et al., 1996 and references therein).

When they occur, gravitational mass wasting events typically create steep head scars on the upper slopes and displace deposits on the seafloor (Moore et al., 1989). Catastrophic lateral flank collapses can remove voluminous sediments into the sea in short period (Mitchell et al., 2003), potentially generating tsunamis and resetting the balanced erosional or depositional status. Small submarine slope valleys in continental slopes have been suggested to be associated with repeated small failures and erosion by sediment gravity flows resulting from disaggregation of the failed material (Pratson and Coakley, 1996). As similar processes also commonly occur on volcanic islands (Masson et al., 2006), slope valleys in volcanic island submarine slopes potentially also develop by those mechanisms.

2.2.4 Biogenic production

Although coral growth is typically restricted to regions in tropical water (Stoddart and Steers, 1977; Chappell, 1980; Spalding and Grenfell, 1997; Dullo, 2005), corals also grow in cool-water temperate and cold-polar environments (James and Clarke, 1997; Pedley and Carannante, 2006). Present-day 'temperate' environments are dominated by heterozoan benthonic assemblages (benthic foraminifera, echinoids, molluscs and bryozoans; James et al., 2011). Coralline algae are the most important phototrophs contributing directly to the sediments. Although the relationship between nutrients and carbonate in marine environments is complex (Lukasik and James, 2003; Mutti and Hallock, 2003), the principal factors affecting growth are seawater temperature, nutrient availability and light. For those volcanic ocean islands in temperate environments, nutrient availability is a more sensitive factor to the growth of plankton foraminifera and heterotrophic metazoans than seawater temperature and light (Mutti and Halleck, 2003). The absence of reef barriers and baffles has major effects on sea cliff development and stability as there is little to prevent direct wave and storm energy reaching the shoreline.

2.2.5 Erosion

Subaerial and submarine erosion are both important processes modifying volcanic islands.

Riverine erosion

Streams are important sources of sediment to coasts at some high volcanic ocean islands, such as the Hawaiian Islands (Stidd and Leopold, 1951) and Reunion Island (Barbary et al., 2019), where orographic rain occurs and the climate is humid. The windward sides of those volcanic edifices receive higher precipitation, enhancing subaerial erosion and the release of terrestrial sedimentary particles. If this applies locally in the Azores, hyperpycnal flows initiated during ephemeral periods of heavy rains and flash flooding (e.g., Babonneau et al., 2013; Quartau et al., 2018) could discharge large volumes of terrestrial sediments into the sea. However, riverine erosion and hyperpycnal river outflows are thought to be less important in the Azores islands, as their rivers are small, storm flows are ephemeral and there is little orographic effect on rainfall due to their low relief (Forjaz et al., 2004; Cruz et al., 2010; Instituto Nacional De Meteorologia, 2012).

Coastal erosion

Wave energy, tides, currents, and wind-driven processes can play important roles in controlling the intensity of marine and coastal erosion (Trenhaile, 2000; 2001). In many volcanic ocean islands where sea cliffs have high reliefs (Quartau et al., 2012; Huppert et al., 2020), wave forcing is probably the main process modifying coastline morphology (Borges, 2003; Quartau et al., 2010), although weathering and large landslides may also contribute. The energy of waves reaching coastal areas varies in space and time as it originates from both near and far-field winds, which vary with climate, and waves are refracted and attenuated by shallow bathymetry. During sea-level fall, sea cliffs can become moribund and isolated from waves. In contrast, increased wave exposure of sea cliffs during the sea-level highstands results in enhanced sea-cliff erosion due to repeated wave impacts (Sunamura, 1977). High-energy storms and tsunamis can extensively modify coastal geomorphology in merely minutes or hours (Noormets et al., 2002; Paris et al., 2009).

Submarine erosion

Submarine erosion can result from sediment gravity flows originating from the disintegration of materials in submarine mass movements (Nisbet and Piper, 1998), agitation of shelf sediment

by waves effects (Porcile et al., 2020) and wind-driven circulation (Normandeau et al., 2020). Other oceanic processes such as internal tidal wave currents resulting from interactions of barotropic tides with seafloor topography (Belde et al., 2015; Ribó et al., 2016) and geostrophic bottom currents originating from the force balance between the pressure gradient and the Coriolis effect (Thran et al., 2018) have been suggested to be capable of modifying deep-marine bathymetry around some volcanic islands (e.g., Canary Islands; Palomino et al., 2016) and in the pelagic caps of guyots (Mitchell et al., 2015). Although these oceanographic processes are not as intense as storms or tsunamis, their sustained effects have been suggested to continue remobilizing finer-grained unconsolidated sediments on continental slopes (e.g., Fuhrmann et al., 2022), which may eventually readjust the slope balance and then induce gravity-driven mass movements.

2.2.6 Eustatic sea-level change

Changes in relative sea-level, which likely follow eustatic sea-level in the Azores Islands as they lie far from changing glacial and hydrostatic loads, have a number of influences on the evolution of volcanic ocean islands. In volcanic islands such as the Azores, higher biogenic production and sea-cliff erosion are expected during sea-level highstands because of broader shelves submerged under shallow water and the increased wave exposure of tall sea cliffs (Quartau et al., 2012).

Increased volcanic eruption frequency of Santorini Volcano has been correlated with periods of falling sea-level, suggested to be due to reduced overburden pressure in the rocks above the magma chamber (Satow et al., 2021). However, other researchers either have not found such an association (Walker et al., 2021) or cannot explain this trend by a single external modulation (Neuberg, 2000). Increased sediment fluxes originating from processes driven by sea-level adjustments may also affect the stability of the submarine slopes, such as by over-steepening and rapid deposition (weak consolidation), ultimately leading to submarine slope failures (e.g., Sansone and Smith, 2006).

2.3 Hazards at/around volcanic islands

Various types of natural hazards can occur at/around volcanic islands. They are either directly, indirectly, or unrelated to volcanic activities. However, a complex scenario of multiple types of hazards overlapping with each other is also likely (e.g., Selva et al., 2019).

2.3.1 Hazards related to eruptive activities

Volcanoes can directly pose multiple types of hazards and severely affect the surrounding area. In this section, only the hazards relevant to this project are introduced.

Lava flows

Lava flows are one of the common volcanic eruption products, and their high temperatures can cause fires in vegetation and buildings along their transport paths. Iron/magnesium-rich basalt lavas have low viscosities and can widely spread in broad and thin sheets. On the other hand, silicon-rich andesite, dacite, and rhyolite lava flows are much less fluid and tend to form steep-sided lava domes restricted to more limited areas. Early works on the Hawaiian (Moore and

Chadwick, 1995) and Canary Islands (Schmincke et al., 1995) suggested that the submerged parts of volcanic ocean islands probably consist of pillow lava (Fornari et al., 1979) volcanoclastic debris of lava fragmentation (Moore and Chadwick, 1995) and explosive eruptions (Schmincke et al., 1995). High-resolution bathymetric data have further revealed varied submarine lava flow structures in the Azores islands (Mitchell et al., 2008), a result of lava flow penetration into the sea. Lava flow emplacements may overload slopes, leading to instability and eventually failures and tsunamis (e.g., Di Traglia et al., 2018).

Pyroclastic density currents (PDCs)

The terms "pyroclastic density current" are used here to refer to both dilute and dense gravity currents of predominantly volcanoclastic particles. PDCs are mixtures of fragmented magma, rock debris and hot gas that flow along the ground and discharge into the sea at high speed (i.e., several hundred m/sec). PDCs deposits are derived from volcanic eruptions of different scales, from small-volume events (e.g., directed blasts and small dome collapses) to caldera-forming eruptions (e.g., Calder et al., 1999). The generated fast-moving pyroclastic flows can cause damage along their transport paths and may also induce other associated hazards (e.g., tsunamis or slope instability) while entering the sea. For instance, the largest dome collapse of Montserrat (0.2 km^3) produced a tsunami that locally ran up to 15 m (Herd et al., 2005). Most ejected coarse volcanic clasts (Lapilli and volcanic bombs) tend to fall or translate on the ground close to volcanoes at distances of tens of kilometres (e.g., Baker, 1969). Trofimovs et al. (2008) comprehensively documented the processes and composition of submarine pyroclastic deposits from the July 2003 Montserrat dome collapse. While pyroclastic flows penetrated into the sea, phreatic explosions (steam-driven explosions occurring when magma overheats the ground or surface water) were observed at the air-ocean interface, creating surge clouds decoupled from the main flow body and travelling several kilometres over the ocean surface before settling. The bulk of the pyroclastic flow was submerged and rapidly mixed with sea water forming a water-saturated mass density current. About 60% of total eruption volume, mostly coarse components, were deposited at proximal distances. The remaining 40% of erupted volume, mostly finer components, evolved into a far-reaching turbidity current.

Pyroclastic tephra fallout

Tephra fallout deposits comprise volcanoclastic particles that have gravitationally settled through air or water. They are usually generated during phreatic activity (steam-driven interaction), dome-collapse, magmatic explosion and ash-venting. Although most of the larger-size tephra particles (>2mm) fall onto slopes close to source vents, smaller and lighter tephra ash (<2mm) can be transported by winds to distances of hundreds to thousands of kilometres from their source vents. Tephra fallout ash tends to consist of fine and angular volcanic fragments and debris. In a multi-hazard scenario, tephra fallout is often accompanied by partial collapses of the eruptive column (and consequent pyroclastic flows) or base surges and atmospheric phenomena (Selva et al., 2019). Local weather conditions can become violent (i.e., heavy raindrops, downbursts and frequent lightning) during the growth of phreatomagmatic eruptive columns, where high water contents in the columns interact with hot magma. Raindrop nucleation is stimulated by volcanic ash particles and magmatic water injected into the atmosphere. Where such rains fall, they can interact with unconsolidated volcanoclasts and may ultimately trigger lahars. The far-reaching fine tephra particles, even in low concentrations, potentially still can disrupt human activity, damage electronics and machinery, interrupt power and transportation systems, and pollute water sources (e.g., Wilson et al., 2012). Aircraft can be endangered by drifting clouds of finer fallout ash even thousands of miles away from their source vents.

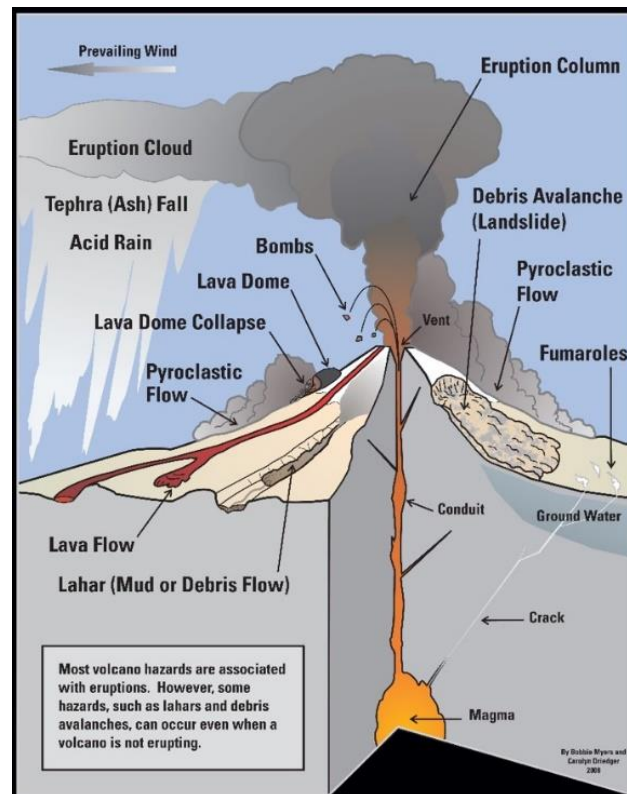


Figure 2.2. Natural hazards that are associated with volcanic activities (USGS: <https://www.usgs.gov/media/images/geologic-hazards-volcanoes-click-larger-version>).

2.3.2 Earthquakes

Two types of earthquakes can occur beneath volcanic islands: volcanic earthquakes caused by the pressure changes of magma or fluids underground (Chouet, 1996) and tectonic earthquakes induced by slip movement of structures (e.g., seismic faults; Yamashina and Nakamura, 1978). Volcanic earthquakes can have long-periods, which helps to identify magma chambers, but are often too small to be detected without broadband seismometers. A tectonic earthquake, in contrast, can cause large vertical ground movement and cracks, leading to volcanic eruptions (Hill et al., 2002), catastrophic caldera collapses (Hürlimann et al., 2000) or submarine landslides (Fine et al., 2005). Besides the direct impacts of earthquakes on the landscape, large earthquakes have also been found to be tsunamigenic due to sudden vertical ocean surface displacement (e.g., Hemphill-Haley, 1995) or voluminous mass failures from the slopes towards the seafloor (e.g., Ward and Day, 2003).

2.3.3 Submarine landslides

"Landslide" is used here as a general term referring to any type of slope failure and resulting mass movement regardless of the initiation location (onshore or offshore). Unstable submarine slopes are subject to landslides, ranging from creep (i.e., downward slow slope movement with low strain rates) to debris flows (i.e., rapid mass movement with high strain rates). Landslides can be triggered by many potential processes (Fig. 2.4) and can ultimately evolve into turbidite currents underwater. Typical causes of submarine landslides proposed in different volcanic settings include explosive volcanic eruptions (e.g., Hunt et al., 2021), cyclic stresses originating from earthquakes (e.g., Hughes Clarke et al., 1990; Watt et al., 2014) and storm-waves (e.g., Dengler et al., 1984; Zhang et al., 2016), and over-steepening of slopes due to stacked lava deltas (e.g., Di Traglia et al., 2018), faults (Nunes, 1999) and lateral magma intrusions (Bonaccorso et al., 2003), and complex interactions between a range of processes (Clare et al., 2018). Submarine landslides can displace infrastructure both on land and undersea. Turbulent sediment gravity flows evolving from downward-moving mass disintegration can also cut off telecommunication cables deployed on the seafloor (e.g., Hsu et al., 2008). Tsunamis can be generated from collapses of volcanic flanks (Barrett et al., 2019) or failures of submarine slopes (e.g., Tinti et al., 2005).

In recent decades, offshore exploration has increased the accessibility of high-resolution bathymetric and seismic data and dense collections of sediment cores, allowing the evolution of submarine landslides or flank collapses to be revealed (i.e., single or multi-stage failures; Hunt et al., 2013, 2014, 2018). The identification of multi-stage failures has a broader implication for tsunami assessment as this type of failure serves to divide the total landslide volume into several smaller events. The smaller failures would produce significantly smaller tsunamis as the volume of a landslide is one of the critical factors affecting tsunami magnitude (Murty, 2003).

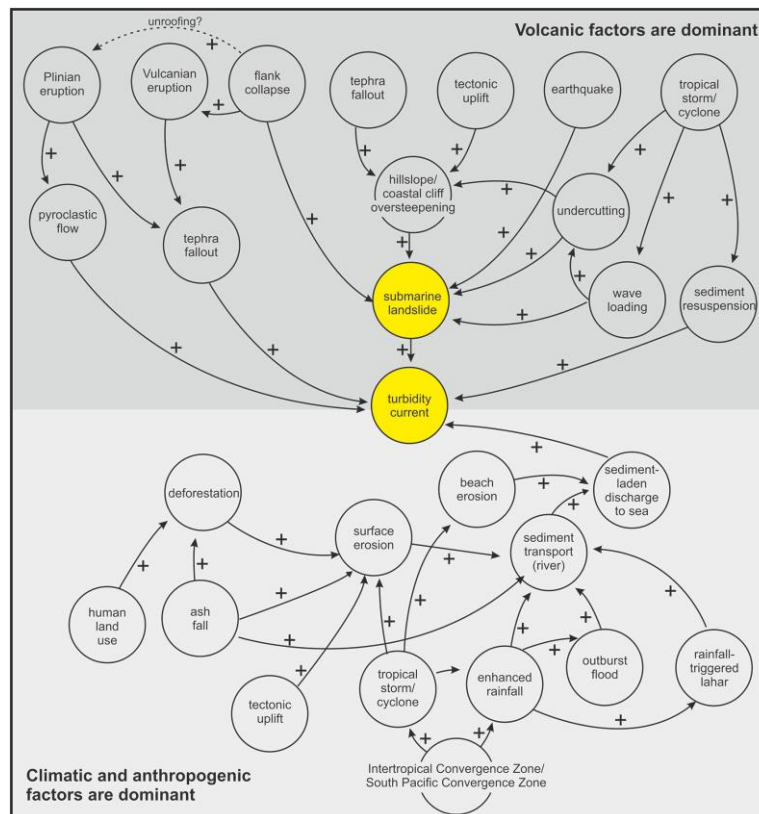


Figure 2.3. Complexity of interacting processes at volcanic islands that may precondition and trigger submarine landslides and turbidity currents (Clare et al., 2018). Plus symbols and arrows indicate how an increase in a variable may make a subsequent process more likely. Dark gray and light gray areas show scenarios where volcanic factors and climatic or anthropogenic factors may dominate.

2.3.4 Tsunamis

A tsunami is a series of propagating waves caused by a large volume of water displacement. Tsunami waves tend to be difficult to detect in deep water due to their small wave heights (<1 m), long wavelengths (100–200 m) and high speeds (>800 km/hr). Once tsunami waves approach shallow water near the coast, the wave shoaling effect increases wave heights because of wave compression due to a decreased wave speed with shallowing water depth. From a global analysis, tsunamis are mostly generated by earthquakes (i.e., ~80%; Reid and Mooney, 2022), but submarine landslides (e.g., Masson et al., 2006; Hunt et al., 2017) and volcanic eruptions (Egorov, 2007) are also important mechanisms, particularly for regions far from the subduction boundaries (i.e., 30–40%, Reid and Mooney, 2022).

Assessing tsunami hazards (e.g., wave amplitude and run-up height) is essential for coastal managements in volcanic island settings. Seismogenic tsunamis typically occur at subduction zones, where frequent inter-plate thrust motions can cause significant vertical seafloor deformations. Assessment for this type of tsunamis requires parameters of the dimensions (slip length and area), dynamic (shear stresses) of the rupture plane and physical properties of surrounding rock (shear modulus and friction coefficients). Landsliding, instead, is a more important tsunamigenic mechanism in the area where large earthquakes ($M > 6$) are less frequent. A first-order landslide-induced tsunami wave amplitude assessment can be done using morphometric parameters of landslides scars, slope gradient and water depth (e.g., Mcadoo and Watts, 2004; Casalbore et al., 2011). A more sophisticated numerical modelling for predicting tsunami generation, propagation and run-up at the coast requires additional in-situ geotechnical data (e.g., landslide density, coefficients of the basal Coulomb friction, skin friction and drag; Fornaciai et al., 2019). Giant tsunamigenic landslides have been extensively studied in the last several decades due to the induced devastating hazards (Lipman et al., 1988; Moore et al., 1994; Masson et al., 2010; Hunt et al., 2013). However, increasing attention is also placed on the smaller tsunamigenic submarine landslides (Fig. 2.5; Casalbore et al., 2011; 2018) because of the more limited response time for tsunami arrival (i.e., tens of minutes) and a far shorter recurrence period (i.e., 100 times more frequent than the giant ones).

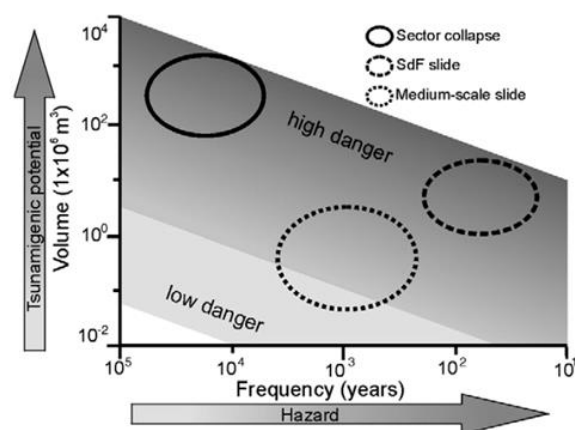


Figure 2.4. Volume-frequency plot illustrating the submarine landslide scales and recurrence periods (Casalbore et al., 2011). The term “danger” used here refers to a combined index generated by considering the frequency and mobilised volume of submarine landslides.

2.3.5 Hazards within the Azores Islands

Located close to plate boundaries and with evidence from widespread fault offsets of Holocene lava flows on land (Madeira and Brum da Silveira, 2003), the Azores islands are seismically active with a recurrence interval of 70 years for large earthquakes ($M > 6.5$) on average (Nunes and Ribeiro, 2001; Nunes et al., 2001). Historical records and recent seismic activity show that most destructive earthquakes occur in the early stage of earthquake sequences that can last for weeks or even months (e.g., events in 1980 and 1998). The effects of large events in the Azores can be exacerbated by the poor preparedness of legacy buildings (Maio et al., 2017). For instance, the strongest Azorean earthquake ($M > 7.4$) on 9th July 1757 occurred close to the north coast of São Jorge (Machado, 1949), causing over 1000 casualties. The first report of a volcanic eruption can be traced back to the settlement of São Miguel Island and relates to a sub-Plinian phreatomagmatic eruption in the caldera. The most recent event in 1998-2001 was a submarine eruption on the Serreta Ridge (Gaspar et al., 2003). Since island settlement, at least 21 major earthquake crises and 27 volcanic eruptions have occurred around the central Azores and São Miguel islands, including events both offshore and onshore (Fig. 1.1.b and 1.1.c). The islands also regularly suffer from coastal flooding during extreme storms, which can cause maximum wave heights of >20 m (e.g., Borges et al., 2011) and occur with a recurrence interval of about seven years (Andrade et al., 2008). Tsunamis are less historically important than earthquake crises. Their appearance sometimes cannot be fully explained by the occurrence of earthquakes, suggesting other mechanisms forming them such as submarine landslides. The various types of natural hazards and their frequency highlight the need for a better understanding of the processes and hazards around the Azores volcanic islands.

Chapter 3. Landslides in the upper submarine slopes of volcanic islands: the central Azores

This chapter is a reproduction of a manuscript published in the Journal of Geochemistry, Geophysics, Geosystems. Chang, Y.-C., Mitchell, N., Quartau, R. 2021. Landslides in the upper submarine slopes of volcanic islands: the central Azores. <https://doi.org/10.1029/2021GC009833>

Y-C.C produced the original draft of the manuscript and figures. All co-authors contributed their opinions and comments to the draft manuscript. The journal reviewers also effectively made contributions by commenting on the article.

In this chapter, I digitised and classified the submarine landslide valleys from the high-resolution bathymetric data. Landslide sizes (area and volumes) and the morphometric parameters (e.g., slope angle, landslide length, width and thickness) were measured. Those measurements were used for landslide size-frequency analysis, including submarine landslide inventory, volume-frequency distribution, sediment cohesion estimates and assessment of tsunami wave heights at source. Earthquake event data were acquired from the International Seismological Centre (ISC) for years from 1964 to 2019 and used to calculate a peak horizontal acceleration map.

High-resolution bathymetric data were collected, processed and provided by co-authors R.Q and N.M (Mitchell et al., 2008; Quartau et al., 2014).

Abstract

Small landslides in the upper submarine slopes of volcanic islands present potential hazards locally because of their high frequency. We examine evidence for landsliding in high-resolution bathymetric data from Faial, Pico, São Jorge and Terceira islands of the Azores. Because the rugged morphology of the upper slopes makes landslides difficult to interpret, we develop two classification schemes for the 1227 identified slope valleys. One scheme addresses how recognizable the valleys were as originating from landslides (whether scarps are prominent or indefinite), whereas the other scheme addresses valley types (whether apparently produced by single or multiple failures). Size distributions are used to assess the relative occurrence of large versus small landslides. Thirteen landslides are predicted to have generated tsunami heights at source of >1 m and one with height of >7 m. Some slopes have gradients far above 30°, the angle of repose of incohesive clastic sediment, so the seabed in those areas is strengthened perhaps by carbonate cementation, by seismic shaking or by the presence of coherent lava or lava talus. Using all types of slope valleys, Faial and Pico have smaller affected volumes per unit slope area than those of São Jorge and Terceira. These differences could be associated with varied seismic activity, with more frequent earthquakes beneath Faial and Pico preventing the build-up of sediments on their slopes. Submarine landslide statistics are therefore potentially useful for assessing long-term earthquake hazards of volcanic islands in seismically active environments such as the Azores.

Key words: submarine landslides, seismic hazards, size-frequency distribution, landslide-induced tsunami, slope stability

3.1 Introduction

Giant landslides have been found around many volcanic ocean islands (those located away from convergent margins), including the Canary archipelago (Masson et al., 2002, 2006; Mitchell et al., 2002; Wynn and Masson, 2003), the Hawaiian Islands (Lipman et al., 1988; Moore et al., 1989, 1994; McMurtry et al., 2004), Cape Verdes (Masson et al., 2008; Ramalho et al., 2015; Barrett et al., 2019), Madeira archipelago (Quartau et al., 2018; Santos et al., 2019), Reunion Island (Labazuy, 1996; Ollier et al., 1998), and islands near mid-ocean ridges (Mitchell, 2003). Smaller submarine landslides have been found in the steep upper flanks of volcanic islands and they have generated tsunamis (Tinti et al., 2005; Rahiman and Pettinga, 2006; Chiocci et al., 2008; Tommasi et al., 2008; Kelfoun et al., 2010; Casalbore et al., 2011; Casas et al., 2016; Alberico et al., 2018; Casalbore et al., 2018; Fornaciai et al., 2019), but their threats are less well known. These smaller landslides are more frequent (Casalbore et al., 2011; Chiocci and Casalbore, 2017) compared with the giant landslides, which recur globally every ~10 ky around volcanic islands and locally every >100 ky in the Canary (Krastel et al., 2001) and Hawaiian Islands (Garcia et al., 2006). Although tsunamis they generate are smaller, those tsunamis may nevertheless be significant geohazards because of their greater frequency. According to historical reports analysed by Andrade et al. (2006), at least 23 tsunamis have affected the Azores since the human settlement of the islands and one with wave height > 10 m. Some of them were not explained by earthquakes so they may have originated from submarine landslides. One motivation for this research was therefore to investigate the sizes and geometries of upper-slope submarine landslides among the islands, in order to assess whether the landslides were large enough to generate tsunamis.

Earthquakes also pose significant geohazards on volcanic ocean islands and can include events of magnitude $M > 7.0$ (Furumoto and Kovach, 1979; Crossen and Endo, 1982; Madeira et al., 2015). Unfortunately, the instrumental record is not sufficient to characterise seismic hazards of small areas (Scholz, 2002). As the central and eastern Azores islands lie in a region of distributed deformation of the Eurasia–Nubia plate boundary (Lourenço et al., 1998; Fig. 3.1),

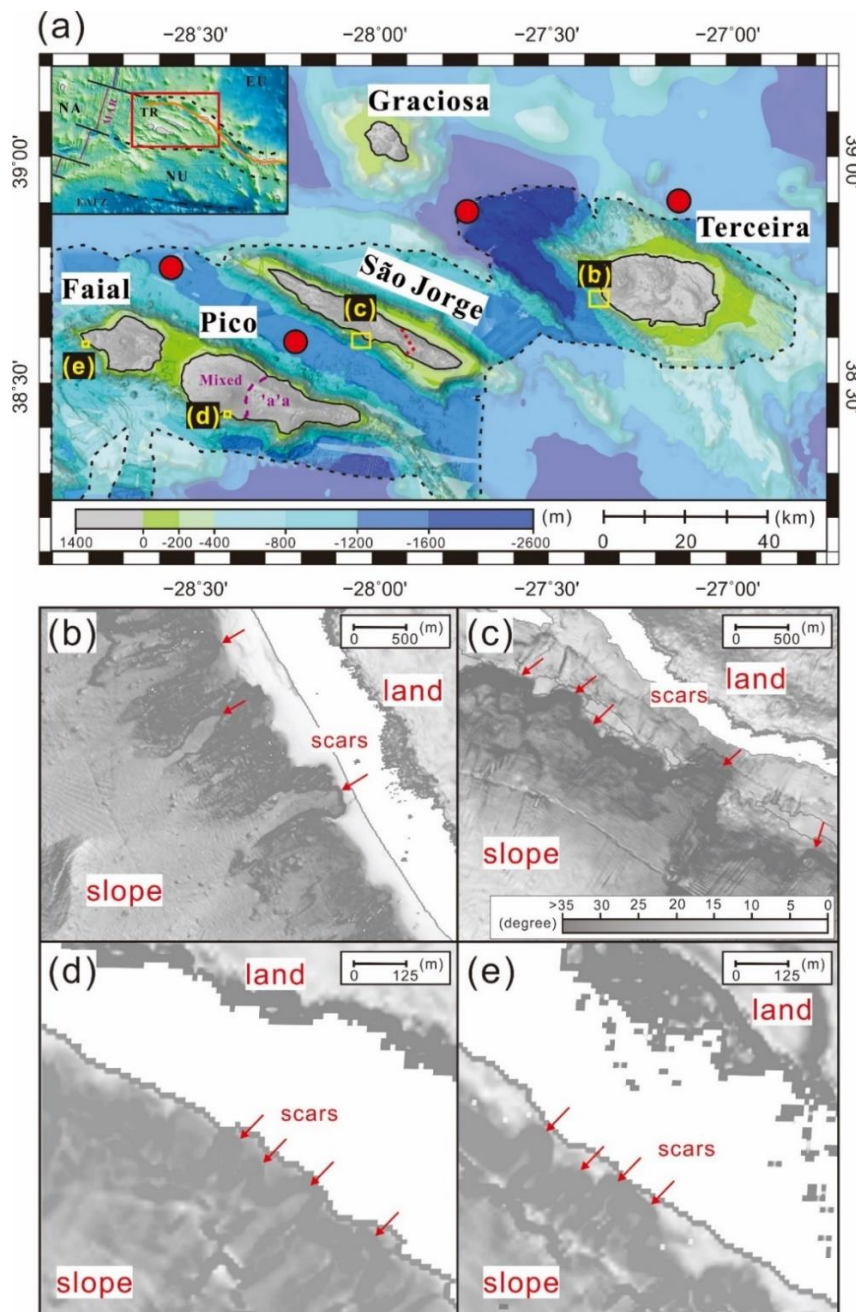


Figure 3.1. (a) Distribution of high-resolution bathymetry data in the central Azores available to this study (outlined by black-dashed lines). Red dashed line on São Jorge island is the boundary separating the old volcanic complex in the southeast from the young volcanic complex in the northwest. Purple dashed line on Pico island is the boundary separating 'a'a lava flow dominated zone of Pico mountain from the zone of mixed lava types in the east of the island. Background bathymetric data are from Ryan et al. (2009). Island elevations above sea-level are shown in gray with black outlines. Red circles locate the sediment cores analysed by Chang et al. (2021). Inset shows the regional tectonic setting of the area in the diffuse boundary between the Eurasia (EU) and Nubia (NU) plates (NA: North American plate). Purple lines locate the Mid-Atlantic Ridge (MAR), solid black lines locate its associated fracture zones, and dashed-dot-dashed line locates the East Azores Fracture Zone (EAFZ). Dashed black lines are

the limits of the diffuse Nu–Eu plate boundary and the orange solid line represents the centre of Terceira Rift (TR). (b), (c), (d), (e) Selected maps of maximum local gradient revealing landslide scars in the steep upper island submarine slopes. Map extents are shown by yellow rectangles in (a). The gradients in these four panels share the scale in (c). Red arrows locate interpreted landslide scars.

they are seismically active. The question of adequacy of the instrumental record is, therefore, important locally. In particular, onshore mapping and sonar data has revealed potentially active faults of 10–20 km in length (Lourenço et al., 1998; Madeira et al., 2015; Mitchell et al., 2012; Casalbore et al., 2015), whereas the north slope of São Jorge, which appears fault controlled (Walker, 1999), is 60 km long and the walls of the Terceira Rift (Fig. 3.1a) reach 100 km in length. Madeira et al. (2015) estimated that earthquakes up to $M=6.8$ could occur based on the lengths of active faults mapped on the islands, but this is likely an underestimate as the submarine faults are longer. From data compiled by Scholz (1994), a strike-slip rupture of 110 km length (the approximate maximum of the faults outlined later) could produce an earthquake with seismic moment $\sim 5 \times 10^{20}$ N·m, (i.e., moment magnitude $M_w \sim 7.4$). Such an earthquake would be similar in size to events that have occurred in the Azores historically (e.g., $M_w \sim 7.2$; Gaspar et al., 2015). If such a large event were to occur in the Azores, its effects would be exacerbated by the poor preparedness of legacy buildings (Maio et al., 2017). Unfortunately, assessing the frequency of large earthquakes is difficult because palaeoseismological methods are not easily applied to volcanic sequences and many of the faults lie underwater. Alternative assessment methods are therefore needed.

High-resolution bathymetric data have revealed evidence of widespread submarine mass wasting along the upper submarine slopes of islands in the Azores (Mitchell et al., 2008, 2012; Quartau et al., 2012, 2014, 2015; Ricchi et al., 2020). Unfortunately, those data such as shown in Figs 3.1b to 3.1e present a difficulty of interpretation. Whereas landslides in continental slopes often occur over decollements parallel to the seabed and create landslide scars that are clearly defined (e.g., ten Brink et al., 2006), this is not the case in the Azores data, which instead

show a rugged morphology likely due to past volcanic history, transfer of slope sediments and multiple small-scale landsliding. We address this problem by adopting the general term “slope valley” for topographic depressions without connotations of origin. Within a database of such identified features, we classify them first according to the degree to which they adhere to the classical features of landslides (Varnes, 1978). A second classification is then used to separate them according to whether they appear to form single landslide scars, amphitheatres created by multiple landslide events (e.g., Pratson and Coakley, 1996) or potential retrogressive failures. We then interrogate this database using the different classes depending on the objective being addressed. The results indicate a significant variation in submarine slope landsliding and hence hazard among the islands.

3.2 Geological setting

It is useful to know aspects of Azorean geology in order to assess how frequently volcanic materials are fed to the coasts during eruptions and earthquakes, both of which may affect landslide frequency and geomorphology. The central Azores islands of Faial, Pico, São Jorge, Graciosa, and Terceira lie east of the Mid-Atlantic Ridge (Fig. 3.1). Rift zones, faults on land and submarine ridges commonly lie perpendicular or oblique to Nubia–Eurasia plate motion suggesting that they were produced by trans-tensional deformation, continuing through the Quaternary to the present-day (Lourenço et al., 1998; Madeira and Brum da Silveira, 2003). Recent $^{40}\text{Ar}/^{39}\text{Ar}$ and K/Ar dating results suggest that Terceira is generally young, with the earliest-formed edifice in the east younger than 0.4 Ma and the most recent edifice in the west ~ 50 ka (Calvert et al., 2006; Hildenbrand et al., 2014). São Jorge Island can be subdivided into old and young volcanic complexes (Fig. 3.1). The oldest complex in the southeast is 1.2–1.85 Ma and the intermediate to young volcanic complex in the northwest is younger than 0.75 Ma based on $^{40}\text{Ar}/^{39}\text{Ar}$ and K/Ar dating (Hildenbrand et al., 2008; Pinto Ribeiro et al., 2010; Marques et al., 2018). The northwest of São Jorge also has had historical eruptions in 1580 and 1808 (Madeira, 1998). Although K/Ar dates suggest the maximum age for Faial Island is 0.85 Ma (Hildenbrand et al., 2012), most parts of the island are widely blanketed by a 10–440 ka volcanic complex (Pacheco, 2001; Pimentel et al., 2015). The youngest part of Faial in the west

(<10 ka) also experienced the historical Capelinhos eruption in 1957/58 (Machado et al., 1962). K/Ar dates suggest an oldest age of 0.19 Ma for Pico Island (Costa et al., 2015), which has had three historical eruptions since 1562. Lava flows of Pico volcano in the west of the island originated from the summit area and some from flank sources. The flows include both pahoehoe and 'a'a lava types. In contrast, 'a'a lava flows are more common in eastern Pico (Fig. 3.1; Scarth and Tanguy, 2001).

Neotectonic structures (Fig. 3.2) can be explained by regional trans-tension (Lourenço et al., 1998). Active strike-slip faults on São Jorge and Pico islands are revealed by sheared cinder cones (Madeira and Brum da Silveira, 2003). Some Holocene lava flows have been displaced by faults (Madeira et al., 2015), which is evidence of pre-historic seismic activity. From 1522 to 1964, at least 10 destructive earthquakes occurred in the central Azores (Fig. 3.2) responsible for hundreds of deaths (Gaspar et al., 2015). Since 1980, seismometers have been installed on several Azores islands (CIVISA, 1998), greatly improving earthquake detection threshold and location accuracy (Carvalho et al., 2001). At least 30 earthquakes of $M_w > 4.5$ were recorded (Fig. 3.2)

The deposits forming the upper submarine slopes have not been directly observed or sampled, but their origins can be speculated on. Quartau et al. (2012 and 2015) showed that the shelves of the Azores Islands have recently been accumulating volcanoclastic particles from subaerial and coastal erosion and carbonate particles from *in situ* biogenic production. Such sediments likely accumulated since the Last Glacial Maximum and are generally only 10 ms thick, although a seismic reflection image in Marques et al. (2018, their Figure 8) reveals an unusually thick 250 ms (~225 m) of sediment in the outer shelf of northeast São Jorge. During sea-level lowerings, such sediments are likely to be remobilised by coastal and subaerial erosion, and some of those sediments redeposited in the upper submarine slopes. Sonar images of the shelves of Pico and Faial reveal Holocene dendritic lava flows, lobes and deltas (Mitchell et al., 2008; Quartau et al., 2012, 2015). During sea-level low-stands, seaward extending shorelines probably allowed such lava flows to reach the outer shelves and hence feed the uppermost slopes. Sedimentary particles released by erosion by streams and waves also likely fed the upper

submarine slopes of the islands at such times. However, during sea-level high-stands, sediment can also be produced and exported from shelves due to greater biogenic production (Droxler and Schlager, 1985). It is presently unclear exactly how the flux of sediment to the island slopes has varied over time.

Offshore sediment gravity cores have been collected around these islands, which contain turbidites likely originating from slope landslides such as those we describe here. Analyses of four of those cores located in Fig. 3.1 (Chang et al., 2021) has revealed that those turbidites comprise mainly silt to sand grade volcanoclastic and minor bioclastic particles. Glass shard analysis and other data suggest that more than half of the turbidites originated as primary volcanoclastic events (i.e., pyroclastic flows). Much of the uppermost slopes of the islands may therefore also include such volcanoclastic deposits.

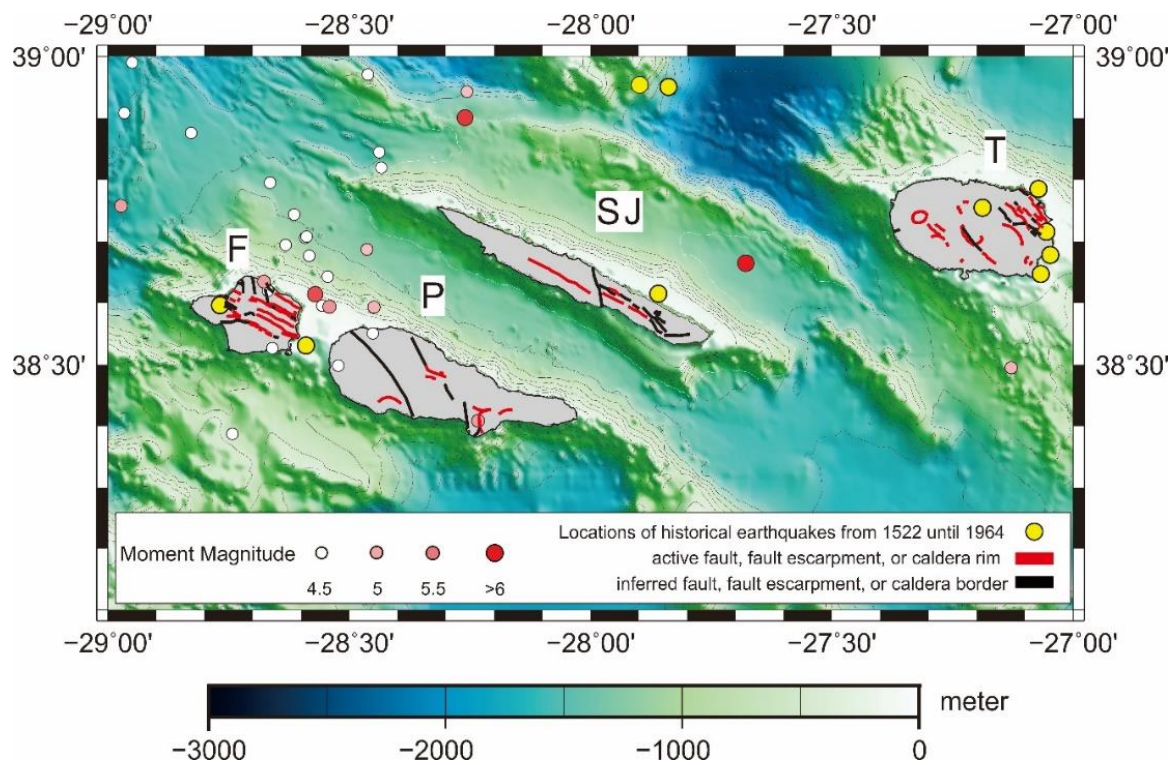


Figure 3.2. Distributions of earthquakes. Earthquakes shown with moment magnitude scaling were recorded between 1964 and 2019 and were derived from the International Seismological Centre catalogue ($M_w > 4.5$ shown). Yellow circles locate historical earthquakes from 1522 until 1964 (Gaspar et al., 2015, their Table 4-1). Red and black lines represent active and inferred faults on land, respectively (Madeira et al., 2015). F, P, SJ and T are Faial, Pico, São Jorge, and Terceira, respectively.

3.3 Materials and methods

3.3.1 Research materials

High-resolution bathymetric data were collected on RV *Arquipélago* in 2003 and RV *l'Atalante* in 2011, providing the coverage outlined in Fig. 3.1. The *Arquipélago* survey was carried out with a portable multibeam sonar (Mitchell et al., 2008) and covered the submarine slopes of Faial, Pico and São Jorge islands. These data suffer from imperfect rigidity of the transducer mounting, which led to an artificial high-frequency cross-track corrugation of the data, which needs to be borne in mind in interpretation (e.g., in the class C example in Fig. 3.2). The 2011 survey was carried out during project Features of Azores and Italian Volcanic Islands (FAIVI). Bathymetry data were collected around Terceira Island, with a survey boat deployed into coastal areas. Those combined data have a resolution of ~1 m in the first 100 m water depth increasing to 50 m at 2000 m depths (Chiocci et al., 2013; Quartau et al., 2014; Casalbore et al., 2015).

The earthquake event data were acquired from the International Seismological Centre (ISC) un-reviewed catalogue for the years 1964 to 2019. Fig. 3.2 shows the 30 largest earthquakes with $M_w > 4.5$. Historical earthquakes from 1522 until 1964 are from Gaspar et al. (2015) and the locations and lengths of active and inferred faults on land are from Madeira et al. (2015).

3.3.2 Landslide identification and calculations of area and volume

An idealised landslide comprises both an embayment or scar created by removed material and an emplaced mound of deposits, sometimes also with a chute in between (Hampton et al., 1996; Clare et al., 2019). Slope valleys that are potential landslide scars were identified by inspecting multiple perspective views of the shaded bathymetric data and seafloor gradient maps, also using tightly spaced contour lines as an indicator of steep gradients. Given the varied data resolutions and poor imaging at deep water depths where the deposits lie, mapping complete landslides was considered to be unrealistic. Therefore, our mapping focused on the heads of landslides only. Even with this focus, subjective decisions were necessary because some headwall escarpments are variably reworked or obscured by later sedimentation. Moreover,

headwalls and boundaries between adjacent valleys can become obscured by subsequent slope failures and some escarpments appeared likely formed from multiple events.

The slope valleys were classified in two ways (Fig. 3.3; see detailed mapping results in Appendix 3.1). The first classification addresses the varied level of recognition of these features as landslides and hence conveys our confidence in their landslide origins. The second classification addresses whether their morphologies suggest they formed by single slope failure events or by multiple events (either subsequent different events or retrogressive failures occurring over finite periods). For the recognition classification, five classes (A to E) were chosen as follows (Fig. 3.3a). Class A: headwalls and sidewalls can be clearly identified by sharp gradient changes and commonly with significant depth changes. Class B: headwalls and sidewalls mostly can be identified by sharp gradient changes and commonly with significant depth changes, though parts of them are less well defined. Class C: headwalls can be mostly identified from gradient changes but sidewalls are obscured or missing. Class D: headwalls and sidewalls are delineated based on modest gradient and depth changes (valleys belonging to this class commonly still have a depression). Class E: headwalls and sidewalls are delineated based on mild gradient and depth changes.

Examples illustrating our second classification scheme are shown in Fig. 3.3b. The slope valleys were subdivided into three types (1 to 3) based on their morphometric features. Type 1 valleys were interpreted as produced by multiple failure events. In this cases, multiple-branching valleys were identified and each of them appears important. Later erosive features can also overprint the main rupture surface. Type 2 valleys were interpreted as each produced by a single major failure event. Each valley contains a prominent headscarp. Type 3 valleys lie above the headscarps of type 1 or 2 valleys, so we interpreted them as the result of retrogressive failures. They have gentler gradients and form depressions of the sediment surface. Although those depressions could be artifacts, such as due to sediment aggradation around them or other factors, landsliding has occurred in similar shallow gradients and layered carbonate-rich deposits (Schwab et al., 1988), so we suggest these were potentially also earthquake-triggered

failures. Type 3 valleys typically occur in the outermost shelves of the islands, which are fully mapped in the multibeam data.

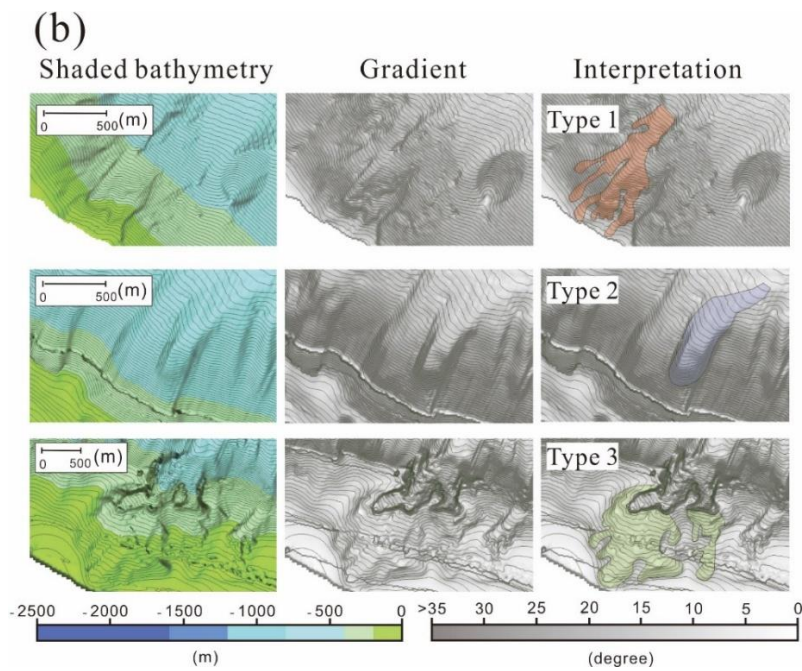
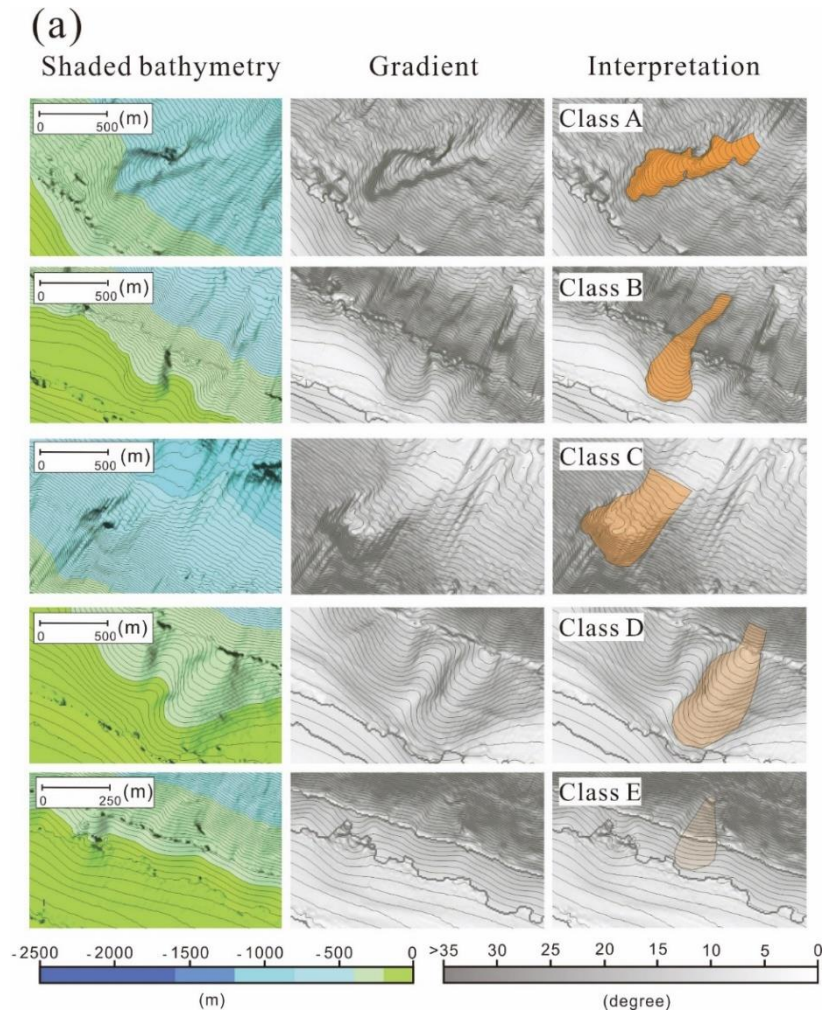


Figure 3.3. *Illustration of different classes and types of valley polygons. Contour interval is 10 m. (a) Classes based on recognition as landslides with A the most recognizable as landslide scars, E the least recognizable as such. (b) Classification based on suspected number of failure events. Type 1 contains multiple branches, suggesting multiple failures. Type 2 contains a single prominent valley, likely created by a single failure. Type 3 contains a valley lying above a prominent escarpment, which potentially developed by retrogressive failure, either during or after the lower failure.*

The areas and volumes of valleys were measured following the methods of ten Brink et al. (2006). We first manually digitised the boundary of each valley encompassing the potentially collapsed region to acquire valley area. We then created a smooth upper surface by interpolating over the perimeter of each digitised polygon. The present-day bathymetry (lower surface) was then subtracted from the interpolated surface (upper surface) to acquire valley volume. As the investigated submarine slope area varies amongst the islands and hence also affects the abundances of landslide valleys, we normalised landslide valley areas and volumes by dividing them by the submarine slope areas.

These measurements have the following potential uncertainties. (1) Later sediments deposited in slope valleys bias volume estimates. (2) Further erosion may be possible from sediment movements during or shortly following each slope failure. (3) Oblique artifacts due to the non-rigid mounting of the 2003 data can influence the topography of headscarps. Uncertainty (3) is minimised, as most slope valleys were located in the upper slopes. We mitigate against uncertainty (1) when assessing tsunami risks by only studying the more distinct landslide scars (classes A–C and type 2). That uncertainty may affect our inter-island comparisons of landslide volume, although we also check variations using scars with prominent scarps. Uncertainty (2) can potentially also affect the landslide volumes (e.g., Sun et al., 2018). However, the variations in landslide volumes can be verified if similar variations also occur in the landslide areas, which are less affected by either depositional or erosional modifications. Furthermore, our results below suggest that the material has significant cohesion and is thus more resistant to erosions by small sedimentary flows in the uppermost island slopes.

3.3.3 Landslide size-frequency analysis

The complementary cumulative distribution function (CCDF) has been used to represent the probability that a landslide greater than a particular size will occur and is helpful for summarizing the distribution of landslide sizes as it emphasizes the larger features (e.g., Malamud et al., 2004). CCDFs of area and volume were generated from slope valleys best representing single-event landslide scars (classes A–C and type 2). Their correspondence with models (goodness-of-fit) was tested using Kolmogorov–Smirnov tests (K-S test) and the p -value suggested by Clauset et al. (2009). The K-S test is a nonparametric test of the equality of continuous or discontinuous variations. It is used to quantify an interval between the empirical cumulative distribution function of the sample and the reference distribution. The p -value can vary from 0 to 1. If it is higher than 0.1, the observed data fit the tested distribution, whereas a p -value equal to or less than 0.1 suggests that the data are unlikely to follow the distribution. These tests have been applied in other submarine landslide studies (Casas et al., 2016; Geist and ten Brink, 2019).

3.3.4 Estimates of peak horizontal accelerations during earthquakes

Earthquake-induced ground motions have been widely suggested to trigger landslides (Heezen and Ewing, 1952; Tappin et al., 2001; Gràcia et al., 2003; Fine et al., 2005). Earthquakes with $M_s > 6.5$, which can create a local peak horizontal acceleration (PHA) $>0.5g$, occur every 70 years on average in the Azores (Nunes and Ribeiro, 2001; Nunes et al., 2001). To compare with the landslide data, we estimated PHA as follows. Moment magnitudes M_w were derived from all 1964–2019 body-wave magnitudes (m_b), duration magnitude (M_d), and local magnitude (M_L) of the ISC catalogue using the following relations (Das et al. (2011) for m_b , Kadirioğlu and Kartal (2016) for M_d , and Castello et al. (2007) for M_L):

$$M_w = \exp(0.719 + 0.212m_b) - 0.737 \quad (1)$$

$$M_w = 0.7947M_d + 1.342 \quad (2)$$

$$M_w = 0.79M_L + 1.2 \quad (3)$$

Based on an empirical study of ground motion recordings in western North America, Boore et al. (1997) suggested the following dependence of PHA (Y in fraction of g) on M_w and closest horizontal distance from source (r_{jb} in km).

$$\ln Y = b_1 + b_2(M_w - 6) + b_3(M_w - 6)^2 + b_5 \ln r + b_V \ln(V_S/V_A) \quad (4)$$

$$r = (r_{jb}^2 + h^2)^{1/2}$$

V_S is average shear-wave velocity of the upper 30 m in m/s used to represent local site conditions. Parameters V_A (m/s) and h (m) are fictitious values found by the regression analysis. Coefficients b_1 , b_2 , b_3 , b_5 , h , b_V , and V_A are determined by nonlinear regression (Joyner and Boore, 1994), which in this study were derived from Boore et al. (1997, their Table 8) corresponding with period 0.75s as suggested by ten Brink et al. (2009). The 200 m/s value used here for V_S is a representative average for 0–30 m depth in marine sediments from data compiled by Hamilton (1976). Equation 4 was derived from larger magnitude earthquakes than we study here and represents effects of attenuation and scattering over continental crust, so the derived PHA could be biased, though we use it here as it is based on a large amount of strong-motion data and lack of suitable alternatives.

3.3.5 Sediment cohesion estimates

Geotechnical data are not available to assess the stability of these slope sediments. However, remarkably steep deposits in headwalls and, in places, chutes of landslides (Figs. 3.1b to 3.1e) around the volcanic islands imply that the slope sediments are cohesive and that in turn has implications for how we interpret them. In contrast, if the slopes were instead purely incohesive sediment, they would be expected to have gradients no greater than the angle of repose of $\sim 30^\circ$. We estimated cohesion by inverting the conventional equations used in static limit-equilibrium analysis using the seabed gradients found. Such analysis is still widely applied due to its simplicity and ease of usage but tends to be conservative (Jibson, 2011), implying that cohesion estimates based on it will be minima. According to that analysis, failure occurs when the factor of safety (FS) (the ratio of resisting to driving stresses on the potential failure surface) is lower

than 1. We use the simplified equations for failure on a surface parallel to the dipping seabed (Fig. 3.4), assuming the structure extends infinitely. FS is then simply given by:

$$FS = [c/(\gamma' H \cos \theta_f \sin \theta_f)] + (\tan \Phi / \tan \theta_f) \quad (5)$$

$$\gamma' = (\rho_s - \rho_w) g$$

where c = sediment cohesion, H = average thickness of failure, γ' = unit weight of submarine deposit in water, ρ_s = sediment wet bulk density and ρ_w = water density, g = gravitational acceleration, θ_f = the angle of failure, and Φ = sediment friction angle. Using parameters given later, we estimated c as the value satisfying $FS=1$. As earthquake shaking was not considered but some of these steep sediments may have survived such shaking, this analysis provides a minimum value for c .

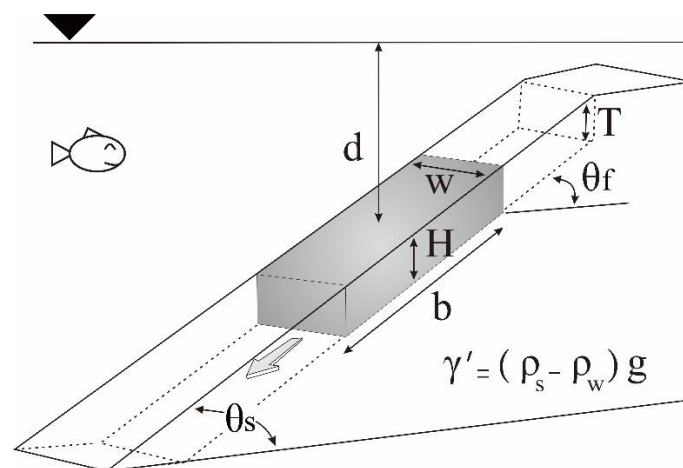


Figure 3.4. Shallow slope failure parameters used in the static limit-equilibrium calculation and estimates of tsunami height at source.

3.3.6 Estimates of tsunami height

Coastal run-up heights of tsunamis are difficult to reconstruct without sophisticated numerical modeling. There is also the uncertainty over whether the valleys were created by single or multiple landslides (Hunt et al., 2011; 2013). Nevertheless, Watts et al. (2003) derived analytical expressions for the initial waves above the landslides that are potentially useful for applying to the Azorean valleys likely produced by single events. Those expressions were derived from laboratory experiments simulating landslides that are large along-slope compared

with the tsunami wavelength. McAdoo and Watts (2004) updated the expressions to allow for landslides that are narrower along-slope than the tsunami wavelength. In their model, the sliding body was idealised as elliptical with specific gravity 1.85. With further corrections by De Lange and Moon (2004), this wave amplitude at source for translational slides is:

$$A = 0.224T [w/(w + \lambda)][(\sin\theta)^{1.29} - 0.75 (\sin\theta)^{2.29} + 0.170 (\sin\theta)^{3.29}](b/d)^{1.25} \quad (6)$$

$$\lambda = 3.87(bd/\sin\theta)^{1/2}$$

where (Fig. 3.4) T = head scarp height, w = along-slope landslide width, λ = tsunami wavelength, θ = average slope angle, b = initial length of the slide measured downslope, and d = depth of landslide initial centre of mass. Sediment density has not been measured here. If, based on the offshore cores, our suspicion that the sediment comprises detrital particles is correct, a wet bulk density of $\sim 2.0 \text{ g/cm}^3$ is appropriate (Hamilton and Bachman, 1982) so the specific gravity of 1.85 should not be far in error. Spreading during wave propagation towards the coasts can reduce wave amplitudes, whereas shoaling typically increases wave amplitudes. Local bathymetry can refract waves, leading to either convergence or divergence. Depending on direction, the incoming waves can also interfere with wave fronts emanating from the landslide deposit area (Geist et al., 2009). Local wave impacts are therefore likely to vary greatly around coasts and differ from these values of A . Nevertheless, Casalbore et al. (2011) found that tsunami run-up heights in the Tyrrhenian Sea roughly compared with those predicted by equation 6. Here, the estimated values of A were used mainly to provide a rough sense of relative scale, in a similar way to how earthquake magnitudes are used to assess relative size.

3.4 Results

3.4.1 Seismic ground shaking

The map of PHA (Fig. 3.5) calculated from the ISC data (Fig. 3.2) suggests that the submarine slopes of the four islands studied here have all experienced $>0.05g$ and locally $>0.4g$ since 1964. Three areas of high acceleration occur around the slopes of Faial and São Jorge associated with

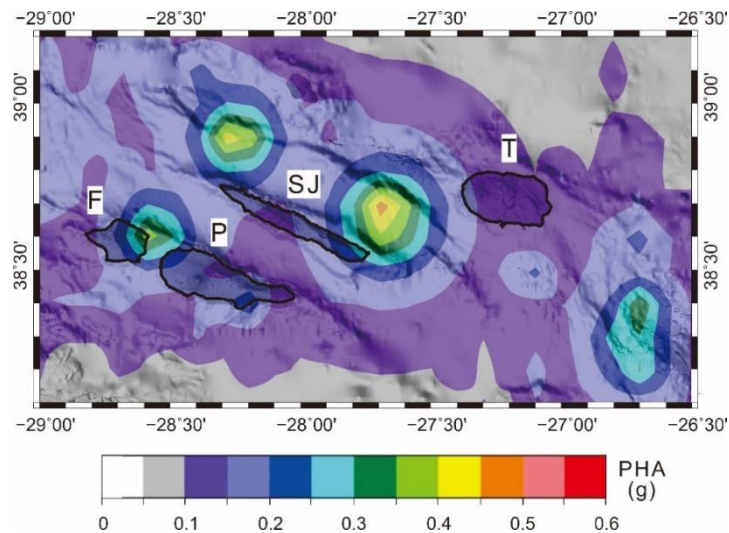


Figure 3.5. Peak horizontal accelerations (PHA) derived from the International Seismological Centre catalog for 1964–2019 earthquakes. *F*, *P*, *SJ*, and *T* are Faial, Pico, São Jorge, and Terceira, respectively.

the largest earthquakes in the ISC catalogue. However, if our suspicion is correct that the landslides have formed over the Holocene, all of these slopes may have experienced as much as 0.5g PHA over that timescale for at least two reasons. First, the historical (1522–1964) record includes 10 large events (Fig. 3.2), many of which occurred on Terceira where seismicity since 1964 has been modest (Fig. 3.2). This suggests a discrepancy with the instrumental data. Although magnitudes of such old events are difficult to estimate accurately, they are likely to have been $M > 6.5$ based on magnitude assessments of historical records elsewhere (Nunes and Ribeiro, 2001; Nunes et al., 2001). Second, active faults are widespread amongst the islands. Madeira et al. (2015) estimated that >20-km-long faults on the islands could produce events of $M = 6.5$ if they ruptured along their whole lengths. However, mapping the full extents of active faults is difficult on land, where they can be masked by subsequent deposits (Hipólito et al., 2014). Identifying active faults between the islands and continuations of faults from land underwater is another challenge. Deep-tow sonar images (Mitchell et al., 2018) show many fault escarpments that lack erosional features seen in older inactive faults (Tucholke et al., 1997), and the FAIVI data also show many “fresh” submarine fault scarps around Terceira

(Chiocci et al., 2013; Quartau et al., 2014; Casalbore et al., 2015). We thus suspect that the submarine areas host active faults, as also implied by the broad distribution of seismicity. Many of these faults have greater lengths than those mapped on land by Madeira et al. (2015) so they likely generate earthquakes larger than the $M=6.5$ that Madeira et al., (2015) suggested as a maximum. Consequently, the pattern of seismic accelerations over the long-term remains uncertain.

3.4.2 Submarine landslide inventory and volume-frequency distribution

We mapped 1227 slope valleys in total. The counts of the different classes and types are shown in Figs. 3.6a and 3.6b. Volumes range from 10^2 to 10^8 m³ with sample mean 7.9×10^5 m³. The volume distribution for all valleys (Fig. 3.6c) has a logarithmic bell shape. The volume distributions for individual islands (Fig. 3.6d) differ from each other. The modes for Pico and Faial (10^4 – 10^5 m³) are smaller than those for São Jorge and Terceira (10^5 – 10^6 m³), but the distributions all have similar bell shapes. Fig. 3.6d also reveals that São Jorge and Terceira have higher percentages (20–25%) of the larger valleys ($V > 10^6$ m³) than Faial and Pico Islands (5–10%). The largest ten valleys (all types) all occur around São Jorge and Terceira. São Jorge and Terceira also have the largest valley cumulative area and volume (Figs. 3.7a and 3.7c), an observation that persists when the data are normalised for slope area (Figs. 3.7b and 3.7d).

The relationship between area (A_l) and volume (V) for valleys most likely to be single landslide scars (type 2 and classes A–C) is shown in Fig. 3.8. Regressing the logarithmic variables suggests $V = 0.234 A_l^{1.3365}$ ($R^2 = 0.924$). Mean thicknesses were also obtained by dividing individual landslide scar volume by area (also for type 2 and classes A–C valleys). The mean thicknesses are 9.2 ± 0.5 , 7.3 ± 0.5 , 12.6 ± 0.8 and 10.6 ± 1.3 m for Faial, Pico, São Jorge and Terceira, respectively (uncertainties of means are 1σ). CCDFs of area and volume were also generated from these valleys (type 2 and classes A–C) as shown in Fig. 3.9. Both CCDFs follow log-normal distributions ($p=0.98$ and 1.0).

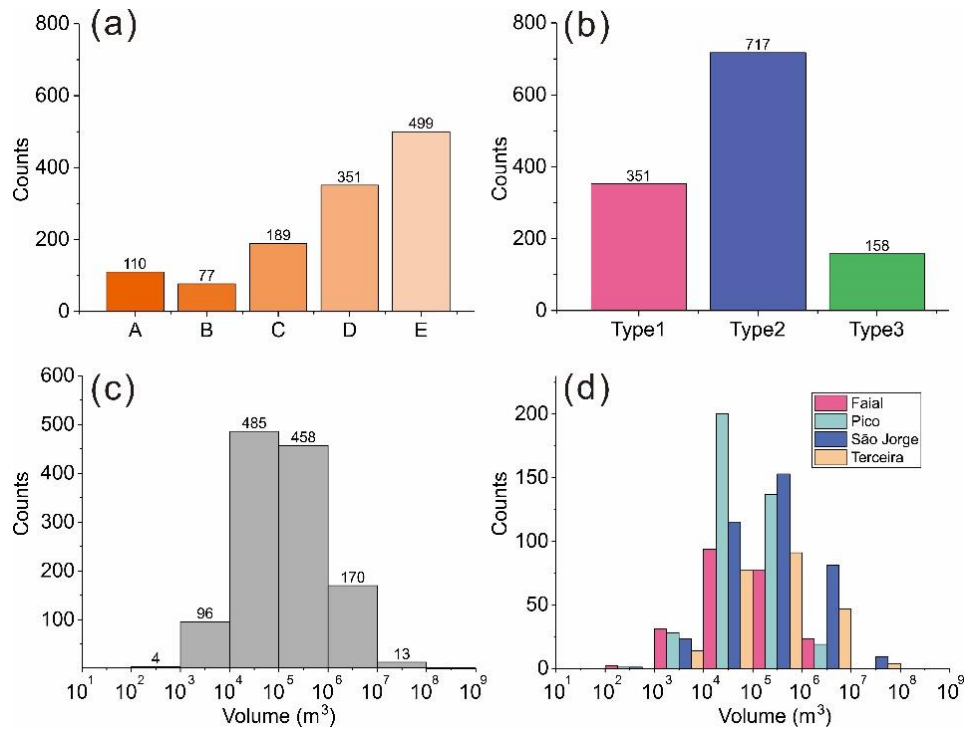


Figure 3.6. Histograms of slope valleys. (a) Counts by class. (b) Counts by type. Colours in (a) and (b) are as Fig. 3.3 (right panels). (c) Counts of volumes of all mapped slope valleys. (d) As (c) for individual islands. Values above bars in (a), (c) and (d) are counts in each interval.

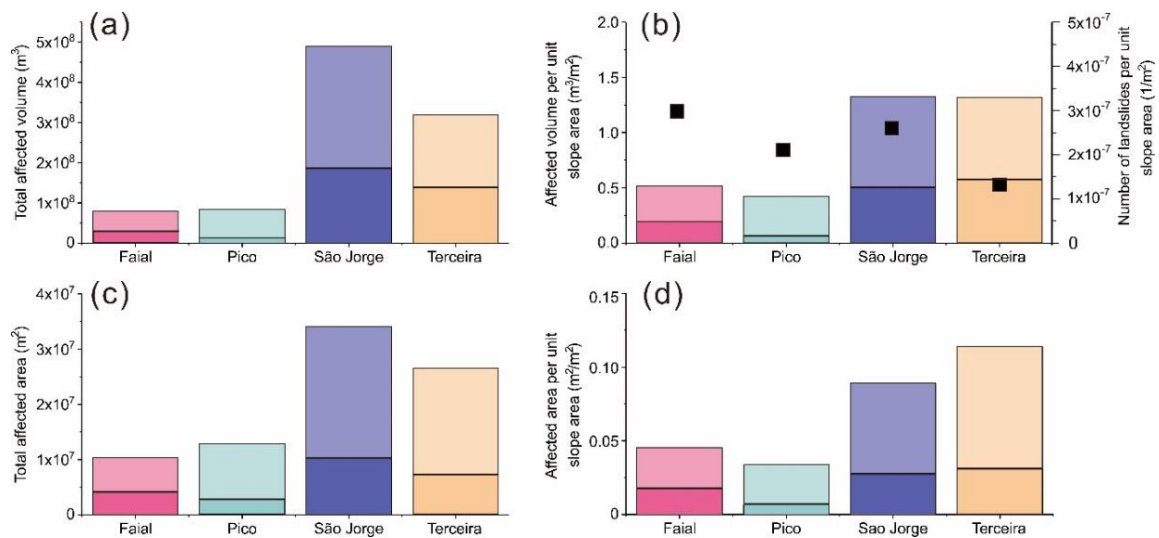


Figure 3.7. Summaries of total areas and volumes of slope valleys of each island (all types and classes; bold colours represent the volumes of the type 2, classes A-C valleys only). (a) Total volume of valleys. (b) As (a) normalised to submarine slope area of each island. Solid squares show the abundances of the type 2, classes A-C valleys (scale to right). (c) Total area of valleys. (d) As (c) normalised to submarine slope area of each island.

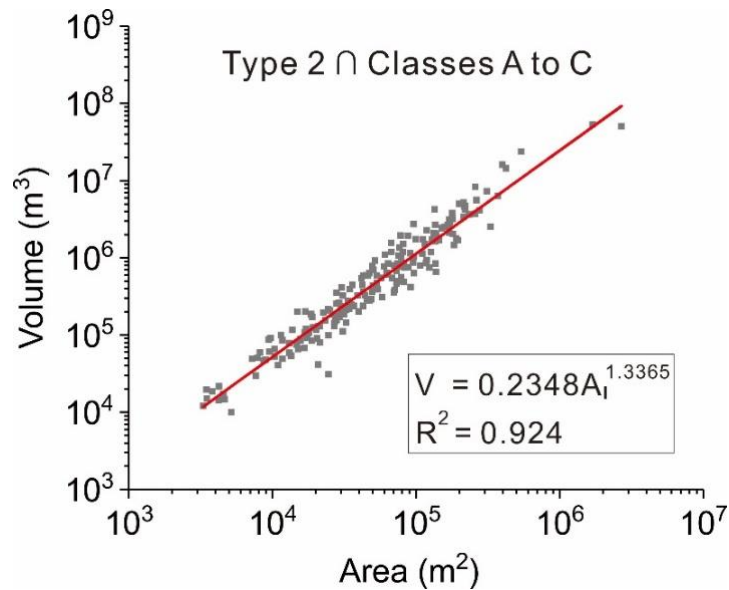


Figure 3.8. Empirical relationship between area (A_i) and volume (V) for the central Azores valleys of type 2 and classes A-C. A least-squares regression of the logarithmic variables suggests the relationship shown (red line).

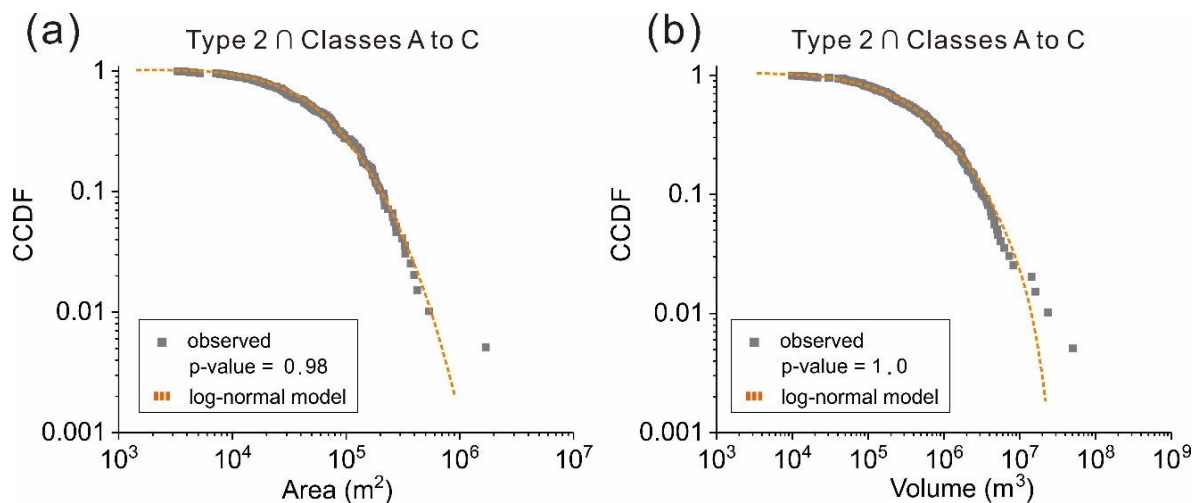


Figure 3.9. Complementary cumulative distribution functions (CCDF) of (a) area and (b) volume for valleys most likely to be landslide scars (type 2 and classes A-C). Orange dashed lines are log-normal models. Note that axes are logarithmic.

3.4.3 Assessment of cohesions of steep deposits

Steep gradients in some headwalls and sidewalls exceed 60° locally and generally reach 30° – 40° (Figs. 3.1b and 3.1c). Using these slope gradient values for the failure gradient angle, we inverted equation 5 for cohesion c . For H , we used the average thickness (10.6 m) of the scars

associated with single landslides (type 2 and classes A–C) found by dividing their volumes by their areas. A bulk density of 1.0 g/cm^3 was used for $(\rho_s - \rho_w)$ representing sand in water (Hamilton et al., 1956; Hamilton and Bachman, 1982). We used 25° – 40° for internal friction angle Φ typical of volcanoclastic sands and calcareous ooze (Lee et al., 1994; Boldini et al., 2009). Repeating the calculation for gradients of 30° to 60° , we estimated c between 9 and 33 kPa (Fig. 3.10). However, these c -values are minima because the infinite-slope calculation is conservative. Furthermore, if some of these steep sediment deposits have survived shaking by earthquakes, such accelerations have not been taken account of by only the gravitational loading used in equation (5), also ensuring that these c -values are minima.

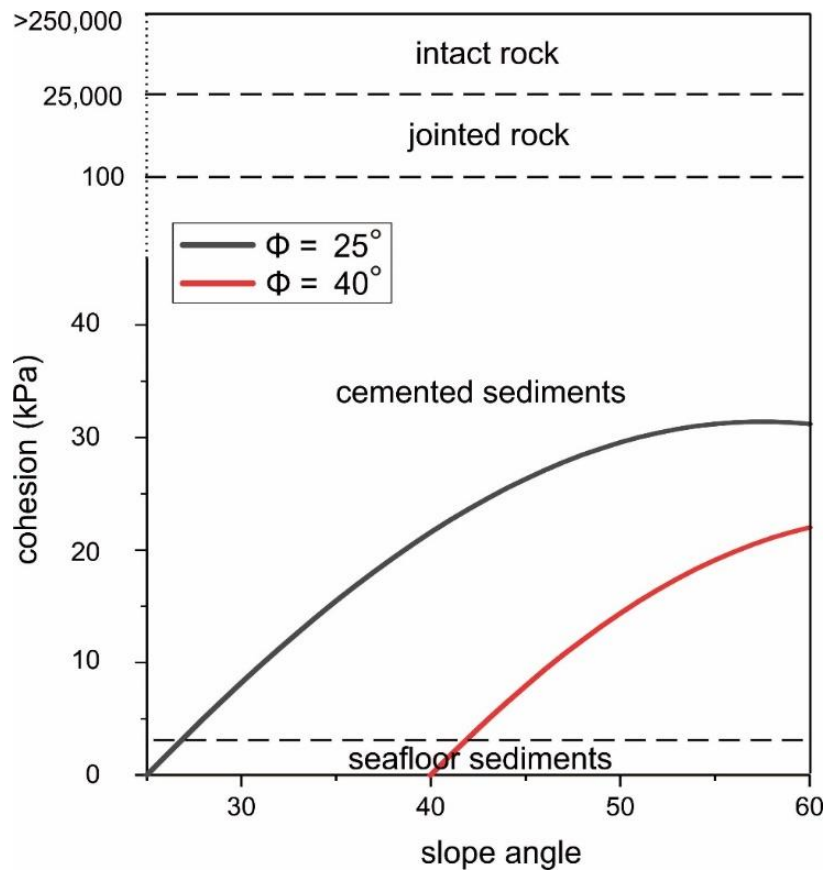


Figure 3.10. Estimates of sediment cohesion with varied slope angles from the pseudo-static analysis with no seismic accelerations. Dashed lines represent typical cohesion values for the materials shown.

The upper-slope sediments lie in water that is saturated with respect to aragonite and calcite (Wisshak et al., 2010; 2015), so cementation may be involved in stabilizing the sediments.

Carbonates are precipitated from seawater on the edges of clasts (Gabitov et al., 2019), binding the sediments (e.g., Tucker et al., 2020). These cohesion values (Fig. 3.10) noticeably overlap with laboratory results of Nafisi et al. (2020), who formed calcium carbonate cements in sand by microbial precipitation and tested the results under 10–100 kPa effective stresses. They showed that cohesion was 9–12 kPa after moderate cementation (1–4 wt% CaCO_3) and 56–65 kPa after high cementation (4–10 wt% CaCO_3). Our 9–33 kPa estimates of sediment cohesion therefore correspond with moderate to high cementation.

These cohesion values are also compatible with test results on some volcanoclastic deposits (e.g., lava-breccia ~30 kPa) found in volcanic islands as here but lower than the ~600 kPa of pyroclastic deposits (Di Traglia et al., 2018). Volcanoclastic deposits lying at up to 40° were also found off the Sciara del Fuoco slope of Stromboli (Casalbore et al., 2020). Some of these cohesions could therefore be compatible locally with lava deltas (Mitchell et al., 2008) underlying parts of these slopes. The cohesions we estimated are logically smaller than found in intact rocks ($c > 25,000$ kPa; Bieniawski, 1975; Marinis and Hoek, 2000).

3.4.4 Assessment of tsunami wave heights at source

Tsunami heights A immediately above landslides were derived for 83 single-failure landslides (type 2) with $V > 10^6$ m³ using equation 7 (detailed morphometric data in Appendix 3.2). The CCDF of wave height in Figs. 3.11a also follows a log-normal model ($p=0.43$). We define an initial wave height at source >1 m as potentially hazardous as such a wave could be amplified to several meters when inundating coasts (e.g., Tinti et al., 2005). At least 13 landslides were found capable of generating tsunamis with $A > 1.0$ m, and one with $A > 7$ m (Fig. 3.11). These landslides were located around São Jorge, Terceira and Faial Islands.

Sophisticated modeling of landslide-triggered tsunami wave propagation is beyond the scope of this paper. Coastal topography, refraction and wave steepening with shallowing water all affect final run-up height (tides are a secondary consideration here as they are only ~1 m (Cruz and Silva, 2001)). However, a first-order estimate of tsunami height at the coast can be made using Green's law (e.g., Federici et al., 2006), which predicts run-up heights relative to source

heights. In our study area, the shoaling factor to 1 m water depth is between 3 and 5, suggesting that there is an underappreciated risk of tsunamis around volcanic islands such as the Azores.

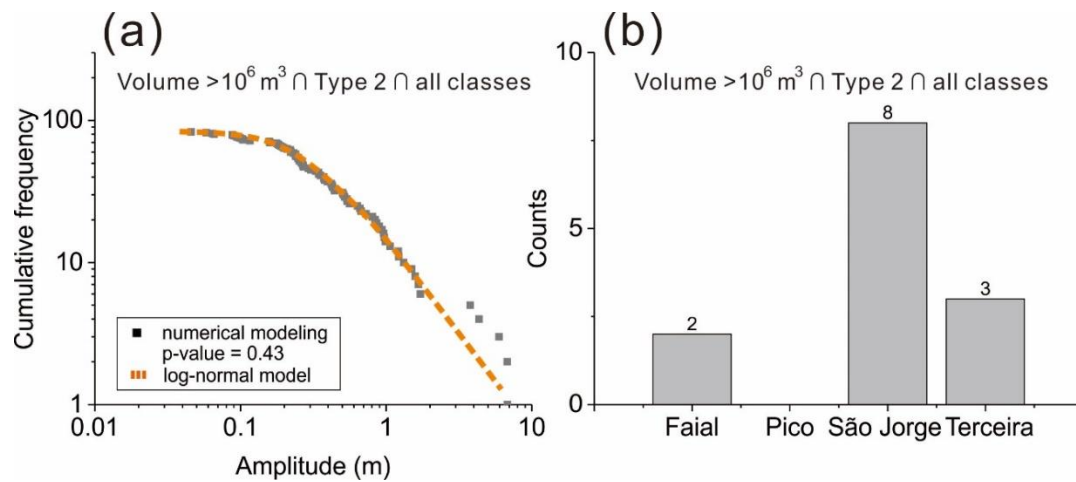


Figure 3.11. Cumulative frequency of tsunami amplitudes (A) at source predicted using equation 7 from landslide scars (volumes $>10^6$ m³, type 2, all classes), depths and other characteristics. (b) Occurrences of potentially hazardous tsunamis ($A > 1$ m) for individual islands.

3.5 Discussion

3.5.1 Assessing varied submarine landslide features in the central Azores

The above analysis has revealed lower cumulative volumes and areas of slope valleys around Faial and Pico islands than around São Jorge and Terceira islands (Fig. 3.7). The density of landslides around São Jorge is comparable with those of Faial and Pico, so landslides around São Jorge are generally larger than those around the other two islands. Accounting for the low density but high affected slope volume of landslides in Terceira island, the landslides there are large as well. As might be expected from their different average volumes, therefore, landslides are modestly thicker on average around São Jorge than around Faial and Pico. We explore these contrasts in this section.

3.5.1.1 Earthquake triggering

ten Brink et al. (2016) suggested that slopes become more stable with decreasing sedimentation rate and increasing frequency of earthquakes. Such increased sediment shear strength arises due

to seismic shaking, causing shear-induced compaction (e.g., Sawyer and DeVore, 2015; ten Brink et al., 2016) or sediment internal structure changes (Wu et al., 2021). This may help to explain the comparatively high 9–33 kPa estimated cohesion of these Azorean sediments besides carbonate cementation and prompts us to ask if earthquakes may explain other aspects of the landslides data also. To represent the regional occurrences of landslides, we prefer the cumulative volumes or areas of all slope valleys (Fig. 3.7) as they form the largest database, although the restricted groups (type 2 and classes A–C) also show a similar tendency for volumes and areas of valleys around São Jorge and Terceira to be larger than those around Faial and Pico islands.

The pattern of extreme shaking in Fig. 3.5 is dominated by the three largest earthquakes occurring since 1964, with two near São Jorge and one in northeast Faial. The pattern does not correspond with the landslide volume and area differences between the islands. However, the lack of correspondence could arise if the ISC catalogue is unrepresentative of the long period over which these submarine landslides likely developed (>ky). E.g., patterns of seismicity can change location over decades due to changes in stress after the largest events (Stein, 1999). The historical record of earthquakes is also subject to uncertainties. The wide distribution of active faults (Fig. 3.2) implies that there is a potential for large earthquakes that is more widespread than suggested by the simplistic reading of either instrumental or historical records.

Sediments accumulating on the upper island slopes originate from various sources; from coastal and subaerial erosion, biological production and volcanic eruptions. Their fluxes are hard to quantify and most likely vary around the islands. However, a simple explanation for the larger landslides around São Jorge and Terceira compared with Faial and Pico could involve a larger time interval between destructive earthquakes, leaving more time for deposits to accumulate. This in turn implies that there could be a higher frequency of larger earthquakes around Faial and Pico islands and thus a greater longer-term threat of earthquakes there. This is an important inference concerning the seismic hazards of the Azores islands. We however temper this inference by assessing other factors below that may have also affected the landslide volumes and areas.

3.5.1.2. Varied lava flow types

Lava flows on east Pico island are mainly 'a'a whereas those of west Pico are more mixed pahoehoe and 'a'a types (Fig. 3.1). Pahoehoe flows typically form stacks of thin sheets whereas 'a'a lava flows are commonly thicker (Macdonald, 1953). Although 'a'a flows can have friable clinkers above and below them, their interiors are commonly more massive and less porous or fractured (Macdonald, 1953). During sea-level low-stands, lava flows would have more easily reached the outer shelves, supplying the uppermost slopes directly. Although we anticipate there being mainly sediments underlying the uppermost slopes because turbidites in offshore cores contain mainly silt-sand grade volcanoclastic and bioclastic particles (Chang et al., 2021), different landslide statistics may occur if there were widespread lava underlying the upper slopes because of differences in geotechnical properties between the two lava flow types.

However, landslide volumes (Fig. 3.12) differ only slightly between west and east Pico. We suggest that, even if lavas are common, volcanoclastic deposits of 'a'a and pahoehoe are probably similarly susceptible to failure, rapidly disaggregating on the steep upper submarine slopes (cf. Sansone and Smith, 2006). Furthermore, varied effusion rates of lava flows and the pre-eruption seafloor morphology can also lead to uneven loading of slopes by lava flows, which ultimately affect slope stability (Bosman et al., 2014; Casalbore et al., 2021), so factors other than merely flow type likely affect landslide occurrences.

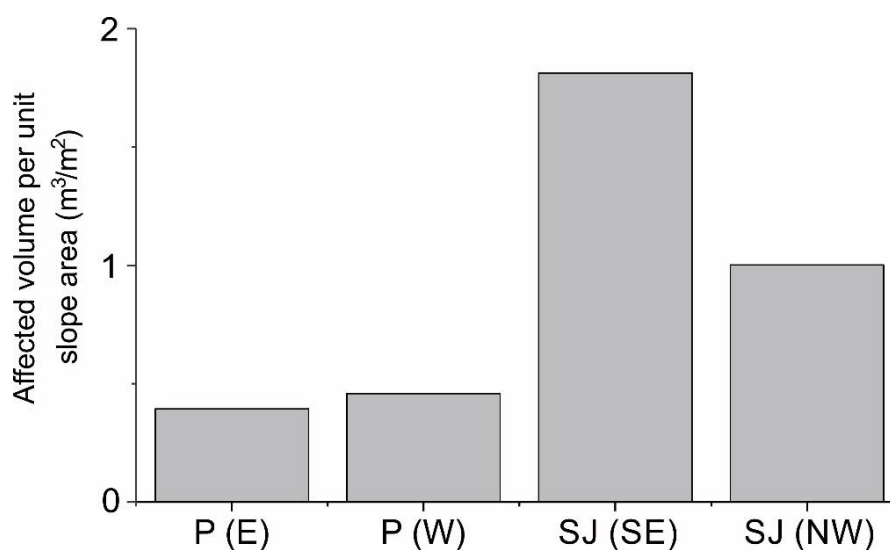


Figure 3.12. Cumulative volumes of slope valley per unit slope area for subdivisions of Pico and São Jorge islands (all valley classes and types).

3.5.1.3 Volcanic ages of adjacent land and shelf widths

The ages of the volcanic sequences comprising each island might be expected to influence landsliding if more recent volcanic building led to steeper slopes of friable material that were susceptible to failure. On the other hand, broad shelves typical of older volcanic islands (Menard, 1986) may host thick sediments and those sediments may be exported to the island submarine slopes by wave erosion and/or mass wasting (e.g., Fornari et al., 1979; Dengler et al., 1984). Based on high-resolution bathymetry data, Quartau et al. (2010, 2014, 2015) confirmed that most of the older volcanoes in the Azores have wider shelves than younger edifices, though shelf width can be affected by vertical tectonic motions, varied wave climate and other factors as well (Ramalho et al., 2013). As sediments are continually produced by biogenic production as well as subaerial erosion and wave abrasion of sea cliffs, we might expect the upper slopes of islands with wide shelves to be capable of accumulating thicker sediment deposits during sea-level high-stands. For instance, the easterly older shelf of São Jorge has a broad sedimented terrain where seismic data reveal an extreme ~250 m of layered sediment (Marques et al., 2018). However, shelf width is likely not the sole pre-conditioner for slope failures. For instance, Santa Maria, which is the oldest island and has the widest shelf of the Azores, has deposits on its shelf of only a few m thick (Ricchi et al., 2020). This is partly because it is a low relief, semi-arid island and hence contributes little sediment from stream erosion. In addition, wide shelves can attenuate waves crossing them, protecting cliffs from erosion (Ricchi et al., 2020).

Although São Jorge has a higher cumulative volume of slope valleys than either Faial or Pico islands, there are also differences between the volcanically old and young parts of São Jorge. The slope valleys in old southeast São Jorge have nearly twice the volume per unit slope area than those in the young northwest part of the island (Fig. 3.12). This favors an explanation involving export of shelf sediment from the broad shelf in southeast São Jorge, leading to thick slope deposits susceptible to failure. Sediment production rates are difficult to anticipate, given that the sediments originate from varied sources such as biogenic particles created on the shelves, subaerial and coastal erosion, and pyroclastic fallout from eruptions (Quartau et al.,

2012), though collecting sediment cores and other data around the islands could in principle help resolve this in the future. Nevertheless, the thick sediment imaged seismically beneath the shelf of São Jorge (Marques et al., 2018) suggests this could indeed partly explain its high cumulative volume of slope valleys. Despite this effect, the cumulative volumes of landslide valleys of west São Jorge ($\sim 1 \text{ m}^3/\text{m}^2$), where the island is volcanically young and the shelf is narrow, is still larger than the volumes for Faial and Pico, which are both $< 0.5 \text{ m}^3/\text{m}^2$, so the difference between the islands still needs an explanation, such as the difference in long-term seismicity.

3.5.2 Comparing the Azores landslide area-volume relationship with those of other settings

The relationship between volume (V) and area (A_l) is generally written as $V = \alpha A_l^\beta$ where α and β are constant parameters for each dataset. Landslides that are perfectly self-similar or show no systematic variation in ratio between the vertical and horizontal dimensions should uniformly have $\beta = 1.5$ (Guzzetti et al., 2009; Klar et al., 2011). With accurate landslide dimensional measurements, Guzzetti et al. (2009) reported $\beta = 1.449$ for subaerial landslides in central Italy, which is close to $\beta = 1.5$.

Table 3.1 shows α and β values for six studies of data from different submarine geological environments for comparison with the Azores results. ten Brink et al. (2006) suggested that diverse β values could result from different failure processes and thicknesses of failed material. For instance, clay-rich debris lobes in the Storegga slide of Haflidason et al. (2005) have β close to 1 ($V = 0.0267A_l^{1.032}$), a result of a nearly constant thickness of the sliding layer regardless of slide area. Other regions with β close to 1 (Chaytor et al., 2009; Hu et al., 2009) are located in open continental slopes where gradients are gentle and sediments have been homogeneously deposited, though likely having layered physical properties. Failure along seabed-parallel layers tends to form tabular landslides. A Mediterranean result (Urgeles and Camerlenghi, 2013) has intermediate $\beta = 1.251$. The Mediterranean slopes have varied geological structure and sedimentary inputs, leading to diverse landslides types and thickness.

The Azores data have intermediate $\beta=1.337$, though closer to a size-invariant ratio ($\beta=1.5$). Landslides have $\beta < 1.5$, perhaps because of later infilling of valleys by sediments or resistance to deep failure (e.g., because of increasing sediment compaction or harder volcanic rocks at depth).

Table 3.1. Synthesis of volume-area relationships.

	Number	α	β	References
Central Azores	197	0.2348	1.337	This study
Southern Tyrrhenian Sea	428	0.0009	1.369	Casas et al. (2016)
US Atlantic margin	106	0.0163	1.099	Chaytor et al. (2009)
East China Sea	102	0.0260	1.020	Hu et al. (2009)
Puerto Rico	160	0.2630	1.292	ten Brink et al. (2006)
Mediterranean Sea	696	0.0050	1.251	Urgeles and Camerlenghi (2013)

3.5.3 Comparing cumulative volume distributions with those of other areas

Fig. 3.13 shows CCDFs of landslide volume from seven different submarine settings. CCDFs are used to assess the maximum size in a region and investigate the relative occurrences of features of differing size, though are affected by completeness and other factors. Substantial sediments can accumulate on open passive continental margins as the slopes are broad and homogenous, with only occasional earthquakes. However, once landslides occur, movements can transport sediment far from their origins so landslides can be large, reflected in their CCDFs (ten Brink et al., 2006). Though landslides in tectonically active areas are usually small (Urgeles and Camerlenghi, 2013), some giant submarine landslides still can be produced there (e.g., large slumps in Hawaii; Masson et al., 2002).

Small landslides ($<10^5 \text{ m}^3$) tend to be identified more readily in higher-resolution datasets. Hence, at least 10 times more landslides were identified in bathymetry grids with 20-m cell sizes than in those with 100-m cell sizes (Fig. 3.13). Comparing datasets of similar grid cell sizes, some differences occur that could be explained by differing sediment physical properties. For instance, the smallest mapped scars in the Azores have volumes 5 times larger than the smallest scars in the southern Tyrrhenian Sea, despite comparable grid cell sizes ($<20 \text{ m}$). One possible explanation could be different sediment cohesions. Limit-equilibrium slope stability modeling has suggested that incohesive sediments tend to form shallow, elongate landslides

with no lower size limit, whereas cohesive sediments tend to develop landslides with a minimum size (Frattini and Crosta, 2013). The 9–33 kPa or larger cohesion of the Azores sediments may explain the larger minimum volumes there compared with those of the Tyrrhenian Sea. However, the variance of geological setting needs to be considered as well, as most of the small landslide scars in the Tyrrhenian Sea were found at the heads or flanks of submarine canyons. Confined spaces there may also have limited landslide development (Casas et al., 2016).

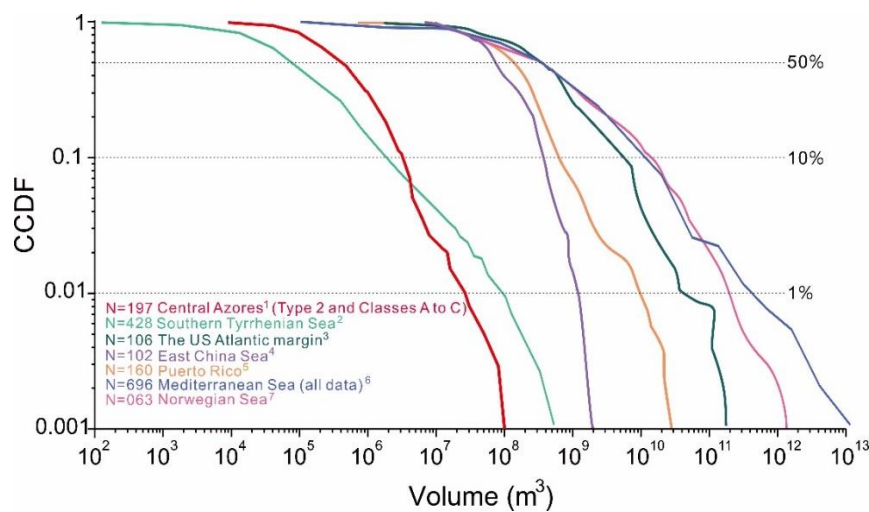


Figure 3.13. CCDFs of landslide volumes. [(1) This study, central Azores; (2) Casas et al. (2016), southern Tyrrhenian Sea; (3) Chaytor et al. (2009), US Atlantic margin; (4) Hu et al. (2009), East China Sea; (5) ten Brink et al. (2006), Puerto Rico; (6) Urgeles and Camerlenghi (2013), Mediterranean Sea; (7) Haflidason et al. (2005), middle Norwegian Sea.]

3.5.4 Lessons for assessing geohazards of volcanic islands

We have suggested that differences in the cumulative volumes and areas of submarine landslides may imply differences in long-term seismicity. Such differences could potentially help to overcome the inadequacy of the instrumental seismic record (Scholz, 2002). Hence, submarine landslide mapping can help in assessing earthquake hazards as well as tsunami hazards. This analysis could easily be repeated around other volcanic islands with suitable bathymetric data, although effort is still needed to assess the other possible causes of varied

landslide properties identified above, e.g., fluxes of sediment from erosion and biogenic production.

Geotechnical data would help evaluating slope responses to earthquakes. Obtaining samples for such tests by vibrocoreing would be challenging on the steep (30°) slopes of islands, but more indirect assessments of sediment rigidity may be possible, e.g., velocities from shallow seismic refraction.

More efforts could be put into assessing landslide frequency. Long-term records can be obtained by dating landslide-origin turbidites (e.g., Hunt et al., 2013). Short-term records could be obtained by repeating multibeam sonar surveys (e.g., Casalbore et al., 2012; 2020; Kelner et al., 2016; Soule et al., 2021), with timings of events obtained from tide gauge records and acoustic recordings (Caplan-Auerback et al., 2001) to help identify possible formative events such as earthquakes.

3.6 Conclusions

We have mapped 1227 submarine slope valleys in the central Azores volcanic islands. To overcome difficulties of interpretation arising from the rugged morphology of the upper submarine slopes, valleys were first categorised based on the levels of recognition as landslides and whether they appear to have formed by single, multiple or retrogressive failures events.

Considering slope valleys of all types and classes, São Jorge and Terceira islands have greater valley volumes and areas per unit slope area, compared with Faial and Pico. We highlight this observation as suggesting that Faial and Pico potentially have greater earthquake hazard. In this interpretation, frequent earthquakes prevent the build-up of unstable sediment deposits on slopes, leading to mostly smaller landslides around Faial and Pico. This suggestion is tempered by an observed greater valley volume in easterly São Jorge where thick sediments are also observed on its shelf. Such sediments are likely exported to slopes during sea-level lowstands, which suggests that greater sediment accumulation has also affected landslide volumes there. Nevertheless, westerly São Jorge has a narrower shelf and its valley volume is still greater than Faial and Pico islands. Thus, differences in factors other than sediment input such as seismicity are still needed to explain the contrast in slope valleys statistics.

Cumulative area and volume distributions for valleys most likely to be single landslides fit log-normal probability density functions, as found elsewhere. Based on an analytical formula, at least 13 of the valleys most likely to have been produced by single landslides would have generated tsunamis with heights >1 m at source. One may have produced a wave of ~ 7 m. Those heights also follow a log-normal probability density function.

Static slope stability analyses suggest that some steep slopes have cohesive strengths of at least 9–33 kPa, much larger than 0.08 to 2 kPa expected of typical superficial incohesive seafloor sediment. This could be explained by moderate to high carbonate cementation, by earthquakes shaking and/or perhaps by the presence of coherent lava or talus.

Overall the study suggests that mapping submarine landslides around volcanic islands in general could also be useful for investigating seismic and tsunami hazards that are not well characterised by other methods, as well as uncovering other aspects of their submarine slope sediments.

Data availability

The 2003 multibeam data are available at 100 m grid resolution from the Marine Geoscience Data Portal (<http://www.marine-geo.org/index.php>). The multibeam data for Terceira are not publicly available due to the sensitive nature of the area and environmental sustainability concerns, but can be made available to researchers with appropriate credentials. Background bathymetric data are from the GeoMapApp (GMRT; www.geomapapp.org, Ryan et al., 2009). The seismic catalog is from International Seismological Centre (2019) (<https://doi.org/10.31905/EJ3B5LV6>; Di Giacomo et al., 2014).

Acknowledgement

YCC thanks the editor Peter van der Beek and reviewers Daniel Casalbore and Uri ten Brink for their constructive comments, which led to significant improvements of this manuscript. He also thanks the Taiwanese government for providing his PhD scholarship and the International Association of Sedimentologists for a travel grant to the annual British Sedimentological Research Group meeting, where some of these ideas were explored. The European Communities 7th Framework Programme under EUROFLEETS funded the bathymetric data collection around Terceira used in this study. Iasmina Cristina Popa is thanked for a preliminary attempt at the peak ground horizontal analysis. Thor Hansteen, Christoph Beier, Adriano Pimentel, Ting-Wei Wu, Sung-Ping Chang and Zhongwei Zhao are thanked for informative discussions. Figures were prepared with the GMT software system (Wessel and Smith, 1991).

Chapter 4. Volcaniclastic deposits and sedimentation processes around volcanic ocean islands: the central Azores

This chapter is a reproduction of a manuscript published in the Journal of Geological Society, London, Special Publications. Chang, Y.-C., Mitchell, N.C., Hansteen, T.H., Schindlbeck-Belo, J.C., Freundt, A. Volcaniclastic deposits and sedimentation processes around volcanic ocean islands: the central Azores. <https://doi.org/10.1144/SP520-2021-62>

Y-C.C produced the original draft of the manuscript and figures. All co-authors contributed their opinions and commented on the draft manuscript. The journal reviewers also effectively made contributions by commenting on the article.

In this chapter, I sampled marine sediments cores stored in the GEOMAR repository at Kiel. I have pre-processed all the samples for geochemical analysis and optical microscope observations. I pictured volcanic grains under a high magnification stereo-microscope and digitally measured their morphometric parameters for angularity and elongation. I made core interpretations based on the compilation of the sedimentary structures, volcanic grain geomorphology and geochemical analytical results.

The four gravity cores and photographic scans were collected during RV *Meteor* cruise M141/1 in 2017 and provided by co-authors T.H.H and A.F. Geochemical analyses were assisted by the senior technicians and research staff. The operation of electron microprobe (EMP) analysis has been helped and carried out by co-author J.C.S. Steffen Kutterolf and Line Herberg at GEOMAR also provided a part of the EMP samples for core 1226. X-ray powder diffraction and pre-test of total organic carbon analysis were operated by senior technicians at the University of Manchester. The published data of organic carbon contents and isotopes were assisted by a senior experimental officer at the University of Liverpool. Multibeam bathymetric data were provided by co-authors N.M and R.Q.

Abstract

Geological histories of volcanic ocean islands can be revealed by the sediments shed by them. Hence there is an interest in studying cores of volcanoclastic sediments that are particularly preserved in the many flat-floored basins lying close to the Azores islands. We analyse four gravity cores collected around the central group of the islands. Three sedimentary facies (F1-F2a, F2b) are recognised based on visual core logging, particle morphometric and geochemical analyses. F1 is clay-rich hemipelagite comprising homogeneous mud with mottled structures from bioturbation. F2a and F2b are both clay-poor volcanoclastic deposits, which are carbonate-rich and carbonate-poor, respectively. More biogenic carbonate in F2a reflects the incorporation of unconsolidated calcareous material from island shelves or bioturbation. Within F2a and F2b we identify deposits emplaced by pyroclastic fallout, primary or secondary turbidity currents by combining multiple information from lithological composition, sedimentary structures, chemical composition of volcanic glass shards and morphometric characteristics of volcanic particles. Primary volcanoclastic sediments were found in all four cores, echoing activity known to have occurred up to historical times on the adjacent islands. These preliminary results suggest that greater details of geological events could be inferred for other volcanic islands by adopting a similar approach to core analysis.

Keywords: volcanoclastic facies, volcanic islands, volcanic hazard, geohazard history, grain-shape analysis

4.1 Introduction

Large volumes of volcanoclastic sedimentary material are denuded from volcanic ocean islands and transferred to their surrounding seafloor (Menard, 1983), so scientific drilling and shallow coring can be used to determine how the transfer of volcanoclastic sediments has varied over time. At more distal sites, turbidity currents associated with mass wasting of islands are typically less erosive, so more dateable hemipelagic sediments between turbidites can be preserved. However, only turbidity currents produced by large events such as flank collapses are likely to reach distal sites (Hunt et al., 2011; 2013). More proximal sites, in contrast, have a good chance of recording smaller volcanic eruption and collapse events (e.g., Wall-Palmer et al., 2014). Examples of sampling sites close to oceanic islands include those of Ocean Drilling Program (ODP) Leg 157 offshore Gran Canaria (Carey et al., 1998; Schmincke and Sumita, 1998), shallow coring offshore Reunion Island (Ollier et al., 1998; Saint-Ange et al., 2013), and Cape Verde islands (Eisele et al., 2015a, b). Intensive sampling near to arc volcanic islands has been carried out near Montserrat, including during International Ocean Discovery Program (IODP) Expedition 340 (Le Friant et al., 2015) and with extensive shallow coring (Trofimovs et al., 2006; Trofimovs et al., 2013; Cassidy et al., 2014). Proximal sites tend to have well-preserved turbidite sequences, although scouring by the turbidity currents can erode their sedimentary substrates as well (e.g., Trofimovs et al., 2006; Solaro et al., 2020). The Montserrat cores in particular reveal how particles in pyroclastic flows are separated when they enter the ocean, with larger clasts rapidly deposited, leaving the finer particles to travel on as turbidity currents (Trofimovs et al. 2006). The IODP core results suggest evidence for seabed failure caused by loading by debris avalanche material (Le Friant et al., 2015). The many flat-floored basins lying within 10–30 km of the Azores islands are potential proximal sediment traps as turbidity currents from the island slopes became depositional upon transformation to subcritical flow (e.g., van Andel and Komar, 1969). These deposits can reveal how the sequence, frequency and style of mass-transport events on and around the islands have varied over time. They should also reveal if and how they differ from the more proximal sampling records obtained at other islands.

Volcaniclastic deposits can be sub-divided into primary and secondary deposits (Fisher, 1961). Primary submarine volcaniclastic deposits are directly derived from volcanic activity, such as ash fallout from eruption columns (e.g., Bonadonna et al., 2002), subaqueously fragmenting lava flows from effusive vents (e.g., Cappello et al., 2015), and pyroclastic flows produced by collapsing eruption columns and domes entering the sea (e.g., Calder et al., 1999). Alongside those, primary deposits also include syn-eruptive deposits whose mode of transport may have included non-eruptive mechanisms, but where the clasts are a product of eruptive activity and where transport occurs without an intervening stage of deposition and remobilisation. For example, the immediate mixing of pyroclastic material with water/ice can generate lahars reaching the sea (e.g., Cronin et al., 1997). Secondary deposits may be indirectly associated with eruptive activity, but most events are unrelated to volcanic activity. Massive landslides can potentially arise from the instability of steep slopes of volcanic islands coupled with various triggers (Lee et al., 1994; Keating and McGuire, 2000). Secondary volcaniclastic deposits unrelated to volcanic activity can also be caused by a wide range of reworking processes, for instance, sediment resuspension during tropical hurricanes or storms (Dengler et al., 1984), submarine slope collapses due to over-steepening of unconsolidated volcanic materials (Fornari et al., 1979) or suspension of particles by coastal waves (Quartau et al., 2012; Zhao et al., 2019) or subaerial erosion (Louvart and Allègre, 1998).

Biogenic production in the shallow waters of the Azores Islands has made carbonate a common non-volcaniclastic component of their shelf deposits (Quartau et al., 2012; 2015; Ávila et al., 2015; Wisshak et al., 2015), which is potentially exported to the basins, where it could be a useful tracer of shelf or upper slope origins. The relative amounts of different types of sediment should vary between islands, e.g., due to different dominant eruption styles (explosive versus effusive) or size and structure of shelves. Biogenic production rates vary with food sources, water clarity and other factors (Wisshak et al., 2015). Coastal and subaerial erosion rates vary with wave, wind and precipitation conditions, even around individual islands due to shadowing (Mitchell et al., 2003).

The chemical compositions of volcanic fragments (typically of glass shards) in volcanoclastic deposits provide clues to their emplacement process and origin. In many instances, a deposit with a tight cluster of geochemical compositions has been interpreted as indicating a single volcanic event and thus primary deposits (e.g., Stokes and Lowe, 1988; Stokes et al., 1992; Lowe et al., 2017), although secondary volcanoclastic deposits may also have homogeneous shard compositions if those shards were derived from the remobilization of shelf-deposited tephra of unique magmatic systems largely stored on the shelf (Schneider et al., 2001). A large geochemical compositional variation instead likely results from reworking of material from different volcanic source deposits. However, in some cases, physically different volcanic sources contributing to deposits can differ only subtly geochemically (Boygale, 1999; Schneider et al., 2001; Gudmundsdóttir et al., 2011; Schindlbeck et al., 2013), making interpretation of resedimented deposits based on geochemistry alone difficult. Such issues may also limit the use of chemical proxies in isolation to determine the origins of volcanoclastic deposits (e.g., Kratzmann et al., 2009; Christopher et al., 2014). Analyses of glass geochemistry integrated with other information are therefore required for accurate and consistent identification of eruption sources.

We seek to reveal the main emplacement mechanism of volcanoclastic deposits on the basin floor of the central Azores by identifying different types of volcanoclastic deposits. The work aims to answer: are most of those deposits derived directly from volcanic eruptions (primary volcanoclastic deposits) or derived from reworked deposits or submarine slope failure (secondary volcanoclastic deposits)? The volcanoclastic bed thicknesses found here also pose the question of how they compare with other islands with different geological histories, as cores typically only sample a limited amount of sediment, both spatially and in terms of age extent, and classification of bed types varies between investigations. Comparing the results of coring in similar relatively proximal locations at other oceanic islands with similar hot-spot origin could reveal interesting variances that reflect differences in style of volcanism, seismicity and turbidite emplacement mechanisms. This article describes sediments in four gravity cores of 13 m total length by integrating visual observations, geochemical measurements and grain-shape

morphometric analyses. Multiple types of sediment characteristics are used to classify the sediments.

4.2 Geological setting

The central Azores group of Terceira, São Jorge, Faial, Pico and Graciosa islands have grown during at least the Quaternary (Féraud et al., 1980) close to the slow spreading Mid-Atlantic Ridge (Fig. 4.1). The crust underlying them is thickened and forms a broad oceanic plateau, created by excess volcanism on a plate or at a plate boundary that has been slowly moving over a mantle hotspot or other source of excess mantle melting (White et al., 1976; Bonatti, 1990; Gente et al., 2003; Vogt and Jung, 2004). Several of the islands are WNW–ESE elongated (Fig. 4.1). Volcanic vents tend to form two distinct geochemical groups with different alignments (N150°E and N110°E–N120°E), possibly a result of regional trans-tensional deformation (Lourenço et al., 1998; Miranda et al., 2015). Eruptive styles have ranged from effusive Hawaiian and mildly explosive Strombolian through phreatomagmatic to Plinian and ignimbrite eruptions associated with caldera formation (Machado, 1959; Weston, 1964; Madeira, 1998; Cole et al., 2001; Calvert et al., 2006; Pimentel, 2007; Larrea et al., 2014; Sibrant et al., 2014). Effusive eruptions producing lava flows have usually been associated with the fissure zones. Besides on-going seismicity (Miranda et al., 2015), fault offsets of Holocene lava flows and cinder cones are evidence of on-going tectonic activity (Madeira and Brum da Silveira, 2003). Volcanic activity, earthquakes and storm-related activity potentially all cause episodic shedding of sediments from the islands.

Volcanoes in the central Azores have been historically active with events occurring since island settlement (Fig. 4.1; Gaspar et al., 2015). Young volcanic products can be found, for example, on Faial as historical lava flows and the <10 ka Capelo volcanic complex in the west of the island (Madeira, 1998; Madeira and Brum da Silveira, 2003). The rest of Faial is widely blanketed by volcanic deposits including ignimbrites, which were emplaced in a 1000 yBP explosive eruption of Caldeira Volcano (Pacheco, 2001; Pimentel et al., 2015). The whole of Pico Island is generally young and has continued growing over the Holocene (Woodhall, 1974).

The latest stages of basaltic lava flows originated from vents along the Fissural System in the middle of Pico Island and from Pico Mountain stratovolcano in the west (e.g., Forjaz, 1968; Woodhall, 1974; Zbyszewski et al., 1974; Madeira, 1998; Nunes, 1999). On São Jorge, the Young Volcanic Complex (<0.1 Ma) was unconformably deposited on both intermediate and old volcanic complexes in the centre of the island (Hildenbrand et al., 2008; Marques et al., 2018). On Terceira, major volcanic activity and the widespread ignimbrite were associated with the latest stages of growth of the west of the island since 23 ka (Self, 1976). Santa Bárbara volcano, Pico Alto Volcano and the fissure zone crossing the island still show signs of activity (Self, 1976; Féraud et al., 1980; Calvert et al., 2006; Gertisser et al., 2010).

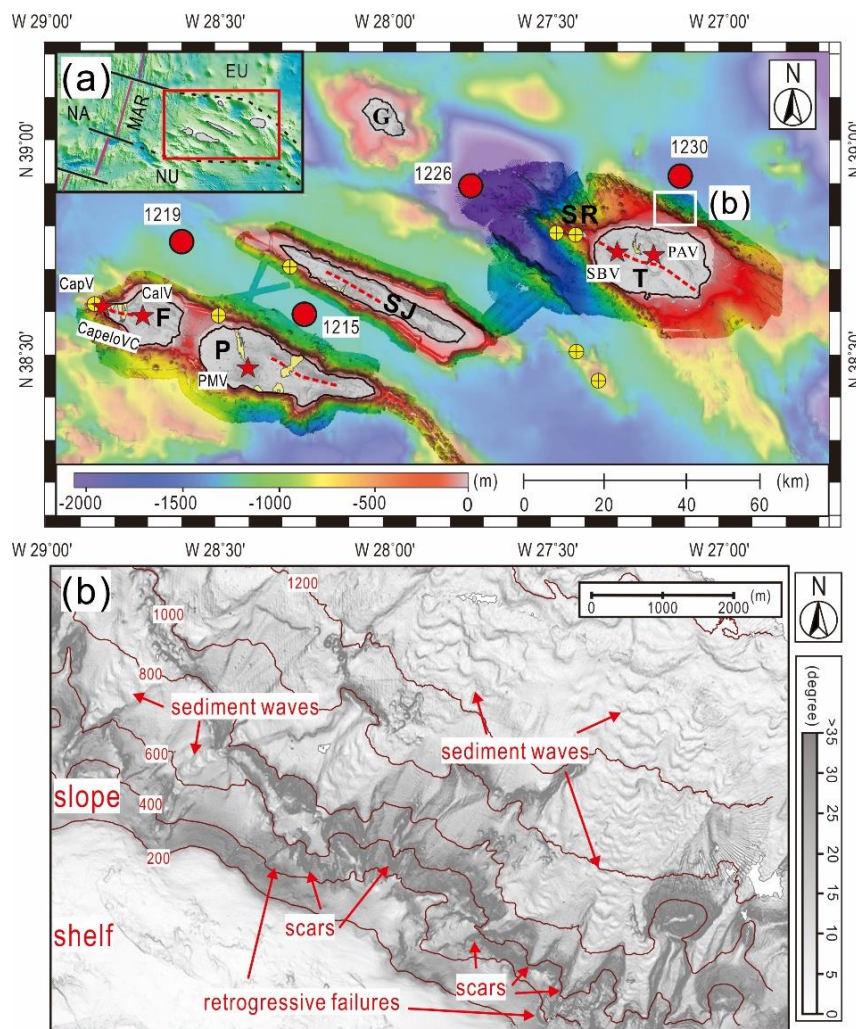


Figure 4.1. (a) Locations of the four investigated gravity cores (numbered red circles) between the five central Azores Islands (shown in grey with black outlines) of Faial (F), Pico (P), São Jorge (SJ), Graciosa (G), and Terceira (T) with the submarine Serreta Ridge (SR). Red stars and dotted lines are recently or presently on-land active volcanoes and fissure zones or cinder cone alignments. Volcanoes active in late Pleistocene and Holocene times are, from the west to east, Capelinhos volcano (CapV), Capelo Volcanic Complex (CapeloVC), Caldeira (CalV), Pico Mountain Volcano (PMV), Santa Bárbara Volcano (SBV), and Pico Alto Volcano (PAV). Yellow areas on land represent historical lava flows (Madeira 1998; Gaspar, 2003; Pimentel et al., 2016). Yellow crossed circles locate submarine eruption sites (Machado 1959; Weston 1964; Queiroz et al. 1995; Gaspar et al., 2015). Background bathymetry is from the Global Multi-Resolution Topography synthesis (GMRT; Ryan et al., 2009); higher-resolution foreground bathymetry (bold colours) is from surveys in 2003 (Mitchell et al., 2008) and 2011 (Chiocci et al., 2013). Upper-left inset: location of the central Azores Islands in the diffuse boundary between the Eurasia (EU) and Nubia (NU) plates. NA: North American plate. Purple lines locate the Mid-Atlantic Ridge (MAR). Solid black lines locate fracture zones near the Mid-Atlantic Ridge and dashed black lines outline the diffuse NU-EU plate boundary (Laughton and Whitmarsh, 1974; Lourenço et al., 1998). (b) Enlarged map of local gradients on the north flank of Terceira revealing morphological features of the submarine slope. Depth contours in 200 m. Map located by white rectangle in (a). The source of map is from surveys in 2011 (Chiocci et al., 2013).

Tall sea cliffs in the Azores indicate that coastal erosion also supplies terrigenous material, either onto shelves during current sea-level high-stand conditions or onto the submarine slopes by shelf spill-over. Zhao et al. (2019) documented the rapid erosion of the Capelinhos Cone since it was created by the eruption in 1957 (coastline initially retreating 164 m/y though with rate quickly declining after the eruption to 2 m/y). Zhao et al. (2020) used dated Holocene lava deltas and evidence of their previous extents underwater to work out retreat rates of 0.08 to 12.5 m/y at those deltas. Using a geochemical method, Louvat and Allègre (1998) inferred chemical denudation rates of 170–500 g/m²/y and mechanical denudation rates of 26–50 g/m²/y for Sao Miguel Island. These rates approximate to 0.06–0.18 m/y and 0.009–0.018 m/y when divided by a typical rock density of 2.7 kg/m³.

Production rates of carbonates on shelves are poorly known though artificial hardground experiments of Wisshak et al. (2010; 2015) southeast of Faial found rates as high as $\sim 631 \text{ g/m}^2/\text{y}$ (i.e., $\sim 0.225 \text{ m/y}$) at 60 m depth. Such high rates are typical of carbonate production, which varies strongly with timescale of measurement, tending to be higher when measured over short timescales (Schlager, 2000), so these values overestimate the production rates on ky-timescales. Nevertheless, carbonate production on shelves, along with material from subaerial and coastal erosion, probably provides significant amounts of sediment to the shelves and slopes that may end up being deposited in the basins around the Azores Islands. Indeed, abundant landslide scars in the upper slopes of the islands (Fig. 4.1b; Mitchell et al., 2008; Quartau et al., 2010; Chang et al., 2019) and sediment waves on their lower flanks (Fig. 4.1b) are evidence for frequent slope failures and transport by sedimentary flows (Casalbore et al., 2020).

4.3 Materials and methods

The four gravity cores described here were collected around the central Azores islands (Fig. 4.1) during RV *Meteor* cruise M141/1 in 2017 (Hansteen et al., 2017) and are curated in the core repository at the GEOMAR-Helmholtz Centre for Ocean Research Kiel, Germany. Sampling points marked by types of analysis are located in Fig. 4.2. Samples are identified by core number and depth (e.g., 1226-90 represents the deposits of core 1226 at 90 cm below the seafloor).

4.3.1 Visual core descriptions and sample selection

Each core was photographed and inspected visually to produce sedimentary logs summarizing grain size changes, sedimentary structures and tephra-rich beds (Fig. 4.2). On the basis of those observations, 66 samples were taken for detailed microscope analysis, 52 for electron microprobe (EMP) analysis, 28 for grain-shape morphometric analyses, 14 for X-ray diffraction (XRD) analysis and 35 for total organic carbon/total nitrogen analysis (TOC/TN) and 23 for carbon isotope analysis ($\delta^{13}\text{C}$).

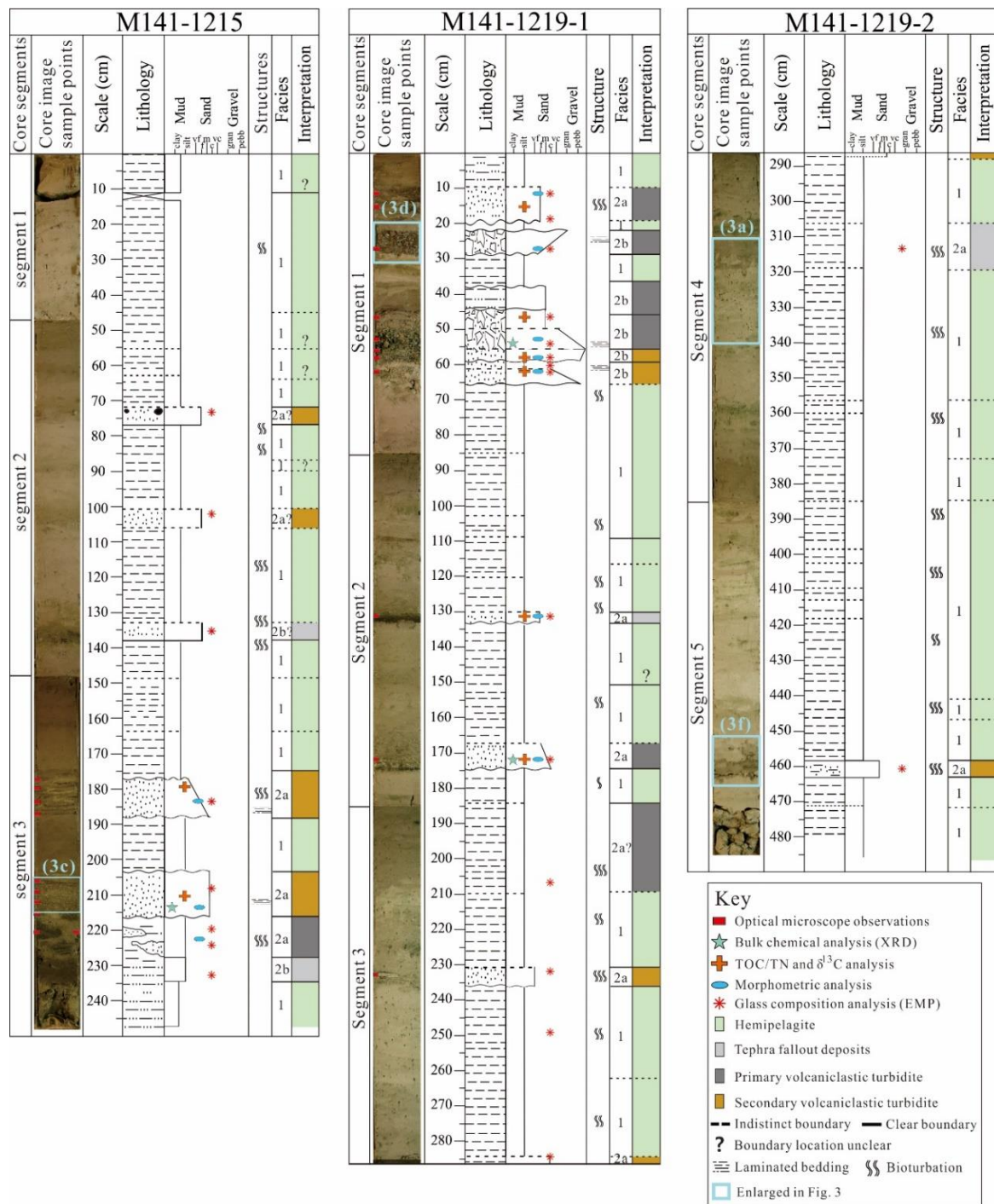


Figure 4.2. Photographic scans, interpreted lithological columns, grain size with locations of analysed samples, sedimentary structures, and facies interpretations of the cores located in Fig. 4.1. The interpreted changes in overall grain size and abundance of microfossils were based on reflecting microscope observations.

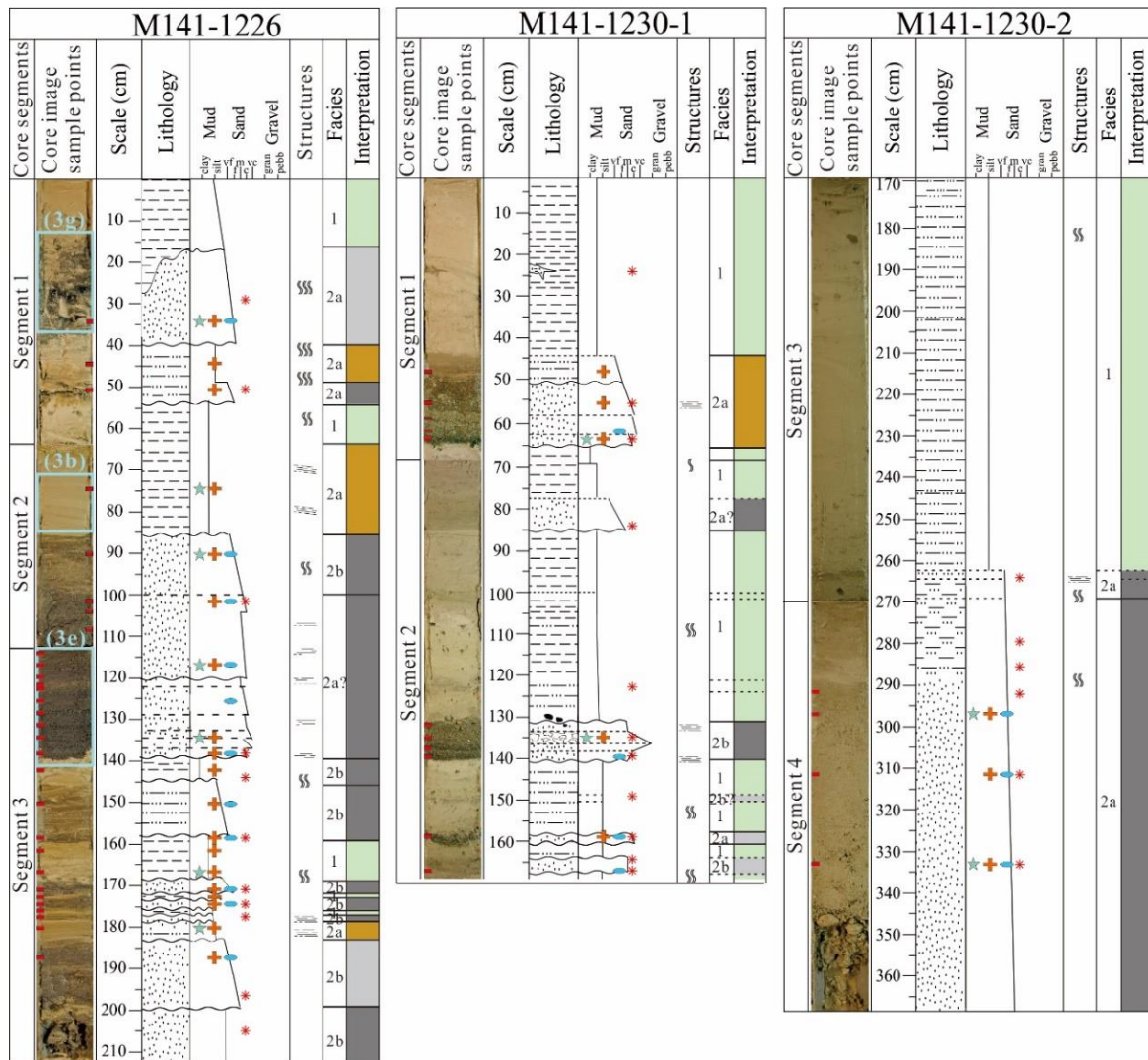


Figure 4.2. Continued

4.3.2 Volcanic glass geochemical analysis

Major element concentrations of volcanic glass shards were obtained by JEOL JXA 8200 wavelength dispersive electron microprobe (EMP) at GEOMAR Helmholtz Centre for Ocean Research, Kiel using procedures of Kutterolf et al. (2011). The size fraction 63–125 μm was extracted by wet-sieving. Glass shards were then selected and embedded in epoxy resin for analysis using a 15-kV accelerating voltage and 6 nA beam current at a defocused beam diameter of 5 μm . Lipari obsidian (peralkaline rhyolite; Hunt and Hill, 2001) and Smithsonian basalt VGA-99 (USNM 113498/1; Jarosewich, 2002) were used as standards. In each sample, 60 individual glass shards were analysed except in very shard-poor samples (<10 vol%), where

all visible glass shards were measured. Every sixty glass shard measurements were bracketed by four standard measurements (two of each standard). Results with total oxides <95 wt% and accidental shots on minerals were excluded. Measured major element concentrations of standard materials deviate by <0.5% from the expected values. All measured values were normalised to 100 wt% to eliminate the effects of varied post-depositional hydration and minor deviations of electron beam focus.

4.3.3 Morphometric analyses of volcanic grains

The volcanic grain shape characterization used in this study was based on the work of Cassidy et al. (2014) with adjustments as follows. Volcanic grains were first manually separated (not sieved) from samples chosen from volcanoclastic-rich deposits, with carbonate-free grains selected (samples were not acid leached). The grains such as those in Figs. 4.3a–4.3d were photographed under a high magnification stereo microscope with white paper as background. Image spatial calibration, transformation and morphometric measurements were carried out with ImageJ software (Rasband WS, 1997–2012, <https://imagej.nih.gov/ij>) as also used by Cassidy et al. (2014). We measured cross-sectional area, aspect ratio and perimeter length of 30 to 60 grains per sample until graphs of the measured characteristics no longer changed with further measurements. Cross-sectional area was calculated from the sum of dark image pixels for each grain. Aspect ratio was calculated from the ratio of long axis to short axis. Perimeter lengths were converted to normalised perimeter lengths (NPLs) by dividing by the circumference of a circle of equivalent cross-sectional area in order to remove the effect of particle size. The characteristic length scale of each particle, representing its grain size, was calculated from square root of grain area and converted to the phi scale.

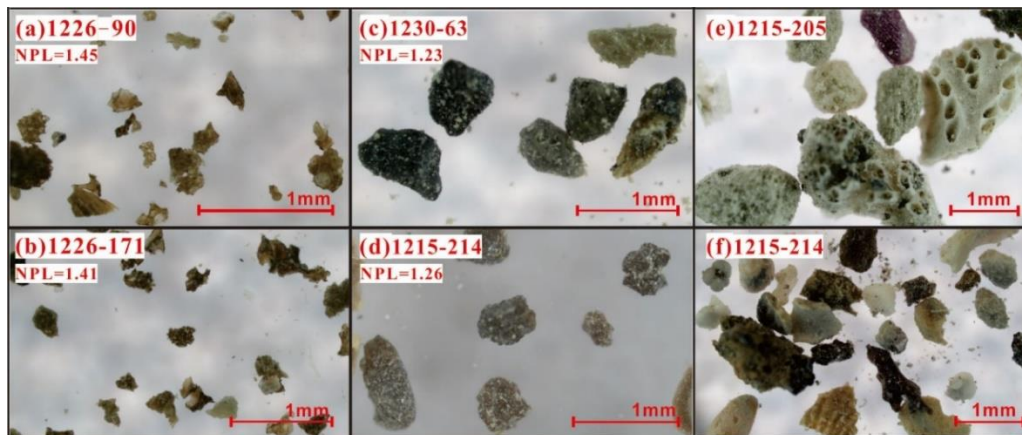


Figure 4.3. Selected photos (reflected light) of volcanic particles and bioclasts from different core samples. Samples are located in Fig. 4.2. (a, b): photos of angular vitric glass fragments from core 1226 at 90 and 173 cm. (c, d): photos of rounded volcanic clasts from core 1230 at 63 cm and core 1215 at 214 cm. (e, f): photos of coralline algae debris from core 1215 at 205 cm and foraminifera and shell fragments from core 1215 at 214 cm. All particles are from facies F2. NPL values were given in the photos of volcanic particles samples.

4.3.4 Bulk mineral assemblage analysis

Bulk sediment mineralogy was determined by X-ray powder diffraction (XRD) analysis. Samples were prepared following the methods of Charlier et al. (2006). Approximately 50 mg samples were powdered and analysed by Bruker D8 Advance diffractometer at the University of Manchester. A voltage of 40 kV and a tube current of 40 mA were used to produce $\text{CuK}\alpha 1$ X-rays at a wavelength of 1.5406\AA . Scanning range of the detector was set from $5\text{--}70^\circ$ (2θ) with a step size of 0.02° and 2s per count. Diffraction angle peaks were evaluated with EVA version 5, with a mineral database originating from the International Centre for Diffraction Data (ICDD). Bulk mineralogy fractions were semi-quantitatively estimated using peak-area measurements with an analytical error of 0.5% (e.g., Schultz, 1964).

4.3.5 Organic carbon and nitrogen and carbon isotope analyses

TOC was measured to assess potential organic carbon preservation and whether organic contents would help discriminate different types of sedimentary flow deposits. TOC/TN ratios and $\delta^{13}\text{C}$ were measured to provide information on carbon sources, in particular, algae and land plant sources (Meyers, 1994). The sediment samples were first powdered and then separated

into acid-untreated and acid-treated groups before measurements in multipurpose mass spectrometers at the University of Liverpool. Total organic carbon and organic carbon isotopes were measured on a subset of samples treated with 10% HCl. Total nitrogen was measured on a subset of samples without that HCl treatment. Standard samples were measured for every ten measurements. The operational detection limit of TOC was quoted as 0.1 wt%, although systematic differences in TOC between F2a and F2b suggests the detection limit may have reached closer to 0.05 wt% in practice. The average precision of $\delta^{13}\text{C}$ from repeated analyses is 0.2‰.

4.3.6 Discriminating pyroclastic fallout, primary turbidite and secondary turbidite

Emplacement mechanisms and origins (i.e., pyroclastic fallout and primary and secondary volcanoclastic turbidite) were determined by assessing all the information available from depositional structures, chemical compositions of volcanic glass shards and morphometric parameters of volcanic grains (Fig. 4.2).

Bed colour, lithological composition, tractional structures and sharp bed contacts allowed the identification of volcanoclastic-rich beds. Laminated bedding, erosive bases and appearance of shelf-derived carbonate fragments indicate emplacement by sediment flows (cf. Bouma, 1962; Stow and Piper, 1984; Talling et al., 2012). Homogeneous volcanic glass compositions probably originate from single eruptions, hence deposits with such compositional homogeneity also conforming to the above features were interpreted as primary turbidites or, if reasonably well sorted and without indication of horizontal transport (traction features), as pyroclastic fallout. Although fallout deposits can share some sedimentary features with primary volcanoclastic turbidites, such as normal grading and sharp basal boundaries (e.g., Sigurdsson et al., 2000; Carey and Schneider, 2011) and homogeneous chemical compositions, the high angularities (from both mean and standard deviation of NPL) are also helpful to distinguish them.

Heterogeneous geochemical compositions in sediment flow deposits instead reflect the mixing of particles from multiple sources, hence these are identified as secondary turbidites. However, interpretation of compositional homogeneity needs to consider possible complications. Erupted

magmas can be compositionally zoned, in which case observed compositions are genetically related although possibly in a complex fashion (e.g., Sigurdsson and Sparks, 1981; Freundt and Schmincke, 1995). Conduit erosion, pyroclastic flows or edifice collapses can also entrain material from previous eruptions of genetically related magmas but possibly also enhance the occurrence of lithic particles. On the other hand, an ocean island volcano may evolve either by repeatedly erupting the same magma compositions over time or by gradually developing more evolved compositions over time so that secondary turbidites originating by multi-stage slope failures can have glass compositions that are homogeneous or follow a genetic trend (Schneider et al., 2001; Hunt et al., 2011).

Although particles transported long distances by sediment flows are expected to become less angular (Manga et al., 2011), those of primary volcanoclastic turbidites transported short distances may remain sub-angular and maintain juvenile textures (e.g., Sigurdsson et al., 1980; Houghton and Landis, 1989), so they can be difficult to distinguish from fallout by morphometric data alone. Moreover, intense post-depositional bioturbation can mix sediments at the tops and bottoms of beds, which can undermine the suggested typical characteristics of different volcanoclastic deposits. The complexity of discrimination highlights that multiple types of parameters are needed to interpret emplacement process and origins of volcanoclastic grains.

Total organic carbon contents were not used as criteria for assigning beds to fallout, primary or secondary volcanoclastic deposits. Nevertheless, they were found to be supportive as some deposits with extremely low TOC are easily explained by rapid deposition of carbon-poor materials, as expected for primary volcanoclastic deposits.

4.4 Results

Three sedimentary facies (F1, F2a and F2b) were distinguished by the characteristics summarised in Table 4.1 with illustrating examples in Fig. 4.3. F1 represents clay-rich hemipelagite and F2 represents clay-poor volcanoclastic deposits. Facies F2 is further subdivided into carbonate-rich F2a and carbonate-poor F2b facies. Assigning the volcanoclastic beds to fallout, primary and secondary turbidite classes was then a complex task involving an

assessment of all the data available, bearing in mind the considerations above. In the following results, we highlight observations that support these choices of classes. Those interpretations are shown in the interpretation columns of Fig. 4.2. The full characteristics and interpretations of individual volcanoclastic-rich layers are provided in Appendix 4.1.

Table 4.1. Characteristics and interpretations of facies identified in sediment cores around the central Azores islands

Facies classification	Facies 1 Clay-rich hemipelagic mud	Facies 2a Carbonate-rich and clay-poor volcanoclastic deposits	Facies 2b Carbonate-poor and clay-poor volcanoclastic deposits
Lithology	Ungraded mud	1.Silt to pebble 2.Light-coloured sediments intercalated in the black sediments	1.Silt to pebble 2.Silt to coarse sand
Abundance of microfossils	Some and evenly distributed	1.Many but usually fragmented 2.Many	1.Few 2.Few
Sedimentary structures	Generally homogeneous mud. Dispersed burrows and mottled structures are common. Volcanic clast pods are occasionally found	1.Sharp scouring surface on the bottom. Apparent normal graded bedding with parallel laminations in the coarse grains. 2.Burrows, and inconsistent laminations	1.Sharp scouring surface at base; usually normal graded beddings, occasionally with inverse graded bedding in the middle 2.Normally graded. Often with bioturbated top
Bed lower boundary	Gradational change	1.Sharp erosive contact 2.Chaotic surface	1.Sharply erosive contact 2.Sharp contact occasionally with tephra intrusion into the lower bedding
Colours	Pale brown or pale grey occasionally with dispersed dark mottles in between	1.light to dark brown base with scattered white dots 2.Dark and light sediments unevenly mixed	1.Generally dark yet gradually lighter upward 2.Generally dark yet gradually lighter upward
Geochemical composition of volcanic glass	Mostly heterogeneous	1.Usually heterogeneous 2.Homogeneous and heterogeneous are possible	1.Usually homogenous 2.Homogeneous
Angularity of volcanic grains	Typically rounded, near-spherical	1.Typically rounded and near-spherical 2.Rounded and angular are possible.	1.Rounded and angular are possible. 2.Angular
Depositional process	Sediment slowly and progressively settled on seabed	1.Volcanoclastic turbidity currents incorporating shelf or slope carbonate material. 2.Intense bioturbation after volcanoclastic deposits were emplaced	1.Volcanoclastic turbidity currents with minor or without carbonate incorporated from shelf or slope. 2.Air fallout
Interpretation	Background sedimentation	1.Can be either primary or secondary event 2.Can be either primary or secondary event	1.Mostly primary event and rarely secondary event 2.Primary fallout

*Numbers in facies 2a and 2b columns associate aspects of the facies that were used to interpret the emplacement mechanisms.

4.4.1 Facies visual descriptions

The sediment was first classified into two facies (F1 and F2) based on the relative abundance of clay and volcanoclastic particles. F1 is mainly composed of homogenous ungraded pale brown/grey mud to silt. Mottled structures, dispersed tephra grains and gradual colour changes are common (Fig. 4.4a). The abundance of microfossils in F1 is intermediate to high.

F2 includes clay-poor volcanoclastic-rich deposits. The grain sizes of F2 beds vary from fine (silt to fine sand) to coarse (medium sand to pebble) beds. F2 varies in colour from light to dark brown (Figs. 4.4b–4.4g). Basal bed contacts are commonly sharp but upper bed contacts can be gradual and diffuse. Sedimentary structures typical of turbidites are common, such as laminations, ripples, internal erosive surfaces and normally graded sequences (cf. Bouma, 1962; Stow and Piper, 1984; Talling et al., 2012), though inverse grading occasionally appears in the middle of beds (Fig. 4.4d). Turbidite structures are more apparent in coarse-grained than in fine-grained deposits (Figs. 4.4c to 4.4e). Burrows (bioturbation) are more common in fine-grained deposits (Figs. 4.4c, 4.4e, 4.4f and 4.4g).

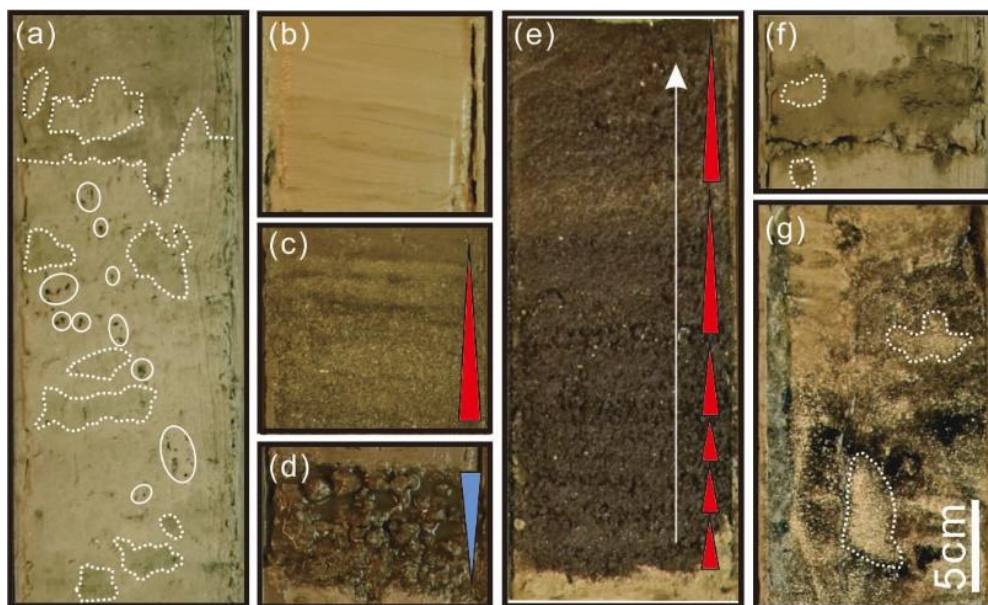


Figure 4.4. Enlargements of core sections located by light blue rectangles in Fig. 4.2 illustrating sedimentary structures in each facies. (a) Bioturbated burrows in F1 (outlined by white dotted lines). Mafic grains dispersed by bioturbation are marked by white ellipses. (b) Gently dipping ripple marks in F2a. (c) Parallel laminations and normally graded bedding (red triangle). (d) Inverse-graded bedding (blue triangle) in F2b with scoured underlying surface. (e) An upward fining sequence (white arrow) in F2b comprising multiple normally graded beds

(red triangles) with sharp underlying boundary. (f) Burrows in a secondary turbidite of F2a. (g) Features caused by intense bioturbation, which have led to incorporation of carbonate in otherwise carbonate-poor volcanoclastic deposits. The distance scale shown is common to all photos.

Interpretation

F1 was formed of fine grains and microfossils such as foraminifers deposited by settling in a largely quiescent ambient environment. Mottled structures are caused by mud-feeding biota burrowing the sediment which are commonly observed in (hemi)pelagic beds (Wetzel and Uchman, 2012). Dispersed volcanic shards are the results from either bioturbation or later settling of ash transported by varied processes through water column (Scudder et al., 2016). The gradual and slight colour variations of these beds are associated with varied organic matter content and redox variations (e.g., Savrda et al., 2001; Hoogakker et al., 2004). Bioturbation can incorporate particles from nearby beds, which may explain dark patches of volcanic-rich sediment found in the two analysed hemipelagic samples (e.g., core 1226 at 55 and 167 cm). The volcanoclastic particles in F2 could be derived either directly from volcanic activity (e.g., pyroclastic fallout or primary volcanoclastic density currents) or from reworking of volcanic material (e.g., submarine landsliding and coastal erosion). In many cases, the fallout beds contain normally-graded vesicular pyroclastic particles with a higher concentration of crystals at their bases and are commonly bioturbated at their tops (Carey and Schneider, 2011). Although normal-grading and bioturbation structures can also commonly appear in the primary and secondary volcanoclastic turbidites, coexisting laminated sedimentary structures and ripples more likely originated from sediment density currents (Bouma, 1962; Stow and Piper, 1984; Talling et al., 2012). We interpret crudely-graded/structureless coarse-grained beds with erosive basal contacts as corresponding with sandy Bouma sub-divisions T_a, laminated coarse-grained beds as corresponding with sandy Bouma sub-divisions T_b to T_c, and fine-grained beds with poorly developed lamination with T_d to T_e (Bouma, 1962; Walker, 1978). Material such as shelf-origin coralline algae debris and shell fragments (Figs. 4.3e and 4.3f) admixed in these volcanoclastic deposits also favor emplacement by turbidity currents over a pyroclastic fallout

origin. However, we are also aware that the typical characteristics of fallout deposits and turbidites may be obscured or modified by post-depositional bioturbation. The complexity and part similarity of sedimentary structures between different types of volcanoclastic deposits reflect that other parameters are still needed to assure the emplacement mechanism interpretation.

4.4.2 Volcanic glass geochemistry

Examples of geochemical variations in MgO and SiO₂ of volcanic glasses extracted from F2 beds are shown in Figs. 4.5 and 4.11 (full glass data are provided in Appendix 4.2). Major element concentrations of volcanic glasses can be classified as three groups based on composition. The geochemical compositions of the volcanoclastic beds in two of the groups tend to cluster tightly (e.g., core 1230 at 158–160 cm shown in Fig.4.5), though rare outliers occur more often in one of them (e.g., core 1230 at 138–140 cm shown in Fig. 4.5). The last group, in contrast, have a scattered range of geochemical compositions (e.g., core 1215 at 208–210 cm shown in Fig. 4.5).

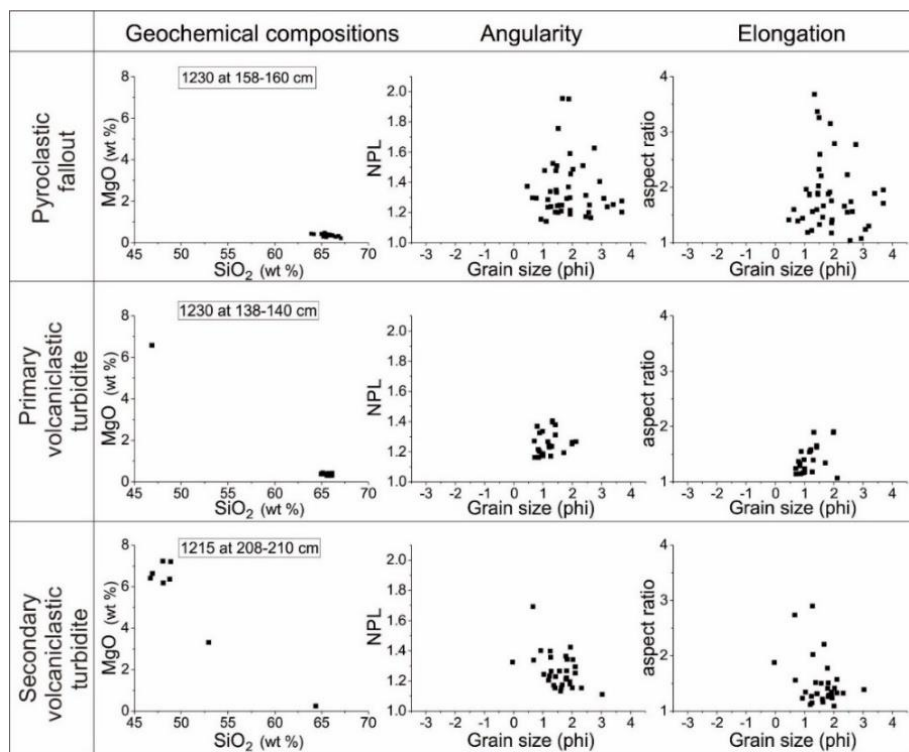


Figure 4.5. Geochemical (left panels) and morphometric characteristics of volcanic particles from selected beds representing the three deposit types found in facies F2. NPL: normalised perimeter length. Diagrams for all analysed beds can be found in appendix 4.1.

Interpretation

A relatively homogeneous chemical composition of vitric particles in a volcanoclastic-rich bed favours a primary syn-eruptive origin, suggesting a probable origin by either fallout or discharge of pyroclastic flows into the sea where they transformed into turbidity currents without significantly eroding earlier volcanoclastic substrates of other compositions (Carey and Schneider, 2011). Volcanic glasses transported through primary processes usually cluster in a narrow range of geochemical compositions due to little mixing with older tephra, although eruptions of compositionally zoned magma or old strata exhumed can produce a genetically related range of glass compositions in the deposit. While the structural and textural appearance of secondary turbidites formed by reworking of volcanoclastic materials is very similar to that of primary turbidites, the glass particles commonly display a broad compositional spectrum instead of a tight cluster because of mixing of particles from multiple sources. Such mixtures can originate from a wide choice of processes ranging from exposed tephra particles eroded by wind and water (Carey and Sigurdsson, 1984; Reid et al., 1996; Le Friant et al., 2004) to large-scale mass wasting such as submarine landsliding (Moore et al., 1994; Masson et al., 2006). However, whether chemical variation is compositionally homogeneous or heterogeneous may be not so straightforward sometimes, so other information is required to reduce uncertainty of interpretation.

4.4.3 Morphologies of volcanic grains

Three examples were selected to illustrate the morphometric features of the different types of volcanoclastic deposits along with their geochemical compositions (Fig. 4.5; full set of morphometric measurements in Appendix 4.3). There is no or only a slight systematic variation of either NPL or aspect ratio with grain size for individual samples (Fig. 4.6). We chose a limiting NPL value of 1.28 to sub-divide the samples into two groups as shown in Fig. 4.6a (black and red colours). There is apparently no corresponding difference in aspect ratio between the two groups (Fig. 4.6b).

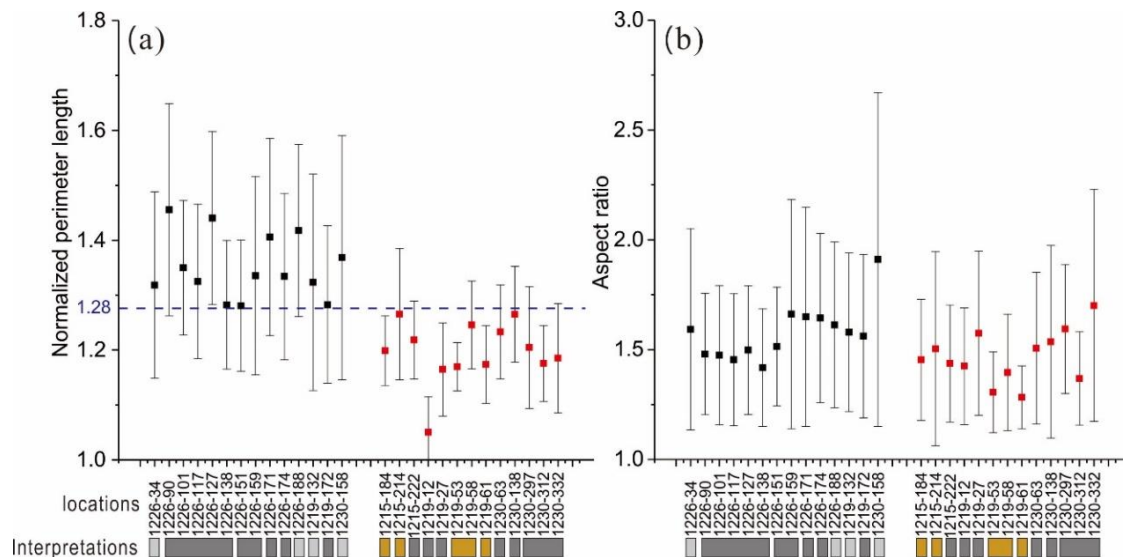


Figure 4.6. Average values (solid squares) and one standard deviations (bars) of (a) normalised perimeter length and (b) aspect ratios of samples located in Fig. 4.2. Colours of rectangles below the graphs correspond with the right-most interpretation panels in Fig. 4.2. Rectangles crossing multiple samples are taken from the same bed but different locations. The data have been sorted into two groups with $NPL > 1.28$ (black symbols) and $NPL < 1.28$ (red symbols), which are interpreted as having without (black) and with (red) intense abrasion.

Interpretations

The shapes of volcanic particles can be clues of transport process (e.g., Manga et al., 2011; Cassidy et al., 2014). Abrasion and comminution of clasts both can occur during transport (e.g., Walker, 1981). Abrasion is expected to increase the roundness of clasts, whereas comminution may decrease roundness. Angular and elongated particles are interpreted to have experienced less grain-grain interactions than rounded and equidimensional particles (e.g., Manga et al., 2011; Cassidy et al., 2014). Angular particles are typical for air-transmitted deposits from low-concentration ash clouds with few grain-grain contacts while rounded particles are commonly observed in deposits from sediment flows, particularly those in which high particle concentration or intense bed-load transport produce frequent intense particle contacts (Wilson and Hildreth, 1998). Cassidy et al. (2014) also suggested that particles emplaced purely by air should be distinguishable from particles emplaced in sedimentary flows if the later involve

intense grain-grain interactions that cause grains to progressively become more spherical and develop smooth surfaces.

As expected, the suggested pyroclastic fallout deposits have NPL values that are higher on average and more varied than those of the suggested secondary turbidite deposits (Fig. 4.5). However, the NPL values of the primary turbidite deposits can be either high or low. Considering that the cores are in proximal locations, the varied NPL values of the primary turbidite deposits may be due to the short distance of transportation, reducing the time for abrasion. Although the NPL values of fallout deposits are distinct from secondary turbidite deposits, a combination of chemical compositions and sedimentary structures are still required to convincingly separate fallout deposits from primary turbidite deposits.

Particles with high NPL are angular and/or elongated; hence aspect ratio is also potentially useful to assess the contribution of elongation to NPL values. The samples of the high NPL group do not typically have high aspect ratios, so the high NPL values are mainly due to grain angularity rather than elongation, as can be seen in sample photos (Figs. 4.3a and 4.3b). While angularity (NPL) is reduced by abrasion (Krumbein, 1941), elongation (aspect ratio) will mainly be reduced by comminution. The similarity of aspect ratios between the high and low NPL groups in Fig. 4.6 implies that particles have only become moderately rounded by abrasion and have not broken up greatly during transport. Alternatively, the source eruptions did not produce significant amounts of elongated grains.

4.4.4 Bulk mineral assemblage

The XRD data of the F2 volcanoclastic turbidites (Fig. 4.7) revealed volcanic minerals (anorthoclase, plagioclase, clinopyroxene, olivine, amphibole and biotite, which are phenocryst phases found in the mildly alkalic or peralkaline volcanic rocks on the Azores islands), marine authigenic and biogenic minerals (e.g., calcite and aragonite) and quartz. Comparatively high abundances of amorphous material exist in some samples and was microscopically identified as glass shards. The light-coloured F2 volcanoclastic turbidites possess more biogenic material (up to 25%) than the dark-coloured F2 turbidites (~5%), although mineralogical assemblages are otherwise similar. We sub-divided facies F2 into F2a and F2b based on carbonate contents

of >10% and <10%, respectively (Fig. 4.7). The biogenic material was microscopically identified as foraminifera, shell fragment and coralline algae debris (e.g., Figs. 4.3e and 4.3f). High carbonate percentages can exist in both primary (e.g., 1230-332) and secondary turbidites (e.g., 1215-214).

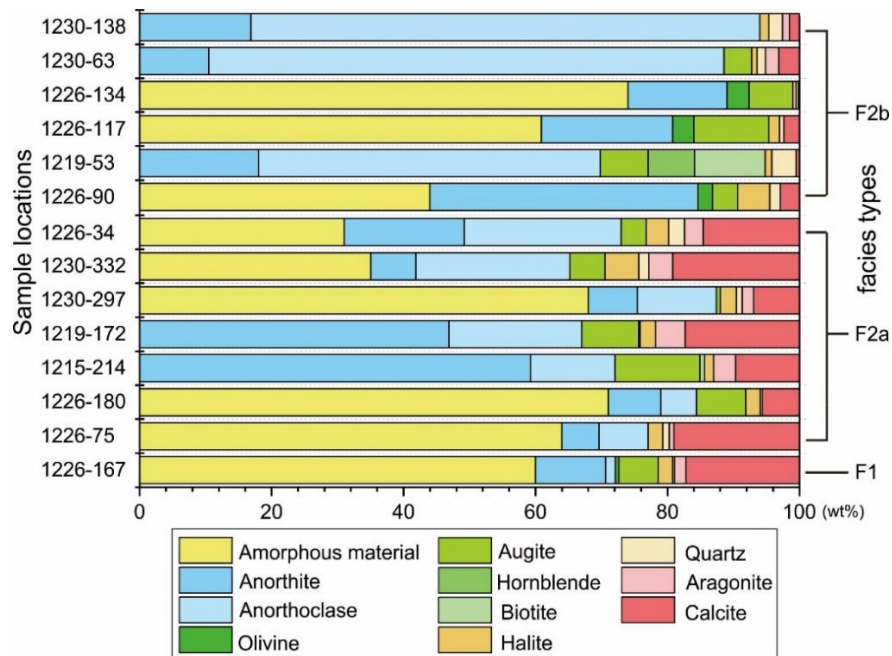


Figure 4.7. Mineral assemblages from XRD analyses of bulk sediment samples. Yellow bars represent amorphous material. The two blue bars represent feldspars. The four green bars represent ferromagnesian minerals. The red and pink bars represent carbonate minerals.

Interpretation

The bulk mineral assemblages of the samples are similar to those on the present-day shelf (e.g., Valente, 2020), although carbonate contents on the shelf vary more greatly and are generally higher (10–90%; Quartau et al., 2015) compared to our F2a volcaniclastic beds (<25%; Fig. 4.7). Remobilization of shelf biogenic material or slope particles originating from shelf spill-over should be the cause of higher carbonate concentrations in F2a than F2b volcaniclastic turbidite deposits, given that most of the biogenic material occurring in F2a is of shelf origin (Figs. 4.3e and 4.3f; Wisshak et al., 2014). The low carbonate content in F2b could be attributed to the lack of incorporated shelf origin bioclasts. For example, volcaniclastic grains may have only settled through the water column (e.g., pyroclastic fallout) or transported over a

carbonate-starved shelf platform. Remobilization can occur in either primary or secondary turbidity currents. For instance, primary volcanoclastic density flows can incorporate unconsolidated shelf bioclasts (e.g., Whitham, 1989; Trofimovs et al., 2008). Alternatively, volcanic island submarine slopes or outer shelves may become unstable and collapse, sourcing secondary turbidity currents containing both volcanoclastics and bioclasts (e.g., Quartau et al., 2015). The high fraction of glass in the volcanoclastic-rich deposits can also indicate the origin of the primary volcanoclastic material. Scarcity of volcanic glass or mixture of volcanic glass compositions probably imply re-deposition from terrestrial deposits.

4.4.5 Total organic carbon, total nitrogen, and carbon isotopes

All facies have low organic carbon contents (Fig. 4.8; full data are provided in Appendix 4.4). F1 has the highest (>0.15 wt%), F2a has intermediate (slightly > 0.1 wt%) and F2b has the lowest organic carbon content (<0.1 wt%). Fine-grained samples of F2a (light orange bars in Fig. 4.8) have slightly higher organic matter contents on average than the coarse-grained samples of F2a (dark orange bars in Fig. 4.8). The F2a TOC/TN ratios are 5–15 and $\delta^{13}\text{C}$ values are -18‰ to -25‰ (Fig. 4.9). The corresponding values for the F2b samples are 5–10 and -22‰ to -27‰, respectively.

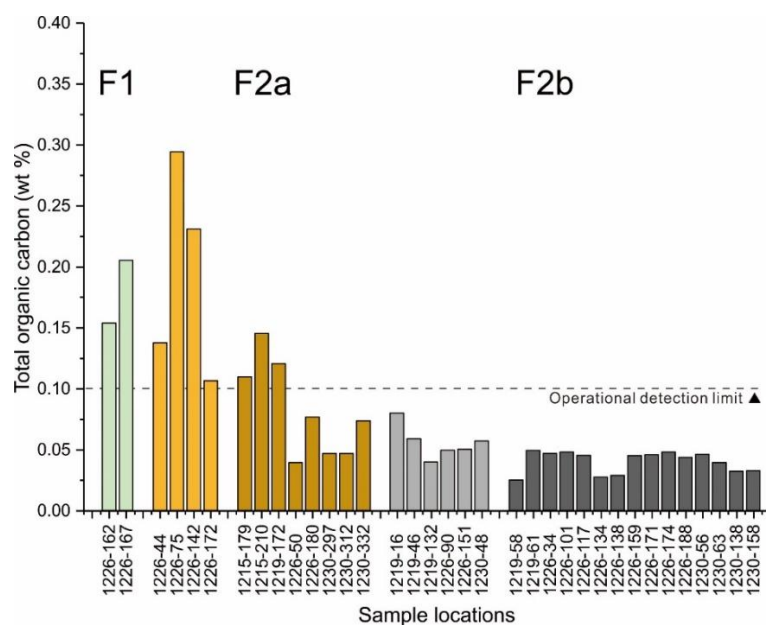


Figure 4.8. Organic carbon contents of the samples located in Fig 4.2 sorted by facies. The light and dark tones of the colour bars are used to represent fine- and coarse-grained sediments of F2a and F2b. The 0.1 wt.% operational detection limit is marked.

Interpretation

The overall low TOC contents could be attributed to low input of organic matter and poor preservation after deposition, such as slow sediment accumulation rates and oxidised bottom water bodies (Cowie et al., 1995). Although lying around the analytical detection limit, the lower TOC contents of F2b compared with F2a are consistent with less or no mobilised shelf or submarine slope biogenic material in F2b, supporting a primary volcanoclastic interpretation for F2b in this study.

The TOC/TN ratios and $\delta^{13}\text{C}$ values help to constrain the origins of the organic matter. According to Meyers (1994), TOC/TN ratios of algae typically vary from 4 to 10, whereas ratios for land plants are usually >20 . Marine organic matter typically has average $\delta^{13}\text{C}$ values between -22 and -20‰ . C_3 and C_4 land plants have average $\delta^{13}\text{C}$ values of -27‰ and $\sim -14\text{‰}$, respectively. The TOC/TN ratios and $\delta^{13}\text{C}$ values of our samples show a dominant marine-algal origin. The F1 and F2a samples also contain minor carbon from land plants (Fig. 4.9). The organic matter in some F2b samples appears to originate from freshwater algae, likely derived from island drainage.

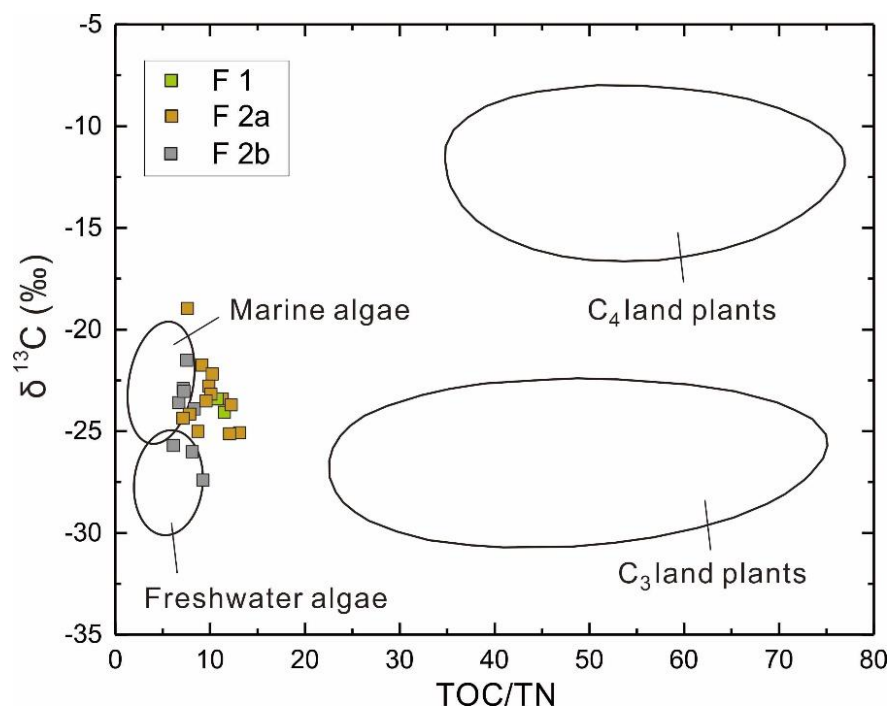


Figure 4.9. $\delta^{13}\text{C}$ and ratios of total organic carbon and total nitrogen for the samples located in Fig 4.2. Reference data fields (ellipses) after Meyers (1994).

The modestly higher organic matter concentration in F2a than in F2b (Fig. 4.8) suggests incorporation by turbidity currents of shelf or slope material (e.g., Figs. 4.3e and 4.3f) containing some organic matter and its subsequent preservation by rapid burial. Although shallow sediments lie in an oxidising environment, organic matter preservation is also facilitated by the high productivity of coastal seas (Martin et al., 1987) and the effects of bioturbation (Emerson and Hedges, 1988). The higher organic matter concentration in finer-grained sediments (F2a) than those in coarse-grained sediments (F2b) may be an effect of total particle surface area (Bergamaschi et al., 1997). Organic matter can be absorbed on mineral surfaces, protecting it and slowing the rate of remineralisation (Keil et al., 1994).

4.5 Discussion

In total 42 volcanoclastic-rich beds were identified. Among these volcanoclastic beds, 24 of them are F2a and 18 of them are F2b. F2a comprises 4 pyroclastic fallout beds, 8 primary turbidites and 13 secondary turbidites. F2b comprises 5 pyroclastic fallout beds and 11 primary turbidites. Although the lack of biogenic material was a characteristic used to discriminate primary and secondary volcanoclastic deposits in offshore Montserrat (Trofimovs et al., 2013; Le Friant et al., 2015), 12 primary volcanoclastic beds have relatively high carbonate contents in these cores. This could be attributed to the incorporation of shelf sediments during transport and/or intense post-depositional bioturbation mixing carbonate particles from the tops or bases of beds (e.g., core 1226 at 18–40 cm). Therefore, we highlight that other data are still needed to interpret transportation mechanisms instead of counting individual characteristics, as illustrated here.

Assigning uncertainties to the volcanoclastic bed emplacement interpretations (fallout, and primary and secondary volcanoclastic turbidites) is difficult given the many parameters were used. Those emplacement interpretations are less certain where individual parameters do not indicate bed type clearly (e.g., core 1215 at 133–137 cm and core 1230 at 78–86 cm). (*The segment in the core 1230 at 168-262 cm will be reinterpreted in Chapter 6 from hemipelagite to primary volcanic turbidites based on new available samples and analyses*) Nevertheless, in most samples, all parameters indicated the emplacement type consistently, so the above relative

proportions of different types should be reliable. To allow readers to assess the interpretations for themselves, the full set of sample classifications and parameters is included in Appendix 4.1.

Landslide scars such as those in Fig. 4.1b are common around the Azores islands and earthquakes potentially triggering slope failure are frequent, suggesting that associated turbidity currents should occur frequently. The modal volume of landslide scars for Faial, Pico, São Jorge and Terceira lies in the 10^5 – 10^6 m³ range (Chang et al., 2021). If a 10^6 m³ volume of mobilised slope sediment were distributed uniformly over basins of roughly 20*20 km dimensions (Fig. 4.1a), they would generate deposits of 2.5 cm in thickness. Although having only half the 10^5 – 10^6 m³ frequency, scars an order of magnitude larger in volume are also common. Therefore, secondary volcanoclastic deposits of 2.5–25 cm thickness derived from slope failure should be common. *(A more comprehensive turbidite volume modelling for different depositional basins will be conducted in Chapter 6)*

The results summarised in Fig. 4.2 (right-most column), however, suggests that secondary volcanoclastic deposits are not the overwhelming majority. Rather the cores are dominated by primary volcanoclastic turbidites, particularly in cores 1226 and 1230. We interpret the dominance of primary over secondary turbidites as either due to sedimentary flows generated by slope failure not all running out to the basin floors or to volcanic eruptions generating the primary beds being more frequent than the slope failures or some combination of these effects.

4.5.1 Origins of volcanoclastic turbidites

Primary volcanoclastic turbidites should mostly reflect adjacent eruption history rather than more distant eruptions. Hence, those in core 1219 should be mainly sourced from Caldera Volcano on Faial island (Fig. 4.1), although the Capelo Volcanic Complex is another possibility. The site is also flanked by submarine cones of NW São Jorge and NW Faial, although it is currently unclear how active they are (Mitchell et al., 2018). Those in core 1230 could be sourced from Santa Bárbara or Pico Alto volcanoes on Terceira. The primary volcanoclastic turbidites in core 1215 may originate from Pico and/or São Jorge Islands. Core 1226 within the

Terceira Rift may have received primary volcanoclastic turbidites from Terceira or from submarine eruptions on the Serreta Ridge, which is volcanically active (Gaspar et al., 2003). The upper submarine slopes of the islands contain abundant scars from upper-slope landslides and retrogressive failures in their outer shelves (Fig. 4.1b), so they are potential sources of the secondary volcanoclastic turbidites. Emplacements of secondary volcanoclastic turbidites seem to be randomly distributed in each core and there are no clear major differences in occurrences between them. Their common occurrences amongst the cores could ultimately reflect triggering of slope failure around all the islands, such as by earthquakes or storm waves. *(The influences of intense effects of ocean surface waves on sediment transport processes will be addressed in Chapter 5)*

4.5.2 Applicability of morphological analysis of volcanic grains in other volcanic settings

Cassidy et al. (2014) presented volcanic grain morphometric data for volcanoclastic beds that had known transport origins. Our analysis method differs from theirs as we measured fewer grains in each sample and classified deposits using a different parameter, normalised perimeter distance (NPL), so we have investigated if our method would also separate the samples of Cassidy et al. (2014) into the same two groups assigned by them.

The results shown in Fig. 4.10 have both slightly lower average and standard deviation of NPL and aspect ratio than those of the Azorean samples in Fig. 4.6. The 1.23–1.20 NPL value that allows a separation between two types of deposits in the results of Cassidy et al. (2014) is smaller than 1.28 in Fig. 4.6. This difference might be either due to higher angularity of grains in the Azores cores or to the ~300 volcanic grains measured by Cassidy et al. (2014) compared with only 30–60 in each of our samples. If the number of grains measured were important, we would expect a more confined range and perhaps also a lower separation value of NPL in the Azorean samples if more measurements were made. Otherwise, a unique separation value of NPL may be found in each volcanic setting if the morphometric characteristics are dominantly controlled by original characteristics such as solid and bulk densities, vesicle textures, primary particle shapes and glass/crystal ratios. Although slight differences exist in the two sets of results, both sets of graphs still show pyroclastic fallout tending to have a higher average and

variability of NPL than the deposits emplaced by turbidity currents. This consistency suggests that the more limited morphometric analysis conducted here is effective and potentially could be applied to other volcanic settings.

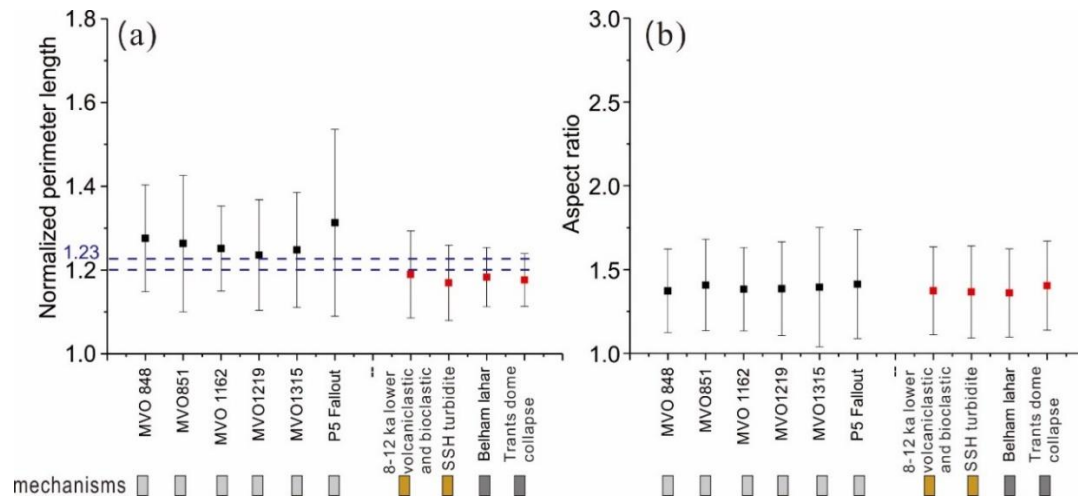


Figure 4.10. Average values (solid squares) and one standard deviations (bars) of (a) normalised perimeter length and (b) aspect ratios of volcaniclastic particles constructed in the same style as Fig. 4.6 from the data of Cassidy et al. (2014), where the transport process was known independently. Colours of rectangles below the graphs correspond with the key in Fig. 4.2. The data have been sorted into pyroclastic fallout (black squares) and primary and secondary volcaniclastic turbidite (red squares) in each panel. Pyroclastic fallout has $NPL > 1.23$ and without intense abrasion (black symbols). Turbidite instead has $NPL < 1.2$ with intense abrasion (red symbols).

4.5.3 Lateral correlation of pyroclastic fallout beds

The glass shard compositions cluster tightly in each of the four cores but differ between the cores, apart from a few outliers (Fig. 4.11). This suggests that fallout beds cannot be correlated between cores and that each core had its own volcanic source. (*Tephra bed correlations between land and sea will be addressed further in Chapter 6*) The highly evolved glasses in core 1230 taken north of Terceira derive from the trachytic/comenditic eruptions on that island (Calvert et al., 2006; Jeffery et al., 2018). Ashes with such evolved compositions did not reach core 1226 between Terceira, Graciosa and São Jorge, which only contains mafic glass shards. The compositions of core 1226 differ from those of glass shards in cores 1215 and 1219 between Faial, Pico and São Jorge, suggesting a closer source, such as basaltic eruption on

Terceira (Self et al. 1976) or at the Serreta Ridge. Association of the glass shards in cores 1215 and 1219 with sources on the surrounding islands is not presently possible, although dating and trace element glass analyses in the future may help. Although sedimentation rates vary with bathymetry and distance from islands, the most extensive volcanic history preserved in those cores is <100 ky, which is roughly estimated from the length of hemipelagic sediments (F1) divided by the hemipelagic sedimentation rate (3.5 cm/ky) in the central Azores basin (Vlag et al., 2004). Hence, the cores contain a comparable range of eruption history to deposits on the islands and partly within ^{14}C dating range. (*Depositional history and sedimentation rates of four sediment cores will be revealed in Chapter 6 based on twelve ^{14}C dates and two correlated ignimbrites.*)

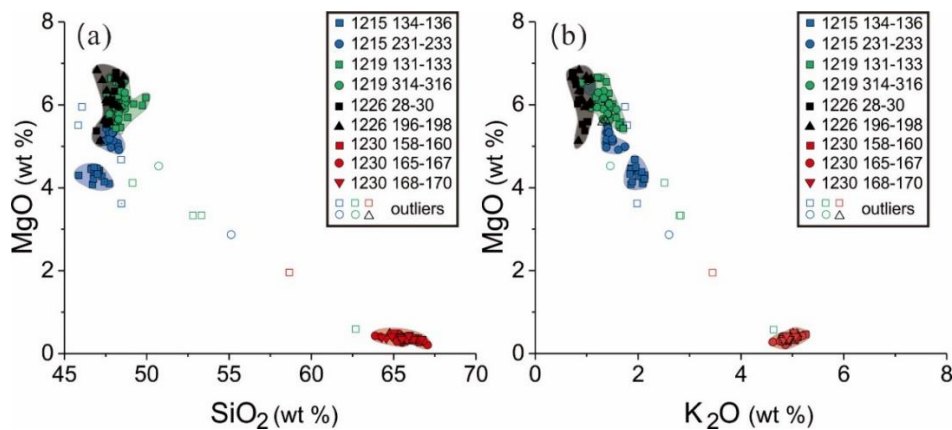


Figure 4.11. Geochemical variations of volcanic glasses in selected samples interpreted as fallout. (a) MgO versus SiO_2 . (b) MgO versus K_2O . Note that outliers have been left unfilled to avoid distraction from the clusters.

4.5.4 Comparing thicknesses of volcanoclastic beds with those near other oceanic islands

Thickness frequency distributions have been used to characterise turbidite sequences from other settings (Hiscott et al., 1992; Beattie and Dade, 1996; Talling, 2001). Such thickness frequency distributions can reflect the relative importance of large versus small turbidite beds. For example, volcanoclastic beds in the Izu-Bonin forearc basin show such a distribution with a magnitude of the gradient β slightly above 1.0 (purple dashed line in Fig. 4.12c; Hiscott *et al.*, 1992).

We use the similar approach, which is useful to compare volcanoclastic bed abundances over certain thickness ranges between the islands. A limited dataset of volcanoclastic bed thicknesses was obtained from near Gran Canaria (Sumita and Schmincke, 1998), Reunion (Saint-Ange *et al.* 2013), the Cape Verde islands (Eisele *et al.* 2015a, b) and the Azores, which allows comparison between island groups of contrasting volcanic history and core sampling proximity to the islands. Due to the varied and commonly less detailed analyses that are available for these cores compared with the Azores cores, the different types of volcanoclastic beds were typically not all well discriminated and some may have been overlooked where they had weakly contrasting colour with other sediments. To compare with the Azores results on the same basis, therefore, we counted bed thicknesses from all types of volcanoclastic-rich beds in each site as though they were a single type.

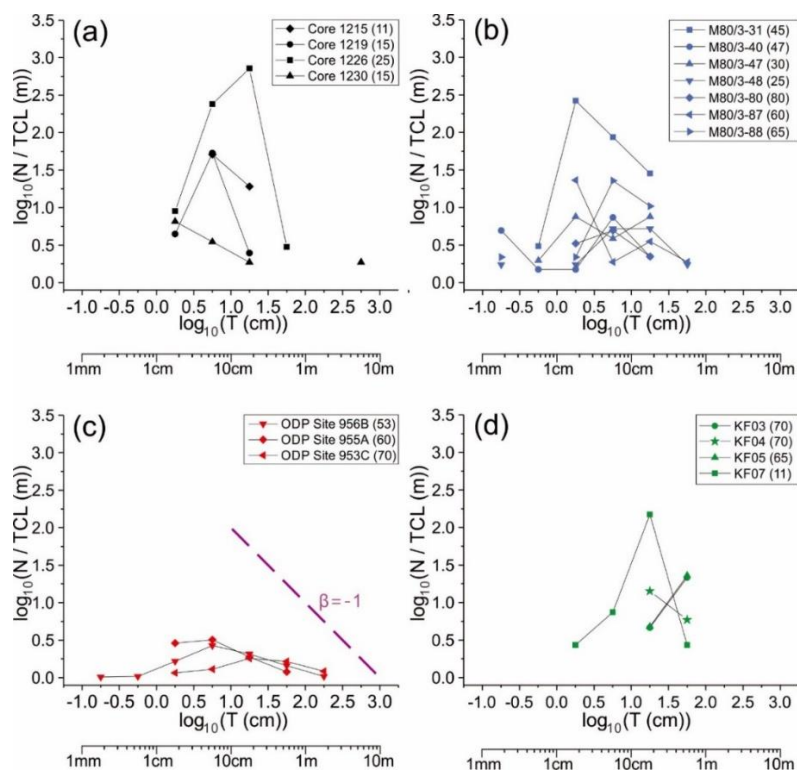


Figure 4.12. Thickness frequency distributions of volcanoclastic beds preserved in comparatively proximal drilling sites of different volcanic settings (a) the central Azores (b) Cape Verde (c) Gran Canaria and (d) Reunion island. Counts of volcanoclastic beds (N) divided by total core length (TCL) are plotted against volcanoclastic bed thickness (T). The distances of cores to the coasts (km) are noted in the legends after the core sites. Note that both axes are logarithmic. The purple dashed line represents a graph-gradient of $\beta = -1$, which is similar to that found for volcanoclastic beds in the Izu-Bonin cores (Hiscott *et al.*, 1992).

The results in Fig. 4.12 show that the central Azores and Cape Verde islands have similar thickness distributions, with both commonly having 2–20 cm volcanoclastic beds. Although the length of cores from the central Azores and Cape Verde islands are too limited to determine their complete distributions, the graphs are compatible with rapid declines in frequency after the peaks, suggesting that small beds are important over the sediment depth sampled by coring. The Gran Canaria cores (Fig. 4.12c), in contrast, have more than an order of magnitude smaller frequency of decimetre-scale beds than either the Azores or Cape Verdes cores. The shallow graph gradient (small magnitude of β) for the data above $\log_{10}(T)$ of 0.5 shows that the larger beds are proportionally more important relative to small beds than for the Izu-Bonin cores (purple dashed line in Fig. 4.12c; Hiscott *et al.*, 1992). Core logs of Gran Canaria shown in Sumita and Schmincke (1998; their figure 21) are also noticeably episodic, with typically 20 m non-volcanoclastic-rich intervals between clusters of volcanoclastic beds. Both features reflect a different volcanic evolution of Gran Canaria, which was episodic and explosive over the period of volcano emergence from the sea that the cores span.

The Reunion island cores were collected on the dipping volcanoclastic apron of the island, at varied distances from the shoreline (Saint-Ange *et al.* 2013), offshore an embayment of the island containing collapse structures (e.g., Ollier *et al.* 1998). Fig. 4.12d shows a high frequency of volcanoclastic beds and a high average bed thickness (>20 cm). The cores commonly contain coarse and poorly-sorted turbidites, so their formative turbidity currents may have been in the upper flow regime or at least more vigorous than the Azores turbidity currents. The cores were also collected on a slope close to a large slump scar, so slope movements may have originated the turbidity currents.

4.6 Conclusions

The four selected Azorean sediment cores contain three sedimentary facies recognised on the basis of sedimentary logging (visual and microscope inspection), geochemical compositions (bulk mineralogy assemblage from XRD measurements, electron microprobe analysis of volcanic glass shards, carbon isotopy and total organic carbon and nitrogen) and morphometric

analysis of volcanic grain shapes (angularity and elongation). They are: F1, clay-rich hemipelagite, F2a, clay-poor and carbonate-rich volcanoclastic deposits, and F2b, clay-poor and carbonate-poor volcanoclastic deposits. Mottled structures caused by bioturbation are common in F1 and sometimes in fine-grained F2. Normally graded, laminated beds with sharp bases are commonly identified in F2a and F2b. All three facies typically possess high contents of volcanogenic minerals and comparatively low organic carbon. F2a possess more carbonate (10–20%) and organic carbon (>0.1 wt%) than F2b, likely from carbonate material incorporated from the shelf and/or submarine slope.

The processes by which the F2 volcanoclastic deposits were emplaced, whether primary or secondary, was determined based on multiple lines of evidence. Primary and secondary volcanoclastic turbidites contain structures associated with turbidity currents and can also contain high amounts of shelf-derived carbonate. Secondary turbidites contain rounded volcanoclastic grains, and their volcanic glass shards have heterogeneous chemical compositions. Primary volcanoclastic grains, in contrast, can be either angular or rounded. Their volcanic glass compositions tend to cluster in a narrow range, sometimes with rare outliers, although a range of glass compositions genetically related to magma fractionation can also be observed. Although the sedimentary structures and chemical compositions of fallout deposits can be similar to primary volcanoclastic turbidites, angular particles and scarcity of biogenic carbonate favour a fallout interpretation. However, depositional environments with intense post-depositional bioturbation can obscure all these suggested characteristics.

Interpreting individual event beds and the mechanisms that emplaced them remains a challenge, although the approach of using multiple characteristics presents a way forward here. Provisional analysis of volcanic glass compositions has revealed that individual cores tend to have relatively homogeneous compositions, which would not be expected if they originated from different islands or source volcanoes. Hence, volcanoclastic beds in the Azorean cores reflect the eruption histories of adjacent islands rather than regional events.

Bed thickness-frequency distributions were used to contrast the volcanoclastic emplacement histories of four island groups. Those distributions for the central Azores and Cape Verde islands are similar, possibly reflecting their similar bed origins. The decimetre beds for Gran Canaria cores are at least an order of magnitude less abundant than the central Azores. That small gradient (β) reflects the large-volume explosive eruptions that occurred during the volcano emergence stage of Gran Canaria, which led to many dominating larger volcanoclastic beds. The cores of Reunion contain poorly sorted, coarser and thicker beds on average than those of the Azores, partly reflecting emplacement by larger and more vigorous turbidity currents.

Acknowledgement

YCC thanks the government of Taiwan funded this research with a PhD scholarship. We thank the editor Sebastian Watt and reviewers James Hunt and Ricardo Ramalho and for providing their constructive comments, which led to significant improvements of this manuscript. We thank the scientific party and crew of RV *Meteor* during cruise M141/1 for their work in collecting the gravity cores. Steffen Kutterolf and Line Herberg provided data for part of the EMP samples. We also thank Doris Maicher for help in shifting heavy cores from the GEOMAR repository, Bart Van Dongen for use of laboratory space for sample preparation, Elsa-Marie Portanyi for help in setting up the preliminary chemical experiments, Kévin Boulesteix for sharing his knowledge of ichnology, Emíly D. Flud, Shunwen Yu, Yu-Huang Chen, Hsing-Chien Juan and Chia-Yu Lin for discussions on the geochemical analyses, John Waters for the XRD measurements and analysis, Alastair Bewsher for pre-testing the TOC analyses in Manchester (data not shown), Stephen Crowley for the TOC, TN and $\delta^{13}\text{C}$ analyses in the University of Liverpool, Michael Cassidy for advice on morphometric analysis and Rui Quartau for providing the high-resolution multibeam data from around Terceira displayed in Fig. 4.1.

Chapter 5. Asymmetric abundances of submarine sediment waves around the Azores volcanic islands

This chapter is a reproduction of a manuscript published in the *Journal of Marine Geology*. Chang, Y.-C., Mitchell, N.C., Quartau R., Hübscher, C., Rusu, L., Tempera, F. Asymmetric abundances of submarine sediment waves around the Azores volcanic islands.

Y-C.C produced the original draft of the manuscript and figures. All co-authors contributed their opinions and comments to the draft manuscript. The journal reviewers also effectively made contributions by commenting on the article.

In this chapter, I identified sedimentary wave trains and produced their density maps in each segment of the islands. I characterised the morphological and seismic reflections features of the sediment waves. I also measured the wavelengths and heights of sediment waves. I evaluated shelf sediment mobility by assessing evidence of drop-down camera and sidescan sonar images, sediment grain-size textures and wave simulations by comparing wave-induced shear stresses with the threshold stresses needed to cause sediment movement.

Wave propagation was simulated for two periods by co-author L.R. providing information on wave properties. Superficial sediments on the shelves were collected and sieved by co-author R.Q during the cruise in 2005 (Quartau et al., 2005). Graphs of critical gradients of internal tidal waves were produced by co-author N.M. High-resolution bathymetric data were collected, processed and provided by co-authors N.M, R.Q, and C.H (Mitchell et al., 2008; Hübscher, 2013; Quartau et al., 2014). Seismic reflection images were collected, processed and provided by co-author C.H. (Hübscher, 2013). Sidescan sonar and drop-down camera images were processed and provided by co-author F.T.

Abstract

Sediment waves are common on the submarine flanks of volcanic islands, but the processes that form them are difficult to decipher from geophysical data alone. Here, we identify downslope-trending trains of sediment waves in multibeam sonar data from five islands of the Azores. Train abundances are derived by counting the train intersections with depth contours around each island, revealing that they are typically twice as common on the north slopes of the islands compared with their south slopes. To provide context, we also characterise the Holocene mobility of sediments on the shelves, ocean density structure (for evaluating internal wave critical gradients) and sediment lithologies in four cores from beneath the slopes, which contain shelf carbonates in some volcanoclastic turbidites. Holocene mobility is assessed using sidescan sonar data, which reveal shelf-crossing sand streams. Using results of a high-resolution wave model, wave-imposed shear stresses are found to have exceeded the stresses at threshold of motion for most of the modern shelf sediments during recent extreme wave conditions.

Sediment waves could potentially arise from sedimentary flows, gravity mass movements (shallow slumping) or ocean internal waves. Sedimentary flow origins are favoured by streamwise changes of wavelengths and upslope bedform migrations suggested by seismic reflections. The asymmetry of abundances north and south of each island is also an important clue. For example, it is unlikely that systematically different sediment geotechnical properties occur on the two sides of the islands, hence no reason to expect greater mass movements on northern slopes. Internal waves originate mainly from the south and hence also do not explain the asymmetry. Primary volcanoclastic flows are likely to be equally important on both sides. Sedimentary flows originating from shelf sediment agitated during storms or from failed slope sediment appear to explain best the asymmetry. In that case, prevailing wind and waves approaching the islands from the northwest lead to more frequent sediment gravity flows because they lead to greater flux of sediment from coastal erosion towards northerly outer shelves and upper slopes, where it is prone to slope failure. Offshore-directed near-bed currents originating from northwesterly wind-driven surface currents also transport shelf sediment efficiently to the north, further aided by greater wave agitation on that side. The high

abundances of wave trains on the north sides of the islands therefore favours origins involving sedimentary gravity flows associated with wind and wave effects.

Keywords: sediment gravity flows, wave-induced turbidity currents, sediment transfer, threshold of sediment motion, bottom current, internal waves

5.1 Introduction

Extensive sediment waves have been identified around the deep submarine flanks of many volcanic islands, in places extending downslope over tens of kilometres (e.g., Wynn et al., 2000; Hoffmann et al., 2008; Casalbore et al., 2014; Mazuel et al., 2016; Clare et al., 2018; Pope et al., 2018; Quartau et al., 2018; Santos et al., 2019). Such waves, which are found in other types of submarine slopes also, have been suggested to be created by (1) sedimentary gravity flows due to transformation of sediment mobilised by gravity-driven slope mass movements (e.g., Pope et al., 2018) or from flooding or pyroclastic flows (e.g., Romagnoli et al., 2013), and (2) effects of geostrophic bottom currents (e.g., Thran et al., 2018) or internal tidal wave currents (Belde et al., 2015; Ribó et al., 2016). (In this study, "sediment waves" are used merely as descriptive terms without connotation of their origins.)

Pope et al. (2018) have suggested morphologic criteria for interpreting sediment wave origins. According to them, sediment waves originating from mass movements comprise rotational landslide blocks with distinct headscarps, laterally confined transport paths, straight crestlines and wave-forms that vary from asymmetrical to symmetrical in downslope sections. Eruption-fed pyroclastic flows, instead, tend to produce radially extensive sediment waves that decrease in wave height and wavelength downslope and have convex and/or bifurcated crestlines. Using a global dataset of morphologic measurements, Casalbore et al. (2020) attempted a comprehensive study of such sediment waves. However, interpreting the origins of sediment waves solely based on bathymetric data is challenging as morphologic characteristics do not indicate the mechanisms for forming the waves unambiguously. Even sediment wave-forms that appear plausibly to have been created by a specific process can turn out to be more likely produced by other process when other measurements or criteria are applied. For example,

sediment waves off the Eel River of California have been re-interpreted as produced by sedimentary flows (Lee et al., 2002), following an earlier mass-movement origin (Gardner et al., 1999). Additional data are typically needed, for example, high-resolution seismic reflection images (e.g., Pope et al., 2018; Quartau et al., 2018). Repeated bathymetric surveys have been used to record the kinematics of sediment waves around volcanic islands (Casalbore et al., 2017) and in other settings (Normandeau et al., 2016; Paull et al., 2018). Such kinematic information can be integrated with other data to provide clues of origins, but interpretation is still commonly uncertain.

Weiß et al. (2016) have noted that large undulated lobe deposits (sediment waves), erosional/non-depositional channels and seismically resolved upslope migrating cyclic steps are more commonly found in the northern submarine slope of São Miguel island than in its southern slope. They speculated that this was linked to the exposure of the north coasts of the island to episodic swells originating mainly from the north. In this study, we expand on their observations by using high-resolution multibeam echo-sounder data from the central Azores islands. We confirm that the central islands also show asymmetric abundances of submarine sediment waves.

5.2 Regional Setting

The central and eastern islands of the Azores are located in or around a diffuse tectonic boundary between the Eurasian and Nubian plates (Fig. 5.1), which includes the Terceira Rift, an extensional graben crossing from São Miguel, Terceira, Graciosa islands towards the Mid-Atlantic Ridge (Machado, 1959). Consequently, the Azores are highly active seismically (Tucholke et al., 1997; Chiocci et al., 2013; Madeira et al., 2015; Miranda et al., 2015). The rift and the islands have developed on a broad oceanic plateau of crust thickened by excess volcanism, possibly associated with a hot-spot (White et al., 1976; Bonatti, 1990; Gente et al., 2003; Vogt and Jung, 2004). Most of the islands and tectonic structures are WNW–ESE elongated (Fig. 5.1). Faults on land have two different alignments (N150°E and N110°E–N120°E), possibly a result of regional transtensional deformation (Lourenço et al., 1998;

Miranda et al., 2015). Besides tectonic activity, the islands and some sea areas are volcanically active (Moore, 1990; Cole et al., 1995; 2001; Gaspar et al., 2003), an activity that has extended at least into the Quaternary (Féraud et al., 1980) if not much earlier. The geologic activity suggests that many conditions exist in the Azores for the generation of sedimentary flows and other processes that have been proposed to create submarine sediment waves (Casalbore et al., 2020).

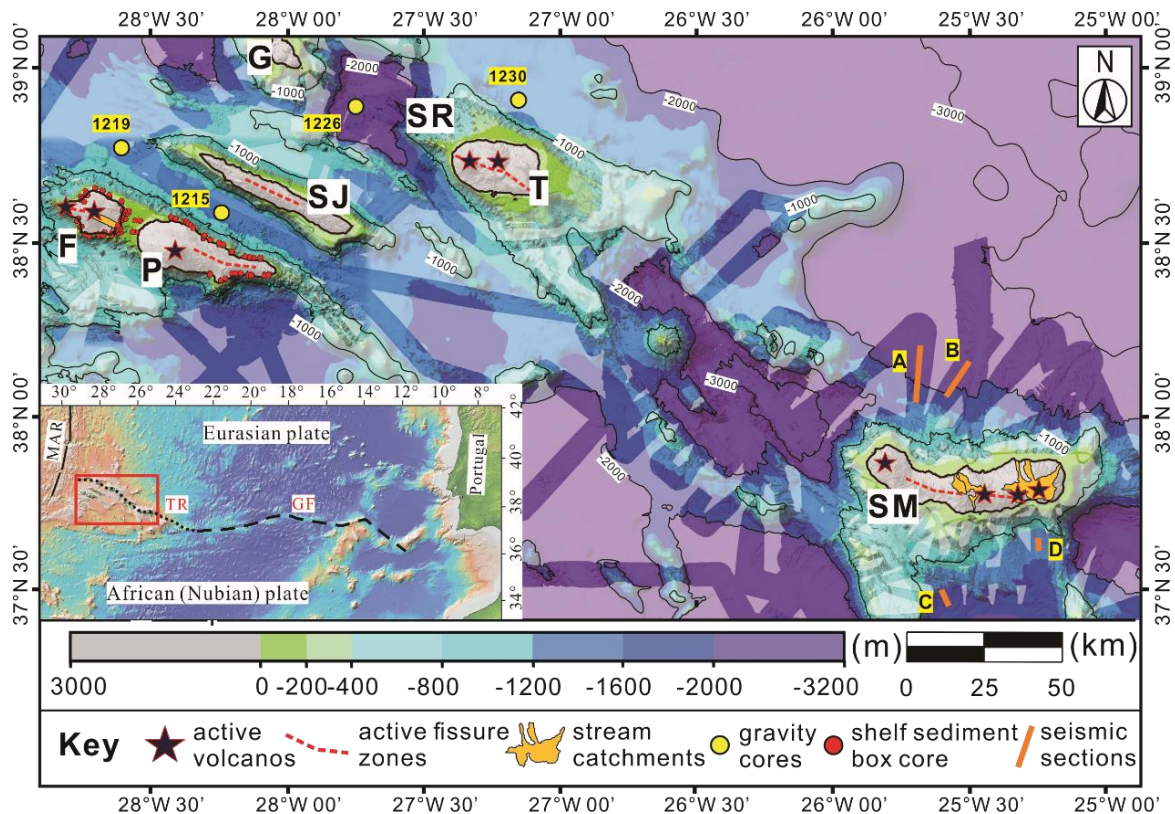


Figure 5.1. Bathymetry of the central and eastern Azores Islands with depth contours every 1000 m. High-resolution multibeam echo-sounder data available to this study are shown in bold colours. Background (faint colours) is derived from the Global Multi-Resolution Topography Synthesis of Ryan et al. (2009). Light grey areas represent the islands of Faial, Pico, São Jorge, Terceira, Graciosa and São Miguel (F, P, SJ, T, G and SM, respectively). SR is submarine Serreta Ridge. Seismic sections corresponding to the orange lines marked A-D are shown in Fig. 5.7. Data from the surface sediments (red circles) on the shelves of Faial and Pico islands are shown in Figs. 5.10 and 5.11. Lower-left inset: red rectangle locates the study area in the diffuse boundary between the Eurasian and Nubian plates. Solid black lines locate the Mid-Atlantic Ridge (MAR). Black long-dashed line locates Gloria Fault (GF). Black dotted line locates the Terceira Rift (TR).

5.2.1 Turbidite census

A recent study by Chang et al. (2021b) is useful to assess the relative importance of different types of sediment flows. They used multiple lines of evidence (mainly sedimentary structures and glass shard geochemistry and morphometrics) to interpret the emplacement of 42 volcanoclastic-rich beds from hemipelagite in four gravity cores collected in the vicinity of the central Azores islands (yellow circles marked in Fig. 5.1). (Hemipelagite is sediment formed slowly from typically fine particles of biogenic or terrigenous origin settling from suspension.) Those beds were subdivided into primary and secondary volcanoclastic deposits following White and Houghton (2006). Pyroclastic fallout and primary volcanoclastic turbidites are both primary deposits derived directly from volcanic eruption columns, without interim deposition and remobilisation. Secondary volcanoclastic turbidites are deposits reworked by sedimentary processes during and after an eruption but before lithification. Evidence included the presence of shelf carbonate grains. The 42 volcanoclastic beds summarised in Fig. 5.2 include nine pyroclastic fallout beds, 20 primary volcanoclastic turbidites and 13 secondary volcanoclastic turbidites. Therefore, turbidity currents formed directly from eruption columns (producing primary volcanoclastic beds) were more common at these core sites than the sedimentary flows producing secondary turbidites.

5.2.2 Flank collapses, pyroclastic and lava flows as submarine sedimentary flow sources

Pyroclastic flows and fallout deposits have been found on Terceira (e.g., Calvert et al., 2006; Pimentel et al., 2015; 2021), Faial (e.g., Cole et al., 2001; Pacheco, 2001), Pico (e.g., Madeira, 1998), São Jorge (e.g., Weston, 1964), São Miguel (e.g., Ferreira, 2000; Ferreira et al., 2015; Sibrant et al., 2015). Sedimentary flows generated by the penetration of pyroclastic flow or fallout material into the sea (e.g., Carey et al., 2000; Trofimovs et al., 2008) are therefore likely to be frequent in the Azores, explaining their high abundance in the cores (Fig. 5.2). Effusive eruptions have occurred often in the Azores (e.g., Weston, 1964). The lava flows they produce may have induced sedimentary flows when their load led to failure of underlying shelf sediments (Lodato et al., 2007; Mitchell et al., 2008; Quartau et al., 2015) or when the lava flow fronts themselves failed (Bergh and Gudmunder, 1991). Although not all reaching the sea, there

have been 35 events in 2000 years on Pico Island (Cappello et al., 2015) suggesting a high frequency of lava flow emplacements. Some mass transport deposits on the southern submarine flank of São Miguel were attributed to multiple flank and caldera collapses associated with the growth of the volcanic island (Sibrant et al., 2015).

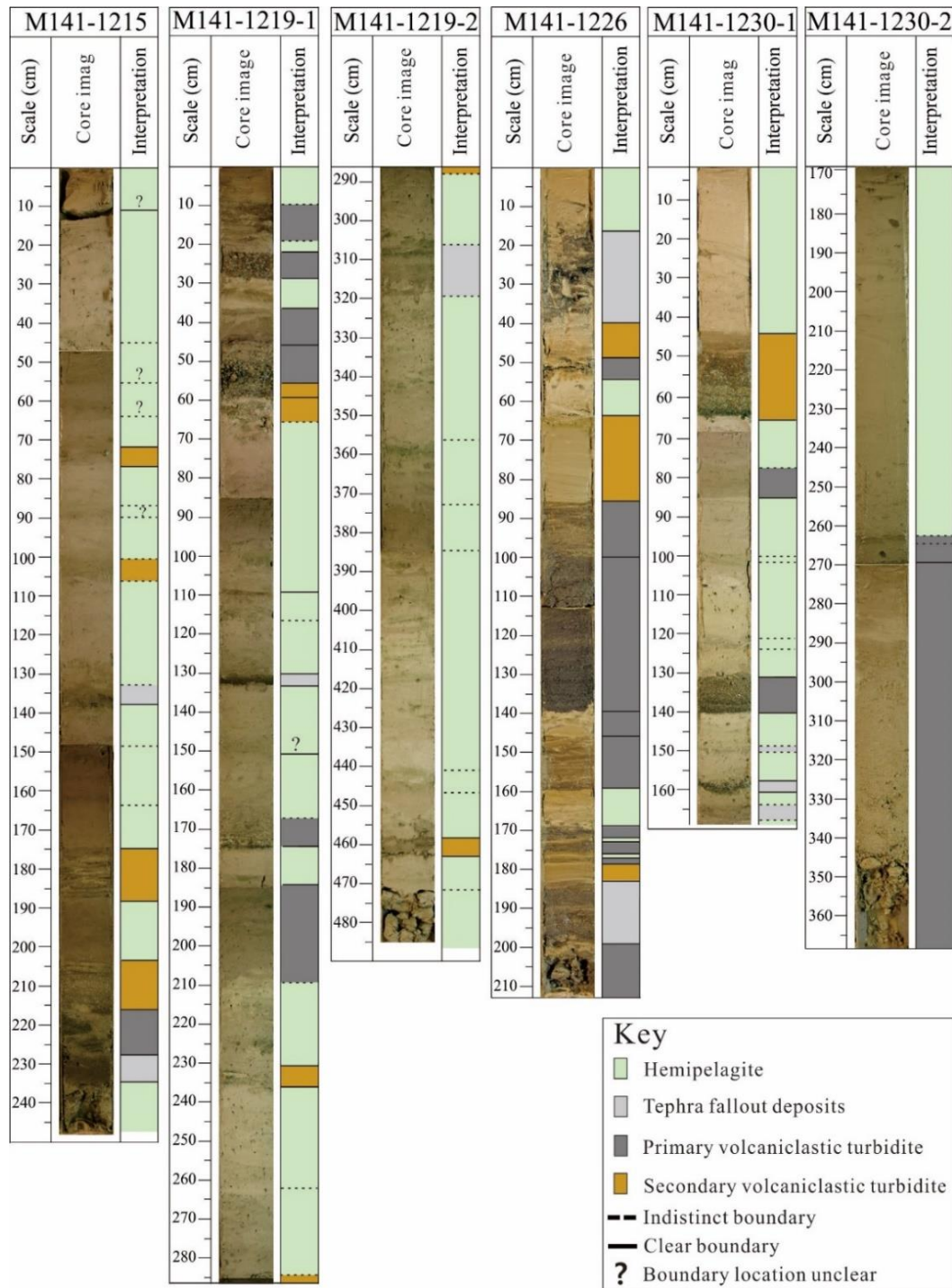


Figure 5.2. Photographic scans of four gravity cores (1215, 1219, 1226 and 1230) and interpreted deposit emplacement mechanisms simplified from Chang et al. (2021b). Core sites are located in Fig. 5.1.

5.2.3 Potential sources of other kinds of sedimentary flows

Sedimentary flows can also be formed from the export of sediments from shelves to slopes (Masson et al., 2006; 2011; Piper and Normark, 2009; Bailey et al., 2021). Mechanisms proposed elsewhere, though also potentially applying to the Azores, include (1) disintegration of sediments during landsliding or other mass movements (e.g., Nisbet and Piper, 1998; Piper et al., 2007), which can be caused by (for example) over-steepening of slopes (e.g., Di Traglia et al., 2018), seismicity (e.g., Hughes Clarke et al., 1990; Watt et al., 2014) or wave-induced stresses during storms (e.g., Dengler et al., 1984; Zhang et al., 2016; Normandeau et al., 2020; Porcile et al., 2020); (2) hyperpycnal flows at river mouths (e.g., Mulder et al., 2003); and (3) suspension of bed particles agitated by waves (Savoie et al., 1990; Mosher et al., 2004). Conditions in the Azores suggest that many of these mechanisms could apply, for example, high seismicity (Gaspar et al., 2015), ephemeral streams prone to flash-flooding during intense rainfall (Marques et al., 2008), submarine landslides (Chang et al., 2021a) and strong surface ocean waves (outlined below).

5.2.4 Oceanographic conditions

Ocean surface circulation and hydrological structure around the Azores are complex (Caldeira and Reis, 2017), but overall the islands are northward bounded by one branch of the Gulf Stream recirculating towards the south and southward bounded by the Azores current propagating towards the west (Klein and Siedler, 1989; Schott et al., 2004).

Strong winds and waves from the west and north frequently cross the Azores archipelago (Rusu and Guedes Soares, 2012), though intense hurricanes occasionally travel across individual islands from the south (e.g., 29–35 events passed the central and eastern islands in the past 160 years (<https://coast.noaa.gov/hurricanes/>)). Wave heights are generally greater in wintertime and on the windward sides of the islands (Ponce de León and Guedes Soares, 2005; Rusu and Guedes Soares, 2012). Modelling by Rusu and Guedes Soares (2012) showed how wave energy is also affected by the islands, e.g., south-eastern (leeward) sides experience sheltering effects (e.g., Pawka et al., 1984; Caldeira and Reis, 2017). On leeward sides, average wave heights are therefore much lower than those on windward sides. That pattern has probably not changed

much in the past since the northern and western shelves of the islands are commonly wider than their leeward shelves, suggesting greater long-term erosion on the former sides (Quartau et al., 2010; 2014; 2015).

During times of strong shoreward winds, the resulting shoreward surface currents can be balanced by downwelling offshore currents near the seabed (Winant, 1980). These offshore-directed currents can mobilise and transport sediments across shelves to the shelf edges and deposit them on submarine slopes (e.g., Myrow and Southard, 1996; Quartau et al., 2012). This process is important for sediment transport on island shelves subject also to high wave energy and may explain some features of uplifted shelf tempestites found subaerially on Santa Maria Island (Meireles et al., 2013). There has been little work done on coastal oceanography in the Azores, but bottom current meter measurements were made off southern Faial in 19 m depth during 2004/2005 (Youssef, 2005). Those data reveal offshore-directed currents reaching 27 cm/s during periods when surface wave heights of up to ~5 m were produced by intense onshore winds. At other narrow continental shelves, across-shelf sediment transport has been found to occur by wave-supported gravity flows occurring during storms/typhoons (Normandeau et al., 2020). Such flows have been interpreted as being responsible for widespread bedforms in submarine slopes (e.g., Porcile et al., 2020).

Weiß et al. (2016) predicted the pattern of bottom currents around São Miguel Island averaged over 9 years using an eddy-resolving simulation (i.e., MITgcm; Marshall et al., 1997). Those currents tend to follow bathymetric contours. They increased seaward north of the island from 3–5 cm/s at the outer shelf edge to 10–15 cm/s in the lower slope. In the lower slope, such currents were intermittently faster than the threshold velocity required for silt resuspension or redistribution (McCave et al., 1995). They were also faster than 2.2 cm/s, an average bottom current speed over contourites in a global modelling study (Thran et al., 2018). Therefore, bottom currents potentially affect the seabed around São Miguel Island, especially in the lower slope (depths > 2000 m) and some influence can be expected in the lower slopes of other islands also.

Internal waves can also re-suspend sediment, causing it to be transported and deposited as sediment waves, or otherwise modulate deposition (Puig et al., 2007; Quaresma et al., 2007; Mitchell et al., 2015; Reiche et al., 2018). In the Azores, internal tidal waves result from interactions of barotropic tides with seamounts lying to a few hundreds of kilometres south of the islands (Fu and Holt, 1982). The waves are therefore northwards propagating and have been observed in satellite images (Fu and Holt, 1982). This wave direction is comparable with predictions from global models (Mertens et al., 2019). Energy fluxes of internal waves reaching the Azores (10^2 – 10^3 W/m²; Löb et al., 2020) are at least one order of magnitude smaller than in areas where internal waves dominate the sedimentary environment (10^3 – 10^4 W/m² in the north-west shelf of Australia and west of Portugal; Rayson et al., 2011; Löb et al., 2020).

5.3 Materials and Methods

5.3.1 Bathymetric, seismic reflection and backscatter data

High-resolution multibeam bathymetric data were collected on *RV Arquipelago* in 2003, *RV l'Atalante* in 2011, *RV Meteor* in 2009 (cruise M79/2; Hübscher, 2013) and *RV Meteor* in 2015 (cruise M113/1; Hübscher et al., 2016). The combined dataset is shown in Fig. 5.1. The *Arquipelago* survey covered the submarine parts of Faial, Pico and São Jorge islands (Mitchell et al., 2008). The *l'Atalante* survey (EUROFLEETS cruise “Features of Azores and Italian Volcanic Islands” (FAIVI)) concentrated predominantly on the shelf and slopes of Terceira Island (Chiocci et al., 2013; Quartau et al., 2014; Casalbore et al., 2015). The *Meteor* surveys mainly focused on the area around São Miguel and partly on the central group. The combined bathymetric dataset almost fully covers these island slopes at a resolution ranging from 0.5 to 1 m in the shallowest 100 meters to 20–50 m at 2000 m depth. Further swath bathymetry and acoustic backscatter data were acquired on the shelf of Faial Island in 2004 using a Submetrix phase-difference swath sonar (Tempera, 2009).

A 2D multichannel seismic reflection dataset was also collected during *Meteor* M79/2 (Hübscher, 2013). For seismic sources, it involved two GI-Guns of 45 and 105 cubic-inch volumes. Signals were recorded with a 600 m long asymmetric digital streamer comprising 144 channels. The main processing steps were editing, CMP binning, bandpass filtering over the

range 10/20–300/400 Hz, gain, stacking, time-migration and fx-deconvolution. Methods are described further by Hübscher and Gohl (2016).

Backscatter data were collected during the 2003 multibeam survey on RV *Arquipélago* (Reson 8160; 50 kHz) and in 2004 in nearshore areas on RV *Águas Vivas* (Submetrix 2000; 117 kHz; Tempera, 2009). Data were processed using CARIS HIPS & SIPS v. 6.0 (© CARIS) including geometrical correction (bottom tracking, removal of altitude and slant range correction) and radiometric compensation (variation across-swath). Further details are provided by Tempera (2009).

5.3.2 Shelf sediment sampling and characterization

Superficial sediments were sampled using a box-corer on the shelves of Faial and Pico islands (Fig. 5.1; Quartau et al., 2005). Eighty-eight sites were sampled in water depths of 20–80 m. Grain sizes coarser than 2 mm (-1Φ) were derived by dry sieving, and those sizes finer than 2 mm were derived by Coulter Counter LS-230, a laser diffraction-based technique allowing finer particles to be measured. The measured grain sizes in the metric scale were converted to the Krumbein phi scale ($\Phi = -\log_2(\text{mm})$) with a unit interval of 1Φ . (Although the Coulter counter measurements have better precision than 1Φ , we use this precision for consistency with the sieve measurements.) Mean grain size and standard deviation were calculated using the moment measures on the sediment whole size distribution after the Folk and Ward (1957). Sediment texture statistics were then generated from the Visual Basic program GSSTAT (Pope et al., 2004).

5.3.3 Wave conditions

Wave conditions in the central and eastern Azores were derived using a Simulating Waves Nearshore (SWAN) model following the procedures of Rusu and Guede Soares (2012) updated using the multibeam bathymetry (Fig. 5.1) to improve wave refraction simulations in shallow waters. Two simulation periods were used. The first simulation is an updated version of the results of Rusu and Guede Soares (2012) run from 1 January 2013 to 31 December 2014. The second simulation (January 2001–March 2001) included an extreme winter storm. All the simulated wave properties were validated against satellite altimeter measurements (Appendix

5.1). Wave rose diagrams were calculated from wave properties at sites that are typically windward of the islands and hence represent conditions without island shadowing.

5.3.4 Sediment wave train identification and density map

Sediment waves were identified by inspecting bathymetric profiles (e.g., Fig. 5.3) and multiple perspective views of both hill-shaded bathymetric data and gradient maps. Gradient maps were found to be the most useful for interpretation (Fig. 5.4). Because of the varied data resolution and a tendency for undulations to be indistinct on the steepest slopes, comprehensive mapping of sediment waves was found to be unrealistic and only wave trains were mapped out. Nevertheless, the bathymetric data for each island was derived from single cruise sources, ensuring a similar resolution at a given depth on both sides of each island. The asymmetry of sediment wave abundance documented below should therefore be genuine.

Sediment waves were mapped where they appeared in trains of downward-oriented undulations (Fig. 5.3) and their geometrical features were recorded from downslope profiles as shown in Fig. 5.3a. Each sediment wave height was measured from the elevation of the wave crest above a line joining successive troughs. Wavelength was derived from the distance between adjacent troughs or crests along the slope. Although some wave trains were isolated, others varied in the degree to which they could be recognised and in the degree to which they formed single trains (e.g., because they merge, diverge or form widespread fields). For the following abundance calculations, wave trains were identified based on whether separate apparent transport paths could be distinguished.

Abundances of wave trains were derived as follows. For each island, a contour level in the lower flank was chosen where it encircled most of the island and crossed the most wave trains. Those contour lines were divided into segments of roughly equal straight-line distance. These were also chosen to encompass many wave trains appearing to form roughly parallel groups. Density maps were then calculated by dividing the number of wave trains by the segment lengths (straight-line distances).

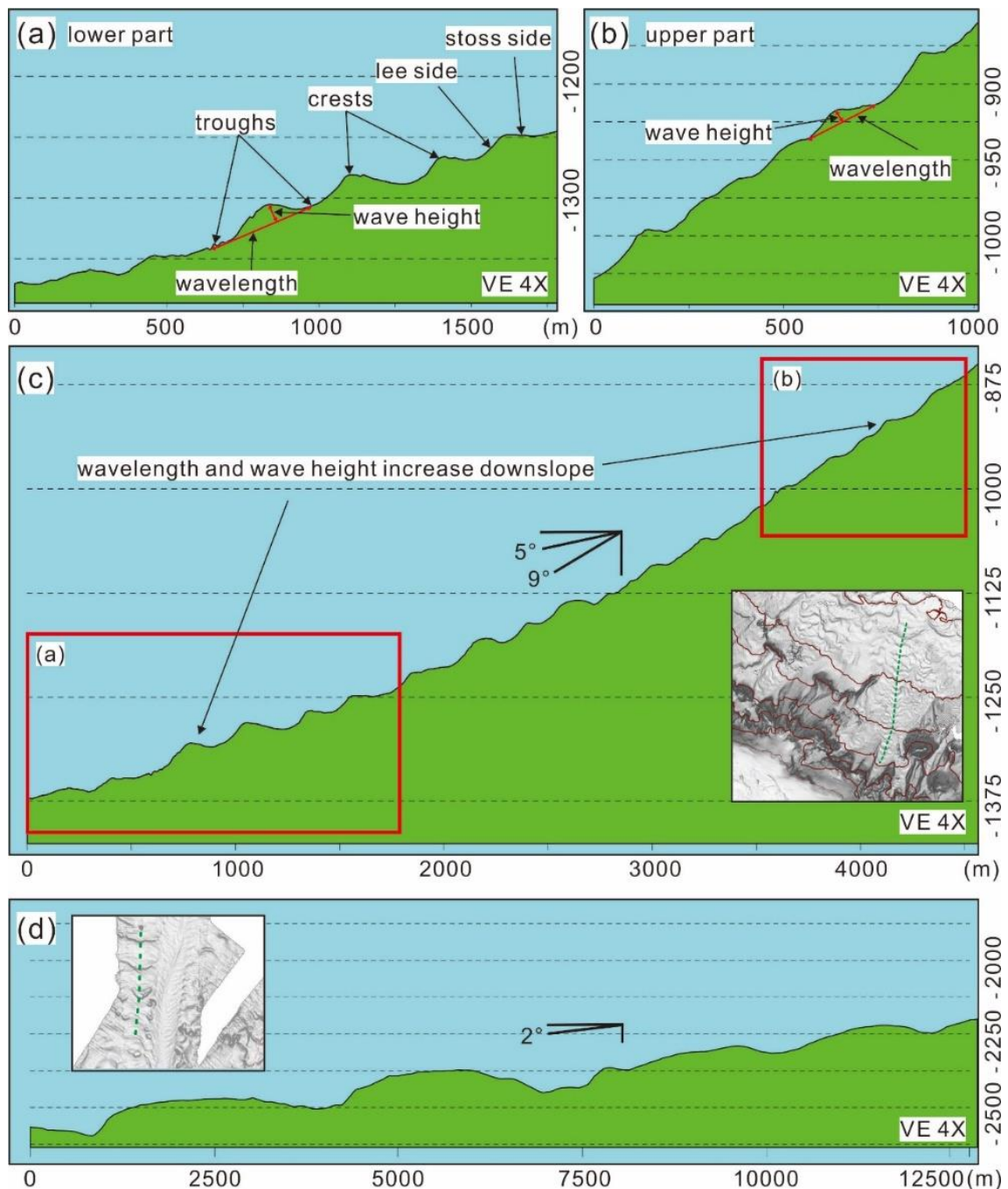


Figure 5.3. Bathymetric profiles along sediment wave trains. (a) Enlargement of the lower part of the wave train in (c) north of Terceira Island. (b) Enlargement of the upper part of the wave train in (c). (c) Complete wave train of panels (a) and (b). (d) Profile down giant wave train in the northern lower slope of São Miguel Island. Vertical exaggeration is 4:1 common to all panels. Location maps (insets) cover the same areas as shown in Figs. 5.5d and 5.5e.

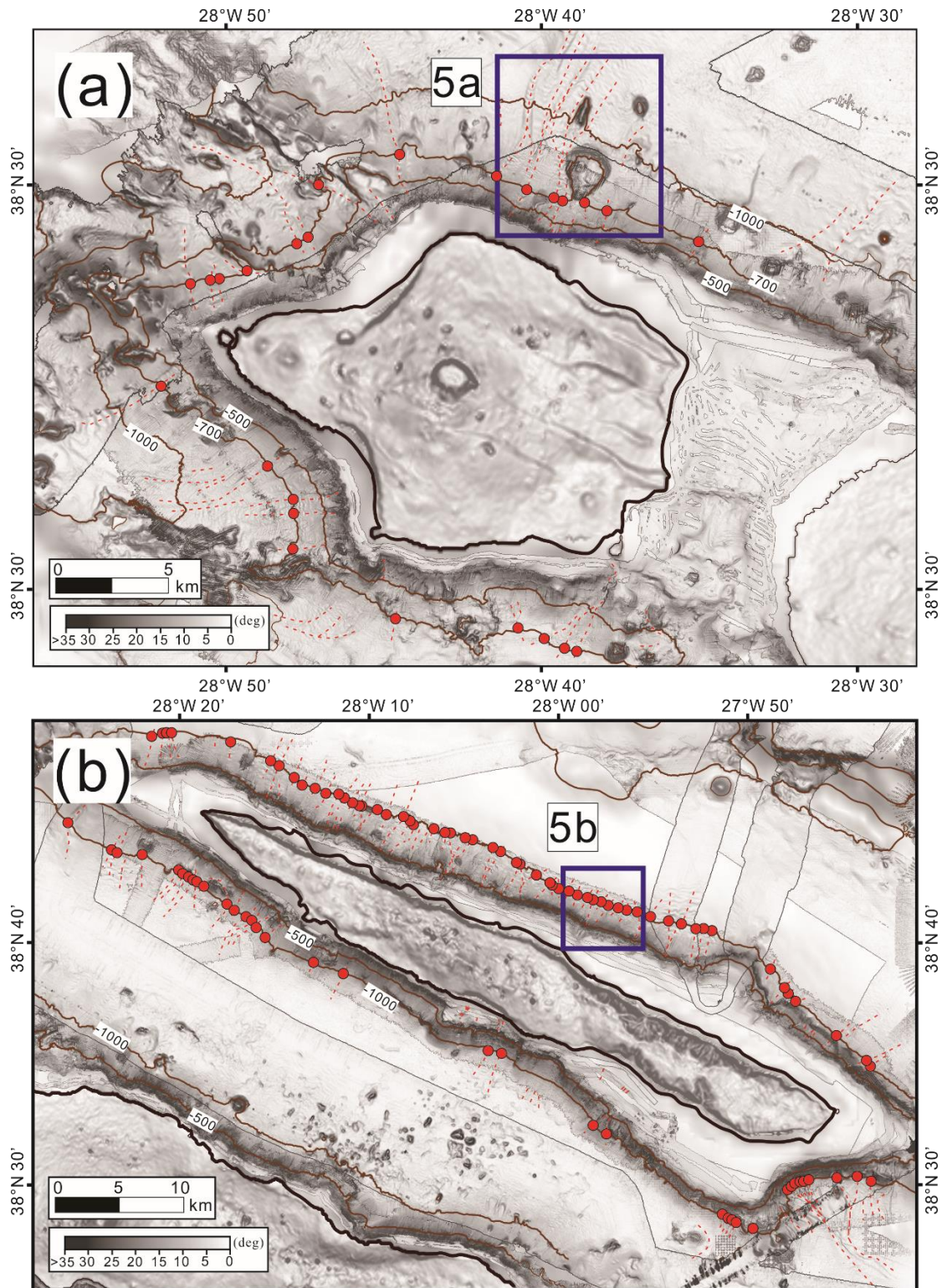


Figure 5.4. Maps of local maximum gradient along with interpreted trains of sediment waves (red dashed lines) around (a) Faial, (b) São Jorge, (c) Pico, (d) Terceira and (f) São Miguel islands. Depth contours in dark brown are spaced every 500 m (note grey lines occur at artifacts caused by the edges of multibeam datasets). Blue rectangles locate the enlargements in Fig. 5.5. Red-filled circles locate where interpreted wave trains intersect selected contours (see text for details).

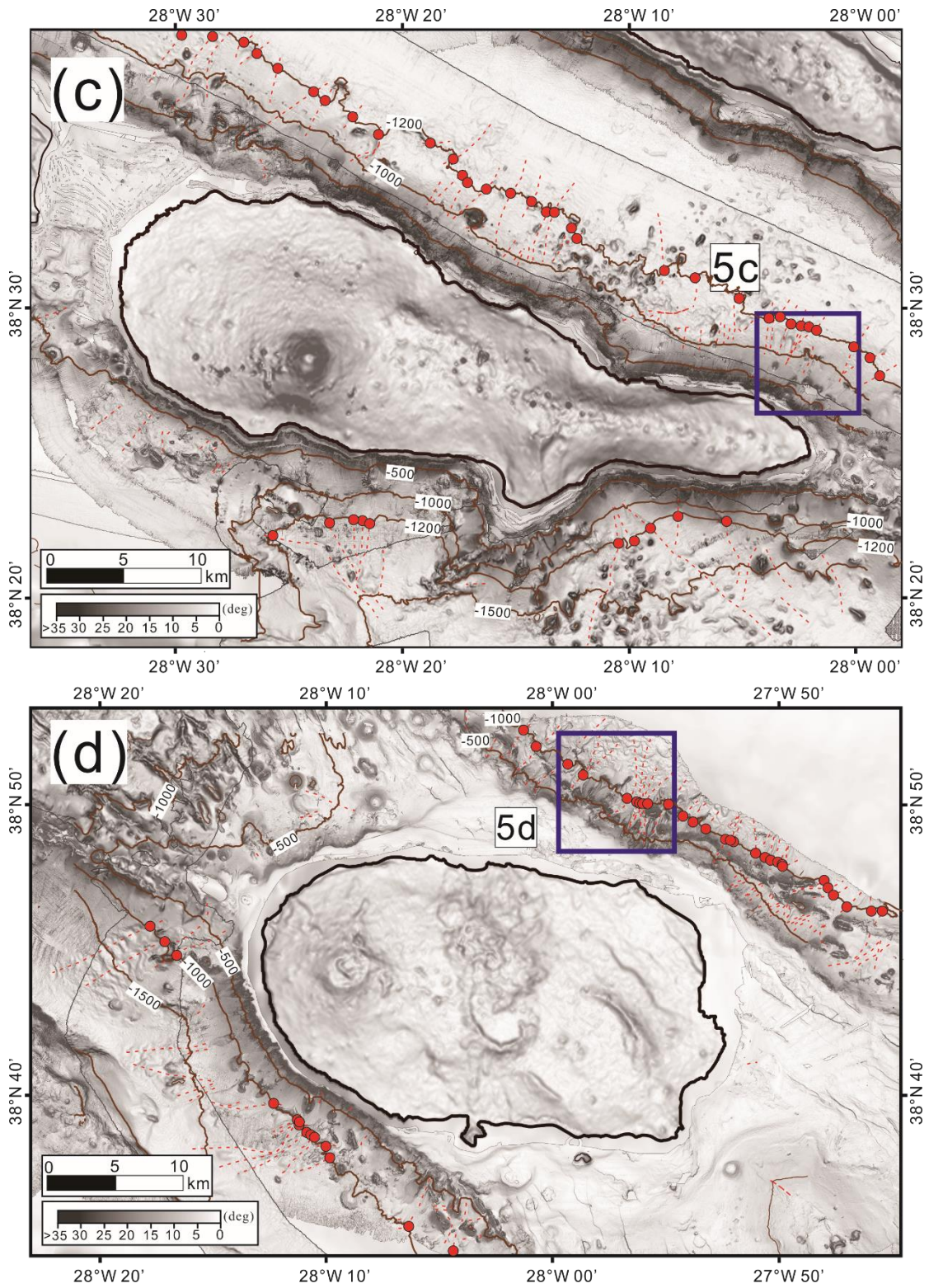


Figure 5.4. continued

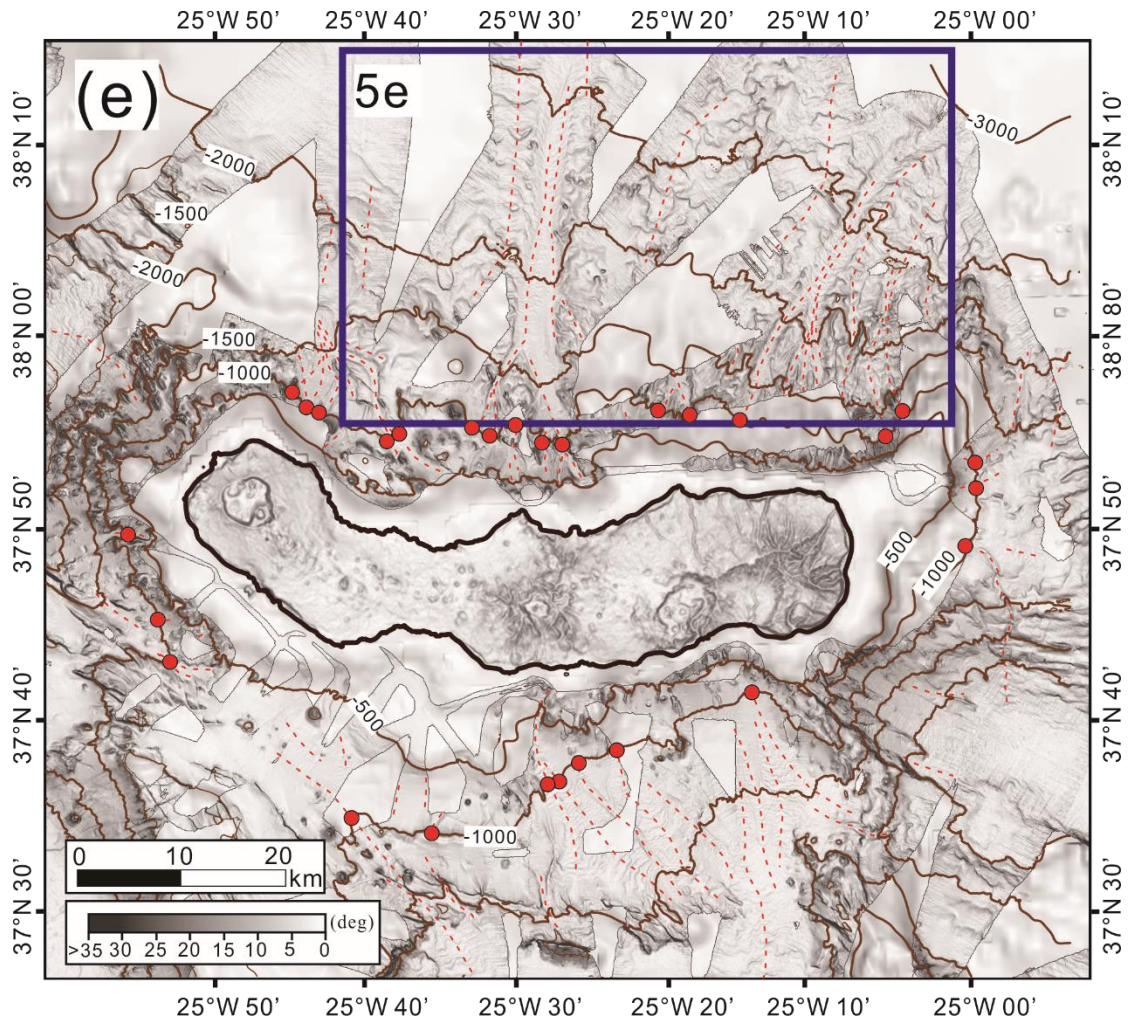


Figure 5.4. continued

5.3.5 Sediment threshold of motion modelling

Threshold of sediment motion modelling was used to assess the effects of waves on initiating movement of sediments on the shelves of Faial and Pico islands, or otherwise maintaining them above threshold of motion so that other currents can more easily transport them (e.g., wind-driven currents). The method follows that of Zhao et al. (2021). Sediment is predicted to have been mobile when the wave-induced shear stress (τ_w) on the seabed exceeds the critical bed shear stress for motion of the bed sediments (τ_{cr}) derived from their grain size.

Oscillating current speed due to ocean surface waves was calculated using linear Airy wave theory (Komar and Miller, 1973) from the 95 percentile of significant wave height H_s (m) and peak period T (s) of the updated SWAN model run over the duration 01/01/2001 to 31/03/2001

and 01/01/2013 to 31/12/2014 (the 95th percentile was used as a more robust measure of stronger conditions than maximum H_s). The wave orbital speed u_m at depth z is thus:

$$u_m = \frac{\pi H_s}{T \sinh(2\pi z/L)} \quad (1)$$

where u_m = the wave orbital speed (m/s), z = water depth (m), L = wavelength (m).

The predicted relationship between wavelength and wave period is given by:

$$L = \frac{gT^2}{2\pi} \tanh\left(\frac{2\pi z}{L}\right) \quad (2)$$

where g = gravitational acceleration (9.81 m/s²). As L occurs on both sides of equation (2), it cannot be calculated simply from. Hunt (1979) overcame this using the following empirical relationship, which is accurate to within 0.1%:

$$(kz)^2 = y^2 + \frac{y}{1+0.666y+0.355y^2+0.161y^3+0.0632y^4+0.0218y^5+0.00654y^6} \quad (3)$$

$$y = \frac{4\pi^2 z}{gT^2} = 4.03 \frac{z}{T^2} \quad (4)$$

where k is wave number (1/m). Using k derived with equations (3) and (4), L can then be derived using:

$$L = \frac{2\pi}{k} \quad (5)$$

Wave-induced shear stresses (τ_w) were then calculated from (Soulsby (1997):

$$\tau_w = 0.5 \rho_w f_w u_m^2 \quad (6)$$

where ρ_w = density of sea water (1,025 kg/m³), f_w = friction factor (dimensionless):

$$f_w = 0.237 \left(\frac{A}{k_s}\right)^{-0.52} \quad (7)$$

Where A = water particle semi-exursion at the top of the boundary layer (m), k_s = equivalent Nikuradse bed roughness empirically shown equal to $2.5D$ (m)

$$A = \frac{u_m T}{2\pi} \quad (8)$$

$$k_s = 2.5D \quad (9)$$

Where D = dimension of the sediment irregularities (here mean grain size in m).

Critical bed shear stress at the threshold of motion (τ_{cr}) was derived from the grain size following the procedures of Soulsby (1997), which were derived from a revised empirical Shields parameter (θ_{cr}) formula of Soulsby and Whitehouse (1997):

$$\tau_{cr} = \theta_{cr} g(\rho_s - \rho_w) D \quad (10)$$

$$\theta_{cr} = \frac{0.3}{1+1.2D_*} + 0.055(1 - \exp(-0.02D_*)) \quad (11)$$

$$D_* = \left(\frac{g(s-1)}{\nu^2}\right)^{1/3} D \quad (12)$$

where D_* = dimensionless grain size, s = the ratio of grain to water density, ν = kinematic viscosity of water ($1.36 \times 10^{-6} \text{ m}^2/\text{s}$), and ρ_s = *in-situ* grain density (2,650 kg/m³ was used here because the main sediment composition is volcanic lithics), ρ_w = density of water (1,027 kg/m³). The parameters used and computed stresses are provided in Appendix 5.2.

5.3.6 Internal tidal waves

Internal tidal waves typically form beams emanating from internal wave generating sites, such as ridges and shelf edges (Simmons, 2008). Where such beams reach a submarine slope of gradient (γ), they can generate currents at the seabed. The critical angle of internal tidal waves (c) to the horizontal is determined by their frequency, the ocean density profile, and latitude. When $c \sim \gamma$, internal tidal wave energy becomes trapped along the bottom, is associated with breaking internal waves, and can affect slope sediment (Cacchione and Drake, 1986; Cacchione et al., 2002). This critical angle is

$$c = \left(\frac{\sigma^2 - f^2}{N^2 - \sigma^2}\right)^{0.5} \quad (13)$$

where σ is the internal wave frequency, f is the local inertial frequency, and N is the Brunt-Vaisala frequency (Wunsch, 1969). For internal semidiurnal tidal waves, $\sigma = 0.081$ cycles/h

(cph) and $f = 2 \Omega \sin(\phi) \text{ s}^{-1}$, where ϕ is latitude (degrees), $\Omega = 7.2921 \times 10^{-5} \text{ rad/s}$ is the rotation rate of the Earth, and N is (Gill, 1982):

$$N = \left(\frac{g}{\rho_0} \frac{\partial \rho}{\partial z} \right)^{0.5} \quad (14)$$

where g is the acceleration due to gravity (9.8 m s^{-2}), ρ_0 is a reference fluid density, $\partial \rho / \partial z$ is density gradient at the depth of interest, and z is water depth. The parameter ρ represents potential density at a given depth in the oceans from local salinity and temperature (Gill, 1982). In order to compare with local bathymetry gradients (γ), we derived c by first calculating potential densities using the procedure in Joint Panel on Oceanographic Tables and Standards (1991) from temperature and salinity profiles across the central Azores islands. Those densities were then differentiated with depth to solve for N (equation 14), allowing c to be derived from equation 13.

5.4 Results

5.4.1 Sediment wave characteristics

5.4.1.1 Geomorphological features

In total, 436 trains of sediment waves were identified (Fig. 5.4). They were found on slope gradients ranging from 21° to 0.52° but mostly $< 8^\circ$. In general, the wavelengths and heights of sediment waves on the lower slopes (deeper than 1000 m) are larger than those on the upper slopes (Fig. 5.3), hence recognizable wave trains were commonly found in water depths > 700 m where seabed gradient declines (Fig. 5.5). Wave trains are almost aligned perpendicular or slightly oblique to the adjacent shelf edges, although some trains can divert around local hills or promontories (Figs. 5.5a and 5.5c). These observations apply to wave trains around the central islands, whereas wave trains in the northern slope of São Miguel are larger and the sediment waves are more irregular.

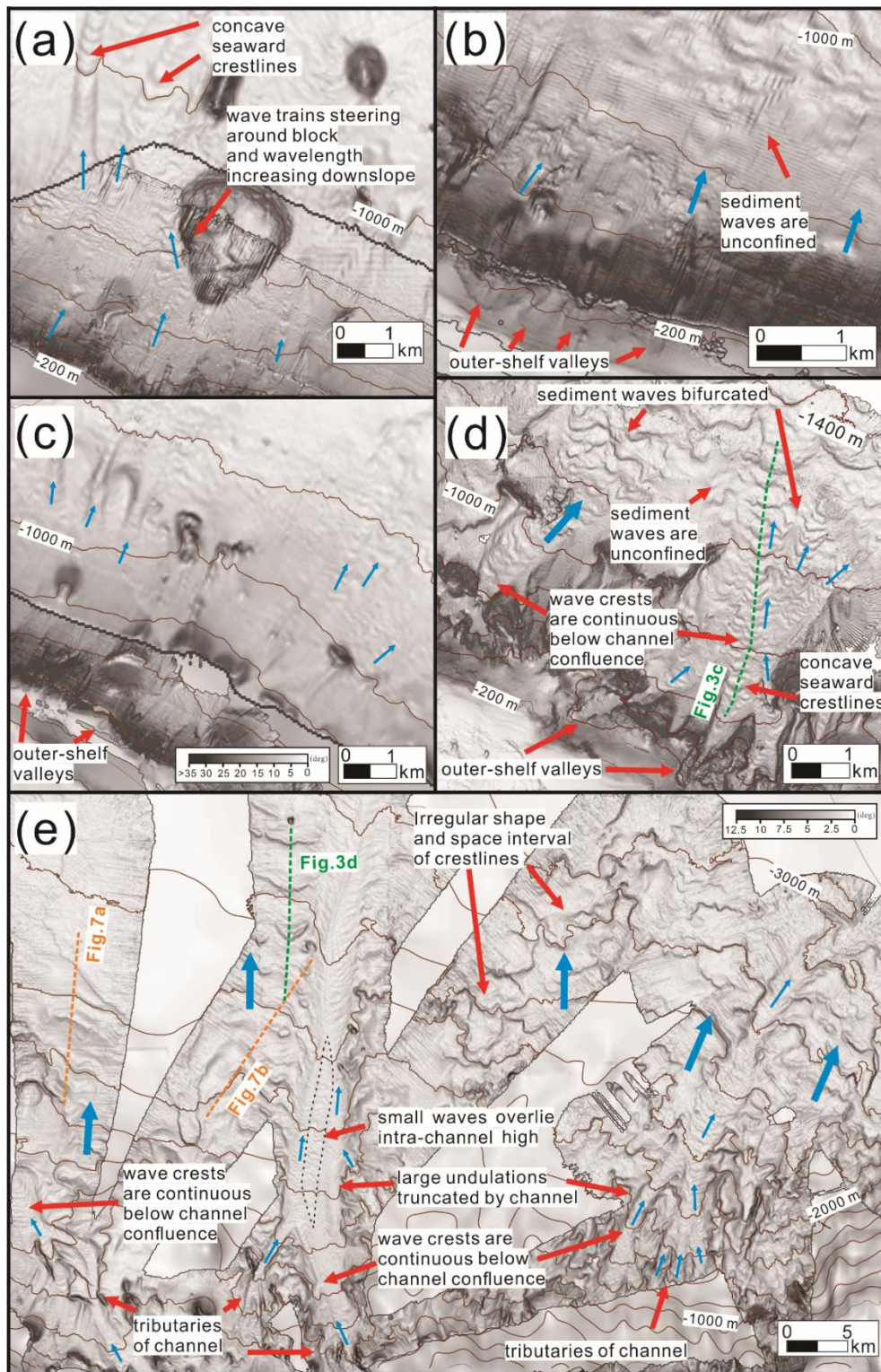


Figure 5.5. Enlarged maps of local maximum gradient to the north of (a) Faial, (b) São Jorge, (c) Pico, (d) Terceira and (e) São Miguel Island located in Fig. 5.4. Depth contours (brown lines) are spaced every 200 m. Blue arrows are oriented perpendicular to sediment wave crestlines, indicating inferred directions of movement. Green and orange dashed lines locate bathymetric profiles in Fig. 5.3 and seismic sections in Fig. 5.7. The gradient scale in (c) is shared with panels of (a) to (d) and is different from that used in (e).

In plan-view, wave trains can form streams (having somewhat uniform width with depth), or fans, or are more irregular. They tend to be narrow with low relief waves in the upper slopes but evolve downward to form the varied plan-view shapes. They can either form independent trains or merge with other trains on the lower slopes. Stream-like wave trains are the most common, dominating the slopes of Pico and Faial Islands and the southern sides of São Jorge and Terceira Islands. They can be constrained within channels (e.g., top-left of Fig. 5.5a) or be laterally confined though otherwise not channelised (e.g., Figs. 5.5a and 5.5c). Wave crestlines tend to be concave-downslope, changing little towards lower slopes. Fan-shaped wave trains (e.g., Figs. 5.5b and 5.5d) commonly appear south of the São Miguel Island and north of the São Jorge and Terceira Islands, where sediment trains become unconfined on the lower slopes. Their crestlines on the upper slopes tend to be concave-downslope but in places gradually bifurcate or become sinuous on lower slopes (e.g., Fig. 5.5d). Stream- and fan-shaped wave trains usually can be traced upslope to morphological features around the shelf edge, such as landslide headscarps or depressions. The margins of those wave trains are also typically more distinct in upper slopes than in lower slopes. More irregular-shaped wave trains were found in the northern slopes of São Miguel Island. There, waves do not form such clear trains, they do not change morphologically downslope and crestlines are more irregular and irregularly spaced (Fig. 5.5e). They occur on the lower slope and tend to be laterally unconfined.

Around the four central islands, mainly stream- and fan-shaped wave trains occur. Usually, their wavelengths are 100–500 m and wave heights are 1–100 m (Fig. 5.6). Their wave height/wavelength (H/L) ratios are mostly $1/5$ to $1/25$. In contrast, around São Miguel Island, although sediment waves of similar dimensions appear there, much larger sediment waves also commonly occur, reaching wavelengths of 1000–3500 m and wave heights of 50–150 m. The largest waves around São Miguel tend to form the most irregular trains in plan view. Their H/L ratios are $1/20$ to $1/75$. Wave fields tend to be broader and longer down-slope than those around the central group islands.

Fig. 5.6c compares the dimensions of the Azorean sediment waves with those of other island groups. The central Azores waves are steeper than some island groups (Selvagens, Madeira) but otherwise in line with others (e.g., Aeolians, Macauley).

Other geomorphological features that may be clues to formative processes were also observed. For instance, wave crests immediately below some confluences are typically continuous across the channels with no break (e.g., Fig. 5.5e). In some areas, different scales of sediment waves appear superimposed and overlapping relationships suggest they formed at different times. For instance, Figs. 5.5d and 5.5e show small waves within channels that appear to have been entrenched into deposits containing larger sedimentary waves (an observation made previously by Weiß et al. (2016).

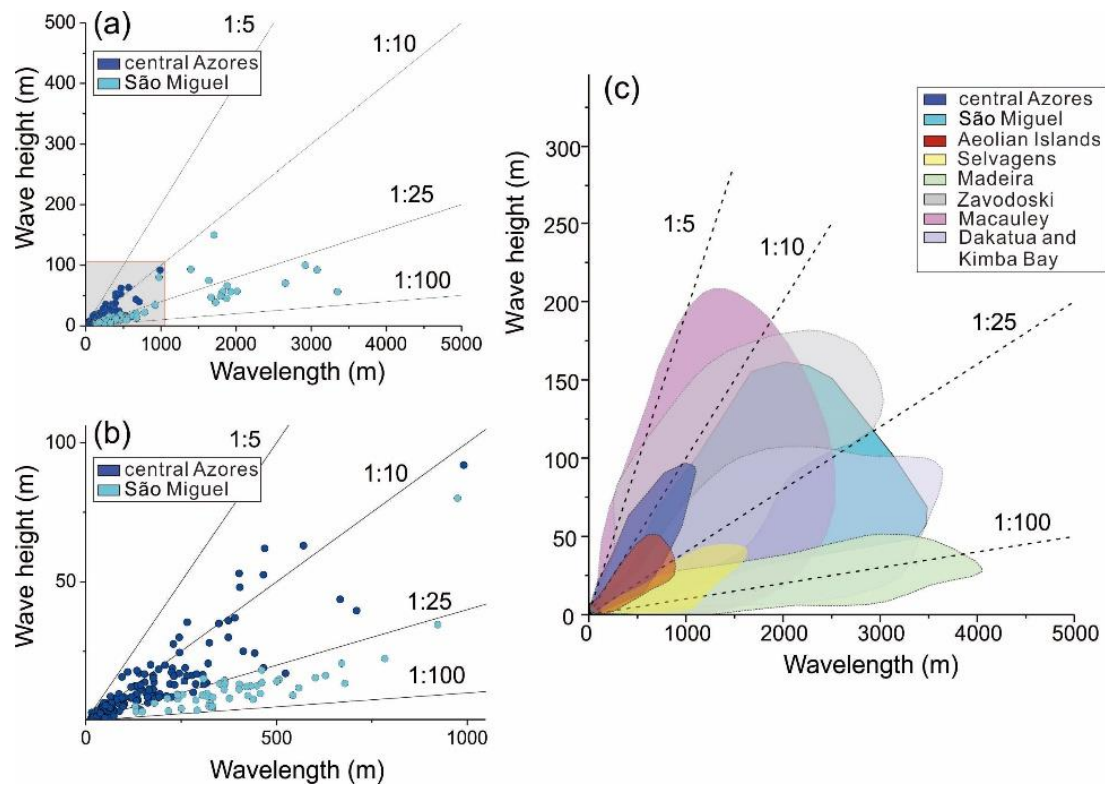


Figure 5.6. Dimensions of selected sediment waves in the Azores and comparison with those of other volcanic islands. (a) Wave heights and wavelengths measured as in Fig. 5.3. Dark and light blue circles represent the measurements in the central Azores and São Miguel Island, respectively. (b) Enlargement of the grey area in (a). Comparison of Azores sediment wave dimensions with sediment waves around other volcanic islands (Casalbore et al. (2020) and references therein).

5.4.1.2 Seismic reflections

In the sections from the northern and southern slopes of São Miguel (Fig. 5.7), reflections within sediment waves are mostly upslope-dipping on stoss sides and turn towards the seabed or are truncated on lee sides. In some sections, earlier-formed waves can be observed but have crests at different locations from the wave crests at the seabed (Figs. 5.7b and 5.7c). Within Fig. 5.7c, bowl-shaped reflection sequences and a downslope dipping band of low reflectivity can be observed. Areas of low-amplitude reflectivity occur in Fig. 5.7c, though some reflections can nevertheless be traced laterally within them.

In the northern lower slope of São Miguel, reflections towards the toe of the slope become nearly parallel to the seabed (Fig. 5.7a). Sediment waves there appear subdued or absent. The reflection sequence paralleling the seabed on either side of the ridge appearing in Fig. 5.7a are analogous to those of contourites (Faugères et al., 1999). In contrast, up-slope of the trough, the upper slope has more subdued sediment waves. Within them, reflections turn towards the seabed or are truncated at the seabed. In some sections of the data (e.g., red arrows in right panel of Fig. 5.7b), large pockmark-like depressions (40–60 m in diameter) occur within irregular-shaped wave trains.

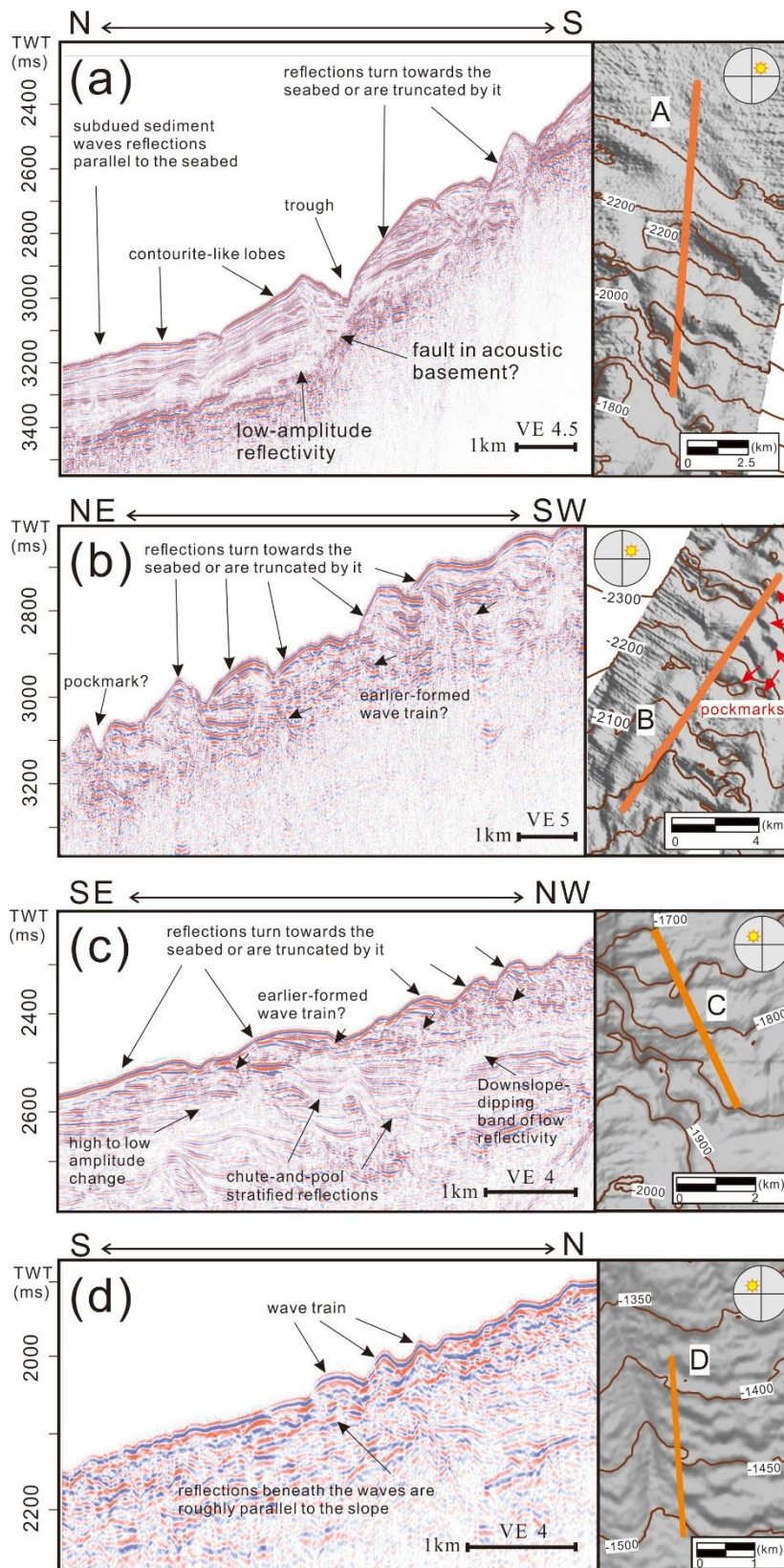


Figure 5.7. Seismic reflection sections from north (a-b) and south (c-d) of São Miguel Island located in Fig. 5.1. VE: vertical exaggeration. In the grey-shaded bathymetric maps on right, orange lines locate the seismic sections. In map for (b), red arrows locate possible pockmarks. Artificial light directions are from the NE in (a) and (b) and from the NW in (c) and (d).

5.4.1.3 Variations in abundance of sediment wave trains

In Fig. 5.8, significant variations in abundance occur around the islands, by up to a factor of two or more. Around Faial Island, the highest density of 0.63/km occurs to the NW and lowest 0.34/km to the SW, while density to the NE is modest (0.48/km). Pico also has higher densities to the north, about a factor of two greater than those to the south. The contrast between the north and south sides of São Jorge is also about a factor of two, although the east of the island also has a high abundance. A similar asymmetry of abundance is seen around Terceira by a little more than a factor of two. Abundances are higher on the north slopes of São Jorge and Terceira (0.72–0.91/km) than they are on the north slopes of Faial and Pico (0.48–0.63/km). In contrast, abundances in their southern slopes are only modestly higher (0.31–0.49/km) compared with those of Faial and Pico (0.24–0.38/km). Wave trains are more abundant on the northern slopes of São Miguel than on its southern slopes, also by about a factor of two. Its west and east slopes also have low abundances (0.10–0.11/km). However, São Miguel also has lower abundances overall compared with the other islands, by about a factor of three or four.

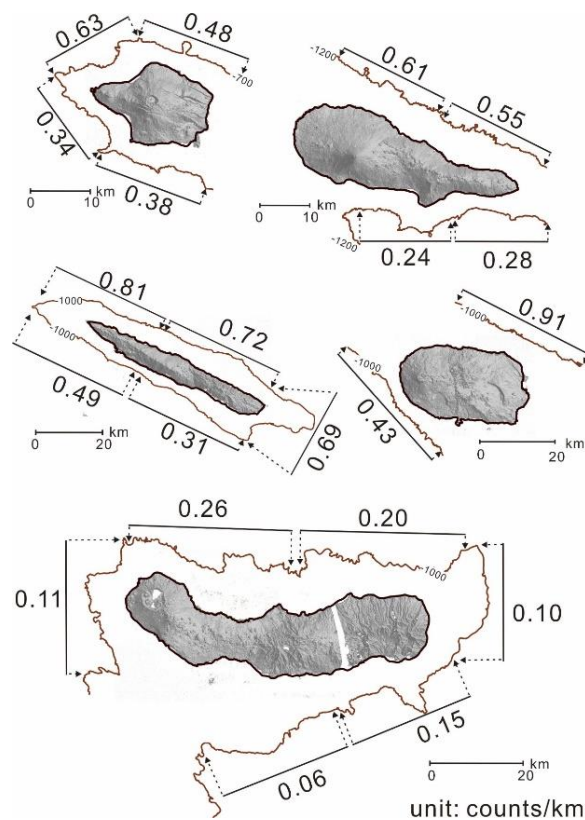


Figure 5.8. Densities of sediment wave trains measured along the contour segments shown between the dashed arrows.

5.4.2 Evidence of shelf sediment mobility

5.4.2.1 Sidescan sonar

The acoustic backscatter data shown in Fig. 5.9 were ground-truthed extensively by Tempera (2009). Where imaged using a drop-down camera (Fig. 5.10g), low backscattering areas with smooth textures correspond to finer sediments (e.g., sand substrates in Fig. 5.10d), whereas high backscattering areas typically contain coarser particles (e.g., boulders in Figs. 5.10a and 10b, gravel in Figs. 5.10c and abundant biogenic particles in Fig. 5.10f).

In the northeast shelf of Faial (Fig. 5.9a), three sets of elongated low backscattering occur, which we refer to as ribbons. Each ribbon is typically oriented sub-perpendicular to the shoreline and orthogonal to depth contours. One large area marked "LB patch" coincides with smooth bathymetry that forms a broad cone, as indicated by the 50 m depth contour. Fig. 5.9b shows some high backscattering streaks, also perpendicular the coastline, though fainter than the ribbons in Fig. 5.9a. To the southwest of Faial, two further broad patches of low backscattering occur.

5.4.2.2 Sediment texture

Sediment mean grain size and standard deviation (a measure of sorting) and carbonate contents obtained from shelf surface samples are shown in Figs. 5.11a to 5.11c. The samples mainly comprise medium to coarse moderately sorted sand (mean grain size 0–2 Φ and standard deviation $<1 \Phi$). Sample sites comprising finer sediments on average tend to have smaller standard deviations, implying that they are better sorted. If sample sites are grouped into across-shelf transects, in many of them the mean grain size increases (Fig. 5.11a) and sediments become progressively less well-sorted (Fig. 5.11b) seawards. High carbonate contents were found south and east of Faial (Fig. 5.11c). Only three transects coarsen landwards (blue arrows).

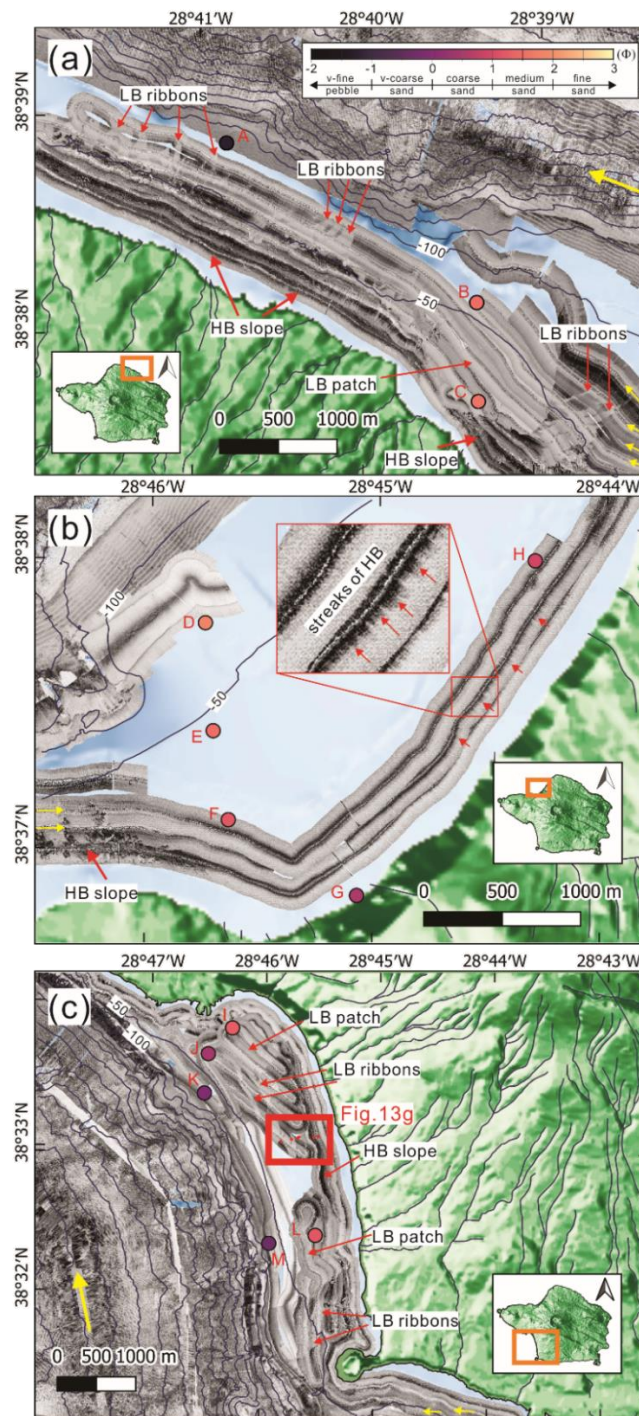


Figure 5.9. Acoustic backscatter mosaics for the (a) northeast, (b) northwest and (c) southwest shelves of Faial Island (dark tones represent high backscatter). Yellow arrows locate some sonar tracks to aid interpretation. Circles labeled A to M represent surface sediment samples with colours following the same grain size scale as in Fig. 5.10a. Red box in (c) locates the backscatter mosaic shown in Fig. 5.10g. HB and LB represent high backscattering and low backscattering, respectively. (LB ribbons running parallel to coast in (c) have positive relief and likely have a different origin from the sand streams discussed in the main text.) Depth contours (blue lines in sea areas) are spaced every 50 m.

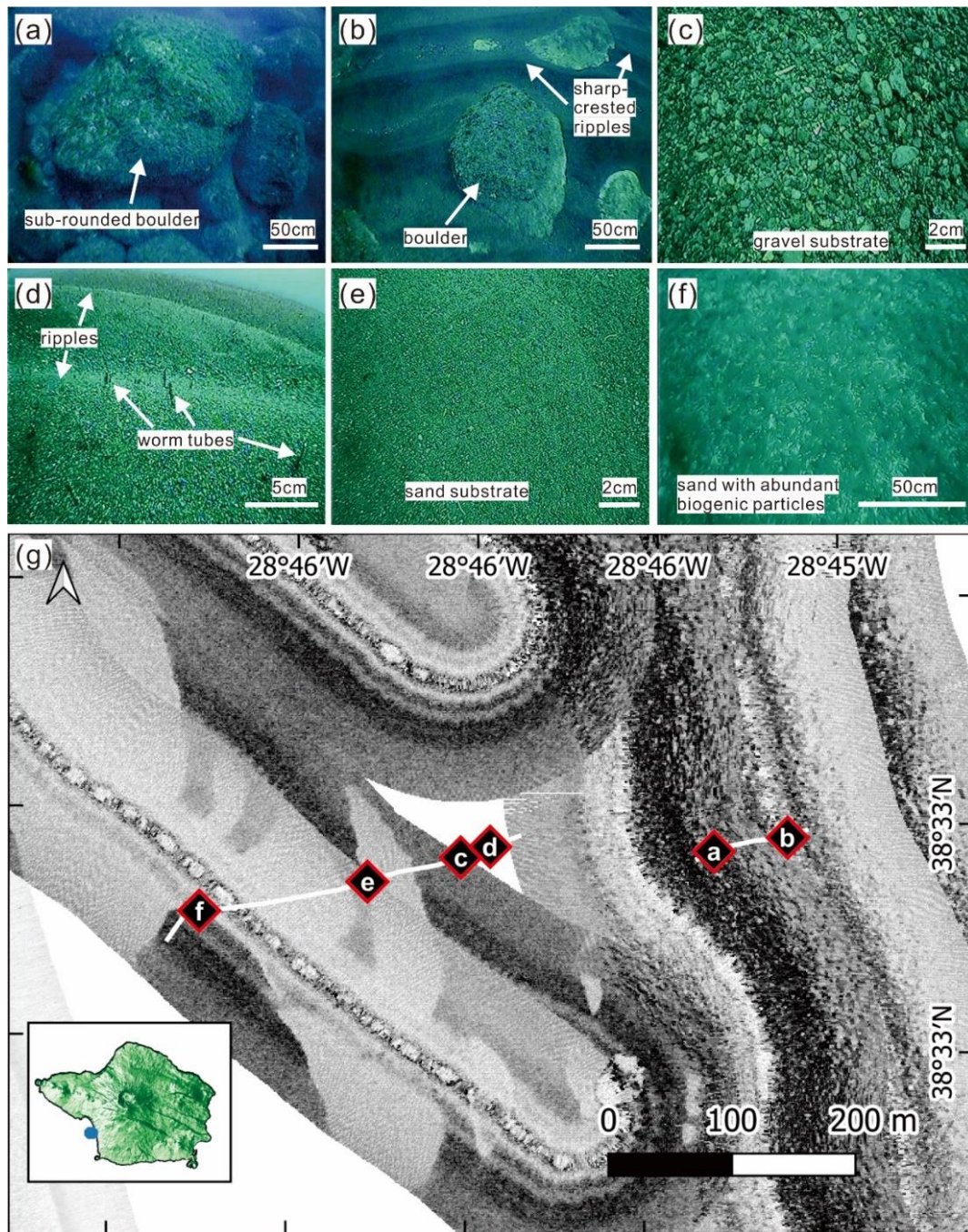


Figure 5.10. Dropdown camera images extracted from a transect of video footage for ground-truthing high (a, b, c and f) to low (e) backscattering areas. (g) Map locating the underwater images (a-f) on acoustic backscatter from the southwestern shelf of Faial Island.

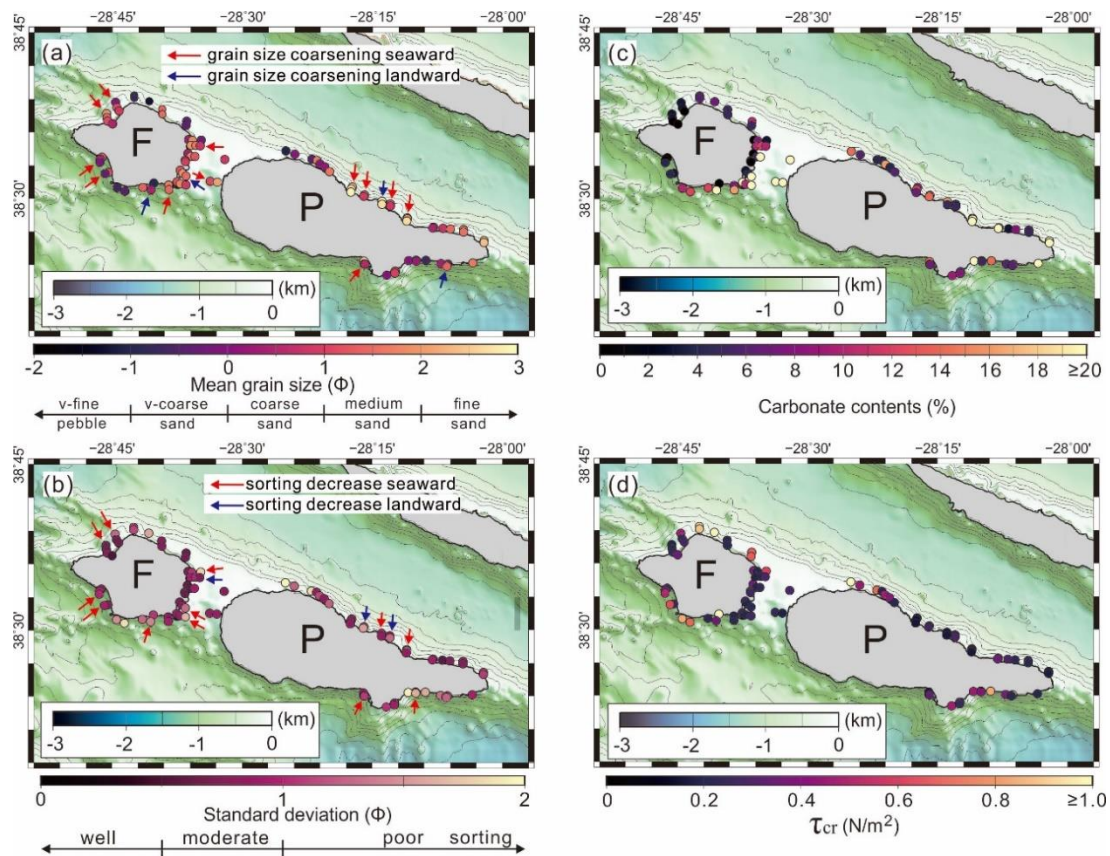


Figure 5.11. Characteristics of surface sediments on the shelves of Faial and Pico (F and P). (a) Mean grain size in phi units ($\phi = -\log_2(\text{mean grain size (mm)})$). (b) Standard deviation of grain size in phi units. (c) Carbonate contents. (d) Bed shear stress at the threshold of sediment motion predicted from the mean grain sizes in (a).

5.4.2.3 Sediment mobility assessment using wave simulations

Waves approaching the Azores from the northwest dominate both durations simulated, though were dispersed by up to $\sim 90^\circ$ (Fig. 5.12). For the shorter duration (2001), although a more westerly origin appears to dominate, the waves from the northwest nevertheless have largest H_s . Significant wave heights reached > 8 m in the 2013–2014 simulation (Figs. 5.12a and 5.12b), which had wave properties similar to other wintertimes through the period 2004 to 2013 (Rusu and Onea, 2016), but were > 10 m in the 2001 simulation (Figs. 5.12c and 5.12d).

Shelf sediment mobility was evaluated by comparing the wave-induced shear stresses (τ_w) with the threshold stresses needed to cause sediment movement (τ_{cr}) derived from the grain sizes, expressed as a ratio in Figs. 5.13c and 5.13d. High wave-induced shear stresses at the seabed

mostly appear on the windward sides of the islands (Figs. 5.13a and 5.13b). Large grain sizes occur on both sides of each island, so high τ_{cr} occurs equally (Fig. 5.11d). Consequently, more sample sites have $\tau_w > \tau_{cr}$ on windward sides, although some sites in the island lee sides are also predicted to have been mobile (Figs. 5.13c and 5.13d). Sediments were more active (68.2% of sites mobile) over the season when the extreme strong storm visited the islands (Fig. 5.13c), compared with the more typical annual conditions (42.1% of sites; Fig. 5.13d).

The above approach can be criticised because the wave-induced stress calculation does not account for (i) possible shielding of the sediment by seabed topography (form drag) and (ii) because the threshold of motion equations were intended for simple round particles of quartz density, whereas the sediments contain biogenic carbonate particles. Zhao et al. (2021) addressed these issues by reducing the stress ratio τ_w/τ_{cr} by a factor of 2–3 to achieve a satisfactory match of predictions of sediment mobility on the shelf of Santa Maria to data indicating where deposition has occurred there. If τ_w/τ_{cr} were increased by a factor of 2.5, the shelf sediments are generally predicted to be less mobile, though still with those NW of Faial mobile (results not shown). However, it is unclear if this large adjustment is needed for the shelf sediments of Faial and Pico, as porous carbonate material is typically only ~10%, in contrast to ~70% on the shelf of Santa Maria. It is also unclear if the irregular shapes of carbonate grains increase (e.g., McCarron et al., 2019) or decrease the threshold of motion (e.g., Komar and Li, 1986; Flemming, 2017; Joshi et al., 2017). Even without making this adjustment to τ_w/τ_{cr} , we suggest this approach is still conservative because the modelled period did not include the most extreme storms, which can produce wave heights of up to 22.2 m (e.g., Borges et al., 2011), which are higher than the 2001 case, and recur every roughly seven years (Andrade et al., 2008). Therefore, over the long term (many years), a higher percentage (>68%) of sites are predicted to have been active from such extreme storms.

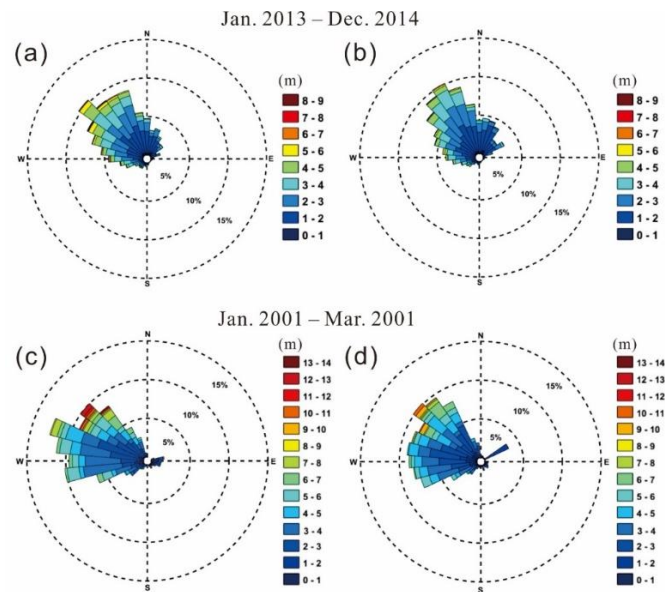


Figure 5.12. Rose diagrams of wave directions and significant wave heights for windward locations of islands in (a, c) the central Azores (29°W, 39°N) and (b, d) eastern Azores (26°W, 38°N). Results extracted from the SWAN model for the periods January 2013–December 2014 (a, b) and January 2001–March 2001 (c, d).

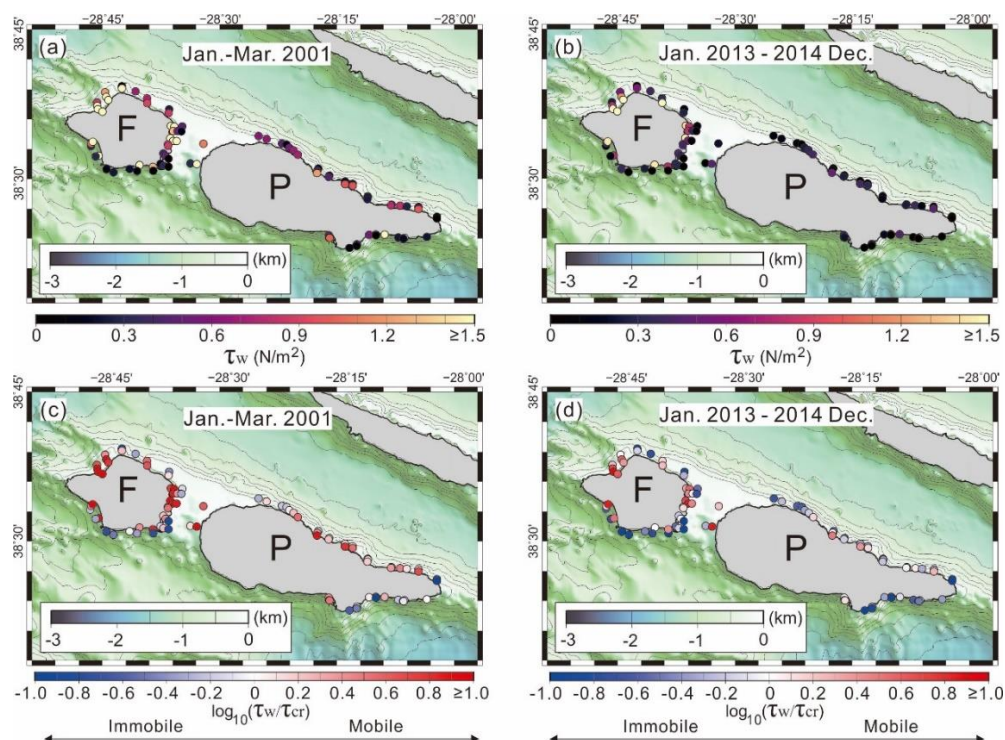


Figure 5.13. Assessment of surface sediment mobility on the shelves of Faial and Pico. (a) and (b): wave-induced shear stress predicted from the wave properties for January–March 2001 and for January 2013 to December 2014, respectively. Stresses were computed from the SWAN model peak wave period (T) and significant wave height (H_s) outputs at the 95% level by H_s at each location (i.e., relatively extreme conditions). (c) and (d): ratios of wave-induced stresses in (a) and (b) to stresses at threshold of sediment motion in Fig. 5.11d

5.4.3 Internal wave effects

In Fig. 5.14a, potential density sharply increases to 100 m (surface mixed layer) before gradually decreasing below there to 2000 m. Critical gradients obtained from those data using equations (13) and (14) are $\sim 0.03\text{--}0.04$ (i.e., up to $\sim 2.3^\circ$) down to 1000 m, but steepen to 0.08 or more by 1500 m depth (Fig. 5.14b). Conditions under which more energetic bottom currents can be expected from internal waves (where seabed gradients are comparable to internal wave critical gradients) only occur in the lower slopes of the islands (Fig. 5.14c), well below the depths of the majority of the sediment waves.

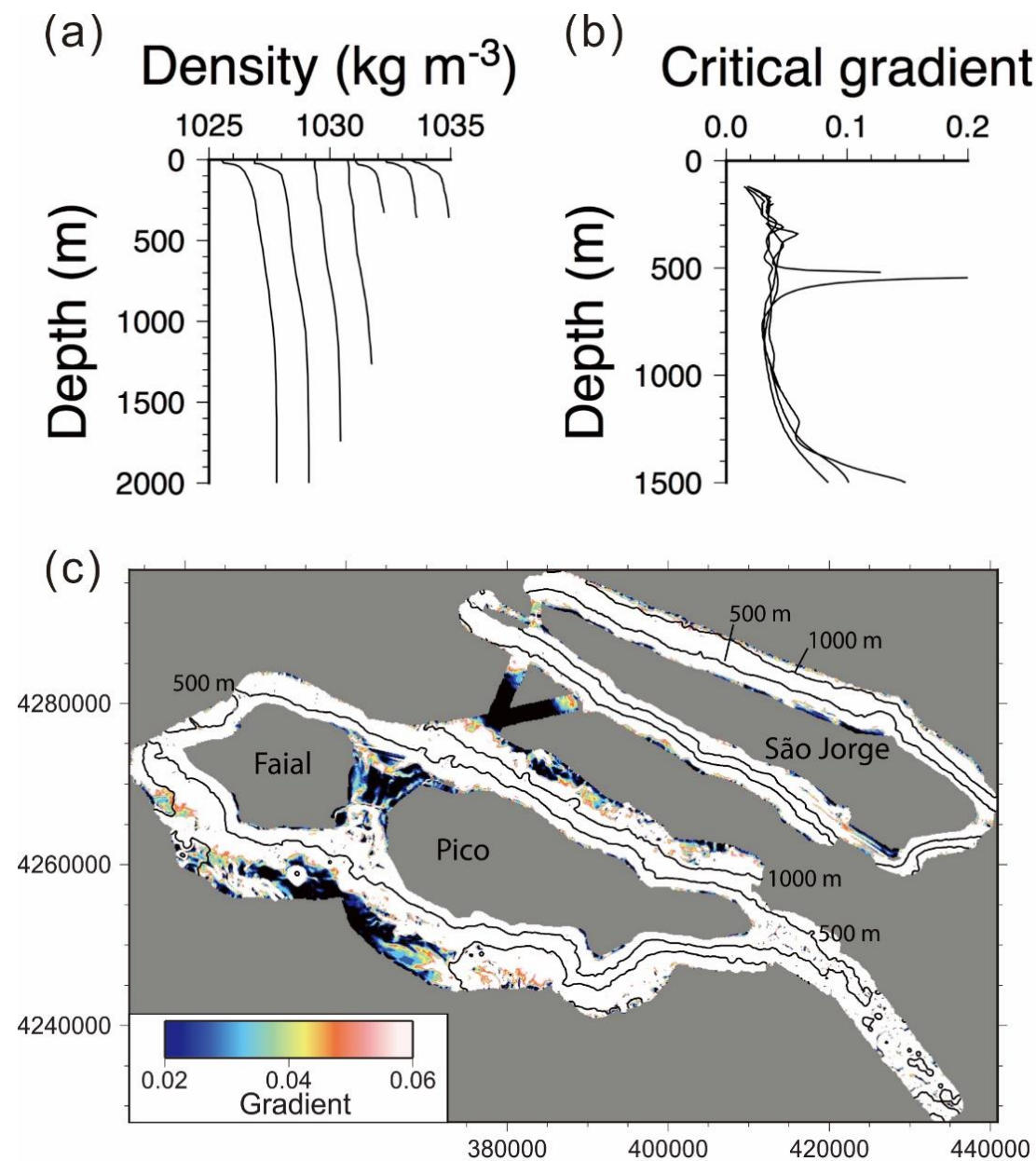


Figure 5.14. Assessment of critical gradients for breaking of internal tidal waves. (a) Profiles of potential density (density without pressure effect) derived from ocean conductivity temperature-depth measurements (left to right: stations 2503, 3201, 3188 and 3187 from GeoMapApp and ARGO float stations 119893, 120095 and 120290). (b) Profiles of critical gradients computed from the data in (a). Note that the critical gradient is undefined for one profile at 600 m depth due to values of N almost equal to σ in equation (13) and hence is an artifact. Otherwise, the results suggest critical gradients of 0.02-0.03 m/m in much of the island flanks, approaching 0.06 m/m towards 1500 m depth. (c) Seabed gradient magnitudes computed from the 2003 Arquipelago multibeam dataset after filtering the bathymetry over 500 m using a box-car filter. Gradients outside the range shown are black and white. Depth contours are every 500 m.

5.5 Discussion

We first evaluate the more recent activity of the shelf sediments because this suggests whether the sediments are being exported from the shelves and are likely to have a role in shaping the sediment waves. This leads us to consider modern processes forming wave trains as at least contributing to explaining aspects of wave geomorphology and in attempting to explain the asymmetry of sediment wave abundances.

5.5.1 Evidence of shelf sediment mobility over the Holocene and at present

The ribbons of high-backscattering (Fig. 5.9) suggest that sand streams occur around Faial Island. Along with the cone-like low-backscattering patches, these imply that sand has been transported roughly perpendicular to shorelines. The varied sizes of the ribbons and cones suggest considerable variability in that transport, with the cones potentially linked to erosive sources on land (e.g., erodible tephra). Because no unconformities are observed in boomer seismic records from the shelves (Mitchell et al., 2008; 2012; Quartau et al., 2012; 2015; Zhao et al., 2020), these features can only have been formed since the early Holocene (Mitchell et al., 2012). The results based on the wave simulations (Fig. 5.12) further suggest that the shelf sediment of Faial and Pico has been regularly mobilised by waves in recent years. Once mobile, such sediment is more easily transported seawards by either offshore currents of the wind-driven circulation (e.g., Normandeau et al., 2020) or by wave-agitated sedimentary gravity

currents (e.g. Porcile et al., 2020), particularly as these shelves are steeper than continental shelves. These currents may be the causes of the sand ribbons and cones in Fig. 5.9.

“Wave-graded shelf” is a set of terms used to describe sediment texture trends occurring where particles have been transported until they have approached equilibrium with wave-induced shear stress (Dunbar and Barrett, 2005). In such shelves, coarser grains in shallow water typically grade into finer grains in deep water. While three transects do show this tendency (blue arrows in Fig. 5.11a), many of them instead coarsen seawards (located by red arrows in Fig. 5.11a). The wave-based simulation results (Fig. 5.13) suggest that the coarser sandy sediments have been transported offshore and accumulated on the outer shelves. Furthermore, depressions in the outer shelves typical of landslides are variably smooth (Chang et al., 2021a), suggesting they have been variably covered by later sediments. The combined evidence suggests that these coarse sediments are not relics of lower sea-level conditions (e.g., Emery, 1968). Rather, the sediment textural data supports the active transport of particles towards the outer shelf and potentially onto the upper submarine slopes of the islands.

5.5.2 Processes forming sediment waves:

5.5.2.1 Morphologic and seismic stratigraphic evidence

1. Almost all sediment trains can be associated up-slope with potential source areas and they are all nearly perpendicular with adjacent shelf edges or, where in areas without adjacent shelves, are oriented down-slope. These features both imply a component of gravity in moving sedimentary materials and are thus compatible with mass movement or sedimentary gravity flow processes, but not with geostrophic currents. In the Azores, internal waves occur with mainly one propagation direction (from the south) and geostrophic currents tend to be along-slope.

2. Increasing wavelength downslope (Fig. 5.3) are expected results of sedimentary flow deposition with decreasing slope gradient (e.g., Cartigny et al., 2011; Kostic, 2011; Dietrich et al., 2016; Slooman and Cartigny, 2020). In contrast, wavelengths are expected to decrease downslope where created by gravity-driven mass movements (e.g., Pope et al., 2018).

3. Wave crestlines are typically concave seaward and typically evolve gradually downslope to other shapes (Fig. 5.5). Crestlines do not maintain linear shapes expected of mass movements.
4. Wave crestlines are continuous immediately below tributary confluences (Fig. 5.5e). In contrast, if mass-movements occurred down adjacent tributaries, it is unlikely they would merge so effectively at the same speeds. No morphologic evidence was found of strike-slip-like movements and/or drag folds resulting from asynchronous gravity-driven mass movement along converging tributaries.
5. Gravity-driven slope mass movements commonly generate tensional regimes upslope and compressional duplex structures in their lower slope where mass accumulates (e.g., Hill et al., 1982). However, there is no evidence for either tension (Fig. 5.7) or duplex structures at the slope base (Weiß et al., 2016).
6. The channel margins that commonly flank the wave trains are typically distinct, suggesting that the core of sedimentary flows creating them were laterally-confined (Fig. 5.5e). This argues against more widespread flows, such as from internal waves or geostrophic currents, though could be compatible with mass-movements.
7. In Fig. 5.7, sediment waves appear to have formed continuously along the seismic sections and their internal reflections are typical of upslope migrating bedforms (e.g., cyclic steps; Zhong et al., 2015) and hence are compatible with a sedimentary flow origin (Cartigny et al., 2014; Slooman et al., 2021). The chute and pool stratigraphy in Fig. 5.7c is also typical of antidunes within cyclic-step sequences (Dietrich et al., 2016; Slooman et al., 2021). Beneath the sediment waves, no single dipping reflection or reflection hiatus can be observed that might otherwise indicate a mass-movement sliding surface.

5.5.2.2 Asymmetric abundances around each island evidence

Densities of sediment wave trains are generally a factor of two larger on northern slopes compared with southern slopes (Fig. 5.8). This asymmetry also helps to rule out some potential origins of the sediment waves discussed above. Based on the core results (Fig. 5.2), the most important sedimentary flows reaching the adjacent basin floors are of primary volcanic origin, so we discuss their role first.

Sedimentary flows fed by volcanic eruption columns

If eruption-fed sediment flows preferentially occur in any one direction, they could conceivably have a strong effect on the wave train distributions. Isopach maps of pyroclastic material for an eruption on Faial at ~1000 yBP suggests that most volcanoclastic particles were deposited NW of the central caldera of the island (Pimentel et al., 2015), opposite in direction to that expected from the prevailing northwesterly winds. In another study, ~25 ka ignimbrites on Terceira thicken to both north and south coasts, though with most material deposited northwards (Pimentel et al., 2021). Although particles in eruption columns might be expected to be deflected more to the SE by the prevailing wind, isopach maps of Plinian material on São Miguel and other islands do not demonstrate any directional preference (Self, 1976; Storey, 1982; Cole et al., 1995; Cole et al., 2001; Pedrazzi et al., 2015; Pensa et al., 2015). In volcanic islands elsewhere, valleys created by asymmetric erosion can guide pyroclastic flows asymmetrically (Hart et al., 2004), but erosion is not strongly asymmetric in the Azores (Forjaz et al., 2004; Instituto Nacional de Meteorologia, 2012). We therefore suggest that volcanic eruptions are unlikely to be the main cause of the asymmetry of sediment wave trains (Fig. 5.8). However, given the high abundance of primary volcanoclastic beds (Fig. 5.2) and that individual eruptions generate large volumes of material (Pimentel et al., 2015, 2021), pyroclastic flows have likely played a role in shaping the sediment waves. If the long-term impact of such flows has been symmetric about each island, they will have contributed to sediment wave train development on north and south sides equally. If their impacts have been more deflected to the SE by ambient winds, the observed asymmetry of sediment wave abundances is even more surprising and other processes are needed to explain it.

Sedimentary flows not sourced directly by eruption columns

Wave trains have been interpreted elsewhere around volcanic islands as caused by sedimentary gravity flows (Cassalbore et al., 2020). Such flows can be generated in shallower water by slope failure and disintegration of the failed sediment mass (Masson et al., 2006), agitation of shelf sediment by waves during storms (Normandeau et al., 2020) or hyperpycnal discharges of rivers

into the sea (Mulder et al., 2003). If any such effects were more common on the north sides of the islands, this may help to explain the asymmetry of wave train abundances.

We have shown earlier that the shelf sediments are presently mobile and likely to have been feeding the upper slopes of the islands with particles through the Holocene. Precipitation is mostly symmetric on each island (Forjaz et al., 2004; Instituto Nacional de Meteorologia, 2012) so hyperpycnal currents, if they occur, are not obviously asymmetric. Landslides are common in the uppermost slopes (Chang et al., 2021a) and secondary volcanoclastic turbidites containing carbonate particles occur in the cores (Chang et al., 2021b). Earthquake triggering of landslides is unlikely to be asymmetric across all the islands, as maps of earthquakes (Gaspar et al., 2015) and active tectonic/volcanic structures (Madeira et al., 2015) do not show any systematic asymmetry. Rather, shaking by earthquakes is likely to occur on all these slopes over geological timescales (Chang et al., 2021a).

Our assessment of sediment mobility revealed that waves affect the northerly shelves of Faial and Pico (Fig. 5.13) and offshore sediment transfer is likely stronger on the windward NW sides (Fig. 5.12). Besides contributing to the slope sediment deposits and therefore forming precursors for landslide-induced flows described above, suspension of sediment by waves on gradients can generate wave-agitated sediment flows (e.g., Flores et al., 2018; Normandeau et al., 2020). Sediment transport towards the outer shelf and uppermost slope may also be enhanced by wind-driven downwelling currents (e.g., Quartau et al., 2012), with wave agitations helping to maintain bed shear stress above the sediment threshold of motion. Wave erosion can also be expected to have mobilised more unconsolidated pyroclastic material on the northerly or northwesterly sides.

Overall, the coincidence between greater abundance of sediment wave trains in the north of these islands with waves and winds mainly originating from the northwest suggests to us that sedimentary gravity flows are the main cause of the wave trains by such mechanisms as described above. The association is admittedly not perfect as some sectors partly exposed to strong waves (e.g., SW Faial) also have low abundances, that is likely due to a longer recurrence

interval of storm waves coming from southwest. It is also unclear to what extent the distribution of pyroclastic deposits has been symmetric or if it has been asymmetric as shown by the Faial and Terceira eruptions (Pimentel et al., 2015; 2019).

5.5.3 Other processes modifying the morphologies of sediment waves

Weiß et al. (2016) suggested that the large sedimentary waves north of São Miguel were created by sedimentary flows over-topping either older channels that are now obscured or the presently observable channels (Fig. 5.5e), similar to those created by over-topping of submarine channel levées (e.g., Peakall et al., 2000; Fildani et al., 2006; Tubau et al., 2015). However, over-topping of the present channels seems unlikely as the orientations of wave crests are inconsistent with a component of flow out of those channels. The crest orientations vary greatly and do not clearly indicate over-topping from earlier channels. Furthermore, the roughly margin-parallel large sediment waves imply formation under very large flows, unlike the sedimentary flows that formed the other wave trains amongst the islands. We therefore interpret the large waves north of São Miguel as originating from pyroclastic flows, which are more likely to have formed flows that were large in vertical extent. They would have also been suitably widespread, based on widespread nature of volcanoclastic deposits on land described earlier.

Nonetheless, effects of bottom currents are also possible and might also help to explain the giant wavelengths and irregular crestlines of sediment waves towards the lower slopes with low amplitude of subdued seismic reflections (Figs. 5.7a). Such complex features have been found where turbidity and bottom currents both actively affect sediment wave fields (e.g., Miramontes et al., 2019; Fuhrmann et al., 2022). The north São Miguel wave trains developed above earlier-formed thick contourite-like channel lobes and likely have been persistently readjusted by effects of weak bottom currents that are nearly perpendicular to the turbidity currents. Sediment wave morphology in areas where bottom currents are slow (10–15 cm/s) is mainly controlled by the passive interaction of turbidity with local depositional relief (Fuhrmann et al., 2022). During the times of reduced turbidity currents, the quasi-steady weak bottom currents would travel along local relief and deposited/partly stripped fine-grained (up to silt sized) sediment on

the lee-sides of sediment waves, causing wave migration or migration oblique to the geostrophic current direction (Flood, 1988; Flood and Shor, 1988).

5.6 Conclusions

Based on high-resolution bathymetric data, 438 sediment wave trains have been identified in the central and east Azores islands. Sediment wave trains are twice as abundant on the northern (windward) submarine slopes of the islands compared with their southern slopes. Different mechanisms forming the wave trains have been discussed, including sedimentary gravity and eruption-fed flows, gravity-driven slope movements, internal waves and geostrophic currents. The most likely mechanism for forming the waves that also explains their asymmetric abundance is under sedimentary gravity flows. Such flows can be linked to waves and winds mainly originating from the northwest, because they can lead to greater mobilisation of shelf sediments (wave agitation), transport by wave-agitated sediment gravity flows and by offshore bottom currents balancing wind-driven onshore currents. Sediment wave morphologic and seismic stratigraphic features also suggest a predominantly sediment-flow origin. That evidence includes downslope-increasing wave size, streamwise evolution of crestline shapes, continuity of waves across channels below tributaries and up-slope migrating stratigraphic sequences in seismic sections.

Various evidence suggests that sediment on the island shelves has been transported towards the shelf edge over the Holocene and more recently. Low-backscattering sand ribbons and cones on the shelf of Faial indicate across-shelf sediment transport. Mean grain sizes in seabed sample transects commonly increase seaward, so sediment textures on the shelves have not reached equilibrium with wave stresses, which would lead to the opposite trend. Using a simulation of surface waves, during extreme conditions (95th percentile wave height), 42–68% of sampling sites exceeded the threshold stresses of the sediments predicted from grain size, mostly on windward sides. Those sediments spilling onto the steep uppermost slopes of the islands are then prone to failure and initiation of sedimentary flows by disintegration of the failed deposits.

Data availability

The 2003 multibeam data are available at 100 m grid resolution from the Marine Geoscience Data Portal (<http://www.marine-geo.org/index.php>). The multibeam data for Terceira and Faial nearshore are not publicly available due to the sensitive nature of the area and environmental sustainability concerns, but can be made available to researchers with appropriate credentials. Requests for access to the São Miguel data should be addressed to co-author CH. Background bathymetric data are from the GeoMapApp (GMRT; www.geomapapp.org, Ryan et al., 2009). CTD data contributing to the profiles in Fig. 5.14a are also from the GeoMapApp or the Coriolis project (<http://www.coriolis.eu.org>).

Acknowledgement

YCC thanks the government of Taiwan for funding this research with a PhD scholarship. Vernon Anak Vincent is thanked for helping with a preliminary analysis at the beginning of this project. The European Communities 7th Framework Programme under EUROFLEETS funded the bathymetric data collection around Terceira used in this study. The Directorate for the Environment (Azores Regional Government) is thanked for sharing GIS data for the islands. The multibeam data collected around Faial, Pico and São Jorge were collected with the support of grants from the Higher Education Funding Council for Wales (NER/F/S/20/00/00146), the Royal Society, British Council and other sources mentioned in Mitchell et al. (2008). Sediment sampling in the shelves of Faial and Pico were conducted in the scope of the GEMAS Project funded by Secretaria Regional do Ambiente dos Açores. Submetrix swath surveying of the nearshore of Faial Island was funded by the Portuguese Foundation for Science and Technology (FCT) in project MAYA (AdI/POSI/2003). Paula Lourinho, Valter Medeiros and Ricardo Medeiros (IMAR-DOP of the University of the Azores) kindly digitised the seabed images in Fig. 5.10 from video footage. Damien Sirjacobs clarified aspects of the Youssef (2005) dataset. ARGO float data contributing to Fig. 5.14 were collected and made freely available by the Coriolis project and programmes that contribute to it (<http://www.coriolis.eu.org>). Chin-Yeh Chen, Zhongwei Zhao and Chih-Chieh Chien help to manage the wave property extraction.

Some figures were prepared with the GMT software system (Wessel and Smith, 1991) and QGIS (QGIS Development Team, 2009). We also thank editor Edward Anthony and two anonymous reviewers for comments that helped to re-focus the article.

**Chapter 6. Emplacement history of volcanoclastic turbidites
around the central Azores volcanic islands: frequencies
of slope landslides and eruptions**

This chapter is a reproduction of a manuscript submitted to the journal *Geosphere* with authors Chang, Y.-C., Mitchell, N., Schindlbeck-Belo, Julie C., Hansteen, T.H., Freundt, A., Hübscher, C., Quartau, R.

Y-C.C produced the original draft of the manuscript and figures. All co-authors contributed their opinions and comments on the draft manuscript.

In this chapter, I sampled, pictured and pre-processed foram from the hemipelagic beds in the cores for radiocarbon datings. I reinterpreted a segment from a hemipelagic bed as a volcanoclastic turbidite bed in core 1230 and correlated tephra beds to other parts of segments in different cores. I built four hemipelagic sediment age-depth models based on the radiocarbon dates and tephrochronology. I modelled turbidite volumes in the four depositional basins around the islands. I compiled the volume estimates from turbidite volume modelling, upper slope submarine landslides and ignimbrite-forming eruptions.

High-resolution bathymetric data were collected, processed and provided by co-authors R.Q and N.M (Mitchell et al., 2008; Quartau et al., 2014). The four gravity cores and photographic scans were collected during RV Meteor cruise M141/1 in 2017 and provided by co-authors T.H.H and A.F. The newly collected samples in core 1230 for electron microprobe (EMP) analysis were sampled and analyses conducted by co-author J.C.S. The ¹⁴C accelerator mass spectrometry (AMS) analyses and age calibrations were carried out by researchers at the Environmental Radiocarbon Laboratory at Scottish Universities of Environmental Research Centre (SUERC).

Abstract

Volcanic islands export clastic material to their surrounding oceans by explosive eruptions and lava emissions, biogenic production on their shelves and failure of their slopes, amongst other processes. This raises the question of whether geological events (in particular, eruptions and landslides) can be detected and dated, and whether any relationships (for example, with climate changes) can be revealed using sediment cores. The volcanically active central Azorean islands (Faial, Pico, São Jorge, and Terceira), with their neighbouring submarine basins are potentially good candidates for such an analysis. Here, chronostratigraphies for four gravity cores collected amongst the islands are constructed based on twelve ^{14}C radiocarbon dates and two dates derived by chemically correlating primary volcanoclastic turbidite horizons with ignimbrites on Faial and Terceira Islands. Age-depth models are built from the hemipelagic intervals to date individual turbidites. Volumes of turbidites are modelled by multiplying basin areas with bed thickness, allowing for various turbidite thinning rates and directions. The volumes of landslide-origin turbidites are only comparable with the largest volumes of their adjacent upper slope submarine landslide valleys, so deposits in the cores likely derive from these largest landslides.

Emplacement intervals of turbidites originating from both landslides and pyroclastic flows are found to be mostly a few thousand years. Frequencies of landslide-origin turbidites and hemipelagic sedimentation rates were both highest in the past 8 k.y. compared to preceding periods up to 50 k.y. High hemipelagic sedimentation rates are interpreted to be related to sea-level rise, allowing more shelf bioproduction and release of particles by coastal erosion. The coincident increased frequencies of submarine landslides may be associated with the increased sediment supply from the islands, resulting in a more rapid build-up of unstable sediments on submarine slopes. Notably, the results for turbidites of pyroclastic flow origins do not suggest a decreased eruption frequency towards the Holocene that has been found elsewhere.

Keywords: volcanic hazard assessment, age-depth modelling, eruption history, tephrostratigraphy, radiocarbon dating, basin analysis, submarine landslide

6.1 Introduction

Climate changes have been suggested to modulate volcanism because of mechanical responses of volcanoes to adjustments in stresses caused by changes in loading by ice (e.g., Hall, 1982; Nakada and Yokose, 1992; Glazner et al., 1999) or, for coastal or submerged volcanoes, by changes in hydrostatic pressure with sea-level fluctuation (e.g., Walcott, 1972; Wallmann et al., 1988). For instance, a lower eruption frequency has been suggested to be correlated with increased glacial loading (e.g., Jellinek et al., 2004). The reduced over-burden pressure during sea-level fall may encourage decompression melting in the mantle (e.g., Walcott, 1972; Wallmann et al., 1988), hence increasing volcanic activity. Satow et al. (2021) compared the past 360 kyr of sea-level change with the tephrochronology of Santorini Volcano. The records in marine sediment cores showed that ~98% of eruptive activity of the Santorini Volcano occurred during periods of sea-level falls and subsequent rises. According to their 2D numerical model, the decreased hydrostatic pressure may have induced relative tensile spreading in the roof of the volcano, leading dyke injections and eruptions. In contrast, Walker et al. (2021) came to a different conclusion, criticizing the oversimplified geometry and dimensionality of the model and the omission of the effects of crustal loading on stress balance.

Large flank collapses have been reported for both intra-plate oceanic islands (e.g., the Hawaiian Islands (Moore et al., 1994), Canary Islands (Masson et al., 2002) and Cape Verde Islands (Masson et al., 2008)), and island arcs (e.g., Montserrat (Wall-Palmer et al., 2014) and Ritter Islands (Ward and Day, 2003)). Coussens et al. (2016) compiled data on 25 volcanic island landslides and found no relationship between the timing of large landslides ($>0.3 \text{ km}^3$) and periods of rapid sea-level rise for intra-plate oceanic islands, but did find a correlation for island arcs. However, the dataset was small, so systematic changes in the timing and frequency of such events are still not well recorded or cannot be ruled out. To address this and potential climatic modulation of eruptions more datasets are needed of emplacement histories of volcanoclastic deposits in a variety of tectonic environments and with a variety of geomorphologies (Kutterolf et al., 2019).

The many flat-floored basins lying around the Azores islands lie only 10–30 km from eruptive centres and island slopes, potentially allowing the deposits of small events (both eruptions and slope failures) to be captured (e.g., Wall-Palmer et al., 2014). Continuing work on an extensive set of samples and geophysical data collected from RV Meteor cruise (Schmidt et al., 2019; Schmidt et al., 2020; Chang et al., 2021a), in this study, information from sediment cores, high-resolution multibeam bathymetric data and seismic reflection profiles (airgun and parasound) were combined to work out the magnitudes of sediment emplacements and how they varied over time. To build chronologies, planktonic foraminifers picked from hemipelagic beds were ^{14}C -dated by accelerator mass spectrometry (AMS) and two primary tephra beds were geochemically correlated with terrestrial volcanic deposits of known dates. Volumes of turbidites in the basins were modelled by considering various lateral flow thinning rates found in other similar basins. Our main aims are to (1) estimate the volumes of volcanoclastic turbidites for comparison with potential source volumes, (2) use a hemipelagic sediment age-depth model derived from ^{14}C dates to construct chronologies of the four cores, and (3), from them, derive emplacement frequencies for volcanoclastic turbidites produced by eruptions and landslides.

6.2 Regional Setting

The Azores islands have developed on a broad plateau of oceanic crust thickened by excessive volcanism, associated with a hotspot or mantle plume (White et al., 1976; Bonatti, 1990; Gente et al., 2003; Vogt and Jung, 2004). The islands are geologically young and active (Féraud et al., 1980; Madeira and Brum da Silveira, 2003). Volcanism and tectonic activity in the Azores have been continuing over at least the Quaternary (Forjaz, 1968; Calvert et al., 2006; Nunes et al., 2006). Moreover, eruption-fed (e.g., pyroclastic turbidite and fallout deposits) and mass transport (e.g., landslide-origin) turbidites are commonly recognised in the cores collected on the basin floors around the islands (Chang et al., 2021a), suggesting that volcanism and submarine mass transportation likely occur frequently in the central Azores.

6.2.1 Explosive eruptions on the central Azores islands

Eruptions in the central group of islands are generally moderate (i.e., from effusive Hawaiian to intermediate phreatomagmatic eruptions (Machado et al., 1962; Madeira and Brum da Silveira, 2003; Cappello et al., 2015; Zanon and Viveiros, 2019), but some explosive sub-Plinian and ignimbrite-forming eruptions have occurred on Faial and Terceira Islands (e.g., Self, 1976; Pacheco, 2001; Gertisser et al., 2010; Pimentel et al., 2015; 2021). The ignimbrite-forming eruptions were usually associated with caldera-forming or –enlarging events that produced widespread pyroclastic fallout dispersal, as well as pyroclastic density currents flowing tens of kilometres (e.g., Pimentel et al., 2015; 2021).

Three prominent ignimbrite-forming eruptions have occurred in the last 30 kyr. The C11 eruption (980 ± 50 years BP) was the most complex and prominent eruption of Caldeira Volcano of Faial Island (Fig. 6.1; Pacheco, 2001; Pimentel et al., 2015). It was the largest eruption on Faial within the last 16 kyr and its deposits widely blanket the island (Fig. 6.1). C11 deposits have been divided into the Brejo, Inverno, and Cedros members, representing three distinct eruptive phases (Pimentel et al., 2015). According to Pimentel et al. (2015), this eruption started with a series of phreatomagmatic explosions, causing ash to fallout on the NW sector of the island. The next phase (sub-Plinian) produced coarse pumice fall deposits over the north flank with narrow NNW dispersal. The final phase involved widespread pyroclastic density currents (PDCs) that reached the north and west sectors of the island. Pimentel et al. (2015) estimated on-land tephra volume for the eruption to be 0.18 km^3 (we refer to these as "bulk volumes", which are not corrected for pore space, i.e., not dense rock equivalent). The total tephra volume including submarine deposits was estimated by them to be $>0.22 \text{ km}^3$ using empirical methods of Sulpizio (2005) combined with those of Fierstein and Nathenson (1992).

Ignimbrites on Terceira Island constitute a significant portion of the island stratigraphy. At least seven ignimbrite sequences were emplaced between ca. 86 ka and ca. 25 ka BP (Calvert et al., 2006; Gertisser et al., 2010). The most recent Lajes-Angra Ignimbrite Formation originated from eruptions of Pico Alto volcano (Fig. 6.1). Two ignimbrites were initially interpreted by Self (1976) as resulting from two eruptions of Pico Alto volcano: the Angra and Lajes ignimbrite-forming eruptions. Although the Angra and Lajes ignimbrites have similar whole-

rock major element compositions and mineral assemblages, their whole-rock trace element and volcanic glass compositions differ considerably (Pimentel et al., 2021). Moreover, the Angra Ignimbrite is only exposed in a narrow valley in the southern part of the island. The Lajes

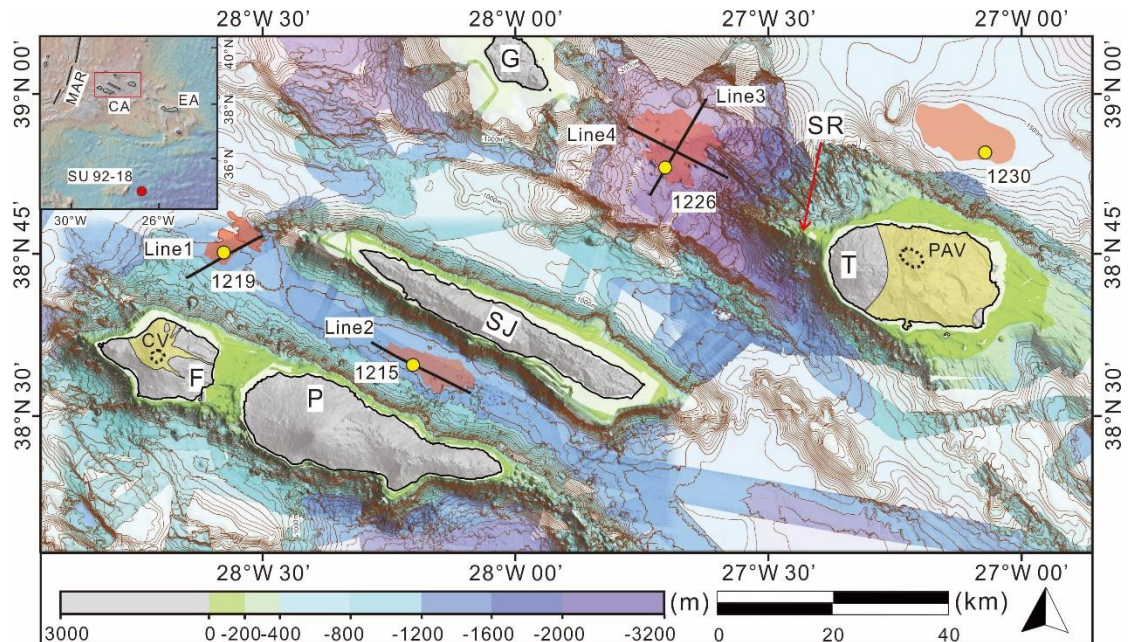


Figure 6.1. Bathymetry of the central Azores Islands contoured every 50 m from 500 to 3200 m. High-resolution multibeam echo-sounder data are shown in bold colours as key. Bathymetry in faint colours is from the Global Multi-Resolution Topography Synthesis of Ryan et al. (2009). Light grey areas represent the islands of Faial, Pico, São Jorge, Terceira, Graciosa (F, P, SJ, T and G, respectively). SR is submarine Serreta Ridge. Black dashed lines outline the inferred calderas of Caldeira Volcano (CV) and Pico Alto Volcano (PAV). Yellow on islands are extents of volcanic deposits on Faial (from the C11 eruption) and Terceira (Lajes eruption), which include volcanic ash and ignimbrites. Yellow circles locate gravity cores summarised in Fig. 6.2. Black lines (1 to 4) locate the seismic sections in Fig. 6.8. Salmon areas outline extents of turbidite depositional basins identified from depth contours and seismic reflection data. Inset locates study area (red rectangle) and reference core site (red circle). CA, EA and MAR represent the central Azores, eastern Azores and Mid-Atlantic ridge, respectively.

Ignimbrite, in contrast, is widely exposed in the southern, middle and northern parts of Terceira (Fig. 6.1). Radiocarbon dates of charcoal below and within the Lajes and Angra ignimbrite (Calvert et al., 2006; Gertisser et al., 2010), calibrated with the IntCal20 calibration curve (Reimer et al., 2020), suggest the Angra Ignimbrite was emplaced 25.3–28.1 cal ka BP (Gertisser et al., 2010) and the Lajes Ignimbrite 23.0–28.8 cal ka BP (Gertisser et al., 2010) or

25.2–25.9 cal ka BP (Calvert et al., 2006). Their juvenile clasts are characterised by coarse porphyritic pumices, including light grey comenditic trachyte pumice and dark grey/black scoriae, but the black clasts are exclusive to the Lajes Ignimbrite (Pimentel et al., 2021). The on-land bulk volumes of the Angra Ignimbrite and Lajes Ignimbrite were estimated to be 0.08 km³ and 0.59 km³ (Pimentel et al., 2021), respectively.

6.2.2 Volcanism-associated sediment gravity flows as turbidite sources

Deposits from pyroclastic flows and fallout have been recognised on the islands (e.g., Cole et al., 2001; Pacheco, 2001) and identified in the four sediment cores near to the islands (Chang et al., 2021a; Fig. 6.2). Effusive eruptions (Hawaiian to mildly explosive Strombolian) have likely occurred frequently (e.g., many times over the period of human habitation, Weston, 1964), so there is also a potential for submarine-emplaced lava flows to initiate sediment flows either due to the flow disintegration arising from rapid transportation on steep slopes (Bergh and Gudmunder, 1991) or flow front failures caused by piling up of lava fragments (Lodato et al., 2007; Mitchell et al., 2008; Quartau et al., 2015). Collapses due to slope overloading and oversteepening (Mitchell et al., 2012; Costa et al., 2014; 2015) result in large-scale mass movements, which can evolve downslope into sediment gravity flows.

Fig. 6.2 shows 41 volcanoclastic-rich beds found in the sediment cores located in Fig. 6.1. These are updated from the identifications of Chang et al. (2021a) as described later in this article. The beds include 9 pyroclastic fallout beds and 33 volcanoclastic turbidites. The turbidites were further classified into primary volcanoclastic turbidites (PVTs) and secondary volcanoclastic turbidites (SVTs). PVTs originate directly from pyroclastic flows where transport occurs without an intervening stage of deposition and remobilization. SVTs instead involve some seabed interaction or other events unrelated to volcanic activity such as slope failure. SVTs were distinguished from PVTs by distinct features, such as rounded volcanic particles and low proportions of glass shards, with usually heterogeneous glass shard compositions. They also always contain detectable organic carbon, whereas PVTs are not necessary. Two-thirds of these turbidites are PVTs. Their thicknesses are typically 0.05–0.15 m, though two PVTs are thicker (0.4 and 2 m). Although the PVTs were likely created by pyroclastic flows from eruptions of

the adjacent islands, core 1226 located within the Terceira Rift may have received PVTs from Terceira or from submarine eruptions on the Serreta Ridge, which is volcanically active (Gaspar et al., 2003).

6.2.3 Other sources of sediment gravity flows

Processes that have been suggested to generate sediment gravity flows on submarine slopes elsewhere also occur in the Azores. For instance, more than a thousand submarine landslide valleys have been identified along the upper slopes of four islands in the central Azores (Chang et al., 2021b). Downslope mass movements (landslides) may transform into turbulent sediment gravity flows if the mass disintegrates during movement (e.g., Nisbet and Piper, 1998; Piper et al., 2007). Landslides in the Azores potentially can be induced by frequent earthquakes (Gaspar et al., 2015). High ocean surface waves, which predominantly approach the islands from the NW, have been suggested to be responsible for more frequent submarine sediment gravity flows on the windward sides of islands (Chang et al., 2022) due to the increased sediment flux from wave erosion (e.g., Quartau et al., 2012; Zhao et al., 2020) supplying unconsolidated sediment to upper slopes, where it is prone to failure, or enhanced wave-agitated turbulent flows (e.g., Normandeau et al., 2020; Porcile et al., 2020).

In the investigated cores (Fig. 6.2), one-third of the turbidites are SVTs and hence involved some reworking of bed material, such as evidenced by fragments of carbonate of shelf origin and higher organic contents. The lower abundance of SVTs compared with PVTs suggests either that volcanic eruptions in the Azores are more frequent than slope failures or that sediment gravity flows generated by slope failures have not all reached the basin floors (Chang et al., 2022). The SVTs thicknesses are similar to PVT thicknesses but no SVTs thicker than 0.2 m have been found.

6.3 Materials and Methods

6.3.1 Sediment cores and sample collections

The four gravity cores were collected during Research Vessel (RV) *Meteor* cruise M141/1 in 2017 (Hansteen et al., 2017). They were sampled for ^{14}C AMS analysis, volcanic glass compositional analysis, and tephra-bed correlations at the positions shown in Fig. 6.2.

6.3.1.1 Samples for radiocarbon dating

Thirteen samples were selected for ^{14}C dating mostly in hemipelagic beds immediately overlying turbidites and tephra beds (Fig. 6.2). For those beds with gradational or bioturbated boundaries, samples were collected where hemipelagite and turbidite are in equal proportions. That proximity should allow reasonable estimates of the turbidite ages to be determined. Pretreatment of samples included sediment disaggregation in 10 wt% sodium hexametaphosphate, ultrasonic bathing, rinsing and wet sieving (Hajdas, 2008; Brock et al., 2010). Approximately 10 mg of planktonic foraminifers showing little sign of damage or alteration were hand-picked under a high-power dissecting microscope (e.g., Fig. 6.3). *Globigerina bulloides* and *Globigerinoides ruber* species were mainly selected due to their abundance. Although we prioritised selecting mono-planktonic species to reduce potential temporal biases (e.g., Ausín et al., 2019), other surface-dwelling planktonic species (e.g., *Globigerinella siphonifera* and *Globigerinoides sacculifer* shown in Figs. 6.3c and 6.3d) were sometimes included where abundance of the preferred species was low.

The AMS analysis was conducted by the National Environmental Isotope Facility (NEIF) radiocarbon laboratory at the Scottish Universities Environmental Research Centre (SUERC). Samples were acid-leached to remove external carbon contamination on outer shell surfaces (Hajdas, 2008; Brock et al., 2010) and then converted into pure and condensed carbon (Povinec et al., 2009) suitable for AMS analysis. $^{13}\text{C}/^{12}\text{C}$ ratios were measured by isotope ratio mass spectrometry (IRMS), and $\delta^{13}\text{C}$ values (deviation from reference $^{13}\text{C}/^{12}\text{C}$) calculated relative to the Vienna Pee Dee Belemnite (VPDB) standards. $^{14}\text{C}/^{12}\text{C}$ ratios were then corrected for fractionation by normalising $\delta^{13}\text{C}$ to -25 ‰ obtained from a pool of woods (a standard). The

conventional radiocarbon years before present (BP) with $\pm 1\sigma$ confidence ranges are shown in Table 6.1.

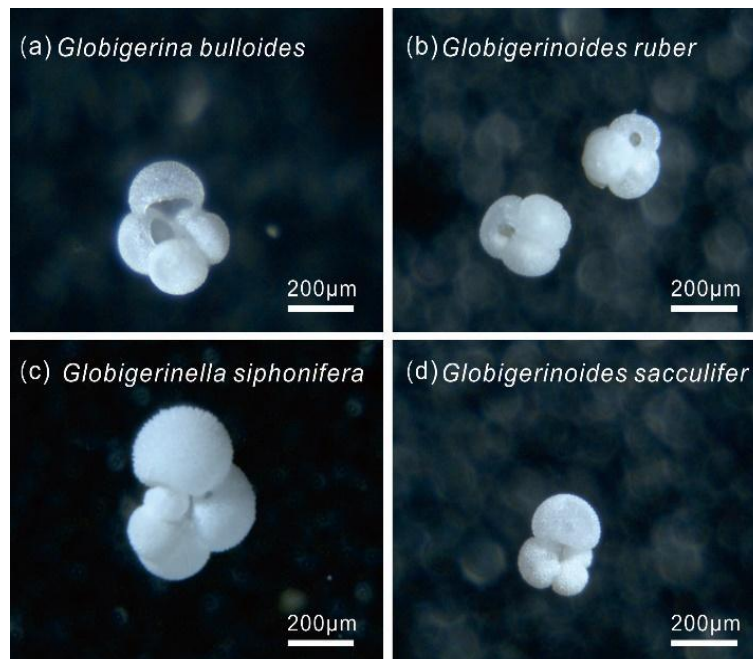


Figure 6.3. Selected photos of planktonic foraminifera species from the samples used for radiocarbon dating. (a) *Globigerina bulloides*. (b) *Globigerinoides ruber*. (c) *Globigerinella siphonifera*. (d) *Globigerinoides sacculifer*. The species in (a) and (b) were the main ones selected for ^{14}C dating in this study. Note glassy surface textures suggesting lack of alteration.

6.3.1.2 Radiocarbon age calibration and age-depth modelling

To correct for varying production rates of ^{14}C through time (Lal and Peters, 1967), radiocarbon ages were converted to calendar ages using Marine20 (Heaton et al., 2020), a marine-specific calibration curve that corrects for the marine reservoir effect (MRE) of non-polar areas and provides global-average marine dates within 0–55 cal kyBP. Correcting for a local MRE (i.e., deviation from the global curve or ΔR) is difficult around the Azores due to the lack of established values and appropriate materials for self-assessment (e.g., Ascough et al., 2005). Comparing global ΔR variations (Reimer and Reimer, 2001) with oceanic circulation in Ascough et al. (2005), however, ΔR around the Azores is probably between -51 and +14 yr. The age shifts due to the ΔR correction within this range are small compared with age differences between samples reported below, so variations in ΔR are ignored in this study.

Volcaniclastic bed thicknesses were subtracted from each core depth to build hemipelagic sediment age-depth models. The use of age-depth modelling relies on two assumptions, which we return to later: (1) no change in hemipelagic sedimentation rate between dates (e.g., Milkert et al., 1996; Lebreiro et al., 2009; Clare et al., 2015; Allin et al., 2016) and (2) negligible surficial deposits have been removed by turbidity currents (e.g., Weaver and Thomson, 1993; Thomson and Weaver, 1994; Gutierrez-Pastor et al., 2009; Gràcia et al., 2010). We used the median as the best estimates of sample calendar age. Age-depth relationships were then created by linear interpolation and those hemipelagic ages allowed the emplacement dates of turbidites and tephra to be estimated. Hemipelagic sedimentation rates were also found by dividing the calendar age differences between samples by the thickness of hemipelagic beds within them. Hemipelagic sedimentation rates were then found for discrete age intervals representing different periods of sea-level (0–8, 8–20 and 20–50 ka) by dividing the hemipelagic thickness of beds by the time span, using the interpolated calendar ages. Rates for those core intervals that do not entirely extend over a full age interval were computed by dividing the hemipelagic thickness by the duration that they spanned. A more regional estimate of the hemipelagic sedimentation rate curve was then computed by averaging the individual interval-averaged hemipelagic sedimentation rates of the four cores. The same calculation was also used to derive individual core and total interval-averaged frequencies of PVTs and SVTs within the selected date intervals.

6.3.1.3 Samples for sediment core reinterpretation and tephrostratigraphic correlations

The classification of bed types of Chang et al. (2021a) shown in Fig. 6.2 was updated in the light of data from six volcaniclastic samples from core 1230 at depths 168 to 262 cm below sea floor (bsf). Sample pretreatment and analytical procedures followed those of Chang et al. (2021a). Backscattered-electron images of whole samples were captured by JEOL JXA 8200 wavelength dispersive electron microprobe (EMP). Major elements were measured on volcanic glass shards by EMP at GEOMAR Helmholtz-Centre for Ocean Research Kiel following procedures described in Kutterolf et al. (2011).

Two PVTs in core 1219 at depths 22–29 cm bsf and core 1230 at 168–368 cm bsf were correlated with ignimbrites on adjacent islands. Correlations followed the established method of Kutterolf et al. (2008) by comparing the major geochemical elements of volcanic glass shards from marine tephras and from island samples, while their stratigraphic positions were validated using the age-depth model based on the radiocarbon dates. Mineral assemblage data and sedimentary features were also considered if they were available. The geochemical correlations are constrained by overlaps of multiple elements. The correlation followed a similar method applied to reconstruct tephra provenance offshore the southern central American volcanic arc (e.g., Schindlbeck et al., 2016; 2018).

6.3.2 Marine geophysical data

High-resolution multibeam bathymetric data were collected in four surveys at resolutions ranging from 0.5 to 1 m in the shallowest 100 metres to 20 to 50 m at 2000 m depth. The combined dataset broadly covers the submarine part of the central group of the Azores (Fig. 6.1). The RV *Arquipélago* survey in 2003 investigated the submarine parts of Faial, Pico and São Jorge islands (Mitchell et al., 2008). The *l'Atalante* survey (EUROFLEETS cruise “Features of Azores and Italian Volcanic Islands” (FAIVI)) in 2011 investigated predominantly the shelf and slopes of Terceira Island (Chiocci et al., 2013; Quartau et al., 2014; Casalbore et al., 2015). Though mainly investigating the area around São Miguel Island, the two RV *Meteor* surveys in 2009 (cruise M79/2; Hübscher, 2013) and 2015 (cruise M113/1; Hübscher et al., 2016) also covered partly the central group, in particular the basin between submarine Serreta Ridge and Graciosa Island.

2D multichannel seismic reflection profiles were collected during cruise M113 (Hübscher, 2016) using two GI-Guns of 45 and 105 cubic-inch volumes as a source. Signals were recorded with a 144-channel acquisition system. The main seismic processing steps involved editing, CMP binning, bandpass filtering over the range 10/20–300/400 Hz, gain, stacking, time-migration and fx-deconvolution. Processing is described further by Hübscher and Gohl (2016).

Also during M113, sediment profiler data were acquired using a hull-mounted Parasound system (Atlas Hydrographics) simultaneously with the multichannel seismic data. This system

operates by emitting two pulses with high primary frequencies (18 kHz and 22 kHz), which combined non-linearly in the water to produce a signal at their difference frequency of 4 kHz. The beams produced by the high primary frequencies form cones of $<4^\circ$ width, resulting in data without diffraction hyperbolae. Hence, Parasound data have high vertical and lateral resolution. Processing applied to the Parasound data included amplitude amplification and frequency filtering. Depth values have been derived from the Parasound data assuming a water velocity of 1500 m/s.

6.3.3 Turbidite volume modelling

If turbidites form simple flat-lying deposits of uniform thickness within basins, turbidite volumes can be estimated by multiplying the basin area with the turbidite thicknesses found in the cores. For such calculations, the area of each basin floor can be delimited using a closed bathymetric contour line (Fig. 6.1) encompassing the core site and located at the base of slope or tectonic structures revealed by the seismic sections. This approach makes the implicit assumption that turbidity currents, which are typically channelled on the slopes, are sufficiently mobile to spread out across the entire flat basin floor.

Such a procedure ignores the possibility of turbidites varying in thickness across each basin floor. To allow for bed thinning, the results of more detailed analysis of turbidite geometries in similar basins was drawn upon, in particular that of Liu et al. (2018). They classified thinning as occurring at low (3–15 %/km) and high (40–65 %/km) rates. Representing the rate with K (1/km), the rate of change is:

$$dT/dx = -KT \quad (1)$$

where T is bed thickness and x is distance. Integrating from a fixed reference point chosen at the origin ($x=0$ km) suggests:

$$T = T_0 \exp(-Kx) \quad (2)$$

where T_0 is the bed thickness at the reference position $x=0$ km. To implement the exponential model, the delimited basins (Fig. 6.4a) were idealised as rectangles of areas equal to the basins (Fig. 6.4b). The length and width of each rectangle were adjusted to represent approximately

the dimensions of each basin. Although turbidity currents potentially entered each basin from any side, we identified those sides that were closest to the most likely sources (for example, PVTs were most likely produced by eruptions of adjacent islands and SVTs by failure of adjacent steep slopes). Volumes calculated with different source directions then represent the effect of this uncertainty.

For each chosen source direction, volumes were estimated in practice by numerically integrating T in a series of 1-km steps over the direction in which the flows are assumed to have entered the basin and multiplying by rectangle width. Thinning rates of 9, 30.75 and 52.5 %/km were used, encompassing the most appropriate rates of Liu et al. (2018). Where the core site is opposite to the assumed source, the calculation results in volumes that are larger than those with no thinning, whereas core sites close to the source resulted in smaller volumes. Best estimates of individual turbidite volumes were derived using the most likely sediment entry direction and thinning rates suggested from seismic reflection data.

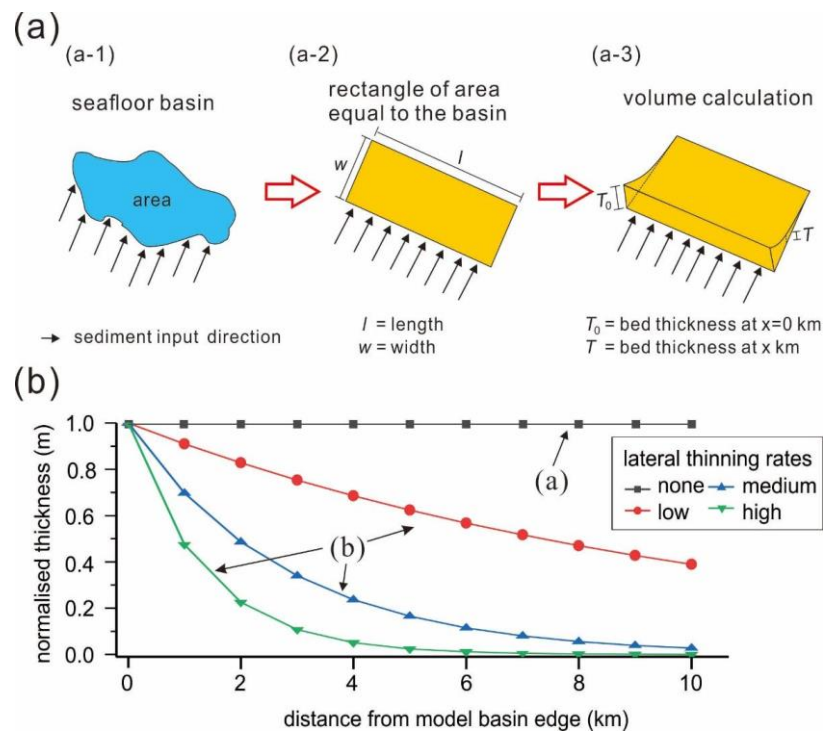


Figure 6.4. Conceptual elements of geometry used in calculation of turbidite volume, which attempts to account for varied degrees of deposit confinement and lateral thinning rate. (a) Flow of turbidite volume calculation. (b) Turbidite thickness change from model basin edge, encompassing four thinning rates. Example bed thicknesses variation with distance are normalised to 1 m.

6.4 Results

6.4.1 Stratigraphy of the sediment cores

The core stratigraphy that we established previously (Chang et al. 2021a) was improved and extended in three steps by: 1. reinterpreting one segment of hemipelagic beds in core 1230 as a primary volcanoclastic turbidite, 2. geochemically correlating two volcanoclastic beds with well-dated ignimbrites on Faial and Terceira Islands, and 3. incorporating the 12 new radiocarbon dates.

6.4.1.1 Bed reinterpretation

Chang et al. (2021a) originally interpreted the 168–262 cm below sea floor (bsf) section of core 1230 as hemipelagic sediment because this fine-grained section lacked tractional structures. However, visual inspection and chemical analyses by EMP of six additional samples (locations shown in Fig. 6.2) have led us to reinterpret it. Selected backscattered-electron images of 63–125 μm fraction from core 1230 at 168–170 cm bsf and 248–252 cm bsf revealed predominant volcanic glass shards and some biogenic matter and lithics (Fig. 6.5a and 6.5b), which are similar to samples at 262–368 cm bsf (Chang et al., 2021a). Besides minor outliers, major elements of four samples from the segment clustered closely (Fig. 6.5c and 6.5d). The consistency of the volcanic glass geochemical compositions across the interval suggests that the upper boundary of the thick turbidite previously placed at 262 cm bsf should be lifted to 168 cm bsf. The geochemical data for these six samples are provided in Appendix 6.1.

6.4.1.2 Tephrostratigraphic correlations

Multiple lines of evidence suggest that samples of core 1219 at 22–29 cm bsf and 1230 at 168–368 cm bsf correspond with ignimbrites on Faial (C11) and Terceira Island (Lajes), respectively.

1. Multiple major elements (MgO, SiO₂, FeO, CaO and TiO₂) derived from the groundmass glasses of the land samples overlap with those of the core samples (Fig. 6.6).
2. The elongated and stretched light grey pumiceous glass shard (e.g., Figs. 6.5a and 6.5b) both dominate the bed of core 1230 and the Lajes ignimbrite (Pimentel et al, 2021). The relative proportions of minerals (e.g., anorthoclase, plagioclase, clinopyroxene, olivine phenocrysts) in core 1230 (Chang et al., 2021a) are also similar to those described in the ignimbrite.
3. The stratigraphic

positions and dates of emplacement of these two ignimbrites (Calvert et al., 2006; Gertisser et al., 2010) are compatible with our hemipelagic age-depth models (see section 6.4.2). For instance, the $^{40}\text{Ar}/^{39}\text{Ar}$ dates of the ignimbrites are (C11) 930–1,030 yr BP and (Angra-Lajes) 23,000–28,800 yr BP (Calvert et al., 2006; Gertisser et al., 2010). Our age-depth model suggests 942–1,020 cal BP for the C11 bed and 27,013–27,240 cal BP for the Lajes bed. As mentioned earlier, we assign this bed to the Lajes ignimbrite given that the Angra ignimbrite only outcrops in a valley on the south of the island (opposite the core site).

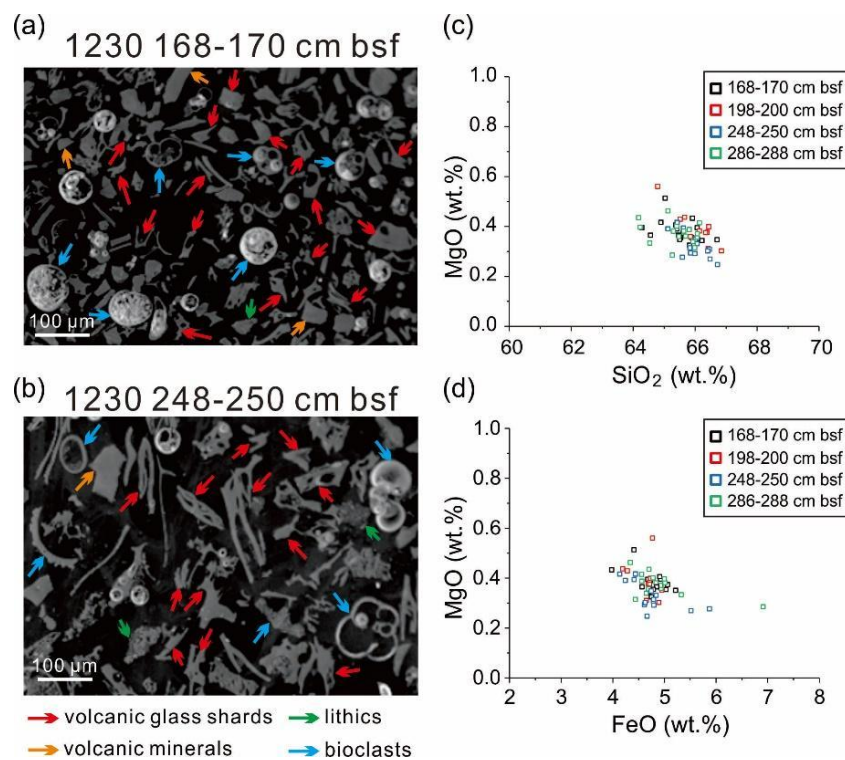


Figure 6.5. Data from samples of primary volcaniclastic beds in core 1230 from core depths 168–262 cm to 262–368 cm bsf. Backscattered-electron images in (a) and (b) are from the core depths marked above each image. Red, orange, blue and green arrows mark interpreted volcanic glass shards, volcanic minerals, biogeniclast and lithics, respectively. Major element compositions in (c) and (d) measured on glass shards taken from the core depths shown in the graph keys. Three outliers out of 80+ analyses were excluded from the graphs.

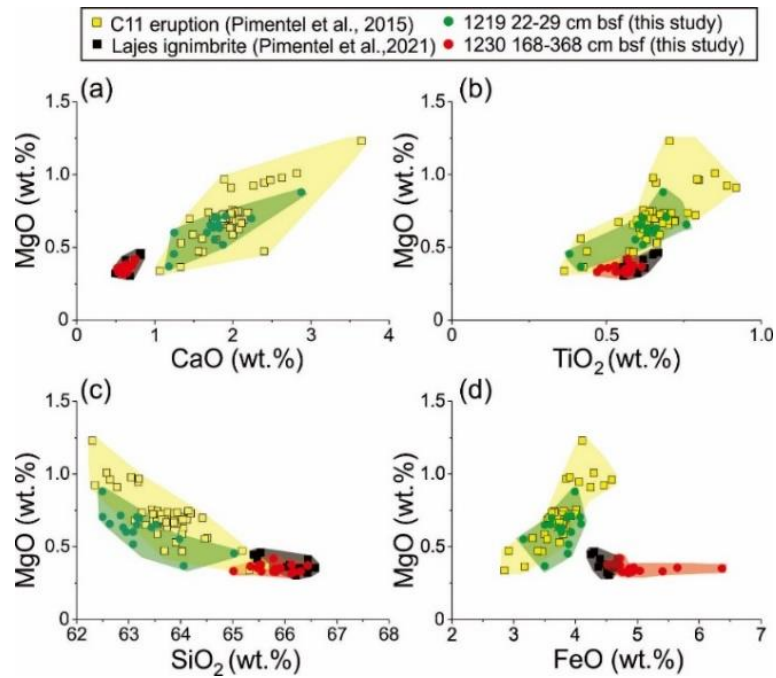


Figure 6.6. Comparison of major element compositions of two well-dated ignimbrites on land with those of volcanic glass shards in the sediment cores. Panels (a to d) compare data from core 1219 (22–29 cm bsf) with products of the Faial C11 eruption (Pimentel et al., 2015) and data from core 1230 (168–368 cm bsf) with products of the Terceira Lajes eruption (Pimentel et al., 2021).

6.4.1.3 Radiocarbon dates and age-depth modelling

The calendar ages and two dates of the ignimbrites correlated with volcaniclastic beds are shown in Figs 6.2 and 6.7. Most calendar dates had narrow uncertainty ranges (~300 yrs) except the fourth sample in core 1219 (~8,000 yrs), where ^{14}C concentration was low. The $\delta^{13}\text{C}$ values (1.0 and -1.0) are typical of marine foraminifera, also indicating low terrestrial contamination. The dates progressively increase down each core with no age reversals. The radiocarbon dates and associated data are listed in Table 6.1.

Table 6.1. Information on microfossil samples and radiocarbon dating results

Publication code	Sample no.	Sample depth (bsf cm)	Sample weight (mg)	Boundary	Dominant dated species	Conventional radiocarbon age ($\pm 1\sigma$, BP)	$\delta^{13}\text{C}$ VPDB (‰)	Calendar age (cal yr BP)	Best calendar age estimate (BP)
SUERC-100215	1215-1	39–40	10.6	gradational	G. bulloides and G. ruber	2,570 \pm 35	0.0	1,911-2,272	2,070
SUERC-100216	1215-4	128–129	10.2	gradational	G. ruber	6,315 \pm 38	-0.3	6,390-6,730	6,559
SUERC-100217	1215-7	201–202	10.5	gradational	G. bulloides	11,901 \pm 52	-1.1	13,065-13,400	13,220
SUERC-100218	1219-1	35–36	10.7	gradational	G. bulloides and G. ruber	2,168 \pm 35	1.0	1,415-1,726	1,582
SUERC-100219	1219-3	162.5–163.5	10.3	gradational	G. bulloides	14,349 \pm 57	-0.9	16,265-16,820	16,535
SUERC-100223	1219-5	229.5–230.5	10.2	gradational	G. bulloides	21,252 \pm 116	-0.6	24,170-24,930	24,543
SUERC-100224	1219-7	322–323	10.4	sharp	G. bulloides	45,384 \pm 2281	-0.6	44,351-54,564	46,992
SUERC-100225	1219-8	456.5–457.5	10.6	gradational	G. bulloides	>46,665	-0.9	Out of range	Out of range
SUERC-100226	1226-3	61–61.5	7.1	gradational	Mixture of four species	1,512 \pm 37	-1.0	743-1,047	894
SUERC-100227	1226-8	167–167.5	8.2	gradational	Mixture of four species	3,064 \pm 37	-1.1	2,507-2,840	2,691
SUERC-100228	1230-2	67–68	10.7	sharp	G. siphonifera and G. ruber	8,301 \pm 37	0.5	8,450-8,853	8,636
SUERC-100229	1230-4	128–129	10.7	sharp	G. bulloides and G. ruber	18,924 \pm 89	-0.7	21,710-22,286	22,006
SUERC-100233	1230-6	156–157	10.5	sharp	G. bulloides	22,473 \pm 134	-1.2	25,543-26,189	25,837

6.4.1.4 Sedimentation history

Fig. 6.7 shows the combined results of the sample datings (twelve ^{14}C dates and two correlated ignimbrites). The timings of inflections in the sea-level curve of Spratt and Lisiecki (2016) shown was used to separate the stratigraphy into periods of highstand (0–8 ka), transgression (8–20 ka) and regression (20–50 ka). Stratigraphy is present within core 1219 that is older than the oldest dateable ^{14}C date (~1.5 m of hemipelagics). One SVT within that interval was dated by extrapolation using the hemipelagic sedimentation rate from the overlying two ^{14}C dates.

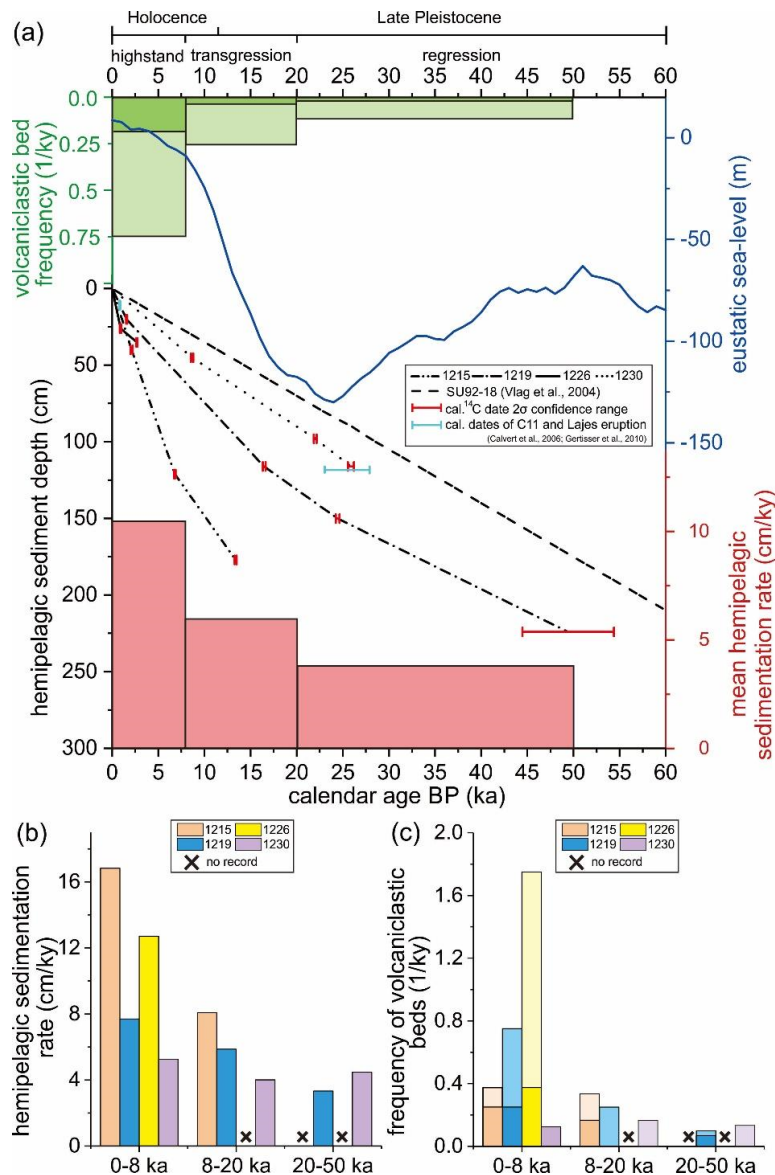


Figure 6.7. Sediment deposition history in the cores based on the ^{14}C dating and two correlated ignimbrites. (a) Black lines (scale to lower left) are hemipelagic age-depth models for the cores based on calendar age intervals (red horizontal bars represent at the 95% confidence level). Double-dashed line is the depth-averaged deep-sea hemipelagic sedimentation rate of 3.5 cm/ky (Vlag et al., 2004) for site located in inset to Fig. 6.1. Blue curve is eustatic sea-level of Spratt et al. (2016). Olive green bars are the interval-averaged frequencies of volcaniclastic turbidites for all cores combined (light and dark tones represent frequencies of primary and secondary volcaniclastic turbidites, respectively). Pink bars are interval-averaged hemipelagic sedimentation rates that have been averaged between the four cores where stratigraphy is present. (b) Interval-averaged hemipelagic sedimentation rates of individual cores. (c) Interval-averaged frequency of volcaniclastic turbidites of individual cores (light and dark tones represent primary and secondary volcaniclastic turbidites, respectively). Black crosses in (b) and (c) mark where cores did not penetrate to the age range shown.

In each of the four hemipelagic sediment age-depth models shown in Fig. 6.7a (black lines), all dates progressively increase with depth with no major change of trend that might indicate sediment abruptly removed by erosion (eroded intervals are not resolved). They mostly steepen into the Holocene. This is reflected in greater average hemipelagic sedimentation rates shown by the pink bars in Fig. 6.7a, which increase from ~5 cm/ky in the regression period to ~11 cm/ky in the highstand period. Focusing on the better-constrained stratigraphy after the regression period, sedimentation rates increased from transgression to highstand periods by nearly a factor of two. These rates are all higher than the average open-ocean sedimentation rate at site SU92-18 (3.5 cm/ky; Vlag et al., 2004) et al., 2004). Fig. 6.7b shows that these variations occurred consistently amongst the cores, though rates increased more modestly into the highstand period for core 1230.

Emplacement ages of turbidites and tephra were derived from the age-depth models using the interpolated calendar ages through the hemipelagic intervals (Table 6.2). The interval-averaged frequencies of emplacements of primary and secondary volcanoclastic turbidites (PVTs and SVTs, respectively) are shown in Fig. 6.7a by light and dark tone olive green bars, respectively. (As mentioned earlier, the PVTs and SVTs are interpreted as respectively caused by pyroclastic flows that entered the sea directly and by sediment gravity flows resulting from remobilisation (such as landsliding) of such deposits on the shelf or slope of the island). Return periods of both types of turbidites are >1 ky. The frequencies of PVT and SVT emplacements were both higher during the transgression and particularly during the highstand period compared to the preceding regression period (Fig. 6.7a). Relative to frequencies during the regression period, PVT emplacements increased by factor 2.5 during transgression and by factor 6 during the highstand. SVT emplacements increased by factors of 4.5 and 7.5 over the corresponding periods. Examining the records from individual cores (Fig. 6.7c), these frequencies vary amongst sites. While emplacement frequencies of all turbidite types in cores 1230 and 1215 were comparable between transgression and highstand, in core 1219 frequencies increased into the highstand period. The PVT frequencies in cores 1215 and 1230 slightly decreased toward the highstand period, whereas that in core 1219 increased. Although core 1226 did not penetrate sediment

older than 8 ka, its PVT frequency was higher than the other cores. SVT frequencies of cores 1215, 1219 and 1230 all consistently increased into the highstand period.

Table 6.2. Modelled ages and volumes of volcanoclastic turbidites

Volcanoclastic deposit number	Core	Bed thickness (cm)	Bed type	Calendar age (cal yr BP)	Best estimates of turbidite volumes (10^6 m^3)
1	1215	4	SVT	3,830–3,888	2.10
2	1215	4	SVT	5,223–5,281	2.10
3	1215	4	PF	6,791–6,915	NA
4	1215	13	SVT	11,489–11,613	6.85
5	1215	13	SVT	13,344–13,467	6.85
6	1215	11	PVT	13,344–13,467	5.79
7	1215	7	PF	>13,344	NA
8	1219	10	PVT	791–870	2.64
9 (C11 eruption)	1219	6	PVT	949–1,028	1.58
10	1219	9	PVT	1,661–1,817	2.37
11	1219	9	PVT	1,661–1,817	2.37
12	1219	4	SVT	1,661–1,817	1.06
13	1219	7	SVT	1,661–1,817	1.85
14	1219	2	PF	11,629–11,785	NA
15	1219	7	PVT	17,243–17,491	1.85
16	1219	26	PVT	19,470–19,717	6.87
17	1219	3	SVT	24,914–25,220	0.79
18	1219	2	SVT	39,892–40,197	0.53
19	1219	14	PF	45,699–46,005	NA
20	1219	5	SVT	88,187–88,492	1.31
21	1226	23	PF	620–657	NA
22	1226	9	SVT	620–657	3.37
23	1226	5	PVT	620–657	6.03
24	1226	23	SVT	949–1,154	8.88
25	1226	14	PVT	949–1,154	16.33
26	1226	40	PVT	949–1,154	48.25
27	1226	7	PVT	949–1,154	8.17
28	1226	13	PVT	949–1,154	15.17
29	1226	4	PVT	2,794–2,999	4.82
30	1226	2	PVT	2,999–3,203	2.41
31	1226	2	PVT	>3,203	2.41
32	1226	4	SVT	>3,203	1.55
33	1226	17	PF	>3,203	NA
34	1226	10	PVT	>3,203	12.05
35	1230	23	SVT	8,252–8,444	11.47
36	1230	8	PVT	11,159–11,411	3.99
37	1230	9	PVT	22,511–22,718	4.49
38	1230	1	PF	24,382–24,590	NA
39	1230	2	PF	26,045–26,253	NA
40	1230	3	PF	26,877–27,084	NA
41 (Lajes Eruption)	1230	200	PVT	>27,084	99.72

PF: pyroclastic fallout, PVT: primary volcanoclastic turbidite, SVT: secondary volcanoclastic turbidite, NA: none applicable

6.4.2 Turbidite volume modelling results

Seismic sections (Figs. 6.8b to 6.8d) and bathymetric data (Fig. 6.9a) show that the sites of cores 1215, 1226 and 1230 are located within closed-contour depressions and/or surrounded by tectonic structures (e.g., faults) so their basin floors are well-constrained. In contrast, core 1219

was collected from the lower slope of Faial island (Fig. 6.8a). For that site, we approximated the depositional basin length as extending from a small escarpment up-slope to the edge of a graben downslope (Fig. 6.8a) and the basin width as the graben length. The model rectangles of equal basin area are shown in Figs 6.8a to 6.8d, which have areas of 3.9×10^7 – 1.1×10^8 m².

The in-situ lateral thinning of beds was assessed using Parasound data collected perpendicular to suspected sediment input directions (Figs. 6.8f and 6.8g). In Fig. 6.8f (northwest of Terceira), an interval encompassing a transparent section (a possible mass-transport deposit) tapers westward from 3.56 to 1.4 m thickness over a distance of 2.83 km, suggesting a thinning rate of 33%/km, close to the moderate thinning rate of Liu et al (2018). A similar thinning rate can be inferred from Fig. 6.8g. Although strictly speaking these observed thinnings likely represent more than single beds, they suggest that the modelling with 30.75%/km (blues curves in Fig. 6.9f) should provide the best volume estimates.

Turbidite volumes were estimated allowing for different thinning rates and input directions (Fig. 6.9f). Sediment input directions for PVTs in cores 1219 and 1230 were both chosen from the south sides of the basins, based on proximity of Faial and Terceira Islands. Core 1215 was interpreted as receiving PVTs and SVTs mainly from Pico and São Jorge Islands. Although some sediment flows originating from large events (either pyroclastic flows or landslides) may have been directed longitudinally along the basin floor, the mostly uniform interval of reflections in the Parasound data collected parallel to Pico and São Jorge (Fig. 6.8e) suggests that such events have been infrequent. We considered three potential sources of turbidity currents for core 1226: Graciosa and Terceira Islands and Serreta Ridge. Frequent observed

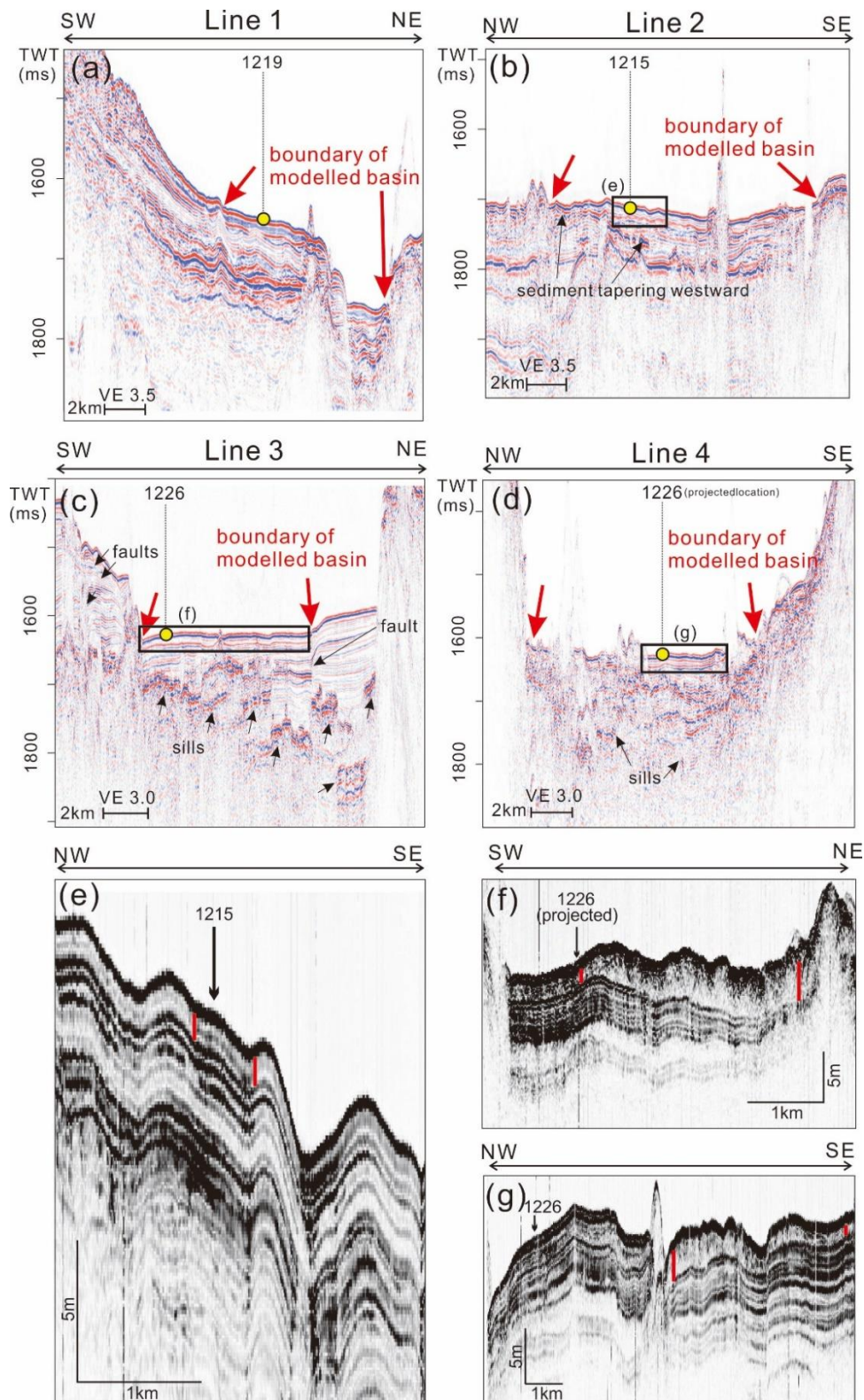


Figure 6.8. Seismic reflection data over core sites. (a to d) Multichannel airgun seismic reflection images collected along the lines shown in Fig. 6.1. Basin boundaries assigned on the basis of the multibeam data are marked by bold red arrows. (e to g) Parasound sediment profiler records corresponding with the rectangles in (b) to (d). Vertical red bars illustrate some varied separations of reflections along these lines.

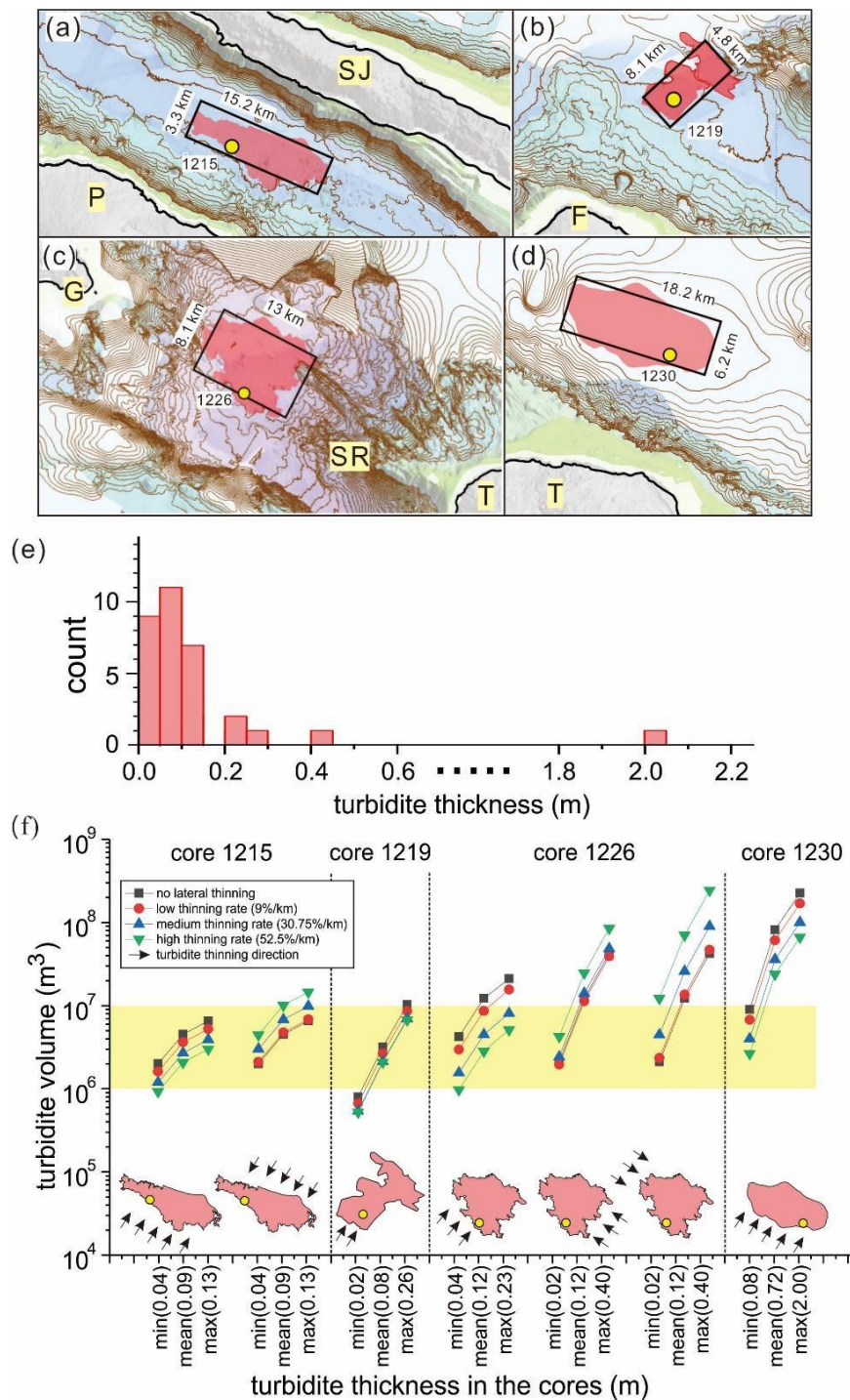


Figure 6.9. Turbidite volume modelling results. (a to d) Bathymetry (contoured every 50 m) with interpreted turbidite basins (pink) superimposed with rectangles of equal area (black outlines). Yellow circles locate sediment cores. (e) Thickness distribution of volcaniclastic beds of the four gravity cores combined. (f) Turbidite volumes for each core modelled with various thinning rates, sediment input directions and range of turbidite thicknesses found in the cores. Yellow block encompasses the dominant range of modelled turbidite volumes.

Holocene pyroclastic particles and relatively low carbonate contents (10–20%; Chang et al., 2021a) in the deposits suggest that PVTs and SVTs in core 1226 probably are not mainly sourced from the Graciosa Island, where explosive eruptions have become mostly inactive (Larrea et al., 2014) and biogenic productions on the shelf have been boosting since the Holocene. Therefore, the PVTs in core 1226 are suggested to have been dominantly emplaced from the southeast, where many active volcanic ridges are adjacent to the depositional basin. In practice, the escarpment southwest of site 1226 likely only sources SVTs as it is a tectonic feature (the southerly fault escarpment of the Terceira Rift). Volume calculations with the southerly source were therefore only applied to SVTs for core 1226. The modelled volumes are 10^5 – 10^9 m³ but mostly 10^6 – 10^7 m³ (yellow bar in Fig. 6.9f).

The best-estimated volumes of individual turbidites were calculated (Table 6.2), allowing for the preferred 30.75%/km thinning rate and the most likely sediment entry direction in each case. As PVTs and SVTs in core 1215 were potentially emplaced from either Pico or São Jorge Islands, the best-estimated turbidite volume for each bed was an average of the volumes estimated with those two alternative origins. Volumes in Fig. 6.9f vary by up to two orders of magnitude due to bed thickness variations and by up to one order of magnitude because of varied thinning rates.

6.5 Discussion

6.5.1 Implications of the turbidite volume estimates

6.5.1.1 Comparing SVT volumes with upper-slope landslide volumes

The estimated volumes of SVTs range from 10^5 to 10^8 m³ (Fig. 6.10). For comparison, the volumes of landslide valleys in the upper submarine slopes adjacent to the core sites are 10^2 to 10^8 m³ (dark orange bars in Fig. 6.10). The estimated SVT volumes only overlap the volumes of the larger landslide valleys, suggesting that only the larger landslide deposits have been preserved in the cores. The sediment gravity flows initiated by smaller landslides probably deposited on the slopes before reaching core sites, producing thin beds in the basin floors that cannot be identified by eye or were obscured by bioturbation. Nonetheless, these results show that moderate-sized landslide deposits should be preserved within such proximal basins. This

contrasts with core sites that are >100 km from volcanic islands which only preserve turbidites originating from giant landslides (e.g., >10¹¹–10¹² m³; Hunt et al., 2013). Our comparison suggests a more comprehensive landsliding history can be preserved in the depositional areas adjacent to the islands, as also found in the continental margins (e.g., Jobe et al., 2018 and references therein). Landsliding inventories are also potentially available for volcanoes with similar proximal basins.

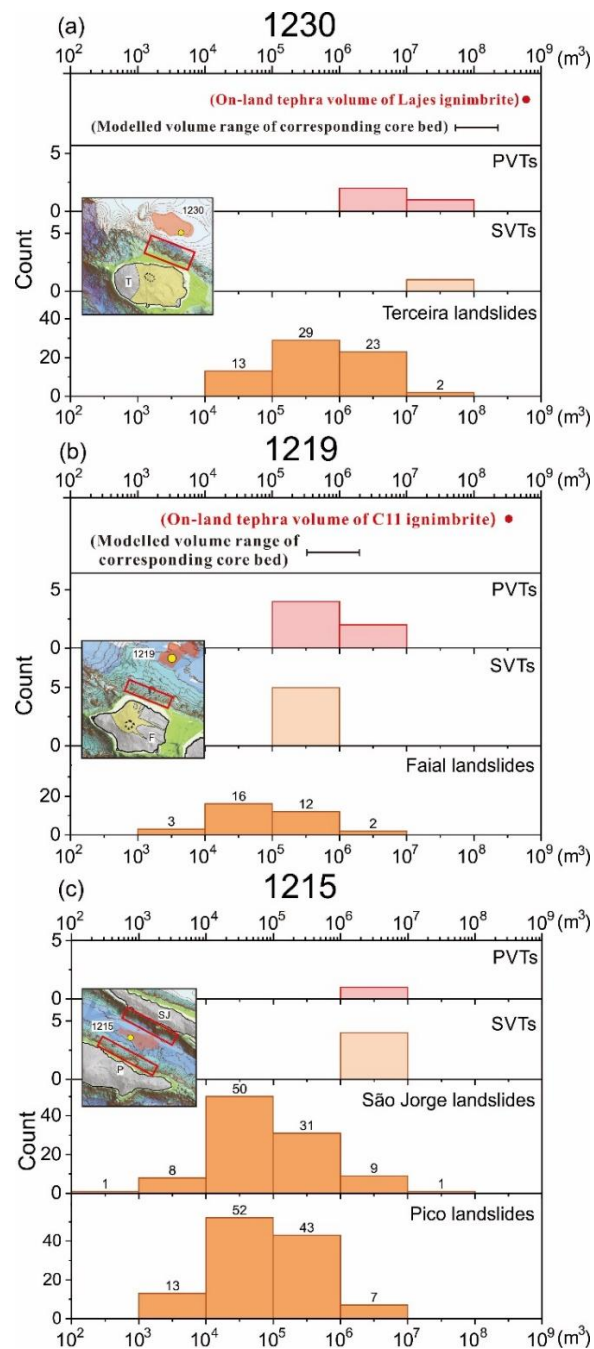


Figure 6.10. Basin-floor volumes of turbidites predicted with 30.75%/km (intermediate) thinning rates (pink and light orange histograms) for cores 1230, 1219 and 1215 compared

with volumes of landslide valleys in their adjacent upper submarine slopes (dark orange histograms) derived from Chang *et al.* (2021b). Also shown are (red dot in (a)) estimated on-land tephra volume of the Lajes erupted materials from Pimentel *et al.* (2021) and (red dot in (b)) estimated tephra volume (on land and offshore) of the C11 erupted materials from Pimentel *et al.* (2015). Slope regions selected for landslide valley volumes are located by red rectangles on maps. SVTs and PVTs represent secondary and primary volcanoclastic turbidites. The volumes of Pimentel *et al.* (2015 and 2021) and our modelled volumes of PVTs and SVTs are tephra volumes, hence not dense rock equivalents (corrected for pore volumes).

6.5.1.2 Comparing PVT volumes for the C11 and Lajes eruptions

The PVT volumes allow an assessment of the proportion of pyroclastic sediments transported into the sea and allow us to update estimates of total volumes from eruptions. The best-estimated volume of the PVT that is associated with the Lajes eruption in core 1230 (Fig. 6.10a) is 10^8 m^3 (5×10^7 to $2 \times 10^8 \text{ m}^3$, a range due to the different thinning rates). The volume is of similar order of magnitude but slightly less than the $5.9 \times 10^8 \text{ m}^3$ of the on-land bulk volume of Lajes ignimbrite estimated by Pimentel *et al.* (2021). A significant portion (i.e., 8–33%) of the erupted material was therefore discharged into the ocean and reached the basin floor. We can thus adjust the total volume of erupted pyroclastic material of the Lajes eruption to $6.9 \times 10^8 \text{ m}^3$. The estimated volume of the PVT corresponding to the C11 eruption (Fig. 6.10b) is $1.58 \times 10^6 \text{ m}^3$. This is at least two orders of magnitude smaller than the volume ($> 2.2 \times 10^8 \text{ m}^3$) of the ignimbrite on land estimated by Pimentel *et al.* (2015). Two factors may explain this contrast. First, the two initial eruptive phases led to deposition mostly towards the north and northwest of the caldera on Faial (inset map to Fig. 6.10b). The basin-floor sediments may have mainly been emplaced during the last phase of pyroclastic density currents, which Pimentel *et al.* (2015) showed had a more north-easterly component. Second, the seismic section in Fig. 6.8a suggests that sediments were likely also deposited widely on the upper island slopes rather than solely in the basin floor, which leads to an underestimation of the actual volume.

As ignimbrite-forming eruptions have occurred repeatedly on Terceira, the island is likely to host similar eruptions in the future (Pimentel *et al.*, 2021). Precisely estimating the areas to be affected by erupted material is difficult for small volcanic islands as the portions of material

transported offshore are usually unclear (Walker, 1981). Our tephra correlations imply that the C11 and Lajes deposits extend offshore at least 20–30 km, a distance 3–5 times further than the outcrops on land had suggested. The turbidite volume modelling also indicates that a significant portion of the Lajes ignimbrite discharged into the sea, probably in a tsunamigenic process. We suggest that further sediment cores from the slopes and around the basins would be desirable to constrain better the lateral thickness variations and total volumes. This should include the southern basin of Terceira, given that the Lajes ignimbrite also extended southwards

6.5.1.3 Comparing sediment fluxes in source areas with depositional fluxes in basins

The ^{14}C -dated sediments allow depositional fluxes in the basins to be compared with fluxes of sediment released by erosion on the islands, eruptive activity and biogenic production on their shelves. For this, we use results of Quartau et al. (2012) for Faial Island. They provided flux estimates for the past 6.5 ky from onshore and shelf sources for around 1/4 of the island (their sectors F and G in their Table 3). We divided those fluxes by a factor of two to allow for the smaller length of the north coastline of Faial adjacent to the basin containing core site 1219.

The estimated total sediment flux of $45.2 \times 10^6 \text{ m}^3/\text{ky}$ includes subaerial sources (pyroclastics from recent eruptions, cliff erosion and riverine erosion) of $44 \times 10^6 \text{ m}^3/\text{ky}$ and submarine sources (bioclasts) of $1.2 \times 10^6 \text{ m}^3/\text{ky}$. All such sediments can be assumed to be Holocene in age as there is no evidence of older stratigraphy in the boomer records.

We can also assess how much particle accumulation has occurred in the hemipelagic deposits, some of which likely comprise fine particles also originating from the island (e.g., remobilised volcanic ash). By assuming a uniform pelagic sedimentation rate in the 0–8 ka period, the hemipelagic flux in the seafloor basin of core 1219 is estimated to have been $3 \times 10^6 \text{ m}^3/\text{ky}$. This is only 6.7% of the island-generated flux. We also assessed the sediment fluxes arising from the island with those of the SVTs. The mean SVT flux was $1.1 \times 10^6 \text{ m}^3/\text{ky}$ obtained by dividing the total turbidite volume in the basin by the SVT emplacement frequency in core 1219 over 0–8 ka. This depositional flux is only ~2.4% of the island-generated flux. Therefore, there is a large difference (90.9%) between the flux supplied from the island and the combined hemipelagic and SVT fluxes in the basin. The discrepancy is a minimum as some of the

hemipelagic particles are tests of pelagic organisms, although some dispersal of ash away from the basin could make it a maximum.

We had inferred earlier that only the largest SVTs are preserved at the core sites, implying that smaller landslides produce sediment gravity flows that deposit on the slopes. The flux discrepancy also supports that inference. Thick sequences of reflections dipping parallel to seabed are commonly observed within the flanks of other oceanic islands (e.g., the Hawaiian Islands (Leslie et al., 2002), the Marquesas Islands (Wolfe et al., 1994) and the Canary Islands (Watts et al., 1997; León et al., 2017)). These are likely at least partly due to clastic deposits from sediment gravity flows that have not fully runout. Some shallow examples of such reflections are shown in Fig. 6.8a.

6.5.2 Has sediment deposition history been affected by climatic changes?

In order to address this question, in the following we discuss our observations that both hemipelagic sedimentation rates and frequencies of submarine landsliding were generally higher during the time of sea-level highstand (0–8 ka) than during the sea-level transgression or regression (Fig. 6.7a), strongly suggesting a direct or indirect climatic influence.

6.5.2.1 Hemipelagic sedimentation rates

Around the Azores islands, riverine supply of sediment is considered to be minor compared to supply by shelf biogenic production, coastal erosion and volcanism (e.g., Quartau et al., 2012; Ramalho et al., 2013). During sea-level highstands, the wide submerged insular shelves of the islands allow increased biogenic productivity that would not occur if the shelves were exposed above sea-level (e.g., Ramalho et al., 2013). Sea-level highstands, such as at present, also allow waves to attack and erode the tall sea cliffs (e.g., Zhao et al., 2020), which Quartau et al. (2012) suggested to be the primary source of sediments to the shelf. In contrast, the sea cliffs would be more protected from attack with sea-level a few tens of m lower than at present. The high emplacement frequencies of PVTs in core 1219 and 1226 (Fig. 6.7c) suggests that increased pyroclastic activity provided an additional supply of easily erodible volcanoclastic material.

6.5.2.2 Frequencies of secondary volcanoclastic turbidite emplacements

Many of the upper-slope landslides in the Azores have been suggested to have been triggered by ground shaking during earthquakes (Chang et al., 2021b). As earthquakes occur randomly over time, they do not clearly explain the increase in SVT emplacements into the sea-level highstand period. Seismogenic faults are common among the islands (Madeira et al., 2015) and many faults in sea areas between them (Casalbore et al., 2015; Mitchell et al., 2018) are likely seismogenic also. GPS-measurements also suggest widespread displacements from distributed tectonic deformation and volcano deformation (D'Araújo et al., 2022).

Sidescan sonar and grain-size data suggest that sediment released by coastal erosion is transported towards the outer shelves and upper slopes of the islands (Chang et al., 2022). As such sediment fluxes are likely greater during high-stand conditions due to exposure of sea cliffs to waves (Quartau et al., 2012), more rapid deposition onto the upper slopes can be expected. The amount of time for such deposits to over-steepen and/or become thick enough to generate large sediment gravity flows when failed will also be shortened. The increased frequency of SVT seems therefore more likely associated with higher sediment fluxes towards the present day.

The enhanced high-stand SVT emplacement and hemipelagic rates prompt us to investigate whether the changes in the source fluxes we propose ultimately affected the volumes of SVTs in the basin, i.e., did a larger flux of sediment from the shelves lead to larger landslides and hence larger SVTs? Chang et al. (2021b) found different landslide scar volumes between the different islands, with larger volumes and scars in the slopes of São Jorge and Terceira islands compared with Pico and Faial Islands. The volume variations were interpreted as being due to greater build-up of sediment around São Jorge and Terceira between major earthquakes. Hence, a larger flux might potentially lead to a thicker accumulation of unstable sediment before failure. Fig. 6.11, however, shows no significant systematic correlation between the best-estimated SVT volume with age. This discrepancy suggests that even if there is any correlation, it cannot be resolved by this small dataset. Further analyses of cores around the islands are needed to investigate this issue.

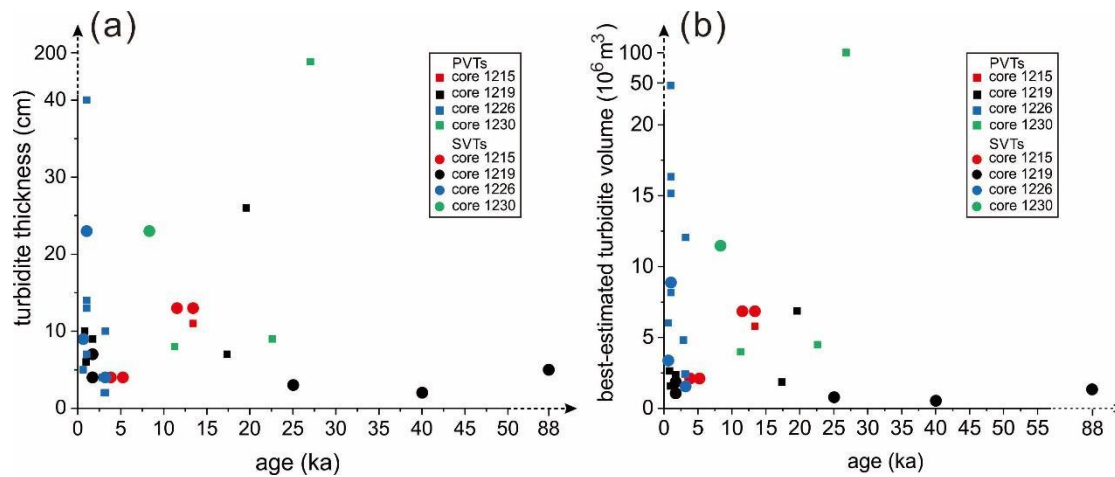


Figure 6.11. Temporal variations in (a) turbidite thicknesses and (b) best-estimated turbidite volumes. PVTs and SVTs are primary volcanoclastic turbidites and secondary volcanoclastic turbidites, respectively.

6.5.2.3 Frequencies of primary volcanoclastic turbidite emplacements

PVT emplacements became more frequent overall in the sea-level highstand period (Fig. 6.7a), but varied PVT frequencies with time in the different cores (light tone colours in Fig. 6.7c) reflected different explosive sources. For instance, PVT frequency was nearly constant from the transgression to the high-stand period in core 1215, whereas it decreased in core 1230. In contrast, PVT frequencies for core 1219 increased into the highstand period. Frequencies for core 1226 were high in that period, although we have no data on previous times. Since each core had different predominant volcanic sources, there is no evidence that those sources reacted in any coordinated way to sea-level and/or climate changes. Thus, we find no evidence for increased volcanic activity due to unloading during the low sea-level stand (Hasenclever et al., 2017) and also find no evidence for the suppression of eruptions by stresses induced by sea-level rise as proposed for Santorini (Satow et al., 2021). The Azores islands also have elevations that are too low for glaciers to have been widespread at this latitude during the last ice age. The equilibrium line altitudes of glaciers in Spain and Portugal at similar latitudes (e.g., Hannah et al., 2017; Palacios et al., 2017; Serrano et al., 2017) are higher than the highest mountain in the Azores (Mount Pico, 2,351m).

There is also no resolvable systematic change in PVT volumes between transgression and high-stand periods overall (Fig. 6.11b). For instance, PVT volumes for cores 1219 and 1226 vary somewhat similarly to the SVT volumes at those sites. PVT volumes in core 1219 are small compared to PVT volumes in other cores. In contrast, PVT volumes in core 1226 vary more greatly, likely a result of many different volcanic eruptions occurring on the Serreta Ridge. The different variation in eruption frequency and erupted volumes with time between the cores suggests that eruptions were not modulated by direct or indirect climatic influence. Rather temporal variations are more likely a result of variations in magma supply or tectonic processes affecting eruptions (e.g., Kappel and Ryan, 1986). Further work on the chronology of eruptions in the Azores would help evaluate if the change in eruption frequency occurred more widely.

6.6 Conclusions

Four chronostratigraphies have been developed based on 12 calibrated ^{14}C radiocarbon dates from hemipelagic beds in the four sediment cores and from two pyroclastic turbidites correlated with ignimbrites formed on Faial Island (C11 at ~1,000 BP) and Terceira Island (Lajes at ~25,000 BP). Age-depth models for the hemipelagic components were reconstructed to date the emplacements of turbidites and tephra in each core to a maximum ~50 ka. Return periods of eruptions and landslides large enough to generate turbidites within the cores were found to be mostly >1 ky for both turbidite types. Hemipelagic sedimentation rates and submarine landslide frequencies were higher in the past 8 k.y. than in the previous few tens of thousands of years. The increased hemipelagic sedimentation rate could be explained by sea-level rise, which enhances erosion of subaerial sea cliffs and biogenic production on shelves. More frequent emplacements of pyroclastic turbidites were found in some cores for the last 8 k.y.; if this occurred more widely, eruptions also supplied more friable volcanoclastic material to both submarine and subaerial areas. The higher submarine landslide frequency of the last 8 k.y. is probably associated with the greater sediment supply, leading to more rapid build-up of unstable sediment on the submarine slopes of the islands. The more frequent emplacement frequency of primary volcanoclastic beds in some cores and lack of increase in others during 0–8 k.y. contradicts models that have been proposed in which higher sea-level loads magma

chamber roofs, leading to lower eruption frequencies. We suggest this different eruption timing may in part be due to temporal variations in magma supply, which can occur in volcanic rifts.

Turbidite volumes have been estimated allowing for varied thinning rates across basin floors and different input directions of sediment flows. The estimated volumes are 10^5 – 10^9 m³ (mostly between 10^6 – 10^7 m³). The volcanoclastic turbidites of landslide origin are comparable in volume with only the largest of their adjacent upper slope submarine landslide valleys, so most landslides lead to mass flows that deposit on the slopes and do not reach the basins. This inference is also supported by a major imbalance of sediment export flux of Faial with the depositional flux of SVTs and hemipelagic sediments in core 1219. We therefore suggest that the dipping reflection found in the flanks of many volcanic ocean islands are mostly due to clastic material that has not fully run-out to the adjacent basin floors.

The volume differences between basin-floor pyroclastic turbidites and their associated erupted units on land allow the total volumes and proportions exported offshore to be addressed. For instance, 8–33% of pyroclastic material from the Lajes eruption was emplaced in the basin north of Terceira, hence the erupted volume was 6.5 – 8.2×10^8 m³ larger than previously suggested. In contrast, the volume of the turbidite associated with the C11 eruption is two orders of magnitude smaller than the corresponding ignimbrite on land, suggesting that deposits in the basin originated only from one of the eruptive phases and/or that deposits exported to the sea largely remained on the slopes without reaching the core site.

Acknowledgement

YCC thanks the government of Taiwan for funding this research with a PhD scholarship. We thank the scientific party and crew of RV Meteor during cruise M141/1 for their work in collecting the gravity cores. This cruise was funded by the DFG (German Research Foundation) and GEOMAR. We also acknowledge the project “Features of Azores and Italian Volcanic Islands (FAIVI)”, supported by the European Communities 7th Framework Programme under EUROFLEETS grant agreement no. 228344, which allowed the acquisition of multibeam

bathymetry around Terceira Island. John Moore, Jon Yarwood and Tom Bishop of Manchester Geography Laboratories was very helpful in providing laboratory space and access to a high-power optical microscope for sample preparation. Bor-Jiun Jong, Shunwen Yu, Pei-Chen Kuo and Chia-Hsin Tsai are thanked for sharing their experience on sample preparation for radiocarbon analysis. Thanks also to Chih-Kai Chuang for sharing his knowledge and experience of identifying foraminiferal species and to Dr Philippa Ascough for assisting in the NERC ^{14}C grant application and project management. We especially thank the research staffs in the environmental Radiocarbon Laboratory at Scottish Universities of Environmental Research Centre for carrying out the ^{14}C analyses.

Chapter 7. Discussion and suggestion

7.1 Synthesis and broader discussion

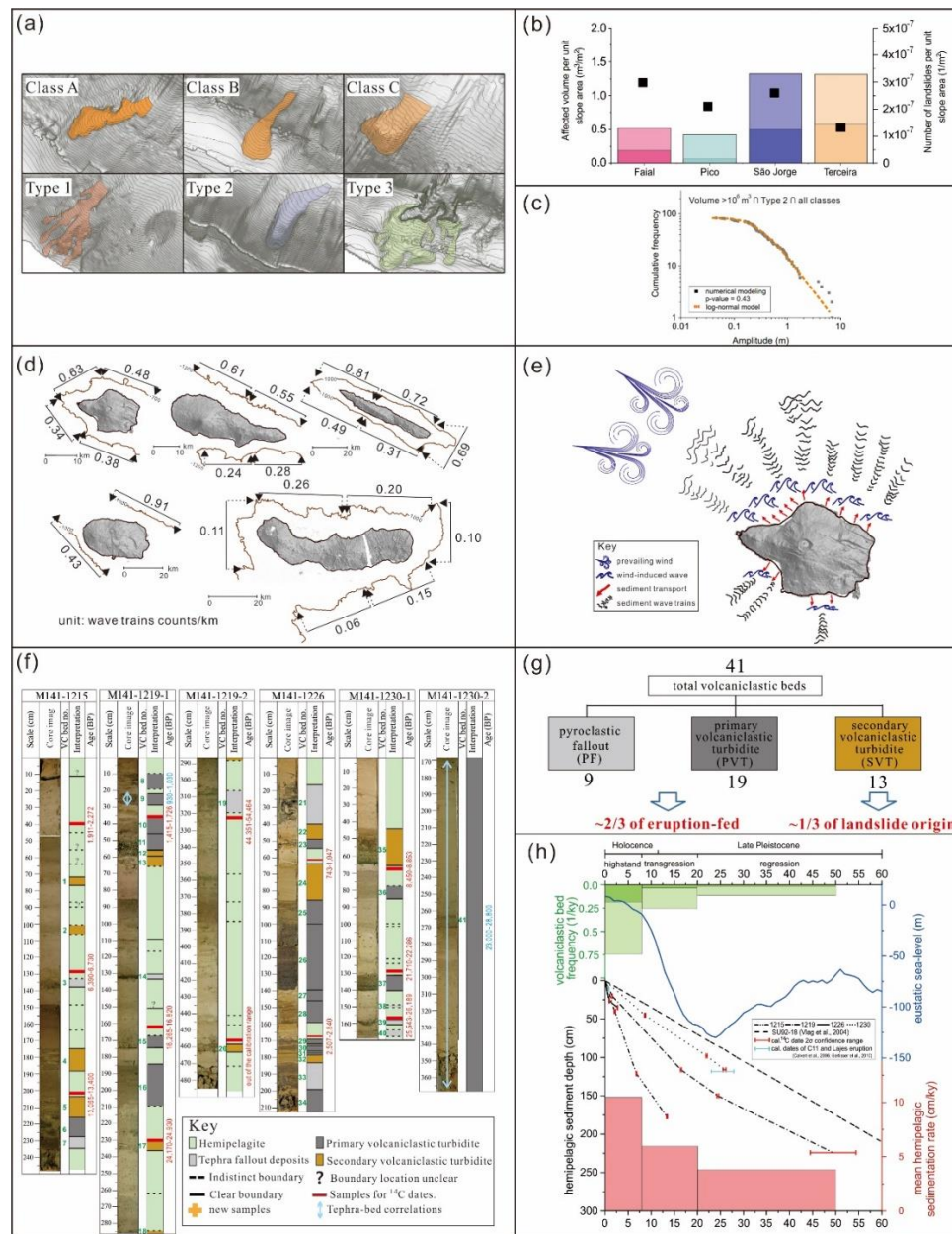


Figure 7.1. Synthesis of key findings of Chapters 3 to 6. (a) Classification and measurements of different types of submarine landslide valleys in volcanic island submarine slopes. (b) Assessment of landslide volume-frequency distributions and their implications for long-term earthquake hazards. (c) Cumulative frequency of tsunami amplitudes at source predicted from landslide scar parameters (volumes $>10^6$ m³, type 2, all classes). (d) Identification of asymmetric abundance of submarine sediment waves around the islands. (e) Identification of prevailing wind and waves from the northwest as associated with asymmetric wave train abundance. (f) Discrimination of different types of beds (hemipelagic beds, pyroclastic fallout and primary and secondary volcanoclastic turbidites) and development of chronostratigraphy

of four sediment cores based on ^{14}C dates and tephrostratigraphy. (g) Bed type discriminations suggesting two-thirds of volcanoclastic-rich beds originate from eruptions, and one-third of them from landslides. (h) Age-depth modelling suggests an association between increased sedimentation rates and greater erosion in the Holocene.

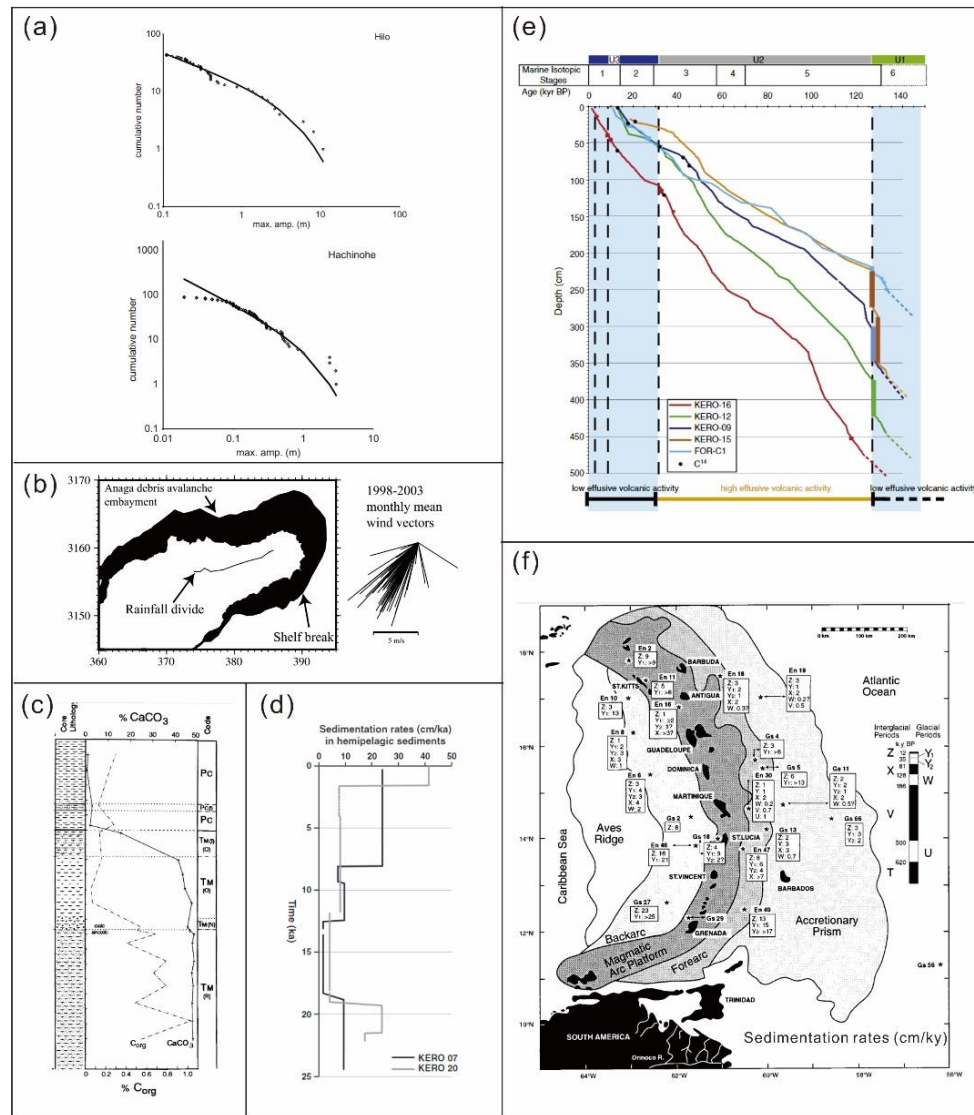


Figure 7.2. Results from other volcanic settings that can be compared with results of this project. (a) Size distribution of tsunami amplitudes (1904–2010) from two locations: Hilo in Hawaii and Hachinohe in Japan (Geist, 2012). Solid line represents tapered Pareto distributions with maximum-likelihood parameter estimates. (b) Asymmetric width of abrasion platform of Tenerife Island and wind vectors (Mitchell et al., 2003). (c) Organic-rich turbidites found in the siliciclastic-volcanoclastic settings of Cape Verde abyssal plain (Robinson et al., 2001). (d) Sedimentation rates derived from the cores proximal to La Réunion Island (Mazuel et al., 2016). (e) Sedimentation rates derived from the cores distal to La Réunion Island (Sisavath et al., 2012). (f) Sedimentation rates derived from cores around the Lesser Antilles island arc (Reid et al., 1996).

Combining information from multiple types of data and samples, and focusing on the results of smaller but frequent sediment transport events in the Azores Islands, has allowed a more comprehensive sediment emplacement history to be obtained, as well as assessment of their hazards. Hazard assessments are needed as significant populations live along coastal areas of some volcanic islands (e.g., Hawaii, Canaries, and Cape Verdes islands). Even where there are only small populations living on the islands, erupted ash plumes and/or tsunamis initiated at them can still disrupt air/sea travel more broadly if they are large (e.g., Hunga Tonga-Hunga Ha'apai Eruption of 2022; Carr et al., 2022). This highlights the need for cross-disciplinary research which allow us to apply appropriate hazard assessment to individual island groups where they present different hazard concerns.

Through classifying and measuring areas and volumes of upper slope submarine landslides (Fig. 7.1a), cumulative volume distributions for Pico and Faial were found to be smaller than those for São Jorge and Terceira (Fig. 7.1b), although they are located in essentially the same regional tectonic setting. This difference was interpreted as a result of varied long-term earthquake recurrences under the two groups of islands. For the Azores Islands, earthquake hazards are the primary concern because of their locations close to or on the plate boundaries. In contrast, more attention is paid to recurrence intervals of explosive eruptions and submarine landslides at volcanic islands more remote from plate boundaries, such as the Canary Islands.

The modelled tsunami height distribution in the Azores follows a similar log-normal distribution to submarine landslides, suggesting that the relative probability of very large events is low (Fig. 7.1c). Fig. 7.2a shows the distributions of the maximum amplitudes of seismogenic tsunamis recorded at coastal tide-gauge stations at Hawaii and Japan from 1904 to 2010 (Burroughs and Tebbens, 2005; Geist and Parsons, 2006; Geist et al., 2009a) were found consistent with the magnitude distribution of earthquakes (Kagan, 2002), following a Pareto distribution. This distribution suggests the counts of the largest tsunamis reduce much faster than the power-law exponent, either resulting from under-sampling at large amplitudes (Burroughs and Tebbens, 2001) or energy dissipation in those with large amplitudes (Korycansky and Lynett, 2005; Geist et al., 2009b). It is still not clear where the difference

comes from, but perhaps it results from different tsunamigenic mechanisms (i.e., submarine landslide versus earthquakes).

The asymmetric abundance of submarine sediment waves found around Azores volcanic islands (Fig. 7.1d) was interpreted as a result of prevailing wind and waves from the northwest (Fig. 7.1e). This conclusion was reached after integrating different types of marine geophysical data, grain size data and hydrodynamical calculations. This method allows an efficient assessment of submarine sediment transport for other islands such as the Canary Islands where subaerial and coastal erosion were found to be asymmetric, potentially also due to prevailing wind and wave effects (Fig. 7.2b; Mitchell et al., 2003).

Volcaniclastic sediment emplacement processes and histories can be revealed by sediment cores collected around the volcanic ocean islands. Discriminating different types of volcaniclastic-rich deposits (Fig. 7.1f) helps to reveal the relative importance of eruption-origin and landslide-origin volcanic sedimentary gravity flows (Fig. 7.1g). Interpreting individual event bed types and the mechanisms that emplaced them remains a challenge due to possible ambiguities. These analyses suggest that chemical compositions and morphometric parameters of volcanic glass shards and the appearance of bioclasts are crucial clues for bed type discrimination. Although only minor differences were found in organic geochemical analyses (TOC, TOC/TN and $\delta^{13}\text{C}$) between the three subtypes of volcaniclastic beds, they are also useful for separating primary and secondary volcaniclastic turbidites. This classification method is particularly applicable for settings that are influenced by both siliciclastic and volcaniclastic systems (e.g., Madeira abyssal plain (Pearce and Jarvis, 1995; 1995; Hunt et al., 2014) and Cape Verde abyssal plain (Robinson, 2001)) due to high preservation of organic matter commonly in the turbidites (e.g., $>0.5\%$; Fig. 7.2c).

The age-depth modelling in the central Azores islands reveals a coincident temporal association between the high frequency of landslides and the increase of hemipelagic sedimentation rates during sea-level highstand in the last 50 ka (Fig. 7.1h). Piston cores proximal to La Réunion Island also found similar high sedimentation rates during the Holocene period (Fig. 7.2d; Mazuel et al., 2016). However, a more extended deposition history (~ 140 ky; Fig. 7.2e) derived

from cores on the submarine fans distal from La Réunion Island revealed slightly lower sedimentation rates during the interglacial (0–30 and 127–140 ka) than glacial times (30–127 ka) when the island was more volcanically active (Sisavath et al., 2012). Similarly, high offshore sedimentation rates were also found in the Lesser Antilles Islands during glacial periods (Fig. 7.2f) when current circulation between interisland passages is intensified.

These hemipelagic sedimentation rates represent the release of fine sediment by erosion and volcanic eruptions at the islands. As coarser sediment is also likely released and accumulated on the uppermost submarine slopes, there could be an association between distal sedimentation rates and slope landsliding. High landslide frequencies for the La Réunion Island and the Lesser Antilles islands are therefore expected to be found during glacial times. In the Lesser Antilles islands, high frequencies of turbidite emplacements were interpreted similarly to the Azores as associated with high sediment input, though the increased sediment fluxes are due to exposure to geostrophic currents (Reid et al., 1996). However, high frequencies of turbidite emplacements in the submarine fans of La Réunion Island were not found during glacial periods but during interglacial periods, a time also of high precipitation. This result was interpreted as the effects of orographic rainfall enhancing riverine erosion on land, causing hyperpycnal sedimentary flows (Sisavath et al., 2012). These differences suggest the long-term relationship between the timing of landsliding and sea-level may not necessarily be the same around different islands, depending on the different predominant mechanisms involved.

A significant difference (~90%) between sediment fluxes in source areas and depositional fluxes in the Azores basins suggests that most of the sedimentary gravity flow deposits were trapped on the island flanks instead of on the basin seafloors. One seismic section also reveals thick sequences of reflections dipping parallel to island slopes within the flanks of the islands (Fig. 6.8a). These results of Chapter 6, though building on those of Chapters 3-5, suggest that most of the flanks of the Azores volcanic islands are composed of unconsolidated fragmental volcanoclastic particles with minor bioclastic particles. Ocean island volcanoes with this internal structure are likely prone to slope failure because of the low resistance of sediments to

large ground motion and planes of weakness dipping parallel to the surface as inferred elsewhere (Ten Brink et al., 2009).

7.2 Future work

The above comments and those in earlier chapters highlight future work that would be useful for moving the subjects of this study forward:

7.2.1 Landslides in the upper submarine slopes of volcanic islands

- It is worth examining whether the landslide volume-frequency statistical method can be applied to predicting long-term hazards of large earthquake at other volcanic islands with suitable data (e.g., the Hawaiian Islands (Moore et al., 1994), Canary Islands; (Masson et al., 2002), Cape Verde Islands (Masson et al., 2008)), and island arcs (e.g., Montserrat (Wall-Palmer et al., 2014) and Ritter Island (Ward and Day, 2003)). This method involving multibeam data allows repeatable analyses to be done efficiently, in contrast to conventional methods that usually require extensive fieldwork on earthquake-related physiographic features (e.g., uplifted terraces and fault-scarp morphology) and deposits to calculate the recurrence interval of successive large earthquakes (e.g., Sieh, 1981 and their references therein). It is also challenging to implement traditional methods at volcanic islands where most faults and deposits are underwater. Nevertheless, its applicability and limitations still await attempts at using it in different volcanic island settings and other tectonic settings.

- In this submarine landslide mapping chapter, a conventional static limit-equilibrium method provided a first-order assessment of sediment cohesion and volcanic island slope stability as no appropriate cores were available. A more sophisticated analysis would require *in-situ* geotechnical measurements (e.g., shear strength and porosity; Lee and Edwards, 1986) and more sophisticated analytical models (e.g., analysis involves stress-deformation or permanent-displacement; Jibson, 2011 and references therein). Such analyses could be viable if samples could be recovered by vibrocoreing.

- Empirical equations are used in this chapter to estimate tsunami heights induced by the many landslides found. Two future works can improve this part of the assessment. 1. Repeated

bathymetric surveys can distinguish slope valleys formed in response to single mass-flows or gradual erosive processes, which imply different tsunami heights (e.g., Di Traglia et al., 2022).

2. Adopting a more sophisticated numerical simulation of tsunami wave generation and propagation such as Cornell multi-grid coupled tsunami model (COMCOT; Liu et al., 1995; Liu et al., 1998) or Non-Hydrostatic WAVE model (NHWAVE; Ma et al., 2012) would allow tsunami propagation, runup and travel time to be assessed more accurately.

- The lower average landslide volumes and areas per unit slope area for Faial and Pico Islands were interpreted as suggesting a higher risk of long-term seismicity compared with São Jorge and Terceira islands. Therefore, it is worth conducting a similar analysis in other settings to examine if this method applies elsewhere.

7.2.2 Volcaniclastic deposits and sedimentation processes around volcanic ocean islands

- The thickness-frequency distribution analysis was found to be useful for characterising the relative importance of different thickness scales of turbidites in different volcanic sites. Despite being capable of recording volcanic history more comprehensively, there have been insufficient sites where coring has penetrated deep enough and in proximal locations for such analyses. Comparing information from cores collected at different volcanic islands (e.g., IODP Exp. 340 Montserrat, IODP Exp. 350 Izu-Bonin Arc and IODP Exp. 398 Hellenic Arc) will potentially help to understand how effectively the spatio-temporal variation of style and magnitude of volcanism have been preserved in the cores.

7.2.3 Asymmetric abundances of submarine sediment waves around volcanic islands

- Hydrodynamic measurements of speed and direction of currents for the entire water column and suspended sediment concentration would allow across-shelf sediment transport to be directly detected. The frequency of the across-shelf sediment emplacements might be estimated if repeat nearshore high-resolution multibeam bathymetric surveys were also available.

- The giant wavelengths and irregular crestlines of sediment wave fields on the north slope of Sao Miguel Island were interpreted as produced from explosive eruption(s) generating large

pyroclastic flows in this study. This speculation can be examined if longer core records were obtained from this area.

7.2.4 Emplacement history of volcanoclastic turbidites around volcanic islands

- The increased higher frequencies of SVTs coincide with higher hemipelagic sedimentation rates during the Holocene, which was interpreted as a result of greater coastal and other erosion at this time, simultaneously feeding more fine sediments to the basins and coarser sediment to the island slopes. However, it is unclear whether there is a more universal relationship applicable to other volcanic islands. This might be revealed if longer sediment cores covering longer age spans and proximal to multiple volcanoes are available.

- It has been possible to link the products of some onshore eruptions and slope landslides with turbidites in the Azores where the turbidites have comparable volumes to ignimbrites and submarine landslide valleys. This is possible because of the relatively short distance to the adjacent flat seafloor basins. A similar analysis could be repeated in other volcanic islands having similar proximal confined depositional basins (e.g., Amsterdam and St Paul islands in the southern Indian Ocean; Conder and Forsyth, 2001).

- The tephra bed correlations between sediment deposited on the seafloor and land can also be applied to other Azores islands where glass shard compositions and radiometric dates are available (e.g., Flores Island; Andrade et al., 2021), allowing age-depth models for sediments deposited near these islands to be produced. The modelled eruption and submarine landsliding histories can also be compared with islands in different groups. Furthermore, tephra bed correlations such as that between core 1230 and the ignimbrite on Terceira Island can also be followed up if additional sediment cores are collected, such as from the southern submarine slopes of Terceira. Given the widespread appearance of ignimbrite also on the south of Terceira, a further upward adjustment of eruptive volume is expected as the current adjustment merely relies on the core collected in the north basin. Therefore, additional cores from the southern slopes would be helpful to constrain the whole coverage area and provide a better prediction of Lajes erupted volume.

Chapter 8. Concluding remarks

The key findings of Chapters 3-6 are organised here as addressing the aims posed in Section 1.3.

***Aim1:** How is sediment created by volcanism, erosion and biological activity transferred to the archaepelagic aprons of volcanic islands?*

From the results of Chapters 3-6, sediment is transported to the aprons of the Azores islands mainly by volcanic activity, slope failures, and sedimentary gravity flows. A high proportion of pyroclastic fallout particles and volcanoclastic turbidites in the cores suggests that the basin-floor sediments mainly originate from volcanic activity. Abundant slope valleys along the upper submarine slopes have been created by landslides, probably triggered mainly by earthquakes. Widespread wave trains on the submarine slopes and basin seafloor were found to originate predominantly from sediment gravity flows. Sediment gravity flow generation was linked to volcanic eruptions, disintegration of sediments during upper-slope landsliding or other mass movements, and suspension of bed particles agitated by strong waves. Sediment gravity flow generation would explain the asymmetric abundances of submarine sediment waves around the central and eastern Azores islands, ultimately because the prevailing wind from the northwest would affect shelf sediments and coastal erosion on that side.

***Aim2:** What processes are responsible for the high abundances and varied characteristics of slope valleys around the submarine flanks of the central Azores volcanic islands?*

Based on high-resolution bathymetric data, more than 1200 submarine slope valleys were identified around the central Azores. They were classified based on the level to which they adhere to classical landslide features, as well as whether they were likely formed by single or multiple landslides or retrogressive failures. Different earthquake frequencies under the islands were suggested to be the main cause of lower densities and higher affected volumes of landslides in Terceira and São Jorge Islands compared to Faial and Pico islands. Landslide statistics do not appear to systematically vary with different lava flow types, ages of adjacent volcanic units or shelf width.

***Aim3:** What are the implications for assessing hazards associated with submarine landslides?*

The CCDF suggested that the relative probability of large submarine landslides (e.g., $>10^8 \text{ m}^3$) in the Azores has been very low ($<0.001\%$). However, some of these submarine landslides were probably still capable of generating tsunamis. At least 13 of them would generate tsunami wave amplitudes (A) at source $>1 \text{ m}$ and one $> 7 \text{ m}$, if they would have occurred with sea-level at its present highstand position. These larger submarine landslides were mainly located around São Jorge and Terceira Islands.

Smaller landslide size but higher frequency of submarine landslides in Faial and Pico islands than those in São Jorge and Terceira Islands could be explained as a consequence of shorter periods between destructive earthquakes, leaving less time for deposits to accumulate. This in turn implies a higher frequency of larger earthquakes around Faial and Pico islands and thus a greater longer-term threat of destructive earthquakes beneath those islands.

Aim 4: What processes are responsible for creating trains of submarine sediment waves around the Azores volcanic islands?

Downslope-trending wave trains are twice as abundant on the northern (windward) submarine slopes of five Azores islands compared to their southern slopes. Geomorphological features from high-resolution bathymetric and seismic reflection data favour their formation under sedimentary gravity flows. The predominant north-westerly waves also help explain their asymmetric abundance. Such waves suggest greater coastal erosion and mobilisation of shelf sediments (wave agitation) transported by wave-agitated sedimentary flows and downwelling currents (offshore bottom currents balancing wind-driven onshore surface currents). Those sediments spilling onto the steep slope edges of the islands are ultimately prone to failure and initiation of sedimentary gravity flows by disintegration of the failed deposits.

Aim5: What are the characteristics and emplacement frequencies of volcanoclastic deposits in sediment cores originating from eruptions and landslides?

Volcanoclastic bed types were discriminated by combining multiple lines of evidence. Primary and secondary volcanoclastic turbidites contain structures associated with turbidity currents (tractional features). Secondary volcanoclastic turbidites contain shelf-derived carbonate particles, rounded volcanoclastic grains, and their volcanic glass compositions tend to be

heterogeneous. Though primary turbidites can be either angular or rounded, their volcanic glass compositions tend to be geochemically homogeneous or genetically related due to magma fractionation. Angular and geochemically homogeneous particles and scarcity of biogenic carbonate favour a tephra fallout interpretation. Combining information is always preferred for emplacement interpretations, as it helps differentiate possible complications such as multistage transport, compositionally zoned magma or intense post-depositional bioturbation. From these interpretations of four sediment cores, two-thirds of the volcanoclastic beds originated from eruptions and only one third from submarine landslides. This suggests either that eruptions are more frequent than submarine landslides in the central Azores or that many sedimentary flows generated by landslides are deposited on the island slopes before reaching basin floors.

Age-depth models based on ^{14}C dates for the hemipelagic intervals were used to estimate the emplacement ages of volcanoclastic turbidites in the cores to a maximum of ~50 ka. The return periods of those submarine landslides and volcanic eruptions were found to be > 1 ky. Hemipelagic sedimentation rates and submarine landslide frequencies were higher in the past 8 k.y. than in the previous few tens of thousands of years. The increased hemipelagic sedimentation rate could be associated with high sea-levels, enhancing erosion of subaerial sea cliffs and biogenic production on shelves. More frequent emplacements of pyroclastic turbidites were found in some cores for the last 8 k.y.; if this occurred more widely, explosive eruptions could also supply more friable volcanoclastic material to both submarine and subaerial areas. The higher submarine landslide frequency of the last 8 k.y. is probably also associated with the greater sediment supply, leading to a more rapid accumulation of unconsolidated sediments on the submarine slopes of the islands, where it then more frequently fails.

***Aim 6:** How do the records in sediment cores near to the Azores islands compare with potential sources on the islands and with sediment records in other volcanic settings?*

A large difference (90.9%) between sediment fluxes in source areas and depositional fluxes in basins (of hemipelagic sediments and SVTs) implies that deposits produced by smaller sediment gravity flows have largely remained on the slopes and have not fully run out to the basin floors. The volumes of turbidites originating from landslides are comparable with the

largest volumes (10^7 – 10^8 m³) of their adjacent upper slope submarine landslide valleys, so secondary volcanoclastic turbidites in the cores likely originate from the largest landslides. These results show that proximal basins still potentially preserve a more comprehensive landslide history than those core sites that are >100 km from their source areas, which only preserve deposits originating from giant landslides (i.e., $>10^{11}$ – 10^{12} m³). Comparisons of volcanic glass geochemical compositions suggest that fallout beds in these four cores are uncorrelatable with other cores or the islands. However, two pyroclastic turbidites can be correlated with ignimbrites on their adjacent islands. The tephra geochemistry suggests that they originated from eruptions on their adjacent volcanic islands. The differences in deposit volumes between PVT on the seafloor basins with the corresponding C11 ignimbrite on Faial were found to be useful for revealing eruptions of multiple eruptive phases. The PVT volume associated with the Lajes ignimbrites was used to adjust their total volumes upward by 8–33%, as well as revise the extent of the Lajes erupted deposits.

Thickness-frequency distributions of volcanoclastic beds in cores collected near oceanic islands can allow comparisons between island groups of different volcanic history. Steep logarithmic frequency distribution gradients ($\beta < -1$) imply that small beds are proportionally more important than large beds, suggesting a more effusive eruptive style, as shown in the Azores and Cape Verde islands. In contrast, a gentle gradient reflects the greater importance of explosive eruptions and episodic eruptive history, as shown for Gran Canaria.

References

- Alberico, I., Budillon, F., Casalbore, D., Di Fiore, V., and Iavarone, R. 2018. A Critical Review of Potential Tsunamigenic Sources as First Step Towards the Tsunami Hazard Assessment for the Napoli Gulf (Southern Italy) Highly Populated Area. *Natural Hazards*, 92, 43-76. <https://doi.org/10.1007/s11069-018-3191-5>.
- Allin, J. R., Hunt, J. E., Talling, P. J., Clare, M. A., Pope, E., and Masson, D. G. 2016. Different Frequencies and Triggers of Canyon Filling and Flushing Events in Nazaré Canyon, Offshore Portugal. *Marine Geology*, 371, 89-105. <https://doi.org/10.1016/j.margeo.2015.11.005>.
- Andrade, C., Trigo, R., Freitas, M., Gallego, M., Borges, P., and Ramos, A. 2008. Comparing Historic Records of Storm Frequency and the North Atlantic Oscillation (Nao) Chronology for the Azores Region. *The Holocene*, 18, 745-754. <https://doi.org/10.1177/0959683608091794>.
- Andrade, C., Borges, P., and Freitas, M. C. 2006. Historical Tsunami in the Azores Archipelago (Portugal). *Journal of Volcanology and Geothermal Research*, 156, 172-185. <https://doi.org/10.1016/j.jvolgeores.2006.03.014>.
- Andrade, M., Ramalho, R. S., Pimentel, A., Hernández, A., Kutterolf, S., Sáez, A., Benavente, M., Raposeiro, P. M., and Giralt, S. 2021. Unraveling the Holocene Eruptive History of Flores Island (Azores) through the Analysis of Lacustrine Sedimentary Records. *Frontiers in Earth Science*, 9. <https://doi.org/10.3389/feart.2021.738178>.
- Ascough, P., Cook, G., and Dugmore, A. 2005. Methodological Approaches to Determining the Marine Radiocarbon Reservoir Effect. *Progress in Physical Geography: Earth and Environment*, 29, 532-547. <https://doi.org/10.1191/0309133305pp461ra>.
- Ausín, B., Haghypour, N., Wacker, L., Voelker, A. H. L., Hodell, D., Magill, C., Looser, N., Bernasconi, S. M., and Eglinton, T. I. 2019. Radiocarbon Age Offsets between Two Surface Dwelling Planktonic Foraminifera Species During Abrupt Climate Events in the Sw Iberian Margin. *Paleoceanography and paleoclimatology*, 34, 63-78. <https://doi.org/10.1029/2018PA003490>.
- Ávila, S. P., Cordeiro, R., Rodrigues, A. R., Rebelo, A. C., Melo, C., Madeira, P., and Pyenson, N. D. 2015. Fossil Mysticeti from the Pleistocene of Santa Maria Island, Azores (Northeast Atlantic Ocean), and the Prevalence of Fossil Cetaceans on Oceanic Islands. *Palaeontol. Electron*, 18, 1-12. <https://doi.org/10.26879/548>.
- Babonneau, N., Delacourt, C., Cancouët, R., Sisavath, E., Bachèlery, P., Mazuel, A., Jorry, S. J., Deschamps, A., Ammann, J., and Villeneuve, N. 2013. Direct Sediment Transfer from Land to Deep-Sea: Insights into Shallow Multibeam Bathymetry at La Réunion Island. *Marine Geology*, 346, 47-57. <https://doi.org/10.1016/j.margeo.2013.08.006>.

- Bailey, L. P., Clare, M. A., Rosenberger, K. J., Cartigny, M. J. B., Talling, P. J., Paull, C. K., Gwiazda, R., Parsons, D. R., Simmons, S. M., Xu, J., Haigh, I. D., Maier, K. L., McGann, M., and Lundsten, E. 2021. Preconditioning by Sediment Accumulation Can Produce Powerful Turbidity Currents without Major External Triggers. *Earth and Planetary Science Letters*, 562, 116845. <https://doi.org/10.1016/j.epsl.2021.116845>.
- Baker, P. E., Gass, I. G., Harris, P. G., Maitre, R. W. L. M., Kennedy, W. Q., Holdgate, M. W., Dickson, J. H., Baird, D. E., Miller, J. A., and Creer, K. M. 1964. The Volcanological Report of the Royal Society Expedition to Tristan Da Cunha, 1962. *Philosophical Transactions of the Royal Society of London. Series A, Mathematical and Physical Sciences*, 256, 439-575. <https://doi.org/10.1098/rsta.1964.0011>.
- Barbary, D., Leroux, M.-D., and Bousquet, O. 2019. The Orographic Effect of Reunion Island on Tropical Cyclone Track and Intensity. *Atmospheric Science Letters*, 20, e882. <https://doi.org/10.1002/asl.882>.
- Barrett, R., Lebas, E., Ramalho, R., Klauke, I., Kutterolf, S., Klügel, A., Lindhorst, K., Gross, F., and Krastel, S. 2019. Revisiting the Tsunamigenic Volcanic Flank-Collapse of Fogo Island in the Cape Verdes, Offshore West Africa. *Geological Society, London, Special Publications*, 500. <https://doi.org/10.1144/SP500-2019-187>.
- Beattie, P. D., and Dade, W. B. 1996. Is Scaling in Turbidite Deposition Consistent with Forcing by Earthquakes? *J. Sed. Res.*, 66, 909-915. <https://doi.org/10.1306/D4268437-2B26-11D7-8648000102C1865D>.
- Belde, J., Back, S., and Reuning, L. 2015. Three-Dimensional Seismic Analysis of Sediment Waves and Related Geomorphological Features on a Carbonate Shelf Exposed to Large Amplitude Internal Waves, Browse Basin Region, Australia. *Sedimentology*, 62, 87-109. <https://doi.org/10.1111/sed.12141>.
- Bergamaschi, B. A., Tsamakidis, E., Keil, R. G., Eglinton, T. I., Montluçon, D. B., and Hedges, J. I. 1997. The Effect of Grain Size and Surface Area on Organic Matter, Lignin and Carbohydrate Concentration, and Molecular Compositions in Peru Margin Sediments. *Geochimica et Cosmochimica Acta*, 61, 1247-1260. [https://doi.org/10.1016/S0016-7037\(96\)00394-8](https://doi.org/10.1016/S0016-7037(96)00394-8).
- Bergh, S. G., and Gudmunder, E. S. 1991. Pleistocene Mass-Flow Deposits of Basaltic Hyaloclastite on a Shallow Submarine Shelf, South Iceland. *Bull. Volcanol.*, 53, 597-611. <https://doi.org/10.1007/BF00493688>.
- Bieniawski, Z. Case Studies: Prediction of Rock Mass Behaviour by the Geomechanics Classification. Second Australia-New Zealand Conference on Geomechanics, 1975. Institution of Engineers, Australia, 36.

- Boldini, D., Wang, F., Sassa, K., and Tommasi, P. 2009. Application of Large-Scale Ring Shear Tests to the Analysis of Tsunamigenic Landslides at the Stromboli Volcano, Italy. *Landslides*, 6, 231-240. <https://doi.org/10.1007/s10346-009-0155-6>.
- Bonaccorso, A., Calvari, S., Garfi, G., Lodato, L., and Patanè, D. 2003. Dynamics of the December 2002 Flank Failure and Tsunami at Stromboli Volcano Inferred by Volcanological and Geophysical Observations. *Geophysical Research Letters*, 30. <https://doi.org/10.1029/2003GL017702>.
- Bonadonna, C., Mayberry, G., Calder, E., Sparks, R., Choux, C., Jackson, P., Lejeune, A., Loughlin, S., Norton, G., and Rose, W. I. 2002. Tephra Fallout in the Eruption of Soufrière Hills Volcano, Montserrat. *Geological Society, London, Memoirs*, 21, 483-516. <https://doi.org/10.1144/GSL.MEM.2002.021.01.22>.
- Bonatti, E. 1990. Not So Hot "Hot Spots" in the Oceanic Mantle. *Science*, 250, 107-111. <https://doi.org/10.1126/science.250.4977.107>.
- Boore, D. M., Joyner, W. B., and Fumal, T. E. 1997. Equations for Estimating Horizontal Response Spectra and Peak Acceleration from Western North American Earthquakes: A Summary of Recent Work. *Seismological Research Letters*, 68, 128-153. <https://doi.org/10.1785/gssrl.68.1.128>.
- Borges, P., Ng, K., and Calado, H. 2011. Coastal Hazards in the Azores Archipelago — Coastal Storms and Flooding. *Journal of Coastal Research*, 474-474. <https://doi.org/10.2112/SI61-001.63>.
- Bosman, A., Casalbore, D., Romagnoli, C., and Chiocci, F. L. 2014. Formation of an 'A' Lava Delta: Insights from Time-Lapse Multibeam Bathymetry and Direct Observations During the Stromboli 2007 Eruption. *Bull. Volcanol.*, 76, [https://doi:10.1007/s00445-014-0838-2](https://doi.org/10.1007/s00445-014-0838-2).
- Bouma, A. H. 1962. *Sedimentology of Some Flysch Deposits; a Graphic Approach to Facies Interpretation*, Amsterdam; New York, Elsevier Pub. Co.
- Boyle, J. 1999. Variability of Tephra in Lake and Catchment Sediments, SviNavatn, Iceland. *Global and Planetary Change*, 21, 129-149. [https://doi.org/10.1016/S0921-8181\(99\)00011-9](https://doi.org/10.1016/S0921-8181(99)00011-9).
- Brock, F., Higham, T., Ditchfield, P., and Ramsey, C. B. 2010. Current Pretreatment Methods for Ams Radiocarbon Dating at the Oxford Radiocarbon Accelerator Unit (Orau). *Radiocarbon*, 52, 103-112. <https://doi.org/10.1017/S0033822200045069>.
- Buchs, D. M., Williams, R., Sano, S.-i., and Wright, V. P. 2018. Non-Hawaiian Lithostratigraphy of Louisville Seamounts and the Formation of High-Latitude Oceanic Islands and Guyots. *Journal of Volcanology and Geothermal Research*, 356, 1-23. <https://doi.org/10.1016/j.jvolgeores.2017.12.019>.

- Burroughs, S. M., and Tebbens, S. F. 2005. Power-Law Scaling and Probabilistic Forecasting of Tsunami Runup Heights. *pure and applied geophysics*, 162, 331-342. <https://doi.org/10.1007/s00024-004-2603-5>.
- Burroughs, S. M., and Tebbens, S. F. 2001. Upper-Truncated Power Laws in Natural Systems. *pure and applied geophysics*, 158, 741-757. <https://doi.org/10.1007/PL00001202>.
- Cacchione, D. A., and Drake, D. E. 1986. Nepheloid Layers and Internal Waves over Continental Shelves and Slopes. *Geo-Mar. Lett.*, 6, 147-152. <https://doi.org/10.1007/BF02238085>.
- Calder, E. S., Cole, P. D., Dade, W. B., Druitt, T. H., Hoblitt, R. P., Huppert, H., Ritchie, L., Sparks, R. S. J., and Young, S. R. 1999. Mobility of Pyroclastic Flows and Surges at the Soufriere Hills Volcano, Montserrat. *Geophysical Research Letters*, 26, 537-540. <https://doi.org/10.1029/1999GL900051>.
- Caldeira, R. M. A., and Reis, J. C. 2017. The Azores Confluence Zone. *Frontiers in Marine Science*, 4. <https://doi.org/10.3389/fmars.2017.00037>.
- Calvert, A. T., Moore, R. B., McGeehin, J. P., and Rodrigues da Silva, A. M. 2006. Volcanic History and ⁴⁰Ar/³⁹Ar and ¹⁴C Geochronology of Terceira Island, Azores, Portugal. *Journal of Volcanology and Geothermal Research*, 156, 103-115. <https://doi.org/10.1016/j.jvolgeores.2006.03.016>.
- Caplan-Auerback, J., Fox, C. G., and Duennebier, F. K. 2001. Hydroacoustic Detection of Submarine Landslides on Kilauea Volcano. *Geophys. Res. Lett.*, 28, 1811-1813. <https://doi.org/10.1029/2000GL012545>.
- Cappello, A., Zanon, V., Del Negro, C., Ferreira, T. J. L., and Queiroz, M. G. P. S. 2015. Exploring Lava-Flow Hazards at Pico Island, Azores Archipelago (Portugal). *Terra Nova*, 27, 156-161. <https://doi.org/10.1111/ter.12143>.
- Caplan-Auerback, J., Fox, C. G., and Duennebier, F. K. 2001. Hydroacoustic Detection of Submarine Landslides on Kilauea Volcano. *Geophys. Res. Lett.*, 28, 1811-1813. <https://doi.org/10.1029/2000GL012545>.
- Carey, S., and Schneider, J.-L. 2011. Chapter 7 - Volcaniclastic Processes and Deposits in the Deep-Sea. In: HüNeke, H., and Mulder, T. (eds.) *Developments in Sedimentology*. Elsevier, 457-515. <https://doi.org/10.1016/B978-0-444-53000-4.00007-X>.
- Carey, S., Sigurdsson, H., Mandeville, C., and Bronto, S. 2000. Volcanic Hazards from Pyroclastic Flow Discharge into the Sea: Examples from the 1883 Eruption of Krakatau, Indonesia. *Special Papers-Geological Society of America*, 1-14. <https://doi.org/10.1130/0-8137-2345-0.1>.
- Carey, S., Maria, T., and Cornell, W. 1998. Processes of Volcaniclastic Sedimentation During the Early Growth Stages of Gran Canaria Based on Sediments from Site 953. In: Weaver, P. P. E., Schmincke, H.-U., Firth, J. V., et al. (eds.) *Proc. Ocean Drill. Progr.*,

- Sci. Res. Vol. 157*. College Station, Texas: Ocean Drilling Program, 183-200. <https://doi.org/doi:10.2973/odp.proc.sr.157.119.1998>.
- Carey, S., and Sigurdsson, H. 1984. A Model of Volcanogenic Sedimentation in Marginal Basins. *Geological Society, London, Special Publications*, 16, 37-58. <https://doi.org/10.1144/gsl.Sp.1984.016.01.04>.
- Carmo, R., Madeira, J., Ferreira, T., Queiroz, G., and Hipólito, A. 2015. Chapter 6 Volcano-Tectonic Structures of São Miguel Island, Azores. *Geological Society, London, Memoirs*, 44, 65-86. <https://doi.org/10.1144/M44.6>.
- Carr, J. L., Horváth, Á., Wu, D. L., and Friberg, M. D. 2022. Stereo Plume Height and Motion Retrievals for the Record-Setting Hunga Tonga-Hunga Ha'apai Eruption of 15 January 2022. *Geophysical Research Letters*, 49, e2022GL098131. <https://doi.org/10.1029/2022GL098131>.
- Carracedo, J. C. 1994. The Canary Islands: An Example of Structural Control on the Growth of Large Oceanic-Island Volcanoes. *J. Volcanol. Geotherm. Res.*, 60, 225-241. [https://doi.org/10.1016/0377-0273\(94\)90053-1](https://doi.org/10.1016/0377-0273(94)90053-1).
- Cartigny, M. J. B., Ventra, D., Postma, G., and van Den Berg, J. H. 2014. Morphodynamics and Sedimentary Structures of Bedforms under Supercritical-Flow Conditions: New Insights from Flume Experiments. *Sedimentology*, 61, 712-748. <https://doi.org/10.1111/sed.12076>.
- Cartigny, M. J. B., Postma, G., van den Berg, J. H., and Mastbergen, D. R. 2011. A Comparative Study of Sediment Waves and Cyclic Steps Based on Geometries, Internal Structures and Numerical Modeling. *Marine Geology*, 280, 40-56. <https://doi.org/10.1016/j.margeo.2010.11.006>.
- Carvalho, A., Sousa, M., Oliveira, C., Campos-Costa, A., Nunes, J., and Forjaz, V. 2001. Seismic Hazard for the Central Group of the Azores Islands. *Bollettino di Geofisica Teorica ed Applicata*, 42, 89-105, 0006-6729.
- Casalbore, D., Di Traglia, F., Bosman, A., Romagnoli, C., Casagli, N., and Chiocci, F. L. 2021. Submarine and Subaerial Morphological Changes Associated with the 2014 Eruption at Stromboli Island. *Remote Sensing*, 13, 2043. <https://doi.org/10.3390/rs13112043>.
- Casalbore, D., Clare, M. A., Pope, E. L., Quartau, R., Bosman, A., Chiocci, F. L., Romagnoli, C., and Santos, R. 2020. Bedforms on the Submarine Flanks of Insular Volcanoes: New Insights Gained from High Resolution Seafloor Surveys. *Sedimentology*. <https://doi.org/10.1111/sed.12725>.
- Casalbore, D., Passeri, F., Tommasi, P., Verrucci, L., Bosman, A., Romagnoli, C., and Chiocci, F. L. 2020. Small-Scale Slope Instability on the Submarine Flanks of Insular Volcanoes: The Case-Study of the Sciara Del Fuoco Slope (Stromboli). *International*

- Journal of Earth Sciences*, 109, 2643-2658. <https://doi.org/10.1007/s00531-020-01853-5>.
- Casalbore, D., Romagnoli, C., Bosman, A., Anzidei, M., and Chiocci, F. L. 2018. Coastal Hazard Due to Submarine Canyons in Active Insular Volcanoes: Examples from Lipari Island (Southern Tyrrhenian Sea). *Journal of Coastal Conservation*, 22, 989-999. <https://doi.org/10.1007/s11852-017-0549-x>.
- Casalbore, D., Romagnoli, C., Pimentel, A., Quartau, R., Casas, D., Ercilla, G., Hipólito, A., Sposato, A., and Chiocci, F. L. 2015. Volcanic, Tectonic and Mass-Wasting Processes Offshore Terceira Island (Azores) Revealed by High-Resolution Seafloor Mapping. *Bulletin of Volcanology*, 77:24. <https://doi.org/10.1007/s00445-015-0905-3>.
- Casalbore, D., Romagnoli, C., Bosman, A., and Chiocci, F. 2014. Large-Scale Seafloor Waveforms on the Flanks of Insular Volcanoes (Aeolian Archipelago, Italy), with Inferences About Their Origin. *Marine Geology*, 355, 318-329. <https://doi.org/10.1016/j.margeo.2014.06.007>.
- Casalbore, D., Bosman, A., and Chiocci, F. L. Study of Recent Small-Scale Landslides in Geologically Active Marine Areas through Repeated Multibeam Surveys: Examples from the Southern Italy. 2012 Dordrecht. Springer Netherlands, 573-582.
- Casalbore, D., Romagnoli, C., Bosman, A., and Chiocci, F. L. 2011. Potential Tsunamigenic Landslides at Stromboli Volcano (Italy): Insight from Marine Dem Analysis. *Geomorphology*, 126, 42-50. <https://doi.org/10.1016/j.geomorph.2010.10.026>.
- Casas, D., Chiocci, F., Casalbore, D., Ercilla, G., and de Urbina, J. O. 2016. Magnitude-Frequency Distribution of Submarine Landslides in the Gioia Basin (Southern Tyrrhenian Sea). *Geo-Marine Letters*, 36, 405-414. <https://doi.org/10.1007/s00367-016-0458-2>.
- Cassidy, M., Watt, S. F. L., Palmer, M. R., Trofimovs, J., Symons, W., Maclachlan, S. E., and Stinton, A. J. 2014. Construction of Volcanic Records from Marine Sediment Cores: A Review and Case Study (Montserrat, West Indies). *Earth-Science Reviews*, 138, 137-155. <https://doi.org/10.1016/j.earscirev.2014.08.008>.
- Castello, B., Olivieri, M., and Selvaggi, G. 2007. Local and Duration Magnitude Determination for the Italian Earthquake Catalog, 1981–2002. *Bulletin of the Seismological Society of America*, 97, 128-139. <https://doi.org/10.1785/0120050258>.
- Chang, Y.-C., Mitchell, N., Quartau, R., Hübscher, C., Rusu, L., and Tempera, F. 2022. Asymmetric Abundances of Submarine Sediment Waves around the Azores Volcanic Islands. *Marine Geology*, 106837. <https://doi.org/10.1016/j.margeo.2022.106837>.
- Chang, Y.-C., Mitchell, N. C., Hansteen, T. H., Schindlbeck-Belo, J. C., and Freundt, A. 2021a. Volcaniclastic Deposits and Sedimentation Processes around Volcanic Ocean Islands:

- The Central Azores. *Geological Society, London, Special Publications*, 520, SP520-2021-62. <https://doi.org/10.1144/SP520-2021-62>.
- Chang, Y.-C., Mitchell, N., Quartau, R., and Hansteen, T. 2021b. Landslides in the Upper Submarine Slopes of Volcanic Islands: The Central Azores. *Geochemistry, Geophysics, Geosystems*. <https://doi.org/10.1029/2021GC009833>.
- Chang, Y.-C., Mitchell, N., Quartau, R., and Hansteen, T., 2019. Size Distribution and Causes of Submarine Landslides, Central Azores Islands. Geophysical Research Abstract, EGU General Assembly, 2019 Vienna, Austria.
- Chappell, J. 1980. Coral Morphology, Diversity and Reef Growth. *Nature*, 286, 249-252. <https://doi.org/10.1038/286249a0>.
- Charlier, B. L. A., Ginibre, C., Morgan, D., Nowell, G. M., Pearson, D. G., Davidson, J. P., and Ottley, C. J. 2006. Methods for the Microsampling and High-Precision Analysis of Strontium and Rubidium Isotopes at Single Crystal Scale for Petrological and Geochronological Applications. *Chemical Geology*, 232, 114-133. <https://doi.org/10.1016/j.chemgeo.2006.02.015>.
- Chaytor, J. D., Uri, S., Solow, A. R., and Andrews, B. D. 2009. Size Distribution of Submarine Landslides Along the US Atlantic Margin. *Marine Geology*, 264, 16-27. <https://doi.org/10.1016/j.margeo.2008.08.007>.
- Chiocci, F. L., Romagnoli, C., Casalbore, D., Sposato, A., Martorelli, E., Alonso, B., Casas, D., Conte, A. M., Bella, L. D., Ercilla, G., Estrada, F., Falese, F., Farran, M., Forleo, V., Frezza, V., Hipolito, A., Lebani, A., Maisto, F., Pacheco, J., Pimentel, A., Quartau, R., Roque, C., Sampaio, I., Santoro, P. C., and Tempera, F. 2013. Bathymorphological Setting of Terceira Island (Azores) after the Faivi Cruise. *Journal of Maps*, 9, 590-595. <https://doi.org/10.1080/17445647.2013.831381>.
- Chiocci, F. L., Romagnoli, C., Tommasi, P., and Bosman, A. 2008. The Stromboli 2002 Tsunamigenic Submarine Slide: Characteristics and Possible Failure Mechanism. *Journal of Geophysical Research: Solid Earth*, 113. <https://doi.org/10.1029/2007JB005172>.
- Christopher, T. E., Humphreys, M. C. S., Barclay, J., Genareau, K., De Angelis, S. M. H., Plail, M., and Donovan, A. 2014. Chapter 17 Petrological and Geochemical Variation During the Soufrière Hills Eruption, 1995 to 2010. *Geological Society, London, Memoirs*, 39, 317-342. <https://doi.org/10.1144/m39.17>.
- Chouet, B. A. 1996. Long-Period Volcano Seismicity: Its Source and Use in Eruption Forecasting. *Nature*, 380, 309-316. <https://doi.org/10.1038/380309a0>.
- CIVISA 1998. *Boletim Sismológico Preliminar Dos Açores. Centro De Coordenação Do Sistema De Vigilância Sismológica Dos Açores (in Portuguese)*.

- Clare, M., Chaytor, J., Dabson, O., Gamboa, D., Georgiopolou, A., Eady, H., Hunt, J., Jackson, C., Katz, O., Krastel, S., León, R., Micallef, A., Moernaut, J., Moriconi, R., Moscardelli, L., Mueller, C., Normandeau, A., Patacci, M., Steventon, M., Urlaub, M., Völker, D., Wood, L., and Jobe, Z. 2019. A Consistent Global Approach for the Morphometric Characterization of Subaqueous Landslides. *Geological Society, London, Special Publications*, 477, SP477.15. <https://doi.org/10.1144/sp477.15>.
- Clare, M. A., Le Bas, T., Price, D. M., Hunt, J. E., Sear, D., Cartigny, M. J. B., Vellinga, A., Symons, W., Firth, C., and Cronin, S. 2018. Complex and Cascading Triggering of Submarine Landslides and Turbidity Currents at Volcanic Islands Revealed from Integration of High-Resolution Onshore and Offshore Surveys. *Frontiers in Earth Science*, 6. <http://dx.doi.org/10.3389/feart.2018.00223>.
- Clare, M. A., Talling, P. J., and Hunt, J. E. 2015. Implications of Reduced Turbidity Current and Landslide Activity for the Initial Eocene Thermal Maximum – Evidence from Two Distal, Deep-Water Sites. *Earth and Planetary Science Letters*, 420, 102-115. <https://doi.org/10.1016/j.epsl.2015.03.022>.
- Clauset, A., Shalizi, C. R., and Newman, M. E. 2009. Power-Law Distributions in Empirical Data. *SIAM review*, 51, 661-703. <https://doi.org/10.1137/070710111>.
- Cole, P., Guest, J., Duncan, A., and Pacheco, J.-M. 2001. Capelinhos 1957–1958, Faial, Azores: Deposits Formed by an Emergent Surtseyan Eruption. *Bulletin of volcanology*, 63, 204-220. <https://doi.org/10.1007/s004450100136>.
- Cole, P. D., Queiroz, G., Wallestein, N., Gaspar, J. L., Duncan, A. M., and Guest, J. E. 1995. An Historic Subplinian/Phreatomagmatic Eruption: The 1630 AD Eruption of Furnas Volcano, Sao Miguel, Azores. *J. Volcanol. Geotherm. Res.*, 69, 117-135. [https://doi.org/10.1016/0377-0273\(95\)00033-X](https://doi.org/10.1016/0377-0273(95)00033-X).
- Conder, J. A., and Forsyth, D. W. 2001. Seafloor Spreading on the Southwest Indian Ridge over the Last One Million Years: A Test of the Capricorn Plate Hypothesis. *Earth Planet. Sci. Lett.*, 188, 91-105. [https://doi.org/10.1016/S0012-821X\(01\)00326-0](https://doi.org/10.1016/S0012-821X(01)00326-0).
- Costa, A. C. G., Hildenbrand, A., Marques, F. O., Sibrant, A. L. R., and Santos de Campos, A. 2015. Catastrophic Flank Collapses and Slumping in Pico Island During the Last 130 Kyr (Pico-Faial Ridge, Azores Triple Junction). *Journal of Volcanology and Geothermal Research*, 302, 33-46. <https://doi.org/10.1016/j.jvolgeores.2015.06.008>.
- Costa, A. C. G., Marques, F. O., Hildenbrand, A., Sibrant, A. L. R., and Catita, C. M. S. 2014. Large-Scale Flank Collapses in a Steep Volcanic Ridge: Pico-Faial Ridge, Azores Triple Junction. *J. Volcanol. Geotherm. Res.*, 272, 111-125. <https://doi.org/10.1016/j.jvolgeores.2014.01.002>.
- Coussens, M., Wall-Palmer, D., Talling, P. J., Watt, S. F. L., Cassidy, M., Jutzeler, M., Clare, M. A., Hunt, J. E., Manga, M., Gernon, T. M., Palmer, M. R., Hatter, S. J., Boudon,

- G., Endo, D., Fujinawa, A., Hatfield, R., Hornbach, M. J., Ishizuka, O., Kataoka, K., Le Friant, A., Maeno, F., McCanta, M., and Stinton, A. J. 2016. The Relationship between Eruptive Activity, Flank Collapse, and Sea Level at Volcanic Islands: A Long-Term (>1 Ma) Record Offshore Montserrat, Lesser Antilles. *Geochemistry, Geophysics, Geosystems*, 17, 2591-2611. <https://doi.org/10.1002/2015GC006053>.
- Cowie, G., Hedges, J., Prah, F., and De Lange, G. 1995. Elemental and Major Biochemical Changes across an Oxidation Front in a Relict Turbidite: An Oxygen Effect. *Geochimica et Cosmochimica Acta*, 59, 33-46. [https://doi.org/10.1016/0016-7037\(94\)00329-K](https://doi.org/10.1016/0016-7037(94)00329-K).
- Cronin, S. J., Neall, V. E., Lecointre, J. A., and Palmer, A. S. 1997. Changes in Whangaehu River Lahar Characteristics During the 1995 Eruption Sequence, Ruapehu Volcano, New Zealand. *Journal of Volcanology and Geothermal Research*, 76, 47-61. [https://doi.org/10.1016/S0377-0273\(96\)00064-9](https://doi.org/10.1016/S0377-0273(96)00064-9).
- Crossen, R. S., and Endo, E. T. 1982. Focal Mechanisms and Locations of Earthquakes in the Vicinity of the 1975 Kalapana Earthquake Aftershock Zone 1970-1979: Implications for Tectonics of the South Flank of Kilauea Volcano, Island of Hawaii. *Tectonics*, 1, 495-452. <https://doi.org/10.1029/TC001i006p00495>.
- Cruz, J. V., Pacheco, D., Coutinho, R., Cymbron, R., Mendes, S., Antunes, P., Fontiela, J., and Freire, P. 2010. Chemical Monitoring of River Water Bodies in an EU Outermost Region: Examples from the Azores Archipelago (Portugal). *Journal of Environmental Monitoring*, 12, 2216-2225. <https://doi.org/10.1039/C0EM00221F>.
- Cruz, J. V., and Silva, M. O. 2001. Hydrogeologic Framework of Pico Island, Azores, Portugal. *Hydrogeol. J.*, 9, 177-189. <https://doi.org/10.1007/s100400000106>.
- Das, R., Wason, H. R., and Sharma, M. L. 2011. Global Regression Relations for Conversion of Surface Wave and Body Wave Magnitudes to Moment Magnitude. *Natural Hazards*, 59, 801-810. <https://doi.org/10.1007/s11069-011-9796-6>.
- D'Araújo, J., Sigmundsson, F., Ferreira, T., Okada, J., Lorenzo, M., and Silva, R. 2022. Plate Boundary Deformation and Volcano Unrest at the Azores Triple Junction Determined from Continuous Gps Measurements, 2002–2017. *Journal of Geophysical Research: Solid Earth*, 127, e2021JB023007. <https://doi.org/10.1029/2021JB023007>.
- De Lange, W., and Moon, V. 2004. Estimating Earthquake and Landslide Tsunami Hazard for the New Zealand Coast. *Bulletin of the New Zealand Society for Earthquake Engineering*, 37, 62-69. <https://doi.org/10.5459/bnzsee.37.2.62-69>.
- Dengler, A. T., Wilde, P., Noda, E. K., and Normark, W. R. 1984. Turbidity Currents Generated by Hurricane Iwa. *Geo-Mar. Lett.*, 4, 5-11. <https://doi.org/10.1007/BF02237967>.

- Di Giacomo, D., Storchak, D., Safronova, N., Ozgo, P., Harris, J., Verney, R., and Bondár, I. 2014. A New Isc Service: The Bibliography of Seismic Events. *Seismological Research Letters*, 85, 354-360. <https://doi.org/10.1785/0220130143>.
- Di Traglia, F., Fornaciai, A., Casalbore, D., Favalli, M., Manzella, I., Romagnoli, C., Chiocci, F. L., Cole, P., Nolesini, T., and Casagli, N. 2022. Subaerial-Submarine Morphological Changes at Stromboli Volcano (Italy) Induced by the 2019–2020 Eruptive Activity. *Geomorphology*, 400, 108093. <https://doi.org/10.1016/j.geomorph.2021.108093>.
- Di Traglia, F., Nolesini, T., Solari, L., Ciampalini, A., Frodella, W., Steri, D., Allotta, B., Rindi, A., Marini, L., and Monni, N. 2018. Lava Delta Deformation as a Proxy for Submarine Slope Instability. *Earth and Planetary Science Letters*, 488, 46-58. <https://doi.org/10.1016/j.epsl.2018.01.038>.
- Dietrich, P., Ghienne, J.-F., Normandeau, A., and Lajeunesse, P. 2016. Upslope-Migrating Bedforms in a Proglacial Sandur Delta: Cyclic Steps from River-Derived Underflows? *Journal of Sedimentary Research*, 86, 112-122. <https://doi.org/10.2110/jsr.2016.4>.
- Droxler, A. W., and Schlager, W. 1985. Glacial Versus Interglacial Sedimentation Rates and Turbidite Frequency in the Bahamas. *Geology*, 13, 799-802. [https://doi.org/10.1130/0091-7613\(1985\)13<799:GVISRA>2.0.CO;2](https://doi.org/10.1130/0091-7613(1985)13<799:GVISRA>2.0.CO;2).
- Dullo, W.-C. 2005. Coral Growth and Reef Growth: A Brief Review. *Facies*, 51, 33-48. <https://doi.org/10.1007/s10347-005-0060-y>.
- Dunbar, G. B., and Barrett, P. J. 2005. Estimating Palaeobathymetry of Wave-Graded Continental Shelves from Sediment Texture. *Sediimentology*, 52, 253-269. <https://doi.org/10.1111/j.1365-3091.2004.00695.x>.
- Egorov, Y. 2007. Tsunami Wave Generation by the Eruption of Underwater Volcano. *Nat. Hazards Earth Syst. Sci.*, 7, 65-69. <https://doi.org/10.5194/nhess-7-65-2007>.
- Eisele, S., Freundt, A., Kutterolf, S., Ramalho, R. S., Kwasnitschka, T., Wang, K. L., and Hemming, S. R. 2015a. Stratigraphy of the Pleistocene, Phonolitic Cão Grande Formation on Santo Antão, Cape Verde. *Journal of Volcanology and Geothermal Research*, 301, 204-220. <https://doi.org/10.1016/j.jvolgeores.2015.03.012>.
- Eisele, S., Reißig, S., Freundt, A., Kutterolf, S., Nürnberg, D., Wang, K. L., and Kwasnitschka, T. 2015b. Pleistocene to Holocene Offshore Tephrostratigraphy of Highly Explosive Eruptions from the Southwestern Cape Verde Archipelago. *Marine Geology*, 369, 233-250. <https://doi.org/10.1016/j.margeo.2015.09.006>.
- Eissler, H. K., and Kanamori, H. 1987. A Single-Force Model for the 1975 Kalapana, Hawaii, Earthquake. *Journal of Geophysical Research: Solid Earth*, 92, 4827-4836. <https://doi.org/10.1029/JB092iB06p04827>.

- Emerson, S., and Hedges, J. 1988. Processes Controlling the Organic Carbon Content of Open Ocean Sediments. *Paleoceanography*, 3, 621-634. <https://doi.org/10.1029/PA003i005p00621>.
- Emery, K. O. 1968. Relict Sediments on Continental Shelves of World1. *AAPG Bulletin*, 52, 445-464. <https://doi.org/10.1306/5D25C2E7-16C1-11D7-8645000102C1865D>.
- Faugères, J.-C., Stow, D. A. V., Imbert, P., and Viana, A. 1999. Seismic Features Diagnostic of Contourite Drifts. *Mar. Geol.*, 162, 1-38. [https://doi.org/10.1016/S0025-3227\(99\)00068-7](https://doi.org/10.1016/S0025-3227(99)00068-7).
- Federici, B., Bacino, F., Cosso, T., Poggi, P., Rebaudengo Landó, L., and Sguerso, D. 2006. Analisi Del Rischio Tsunami Applicata Ad Un Tratto Della Costa Ligure. *MondoGIS*, 57, 53-57.
- Féraud, G., Kaneoka, I., and Allegre, C. J. 1980. K/Ar Ages and Stress Pattern in the Azores: Dynamic Implications. *Earth Planet. Sci. Lett.*, 46, 275-286. [https://doi.org/10.1016/0012-821X\(80\)90013-8](https://doi.org/10.1016/0012-821X(80)90013-8).
- Ferreira, T., Gomes, A., Gaspar, J. L., and Guest, J. 2015. Chapter 10 Distribution and Significance of Basaltic Eruptive Centres: São Miguel, Azores. *Geological Society, London, Memoirs*, 44, 135-146. <https://doi.org/10.1144/m44.10>.
- Ferreira, T. 2000. Caracterização Da Actividade Vulcânica Recente Da Ilha De S. Miguel (Açores): Vulcanismo Basáltico Subaéreo E Zonas De Desgaseificação. Avaliação De Riscos. PhD thesis, Universidade dos Açores.
- Fierstein, J., and Nathenson, M. 1992. Another Look at the Calculation of Fallout Tephra Volumes. *Bulletin of Volcanology*, 54, 156-167. <https://doi.org/10.1007/BF00278005>.
- Fildani, A., Normark, W. R., Kostic, S., and Parker, G. 2006. Channel Formation by Flow Stripping: Large-Scale Scour Features Along the Monterey East Channel and Their Relation to Sediment Waves. *Sedimentology*, 23, 1265-1287. <https://doi.org/10.1111/j.1365-3091.2006.00812.x>.
- Fine, I. V., Rabinovich, A. B., Bornhold, B. D., Thomson, R. E., and Kulikov, E. A. 2005. The Grand Banks Landslide-Generated Tsunami of November 18, 1929: Preliminary Analysis and Numerical Modeling. *Marine Geology*, 215, 45-57. <https://doi.org/10.1016/j.margeo.2004.11.007>.
- Fisher, R. V. 1961. Proposed Classification of Volcaniclastic Sediments and Rocks. *Geological Society of America Bulletin*, 72, 1409-1414. [https://doi.org/10.1130/0016-7606\(1961\)72\[1409:PCOVSA\]2.0.CO;2](https://doi.org/10.1130/0016-7606(1961)72[1409:PCOVSA]2.0.CO;2).
- Flemming, B. W. 2017. Particle Shape-Controlled Sorting and Transport Behaviour of Mixed Siliciclastic/Bioclastic Sediments in a Mesotidal Lagoon, South Africa. *Geo-Marine Letters*, 37, 397-410. <https://doi.org/10.1007/s00367-016-0457-3>.

- Flood, R. D. 1988. A Lee Wave Model for Deep-Sea Mudwave Activity. *Deep-Sea Res.*, 35, 973-983. [https://doi.org/10.1016/0198-0149\(88\)90071-4](https://doi.org/10.1016/0198-0149(88)90071-4).
- Flood, R. D., and Shor, A. N. 1988. Mud Waves in the Argentine Basin and Their Relationship to Regional Bottom Circulation Patterns. *Deep Sea Research Part A. Oceanographic Research Papers*, 35, 943-971. [https://doi.org/10.1016/0198-0149\(88\)90070-2](https://doi.org/10.1016/0198-0149(88)90070-2).
- Flores, R. P., Rijnsburger, S., Meirelles, S., Horner-Devine, A. R., Souza, A. J., Pietrzak, J. D., Henriquez, M., and Reniers, A. 2018. Wave Generation of Gravity-Driven Sediment Flows on a Predominantly Sandy Seabed. *Geophysical Research Letters*, 45, 7634-7645. <https://doi.org/10.1029/2018GL077936>.
- Folk, R. L., and Ward, W. C. 1957. Brazos River Bar [Texas]; a Study in the Significance of Grain Size Parameters. *Journal of Sedimentary Research*, 27, 3-26. <https://doi.org/10.1306/74D70646-2B21-11D7-8648000102C1865D>.
- Forjaz, V. H., Tavares, J. M., Azevedo, E. M. V. B., J.C. Nunes, R.S. Santos, Barreiros, J. P., Gallagher, L., Barcelos, P. J. M., Silva, P. H., Cardigos, F., França, Z. T. M., Dentinho, T., Costa, M. P., Magalhães, L., Rodrigues, M. C., Gonçalves, J. F., Silva, V., and Serpa, V. 2004. *Atlas Básico Dos Açores (2nd Edition)*, Observatório Vulcanológico dos Açores, Ponta Delgada.
- Forjaz, V. 1968. Carta Geológica Do Sistema Vulcânico Faial-Pico-S. Jorge. Escala 1: 200 000. *A actividade vulcânica na ilha do Faial (1957 67)*.
- Fornaciai, A., Favalli, M., and Nannipieri, L. 2019. Numerical Simulation of the Tsunamis Generated by the Sciara Del Fuoco Landslides (Stromboli Island, Italy). *Scientific reports*, 9, 1-12. <https://doi.org/10.1038/s41598-019-54949-7>.
- Fornari, D. J., Moore, J. G., and Calk, L. 1979. A Large Submarine Sand-Rubble Flow on Kilauea Volcano, Hawaii. *J. Volcanol. Geotherm. Res.*, 5, 239-256. [https://doi.org/10.1016/0377-0273\(79\)90018-0](https://doi.org/10.1016/0377-0273(79)90018-0).
- Frattini, P., and Crosta, G. B. 2013. The Role of Material Properties and Landscape Morphology on Landslide Size Distributions. *Earth and Planetary Science Letters*, 361, 310-319. <https://doi.org/10.1016/j.epsl.2012.10.029>.
- Freundt, A., and Schmincke, H.-U. 1995. Petrogenesis of Rhyolite-Trachyte-Basalt Composite Ignimbrite P1, Gran Canaria, Canary Islands. *Journal of Geophysical Research: Solid Earth*, 100, 455-474. <https://doi.org/10.1029/94JB02478>.
- Fu, L.-L., and Holt, B. 1982. *Seasat Views Oceans and Sea Ice with Synthetic-Aperture Radar*, California Institute of Technology, Jet Propulsion Laboratory.
- Fuhrmann, A., Kane, I. A., Schomacker, E., Clare, M. A., and Pontén, A. 2022. Bottom Current Modification of Turbidite Lobe Complexes. *Frontiers in Earth Science*, 9. <https://doi.org/10.3389/feart.2021.752066>.

- Furumoto, A. S., and Kovach, R. L. 1979. The Kalapana Earthquake and Its Relation to Geothermal Processes. *Phys. Earth Planet. Inter.*, 18, 197-208. [https://doi.org/10.1016/0031-9201\(79\)90114-6](https://doi.org/10.1016/0031-9201(79)90114-6).
- Gabitov, R., Sadekov, A., Yapaskurt, V., Borrelli, C., Bychkov, A., Sabourin, K., and Perez-Huerta, A. 2019. Elemental Uptake by Calcite Slowly Grown from Seawater Solution: An in-Situ Study Via Depth Profiling. *Frontiers in Earth Science*, 7. <https://doi.org/10.3389/feart.2019.00051>.
- Gandino, A., Guidi, M., Merlo, C., Mete, L., Rossi, R., and Zan, L. 1985. Preliminary Model of the Ribeira Grande Geothermal Field (Azores Islands). *Geothermics*, 14, 91-105. [https://doi.org/10.1016/0375-6505\(85\)90096-3](https://doi.org/10.1016/0375-6505(85)90096-3).
- Garcia, M. O., Sherman, S. B., Moore, G. F., Goll, R., Popova-Goll, I., Natland, J. H., and Acton, G. 2006. Frequent Landslides from Koolau Volcano: Results from Odp Hole 1223a. *Journal of Volcanology and Geothermal Research*, 151, 251-268. <https://doi.org/10.1016/j.jvolgeores.2005.07.035>.
- Gardner, J. V., Prior, D. B., and Field, M. E. 1999. Humboldt Slide — a Large Shear-Dominated Retrogressive Slope Failure. *Marine Geology*, 154, 323-338. [https://doi.org/10.1016/S0025-3227\(98\)00121-2](https://doi.org/10.1016/S0025-3227(98)00121-2).
- Gaspar, J. L., Queiroz, G., Ferreira, T., Medeiros, A. R., Goulart, C., and Medeiros, J. 2015. Chapter 4 Earthquakes and Volcanic Eruptions in the Azores Region: Geodynamic Implications from Major Historical Events and Instrumental Seismicity. *Geological Society, London, Memoirs*, 44, 33-49. <https://doi.org/10.1144/m44.4>.
- Gaspar, J. L., Queiroz, G., Pacheco, J. A., Ferreira, T., Wallenstein, N., Almeida, M. H., and Coutinho, R. 2003. Basaltic Lava Balloons Produced During the 1998-2001 Serreta Submarine Ridge Eruption (Azores). In: White, J. D. L., Smellie, J. L., and Clague, D. A. (eds.) *Subaqueous Explosive Volcanism, Am. Geophys. Union Geophysical Monogr. 140*. Washington, DC: Am. Geophys. Union, 205-212. <https://doi.org/10.1029/140GM13>.
- Geist, E. L., and ten Brink, U. S. 2019. Offshore Landslide Hazard Curves from Mapped Landslide Size Distributions. *Journal of Geophysical Research: Solid Earth*, 124, 3320-3334. <https://doi.org/10.1029/2018jb017236>.
- Geist, E. L. 2012. Chapter Two - Phenomenology of Tsunamis II: Scaling, Event Statistics, and Inter-Event Triggering. In: Dmowska, R. (ed.) *Advances in Geophysics*. Elsevier, 35-92. <https://doi.org/10.1016/B978-0-12-380938-4.00002-1>.
- Geist, E. L., Lynett, P. J., and Chaytor, J. D. 2009a. Hydrodynamic Modeling of Tsunamis from the Currituck Landslide. *Marine Geology*, 264, 41-52. <https://doi.org/10.1016/j.margeo.2008.09.005>.

- Geist, E. L., Lynett, P. J., and Chaytor, J. D. 2009b. Hydrodynamic Modeling of Tsunamis from the Currituck Landslide. *Marine Geology*, 264, 41-52. <https://doi.org/10.1016/j.margeo.2008.09.005>.
- Geist, E. L., and Parsons, T. 2006. Probabilistic Analysis of Tsunami Hazards*. *Natural Hazards*, 37, 277-314. <https://doi.org/10.1007/s11069-005-4646-z>.
- Gente, P., Dymont, J., Maia, M., and Goslin, J. 2003. Interaction between the Mid-Atlantic Ridge and the Azores Hot Spot During the Last 85 Myr: Emplacement and Rifting of the Hot Spot-Derived Plateaus. *Geochem. Geophys. Geosys.*, 4. <https://doi.org/8510.1029/2003GC000527>.
- Gertisser, R., Self, S., Gaspar, J. L., Kelley, S. P., Pimentel, A., Eikenberg, J., Barry, T. L., Pacheco, J. M., Queiroz, G., and Vespa, M. 2010. Ignimbrite Stratigraphy and Chronology on Terceira Island, Azores. *The Geological Society of America, Special Paper*, 464, 133-154. [https://doi.org/10.1130/2010.2464\(07\)](https://doi.org/10.1130/2010.2464(07)).
- Gill, A. E. 1982. *Atmosphere-Ocean Dynamics*, New York, Academic Press.
- Glazner, A. F., Manley, C. R., Marron, J. S., and Rojstaczer, S. 1999. Fire or Ice: Anticorrelation of Volcanism and Glaciation in California over the Past 800,000 Years. *Geophysical Research Letters*, 26, 1759-1762. <https://doi.org/10.1029/1999GL900333>.
- Gràcia, E., Vizcaino, A., Escutia, C., Asioli, A., Rodés, Á., Pallàs, R., Garcia-Orellana, J., Lebreiro, S., and Goldfinger, C. 2010. Holocene Earthquake Record Offshore Portugal (Sw Iberia): Testing Turbidite Paleoseismology in a Slow-Convergence Margin. *Quaternary Science Reviews*, 29, 1156-1172. <https://doi.org/10.1016/j.quascirev.2010.01.010>.
- Gràcia, E., Danobeitia, J., Vergés, J., and team, P. 2003. Mapping Active Faults Offshore Portugal (36 N–38 N): Implications for Seismic Hazard Assessment Along the Southwest Iberian Margin. *Geology*, 31, 83-86. [https://doi.org/10.1130/0091-7613\(2003\)031<0083:MAFOPN>2.0.CO;2](https://doi.org/10.1130/0091-7613(2003)031<0083:MAFOPN>2.0.CO;2).
- Gudmundsdóttir, E. R., Eiríksson, J., and Larsen, G. 2011. Identification and Definition of Primary and Reworked Tephra in Late Glacial and Holocene Marine Shelf Sediments Off North Iceland. *Journal of Quaternary Science*, 26, 589-602. <https://doi.org/10.1002/jqs.1474>.
- Gutierrez-Pastor, J., Nelson, C. H., Goldfinger, C., Johnson, J. E., Escutia, C., Eriksson, A., Morey, A. E., and The Shipboard Scientific, P. 2009. Earthquake Control of Holocene Turbidite Frequency Confirmed by Hemipelagic Sedimentation Chronology on the Cascadia and Northern California Active Continental Margins. In: Kneller, B., Martinsen, O. J., and McCaffrey, B. (eds.) *External Controls on Deep-Water*

- Depositional Systems*. SEPM Society for Sedimentary Geology, 0. <https://doi.org/10.2110/sepmsp.092.179>.
- Guzzetti, F., Ardizzone, F., Cardinali, M., Rossi, M., and Valigi, D. 2009. Landslide Volumes and Landslide Mobilization Rates in Umbria, Central Italy. *Earth and Planetary Science Letters*, 279, 222-229. <https://doi.org/10.1016/j.epsl.2009.01.005>.
- Haflidason, H., Lien, R., Sejrup, H. P., Forsberg, C. F., and Bryn, P. 2005. The Dating and Morphometry of the Storegga Slide. *Marine and Petroleum Geology*, 22, 123-136. <https://doi.org/10.1016/j.marpetgeo.2004.10.008>.
- Hajdas, I. 2008. Radiocarbon Dating and Its Applications in Quaternary Studies. *E&G Quaternary Sci. J.*, 57, 2-24. <https://doi.org/10.3285/eg.57.1-2.1>.
- Hall, K. 1982. Rapid Deglaciation as an Initiator of Volcanic Activity: An Hypothesis. *Earth Surface Processes and Landforms*, 7, 45-51. <https://doi.org/10.1002/esp.3290070106>.
- Hamilton, E. L., and Bachman, R. T. 1982. Sound Velocity and Related Properties of Marine Sediments. *J. Acoust. Soc. Am.*, 72, 1891-1904. <https://doi.org/10.1121/1.388539>.
- Hamilton, E. L. 1976. Shear-Wave Velocity Versus Depth in Marine Sediments: A Review. *Geophysics*, 41, 985-996. <https://doi.org/10.1190/1.1440676>.
- Hamilton, E. L., Shumway, G., Menard, H. W., and Shipek, C. J. 1956. Acoustic and Other Physical Properties of Shallow-Sater Sediments Off San Diego. *The Journal of the Acoustical Society of America*, 28, 1-1. <https://doi.org/10.1121/1.1908210>.
- Hammer, C. U. 1977. Past Volcanism Revealed by Greenland Ice Sheet Impurities. *Nature*, 270, 482-486. <https://doi.org/10.1038/270482a0>.
- Hampton, M. A., Lee, H. J., and Locat, J. 1996. Submarine Landslides. *Reviews of Geophysics*, 34, 33-59. <https://doi.org/10.1029/95RG03287>.
- Hannah, G., Hughes, P. D., and Gibbard, P. L. 2017. Pleistocene Plateau Ice Fields in the High Atlas, Morocco. *Geological Society, London, Special Publications*, 433, 25-53. <https://doi.org/10.1144/SP433.12>.
- Hansteen, T. H., Freundt, A., and Kutterolf, S. 2017. *Short Cruise Report Rv Meteor M141/1: Azores Tephra*s, GEOMAR Helmholtz-Zentrum für Ozeanforschung Kiel, Germany.
- Hansen, J., Johnson, D., Lacis, A., Lebedeff, S., Lee, P., Rind, D., and Russell, G. 1981. Climate Impact of Increasing Atmospheric Carbon Dioxide. *Science*, 213, 957-966. <https://doi.org/10.1126/science.213.4511.957>.
- Hart, K., Carey, S., Sigurdsson, H., Sparks, R. S. J., and Robertson, R. E. A. 2004. Discharge of Pyroclastic Flows into the Sea During the 1996-1998 Eruptions of the Soufrière Hills Volcano, Montserrat. *Bull. Volcanol.*, 66, 599-614. <https://doi.org/10.1007/s00445-004-0342-1>.
- Hasenclever, J., Knorr, G., Rüpke, L. H., Köhler, P., Morgan, J., Garofalo, K., Barker, S., Lohmann, G., and Hall, I. R. 2017. Sea Level Fall During Glaciation Stabilized

- Atmospheric CO₂ by Enhanced Volcanic Degassing. *Nature Communications*, 8, 15867. <https://doi.org/10.1038/ncomms15867>.
- Heaton, T. J., Köhler, P., Butzin, M., Bard, E., Reimer, R. W., Austin, W. E. N., Bronk Ramsey, C., Grootes, P. M., Hughen, K. A., Kromer, B., Reimer, P. J., Adkins, J., Burke, A., Cook, M. S., Olsen, J., and Skinner, L. C. 2020. Marine20—the Marine Radiocarbon Age Calibration Curve (0–55,000 Cal Bp). *Radiocarbon*, 62, 779-820. <https://doi.org/10.1017/RDC.2020.68>.
- Heezen, B. C., and Ewing, M. 1952. Turbidity Currents and Submarine Slumps, and the 1929 Grand Banks Earthquake. *American Journal of Science*, 250, 849-873. <https://doi.org/10.2475/ajs.250.12.849>.
- Hemphill-Haley, E. 1995. Diatom Evidence for Earthquake-Induced Subsidence and Tsunami 300 Yr Ago in Southern Coastal Washington. *GSA Bulletin*, 107, 367-378. [https://doi.org/10.1130/0016-7606\(1995\)107<0367:DEFEIS>2.3.CO;2](https://doi.org/10.1130/0016-7606(1995)107<0367:DEFEIS>2.3.CO;2).
- Herd, R. A., Edmonds, M., and Bass, V. A. 2005. Catastrophic Lava Dome Failure at Soufrière Hills Volcano, Montserrat, 12–13 July 2003. *Journal of Volcanology and Geothermal Research*, 148, 234-252. <https://doi.org/10.1016/j.jvolgeores.2005.05.003>.
- Hildenbrand, A., Weis, D., Madureira, P., and Marques, F. O. 2014. Recent Plate Re-Organization at the Azores Triple Junction: Evidence from Combined Geochemical and Geochronological Data on Faial, S. Jorge and Terceira Volcanic Islands. *Lithos*, 210-211, 27-39. <https://doi.org/10.1016/j.lithos.2014.09.009>.
- Hildenbrand, A., Marques, F. O., Catalão, J., Catita, C. M. S., and Costa, A. C. G. 2012. Large-Scale Active Slump of the Southeastern Flank of Pico Island, Azores. *Geology*, 10, 939-942. <https://doi.org/10.1130/G33303.1>.
- Hildenbrand, A., Madureira, P., Marques, F. O., Cruz, I., Henry, B., and Silva, P. 2008. Multi-Stage Evolution of a Sub-Aerial Volcanic Ridge over the Last 1.3 myr: S. Jorge Island, Azores Triple Junction. *Earth and Planetary Science Letters*, 273, 289-298. <https://doi.org/10.1016/j.epsl.2008.06.041>.
- Hill, D. P., Pollitz, F., and Newhall, C. 2002. Earthquake–Volcano Interactions. *Physics Today*, 55, 41-47. <https://doi.org/10.1063/1.1535006>.
- Hill, P. R., Moran, K. M., and Blasco, S. M. 1982. Creep Deformation of Slope Sediments in the Canadian Beaufort Sea. *Geo-Mar. Lett.*, 2, 163-170. <https://doi.org/10.1007/BF02462758>.
- Hiscott, R., Colella, A., Pezard, P., Lovell, M., and Malinverno, A. 1992. Sedimentology of Deep-Water Volcaniclastics, Oligocene Izu-Bonin Forearc Basin, Based on Formation Microscanner Images. *Proceedings of the Ocean Drilling Program, Scientific Results*, 126, 75-96. <https://doi.org/10.2973/odp.proc.sr.126.118.1992>.

- Hipólito, A., Madeira, J., Carmo, R., and Gaspar, J. L. 2014. Neotectonics of Graciosa Island (Azores): A Contribution to Seismic Hazard Assessment of a Volcanic Area in a Complex Geodynamic Setting. *Annals of Geophysics*, 56. <https://doi.org/10.4401/ag-6222>.
- Hoffmann, G., Silver, E., Day, S., Morgan, E., Driscoll, N., Orange, D., Draut, A. E., Clift, P. D., and Scholl, D. W. 2008. Sediment Waves in the Bismarck Volcanic Arc, Papua New Guinea. *Formation and Applications of the Sedimentary Record in Arc Collision Zones*. Geological Society of America, 0. [https://doi.org/10.1130/2008.2436\(05\)](https://doi.org/10.1130/2008.2436(05)).
- Hoogakker, B. A. A., Rothwell, R. G., Rohling, E. J., Paterne, M., Stow, D. A. V., Herrle, J. O., and Clayton, T. 2004. Variations in Terrigenous Dilution in Western Mediterranean Sea Pelagic Sediments in Response to Climate Change During the Last Glacial Cycle. *Marine Geology*, 211, 21-43. <https://doi.org/10.1016/j.margeo.2004.07.005>.
- Houghton, B. F., and Landis, C. A. 1989. Sedimentation and Volcanism in a Permian Arc-Related Basin, Southern New Zealand. *Bulletin of Volcanology*, 51, 433-450. <https://doi.org/10.1007/BF01078810>.
- Hsu, S. K., Kuo, J., Lo, C. L., Tsai, C. H., Doo, W. B., Ku, C. Y., and Sibuet, J. C. 2008. Turbidity Currents, Submarine Land- Slides and the 2006 Pingtung Earthquake Off Sw Taiwan. *Terr. Atmos. Ocean Sci.*, 19, 767-772. [https://doi.org/10.3319/TAO.2008.19.6.767\(PT\)](https://doi.org/10.3319/TAO.2008.19.6.767(PT)).
- Hu, G., Yan, T., Liu, Z., Vanneste, M., and Dong, L. 2009. Size Distribution of Submarine Landslides Along the Middle Continental Slope of the East China Sea. *Journal of Ocean University of China*, 8, 322. <https://doi.org/10.1007/s11802-009-0322-3>.
- Hübscher, C., Beier, C., Al-Hseinat, M., Batista, L., Blum, M., Bobsin, M., Bülow, J., Frahm, L., Grob, H., Hildenbrandt, A., Kalvelage, C., Kammann, J., Knevels, K., Levanos, I., Nomikou, P., Reichel, H., Petry, F., Spickermann, D., Stackemann, F., Stratmann, S., Terrinha, P., Vögele, M., Winter, S., Schaaf, T., Schleifer, B., Stelzner, M., Spitzky, S., Weinzierl, C., and Weiß, B. 2016. *Azores Plateau - Cruise No. M113/1 - December 29, 2014 - January 22, 2015 - Ponta Delgada (Portugal) - Ponta Delgada (Portugal)*, Bremen. https://doi.org/10.2312/cr_m113_1.
- Hübscher, C., and Gohl, K. 2016. Reflection/Refraction Seismology. In: Harff, J., Meschede, M., Petersen, S., et al. (eds.) *Encyclopedia of Marine Geosciences*. Dordrecht: Springer Netherlands, 721-731. https://doi.org/10.1007/978-94-007-6238-1_128.
- Hübscher, C. 2013. *Tragica - Cruise No. M79/2 - August 26 – September 21, 2009 - Ponta Delgada (Azores / Portugal) – Las Palmas (Canary Islands / Spain)*, Bremen. https://doi.org/10.2312/cr_m79_2.
- Hughes Clarke, J. E., Shor, A. N., Piper, D. J. W., and Mayer, L. A. 1990. Large-Scale Current-Induced Erosion and Deposition in the Path of the 1929 Grand Banks Turbidity

- Current. *Sedimentology*, 37, 613-629. <https://doi.org/10.1111/j.1365-3091.1990.tb00625.x>.
- Hunt, J. B., and Hill, P. G. 2001. Tephrological Implications of Beam Size—Sample-Size Effects in Electron Microprobe Analysis of Glass Shards. *Journal of Quaternary Science*, 16, 105-117. <https://doi.org/10.1002/jqs.571>.
- Hunt, J. E., Tappin, D. R., Watt, S. F. L., Susilohadi, S., Novellino, A., Ebmeier, S. K., Cassidy, M., Engwell, S. L., Grilli, S. T., Hanif, M., Priyanto, W. S., Clare, M. A., Abdurrachman, M., and Udrek, U. 2021. Submarine Landslide Megablocks Show Half of Anak Krakatau Island Failed on December 22nd, 2018. *Nature Communications*, 12, 2827. <https://doi.org/10.1038/s41467-021-22610-5>.
- Hunt, J. E., Cassidy, M., and Talling, P. J. 2018. Multi-Stage Volcanic Island Flank Collapses with Coeval Explosive Caldera-Forming Eruptions. *Scientific Reports*, 8, 1146. <https://doi.org/10.1038/s41598-018-19285-2>.
- Hunt, J. E., Talling, P. J., Clare, M. A., Jarvis, I., and Wynn, R. B. 2014. Long-Term (17 Ma) Turbidite Record of the Timing and Frequency of Large Flank Collapses of the Canary Islands. *Geochemistry, Geophysics, Geosystems*, 15, 3322-3345. <https://doi.org/10.1002/2014gc005232>.
- Hunt, J. E., Wynn, R. B., Talling, P. J., and Masson, D. G. 2013. Multistage Collapse of Eight Western Canary Island Landslides in the Last 1.5 Ma: Sedimentological and Geochemical Evidence from Subunits in Submarine Flow Deposits. *Geochemistry, Geophysics, Geosystems*, 14, 2159-2181. <https://doi.org/10.1002/ggge.20138>.
- Hunt, J. E., Wynn, R. B., Masson, D. G., Talling, P. J., and Teagle, D. A. H. 2011. Sedimentological and Geochemical Evidence for Multistage Failure of Volcanic Island Landslides: A Case Study from Icod Landslide on North Tenerife, Canary Islands. *Geochemistry, Geophysics, Geosystems*, 12. <https://doi.org/10.1029/2011gc003740>.
- Hunt, J. N. 1979. Direct Solution of Wave Dispersion Equation. *Journal of the Waterway, Port, Coastal and Ocean Division*, 105, 457-459. <https://doi.org/10.1061/JWPCDX.0000168>.
- Huppert, K. L., Perron, J. T., and Ashton, A. D. 2020. The Influence of Wave Power on Bedrock Sea-Cliff Erosion in the Hawaiian Islands. *Geology*, 48, 499-503. <https://doi.org/10.1130/G47113.1>.
- Hürlimann, M., Martí, J., and Ledesma, A. 2000. Mechanical Relationship between Catastrophic Volcanic Landslides and Caldera Collapses. *Geophysical Research Letters*, 27, 2393-2396. <https://doi.org/10.1029/2000GL011564>.
- Instituto Nacional de Meteorología 2012. *Atlas Climático De Los Archipiélagos De Canarias, Madeira Y Azores Temperatura Del Aire Y Precipitación (1971 - 2000)*, Lisboa, Inst. de Meteorología.

- James, N. P., Jones, B., Nelson, C. S., Campbell, H. J., and Titjen, J. 2011. Cenozoic Temperate and Sub-Tropical Carbonate Sedimentation on an Oceanic Volcano – Chatham Islands, New Zealand. *Sedimentology*, 58, 1007-1029. <https://doi.org/10.1111/j.1365-3091.2010.01193.x>.
- James, N. P., and Clarke, J. A. D. 1997. *Cool-Water Carbonates*, SEPM Society for Sedimentary Geology. <https://doi.org/10.2110/pec.97.56>.
- Jarosewich, E. 2002. Smithsonian Microbeam Standards. *Journal of Research of the National Institute of Standards and Technology*, 107, 681. <https://doi.org/10.6028/jres.107.054>.
- Jeffery, A. J., Gertisser, R., Self, S., Pimentel, A., O'Driscoll, B., and Pacheco, J. M. 2018. Petrogenesis of the Peralkaline Ignimbrites of Terceira, Azores. *Journal of Petrology*, 58, 2365-2402. <https://doi.org/10.1093/petrology/egy012>.
- Jellinek, A. M., Manga, M., and Saar, M. O. 2004. Did Melting Glaciers Cause Volcanic Eruptions in Eastern California? Probing the Mechanics of Dike Formation. *Journal of Geophysical Research: Solid Earth*, 109. <https://doi.org/10.1029/2004JB002978>.
- Jibson, R. W. 2011. Methods for Assessing the Stability of Slopes During Earthquakes—A Retrospective. *Engineering Geology*, 122, 43-50. <https://doi.org/10.1016/j.enggeo.2010.09.017>.
- Jobe, Z. R., Howes, N., Romans, B. W., and Covault, J. A. 2018. Volume and Recurrence of Submarine-Fan-Building Turbidity Currents. *The Depositional Record*, 4, 160-176. <https://doi.org/10.1002/dep2.42>.
- Joint_Panel_on_Oceanographic_Tables_and_Standards 1991. *Processing of Oceanographic Station Data*, Paris, UNESCO.
- Johnson, C. L., Wijbrans, J. R., Constable, C. G., Gee, J., Staudigel, H., Tauxe, L., Forjaz, V.-H., and Salgueiro, M. 1998. 40Ar/39Ar Ages and Paleomagnetism of São Miguel Lavas, Azores. *Earth and Planetary Science Letters*, 160, 637-649. [https://doi.org/10.1016/S0012-821X\(98\)00117-4](https://doi.org/10.1016/S0012-821X(98)00117-4).
- Joshi, S., Duffy, G. P., and Brown, C. 2017. Critical Bed Shear Stress and Threshold of Motion of Maerl Biogenic Gravel. *Estuarine, Coastal and Shelf Science*, 194, 128-142. <https://doi.org/10.1016/j.ecss.2017.06.010>.
- Joyner, W. B., and Boore, D. M. 1994. Methods for Regression Analysis of Strong-Motion Data. *Bulletin of the Seismological Society of America*, 84, 955-956, 1943-3573.
- Kadirioğlu, F. T., and Kartal, R. F. 2016. The New Empirical Magnitude Conversion Relations Using an Improved Earthquake Catalogue for Turkey and Its near Vicinity (1900-2012). *Turkish Journal of Earth Sciences*, 25, 300-310. <https://doi.org/10.3906/yer-1511-7>.

- Kagan, Y. Y. 2002. Seismic Moment Distribution Revisited: I. Statistical Results. *Geophysical Journal International*, 148, 520-541. <https://doi.org/10.1046/j.1365-246x.2002.01594.x>.
- Kappel, E. S., and Ryan, W. B. F. 1986. Volcanic Episodicity and a Non-Steady State Rift Valley Along Northeast Pacific Spreading Centers: Evidence from Sea Marc I. *J. Geophys. Res.*, 91, 13925-13940. <https://doi.org/10.1029/JB091iB14p13925>.
- Keating, B. H., and McGuire, W. J. 2000. Island Edifice Failure and Associated Tsunami Hazards. *Pure Appl. Geophys.*, 157, 899-955. <https://doi.org/10.1007/s000240050011>.
- Keefer, D. K. 1994. The Importance of Earthquake-Induced Landslides to Long-Term Slope Erosion and Slope-Failure Hazards in Seismically Active Regions. In: Morisawa, M. (ed.) *Geomorphology and Natural Hazards*. Amsterdam: Elsevier, 265-284. <https://doi.org/10.1016/B978-0-444-82012-9.50022-0>.
- Keil, R. G., Montluçon, D. B., Prahl, F. G., and Hedges, J. I. 1994. Sorptive Preservation of Labile Organic Matter in Marine Sediments. *Nature*, 370, 549-552. <https://doi.org/10.1038/370549a0>.
- Kelfoun, K., Giachetti, T., and Labazuy, P. 2010. Landslide-Generated Tsunamis at Réunion Island. *Journal of Geophysical Research: Earth Surface*, 115. <https://doi.org/10.1029/2009jf001381>.
- Kelner, M., Migeon, S., Tric, E., Couboux, F., Dano, A., Lebourg, T., and Taboada, A. 2016. Frequency and Triggering of Small-Scale Submarine Landslides on Decadal Timescales: Analysis of 4d Bathymetric Data from the Continental Slope Offshore Nice (France). *Marine Geology*, 379, 281-297. <https://doi.org/10.1016/j.margeo.2016.06.009>.
- Klar, A., Aharonov, E., Kalderon-Asael, B., and Katz, O. 2011. Analytical and Observational Relations between Landslide Volume and Surface Area. *Journal of Geophysical Research: Earth Surface*, 116. <https://doi.org/10.1029/2009JF001604>.
- Klein, B., and Siedler, G. 1989. On the Origin of the Azores Current. *Journal of Geophysical Research: Oceans*, 94, 6159-6168. <https://doi.org/10.1029/JC094iC05p06159>.
- Komar, P. D., and Li, Z. 1986. Pivoting Analyses of the Selective Entrainment of Sediments by Shape and Size with Application to Gravel Threshold. *Sedimentology*, 33, 425-436. <https://doi.org/10.1111/j.1365-3091.1986.tb00546.x>.
- Komar, P. D., and Miller, M. C. 1973. The Threshold of Movement under Oscillatory Water Waves. *J. Sediment. Petrol.*, 43, 1101-1110. <https://doi.org/10.1306/74D7290A-2B21-11D7-8648000102C1865D>.
- Korycansky, D. G., and Lynett, P. J. 2005. Offshore Breaking of Impact Tsunami: The Van Dorn Effect Revisited. *Geophysical Research Letters*, 32. <https://doi.org/10.1029/2004GL021918>.

- Kostic, S. 2011. Modeling of Submarine Cyclic Steps: Controls on Their Formation, Migration, and Architecture. *Geosphere*, 7, 294-304. <https://doi.org/10.1130/GES00601.1>.
- Krastel, S., Schmincke, H.-U., Jacobs, C. L., Rihm, R., Le Bas, T. P., and Alibes, B. 2001. Submarine Landslides around the Canary Islands. *Journal of Geophysical Research: Solid Earth*, 106, 3977-3997. <https://doi.org/10.1029/2000JB900413>.
- Kratzmann, D. J., Carey, S., Scasso, R., and Naranjo, J.-A. 2009. Compositional Variations and Magma Mixing in the 1991 Eruptions of Hudson Volcano, Chile. *Bulletin of Volcanology*, 71, 419. <https://doi.org/10.1007/s00445-008-0234-x>.
- Krumbein, W. C. 1941. Measurement and Geological Significance of Shape and Roundness of Sedimentary Particles. *Journal of Sedimentary Research*, 11, 64-72. <https://doi.org/10.1306/D42690F3-2B26-11D7-8648000102C1865D>.
- Kutterolf, S., Schindlbeck, J. C., Jegen, M., Freundt, A., and Straub, S. M. 2019. Milankovitch Frequencies in Tephra Records at Volcanic Arcs: The Relation of Kyr-Scale Cyclic Variations in Volcanism to Global Climate Changes. *Quaternary Science Reviews*, 204, 1-16. <https://doi.org/10.1016/j.quascirev.2018.11.004>.
- Kutterolf, S., Freundt, A., and Burkert, C. 2011. Eruptive History and Magmatic Evolution of the 1.9 Kyr Plinian Dacitic Chiltepe Tephra from Apoyeque Volcano in West-Central Nicaragua. *Bulletin of Volcanology*, 73, 811-831. <https://doi.org/10.1007/s00445-011-0457-0>.
- Kutterolf, S., Freundt, A., Perez, W., Mörz, T., Schacht, U., Wehrmann, H., and Schmincke, H. U. 2008. Pacific Offshore Record of Plinian Arc Volcanism in Central America: 1. Along-Arc Correlations. *Geochemistry, Geophysics, Geosystems*, 9. <https://doi.org/10.1029/2007GC001631>
- Labazuy, P. 1996. Recurrent Landsliding Events on the Submarine Flank of Piton De La Fournaise Volcano (Reunion Island). In: McGuire, W. J., Jones, A. P., and Neuberg, J. (eds.) *Volcano Instability on the Earth and Other Planets*. London: Geological Society, 295-306. <https://doi.org/10.1144/GSL.SP.1996.110.01.23>.
- Lal, D., and Peters, B. 1967. Cosmic Ray Produced Radioactivity on the Earth. In: Sitte, K. (ed.) *Kosmische Strahlung II / Cosmic Rays II*. Berlin, Heidelberg: Springer Berlin Heidelberg, 551-612. https://doi.org/10.1007/978-3-642-46079-1_7.
- Larrea, P., Wijbrans, J. R., Galé, C., Ubide, T., Lago, M., França, Z., and Widom, E. 2014. $^{40}\text{Ar}/^{39}\text{Ar}$ Constraints on the Temporal Evolution of Graciosa Island, Azores (Portugal). *Bulletin of Volcanology*, 76, 1-15. <https://doi.org/10.1007/s00445-014-0796-8>.
- Laughton, A., and Whitmarsh, R. 1974. The Azores-Gibraltar Plate Boundary. *Geodynamics of Iceland and the North Atlantic Area*. Springer, 63-81. https://doi.org/10.1007/978-94-010-2271-2_5.

- Le Friant, A., Ishizuka, O., Boudon, G., Palmer, M. R., Talling, P. J., Villemant, B., Adachi, T., Aljahdali, M., Breitreuz, C., Brunet, M., Caron, B., Coussens, M., Deplus, C., Endo, D., Feuillet, N., Fraas, A. J., Fujinawa, A., Hart, M. B., Hatfield, R. G., Hornbach, M., Jutzeler, M., Kataoka, K. S., Komorowski, J.-C., Lebas, E., Lafuerza, S., Maeno, F., Manga, M., Martínez-Colón, M., McCanta, M., Morgan, S., Saito, T., Slagle, A., Sparks, S., Stinton, A., Stroncik, N., Subramanyam, K. S. V., Tamura, Y., Trofimovs, J., Voight, B., Wall-Palmer, D., Wang, F., and Watt, S. F. L. 2015. Submarine Record of Volcanic Island Construction and Collapse in the Lesser Antilles Arc: First Scientific Drilling of Submarine Volcanic Island Landslides by Iodp Expedition 340. *Geochemistry, Geophysics, Geosystems*, 16, 420-442. <https://doi.org/10.1002/2014GC005652>.
- Le Friant, A., Harford, C. L., Deplus, C., Boudon, G., Sparks, R. S. J., Herd, R. A., and Komorowski, J. C. 2004. Geomorphological Evolution of Montserrat (West Indies): Importance of Flank Collapse and Erosional Process. *J. Geol. Soc. Lond.*, 161, 147-160. <https://doi.org/10.1144/0016-764903-017>.
- Lebreiro, S. M., Voelker, A. H. L., Vizcaino, A., Abrantes, F. G., Alt-Epping, U., Jung, S., Thouveny, N., and Gràcia, E. 2009. Sediment Instability on the Portuguese Continental Margin under Abrupt Glacial Climate Changes (Last 60kyr). *Quaternary Science Reviews*, 28, 3211-3223. <https://doi.org/10.1016/j.quascirev.2009.08.007>.
- Lee, H. J., Syvitski, J. P. M., Parker, G., Orange, D., Locat, J., Hutton, J. W. H., and Imran, J. 2002. Distinguishing Sediment Waves from Slope Failure Deposits: Field Examples, Including the "Humboldt Slide" and Modelling Results. *Mar. Geol.*, 192, 79-104. [https://doi.org/10.1016/S0025-3227\(02\)00550-9](https://doi.org/10.1016/S0025-3227(02)00550-9).
- Lee, H. J., Torresan, M. E., and McArthur, W. 1994. Stability of Submerged Slopes on the Flanks of the Hawaiian Islands, a Simplified Approach. *Open-File Report*, 94-638, 1-54. <https://doi.org/10.2172/90387>.
- Lee, H. J., and Edwards, B. D. 1986. Regional Method to Assess Offshore Slope Stability. *J. Geotech. Eng.*, 112, 489-509. [https://doi.org/10.1061/\(ASCE\)0733-9410\(1986\)112:5\(489\)](https://doi.org/10.1061/(ASCE)0733-9410(1986)112:5(489)).
- León, R., Somoza, L., Urgeles, R., Medialdea, T., Ferrer, M., Biain, A., García-Crespo, J., Mediato, J. F., Galindo, I., Yepes, J., González, F. J., and Gimenez-Moreno, J. 2017. Multi-Event Oceanic Island Landslides: New Onshore-Offshore Insights from El Hierro Island, Canary Archipelago. *Marine Geology*, 393, 156-175. <https://doi.org/10.1016/j.margeo.2016.07.001>.
- Leslie, S. C., Moore, G. F., Morgan, J. K., and Hills, D. J. 2002. Seismic Stratigraphy of the Frontal Hawaiian Moat: Implications for Sedimentary Processes at the Leading Edge

- of an Oceanic Hotspot Trace. *Marine Geology*, 184, 143-162. [https://doi.org/10.1016/S0025-3227\(01\)00284-5](https://doi.org/10.1016/S0025-3227(01)00284-5).
- Lipman, P. W., Normark, W. R., Moore, J. G., Wilson, J. B., and Gutmacher, C. E. 1988. The Giant Submarine Alike Debris Slide, Mauna Loa, Hawaii. *Journal of Geophysical Research*, 93, 4279-4299. <https://doi.org/10.1029/JB093iB05p04279>.
- Liu, P. L.-F., Woo, S.-B., and Cho, Y.-S. 1998. Computer Programs for Tsunami Propagation and Inundation. *Cornell University*, 25.
- Liu, P. L. F., Cho, Y. S., Yoon, S. B., and Seo, S. N. 1995. Numerical Simulations of the 1960 Chilean Tsunami Propagation and Inundation at Hilo, Hawaii. In: Tsuchiya, Y., and Shuto, N. (eds.) *Tsunami: Progress in Prediction, Disaster Prevention and Warning*. Dordrecht: Springer Netherlands, 99-115. https://doi.org/10.1007/978-94-015-8565-1_7.
- Liu, Q., Kneller, B., Fallgatter, C., Valdez Buso, V., and Milana, J. P. 2018. Tabularity of Individual Turbidite Beds Controlled by Flow Efficiency and Degree of Confinement. *Sedimentology*, 65, 2368-2387. <https://doi.org/10.1111/sed.12470>.
- Löb, J., Köhler, J., Mertens, C., Walter, M., Li, Z., von Storch, J.-S., Zhao, Z., and Rhein, M. 2020. Observations of the Low-Mode Internal Tide and Its Interaction with Mesoscale Flow South of the Azores. *Journal of Geophysical Research: Oceans*, 125, e2019JC015879. <https://doi.org/10.1029/2019JC015879>.
- Lodato, L., Spampinato, L., Harris, A., Calvari, S., Dehn, J., and Patrick, M. 2007. The Morphology and Evolution of the Stromboli 2002-2003 Lava Flow Field: An Example of a Basaltic Flow Field Emplaced on a Steep Slope. *Bull. Volcanol.*, 69, 661-679. <https://doi.org/10.1007/s00445-006-0101-6>.
- Lourenço, N., Miranda, J. M., Luis, J. F., Ribeiro, A., Victor, L. A. M., Madeira, J., and Needham, H. D. 1998. Morpho-Tectonic Analysis of the Azores Volcanic Plateau from a New Bathymetric Compilation of the Area. *Marine Geophysical Research*, 20, 141-156. <https://doi.org/10.1023/A:1004505401547>.
- Louvat, P., and Allègre, C. J. 1998. Riverine Erosion Rates on Sao Miguel Volcanic Island, Azores Archipelago. *Chem. Geol.*, 148, 177-200. [https://doi.org/10.1016/S0009-2541\(98\)00028-X](https://doi.org/10.1016/S0009-2541(98)00028-X).
- Lowe, D. J., Pearce, N. J. G., Jorgensen, M. A., Kuehn, S. C., Tryon, C. A., and Hayward, C. L. 2017. Correlating Tephra and Cryptotephra Using Glass Compositional Analyses and Numerical and Statistical Methods: Review and evaluation. *Quaternary Science Reviews*, 175, 1-44. <https://doi.org/10.1016/j.quascirev.2017.08.003>.
- Lukasik, J. J., and James, N. P. 2003. Deepening-Upward Subtidal Cycles, Murray Basin, South Australia. *Journal of Sedimentary Research*, 73, 653-671. <https://doi.org/10.1306/031003730653>.

- Ma, G., Shi, F., and Kirby, J. T. 2012. Shock-Capturing Non-Hydrostatic Model for Fully Dispersive Surface Wave Processes. *Ocean Modelling*, 43-44, 22-35. <https://doi.org/10.1016/j.ocemod.2011.12.002>.
- Macdonald, G. A. 1953. Pahoehoe, Aa, and Block Lava. *American Journal of Science*, 251, 169-191. <https://doi.org/10.2475/ajs.251.3.169>.
- Machado, F., Parsons, W. H., Richards, A. F., and Mulford, J. W. 1962. Capelinhos Eruption of Fayal Volcano, Azores, 1957–1958. *Journal of Geophysical Research (1896-1977)*, 67, 3519-3529. <https://doi.org/10.1029/JZ067i009p03519>.
- Machado, F. 1959. Submarine Pits of the Azores Plateau. *Bulletin Volcanologique*, 21, 109-116. <https://doi.org/10.1007/BF02596510>.
- Machado, F. 1949. O Terramoto De S. Jorge, Em 1757. *Açoreana*, 4, 311-324.
- Madeira, J., Brum da Silveira, A., Hipólito, A., and Carmo, R. 2015. Chapter 3 Active Tectonics in the Central and Eastern Azores Islands Along the Eurasia–Nubia Boundary: A Review. *Geological Society, London, Memoirs*, 44, 15-32. <https://doi.org/10.1144/m44.3>.
- Madeira, J., and Brum da Silveira, A. 2003. Active Tectonics and First Paleoseismological Results in Faial, Pico and S. Jorge Islands (Azores, Portugal). *Annals of Geophys.*, 46, 733-761. <https://doi.org/10.4401/ag-3453>.
- Madeira, J. 1998. Estudos De Neotectónica Nas Ilhas Do Faial, Pico E S. Jorge: Uma Contribuição Para O Conhecimento Geodinâmico Da Junção Tripla Dos Açores. Ph.D thesis, Lisbon University.
- Maio, R., Estêvão, J. M. C., Ferreira, T. M., and Vicente, R. 2017. The Seismic Performance of Stone Masonry Buildings in Faial Island and the Relevance of Implementing Effective Seismic Strengthening Policies. *Engineering Structures*, 141, 41-58. <https://doi.org/10.1016/j.engstruct.2017.03.009>.
- Malamud, B. D., Turcotte, D. L., Guzzetti, F., and Reichenbach, P. 2004. Landslides, Earthquakes, and Erosion. *Earth and Planetary Science Letters*, 229, 45-59. <https://doi.org/10.1016/j.epsl.2004.10.018>.
- Manga, M., Patel, A., and Dufek, J. 2011. Rounding of Pumice Clasts During Transport: Field Measurements and Laboratory Studies. *Bulletin of Volcanology*, 73, 321-333. <https://doi.org/doi:10.1007/s00445-010-0411-6>.
- Marinos, P., and Hoek, E. 2000. Gsi: A Geologically Friendly Tool for Rock Mass Strength Estimation. *ISRM international symposium*. Melbourne, Australia: International Society for Rock Mechanics and Rock Engineering.
- Marques, F. O., Hildenbrand, A., and Hübscher, C. 2018. Evolution of a Volcanic Island on the Shoulder of an Oceanic Rift and Geodynamic Implications: S. Jorge Island on the

- Terceira Rift, Azores Triple Junction. *Tectonophysics*, 738-739, 41-50. <https://doi.org/10.1016/j.tecto.2018.05.012>.
- Martin, J. H., Knauer, G. A., Karl, D. M., and Broenkow, W. W. 1987. Vertex: Carbon Cycling in the Northeast Pacific. *Deep Sea Research Part A. Oceanographic Research Papers*, 34, 267-285. [https://doi.org/10.1016/0198-0149\(87\)90086-0](https://doi.org/10.1016/0198-0149(87)90086-0).
- Marshall, J., Adcroft, A., Hill, C., Perelman, L., and Heisey, C. 1997. A Finite-Volume, Incompressible Navier Stokes Model for Studies of the Ocean on Parallel Computers. *Journal of Geophysical Research: Oceans*, 102, 5753-5766. <https://doi.org/10.1029/96JC02775>.
- Masson, D. G., Arzola, R. G., Wynn, R. B., Hunt, J. E., and Weaver, P. P. E. 2011. Seismic Triggering of Landslides and Turbidity Currents Offshore Portugal. *Geochemistry, Geophysics, Geosystems*, 12. <https://doi.org/10.1029/2011GC003839>.
- Masson, D., Le Bas, T., Grevemeyer, I., and Weinrebe, W. 2008. Flank Collapse and Large-Scale Landsliding in the Cape Verde Islands, Off West Africa. *Geochemistry, Geophysics, Geosystems*, 9. <https://doi.org/10.1029/2008GC001983>.
- Masson, D. G., Harbitz, C. B., Wynn, R. B., Pedersen, G., and Lovholt, F. 2006. Submarine Landslides: Processes, Triggers and Hazard Prediction. *Philosophical Transactions of the Royal Society*, A364, 2009-2039. <https://doi.org/10.1098/rsta.2006.1810>.
- Masson, D. G., Watts, A. B., Gee, M. J. R., Urgeles, R., Mitchell, N. C., and Le Bas, T. P. 2002. Slope Failures on the Flanks of the Western Canary Islands. *Earth-Science Reviews*, 57, 1-35. [https://doi.org/10.1016/S0012-8252\(01\)00069-1](https://doi.org/10.1016/S0012-8252(01)00069-1).
- Mazuel, A., Sisavath, E., Babonneau, N., Jorry, S. J., Bachèlery, P., and Delacourt, C. 2016. Turbidity Current Activity Along the Flanks of a Volcanic Edifice: The Mafate Volcaniclastic Complex, La Réunion Island, Indian Ocean. *Sedimentary Geology*, 335, 34-50. <https://doi.org/10.1016/j.sedgeo.2016.01.020>.
- McAdoo, B. G., and Watts, P. 2004. Tsunami Hazard from Submarine Landslides on the Oregon Continental Slope. *Marine Geology*, 203, 235-245. [https://doi.org/10.1016/S0025-3227\(03\)00307-4](https://doi.org/10.1016/S0025-3227(03)00307-4).
- McCarron, C. J., Van Landeghem, K. J. J., Baas, J. H., Amoudry, L. O., and Malarkey, J. 2019. The Hiding-Exposure Effect Revisited: A Method to Calculate the Mobility of Bimodal Sediment Mixtures. *Marine Geology*, 410, 22-31. <https://doi.org/10.1016/j.margeo.2018.12.001>.
- McCave, I. N., Manighetti, and Robinson, S. G. 1995. Sortable Silt and Fine Sediment Size/Composition Slicing: Parameters for Palaeocurrent Speed and Paleoceanography. *Paleocean.*, 10, 593-610. <https://doi.org/10.1029/94PA03039>.

- McMurtry, G., Watts, P., Fryer, G., Smith, J., and Imamura, F. 2004. Giant Landslides, Mega-Tsunamis, and Paleo-Sea Level in the Hawaiian Islands. *Marine Geology*, 203, 219-233. [https://doi.org/10.1016/S0025-3227\(03\)00306-2](https://doi.org/10.1016/S0025-3227(03)00306-2).
- Meireles, R. P., Quartau, R., Ramalho, R. S., Rebelo, A. C., Madeira, J., Zanon, V., and Ávila, S. P. 2013. Depositional Processes on Oceanic Island Shelves – Evidence from Storm-Generated Neogene Deposits from the Mid-North Atlantic. *Sedimentology*, 60, 1769-1785. <https://doi.org/10.1111/sed.12055>.
- Menard, H. W. 1986. *Islands*, New York, Scientific American Books.
- Menard, H. W. 1983. Insular Erosion, Isostasy, and Subsidence. *Science*, 220, 913-918. <https://doi.org/10.1126/science.220.4600.913>.
- Mertens, C., Köhler, J., Walter, M., von Storch, J.-S., and Rhein, M. 2019. Observations and Models of Low-Mode Internal Waves in the Ocean. In: Eden, C., and Iske, A. (eds.) *Energy Transfers in Atmosphere and Ocean*. Cham: Springer International Publishing, 127-143. https://doi.org/10.1007/978-3-030-05704-6_4.
- Meyers, P. A. 1994. Preservation of Elemental and Isotopic Source Identification of Sedimentary Organic Matter. *Chemical geology*, 114, 289-302. [https://doi.org/10.1016/0009-2541\(94\)90059-0](https://doi.org/10.1016/0009-2541(94)90059-0).
- Miramontes, E., Penven, P., Fierens, R., Droz, L., Toucanne, S., Jorry, S. J., Jouet, G., Pastor, L., Silva Jacinto, R., Gaillot, A., Giraudeau, J., and Raison, F. 2019. The Influence of Bottom Currents on the Zambezi Valley Morphology (Mozambique Channel, Sw Indian Ocean): In Situ Current Observations and Hydrodynamic Modelling. *Marine Geology*, 410, 42-55. <https://doi.org/10.1016/j.margeo.2019.01.002>.
- Miranda, J. M., Luis, J. F., Lourenço, N., and Fernandes, R. M. S. 2015. The Structure and Evolution of the Azores Triple Junction: Implications for S. Miguel Island. In: Gaspar, J. L., Guest, J. E., Duncan, A. M., et al. (eds.) *Volcanic Geology of São Miguel Island (Azores Archipelago)*. London: Geol. Soc., Lond., 5-13. <https://doi.org/10.1144/M44.2>.
- Milkert, D., Alonso, B., Liu, L., Zhao, X., Comas, M., and De Kaenel, E. 1996. 45. Sedimentary Facies and Depositional History of the Iberia Abyssal Plain1. <https://doi.org/10.2973/odp.proc.sr.149.202.1996>.
- Mitchell, N. C., Stretch, R., Tempera, F., and M., L. 2018. Volcanism in the Azores: A Marine Geophysical Perspective. In: Beier, C., and Küppers, U. (eds.) *Volcanoes of the Azores*. Springer, Berlin, Heidelberg. https://doi.org/10.1007/978-3-642-32226-6_7.
- Mitchell, N. C., Simmons, H. L., and Lear, C. H. 2015. Modern and Ancient Hiatuses in the Pelagic Caps of Pacific Guyots and Seamounts and Internal Tides. *Geosphere*, 11. <https://doi.org/10.1130/GES00999.1>.

- Mitchell, N. C., Quartau, R., and Madeira, J. 2012. Assessing Landslide Movements in Volcanic Islands Using near-Shore Marine Geophysical Data: South Pico Island, Azores. *Bulletin of Volcanology*, 74, 483-496. <https://doi.org/10.1007/s00445-011-0541-5>.
- Mitchell, N. C., Beier, C., Rosin, P., Quartau, R., and Tempera, F. 2008. Lava Penetrating Water: Submarine Lava Flows around the Coasts of Pico Island, Azores. *Geochemistry, Geophysics, Geosystems*, 9, Paper Q03024. <https://doi.org/10.1029/2007GC001725>.
- Mitchell, N. C. 2003. Susceptibility of Mid-Ocean Ridge Volcanic Islands and Seamounts to Large-Scale Landsliding. *Journal of Geophysical Research*, 108. <https://doi.org/10.1029/2002JB001997>.
- Mitchell, N. C., Dade, W. B., and Masson, D. G. 2003. Erosion of the Submarine Flanks of the Canary Islands. *J. Geophys. Res.*, 108. <https://doi.org/10.1029/2002JF000003>.
- Mitchell, N. C., Masson, D. G., Watts, A. B., Gee, M. J. R., and Urgeles, R. 2002. The Morphology of the Flanks of Volcanic Ocean Islands: A Comparative Study of the Canary and Hawaiian Hotspot Islands. *Journal of Volcanology and Geothermal Research*, 115, 83-107. [https://doi.org/10.1016/S0377-0273\(01\)00310-9](https://doi.org/10.1016/S0377-0273(01)00310-9).
- Moore, J. G., Ingram, B. L., Ludwig, K. R., and Clague, D. A. 1996. Coral Ages and Island Subsidence, Hilo Drill Hole. *J. Geophys. Res.*, 101, 11599-11605. <https://doi.org/10.1029/95JB03215>.
- Moore, J. G., and Chadwick, W. W. 1995. Offshore Geology of Mauna Loa and Adjacent Areas, Hawaii. In: Rhodes, J. M., and Lockwood, J. P. (eds.) *Mauna Loa Revealed: Structure, Composition, History and Hazards*. American Geophysical Union, 21-44. <https://doi.org/10.1029/GM092p0021>.
- Moore, J. G., Bryan, W. B., Beeson, M. H., and Normark, W. R. 1995. Giant Blocks in the South Kona Landslide, Hawaii. *Geology*, 23, 125-128. [https://doi.org/10.1130/0091-7613\(1995\)023<0125:GBITSK>2.3.CO;2](https://doi.org/10.1130/0091-7613(1995)023<0125:GBITSK>2.3.CO;2).
- Moore, J. G., Normark, W. R., and Holcomb, R. T. 1994. Giant Hawaiian Landslides. *Annual Review of Earth and Planetary Sciences*, 22, 119-144. <https://doi.org/10.1146/annurev.ea.22.050194.001003>.
- Moore, J. G., Clague, D. A., Holcomb, R. T., Lipman, P. W., Normark, W. R., and Torresan, M. E. 1989. Prodigious Submarine Landslides on the Hawaiian Ridge. *Journal of Geophysical Research*, 94, 17465-17484. <https://doi.org/10.1038/s41467-017-02100-3>.
- Moore, J. G., and Fiske, R. S. 1969. Volcanic Substructure Inferred from Dredge Samples and Ocean-Bottom Photographs, Hawaii. *Geol. Soc. Am. Bull.*, 80, 1191-1202. [https://doi.org/10.1130/0016-7606\(1969\)80\[1191:VSIFDS\]2.0.CO;2](https://doi.org/10.1130/0016-7606(1969)80[1191:VSIFDS]2.0.CO;2).

- Moore, R. B. 1990. Volcanic Geology and Eruption Frequency, São Miguel, Azores. *Bull. Volcanol.*, 52, 602-614. <https://doi.org/10.1007/BF00301211>.
- Mosher, D. C., Piper, D. J. W., Calvin Campbell, D., and Jenner, K. A. 2004. Near-Surface Geology and Sediment-Failure Geohazards of the Central Scotian Slope. *AAPG Bulletin*, 88, 703-723. <https://doi.org/10.1306/01260403084>.
- Muecke, G. K., Ade-Hall, J. M., Aumento, F., MacDonald, A., Reynolds, P. H., Hyndman, R. D., Quintino, J., Opdyke, N., and Lowrie, W. 1974. Deep Drilling in an Active Geothermal Area in the Azores. *Nature*, 252, 281-285. <https://doi.org/10.1038/252281a0>.
- Mulder, T., Syvitski, J. P. M., Migeon, S., Faugères, J.-C., and Savoye, B. 2003. Marine Hyperpycnal Flows: Initiation, Behavior and Related Deposits. A Review. *Marine and Petroleum Geology*, 20, 861-882. <https://doi.org/10.1016/j.marpetgeo.2003.01.003>.
- Murty, T. S. 2003. Tsunami Wave Height Dependence on Landslide Volume. In: Bardet, J.-P., Imamura, F., Synolakis, C. E., et al. (eds.) *Landslide Tsunamis: Recent Findings and Research Directions*. Basel: Birkhäuser Basel, 2147-2153. https://doi.org/10.1007/978-3-0348-7995-8_17.
- Mutti, M., and Hallock, P. 2003. Carbonate Systems Along Nutrient and Temperature Gradients: Some Sedimentological and Geochemical Constraints. *International Journal of Earth Sciences*, 92, 465-475. <https://doi.org/10.1007/s00531-003-0350-y>.
- Myrow, P. M., and Southard, J. B. 1996. Tempestite Deposition. *Journal of Sedimentary Research*, 66, 875-887. <https://doi.org/10.1306/D426842D-2B26-11D7-8648000102C1865D>.
- Nafisi, A., Montoya, B. M., and Evans, T. M. 2020. Shear Strength Envelopes of Biocemented Sands with Varying Particle Size and Cementation Level. *Journal of Geotechnical and Geoenvironmental Engineering*, 146, 04020002. [https://doi.org/10.1061/\(ASCE\)GT.1943-5606.0002201](https://doi.org/10.1061/(ASCE)GT.1943-5606.0002201).
- Nakada, M., and Yokose, H. 1992. Ice Age as a Trigger of Active Quaternary Volcanism and Tectonism. *Tectonophysics*, 212, 321-329. [https://doi.org/10.1016/0040-1951\(92\)90298-K](https://doi.org/10.1016/0040-1951(92)90298-K).
- Neuberg, J. 2000. External Modulation of Volcanic Activity. *Geophysical Journal International*, 142, 232-240. <https://doi.org/10.1046/j.1365-246x.2000.00161.x>.
- Nisbet, E. G., and Piper, D. J. W. 1998. Giant Submarine Landslides. *Nature*, 392, 329-330. <https://doi.org/10.1038/32765>.
- Noormets, R., Felton, E. A., and Crook, K. A. W. 2002. Sedimentology of Rocky Shorelines: 2: Shoreline Megaclasts on the North Shore of Oahu, Hawaii—Origins and History. *Sedimentary Geology*, 150, 31-45. [https://doi.org/10.1016/S0037-0738\(01\)00266-4](https://doi.org/10.1016/S0037-0738(01)00266-4).

- Normandeau, A., Bourgault, D., Neumeier, U., Lajeunesse, P., St-Onge, G., Gostiaux, L., and Chavanne, C. 2020. Storm-Induced Turbidity Currents on a Sediment-Starved Shelf: Insight from Direct Monitoring and Repeat Seabed Mapping of Upslope Migrating Bedforms. *Sedimentology*, 67, 1045-1068. <https://doi.org/10.1111/sed.12673>.
- Normandeau, A., Lamoureux, S. F., Lajeunesse, P., and Francus, P. 2016. Sediment Dynamics in Paired High Arctic Lakes Revealed from High-Resolution Swath Bathymetry and Acoustic Stratigraphy Surveys. *Journal of Geophysical Research: Earth Surface*, 121, 1676-1696. <https://doi.org/10.1002/2016JF003873>.
- Nunes, J. C., Camacho, A., França, Z., Montesinos, F. G., Alves, M., Vieira, R., Velez, E., and Ortiz, E. 2006. Gravity Anomalies and Crustal Signature of Volcano-Tectonic Structures of Pico Island (Azores). *J. Volc. Geothermal Res.*, 156, 55-70. <https://doi.org/10.1016/j.jvolgeores.2006.03.023>.
- Nunes, J., and Ribeiro, E. 2001. Caracterização Da Sismicidade Instrumental Dos Açores No Período 1950–1980. *SISMICA, Encontro Nacional de Sismologia e Engenharia Sísmica, Açores*, http://www.hms.civil.uminho.pt/events/sismica2004/349-358%20c56%20Jo%C3%A3o%20Carlos%20Nunes%20_10p_.pdf.
- Nunes, J. C., Forjaz, V. H., França, Z., and Fragoso, M. 2001. Principais Sismos Destrutivos No Arquipélago Dos Açores—Uma Revisão. *5º Encontro Nacional de Sismologia e Engenharia Sísmica—SÍSMICA*, 119-131.
- Nunes, J. C. 1999. A Actividade Vulcânica Na Ilha Do Pico Do Plistocénico Superior Ao Holocénico: Mecanismo Eruptivo E Hazard Vulcânico. PhD, Universidade dos Açores, <http://dited.bn.pt:80/30404>.
- Ollier, Cochonat, Lénat, and Labazuy 1998. Deep-Sea Volcaniclastic Sedimentary Systems: An Example from La Fournaise Volcano, Réunion Island, Indian Ocean. *Sedimentology*, 45, 293-330. <https://doi.org/10.1046/j.1365-3091.1998.0152e.x>.
- Pacheco, J. 2001. Processos Associados Ao Desenvolvimento De Erupções Vulcânicas Hidromagmáticas Explosivas Na Ilha Do Faial E Sua Interpretação Numa Perspectiva De Avaliação Do Hazard E Minimização Do Risco. PhD thesis, Universidade dos Açores, <http://hdl.handle.net/10400.3/117>.
- Palacios, D., de Andrés, N., Gómez-Ortiz, A., and García-Ruiz, J. M. 2017. Evidence of Glacial Activity During the Oldest Dryas in the Mountains of Spain. *Geological Society, London, Special Publications*, 433, 87-110. <https://doi.org/10.1144/SP433.10>.
- Palomino, D., Vázquez, J.-T., Somoza, L., León, R., López-González, N., Medialdea, T., Fernández-Salas, L.-M., González, F.-J., and Rengel, J. A. 2016. Geomorphological Features in the Southern Canary Island Volcanic Province: The Importance of Volcanic Processes and Massive Slope Instabilities Associated with Seamounts. *Geomorphology*, 255, 125-139. <https://doi.org/10.1016/j.geomorph.2015.12.016>.

- Paris, R., Bravo, J. J. C., González, M. E. M., Kelfoun, K., and Nauret, F. 2017. Explosive Eruption, Flank Collapse and Megatsunami at Tenerife Ca. 170 Ka. *Nature Communications*, 8, 15246. <https://doi.org/10.1038/ncomms15246>.
- Paris, R., Wassmer, P., Sartohadi, J., Lavigne, F., Barthomeuf, B., Desgages, E., Grancher, D., Baumert, P., Vautier, F., Brunstein, D., and Gomez, C. 2009. Tsunamis as Geomorphic Crises: Lessons from the December 26, 2004 Tsunami in Lhok Nga, West Banda Aceh (Sumatra, Indonesia). *Geomorphology*, 104, 59-72. <https://doi.org/10.1016/j.geomorph.2008.05.040>.
- Paull, C. K., Talling, P. J., Maier, K. L., Parsons, D., Xu, J., Caress, D. W., Gwiazda, R., Lundsten, E. M., Anderson, K., and Barry, J. P. 2018. Powerful Turbidity Currents Driven by Dense Basal Layers. *Nature communications*, 9, 1-9. <https://doi.org/10.1038/s41467-018-06254-6>.
- Pawka, S., Inman, D., and Guza, R. 1984. Island Sheltering of Surface Gravity Waves: Model and Experiment. *Continental Shelf Research*, 3, 35-53. [https://doi.org/10.1016/0278-4343\(84\)90042-6](https://doi.org/10.1016/0278-4343(84)90042-6).
- Peakall, J., McCaffrey, B., and Kneller, B. 2000. A Process Model for the Evolution, Morphology, and Architecture of Sinuous Submarine Channels. *Journal of Sedimentary Research*, 70, 434-448. <https://doi.org/10.1306/2DC4091C-0E47-11D7-8643000102C1865D>.
- Pearce, T. J., and Jarvis, I. 1995. High-Resolution Chemostratigraphy of Quaternary Distal Turbidites: A Case Study of New Methods for the Analysis and Correlation of Barren Sequences. *Geological Society, London, Special Publications*, 89, 107-143. <https://doi.org/10.1144/GSL.SP.1995.089.01.07>.
- Pearce, T. J., and Jarvis, I. 1992. Composition and Provenance of Turbidite Sands: Late Quaternary, Madeira Abyssal Plain. *Marine Geology*, 109, 21-51. [https://doi.org/10.1016/0025-3227\(92\)90219-8](https://doi.org/10.1016/0025-3227(92)90219-8).
- Pedrazzi, D., Cappello, A., Zanon, V., and Del Negro, C. 2015. Impact of Effusive Eruptions from the Eguas–Carvão Fissure System, São Miguel Island, Azores Archipelago (Portugal). *Journal of Volcanology and Geothermal Research*, 291, 1-13. <https://doi.org/10.1016/j.jvolgeores.2014.12.012>.
- Pensa, A., Cas, R., Giordano, G., Porreca, M., and Wallenstein, N. 2015. Transition from Steady to Unsteady Plinian Eruption Column: The Vei 5, 4.6 Ka Fogo a Plinian Eruption, São Miguel, Azores. *Journal of Volcanology and Geothermal Research*, 305, 1-18. <https://doi.org/10.1016/j.jvolgeores.2015.09.012>.
- Peterson, D. W. Process of Volcanic Island Growth, Kilauea Volcano, Hawaii, 1969-1973. *International Association of Volcanology and Chemistry of the Earth's Interior*,

- Symposium on Andes and Antarctic volcanology problems (proceedings), 1976 1976. 172-189.
- Pimentel, A., Self, S., Pacheco, J. M., Jeffery, A. J., and Gertisser, R. 2021. Eruption Style, Emplacement Dynamics and Geometry of Peralkaline Ignimbrites: Insights from the Lajes-Angra Ignimbrite Formation, Terceira Island, Azores. *Frontiers in Earth Science*, 9. <https://doi.org/10.3389/feart.2021.673686>.
- Pimentel, A., Pacheco, J., and Self, S. 2015. The ~1000-Years Bp Explosive Eruption of Caldeira Volcano (Faial, Azores): The First Stage of Incremental Caldera Formation. *Bulletin of Volcanology*, 77, 1-26. <https://doi.org/10.1007/s00445-015-0930-2>.
- Pimentel, A. H. G. 2007. Domos E Coulées Da Ilha Terceira (Açores): Contribuição Para O Estudo Dos Mecanismos De Instalação. MSc dissertation, Universidade dos Açores, https://www.proquest.com/openview/129f0b4a4e73d45fadd1fada0a34e910/1?pq-origsite=gscholar&cbl=2026366&diss=y&casa_token=Y0Iye5cVhq0AAAAA:PpUdU0eeSOOrPHzHDUwPAZRiwF6BiB7dWZKS_Z9fFmHibN8GJysl3mzQLiybfXLhao7LFa1O8Gg.
- Pinto Ribeiro, L., Calvert, A., França, Z., Rodrigues, B., and Pinto de Abreu, M. 2010. New $^{40}\text{Ar}/^{39}\text{Ar}$ and Geochemical Constraints on São Jorge Island, Azores. *1st International Workshop on Volcano Geology, at Madeira*. Portugal.
- Piper, D. J. W., Shaw, J., and Skene, K. I. 2007. Stratigraphic and Sedimentological Evidence for Late Wisconsinan Sub-Glacial Outburst Floods to Laurentian Fan. *Palaeogeography, Palaeoclimatology, Palaeoecology*, 246, 101-119. <https://doi.org/10.1016/j.palaeo.2006.10.029>.
- Ponce de León, S., and Guedes Soares, C. 2005. On the Sheltering Effect of Islands in Ocean Wave Models. *Journal of Geophysical Research: Oceans*, 110. <https://doi.org/10.1029/2004JC002682>.
- Pope, E. L., Jutzeler, M., Cartigny, M. J., Shreeve, J., Talling, P. J., Wright, I. C., and Wysoczanski, R. J. 2018. Origin of Spectacular Fields of Submarine Sediment Waves around Volcanic Islands. *Earth and Planetary Science Letters*, 493, 12-24. <https://doi.org/10.1016/j.epsl.2018.04.020>.
- Poppe, L. J., Eliason, A. H., and Hastings, M. E. 2004. A Visual Basic Program to Generate Sediment Grain-Size Statistics and to Extrapolate Particle Distributions. *Computers & Geosciences*, 30, 791-795. <https://doi.org/10.1016/j.cageo.2004.05.005>.
- Porcile, G., Bolla Pittaluga, M., Frascati, A., and Sequeiros, O. E. 2020. Typhoon-Induced Megarips as Triggers of Turbidity Currents Offshore Tropical River Deltas. *Communications Earth & Environment*, 1, 2. <https://doi.org/10.1038/s43247-020-0002-1>.

- Pratson, L. F., and Coakley, B. J. 1996. A Model for the Headward Erosion of Submarine Canyons Induced by Downslope-Eroding Sediment Flows. *Geol. Soc. Am. Bull.*, 108, 225-234. [https://doi.org/10.1130/0016-7606\(1996\)108<0225:AMFTHE>2.3.CO;2](https://doi.org/10.1130/0016-7606(1996)108<0225:AMFTHE>2.3.CO;2).
- Povinec, P. P., Litherland, A. E., and von Reden, K. F. 2009. Developments in Radiocarbon Technologies: From the Libby Counter to Compound-Specific Ams Analyses. *Radiocarbon*, 51, 45-78. <https://doi.org/10.1017/S0033822200033701>.
- Puig, P., Ogston, A. S., Guillén, J., Fain, A. M. V., and Palanques, A. 2007. Sediment Transport Processes from the Topset to the Foreset of a Crenulated Clinof orm (Adriatic Sea). *Continental Shelf Research*, 27, 452-474. <https://doi.org/10.1016/j.csr.2006.11.005>.
- QGIS Development Team 2009. *QGIS Geographic Information System. Open Source Geospatial Foundation Project*, <http://qgis.org>.
- Quaresma, L. S., Vitorino, J., Oliveira, A., and da Silva, J. 2007. Evidence of Sediment Resuspension by Nonlinear Internal Waves on the Western Portuguese Mid-Shelf. *Marine Geology*, 246, 123-143. <https://doi.org/10.1016/j.margeo.2007.04.019>.
- Quartau, R., Ramalho, R. S., Madeira, J., Santos, R., Rodrigues, A., Roque, C., Carrara, G., and da Silveira, A. B. 2018. Gravitational, Erosional and Depositional Processes on Volcanic Ocean Islands: Insights from the Submarine Morphology of Madeira Archipelago. *Earth and Planetary Science Letters*, 482, 288-299. <https://doi.org/10.1016/j.epsl.2017.11.003>.
- Quartau, R., Madeira, J., Mitchell, N. C., Tempera, F., Silva, P. F., and Brandão, F. 2015. The Insular Shelves of the Faial-Pico Ridge (Azores Archipelago): A Morphological Record of Its Evolution. *Geochemistry, Geophysics, Geosystems*, 16, 1401-1420. <https://doi.org/10.1002/2015GC005733>
- Quartau, R., Hipólito, A., Romagnolii, C., Casalbore, D., Madeira, J., Tempera, F., Roque, C., and Chiocci, F. L. 2014. The Morphology of Insular Shelves as a Key for Understanding the Geological Evolution of Volcanic Islands: Insights from Terceira Island (Azores). *Geochemistry, Geophysics, Geosystems*, 15. <https://doi.org/10.1002/2014GC005248>.
- Quartau, R., Tempera, F., Mitchell, N. C., Pinheiro, L. M., Duarte, H., Brito, P. O., Bates, C. R., and Monteiro, J. H. 2012. Morphology of Faial Island's Shelf: The Results of Volcanic, Erosional, Depositional and Mass-Wasting Processes. *Geochemistry, Geophysics, Geosystems*, 13. <https://doi.org/10.1029/2011GC003987>.
- Quartau, R., Trenhaile, A. S., Mitchell, N. C., and Tempera, F. 2010. Development of Volcanic Insular Shelves: Insights from Observations and Modelling of Faial Island in the Azores Archipelago. *Marine Geology*, 275, 66-83. <https://doi.org/10.1016/j.margeo.2010.04.008>.

- Quartau, R., Duarte, H., and Brito, P. 2005. *Projecto Gemas – Relatório Da Campanha De Amostragem De Sedimentos (Fapi-3) Realizada Na Plataforma E Na Orla Costeira Das Ilhas Do Faial E Do Pico. Relatório Técnico Ingmardep 2/2005*, Lisbon, Portugal.
- Rahiman, T. I. H., and Pettinga, J. R. 2006. The Offshore Morpho-Structure and Tsunami Sources of the Viti Levu Seismic Zone, Southeast Viti Levu, Fiji. *Marine Geology*, 232, 203-225. <https://doi.org/10.1016/j.margeo.2006.07.007>.
- Ramalho, R. S., Winckler, G., Madeira, J., Helffrich, G. R., Hipólito, A., Quartau, R., Adena, K., and Schaefer, J. M. 2015. Hazard Potential of Volcanic Flank Collapses Raised by New Megatsunami Evidence. *Science Advances*, 1, e1500456. <https://doi.org/10.1126/sciadv.1500456>.
- Ramalho, R. S., Quartau, R., Trenhaile, A. S., Mitchell, N. C., Woodroffe, C. D., and Ávila, S. P. 2013. Coastal Evolution on Volcanic Oceanic Islands: A Complex Interplay between Volcanism, Erosion, Sedimentation, Sea-Level Change and Biogenic Production. *Earth-Science Reviews*, 127, 140-170. <https://doi.org/10.1016/j.earscirev.2013.10.007>.
- Rampino, M. R., and Self, S. 1982. Historic Eruptions of Tambora (1815), Krakatau (1883), and Agung (1963), Their Stratospheric Aerosols, and Climatic Impact. *Quaternary Research*, 18, 127-143. [https://doi.org/10.1016/0033-5894\(82\)90065-5](https://doi.org/10.1016/0033-5894(82)90065-5).
- Rayson, M. D., Ivey, G. N., Jones, N. L., Meuleners, M. J., and Wake, G. W. 2011. Internal Tide Dynamics in a Topographically Complex Region: Browse Basin, Australian North West Shelf. *Journal of Geophysical Research: Oceans*, 116. <https://doi.org/10.1029/2009JC005881>.
- Reiche, S., Hübscher, C., Brenner, S., Betzler, C., and Hall, J. K. 2018. The Role of Internal Waves in the Late Quaternary Evolution of the Israeli Continental Slope. *Marine Geology*, 406, 177-192. <https://doi.org/10.1016/j.margeo.2018.09.013>.
- Reid, J. A., and Mooney, W. D. 2022. Tsunami Occurrence 1900–2020: A Global Review, with Examples from Indonesia. *Pure and Applied Geophysics*. <https://doi.org/10.1007/s00024-022-03057-1>.
- Reid, M. E. 2004. Massive Collapse of Volcano Edifices Triggered by Hydrothermal Pressurization. *Geology*, 32, 373-376. <https://doi.org/10.1130/G20300.1>.
- Reid, R. P., Carey, S. N., and Ross, D. R. 1996. Late Quaternary Sedimentation in the Lesser Antilles Island Arc. *Geological Society of America Bulletin*, 108, 78-100. [https://doi.org/10.1130/0016-7606\(1996\)108<0078:LQSITL>2.3.CO;2](https://doi.org/10.1130/0016-7606(1996)108<0078:LQSITL>2.3.CO;2).
- Reimer, P. J., Austin, W. E. N., Bard, E., Bayliss, A., Blackwell, P. G., Bronk Ramsey, C., Butzin, M., Cheng, H., Edwards, R. L., Friedrich, M., Grootes, P. M., Guilderson, T. P., Hajdas, I., Heaton, T. J., Hogg, A. G., Hughen, K. A., Kromer, B., Manning, S. W., Muscheler, R., Palmer, J. G., Pearson, C., van der Plicht, J., Reimer, R. W., Richards, D. A., Scott, E. M., Southon, J. R., Turney, C. S. M., Wacker, L., Adolphi, F., Büntgen,

- U., Capano, M., Fahrni, S. M., Fogtmann-Schulz, A., Friedrich, R., Köhler, P., Kudsk, S., Miyake, F., Olsen, J., Reinig, F., Sakamoto, M., Sookdeo, A., and Talamo, S. 2020. The Intcal20 Northern Hemisphere Radiocarbon Age Calibration Curve (0–55 Cal Kbp). *Radiocarbon*, 62, 725-757. <https://doi.org/10.1017/RDC.2020.41>.
- Reimer, P. J., and Reimer, R. W. 2001. A Marine Reservoir Correction Database and on-Line Interface. *Radiocarbon*, 43, 461-463. <https://doi.org/10.1017/S0033822200038339>.
- Ribó, M., Puig, P., Muñoz, A., Lo Iacono, C., Masqué, P., Palanques, A., Acosta, J., Guillén, J., and Gómez Ballesteros, M. 2016. Morphobathymetric Analysis of the Large Fine-Grained Sediment Waves over the Gulf of Valencia Continental Slope (Nw Mediterranean). *Geomorphology*, 253, 22-37. <https://doi.org/10.1016/j.geomorph.2015.09.027>.
- Ricchi, A., Quartau, R., Ramalho, R. S., Romagnoli, C., Casalbore, D., and Zhao, Z. 2020. Imprints of Volcanic, Erosional, Depositional, Tectonic and Mass-Wasting Processes in the Morphology of Santa Maria Insular Shelf. *Marine Geology*, 106163. <https://doi.org/10.1016/j.margeo.2020.106163>.
- Robinson, C. J., Bickle, M. J., Minshall, T. A., White, R. S., and Nichols, A. R. L. 2001. Low Degree Melting under the Southwest Indian Ridge: The Roles of Mantle Temperature, Conductive Cooling and Wet Melting. *Earth Planet. Sci. Lett.*, 188, 383-398. [https://doi.org/10.1016/S0012-821X\(01\)00329-6](https://doi.org/10.1016/S0012-821X(01)00329-6).
- Romagnoli, C., Casalbore, D., Bosman, A., Braga, R., and Chiocci, F. L. 2013. Submarine Structure of Vulcano Volcano (Aeolian Islands) Revealed by High-Resolution Bathymetry and Seismo-Acoustic Data. *Marine Geology*, 338, 30-45. <https://doi.org/10.1016/j.margeo.2012.12.002>.
- Rusu, E., and Onea, F. 2016. Estimation of the Wave Energy Conversion Efficiency in the Atlantic Ocean Close to the European Islands. *Renewable Energy*, 85, 687-703. <https://doi.org/10.1016/j.renene.2015.07.042>.
- Rusu, L., and Guedes Soares, C. 2012. Wave Energy Assessments in the Azores Islands. *Renewable Energy*, 45, 183-196. <https://doi.org/10.1016/j.renene.2012.02.027>.
- Ryan, W. B. F., Carbotte, S. M., Coplan, J. O., O'Hara, S., Melkonian, A., Arko, R., Wiessel, R. A., Ferrini, V., Goodwillie, A., Nitsche, F., Bonczkowski, J., and Zemsky, R. 2009. Global Multi-Resolution Topography Synthesis. *Geochemistry, Geophysics, Geosystems*, 10, Q03014. <https://doi.org/10.1029/2008GC002332>.
- Sager, W., Hoernle, K., Höfig, T., and Scientists, E. 2022. Expedition 391 Preliminary Report: Walvis Ridge Hotspot: Drilling Walvis Ridge, Southeast Atlantic Ocean, to Test Models of Ridge-Hotspot Interaction, Isotopic Zonation, and the Hotspot Reference Frame, 6 December 2021–5 February 2022. <https://doi.org/10.14379/iodp.pr.391.2022>.

- Saint-Ange, F., Bachèlery, P., Babonneau, N., Michon, L., and Jorry, S. J. 2013. Volcaniclastic Sedimentation on the Submarine Slopes of a Basaltic Hotspot Volcano: Piton De La Fournaise Volcano (La Réunion Island, Indian Ocean). *Marine Geology*, 337, 35-52. <https://doi.org/10.1016/j.margeo.2013.01.004>.
- Sansone, F. J., and Smith, J. R. 2006. Rapid Mass Wasting Following Nearshore Submarine Volcanism on Kilauea Volcano, Hawaii. *J. Volcanol. Geotherm. Res.*, 151, 133-139. <https://doi.org/10.1016/j.jvolgeores.2005.07.026>.
- Santos, R., Quartau, R., da Silveira, A. B., Ramalho, R., and Rodrigues, A. 2019. Gravitational, Erosional, Sedimentary and Volcanic Processes on the Submarine Environment of Selvagens Islands (Madeira Archipelago, Portugal). *Marine Geology*, 415, 105945. <https://doi.org/10.1016/j.margeo.2019.05.004>.
- Satow, C., Gudmundsson, A., Gertisser, R., Ramsey, C. B., Bazargan, M., Pyle, D. M., Wulf, S., Miles, A. J., and Hardiman, M. 2021. Eruptive Activity of the Santorini Volcano Controlled by Sea-Level Rise and Fall. *Nature Geoscience*, 14, 586-592. <https://doi.org/10.1038/s41561-021-00783-4>.
- Savoie, B., Cochonat, P., and Piper, D. J. W. 1990. Seismic Evidence for a Complex Slide near the Wreck of the Titanic: Model of an Instability Corridor for Non-Channeled Gravity Events. *Marine Geology*, 91, 281-298. [https://doi.org/10.1016/0025-3227\(90\)90050-T](https://doi.org/10.1016/0025-3227(90)90050-T).
- Savrda, C. E., Krawinkel, H., McCarthy, F. M. G., McHugh, C. M. G., Olson, H. C., and Mountain, G. 2001. Ichnofabrics of a Pleistocene Slope Succession, New Jersey Margin: Relations to Climate and Sea-Level Dynamics. *Palaeogeography, Palaeoclimatology, Palaeoecology*, 171, 41-61. [https://doi.org/10.1016/S0031-0182\(01\)00266-8](https://doi.org/10.1016/S0031-0182(01)00266-8).
- Sawyer, D. E., and DeVore, J. R. 2015. Elevated Shear Strength of Sediments on Active Margins: Evidence for Seismic Strengthening. *Geophysical Research Letters*, 42, 10,216-10,221. <https://doi.org/10.1002/2015GL066603>.
- Scarth, A., and Tanguy, J.-C. 2001. *Volcanoes of Europe*, Harpenden, England, Terra, ISBN 1-903544-03-3.
- Schindlbeck, J. C., Kutterolf, S., Freundt, A., Eisele, S., Wang, K.-L., and Frische, M. 2018. Miocene to Holocene Marine Tephrostratigraphy Offshore Northern Central America and Southern Mexico: Pulsed Activity of Known Volcanic Complexes. *Geochemistry, Geophysics, Geosystems*, 19, 4143-4173. <https://doi.org/10.1029/2018GC007832>.
- Schindlbeck, J. C., Kutterolf, S., Freundt, A., Straub, S. M., Vannucchi, P., and Alvarado, G. E. 2016. Late Cenozoic Tephrostratigraphy Offshore the Southern Central American Volcanic Arc: 2. Implications for Magma Production Rates and Subduction Erosion.

- Geochemistry, Geophysics, Geosystems*, 17, 4585-4604.
<https://doi.org/10.1002/2016GC006504>.
- Schindlbeck, J. C., Kutterolf, S., Freundt, A., Scudder, R. P., Pickering, K. T., and Murray, R. W. 2013. Emplacement Processes of Submarine Volcaniclastic Deposits (Iodp Site C0011, Nankai Trough). *Marine Geology*, 343, 115-124.
<https://doi.org/10.1016/j.margeo.2013.06.017>.
- Schlager, W. 2000. Sedimentation Rates and Growth Potential of Tropical, Cool-Water and Mud-Mound Carbonate Systems. *Geological Society, London, Special Publications*, 178, 217-227. <https://doi.org/10.1144/GSL.SP.2000.178.01.14>.
- Schmidt, C., Hensen, C., Hübscher, C., Wallmann, K., Liebetrau, V., Schmidt, M., Kutterolf, S., and Hansteen, T. H. 2020. Geochemical Characterization of Deep-Sea Sediments on the Azores Plateau – from Diagenesis to Hydrothermal Activity. *Marine Geology*, 429, 106291. <https://doi.org/10.1016/j.margeo.2020.106291>.
- Schmidt, C., Hensen, C., Wallmann, K., Liebetrau, V., Tatzel, M., Schurr, S. L., Kutterolf, S., Haffert, L., Geilert, S., Hübscher, C., Lebas, E., Heuser, A., Schmidt, M., Strauss, H., Vogl, J., and Hansteen, T. 2019. Origin of High Mg and So4 Fluids in Sediments of the Terceira Rift, Azores-Indications for Caminite Dissolution in a Waning Hydrothermal System. *Geochemistry, Geophysics, Geosystems*, 20, 6078-6094.
<https://doi.org/10.1029/2019GC008525>.
- Schmincke, H.-U., and Sumita, M. 1998. Tephra Event Stratigraphy and Emplacement of Volcaniclastic Sediments, Mogán and Fataga Stratigraphic Intervals, Part II: Origin and Emplacement of Volcaniclastic Layers. *Proc. ODP, Sci. Results*, 157, 267-291.
<https://doi.org/10.2973/odp.proc.sr.157.113.1998>.
- Schmincke, H.-U., Weaver, P. P. E., Firth, J. V., and al., e. 1995. Background, Objectives, and Principal Results of Drilling the Clastic Apron of Gran Canaria (Vicap). In: Schmincke, H.-U., Weaver, P. P. E., and Firth, J. V. (eds.) *Proc. ODP, Init. Repts*, 157. College Station, Texas: Ocean Drilling Program, 11-25.
<https://doi.org/10.2973/odp.proc.ir.157.102.1995>.
- Schneider, J.-L., Le Ruyet, A., Chanier, F., Buret, C., Ferrière, J., Proust, J.-N., and Rosseel, J.-B. 2001. Primary or Secondary Distal Volcaniclastic Turbidites: How to Make the Distinction? An Example from the Miocene of New Zealand (Mahia Peninsula, North Island). *Sedimentary Geology*, 145, 1-22. [https://doi.org/10.1016/S0037-0738\(01\)00108-7](https://doi.org/10.1016/S0037-0738(01)00108-7).
- Scholz, C. H. 2002. *The Mechanics of Earthquakes and Faulting*, New York, Cambridge University Press. <https://doi.org/10.1017/9781316681473>.
- Scholz, C. H. 1994. A Reappraisal of Large Earthquake Scaling. *Bull. Seis. Soc. Am.*, 84, 215-218.

- Schott, F. A., Zantopp, R., Stramma, L., Dengler, M., Fischer, J., and Wibaux, M. 2004. Circulation and Deep-Water Export at the Western Exit of the Subpolar North Atlantic. *Journal of Physical Oceanography*, 34, 817-843. [https://doi.org/10.1175/1520-0485\(2004\)034<0817:CADEAT>2.0.CO;2](https://doi.org/10.1175/1520-0485(2004)034<0817:CADEAT>2.0.CO;2).
- Schwab, W. C., Lee, H. J., Kayen, R. E., Quintero, P. J., and Tate, G. B. 1988. Erosion and Slope Instability on Horizon Guyot, Mid-Pacific Mountains. *Geo-Mar. Lett.*, 8, 1-10. <https://doi.org/10.1007/BF02238000>.
- Scudder, R. P., Murray, R. W., Schindlbeck, J. C., Kutterolf, S., Hauff, F., Underwood, M. B., Gwizd, S., Lauzon, R., and McKinley, C. C. 2016. Geochemical Approaches to the Quantification of Dispersed Volcanic Ash in Marine Sediment. *Progress in Earth and Planetary Science*, 3, 1. <https://doi.org/10.1186/s40645-015-0077-y>.
- Searle, R. C. 1980. Tectonic Pattern of the Azores Spreading Centre and Triple Junction. *Earth and Planetary Science Letters*, 51, 415-434.
- Self, S. 1976. The Recent Volcanology of Terceira, Azores. *J. Geol. Soc. Lond.*, 132, 645-666. <https://doi.org/10.1144/gsjgs.132.6.0645>.
- Selva, J., Acocella, V., Bisson, M., Caliro, S., Costa, A., Della Seta, M., De Martino, P., de Vita, S., Federico, C., Giordano, G., Martino, S., and Cardaci, C. 2019. Multiple Natural Hazards at Volcanic Islands: A Review for the Ischia Volcano (Italy). *Journal of Applied Volcanology*, 8, 5. <https://doi.org/10.1186/s13617-019-0086-4>.
- Serrano, E., González-Trueba, J. J., Pellitero, R., and Gómez-Lende, M. 2017. Quaternary Glacial History of the Cantabrian Mountains of Northern Spain: A New Synthesis. *Geological Society, London, Special Publications*, 433, 55-85. <https://doi.org/10.1144/SP433.8>.
- Sibrant, A. L. R., Hildenbrand, A., Marques, F. O., Weiss, B., Boulesteix, T., Hübscher, C., Lüdmann, T., Costa, A. C. G., and Catalão, J. C. 2015. Morpho-Structural Evolution of a Volcanic Island Developed inside an Active Oceanic Rift: S. Miguel Island (Terceira Rift, Azores). *J. Volc. Geothermal Res.*, 301, 90-106. <https://doi.org/10.1016/j.jvolgeores.2015.04.011>.
- Sibrant, A. L. R., Marques, F. O., and Hildenbrand, A. 2014. Construction and Destruction of a Volcanic Island Developed inside an Oceanic Rift: Graciosa Island, Terceira Rift, Azores. *Journal of Volcanology and Geothermal Research*, 284, 32-45. <https://doi.org/10.1016/j.jvolgeores.2014.07.014>.
- Sieh, K. E. 1981. A Review of Geological Evidence for Recurrence Times of Large Earthquakes. *Earthquake Prediction*. 181-207. <https://doi.org/10.1029/ME004p0181>.
- Sigurdsson, H., Kelley, S., Leckie, R., Carey, S., Bralower, T., and King, J. 2000. 20: History of Circum-Caribbean Explosive Volcanism: $^{40}\text{Ar}/^{39}\text{Ar}$ Dating of Tephra Layers.

- Proceedings of the Ocean Drilling Program, Scientific Results. College Station TX, Texas A&M*, 299-314. <https://doi.org/10.2973/odp.proc.sr.165.021.2000>.
- Sigurdsson, H. 1982. Volcanic Pollution and Climate: The 1783 Laki Eruption. *Eos, Transactions American Geophysical Union*, 63, 601-602. <https://doi.org/10.1029/EO063i032p00601>.
- Sigurdsson, H., and Sparks, R. 1981. Petrology of Rhyolitic and Mixed Magma Ejecta from the 1875 Eruption of Askja, Iceland. *Journal of Petrology*, 22, 41-84. <https://doi.org/10.1093/petrology/22.1.41>.
- Sigurdsson, H., Sparks, R., Carey, S. t., and Huang, T. 1980. Volcanogenic Sedimentation in the Lesser Antilles Arc. *The Journal of Geology*, 88, 523-540. <https://doi.org/10.1086/628542>.
- Simmons, H. L. 2008. Spectral Modification and Geographic Distribution of the Semi-Diurnal Internal Tide. *Ocean Modelling*, 21, 126-138. <https://doi.org/10.1016/j.ocemod.2008.01.002>.
- Sisavath, E., Mazuel, A., Jorry, S. J., Babonneau, N., Bachèlery, P., de Voogd, B., Salpin, M., Emmanuel, L., Beaufort, L., and Toucanne, S. 2012. Processes Controlling a Volcaniclastic Turbiditic System During the Last Climatic Cycle: Example of the Cilaos Deep-Sea Fan, Offshore La Réunion Island. *Sedimentary Geology*, 281, 180-193. <https://doi.org/10.1016/j.sedgeo.2012.09.010>.
- Slotman, A., Vellinga, A. J., Moscariello, A., and Cartigny, M. J. B. 2021. The Depositional Signature of High-Aggradation Chute-and-Pool Bedforms: The Build-and-Fill Structure. *Sedimentology*, 68, 1640-1673. <https://doi.org/10.1111/sed.12843>.
- Slotman, A., and Cartigny, M. J. B. 2020. Cyclic Steps: Review and Aggradation-Based Classification. *Earth-Science Reviews*, 201, 102949. <https://doi.org/10.1016/j.earscirev.2019.102949>.
- Solaro, C., Boudon, G., Le Friant, A., Balcone-Boissard, H., Emmanuel, L., and Paterne, M. 2020. New Insights into the Recent Eruptive and Collapse History of Montagne Pelée (Lesser Antilles Arc) from Offshore Marine Drilling Site U1401a (Iodp Expedition 340). *Journal of Volcanology and Geothermal Research*, 403, 107001. <https://doi.org/10.1016/j.jvolgeores.2020.107001>.
- Soule, S. A., Zoeller, M., and Parcheta, C. 2021. Submarine Lava Deltas of the 2018 Eruption of Kīlauea Volcano. *Bulletin of Volcanology*, 83, 23. <https://doi.org/10.1007/s00445-020-01424-1>.
- Soulsby, R. 1997. *Dynamics of Marine Sands*. <https://doi.org/10.1680/doms.25844>.
- Soulsby, R. L., and Whitehouse, R. J. S. W. 1997. Threshold of Sediment Motion in Coastal Environments. *Proc. Pacific Coasts and Ports '97 Conf., Christchurch, 1*. Canterbury: University of Canterbury, New Zealand, 149-154.

- Spalding, M. D., and Grenfell, A. M. 1997. New Estimates of Global and Regional Coral Reef Areas. *Coral Reefs*, 16, 225-230. <https://doi.org/10.1007/s003380050078>.
- Spratt, R. M., and Lisiecki, L. E. 2016. A Late Pleistocene Sea Level Stack. *Clim. Past*, 12, 1079-1092. <https://doi.org/10.5194/cp-12-1079-2016>.
- Staudigel, H., and Schmincke, H.-U. 1984. The Pliocene Seamount Series of La Palma/Canary Islands. *Journal of Geophysical Research: Solid Earth*, 89, 11195-11215. <https://doi.org/10.1029/JB089iB13p11195>.
- Stein, R. S. 1999. The Role of Stress Transfer in Earthquake Occurrence. *Nature*, 402, 605-609. <https://doi.org/10.1038/45144>.
- Stidd, C. K., and Leopold, L. B. 1951. The Geographic Distribution of Average Monthly Rainfall, Hawaii. On the Rainfall of Hawaii: A Group of Contributions. Boston, MA: American Meteorological Society, 24-33. https://doi.org/10.1007/978-1-940033-01-3_3.
- Stoddart, D. R., and Steers, J. A. 1977. The Nature and Origin of Coral Reef Islands. In: Jones, O. A., and Endean, R. (eds.) *Biology and Geology of Coral Reefs*. Academic Press, 59-105. <https://doi.org/10.1016/B978-0-12-395528-9.50011-7>.
- Stokes, S., Lowe, D. J., and Froggatt, P. C. 1992. Discriminant Function Analysis and Correlation of Late Quaternary Rhyolitic Tephra Deposits from Taupo and Okataina Volcanoes, New Zealand, Using Glass Shard Major Element Composition. *Quaternary International*, 13-14, 103-117. [https://doi.org/10.1016/1040-6182\(92\)90016-U](https://doi.org/10.1016/1040-6182(92)90016-U).
- Stokes, S., and Lowe, D. J. 1988. Discriminant Function Analysis of Late Quaternary Tephra from Five Volcanoes in New Zealand Using Glass Shard Major Element Chemistry. *Quaternary Research*, 30, 270-283. [https://doi.org/10.1016/0033-5894\(88\)90003-8](https://doi.org/10.1016/0033-5894(88)90003-8).
- Storey, M. 1982. Trachytic Pyroclastics from Agua De Pau Volcano, Sao Miguel, Azores: Evolution of a Magma Body over 4,000 Years. *Contributions to Mineralogy and Petrology*, 78, 423-432. <https://doi.org/10.1007/BF00375204>.
- Stow, D. A. V., and Piper, D. J. W. 1984. Deep-Water Fine-Grained Sediments: Facies Models. *Geological Society, London, Special Publications*, 15, 611-646. <https://doi.org/10.1144/gsl.Sp.1984.015.01.38>.
- Sulpizio, R. 2005. Three Empirical Methods for the Calculation of Distal Volume of Tephra-Fall Deposits. *Journal of Volcanology and Geothermal Research*, 145, 315-336. <https://doi.org/10.1016/j.jvolgeores.2005.03.001>.
- Sumita, M., and Schmincke, H.-U. 1998. Tephra Event Stratigraphy and Emplacement of Volcaniclastic Sediments, Mogán and Fataga Stratigraphic Intervals, Part I: Mineral and Chemical Stratigraphy of Volcaniclastic Units and Correlation to the Subaerial Record. *Proc. ODP, Sci. Results*, 219-266. <https://doi.org/10.2973/odp.proc.sr.157.114.1998>.

- Sun, Q., Alves, T. M., Lu, X., Chen, C., and Xie, X. 2018. True Volumes of Slope Failure Estimated from a Quaternary Mass-Transport Deposit in the Northern South China Sea. *Geophysical Research Letters*, 45, 2642-2651. <https://doi.org/10.1002/2017gl076484>.
- Sunamura, T. 1977. A Relationship between Wave-Induced Cliff Erosion and Erosive Force of Waves. *The Journal of Geology*, 85, 613-618. <https://doi.org/10.1086/628340>.
- Talling, P. J., Masson, D. G., Sumner, E. J., and Malgesini, G. 2012. Subaqueous Sediment Density Flows: Depositional Processes and Deposit Types. *Sedimentology*, 59, 1937-2003. <https://doi.org/10.1111/j.1365-3091.2012.01353.x>.
- Talling, P. J. 2001. On the Frequency Distribution of Turbidite Thickness. *Sedimentology*, 48, 1297-1329. <https://doi.org/10.1046/j.1365-3091.2001.00423.x>.
- Tappin, D. R., Watts, P., McMurtry, G. M., Lafoy, Y., and Matsumoto, T. 2001. The Sissano, Papua New Guinea Tsunami of July 1998 - Offshore Evidence of the Source Mechanism. *Marine Geology*, 175, 1-23. [https://doi.org/10.1016/S0025-3227\(01\)00131-1](https://doi.org/10.1016/S0025-3227(01)00131-1).
- Tempera, F. 2009. Benthic Habitats of the Extended Faial Island Shelf and Their Relationship to Geologic, Oceanographic and Infralittoral Biologic Features. PhD Thesis, University of St. Andrews.
- ten Brink, U. S., Andrews, B., and Miller, N. 2016. Seismicity and Sedimentation Rate Effects on Submarine Slope Stability. *Geology*, 44, 563-566. <https://doi.org/10.1130/G37866.1>.
- ten Brink, U. S., Barkan, R., Andrews, B. D., and Chaytor, J. D. 2009. Size Distribution and Failure Initiation of Submarine and Subaerial Landslides. *Earth and Planet. Sci. Letts.*, 287, 31-42. <https://doi.org/10.1016/j.epsl.2009.07.031>.
- ten Brink, U. S., Geist, E. L., and Andrews, B. D. 2006. Size Distribution of Submarine Landslides and Its Implication to Tsunami Hazard in Puerto Rico. *Geophysical Research Letters*, 33. <https://doi.org/10.1029/2006gl026125>.
- Thomson, J., and Weaver, P. P. E. 1994. An Ams Radiocarbon Method to Determine the Emplacement Time of Recent Deep-Sea Turbidites. *Sedimentary Geology*, 89, 1-7. [https://doi.org/10.1016/0037-0738\(94\)90079-5](https://doi.org/10.1016/0037-0738(94)90079-5).
- Thorarinsson, S. 1979. 5 - on the Damage Caused by Volcanic Eruptions with Special Reference to Tephra and Gases. In: Sheets, P. D., and Grayson, D. K. (eds.) *Volcanic Activity and Human Ecology*. Academic Press, 125-159. <https://doi.org/10.1016/B978-0-12-639120-6.50010-8>.
- Thran, A. C., Dutkiewicz, A., Spence, P., and Müller, R. D. 2018. Controls on the Global Distribution of Contourite Drifts: Insights from an Eddy-Resolving Ocean Model. *Earth and Planetary Science Letters*, 489, 228-240. <https://doi.org/10.1016/j.epsl.2018.02.044>.

- Tinti, S., Manucci, A., Pagnoni, G., Armigliato, A., and Zaniboni, F. 2005. The 30 December 2002 Landslide-Induced Tsunamis in Stromboli: Sequence of Events Reconstructed from the Eyewitness Accounts. *Natural Hazards and Earth System Science*, 5, 763-775. <https://doi.org/10.5194/nhess-5-763-2005>.
- Tommasi, P., Baldi, P., Chiocci, F. L., Coltelli, M., Marsella, M., and Romagnoli, C. 2008. Slope Failures Induced by the December 2002 Eruption at Stromboli Volcano. *Washington DC American Geophysical Union Geophysical Monograph Series*, 182, 129-145. <https://doi.org/10.1029/182GM12>.
- Trenhaile, A. S. 2001. Modeling the Quaternary Evolution of Shore Platforms and Erosional Continental Shelves. *Earth Surf. Processes Landforms*, 26, 1103-1128. <https://doi.org/10.1002/esp.255>.
- Trenhaile, A. S. 2000. Modeling the Development of Wave-Cut Shore Platforms. *Mar. Geol.*, 166, 163-178. [https://doi.org/10.1016/S0025-3227\(00\)00013-X](https://doi.org/10.1016/S0025-3227(00)00013-X).
- Trofimovs, J., Talling, P. J., Fisher, J. K., Sparks, R. S. J., Watt, S. F. L., Hart, M. B., Smart, C. W., Le Friant, A., Cassidy, M., Moreton, S. G., and Leng, M. J. 2013. Timing, Origin and Emplacement Dynamics of Mass Flows Offshore of Se Montserrat in the Last 110 Ka: Implications for Landslide and Tsunami Hazards, Eruption History, and Volcanic Island Evolution. *Geochemistry, Geophysics, Geosystems*, 14, 385-406. <https://doi.org/10.1002/ggge.20052>.
- Trofimovs, J., Sparks, R. S. J., and Talling, P. J. 2008. Anatomy of a Submarine Pyroclastic Flow and Associated Turbidity Current: July 2003 Dome Collapse, Soufrière Hills Volcano, Montserrat, West Indies. *Sedimentology*, 55, 617-634. <https://doi.org/10.1111/j.1365-3091.2007.00914.x>.
- Trofimovs, J., Amy, L., Boudon, G., Deplus, C., Doyle, E., Fournier, N., Hart, M. B., Komorowski, J. C., and Le, A. 2006. Submarine Pyroclastic Deposits Formed at the Soufrière Hills Volcano, Montserrat (1995 -2003): What Happens When Pyroclastic Flows Enter the Ocean? *Geology*, 34, 549-552. <https://doi.org/10.1130/G22424.1>.
- Tubau, X., Paull, C. K., Lastras, G., Caress, D. W., Canals, M., Lundsten, E., Anderson, K., Gwiazda, R., and Amblas, D. 2015. Submarine Canyons of Santa Monica Bay, Southern California: Variability in Morphology and Sedimentary Processes. *Marine Geology*, 365, 61-79. <https://doi.org/10.1016/j.margeo.2015.04.004>.
- Tucholke, B. E., Lin, J., Kleinrock, M. C., Tivey, M. A., Reed, T. B., Goff, J., and Jaroslow, G. E. 1997. Segmentation and Crustal Structure of the Western Mid-Atlantic Ridge Flank, 25°25'-27°10'n and 0-29 M.Y. *Journal of Geophysical Research: Solid Earth*, 102, 10203-10223. <https://doi.org/10.1029/96JB03896>.
- Tucker, M. E., Carey, S. N., Sparks, R. S. J., Stinton, A., Leng, M., Robinson, L., Li, T., Lewis, J., and Cotton, L. 2020. Carbonate Crusts around Volcanic Islands: Composition,

- Origin and Their Significance in Slope Stability. *Marine Geology*, 429, 106320. <https://doi.org/10.1016/j.margeo.2020.106320>.
- Urgeles, R., and Camerlenghi, A. 2013. Submarine Landslides of the Mediterranean Sea: Trigger Mechanisms, Dynamics, and Frequency-Magnitude Distribution. *Journal of Geophysical Research: Earth Surface*, 118, 2600-2618. <https://doi.org/10.1002/2013jf002720>.
- Valente, E. M. L. 2020. Sedimentary Dynamics on Insular Shelves of Volcanic Islands: Insights from Two Marine Cores of Faial Shelf, Azores. Master thesis, Universidade de Lisboa
- van Andel, T. H., and Komar, P. D. 1969. Ponded Sediments of the Mid-Atlantic Ridge between 22° and 23° North Latitude. *Geol. Soc. Am. Bull.*, 80, 1163-1190. [https://doi.org/10.1130/0016-7606\(1969\)80\[1163:PSOTMR\]2.0.CO;2](https://doi.org/10.1130/0016-7606(1969)80[1163:PSOTMR]2.0.CO;2).
- Varnes, D. J. 1978. Slope Movement Types and Processes. In: Schuster, R. L., and Krizek, R. J. (eds.) *Landslides, Analysis and Control, Special Report 176*. Washington, D.C.: National Academy of Sciences, 11-33.
- Vlag, P. A., Kruiver, P. P., and Dekkers, M. J. 2004. Evaluating Climate Change by Multivariate Statistical Techniques on Magnetic and Chemical Properties of Marine Sediments (Azores Region). *Palaeogeography, Palaeoclimatology, Palaeoecology*, 212, 23-44. <https://doi.org/10.1016/j.palaeo.2004.05.015>.
- Vogt, P. R., and Jung, W. Y. 2004. The Terceira Rift as a Hyper-Slow, Hotspot-Dominated Oblique Spreading Axis: A Comparison with Other Slow-Spreading Plate Boundaries. *Earth and Planet. Sci. Letts.*, 218, 77-90. [https://doi.org/10.1016/S0012-821X\(03\)00627-7](https://doi.org/10.1016/S0012-821X(03)00627-7).
- Walcott, R. I. 1972. Past Sea Levels, Eustasy and Deformation of the Earth. *Quaternary Research*, 2, 1-14. [https://doi.org/10.1016/0033-5894\(72\)90001-4](https://doi.org/10.1016/0033-5894(72)90001-4).
- Walker, R., Gill, S., Greenfield, C., McCaffrey, K., and Stephens, T. 2021. No Demonstrated Link between Sea-Level and Eruption History at Santorini. *EarthArXiv*. <https://doi.org/10.31223/X5961N>.
- Walker, G. P. L. 1999. Volcanic Rift Zones and Their Intrusion Swarms. *J. Volcanol. Geotherm. Res.*, 94, 21-34. [https://doi.org/10.1016/S0377-0273\(99\)00096-7](https://doi.org/10.1016/S0377-0273(99)00096-7).
- Walker, G. P. L. 1981. Generation and Dispersal of Fine Ash and Dust by Volcanic Eruptions. *Journal of Volcanology and Geothermal Research*, 11, 81-92. [https://doi.org/10.1016/0377-0273\(81\)90077-9](https://doi.org/10.1016/0377-0273(81)90077-9).
- Walker, G. P. L. 1960. Zeolite Zones and Dike Distribution in Relation to the Structure of the Basalts of Eastern Iceland. *The Journal of Geology*, 68, 515-528. <https://doi.org/10.1086/626685>.

- Walker, R., Gill, S., Greenfield, C., McCaffrey, K., and Stephens, T. 2021. No Demonstrated Link between Sea-Level and Eruption History at Santorini. EarthArXiv. <https://doi.org/10.31223/X5961N>.
- Wall-Palmer, D., Coussens, M., Talling, P. J., Jutzeler, M., Cassidy, M., Marchant, I., Palmer, M. R., Watt, S. F. L., Smart, C. W., Fisher, J. K., Hart, M. B., Fraass, A., Trofimovs, J., Le Friant, A., Ishizuka, O., Adachi, T., Aljahdali, M., Boudon, G., Breikreuz, C., Endo, D., Fujinawa, A., Hatfield, R., Hornbach, M. J., Kataoka, K., Lafuerza, S., Maeno, F., Manga, M., Martinez-Colon, M., McCanta, M., Morgan, S., Saito, T., Slagle, A. L., Stinton, A. J., Subramanyam, K. S. V., Tamura, Y., Villemant, B., and Wang, F. 2014. Late Pleistocene Stratigraphy of Iodp Site U1396 and Compiled Chronology Offshore of South and South West Montserrat, Lesser Antilles. *Geochemistry, Geophysics, Geosystems*, 15, 3000-3020. <https://doi.org/10.1002/2014GC005402>.
- Wallmann, P. C., Mahood, G. A., and Pollard, D. D. 1988. Mechanical Models for Correlation of Ring-Fracture Eruptions at Pantelleria, Strait of Sicily, with Glacial Sea-Level Drawdown. *Bulletin of Volcanology*, 50, 327-339. <https://doi.org/10.1007/BF01073589>.
- Ward, S. N., and Day, S. 2003. Ritter Island Volcano—Lateral Collapse and the Tsunami of 1888. *Geophysical Journal International*, 154, 891-902. <https://doi.org/10.1046/j.1365-246X.2003.02016.x>.
- Watt, S. F., Talling, P. J., and Hunt, J. E. 2014. New Insights into the Emplacement Dynamics of Volcanic Island Landslides. *Oceanography*, 27, 46-57. <https://doi.org/10.5670/oceanog.2014.39>.
- Watts, P., Grilli, S. T., Kirby, J. T., Fryer, G. J., and Tappin, D. R. 2003. Landslide Tsunami Case Studies Using a Boussinesq Model and a Fully Nonlinear Tsunami Generation Model. *Natural Hazards and Earth System Sciences*, 3, 391-402. <https://doi.org/10.5194/nhess-3-391-2003>.
- Watts, A. B., Peirce, C., Collier, J., Dalwood, R., Canales, J. P., and Henstock, T. J. 1997. A Seismic Study of Lithospheric Flexure in the Vicinity of Tenerife, Canary Islands. *Earth Planet. Sci. Lett.*, 146, 431-447. [https://doi.org/10.1016/S0012-821X\(96\)00249-X](https://doi.org/10.1016/S0012-821X(96)00249-X).
- Weaver, P. P. E., and Thomson, J. 1993. Calculating Erosion by Deep-Sea Turbidity Currents During Initiation and Flow. *Nature*, 364, 136-138. <https://doi.org/10.1038/364136a0>.
- Wei, B. J., Hbscher, C., Ldmann, T., and Serra, N. 2016. Submarine Sedimentation Processes in the Southeastern Terceira Rift/So Miguel Region (Azores). *Marine Geology*, 374, 42-58. <https://doi.org/10.1016/j.margeo.2016.02.004>.

- Weiß, B. J., Hübscher, C., and Lüdmann, T. 2015. The Tectonic Evolution of the Southeastern Terceira Rift/São Miguel Region (Azores). *Tectonophysics*, 654, 75-95. <https://doi.org/10.1016/j.tecto.2015.04.018>.
- Weston, F. S. 1964. A List of Recorded Volcanic Eruptions in the Azores with Brief Reports. PhD thesis, Universidade de Lisboa.
- Wessel, P., and Smith, W. H. F. 1991. Free Software Helps Map and Display Data. *Eos, Transactions, American Geophysical Union*, 72, 441. <https://doi.org/10.1029/90eo00319>.
- Wetzel, A., and Uchman, A. 2012. Chapter 22 - Hemipelagic and Pelagic Basin Plains. In: Knaust, D., and Bromley, R. G. (eds.) *Developments in Sedimentology*. Elsevier, 673-701. <https://doi.org/10.1016/B978-0-444-53813-0.00022-8>.
- White, J. D. L., and Houghton, B. F. 2006. Primary Volcaniclastic Rocks. *Geology*, 34, 677-680. <https://doi.org/10.1130/g22346.1>.
- White, W., Schilling, J.-G., and Hart, S. 1976. Evidence for the Azores Mantle Plume from Strontium Isotope Geochemistry of the Central North Atlantic. *Nature*, 263, 659-663. <https://doi.org/10.1038/263659a0>.
- Whitham, A. G. 1989. The Behaviour of Subaerially Produced Pyroclastic Flows in a Subaqueous Environment: Evidence from the Roseau Eruption, Dominica, West Indies. *Marine Geology*, 86, 27-40. [https://doi.org/10.1016/0025-3227\(89\)90016-9](https://doi.org/10.1016/0025-3227(89)90016-9).
- Wilson, C. J., and Hildreth, W. 1998. Hybrid Fall Deposits in the Bishop Tuff, California: A Novel Pyroclastic Depositional Mechanism. *Geology*, 26, 7-10. [https://doi.org/10.1130/0091-7613\(1998\)026<0007:HFDITB>2.3.CO;2](https://doi.org/10.1130/0091-7613(1998)026<0007:HFDITB>2.3.CO;2).
- Wilson, T. M., Stewart, C., Sword-Daniels, V., Leonard, G. S., Johnston, D. M., Cole, J. W., Wardman, J., Wilson, G., and Barnard, S. T. 2012. Volcanic Ash Impacts on Critical Infrastructure. *Physics and Chemistry of the Earth, Parts A/B/C*, 45-46, 5-23. <https://doi.org/10.1016/j.pce.2011.06.006>.
- Winant, C. D. 1980. Downwelling over the Southern California Shelf. *J. Phys. Oceanogr.*, 10, 791-799. [https://doi.org/10.1175/1520-0485\(1980\)010<0791:DOTSCS>2.0.CO;2](https://doi.org/10.1175/1520-0485(1980)010<0791:DOTSCS>2.0.CO;2).
- Wisshak, M., Berning, B., Jakobsen, J., and Freiwald, A. 2015. Temperate Carbonate Production: Biodiversity of Calcareous Epiliths from Intertidal to Bathyal Depths (Azores). *Marine Biodiversity*, 45, 87-112. <https://doi.org/10.1007/s12526-014-0231-6>.
- Wisshak, M., Form, A., Jakobsen, J., and Freiwald, A. 2010. Temperate Carbonate Cycling and Water Mass Properties from Intertidal to Bathyal Depths (Azores). *Biogeosciences*, 7, 2379-2396. <https://doi.org/10.5194/bg-7-2379-2010>.

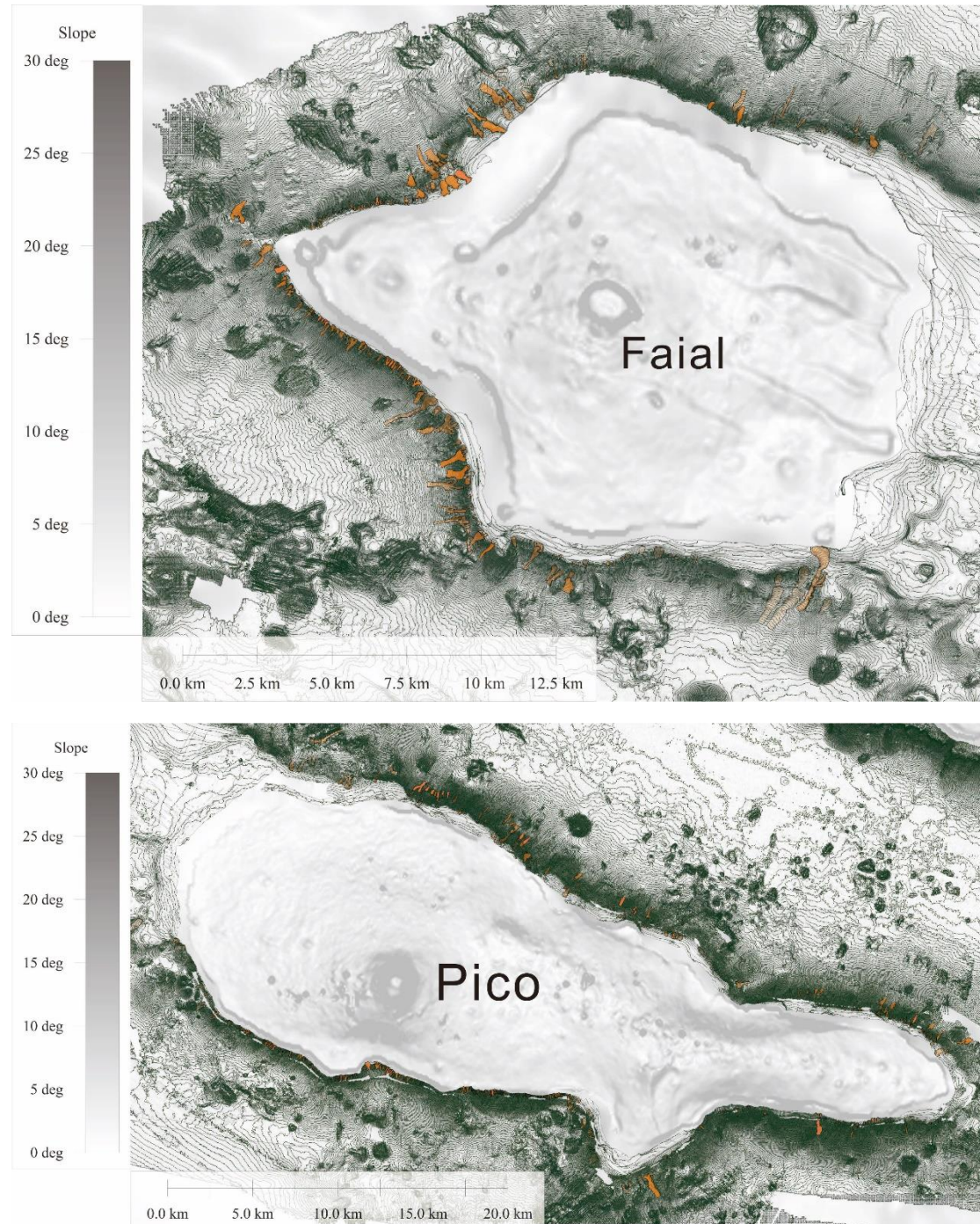
- Wolfe, C. J., McNutt, M. K., and Detrick, R. S. 1994. The Marquesas Archipelagic Apron: Seismic Stratigraphy and Implications for Volcano Growth, Mass Wasting, and Underplating. *J. Geophys. Res.*, 99, 13591-13608. <https://doi.org/10.1029/94JB00686>.
- Woodhall, D. 1974. Geology and Volcanic History of Pico Island Volcano, Azores. *Nature*, 248, 663-665. <https://doi.org/10.1038/248663a0>.
- Wu, T.-W., Suzuki, Y., Carlton, B., Harbitz, C., and Kopf, A. 2021. Effect of Prior Small to Moderate Seismic Events on Monotonic Undrained Shear Strength of Sand. *Soil Dynamics and Earthquake Engineering*, 141, 106465. <https://doi.org/10.1016/j.soildyn.2020.106465>.
- Wunsch, C. 1969. Progressive Internal Waves on Slopes. *J. Fluid Mech.*, 35, 131-144. <https://doi.org/10.1017/S0022112069001005>.
- Wynn, R., and Masson, D. 2003. Canary Islands Landslides and Tsunami Generation: Can We Use Turbidite Deposits to Interpret Landslide Processes? *Submarine Mass Movements and Their Consequences*. Springer, 325-332. https://doi.org/10.1007/978-94-010-0093-2_36.
- Wynn, R. B., Masson, D. G., Stow, D. A. V., and Weaver, P. P. E. 2000. Turbidity Current Sediment Waves on the Submarine Slopes of the Western Canary Islands. *Marine Geology*, 163, 185-198. [https://doi.org/10.1016/S0025-3227\(99\)00101-2](https://doi.org/10.1016/S0025-3227(99)00101-2).
- Yamashina, K. I., and Nakamura, K. 1978. Correlations between Tectonic Earthquakes and Volcanic Activity of Izu-Oshima Volcano, Japan. *Journal of Volcanology and Geothermal Research*, 4, 233-250. [https://doi.org/10.1016/0377-0273\(78\)90015-X](https://doi.org/10.1016/0377-0273(78)90015-X).
- Youssef, W. B. H. 2005. Caractérisation in Situ De L'environnement Physique Des Habitats Benthiques Occupés Par *Codium Elisabethae* Au Sein De Sites D'études Particuliers (Faial, Açores). Master thesis, Université de Liège.
- Zanon, V., and Viveiros, F. 2019. A Multi-Methodological Re-Evaluation of the Volcanic Events During the 1580 Ce and 1808 Eruptions at São Jorge Island (Azores Archipelago, Portugal). *Journal of Volcanology and Geothermal Research*, 373, 51-67. <https://doi.org/10.1016/j.jvolgeores.2019.01.028>.
- Zbyszewski, G., Candido de Mederos, A., da Veiga Ferreira, O., Rodrigues, L., and Rodrigues, A. 1974. *Carta Geologica De Portugal: Ilha Da Madeira B*. Lisbon: Instituto Geografico e Cadestral.
- Zhang, M., Huang, Y., and Bao, Y. 2016. The Mechanism of Shallow Submarine Landslides Triggered by Storm Surge. *Natural Hazards*, 81, 1373-1383. <https://doi.org/10.1007/s11069-015-2112-0>.
- Zhao, Z., Mitchell, N., Quartau, R., Moreira, S., Rusu, L., Melo, C., Ávila, S. P., Das, D., Afonso, P., Pombo, J., Duarte, J. F., and Rodrigues, A. 2021. Wave-Influenced

- Deposition of Carbonate-Rich Sediment on the Insular Shelf of Santa Maria Island, Azores. *Sedimentology*. <https://doi.org/10.1111/sed.12963>.
- Zhao, Z., Mitchell, N. C., Quartau, R., Ramalho, R. S., and Rusu, L. 2020. Coastal Erosion Rates of Lava Deltas around Oceanic Islands. *Geomorphology*, 370, 107410. <https://doi.org/10.1016/j.geomorph.2020.107410>.
- Zhao, Z., Mitchell, N. C., Quartau, R., Tempera, F., and Bricheno, L. 2019. Submarine Platform Development by Erosion of a Surtseyan Cone at Capelinhos, Faial Island, Azores. *Earth Surface Processes and Landforms*, 44, 2982-3006. <https://doi.org/doi:10.1002/esp.4724>.
- Zhong, G., Cartigny, M. J., Kuang, Z., and Wang, L. 2015. Cyclic Steps Along the South Taiwan Shoal and West Penghu Submarine Canyons on the Northeastern Continental Slope of the South China Sea. *Bulletin*, 127, 804-824. <https://doi.org/10.1130/B31003.1>.

Appendix

Sections are numbered to link with their associated chapters, hence Appendix 3.1 accompanies Chapter 3.

Appendix 3.1 Detailed submarine landslide mapping results for individual islands. High-resolution full images can be free download from the G-cubed website (supporting information) : <https://agupubs.onlinelibrary.wiley.com/doi/full/10.1029/2021GC009833>





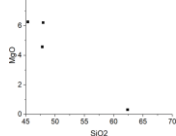
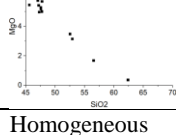
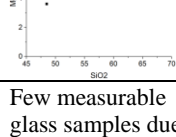
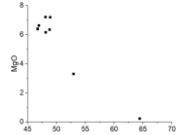
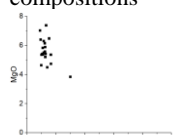
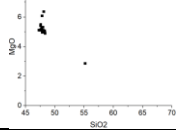
Appendix 3.2 Morphometric parameters of the landslide valleys used to compute the tsunami amplitude above them.

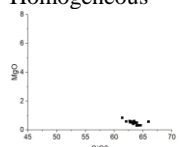
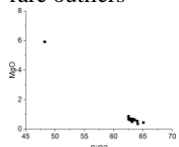
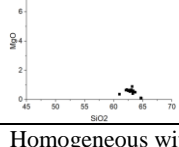
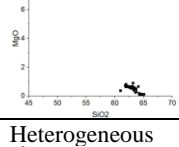
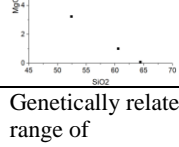
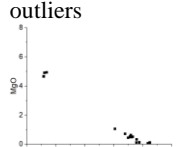
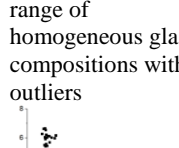
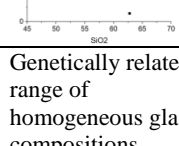
Landslide valley ID	Head scarp height	Average slope angle	Initial length of the slide measured downslope	Depth of landslide initial centre of mass	Along-slope landslide width	Volume	Amplitude
	H (m)	θ ($^{\circ}$)	b (m)	d (m)	w (m)	V_l (m ³)	A (m)
Faial-003	30	20	475	400	350	1,178,526	0.26
Faial-009	18	10	1,625	480	466	3,517,072	0.34
Faial-011	16	10	1,395	485	342	1,891,262	0.20
Faial-016	50	30	410	313	286	1,913,711	0.37
Faial-046	60	30	708	327	236	1,507,768	0.54
Faial-114	45	30	595	255	390	2,517,440	0.84
Faial-121	47	25	1,910	371	355	3,069,340	1.32
Faial-170	41	12.5	2,288	256	540	6,769,416	3.79
Faial-213	30	12.5	754	169	200	2,498,963	0.94
Pico-010	7	10	1,840	278	250	6,493,354	0.21
Pico-108	30	30	580	388	85	1,101,067	0.07
Pico-128	32	30	540	220	131	1,306,099	0.27
Pico-134	26	30	536	517	155	1,144,809	0.06
Pico-172	29	15	2,037	602	238	2,983,407	0.27
Pico-353	67	30	830	284	270	1,659,074	0.99
São Jorge-022	51	30	835	445	415	16,139,145	0.52
São Jorge-024	83	30	407	357	382	1,831,374	0.63
São Jorge-029	92	30	421	417	284	1,077,200	0.43
São Jorge-045	45	30	269	345	318	1,187,639	0.22
São Jorge-057	79	30	756	452	470	7,304,837	0.81
São Jorge-063	36	30	503	398	521	4,658,369	0.35
São Jorge-073	20	10	1,334	225	470	1,367,822	1.21
São Jorge-078	10	20	1,779	418	362	2,180,957	0.24
São Jorge-079	40	30	480	528	186	1,191,508	0.09
São Jorge-080	70	20	940	480	300	3,808,317	0.68
São Jorge-083	50	30	500	599	182	2,736,948	0.10
São Jorge-085	20	17.5	784	457	139	1,042,595	0.09
São Jorge-088	23	15	941	245	563	2,511,797	1.22
São Jorge-089	17	15	751	245	487	1,070,469	0.66
São Jorge-092	60	30	956	484	268	2,433,058	0.40
São Jorge-102	50	7.5	947	250	414	5,284,523	1.49
São Jorge-103	32	7.5	710	235	441	1,983,985	0.90
São Jorge-116	44	30	488	420	220	1,754,421	0.18
São Jorge-118	35	15	992	335	412	1,688,577	0.86
São Jorge-124	48	20	886	614	268	3,370,252	0.26
São Jorge-144	57	30	1,053	550	370	2,934,952	0.44
São Jorge-156	32	12.5	622	144	290	1,136,100	1.59
São Jorge-166	52	30	354	401	232	1,951,404	0.19
São Jorge-175	40	30	443	346	287	1,183,709	0.27
São Jorge-192	42	10	461	70	410	2,072,286	6.78
São Jorge-215	42	22.5	952	578	227	2,123,163	0.22
São Jorge-222	50	30	502	434	246	1,033,460	0.22
São Jorge-255	69	30	530	493	243	1,072,902	0.25
São Jorge-290	51	30	678	375	395	4,213,210	0.56
São Jorge-292	30	12.5	529	230	504	1,142,006	0.96
São Jorge-299	56	12.5	1,190	171	372	3,118,526	4.36
São Jorge-300	77	17.5	971	453	385	5,184,235	1.07
São Jorge-308	66	30	513	434	317	2,053,512	0.37
São Jorge-314	53	30	847	435	240	2,290,469	0.34
São Jorge-319	40	25	1,220	707	259	3,655,155	0.19
São Jorge-321	157	30	1,540	605	468	23,728,878	1.72
São Jorge-331	120	30	920	760	420	14,410,958	0.54
São Jorge-333	40	30	483	899	328	2,689,926	0.06
São Jorge-335	70	22.5	867	940	488	6,296,373	0.31

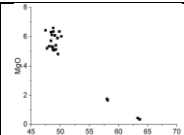
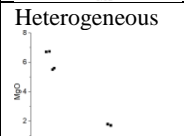
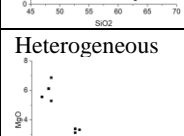
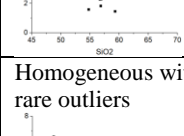
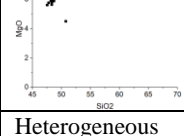
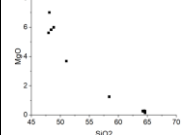
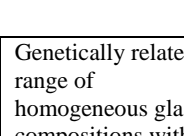
São Jorge-336	62	22.5	918	950	314	4,147,094	0.18
São Jorge-343	55	20	644	570	450	2,324,417	0.43
São Jorge-344	51	25	410	670	363	1,725,008	0.16
São Jorge-349	35	17.5	1,042	750	202	1,465,739	0.12
São Jorge-351	50	25	652	624	330	3,127,637	0.23
São Jorge-358	47	30	600	585	173	1,346,651	0.10
São Jorge-360	49	25	970	595	240	3,199,191	0.25
São Jorge-362	70	30	417	277	213	1,569,717	0.50
São Jorge-365	72	25	794	664	426	4,682,098	0.44
São Jorge-370	40	25	771	663	175	1,713,697	0.10
São Jorge-371	39	25	1,116	670	402	5,585,190	0.29
São Jorge-374	21	25	1,004	808	378	1,387,081	0.10
São Jorge-375	37	30	565	647	520	2,691,511	0.18
São Jorge-377	110	30	807	767	220	4,278,619	0.24
São Jorge-378	77	30	858	827	350	5,040,977	0.24
Terceira-015	74	30	694	608	260	1,696,724	0.25
Terceira-049	65	15	2,964	416	1171	50,445,730	6.81
Terceira-050	50	15	1,745	318	1350	53,205,372	5.97
Terceira-059	40	30	1,251	593	183	1,326,954	0.16
Terceira-113	32	12.5	1,191	353	376	2,534,499	0.73
Terceira-114	38	20	500	225	370	1,630,599	0.97
Terceira-118	93	30	914	266	272	8,291,128	1.67
Terceira-123	47	17.5	1,007	392	221	2,041,050	0.51
Terceira-142	23	22.5	1,379	335	230	1,282,049	0.42
Terceira-167	56	17.5	1,040	544	205	1,794,725	0.33
Terceira-174	30	30	700	882	220	1,736,484	0.05
Terceira-183	84	30	1,492	726	261	3,738,421	0.38
Terceira-210	45	30	320	722	400	1,507,073	0.09
Terceira-225	33	22.5	859	319	125	1,024,926	0.25

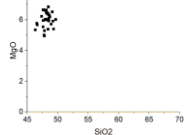
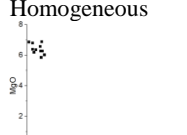
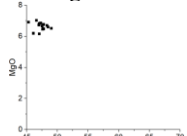
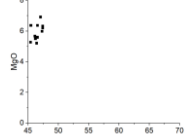
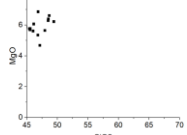
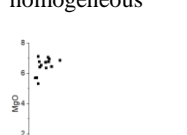
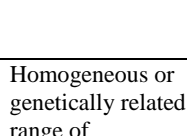
All generated geochemical and geomorphometric numerical data used in Chapter 4 can be obtained via Figshare (<https://doi.org/10.6084/m9.figshare.c.5602176>).

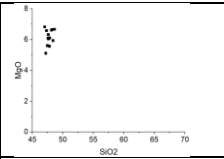
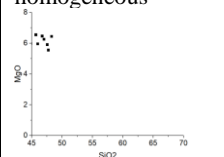
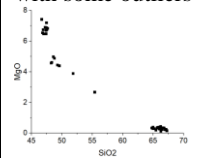
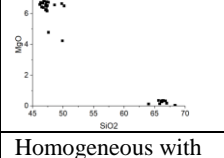
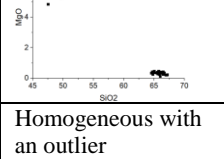
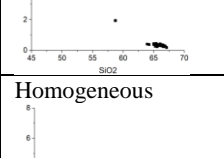
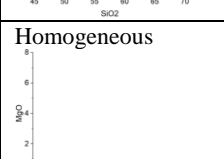

Appendix 4.1 Characteristics and interpretations of volcanoclastic-rich layers "Hand lens" or "microscope" indicates method of observation.

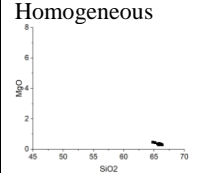
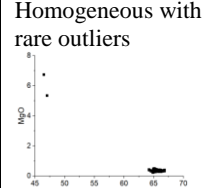
Sample position (cm bsf)	Carbonate (Figure 4.7)	Grain size assessment (Figure 4.2)	Bed basal boundary type and sedimentary structures (Figure 4.2)	Glass shard compositional variability (Appendix 4.2)	Particle morphology (Appendix 4.3)	Interpreted facies and emplacement mechanism
1215						
73-77		Fine to medium sand (microscope)	Reworked and irregular contact	Few measurable glass samples due to oxidation but those measured appear heterogeneous 		F2a? Secondary volcanoclastic turbidite.
102-106		Fine to medium sand (hand-lens)	Diffuse bioturbated contact	Heterogeneous 		F2a? Secondary volcanoclastic turbidite F2a?
133-137		Fine to medium sand (hand-lens)	Irregular bioturbated contact	Homogeneous 		F2b? Primary fallout (?)
175-188	Many bioclasts (microscope)	Fine to coarse sand (microscope)	Sharp and erosive contact, irregular stratification in middle of bed	Few measurable glass samples due to oxidation but those measured appear heterogeneous	Low NPL (rounded)	F2a, Secondary volcanoclastic turbidite (?)
203-216	high carbonate content (XRD)	Medium to coarse sand (microscope)	Slightly erosive and irregular contact, vaguely laminated bed	Heterogeneous 	Low NPL (rounded)	F2a, Secondary volcanoclastic turbidite (?)
216-227	Many bioclasts (microscope)	Tuffaceous sandy silt (microscope)	Diffusive bioturbated contact. Two lenses of coarse ash in the bed centre.	Genetically related range of homogeneous glass compositions 	Low NPL (rounded)	F2a, Primary volcanoclastic turbidite
227-234		Tuffaceous silt (hand-lens)	Irregular, slightly bioturbated contact	Homogeneous 	Angular lapilli (visual)	F2b? Primary fallout or primary volcanoclastic turbidite
1219						

10-20	Many bioclasts (microscope)	Sandy silt (microscope)	Diffuse bioturbated contact. Lower part of bed is laminated	Homogeneous 	Low NPL (rounded)	F2a, Primary volcaniclastic turbidite
22-28	Rare bioclasts (microscope)	Fine sand to gravel (microscope)	Sharp, slightly erosive boundary, inversely graded bed	Homogeneous with rare outliers 	Low NPL (rounded)	F2b, Primary volcaniclastic turbidite
37-46	Rare bioclasts (microscope)	Medium sand (hand-lens)	Irregular contact, normally graded and laminated ash at the top	Homogeneous 		F2b, Primary volcaniclastic turbidite (?)
46-55	Rare bioclasts	Medium sand (microscope)	Irregular contact	Homogeneous with rare outlier 	Low NPL (rounded)	F2b, Primary volcaniclastic turbidite
55-59	low carbonate content (XRD)	Very coarse sand to pebble (microscope)	Irregular contact, inversely graded bed	Heterogeneous 	Low NPL (rounded)	F2b, Secondary volcaniclastic turbidite
59-66	Rare bioclasts (microscope)	Coarse sand to very coarse sand (microscope)	Diffusive contact. Normally graded	Genetically related range of homogeneous glass compositions with outliers 	Low NPL (rounded)	F2b, Secondary volcaniclastic turbidite
130-132	Biogenic material likely introduced by later bioturbation (microscope)	Fine to medium sand (microscope)	Sharp irregular contact	Genetically related range of homogeneous glass compositions with outliers 	High NPL (angular)	F2a, Primary fallout (?)
168-175	high carbonate content (XRD)	Fine to medium (microscope)	Sharp irregular contact	Genetically related range of homogeneous glass compositions 	High NPL (angular)	F2a, Primary volcaniclastic turbidite
184-210	biofragments	Sandy silt	Diffusive lower contact, weakly laminated	Genetically related range of homogeneous glass compositions		F2a, Primary volcaniclastic turbidite

						
232-235	Many bioclasts (microscope)	Sandy silt (microscope)	Bioturbated contact, slightly laminated bed	Heterogeneous 		F2a, Secondary volcanoclastic turbidite
284-286	Biogenic material (microscope)	Coarse sand (hand-lens)	Diffusive contact	Heterogeneous 		F2a, Secondary volcanoclastic turbidite
305-319	Biogenic material likely introduced by bioturbation	Sandy silt (hand-lens)	Bioturbated irregular contact	Homogeneous with rare outliers 		F2a, Primary fallout (?)
458-463	Biogenic material (microscope)		Irregular bioturbated contact	Heterogeneous 		F2a, Secondary volcanoclastic turbidite
1226						
17-40	high carbonate content (XRD) likely introduced by bioturbation	Fine to medium sand (microscope)	Irregular bioturbated contact	Genetically related range of homogeneous glass compositions with outliers 	High NPL (angular)	F2a, Primary fallout or primary volcanoclastic turbidite
40-49	Many bioclasts (microscope)	Sandy silt (hand-lens)	Bioturbated contact, bioclasts and reworked ash from above and below			F2a, Secondary volcanoclastic turbidite
49-54	Many bioclasts likely introduced by bioturbation	Medium to coarse sand (hand-lens)	Bioturbated contact.	Homogeneous with outliers 		F2a, Primary volcanoclastic turbidite
63-86	high carbonate content (XRD)	Silty clay with dispersed sand. Medium sand at below (hand-lens)	Sharp erosive contact, cross-laminated ripple structures. Thick bed			F2a, Secondary volcanoclastic turbidite

86-140	low carbonate content (XRD)	Medium to coarse sand (microscope)	Irregular contact, normally graded massive bed with vague stratification in between. Particles at 86-100 cm are reworked by bioturbation	Homogeneous 	High NPL (angular)	F2b, Primary volcaniclastic turbidite (?)
140-147	Many bioclasts (microscope) likely introduced by bioturbation	Clayey silt (hand-lens)	Erosive contact. Highly bioturbated and dispersed reworked ash from below. Two lenses of coarse ash in the middle.	Homogeneous 		F2a?, Secondary volcaniclastic turbidite
147-160	Rare bioclasts (microscope)	Fine sand (microscope)	Sharp and erosive contact. Laminated and stratified bed.	Homogeneous 	High NPL (angular)	F2b, Primary volcaniclastic turbidite
169-173	Rare bioclasts (microscope)	Coarse sand (microscope)	Sharp and erosive contact. Bioturbated at top	Genetically related range of homogeneous glass compositions (?) 	High NPL (angular)	F2b, Primary volcaniclastic turbidite
174-176	Rare bioclasts (microscope)	Sandy silt (microscope)	Sharp contact	Genetically related range of homogeneous glass compositions? 	High NPL (angular)	F2b, Primary volcaniclastic turbidite (?)
177-179	Rare bioclasts (microscope)	Sandy silt (microscope)	Irregular contact, weakly laminated bed	Homogeneous with outliers or genetically related range of homogeneous 		F2b, Primary volcaniclastic turbidite (?)
179-183	high carbonate content (XRD)	Silt with dispersed reworked fine sand (microscope)	Sharp contact, laminated bed			F2a, Primary or secondary volcaniclastic turbidite
183-200	Rare bioclasts (microscope)	Very fine to coarse sand (microscope)	Sharp contact. Normally graded bed.	Homogeneous or genetically related range of homogeneous 	High NPL (angular)	F2b, Primary fallout or primary volcaniclastic turbidite

						
200-210	Rare bioclasts (microscope)	Medium to coarse sand (hand-lens)	Base of bed not penetrated. Irregular top.	Homogeneous or genetically related range of homogeneous 		F2b, Primary volcanoclastic turbidite (?)
1230						
43-66	Many bioclasts in bed (microscope) but low carbonate content (XRD) near bed base	Very fine sand to coarse sand (microscope)	Sharp contact. Normally graded. Thick bed.	Appears heterogeneous, or might be bimodal with some outliers 	Low NPL (rounded)	F2a, Secondary volcanoclastic turbidite
78-86		Very fine sand to fine sand (hand-lens)	Sharp and slightly irregular contact	Bimodal with rare outliers 		F2a? Primary volcanoclastic turbidite
131-140	Low carbonate content (XRD)	Coarse to very coarse sand (microscope)	Sharp contact. Weakly stratified bed	Homogeneous with outliers 	Low NPL (rounded)	F2b, Primary volcanoclastic turbidite
149-150		Sandy silt (hand-lens)	Irregular and diffuse contact	Homogeneous with an outlier 		F2b?, Primary fallout (?)
157-159	Bioclasts (microscope) likely introduced by bioturbation	Coarse sand (microscope)	Wavy basal contact and irregular reworked top	Homogeneous 	High NPL (angular)	F2a (?), Primary fallout
164-167	Rare bioclasts (microscope)	Medium sand (hand-lens)	Gradual basal contact and reworked top	Homogeneous 		F2b(?), Primary fallout

168-170		Silty clay (hand lens)	Gradual and unclear basal contact	Homogeneous 		F2b(?), Primary fallout
262-368	high carbonate content (XRD)	Fine sand to very coarse sand (microscope)	Base of bed not penetrated, irregular top. Massive normally graded bed.	Homogeneous with rare outliers 	Low NPL (rounded)	F2a, Primary volcaniclastic turbidite

Appendix 4.2 Geochemical composition of full glass data

Sample positions-ID	Na ₂ O	K ₂ O	FeO	SiO ₂	TiO ₂	MgO	CaO	MnO	Al ₂ O ₃	P ₂ O ₅	TAS	Total
(cm bsf)	(%)	(%)	(%)	(%)	(%)	(%)	(%)	(%)	(%)	(%)	(%)	(%)
1215												
73-75-1	3.3	1.3	10.3	47.9	3.2	6.2	11.8	0.2	15.4	0.4	4.59	100
73-75-2	4	1.3	11.3	45.3	3	6.3	12.1	0.2	16	0.4	5.35	100
73-75-3	4.5	2.1	11.6	47.8	3.8	4.6	8.3	0.2	16.6	0.6	6.53	100
73-75-4	7.7	5.8	3.9	62.3	0.5	0.3	0.8	0.1	18.5	0.1	13.49	100
102-104-2	3.7	1.1	10.5	47.5	3.3	5.3	11.2	0.2	16.7	0.4	4.81	100
102-104-3	4.2	1.5	11.6	45.6	4	5.5	11.1	0.2	16.1	0.5	5.63	100
102-104-5	3.6	1.1	10.3	47.4	2.8	6.4	11.6	0.2	16.1	0.4	4.74	100
102-104-6	3.8	1.4	12.1	47.2	3.7	5.4	10.5	0.2	15.3	0.5	5.2	100
102-104-7	3.2	1.1	11.2	47.3	3.3	6.2	12.1	0.2	15.1	0.3	4.29	100
102-104-10	4.3	1.6	12	47.2	4	5	9.5	0.2	15.6	0.6	5.96	100
102-104-12	4.1	1.4	12	47	3.8	5.8	10.4	0.1	14.9	0.5	5.54	100
102-104-13	3.2	1.2	10.9	45.9	2.8	7.4	13	0.2	15	0.3	4.38	100
102-104-14	3.7	1.5	11.3	45.4	3.6	6.1	11.7	0.3	15.9	0.5	5.14	100
102-104-15	3.7	1.2	10.6	47.7	3.4	5.7	11.2	0.2	16	0.4	4.87	100
102-104-16	3.8	1.5	12.2	47.7	4	5	10.6	0.2	14.5	0.5	5.29	100
102-104-17	4.1	1.5	11.9	47.5	3.8	5.2	9.9	0.2	15.4	0.5	5.65	100
102-104-18	3.1	1	10	48.3	3	7.4	12.5	0.1	14.3	0.4	4.09	100
102-104-1	5.2	2.5	9.5	52.9	2.2	3.2	6.4	0.3	17	0.8	7.71	100
102-104-8	5.8	2.5	7.5	56.5	1.5	1.7	5.3	0.3	18.4	0.5	8.34	100
102-104-9	5.2	2.2	9.6	52.5	2.4	3.5	6.7	0.2	16.8	0.8	7.45	100
102-104-11	7.5	6.1	3.3	62.4	0.6	0.4	1.1	0.1	18.5	0.1	13.58	100
134-136-1	4.8	2.1	12	47.7	4.2	4.1	9.1	0.2	14.9	0.9	6.9	100
134-136-2	4.8	1.9	11.8	48.5	4.3	4.7	7.6	0.2	15.7	0.6	6.77	100
134-136-4	4.9	2.1	12.4	45.9	4.4	4.3	9.3	0.2	15.7	0.9	7.04	100
134-136-6	4.6	2	12.5	46.8	4.6	4.3	9.5	0.2	14.6	0.9	6.63	100
134-136-7	4.6	1.9	12.3	46.9	4.6	4.4	9.7	0.3	14.6	0.8	6.46	100
134-136-8	4.6	2	12	47.3	4.5	4.3	9.4	0.2	14.7	1	6.62	100
134-136-9	4.5	2	12	47.1	4.5	4.4	9.6	0.2	14.8	0.8	6.42	100
134-136-10	4.5	1.9	12.1	46.7	4.4	4.1	9.6	0.2	15.6	0.9	6.34	100
134-136-12	4.8	2.1	11.9	47.1	4.4	4.4	9.4	0.2	14.9	0.9	6.9	100
134-136-13	4.6	1.7	12.7	46.1	4.4	5.9	9.4	0.2	14.2	0.8	6.31	100
134-136-14	4.5	1.9	12	47	4.6	4.5	9.6	0.2	14.9	0.9	6.39	100
134-136-15	4.5	1.9	12.5	46.7	4.6	4.5	9.7	0.2	14.8	0.8	6.32	100
134-136-16	4.6	2.1	12.7	46.8	4.4	4.2	9.3	0.2	14.6	1	6.75	100
134-136-17	4.5	1.8	12.4	45.8	4.4	5.5	9.4	0.2	15.2	0.8	6.24	100
134-136-18	4.9	2	10.8	48.5	3.8	3.6	9.1	0.2	16.2	0.9	6.89	100
134-136-19	4.3	1.9	12.5	46.6	4.7	4.4	9.6	0.3	14.8	0.8	6.2	100
134-136-20	4.7	2	12.1	46.8	4.4	4.5	9.7	0.2	14.7	0.9	6.7	100
134-136-21	4.8	1.9	11.7	47.4	4.2	4.1	9.5	0.2	15.2	0.9	6.68	100
134-136-22	4.5	1.8	12.1	47	4.5	4.3	9.7	0.2	15	0.8	6.33	100

180-183-2	7.6	3	2.3	62	0.3	0.3	3.4	0	21	0.1	10.62	100
208-210-2	3.3	1.2	10	48.1	3.2	6.2	11.9	0.2	15.6	0.3	4.58	100
208-210-3	3.8	1.3	9	48.8	2.7	6.3	11.9	0.2	15.5	0.4	5.13	100
208-210-4	4.1	1.2	10.8	46.7	3.1	6.4	11.2	0.2	15.9	0.4	5.26	100
208-210-5	3.9	1.1	10.6	46.9	3.1	6.6	11.3	0.1	16	0.4	5.04	100
208-210-7	2.9	1.4	10.8	48.9	3.1	7.2	11.6	0.2	13.7	0.3	4.27	100
208-210-8	3.5	1	10.1	48.1	2.5	7.2	12.9	0.2	14.3	0.3	4.55	100
208-210-6	7	5.9	3.1	64.4	0.5	0.2	1	0.2	17.6	0	12.92	100
208-210-9	5.6	2.8	8.5	52.9	2.4	3.3	6.4	0.2	17.1	0.7	8.38	100
219-221-1	3.9	1.5	11.7	47.8	3.8	5.2	9.9	0.2	15.3	0.5	5.41	100
219-221-2	3.3	1.4	10.4	48.3	3.4	5.4	11.4	0.2	15.8	0.4	4.65	100
219-221-3	4.1	1.6	11.7	47.7	3.9	5.1	9.9	0.2	15.4	0.5	5.65	100
219-221-4	3	1.2	9.9	48.4	2.8	6.9	12.5	0.2	14.7	0.4	4.23	100
219-221-5	3	1.1	9.6	48.4	2.7	7.6	12.9	0.2	14.1	0.3	4.16	100
219-221-6	3.6	1.4	11.2	48.3	3.7	5.6	10.8	0.3	14.5	0.5	5.06	100
219-221-7	3.6	1.1	10.4	47.6	2.8	6.6	12.3	0.2	15.1	0.4	4.71	100
219-221-8	3.5	1.3	11.8	47.5	3	6.1	11.5	0.2	14.9	0.3	4.76	100
224-226-1	3.6	1.2	11.3	48.1	3.5	5.6	10.8	0.2	15.4	0.4	4.87	100
224-226-2	4.2	1.4	12.2	47.4	3.8	4.6	10.7	0.2	15.1	0.5	5.58	100
224-226-3	3.5	0.6	9.8	48.1	3.6	5.2	13	0.1	15.7	0.4	4.15	100
224-226-4	3.8	1.4	10.2	48.5	3.4	4.5	10.9	0.2	16.9	0.4	5.18	100
224-226-6	3.8	1.4	11.5	48.2	3.8	5.4	10.4	0.1	14.9	0.5	5.19	100
224-226-7	4.1	1.4	11.5	47.6	3.7	5.4	10.7	0.1	14.9	0.5	5.48	100
224-226-8	3.6	1.4	11.6	47.9	3.8	5.5	10.7	0.2	14.9	0.5	5	100
224-226-9	3.7	1.4	12.5	47.2	3.5	7	9.7	0.2	14.3	0.4	5.12	100
224-226-10	3.5	1.2	11.3	47.7	3.5	5.8	11.2	0.2	15.3	0.4	4.66	100
224-226-11	3.7	1	10.8	47.3	2.9	6.4	12	0.2	15.2	0.3	4.68	100
224-226-12	3.6	1.2	10.4	49.1	3.5	4.7	11.2	0.2	15.6	0.4	4.84	100
224-226-13	1.5	1.2	11	48.8	3.2	6.5	11.9	0.2	15.5	0.4	2.67	100
224-226-14	3.3	1.2	10.4	48.3	2.8	7.4	12	0.2	14	0.4	4.56	100
224-226-15	3.9	1.4	11.8	47.7	3.6	5.4	10.7	0.3	14.8	0.4	5.27	100
224-226-16	3.2	1.1	10.5	47.8	3.1	6.3	12.1	0.2	15.3	0.4	4.24	100
224-226-18	4	1.3	11.6	49.1	3.9	5.4	8.3	0.2	15.7	0.5	5.3	100
224-226-19	3.8	1.4	11.9	47.5	3.8	5.4	10.7	0.2	15	0.5	5.13	100
224-226-20	3.3	1.3	10.5	48	3.4	6.2	11.5	0.2	15.3	0.4	4.59	100
224-226-21	3.6	1.2	10.9	48.1	3.6	5.9	11.1	0.2	15.2	0.4	4.78	100
224-226-17	5.3	1.6	11	52.5	3.2	3.9	4.7	0.2	16.8	0.8	6.89	100
231-233-1	4.1	1.5	11.7	47.2	3.8	5.1	10.6	0.2	15.4	0.5	5.54	100
231-233-2	3.8	1.4	11.8	47.6	3.8	5.5	10.6	0.1	15	0.4	5.16	100
231-233-4	4	1.4	11.5	47.7	3.7	5.3	10.6	0.2	15.2	0.4	5.41	100
231-233-5	3.8	1.4	11.6	48.2	3.8	5.1	10.4	0.2	15.2	0.5	5.14	100
231-233-6	3.5	1.4	12	47.5	3.8	5.4	10.7	0.2	15	0.4	4.95	100
231-233-8	3.7	1.4	11.4	48	3.7	5.3	10.7	0.2	15	0.6	5.14	100
231-233-9	3.8	1.4	12	47.7	3.7	5.3	10.5	0.2	14.9	0.4	5.21	100
231-233-10	4.2	1.7	12.1	48.3	3.7	5	8.7	0.2	15.5	0.5	5.95	100

231-233-11	4.1	1.4	11.6	48	3.7	5.1	10.3	0.2	15.1	0.5	5.51	100
231-233-12	4	1.5	12.1	47.6	3.9	5.1	9.8	0.2	15.4	0.5	5.5	100
231-233-13	4.6	1.6	11.5	48.3	3.8	4.9	9.8	0.2	14.8	0.5	6.2	100
231-233-14	4	1.4	12.1	47.6	3.7	5.2	10.5	0.3	14.8	0.5	5.4	100
231-233-15	3.4	1.1	10.2	48.1	2.8	6.4	12.4	0.1	15.1	0.3	4.49	100
231-233-16	3.5	1.2	10.5	47.8	3.2	6.1	11.1	0.2	15.9	0.4	4.71	100
231-233-17	4	1.5	12.1	47.4	3.9	5.1	10.4	0.2	14.9	0.5	5.53	100
231-233-18	3.9	1.5	11.7	47.7	3.7	5.2	10.1	0.2	15.4	0.5	5.44	100
231-233-19	3.8	1.4	11.8	47.8	3.8	5	10.8	0.2	14.8	0.5	5.17	100
231-233-20	3.9	1.4	11.8	47.9	3.8	5.3	10.5	0.2	14.7	0.5	5.38	100
231-233-7	5.1	2.6	8.6	55.1	2.3	2.9	5.9	0.2	16.8	0.5	7.68	100
1219												
12-14-5	7.48	4.44	4.28	61.35	0.79	0.85	2.13	0.15	18.31	0.21	11.91	100
12-14-6	7.95	4.65	3.03	63.84	0.41	0.32	1.43	0.12	18.14	0.12	12.61	100
12-14-7	7.08	5	3.63	64.28	0.42	0.33	1.19	0.13	17.84	0.1	12.08	100
12-14-8	7.14	4.66	3.8	63.26	0.56	0.56	1.58	0.24	18.13	0.09	11.8	100
12-14-9	7.29	4.84	4.2	62.77	0.56	0.59	1.41	0.29	17.91	0.14	12.13	100
12-14-10	7.12	4.71	4.11	62.84	0.53	0.56	1.58	0.17	18.29	0.1	11.82	100
12-14-11	7.47	4.62	3.78	62.72	0.56	0.54	1.59	0.17	18.43	0.11	12.09	100
12-14-13	7.38	4.69	3.83	63.2	0.54	0.51	1.48	0.15	18.13	0.07	12.07	100
12-14-15	7.58	3.65	3.54	63.4	0.65	0.63	2.36	0.07	18.06	0.06	11.24	100
12-14-16	7.36	4.61	3.64	63.2	0.52	0.51	1.58	0.23	18.25	0.1	11.97	100
12-14-17	7.21	4.69	3.7	63.5	0.51	0.5	1.47	0.12	18.2	0.11	11.9	100
12-14-18	7.55	4.97	3.57	64.07	0.43	0.33	1.19	0.18	17.66	0.05	12.51	100
12-14-19	7.36	4.64	3.57	63.16	0.55	0.54	1.58	0.17	18.26	0.18	12	100
12-14-20	7.37	4.69	3.64	63.38	0.54	0.56	1.49	0.19	17.99	0.15	12.05	100
12-14-21	3.59	4.87	3.85	65.91	0.54	0.58	1.59	0.24	18.68	0.16	8.46	100
12-14-22	7.35	4.57	4.04	63.03	0.5	0.53	1.52	0.22	18.13	0.1	11.92	100
12-14-23	7.43	4.53	3.67	64.52	0.42	0.33	1.33	0.14	17.55	0.1	11.96	100
18-19-8	7.53	4.68	4.18	63.24	0.48	0.43	1.39	0.21	17.77	0.1	12.21	100
18-19-10	6.95	4.73	4	63.15	0.56	0.55	1.51	0.16	18.3	0.09	11.68	100
18-19-11	7.48	4.96	4.4	63.5	0.54	0.52	1.17	0.23	17.15	0.04	12.44	100
18-19-12	7.26	4.68	4.12	62.99	0.52	0.55	1.54	0.15	18.07	0.11	11.94	100
18-19-13	6.14	4.71	4	63.89	0.57	0.51	1.56	0.14	18.31	0.15	10.85	100
18-19-15	7.2	5.16	3.61	63.88	0.43	0.33	1.11	0.23	17.97	0.09	12.36	100
18-19-16	7.06	5.66	3.98	62.91	0.56	0.55	1.28	0.17	17.67	0.16	12.72	100
18-19-17	7.28	5.13	4.41	62.62	0.62	0.62	1.32	0.19	17.64	0.16	12.41	100
18-19-18	7.49	4.92	4.16	62.03	0.63	0.6	1.61	0.22	18.1	0.25	12.42	100
18-19-20	7.42	4.71	3.86	63	0.54	0.52	1.58	0.16	18.07	0.12	12.13	100
18-19-21	7.26	4.59	3.76	63.35	0.54	0.52	1.54	0.12	18.16	0.13	11.85	100
18-19-22	7.59	4.66	3.62	63.16	0.54	0.53	1.57	0.13	18.07	0.13	12.25	100
18-19-23	7.52	3.97	4	63.57	0.6	0.53	2.08	0.11	17.53	0.11	11.48	100
18-19-24	7.62	4.82	3.95	63	0.51	0.57	1.44	0.15	17.82	0.11	12.44	100
18-19-25	7.59	4.44	4.3	62.84	0.53	0.54	1.7	0.17	17.76	0.13	12.03	100
18-19-3	3.44	1.31	10.44	48.24	3.04	6.55	11.17	0.26	15.15	0.42	4.75	100

18-19-4	4.57	1.95	11.43	48.11	3.72	4.78	9.81	0.14	15.02	0.46	6.53	100
18-19-5	3.66	1.32	9.02	48.31	2.83	6.45	11.96	0.2	15.83	0.42	4.98	100
18-19-14	5.82	3.07	9.79	51.04	3.24	3.47	7.22	0.2	15.29	0.86	8.89	100
25-27-1	7.51	3.96	3.89	63.09	0.62	0.52	1.87	0.1	18.3	0.13	11.47	100
25-27-2	7.11	4.81	3.78	62.9	0.66	0.63	1.83	0.2	17.9	0.18	11.91	100
25-27-6	7.5	4.32	3.72	63.44	0.63	0.63	1.75	0.17	17.67	0.15	11.83	100
25-27-8	7.48	3.61	3.61	63.21	0.62	0.7	2.24	0.2	18.18	0.15	11.09	100
25-27-9	7.64	3.96	3.16	63.98	0.59	0.55	1.77	0.13	18.06	0.15	11.6	100
25-27-10	7.5	4.38	4.09	62.64	0.76	0.66	1.82	0.19	17.84	0.13	11.88	100
25-27-11	7.08	4.48	3.93	62.85	0.69	0.71	1.91	0.11	18.02	0.2	11.56	100
25-27-13	7.38	5	3.5	64.06	0.42	0.37	1.18	0.15	17.91	0.03	12.38	100
25-27-14	7.56	3.3	3.99	62.5	0.68	0.88	2.88	0.18	17.91	0.12	10.85	100
25-27-15	7.41	4.62	4.08	62.5	0.69	0.7	1.77	0.17	17.9	0.15	12.02	100
25-27-16	7.12	4.9	3.87	65.03	0.38	0.45	1.25	0.22	16.71	0.07	12.02	100
25-27-17	7.2	4.51	3.85	63.16	0.62	0.7	1.81	0.18	17.85	0.12	11.71	100
25-27-18	7.24	4.58	3.5	63.16	0.61	0.65	1.74	0.1	18.28	0.15	11.81	100
25-27-21	7.41	4.73	3.78	63.09	0.63	0.6	1.67	0.19	17.67	0.23	12.14	100
25-27-22	7.27	5.42	3.93	62.95	0.65	0.6	1.25	0.17	17.63	0.12	12.69	100
25-27-24	7.19	4.64	3.6	63.53	0.6	0.65	1.71	0.14	17.84	0.1	11.83	100
25-27-1	3.86	1.56	10	48.19	3.15	5.92	11.55	0.17	15.16	0.43	5.42	100
45-46-1	8.38	4.93	4.63	64.71	0.26	0.1	0.53	0.25	16.19	0.04	13.31	100
45-46-2	7.95	4.15	2.91	63.23	0.49	0.41	1.75	0.08	18.96	0.07	12.09	100
45-46-3	7.41	3.84	4.1	63	0.77	0.67	2.07	0.16	17.83	0.15	11.25	100
45-46-4	7.11	4.93	4	62.24	0.83	0.69	1.73	0.19	18.06	0.21	12.04	100
45-46-5	8.63	4.9	4.89	64.62	0.24	0.12	0.47	0.27	15.84	0.02	13.53	100
45-46-6	7.32	4.53	4.08	62.8	0.69	0.67	1.54	0.24	17.96	0.17	11.85	100
45-46-7	7.55	4.96	4.16	62.56	0.67	0.64	1.46	0.16	17.7	0.15	12.51	100
45-46-8	7.56	4.52	3.66	63.07	0.63	0.59	1.59	0.13	18.08	0.16	12.09	100
45-46-9	7.83	3.54	3.04	62.94	0.56	0.58	2.38	0.18	18.8	0.14	11.37	100
45-46-10	7.3	4.15	3.36	63.67	0.6	0.51	1.88	0.11	18.27	0.15	11.44	100
45-46-13	7.71	4.43	3.92	62.74	0.64	0.55	1.89	0.15	17.74	0.23	12.15	100
45-46-14	7.22	5.07	4.23	62.48	0.7	0.61	1.52	0.13	17.92	0.11	12.29	100
45-46-15	7.56	3.24	2.68	60.95	0.41	0.38	4.43	0.13	18.8	1.41	10.8	100
45-46-15	7.64	3.68	3.15	63.47	0.53	0.52	2.19	0.13	18.54	0.14	11.32	100
45-46-17	6.65	5.38	3.92	63.3	0.7	0.62	1.33	0.16	17.77	0.17	12.03	100
45-46-20	7.56	4.9	4.09	62.06	0.68	0.66	1.51	0.16	18.23	0.15	12.46	100
45-46-25	7.32	4.63	3.78	63.02	0.67	0.69	1.62	0.13	18.01	0.13	11.95	100
45-46-22	7.6	4.56	4.05	62.81	0.67	0.63	1.66	0.2	17.65	0.18	12.15	100
45-46-24	7.28	3.85	3.56	63.13	0.58	0.91	2.31	0.13	18.14	0.11	11.13	100
53-55-1	7.63	4.03	5.16	61.8	0.82	0.74	2.18	0.17	17.25	0.22	11.66	100
53-55-2	8.81	4.73	5.08	63.57	0.31	0.26	0.73	0.29	16.15	0.07	13.54	100
53-55-3	8.43	4.95	3.66	65	0.23	0.13	0.56	0.22	16.79	0.03	13.38	100
53-55-4	8.7	4.8	4.7	64.28	0.24	0.12	0.56	0.27	16.33	0	13.5	100
53-55-6	7.72	4.24	3.93	61.9	0.6	0.65	2.04	0.18	18.59	0.16	11.96	100
53-55-7	8.41	4.53	4.93	64.21	0.31	0.19	0.72	0.32	16.29	0.08	12.95	100

53-55-8	8.69	4.78	4.77	64.39	0.27	0.14	0.59	0.33	15.99	0.04	13.47	100
53-55-9	8.52	5	4.9	64.52	0.25	0.14	0.51	0.29	15.86	0.02	13.52	100
53-55-10	8.44	4.43	4.51	65.07	0.26	0.13	0.83	0.19	16.08	0.06	12.87	100
53-55-11	8.06	4.91	4.17	63.71	0.43	0.32	0.92	0.19	17.19	0.07	12.98	100
53-55-13	7.15	4.49	4.21	62.78	0.65	0.67	1.75	0.05	18.05	0.2	11.64	100
53-55-14	7.43	4.21	4.64	61.93	0.72	0.82	2.24	0.2	17.63	0.17	11.64	100
53-55-15	7.77	3.65	4.24	62.52	0.68	0.64	2.24	0.23	17.93	0.1	11.41	100
53-55-16	5.4	4.35	4	64.06	0.65	0.67	1.97	0.1	18.67	0.15	9.75	100
53-55-17	7.44	4.74	4.26	62.77	0.58	0.57	1.62	0.12	17.74	0.15	12.19	100
53-55-18	8.48	4.97	4.83	64.4	0.23	0.11	0.52	0.31	16.14	0.01	13.45	100
53-55-19	7.26	4.65	3.96	62.76	0.53	0.54	1.55	0.14	18.48	0.14	11.91	100
53-55-12	3.47	1.28	9.18	48.45	2.78	6.53	12.17	0.13	15.6	0.38	4.76	100
57-59-2	4.81	1.81	10.29	48.23	3.62	4.9	10.05	0.11	15.69	0.48	6.62	100
57-59-3	4.27	2.75	8.78	52.38	2.37	3.24	7.56	0.24	16.69	1.74	7.01	100
57-59-7	3.34	1.38	9.24	48.14	2.8	6.46	12.24	0.13	15.87	0.41	4.72	100
57-59-4	8.87	4.88	4.59	64.37	0.22	0.1	0.53	0.17	16.26	0	13.75	100
57-59-5	7.34	3.98	5.43	60.51	0.82	1.03	2.41	0.28	18	0.19	11.32	100
60-61-4	4.79	1.79	10.89	48	3.61	4.92	9.57	0.13	15.77	0.53	6.58	100
60-61-6	4.66	2.19	11.32	47.87	3.95	4.67	9.28	0.21	15.28	0.56	6.85	100
60-61-8	4.63	1.88	10.55	48.39	3.66	4.95	9.88	0.24	15.34	0.49	6.51	100
60-61-5	7.47	5.38	3.86	63.91	0.48	0.35	0.91	0.15	17.38	0.11	12.85	100
60-61-7	8.76	4.82	4.51	64.39	0.24	0.13	0.6	0.28	16.23	0.03	13.58	100
62-63-2	7.71	5.27	4.39	62.45	0.51	0.46	1.14	0.22	17.76	0.08	12.99	100
62-63-3	8.82	4.82	4.77	63.87	0.26	0.13	0.62	0.23	16.42	0.06	13.65	100
62-63-4	8.96	4.9	4.39	64.38	0.3	0.14	0.58	0.29	16.04	0.02	13.86	100
62-63-5	7.46	4.52	3.95	62.91	0.65	0.63	1.7	0.07	17.95	0.18	11.97	100
62-63-6	7.54	4.28	4.23	62.8	0.67	0.54	1.41	0.15	18.22	0.14	11.82	100
62-63-7	7.14	4.73	3.78	63.06	0.54	0.51	1.55	0.08	18.47	0.13	11.87	100
62-63-8	7.4	4.51	3.83	66.18	0.2	0.13	0.58	0.22	16.96	0	11.91	100
62-63-9	7.46	4.71	3.79	62.78	0.52	0.53	1.51	0.07	18.49	0.13	12.16	100
62-63-10	7.3	4.74	3.83	62.95	0.51	0.5	1.55	0.21	18.24	0.17	12.04	100
62-63-11	7.26	4.84	3.69	63.22	0.53	0.53	1.52	0.15	18.13	0.13	12.1	100
62-63-12	7.27	5.51	5.18	61.91	0.66	0.73	1.21	0.17	17.2	0.15	12.78	100
62-63-13	7.71	5.53	3.11	65.83	0.18	0.07	0.6	0.16	16.76	0.02	13.24	100
62-63-15	7.39	3.73	4.77	60.17	0.89	1.07	3.11	0.2	18.4	0.27	11.12	100
131-133-2	3.84	1.23	9.33	49.73	2.65	5.98	10.78	0.14	15.83	0.48	5.07	100
131-133-3	3.76	1.36	9.56	48.57	3	6.13	11.52	0.14	15.53	0.4	5.12	100
131-133-4	3.61	1.18	9.59	49.94	2.61	6.17	10.81	0.16	15.55	0.39	4.79	100
131-133-5	3.75	1.37	9.43	48.26	3.03	6.22	11.66	0.19	15.67	0.43	5.12	100
131-133-7	3.8	1.51	9.02	49.2	2.84	6.02	11.4	0.16	15.6	0.45	5.31	100
131-133-8	4.13	1.66	10.72	48.24	3.21	5.58	10.64	0.16	15.13	0.54	5.79	100
131-133-9	4.09	1.66	10.52	48.4	3.18	5.45	10.68	0.16	15.3	0.54	5.75	100
131-133-10	4.02	1.58	10.32	48.84	3.19	5.69	10.51	0.21	15.15	0.5	5.6	100
131-133-11	4.2	1.63	10.83	47.98	3.34	5.51	10.57	0.16	15.34	0.44	5.84	100
131-133-13	3.7	1.4	9.5	48.37	2.91	6.02	11.8	0.27	15.6	0.43	5.1	100

131-133-15	4.2	1.71	11	48.14	3.36	5.43	10.51	0.13	14.99	0.53	5.92	100
131-133-16	3.63	1.27	9.6	47.84	2.64	6.63	12.25	0.17	15.52	0.44	4.91	100
131-133-17	3.86	1.36	10.14	48.79	2.79	6.13	11.27	0.17	15.08	0.41	5.22	100
131-133-18	3.84	1.45	9.56	48.1	2.87	5.92	11.69	0.12	15.99	0.46	5.29	100
131-133-19	4.27	1.49	10.31	48.11	2.9	5.94	10.24	0.12	16.22	0.39	5.76	100
131-133-20	3.9	1.44	9.84	47.55	2.93	6.27	11.66	0.24	15.75	0.43	5.34	100
131-133-21	5.01	2.51	11.42	49.15	3.88	4.12	8.14	0.25	14.69	0.85	7.52	100
131-133-22	3.47	1.38	9.53	48.16	2.71	6.55	12.28	0.12	15.42	0.4	4.85	100
131-133-23	3.42	1.22	9.49	48.06	2.81	6.65	12.06	0.13	15.84	0.31	4.64	100
131-133-24	3.96	1.42	9.79	48.03	3.08	6.06	11.68	0.12	15.34	0.52	5.38	100
131-133-1	7.56	4.63	3.87	62.73	0.56	0.58	1.6	0.17	18.14	0.15	12.2	100
131-133-12	5.49	2.83	8.86	52.83	2.46	3.33	6.18	0.19	16.97	0.87	8.32	100
131-133-6	5.46	2.81	8.64	53.34	2.48	3.33	6.29	0.15	16.73	0.76	8.27	100
172-174-1	4.56	1.64	9.25	49.02	2.99	5.3	9.76	0.14	16.72	0.63	6.2	100
172-174-2	4.05	1.41	9.08	48.93	2.62	6.05	11.55	0.15	15.75	0.4	5.46	100
172-174-3	4.75	1.88	10.28	48.4	2.97	5.08	9.92	0.19	15.91	0.62	6.63	100
172-174-4	4.37	1.86	10.24	48.81	3	5.16	10	0.2	15.82	0.54	6.23	100
172-174-5	4.28	1.85	10.17	48.76	2.97	5.22	10.07	0.16	16.03	0.48	6.13	100
172-174-6	4.82	2	10.78	48.49	3.3	4.71	9.5	0.14	15.66	0.59	6.82	100
172-174-7	4.39	1.67	10.97	48.77	3.32	5.09	9.84	0.2	15.23	0.51	6.07	100
172-174-8	3.88	1.39	9.66	48.15	3.01	5.92	11.55	0.2	15.81	0.44	5.27	100
172-174-9	4.58	1.81	10.37	48.75	2.99	5.18	10.01	0.21	15.62	0.48	6.39	100
172-174-10	5.41	0.96	9.82	48.91	2.93	6.19	9.32	0.23	15.81	0.42	6.37	100
172-174-11	4.88	2.19	10.55	49.03	3.41	4.33	9.03	0.21	15.69	0.68	7.06	100
172-174-12	4.18	1.87	10.41	48.82	3	5.09	10.04	0.19	15.88	0.5	6.05	100
172-174-13	3.52	1.17	9.72	49.99	2.59	6.05	10.68	0.19	15.74	0.36	4.69	100
172-174-14	4.98	2.11	10.84	48.58	3.27	4.53	9.3	0.23	15.51	0.64	7.09	100
172-174-15	4.55	1.62	11.38	47.45	3.29	5.18	10.64	0.24	15.09	0.55	6.17	100
172-174-16	4.07	1.44	9.66	49.31	2.84	5.43	10.12	0.15	16.51	0.48	5.51	100
172-174-18	3.96	1.52	9.54	49.17	2.72	5.83	11.07	0.1	15.62	0.44	5.49	100
172-174-19	4.06	1.49	9.74	48.85	2.71	5.74	11.16	0.16	15.61	0.49	5.55	100
206-208-1	3.37	1.3	9.06	48.74	2.57	6.61	12.23	0.17	15.61	0.34	4.67	100
206-208-3	4.47	1.58	10.78	48.66	3.16	5.26	9.99	0.24	15.31	0.55	6.05	100
206-208-4	3.73	1.6	11.94	46.62	2.77	11.15	8.19	0.22	13.19	0.58	5.34	100
206-208-5	4.18	1.69	10.72	48.55	3.31	5.34	9.93	0.14	15.59	0.55	5.87	100
206-208-6	4.17	1.44	9.98	48.36	2.86	5.73	10.35	0.19	16.36	0.54	5.61	100
206-208-7	3.75	1.3	9.94	47.43	3.07	6.45	11.78	0.23	15.65	0.41	5.05	100
206-208-8	4.05	1.44	9.42	48.48	2.96	6.13	11.03	0.17	15.76	0.55	5.49	100
206-208-9	3.94	1.98	10.29	48.05	3.53	5.36	10.99	0.14	15.2	0.54	5.92	100
206-208-11	5.33	2.25	10.97	49.01	3.4	6.1	6.5	0.22	15.75	0.47	7.58	100
206-208-12	4.35	1.93	10.46	48.71	3.5	5.11	9.88	0.17	15.33	0.57	6.28	100
206-208-13	4.16	1.64	10.78	48.84	3.14	5.08	10.31	0.19	15.31	0.56	5.8	100
206-208-14	4.2	1.61	10.24	49.21	3.24	5.15	10.02	0.17	15.58	0.58	5.82	100
206-208-15	3.58	1.24	10.13	48.35	2.87	6.32	11.69	0.18	15.23	0.4	4.82	100
206-208-16	3.74	1.42	9.75	49.48	2.75	5.91	10.68	0.12	15.76	0.38	5.16	100

206-208-17	4.59	1.87	10.07	49.56	3.21	4.82	9.18	0.2	15.82	0.68	6.46	100
206-208-18	3.9	1.65	10.04	49.19	3.08	5.43	10.65	0.13	15.46	0.47	5.55	100
206-208-20	3.84	1.22	9.61	50.13	2.51	6.04	10.62	0.15	15.51	0.38	5.06	100
206-208-21	4.37	1.68	10.91	48.93	3.28	5.1	9.96	0.21	15.01	0.56	6.06	100
206-208-23	3.51	1.28	9.23	48.77	2.69	6.36	12.32	0.17	15.3	0.36	4.79	100
206-208-24	4.1	1.72	11.4	47.67	3.81	5.22	10.6	0.17	14.81	0.5	5.83	100
206-208-25	3.72	1.4	9.11	49.8	2.72	6.37	10.6	0.19	15.67	0.41	5.13	100
206-208-22	7.82	4.9	3.82	63.58	0.44	0.36	1.22	0.18	17.6	0.05	12.72	100
206-208-19	7.28	5.3	4.5	63.24	0.51	0.46	1.08	0.15	17.4	0.04	12.58	100
206-208-10	7.08	3.85	5.5	58.09	1.37	1.67	3.57	0.17	18.24	0.46	10.92	100
206-208-2	6.89	3.66	6.17	57.95	1.31	1.76	3.7	0.19	18.03	0.34	10.55	100
233-235-2	4.02	1.61	10.54	48.71	3.07	5.51	10.73	0.23	15.18	0.39	5.63	100
233-235-3	4.12	1.49	9.97	48.99	2.9	5.61	10.21	0.15	16.07	0.49	5.61	100
233-235-5	3.5	1.22	9.95	48.17	2.85	6.74	12.46	0.1	14.64	0.38	4.71	100
233-235-7	3.22	1.15	10.22	47.62	3.05	6.72	11.35	0.05	16.23	0.39	4.36	100
233-235-8	4.47	2.27	13.69	46.76	2.17	12.78	4.19	0.27	12.57	0.81	6.74	100
233-235-1	6.93	3.69	5.57	58.69	1.39	1.71	3.69	0.08	17.83	0.4	10.62	100
233-235-4	7	3.82	5.77	58.17	1.48	1.8	3.6	0.15	17.82	0.39	10.82	100
233-235-6	6.78	3.63	5.78	58.15	1.46	1.79	3.64	0.21	18.06	0.51	10.41	100
233-235-9	7.73	5.11	3.9	62.87	0.48	0.34	1.2	0.13	18.14	0.09	12.85	100
233-235-10	7.42	5.51	5.67	62.73	0.62	0.64	1.15	0.23	15.88	0.13	12.93	100
255-256-3	6.7	3.84	7.5	55.72	2.14	1.97	4.67	0.34	16.57	0.55	10.54	100
255-256-2	5.74	2.79	8.66	51.87	2.58	3.34	7.1	0.19	16.46	1.26	8.52	100
255-256-4	5.56	2.65	8.99	52.33	2.5	3.44	6.78	0.26	16.6	0.88	8.22	100
255-256-6	7.35	5.88	2.93	64.28	0.56	0.36	0.85	0.29	17.45	0.05	13.23	100
255-256-7	8.25	4.97	2.83	65.35	0.13	0.04	0.73	0.14	17.55	0.01	13.22	100
284-285-11	6.05	2.96	6.21	59.27	1.4	1.46	4.48	0.17	17.56	0.42	9.02	100
284-285-5	5.91	2.7	7.89	56.68	1.51	2.29	5.06	0.16	17.22	0.57	8.61	100
284-285-15	6.06	2.19	7.09	56.82	1.37	1.83	5.61	0.17	18.4	0.47	8.25	100
284-285-19	6.09	2.94	8.19	56.89	1.56	2.3	4.84	0.29	16.36	0.53	9.03	100
284-285-1	5.75	2.31	5.76	54.75	1.59	1.59	7.88	0.14	19.48	0.75	8.06	100
284-285-2	4.87	2	9.38	52.42	2.53	3.4	7.4	0.23	16.97	0.79	6.87	100
284-285-18	5.26	2.04	10.13	52.41	2.77	3.14	7.37	0.27	15.67	0.94	7.3	100
284-285-8	5.68	2.71	8.75	53.18	2.45	3.34	6.15	0.22	16.76	0.77	8.39	100
284-285-17	3.49	1.03	10.2	47.87	2.71	6.13	12.63	0.14	15.44	0.36	4.52	100
284-285-13	3.76	1.46	11.91	48.31	3.76	5.3	9.94	0.21	14.82	0.53	5.23	100
284-285-14	3.72	1.31	9.93	47.87	3.08	6.14	10.96	0.23	16.35	0.43	5.03	100
284-285-6	3.83	1.47	11.79	46.73	4.03	5.57	10.88	0.17	14.98	0.55	5.31	100
284-285-16	3.11	1.12	10.51	48.33	2.85	6.88	12.59	0.17	14.04	0.4	4.23	100
314-316-1	3.97	1.44	9.74	48.69	2.87	6.02	11.13	0.1	15.56	0.48	5.41	100
314-316-2	3.87	1.34	10.37	48.43	3.37	6.33	9.82	0.11	15.9	0.47	5.2	100
314-316-3	3.73	1.33	9.4	48.7	3.07	6.16	11.8	0.08	15.31	0.41	5.06	100
314-316-4	3.59	1.23	10.23	48.67	2.89	6.29	11.28	0.13	15.29	0.4	4.81	100
314-316-5	3.77	1.44	11.41	47.51	3.26	5.63	11.35	0.15	15.01	0.48	5.21	100
314-316-6	3.56	1.32	9.99	48.68	3.28	5.9	11.41	0.07	15.33	0.46	4.89	100

314-316-7	4.1	1.58	9.96	48.33	3.13	5.88	10.73	0.21	15.61	0.46	5.68	100
314-316-8	3.44	1.03	9.57	48.63	2.73	6.59	11.64	0.21	15.77	0.38	4.46	100
314-316-9	4.12	1.42	10.14	48.3	2.94	5.77	10.26	0.25	16.3	0.5	5.55	100
314-316-11	3.62	1.07	10.57	48.12	2.85	5.93	12.15	0.14	15.23	0.29	4.69	100
314-316-12	3.88	1.32	10.73	48.29	3.1	5.65	10.72	0.14	15.78	0.37	5.2	100
314-316-13	3.83	1.41	10.68	47.75	3.29	5.78	11.24	0.18	15.41	0.43	5.24	100
314-316-14	3.7	1.2	9.97	48.46	3.02	5.94	11.47	0.14	15.74	0.36	4.91	100
314-316-15	3.48	0.91	10.84	48.34	2.45	6.54	12.38	0.16	14.59	0.31	4.38	100
314-316-17	2.77	1.46	11.95	50.73	4.09	4.52	7.81	0.21	15.84	0.63	4.23	100
461-463-3	7.56	5.46	6.2	58.37	1.59	1.26	1.78	0.23	17.03	0.52	13.02	100
461-463-2	7.35	6.06	2.93	64.37	0.48	0.26	0.9	0.09	17.51	0.06	13.41	100
461-463-11	7.08	5.99	3.3	64.22	0.49	0.29	0.93	0.22	17.43	0.05	13.07	100
461-463-13	8.01	5.15	3.62	64.55	0.32	0.16	0.73	0.31	17.11	0.06	13.16	100
461-463-14	7.33	5.83	2.98	64.41	0.48	0.3	0.93	0.16	17.54	0.04	13.16	100
461-463-21	7.04	6.06	3.01	64.48	0.47	0.27	0.85	0.14	17.66	0.02	13.11	100
461-463-22	7.16	5.97	3.04	64.45	0.51	0.28	0.9	0.16	17.47	0.07	13.13	100
461-463-23	7.33	5.9	3.16	64.17	0.48	0.28	0.93	0.22	17.47	0.05	13.23	100
461-463-27	7.26	5.92	3.08	64.57	0.47	0.26	0.96	0.17	17.24	0.06	13.18	100
461-463-4	4.21	1.44	10.27	47.91	3.11	5.63	10.64	0.13	16.18	0.49	5.65	100
461-463-7	3.37	1.18	10.1	48.06	2.7	7.02	13.04	0.19	13.94	0.4	4.55	100
461-463-15	3.89	1.4	9.97	48.37	3.07	5.84	10.61	0.13	16.27	0.44	5.29	100
461-463-18	5.36	2.66	9.94	50.99	2.96	3.7	6.9	0.23	16.44	0.81	8.01	100
461-463-24	3.62	1.14	9.61	48.82	2.82	6	11.7	0.14	15.72	0.43	4.76	100
1226												
3-4-1		0.94	12.54	46.87		5.69	11.07					
3-4-2		0.8	9.28	47.62		6.91	12.57					
3-4-3		1.15	10.11	47.45		6.18	12.1					
3-4-4		0.98	10.59	45.47		8.79	11.34					
3-4-5		0.7	11.97	46.92		6.65	13.02					
3-4-6		1	10.81	46.75		6.4	11.62					
3-4-7		0.71	12.51	45.46		6.95	13.27					
3-4-9		0.9	12.04	46.38		6.16	11.78					
3-4-10		0.85	11.31	46.56		6.44	11.77					
3-4-11		0.99	10.28	46.25		6.82	12.81					
3-4-12		0.86	11.36	46.51		6.5	11.95					
3-4-14		1.19	11.28	45.07		6.32	11.84					
3-4-15		1.1	11.94	46.61		5.73	11.39					
3-4-13		0.98	13.74	45.05		5.75	11.92					
14-15-1		0.9	10.97	47.34		6.39	11.95					
14-15-2		1	12.61	47		5.52	11.12					
14-15-4		0.75	11.51	47.03		5.02	11.26					
14-15-5		0.81	11.4	46.25		5.8	12.45					
14-15-6		0.92	11.65	46.67		6.6	12.05					
14-15-7		1.01	12.98	45.8		5.54	11.38					
14-15-8		0.99	12.7	47.25		5.41	11.1					

14-15-9		1.15	11.51	47.41		5.62	11.03					
14-15-10		0.86	11.18	46.55		6.59	12.2					
14-15-11		1.02	10.02	47.2		6.4	12.08					
14-15-13		1.11	9.84	47.26		6.15	12.53					
14-15-15		0.91	12.51	47.68		5.18	10.74					
14-15-3		0.89	9.32	47.02		7.01	13.35					
21-22-8		0.8	9.47	48.25		6.84	12.52					
21-22-12		0.92	9.79	48.24		6.24	12.02					
21-22-4		0.75	9.92	48.37		6.84	12.37					
21-22-15		0.79	10.15	48.02		5.61	12.16					
21-22-9		0.86	10.29	47.84		6.45	12.48					
21-22-3		0.91	10.57	47.84		6.23	11.67					
21-22-13		0.8	10.74	47.53		6.92	12.05					
21-22-5		0.86	10.86	47.6		6.44	11.78					
21-22-11		0.68	11.22	47.84		6.72	12.86					
21-22-10		0.94	12.48	46.5		5.97	11.25					
21-22-2		1.03	12.71	47.03		5.55	11.12					
21-22-14		0.98	12.79	47.22		5.56	11.26					
21-22-1		0.88	12.84	48		5.38	10.57					
22-23-1		0.88	11.8	46.97		6.35	11.86					
22-23-2		0.95	10.03	47.04		6.54	11.88					
22-23-3		0.84	10.59	47.8		6.63	12.75					
22-23-4		0.96	11.65	45.84		6.52	12.07					
22-23-5		0.86	10.24	46.85		6.59	12.7					
22-23-6		0.86	10.97	47.67		6.47	11.8					
22-23-7		0.9	10.34	45.25		6.97	12.96					
22-23-11		0.95	10.28	46.87		6.38	12.34					
22-23-12		0.86	11.24	46.22		6.31	12.33					
22-23-13		0.77	9.71	48.63		6.75	12.01					
22-23-14		0.87	11.51	46.55		6.5	12.09					
22-23-15		1.06	11.98	45.75		6.18	12.13					
23-24-8		0.72	9.84	46.54		4.96	12.41					
23-24-9		0.91	9.86	47.12		6.6	12.36					
23-24-1		1.33	9.93	47.02		5.82	11.57					
23-24-2		0.95	12.38	45.73		6.12	11.59					
23-24-3		1.01	10.71	47.92		5.8	11.45					
23-24-4		0.98	12.69	48.34		5.22	10.7					
23-24-5		1.09	10.26	46		6.31	12.47					
23-24-7		0.93	12.49	47.11		5.81	11.34					
23-24-10		0.85	11.03	46.61		6.56	12.15					
23-24-11		0.92	12.41	45.78		6.1	11.28					
23-24-12		0.67	11.56	45.63		7.28	13.46					
23-24-13		0.83	10.99	47.62		6.13	12.02					
23-24-14		1.21	11.89	47.38		5.37	10.29					
23-24-15		0.87	10.03	46.43		6.94	12.65					

28-30-1		0.74	9.59	48.12		6.66	12.54						
28-30-2		0.73	9.83	48.14		6.78	12.39						
28-30-3		0.92	12.11	47.59		5.53	11.45						
28-30-4		1.06	11.35	47.94		6	11.85						
28-30-5		0.85	11.17	47.89		6.12	11.66						
28-30-6		0.83	11.57	48.07		6.02	11.44						
28-30-7		0.88	11.21	48.06		6.33	11.75						
28-30-8		0.79	9.44	48.48		6.49	12.5						
28-30-10		0.96	12.84	46.95		5.37	10.97						
28-30-11		1.02	11.48	47.63		5.59	11.85						
28-30-12		0.78	9.66	48.41		6.6	12.44						
28-30-13		0.73	10.03	48.14		6.76	12.4						
28-30-15		1.01	11.22	47.73		5.59	11.74						
50-51-11		0.86	9.2	48.17		6.94	13.21						
50-51-2		0.8	9.21	48.93		6.7	12.01						
50-51-8		0.82	9.34	48.82		6.78	12.56						
50-51-4		0.77	9.55	48.68		6.65	12.39						
50-51-7		0.87	9.71	47.44		6.96	13.28						
50-51-3		0.84	9.81	48.39		6.5	12.09						
50-51-10		1.18	11.64	48.23		5.09	10.45						
50-51-9		1.16	11.79	48.28		4.94	10.43						
50-51-12		1.21	11.95	48.48		4.94	10.32						
50-51-6		0.97	13.56	46.6		5.28	11.43						
94-96-1		0.9	10.42	48.02		6.11	12.24						
94-96-2		0.85	10.35	47.86		6.12	12.27						
94-96-3		0.84	8.88	48.54		6.66	12.61						
94-96-4		1.1	10.45	48.09		5.93	11.26						
94-96-5		0.94	10.03	48.94		6.14	12.6						
94-96-6		0.86	9.44	48.66		6.51	12.32						
94-96-7		0.73	10.13	47.61		6.8	12.17						
94-96-8		0.84	8.8	49.17		4.95	11.66						
94-96-9		0.81	10.5	47.5		6.68	11.72						
94-96-10		1	10.66	47.22		6.03	12.06						
94-96-11		1.12	10.21	47.19		6.14	11.63						
94-96-12		0.85	9.83	47.67		6.64	12.29						
94-96-13		0.94	11.22	47.67		5.99	11.66						
94-96-14		0.92	9.95	47.55		6.69	12.07						
94-96-15		1.01	10.21	46.57		6.84	13.01						
110-112-1		0.87	9.99	49.28		5.41	12.79						
110-112-2		0.86	11.52	48.37		5.4	11.67						
110-112-4		0.8	10.01	48.1		6.65	12.61						
110-112-5		0.97	10.8	48.08		6.01	12.04						
110-112-6		0.88	9.37	48.05		6.65	13.17						
110-112-7		0.93	10.34	47.94		6.05	12.05						
110-112-8		1.05	10.51	48.89		5.73	11.3						

110-112-10		0.98	10.19	49.17		5.92	11.65					
110-112-11		0.83	8.98	49.05		6.53	12.66					
110-112-12		0.79	9.96	48.65		6.2	12.27					
110-112-13		0.8	8.99	48.42		6.85	12.74					
110-112-14		0.9	10.54	48.49		6.1	12.18					
110-112-15		1	10.84	48.48		5.94	11.45					
110-112-9		0.85	13.26	46.54		5.78	11.69					
110-112-3		0.95	13.5	46.27		5.36	11.33					
137-139-1		0.81	11.02	47.31		6.24	11.83					
137-139-2		0.89	10.19	48.55		6.32	12.26					
137-139-3		0.81	9.94	48.1		6.46	12.75					
137-139-4		1.06	11.55	47.58		5.55	11.4					
137-139-5		1.17	11.61	47.72		5.02	10.55					
137-139-6		0.89	10	48.34		6.45	12.26					
137-139-7		0.95	9.2	49.64		6.03	11.95					
137-139-8		1.02	9.84	48.34		6	12.29					
137-139-9		0.87	9.84	48.01		6.6	12.18					
137-139-10		0.94	11.06	47.78		4.96	11.32					
137-139-11		1.11	9.78	47.59		5.97	12.4					
137-139-12		1.08	9.31	48.31		6.38	11.96					
137-139-13		0.91	10.1	47.58		6.65	12.02					
137-139-14		1.11	11.67	47.78		5.3	11.07					
137-139-15		1	12.02	46.6		5.69	11.65					
144-145-1		1.37	9.64	47.23		6.28	11.53					
144-145-3		1.27	10.49	47.3		5.86	11.48					
144-145-4		1	10.34	47.14		6.58	12.7					
144-145-6		1.17	9.88	45.27		6.87	12.39					
144-145-7		1.08	9.63	47.5		6.28	11.56					
144-145-8		1.01	10.54	45.9		6.81	11.99					
144-145-10		1.08	10.11	45.89		6.4	11.88					
144-145-11		0.97	11.08	46.42		6.36	12.01					
144-145-12		0.74	10.55	47.38		6.89	12.67					
144-145-14		0.84	11.65	46.12		6.19	11.57					
144-145-15		1.38	9.98	47.83		6.03	10.9					
159-160-1		0.81	10.53	47.27		6.86	11.73					
159-160-2		0.84	11.07	47.03		6.83	11.58					
159-160-3		0.91	9.36	47.67		6.48	11.96					
159-160-4		0.9	10.32	46.97		6.74	12.23					
159-160-5		0.93	10.33	47.74		6.49	11.64					
159-160-6		1.06	10.95	47.04		6.17	12.18					
159-160-7		0.93	9.72	46.56		7.04	12.52					
159-160-8		0.85	10.14	48.99		6.52	12.28					
159-160-9		0.86	10.27	47.73		6.77	12.34					
159-160-10		0.82	11.13	45.29		6.92	12.62					
159-160-11		0.96	10.04	47.49		6.67	12.25					

159-160-12		0.92	9.83	47.58		6.47	11.72						
159-160-13		1.19	10	46.07		6.2	12.18						
159-160-14		0.97	10.02	48.46		6.61	11.84						
159-160-15		0.88	9.78	48.27		6.7	12.62						
170-172-9		1.01	10.17	47.39		6.34	12.29						
170-172-6		1.13	10.41	46.19		5.52	11.8						
170-172-8		0.78	10.49	47.04		6.93	13.02						
170-172-13		0.99	10.71	46.52		6.37	12.82						
170-172-4		1.59	11.57	46.39		5.22	10.97						
170-172-14		0.87	11.9	47.4		6.22	11.47						
170-172-1		0.87	12.33	47.29		6	11.7						
170-172-5		0.96	13.22	46.51		5.61	11.65						
170-172-12		0.88	13.23	45.44		6.38	11.89						
170-172-15		0.9	13.37	46.11		5.69	11.51						
170-172-11		1	14.28	45.39		5.28	11.58						
170-172-3		0.93	14.35	44.74		5.62	11.66						
170-172-2		0.97	14.52	44.61		6.4	11.2						
174-175-9		0.91	9.68	48.64		6.62	12.66						
174-175-4		0.91	9.87	49.38		6.23	11.96						
174-175-12		0.74	9.91	48.5		6.41	12.52						
174-175-5		0.87	10.21	46.81		6.87	12.85						
174-175-13		0.86	10.27	48.46		6.29	12.11						
174-175-8		0.81	11.07	46.77		5.35	12.12						
174-175-14		0.71	11.34	47.1		4.69	12.01						
174-175-7		1.14	11.61	47.92		5.65	10.98						
174-175-15		0.84	12.72	46.1		6.07	12.01						
174-175-6		0.85	13.68	45.99		5.62	11.66						
174-175-3		0.9	13.72	45.4		5.77	11.69						
174-175-1		0.88	13.87	44.8		5.89	11.87						
174-175-10		0.89	13.87	45.51		5.77	11.93						
174-175-2		0.91	13.88	45.48		5.7	11.5						
177-178-13		0.91	9.16	48.23		6.77	12.58						
177-178-3		0.9	9.38	47.73		6.74	12.95						
177-178-12		0.87	9.42	48.14		7.07	13.32						
177-178-6		1.05	9.91	46.99		6.54	12.72						
177-178-2		0.75	10.08	48.73		6.46	12.28						
177-178-1		1.07	10.19	46.76		6.43	12.53						
177-178-8		0.86	10.29	48.34		6.96	12.71						
177-178-4		0.66	10.73	46.49		7.12	12.76						
177-178-7		0.87	10.83	47.82		6.36	11.96						
177-178-11		0.87	10.89	46.67		6.77	12.38						
177-178-9		0.84	12.38	46.49		5.33	11.79						
177-178-15		0.87	13.18	46.23		5.72	11.76						
177-178-5		0.88	13.54	46.01		5.71	11.59						
177-178-10		0.65	9.63	50.15		6.87	12.54						

196-198-1		0.97	11.28	48.34		5.95	11.6					
196-198-2		0.71	10.3	48.17		6.67	12.64					
196-198-3		1.03	10.12	47.3		6.59	12.23					
196-198-4		0.84	12.49	47.18		5.12	11.54					
196-198-5		0.88	11.85	47.67		6.09	11.26					
196-198-6		0.85	10.81	46.98		6.83	11.63					
196-198-7		1.37	10.43	47.44		5.62	11.45					
196-198-9		1.31	10.22	47.77		5.58	11.44					
196-198-10		0.91	10.29	47.79		6.12	12.72					
196-198-11		1.08	9.49	48.09		6.62	11.96					
196-198-12		0.85	11.56	47.58		6.33	11.48					
196-198-13		0.87	11.71	47.54		6.11	11.51					
196-198-14		1.07	9.55	47.61		6.05	12.34					
196-198-15		1	9.37	48.6		6.67	12.39					
204-206-8		1	12.63	44.83		5.98	11.79					
204-206-14		0.83	11.88	45.66		6.56	11.8					
204-206-9		1.33	10.52	45.96		5.97	11.61					
204-206-12		0.84	11.61	46.69		6.47	11.8					
204-206-11		1.12	10.09	46.99		6.27	12.27					
204-206-10		1.25	9.4	47.53		5.92	11.75					
204-206-7		1.35	10.89	47.71		5.56	11.35					
204-206-15		0.91	10.25	48.23		6.45	11.88					
196-198-1		0.97	11.28	48.34		5.95	11.6					
196-198-2		0.71	10.3	48.17		6.67	12.64					
196-198-3		1.03	10.12	47.3		6.59	12.23					
196-198-4		0.84	12.49	47.18		5.12	11.54					
196-198-5		0.88	11.85	47.67		6.09	11.26					
196-198-6		0.85	10.81	46.98		6.83	11.63					
196-198-7		1.37	10.43	47.44		5.62	11.45					
196-198-9		1.31	10.22	47.77		5.58	11.44					
196-198-10		0.91	10.29	47.79		6.12	12.72					
196-198-11		1.08	9.49	48.09		6.62	11.96					
196-198-12		0.85	11.56	47.58		6.33	11.48					
196-198-13		0.87	11.71	47.54		6.11	11.51					
196-198-14		1.07	9.55	47.61		6.05	12.34					
196-198-15		1	9.37	48.6		6.67	12.39					
204-206-8		1	12.63	44.83		5.98	11.79					
204-206-14		0.83	11.88	45.66		6.56	11.8					
204-206-9		1.33	10.52	45.96		5.97	11.61					
204-206-12		0.84	11.61	46.69		6.47	11.8					
204-206-11		1.12	10.09	46.99		6.27	12.27					
204-206-10		1.25	9.4	47.53		5.92	11.75					
204-206-7		1.35	10.89	47.71		5.56	11.35					
204-206-15		0.91	10.25	48.23		6.45	11.88					
1230												

23-24-17	3.4	0.91	10.4	47	3.37	6.74	12.29	0.25	15.32	0.32	4.31	100
23-24-5	3.11	0.71	10.96	46.42	3.59	7	12.41	0.16	15.39	0.26	3.82	100
23-24-6	3.25	0.78	11.24	47.15	3.4	7.13	11.91	0.15	14.72	0.28	4.03	100
23-24-3	8.05	4.58	6.92	67.12	0.45	0.13	0.5	0.27	11.94	0.03	12.64	100
23-24-4	7.35	4.84	3.76	67.72	0.21	0.04	0.67	0.11	15.25	0.04	12.2	100
23-24-8	7.54	4.95	5.01	64.62	0.53	0.35	1.01	0.19	15.74	0.05	12.49	100
23-24-9	7.18	4.24	3.95	66.65	0.41	0.24	1.17	0.12	15.98	0.04	11.43	100
23-24-10	7.4	4.78	5.95	66.52	0.51	0.26	0.66	0.33	13.56	0.03	12.18	100
23-24-11	7.8	4.79	5.97	66.15	0.52	0.22	0.65	0.34	13.52	0.04	12.59	100
23-24-12	7.99	4.82	5.88	64.39	0.56	0.26	0.85	0.29	14.9	0.05	12.82	100
23-24-13	8.05	4.83	5.81	64.59	0.54	0.27	0.86	0.16	14.84	0.05	12.88	100
23-24-14	7.54	4.96	4.46	64.94	0.65	0.46	0.81	0.13	15.97	0.09	12.5	100
23-24-15	8.39	4.28	6.78	68.36	0.35	0.05	0.38	0.22	11.18	0.01	12.67	100
23-24-16	6.86	4.62	3.75	68.22	0.28	0.09	0.72	0.23	15.21	0.02	11.48	100
55-59-1	7.14	5.01	5.01	66.51	0.39	0.34	0.67	0.26	14.66	0.02	12.15	100
55-59-6	7.68	4.9	6.27	66.2	0.62	0.34	0.58	0.35	13.03	0.05	12.58	100
55-59-7	7.29	4.9	4.59	66.79	0.55	0.35	0.62	0.19	14.67	0.03	12.2	100
55-59-14	7.52	4.8	6.5	67.11	0.47	0.25	0.5	0.26	12.54	0.04	12.32	100
55-59-17	7.4	5.05	4.88	65.82	0.52	0.36	0.7	0.26	14.96	0.05	12.44	100
55-59-22	7.54	5.07	5.01	66.5	0.44	0.24	0.56	0.27	14.32	0.03	12.61	100
55-59-23	7.42	4.87	5.33	64.95	0.61	0.4	0.86	0.27	15.23	0.06	12.3	100
55-59-25	8.2	4.71	6.31	65.42	0.53	0.23	0.53	0.25	13.77	0.06	12.91	100
55-59-26	7.76	5.14	5.18	64.74	0.57	0.34	0.69	0.29	15.22	0.07	12.89	100
55-59-8	7.66	4.93	4.81	66.44	0.41	0.28	0.52	0.15	14.76	0.05	12.59	100
55-59-27	7.24	5	4.21	65.96	0.51	0.38	0.83	0.19	15.63	0.06	12.24	100
55-59-4	3.19	0.79	11.81	46.9	3.56	6.75	11.58	0.14	14.93	0.35	3.98	100
55-59-5	4.21	1.6	12.47	48.3	4.23	4.61	9.25	0.19	14.46	0.67	5.81	100
55-59-9	2.88	0.81	10.99	47.46	2.99	6.87	12.57	0.21	14.88	0.33	3.69	100
55-59-10	3.07	0.91	10.5	47.22	3.28	6.89	12.31	0.18	15.25	0.38	3.98	100
55-59-11	2.99	0.86	11.55	47.39	3.91	6.48	11.68	0.11	14.68	0.33	3.85	100
55-59-13	4.24	1.59	12.17	48.2	4.25	4.57	9.21	0.24	14.8	0.73	5.83	100
55-59-15	2.88	0.84	11.31	47.64	3.72	6.83	11.66	0.19	14.58	0.36	3.73	100
55-59-16	4.57	1.68	11.21	51.82	3.03	3.89	7.72	0.26	14.71	1.12	6.25	100
55-59-19	4.49	1.64	11.72	49.54	3.77	4.4	8.8	0.15	14.68	0.8	6.13	100
55-59-20	3.26	1	10.11	47.48	3.22	6.75	12.05	0.18	15.61	0.33	4.26	100
55-59-21	2.79	0.8	10.98	47.44	3.34	7.2	12.05	0.22	14.84	0.33	3.59	100
55-59-24	3.05	0.87	11.53	47.37	3.72	6.71	11.6	0.13	14.7	0.33	3.92	100
55-59-28	2.74	0.61	11.27	46.66	3.29	7.42	12.94	0.15	14.61	0.3	3.36	100
55-59-29	3.1	0.86	12.14	46.8	3.7	6.55	11.64	0.17	14.71	0.33	3.95	100
64-66-2	7.2	5	4.8	66	0.6	0.4	0.6	0.2	15.2	0.1	12.17	100
64-66-3	7.1	4.9	4.8	67	0.5	0.2	0.5	0.3	14.7	0	12.03	100
64-66-4	7.5	5	4.8	65.7	0.6	0.4	0.6	0.2	15.2	0	12.52	100
64-66-5	7.4	4.9	5.2	65.9	0.5	0.4	0.6	0.2	14.9	0.1	12.31	100
64-66-6	7.3	5	4.6	65.8	0.5	0.4	0.7	0.2	15.4	0.1	12.3	100
64-66-7	7.2	5	4.7	66	0.5	0.3	0.7	0.2	15.2	0.1	12.16	100

64-66-8	6.9	5	4.8	66.6	0.5	0.4	0.6	0.2	14.9	0.1	11.86	100
64-66-10	6.8	5.2	4.8	66.2	0.6	0.4	0.7	0.2	15	0.1	11.96	100
64-66-11	7.2	5	5	66.4	0.5	0.3	0.6	0.2	14.7	0	12.23	100
64-66-12	7.3	4.8	5.1	67.1	0.5	0.2	0.5	0.3	14.2	0	12.12	100
64-66-15	7.2	4.8	4.1	66.2	0.6	0.4	0.7	0.2	15.7	0.1	12.02	100
64-66-17	7.4	4.7	5.8	67.2	0.4	0.2	0.5	0.3	13.5	0	12.08	100
64-66-18	7.3	4.6	4.2	65.9	0.5	0.3	0.8	0.2	16.1	0	11.93	100
64-66-19	7.3	4.7	5.2	65.1	0.5	0.3	0.9	0.3	15.6	0.1	12.03	100
64-66-20	7.8	4.9	4.1	65.4	0.4	0.2	0.7	0.1	16.2	0.1	12.75	100
64-66-21	7.5	4.8	5.3	65	0.5	0.3	1	0.2	15.3	0.1	12.33	100
64-66-22	7.4	5	2.5	66.2	0.2	0.1	0.8	0.1	17.6	0	12.36	100
64-66-23	7.1	5.4	4.2	66	0.5	0.3	0.7	0.2	15.6	0	12.46	100
64-66-25	7.2	4.9	4.5	65.8	0.6	0.4	0.7	0.1	15.5	0.1	12.18	100
64-66-1	4	1.6	12.3	49.3	3.6	4.4	9.3	0.2	14.8	0.6	5.6	100
64-66-9	4.1	1.2	12.2	48.7	3.7	4.9	9.7	0.2	14.7	0.7	5.31	100
64-66-13	4.2	1.4	12.2	48.6	3.5	5	9.5	0.3	14.9	0.5	5.58	100
64-66-16	3.2	0.8	11.7	46.9	4	6.5	11.5	0.2	14.8	0.4	4.05	100
64-66-14	5.9	2.5	8.9	55.4	2.3	2.7	5.7	0.2	15.9	0.8	8.33	100
84-86-3	3.2	0.8	11.1	46.9	3.5	6.8	11.9	0.2	15.3	0.3	3.99	100
84-86-5	3	0.7	10.5	48.6	2.8	6.6	12.2	0.2	15.1	0.3	3.72	100
84-86-6	3.1	0.9	11.9	47.1	3.8	6.6	11.5	0.1	14.6	0.5	3.93	100
84-86-9	3	0.7	11.7	47.3	3.9	6.2	11.8	0.1	14.9	0.4	3.69	100
84-86-10	3.2	0.7	10.2	49.7	2.8	6.7	11.4	0.2	14.9	0.4	3.86	100
84-86-12	2.9	0.8	12.5	46.4	4.2	6.4	12	0.2	14.1	0.4	3.72	100
84-86-14	3.2	1	10.4	47.3	3.3	6.8	12.3	0.1	15.3	0.4	4.13	100
84-86-15	2.9	0.7	12	46.3	3.8	6.7	12.5	0.2	14.5	0.3	3.62	100
84-86-17	3.2	1	11	47.4	3.6	6.5	12.1	0.1	14.7	0.4	4.19	100
84-86-22	4.3	2.2	12.2	47.6	4.5	4.8	9.5	0.2	14.1	0.7	6.55	100
84-86-23	3.3	1	10.2	47.3	3.2	6.8	12.2	0.2	15.5	0.4	4.23	100
84-86-24	3.3	0.7	10.3	50.1	2.9	6.5	11	0.2	14.8	0.3	3.96	100
84-86-25	4	1.7	11.9	49.8	3.7	4.2	8.7	0.3	15	0.7	5.77	100
84-86-26	3.1	0.8	11.9	47.3	3.8	6.5	11.7	0.2	14.4	0.3	3.88	100
84-86-28	3.2	0.8	12	47.1	4	6.2	11.8	0.2	14.4	0.3	4.03	100
84-86-30	2.8	0.8	12	46.7	4.1	6.4	12	0.1	14.7	0.3	3.63	100
84-86-32	3.1	0.9	12.4	46.6	3.8	6.7	11.5	0.2	14.4	0.4	4.04	100
84-86-33	3	0.8	10.9	47.5	3.4	7.2	11.9	0.2	14.9	0.4	3.8	100
84-86-34	3.3	0.9	11.8	47.2	3.8	6.3	11.8	0.2	14.4	0.3	4.2	100
84-86-35	3	1	10.4	47.6	3.2	6.8	12.4	0.2	15.1	0.4	3.98	100
84-86-38	3	0.8	11.6	47.2	3.8	6.6	11.6	0.2	14.9	0.4	3.82	100
84-86-39	3.1	0.9	11.7	46.2	4.2	6.6	12.1	0.2	14.7	0.4	3.94	100
84-86-40	3	0.8	11.5	46.8	3.5	6.8	11.5	0.2	15.5	0.4	3.78	100
84-86-4	7.4	4.8	6.6	66.1	0.5	0.3	0.6	0.2	13.3	0.1	12.21	100
84-86-7	7.5	4.9	4.6	66.2	0.6	0.3	0.7	0.2	14.9	0	12.38	100
84-86-8	7.5	5	4.9	65.6	0.6	0.4	0.7	0.3	15	0	12.53	100
84-86-11	7.9	4.6	4.8	66.9	0.4	0.2	0.4	0.2	14.6	0	12.44	100

84-86-13	8.7	4.8	4.8	64	0.3	0.1	0.7	0.3	16.2	0	13.5	100
84-86-16	7.7	4.7	5.9	66.2	0.5	0.3	0.6	0.2	13.8	0.1	12.38	100
84-86-18	6.8	5	4.9	66.7	0.6	0.3	0.7	0.2	14.6	0.1	11.85	100
84-86-19	7.2	5	4.9	66.1	0.5	0.3	0.7	0.3	14.9	0.1	12.19	100
84-86-20	6.6	4.9	3.9	68.4	0.2	0	0.7	0.1	15	0	11.51	100
84-86-21	6.7	4.9	3.7	68.3	0.3	0.1	0.7	0.1	15.2	0	11.64	100
84-86-31	6.9	5	4.8	66.4	0.6	0.4	0.7	0.2	15	0.1	11.88	100
84-86-37	7.4	4.9	4.8	66.1	0.5	0.3	0.7	0.2	14.9	0.1	12.34	100
84-86-29	7.9	4.7	6.5	65.8	0.5	0.2	0.7	0.3	13.4	0	12.64	100
84-86-27	7.1	5	4.8	66.1	0.6	0.4	0.7	0.2	15.1	0.1	12.06	100
122-124-1	7	5.1	5	65.2	0.6	0.3	0.9	0.3	15.7	0.1	12.12	100
122-124-5	9	5.2	3.9	62.8	0.4	0.2	0.8	0.3	17.3	0	14.24	100
122-124-6	7.6	4.7	6.4	65.6	0.5	0.2	0.8	0.2	13.8	0.1	12.36	100
122-124-7	7.4	5	4.6	66.1	0.6	0.3	0.8	0.2	15	0.1	12.34	100
122-124-8	7.7	5.2	5	63.9	0.6	0.4	0.7	0.3	16.2	0	12.86	100
122-124-9	7.6	4.9	5	65.3	0.6	0.4	0.8	0.3	15.2	0.1	12.5	100
122-124-10	7.4	4.9	4.8	66.2	0.6	0.3	0.8	0.3	14.7	0.1	12.28	100
122-124-11	7.3	4.9	4.6	67	0.5	0.2	0.5	0.2	14.7	0.1	12.18	100
122-124-13	7.2	5	4.7	66	0.6	0.4	0.7	0.3	15.1	0	12.27	100
122-124-14	7.3	5	4.9	66.1	0.5	0.4	0.7	0.3	14.8	0	12.27	100
122-124-15	7.1	3.2	4.9	62.1	0.7	0.6	3.3	0.1	17.9	0.2	10.24	100
122-124-16	7.7	4.9	4.6	65.7	0.6	0.4	0.8	0.3	15	0.1	12.59	100
122-124-17	7.7	5	4.7	65.7	0.5	0.4	0.7	0.3	15.1	0.1	12.65	100
122-124-18	7.2	4.9	4.7	66.6	0.6	0.3	0.7	0.2	14.8	0.1	12.11	100
122-124-19	7.8	4.9	5.1	65.7	0.5	0.3	0.6	0.2	14.7	0	12.74	100
122-124-20	7.6	4.9	4.6	65.9	0.5	0.4	0.7	0.2	15.1	0.1	12.56	100
122-124-22	7.3	5	4.8	65.9	0.6	0.4	0.7	0.1	15.2	0.1	12.23	100
122-124-26	7.3	5	4.5	65.9	0.6	0.4	0.7	0.2	15.3	0	12.28	100
122-124-27	7.8	4.6	5.3	66.4	0.4	0.2	0.5	0.2	14.6	0	12.44	100
122-124-2	4.1	1.4	12.4	47.3	4	5	9.9	0.2	14.8	1	5.49	100
122-124-3	4.1	1.4	11.4	49.1	4.5	5	9.7	0.2	14.1	0.6	5.49	100
122-124-4	4.4	1.4	12.6	47.3	4.1	4.7	9.4	0.2	14.6	1.3	5.89	100
122-124-25	4.4	1.4	12.2	47.2	3.8	4.9	9.9	0.2	15	1	5.75	100
122-124-23	4.5	1.6	10.6	50.6	3.1	4.5	8.6	0.2	15.6	0.8	6.18	100
132-134-1	6.7	4.9	4.3	65.8	0.7	0.4	0.8	0.3	15.9	0.1	11.63	100
132-134-2	7.6	4.7	6.1	66.6	0.6	0.3	0.5	0.3	13.4	0.1	12.24	100
132-134-5	7.6	4.9	5.2	65.8	0.5	0.3	0.5	0.3	14.7	0.1	12.53	100
132-134-6	7.6	4.9	5.2	66.5	0.5	0.3	0.5	0.2	14.2	0.1	12.53	100
132-134-8	8.3	4.6	6.6	65.9	0.5	0.3	0.5	0.4	13	0.1	12.88	100
132-134-10	7.9	5	5.1	65.5	0.6	0.3	0.6	0.3	14.6	0.1	12.93	100
132-134-11	7.4	4.8	5.1	65.8	0.6	0.3	0.6	0.2	15.1	0.1	12.22	100
132-134-12	7	5.1	4.7	66.6	0.6	0.4	0.6	0.3	14.7	0.1	12.11	100
132-134-13	7.5	4.9	4.8	66	0.6	0.4	0.6	0.3	14.9	0.1	12.41	100
132-134-14	7.3	4.9	4.7	66.4	0.6	0.3	0.6	0.2	14.8	0	12.2	100
132-134-15	7	5	4.3	65.5	0.7	0.4	0.8	0.2	16.1	0.1	11.96	100

132-134-16	7.6	4.6	4.6	66.1	0.5	0.3	0.7	0.2	15.5	0	12.15	100
132-134-17	7.7	4.8	5.5	66.9	0.4	0.2	0.5	0.3	13.7	0	12.46	100
132-134-18	7.6	4.9	4.7	65.9	0.6	0.3	0.6	0.2	15	0.1	12.48	100
132-134-19	6.8	4.9	5.2	66.5	0.6	0.3	0.6	0.2	14.9	0	11.73	100
132-134-20	7.1	5	4.8	66.2	0.6	0.3	0.6	0.2	15	0.1	12.16	100
132-134-3	3	0.7	10	50.1	2.8	6.6	11.2	0.1	15.1	0.3	3.71	100
132-134-7	4	1.5	11	49.7	3.2	5.3	9.2	0.2	15.1	0.7	5.55	100
132-134-9	4.4	1.4	12	47.5	4	4.8	9.7	0.3	14.7	1	5.85	100
138-140-1	7.1	4.9	4.7	66.1	0.6	0.4	0.7	0.3	15.2	0.1	12.07	100
138-140-2	7.9	4.8	5.1	67	0.4	0.2	0.4	0.2	13.9	0	12.71	100
138-140-3	7.7	4.8	5.3	65.7	0.6	0.3	0.6	0.2	14.6	0.1	12.45	100
138-140-4	7.1	4.8	4.3	65.7	0.7	0.5	0.8	0.3	15.7	0.1	11.91	100
138-140-5	7.3	4.9	4.6	66	0.4	0.1	0.8	0.2	15.6	0.1	12.28	100
138-140-6	7	4.9	5.5	65.6	0.5	0.3	0.9	0.3	14.9	0.1	11.94	100
138-140-7	7.4	5	4.5	66	0.6	0.4	0.7	0.2	15	0.1	12.41	100
138-140-8	8.2	4.9	5.4	65.8	0.5	0.3	0.5	0.3	14.2	0	13.05	100
138-140-10	7.6	4.9	5.3	64.8	0.5	0.3	0.9	0.3	15.4	0.1	12.44	100
138-140-11	7.2	5	4.6	65.9	0.6	0.4	0.7	0.2	15.3	0.1	12.2	100
138-140-12	7.6	4.8	6.4	66.5	0.6	0.4	0.5	0.3	12.8	0.1	12.32	100
138-140-13	7.8	5.2	5	64.5	0.5	0.3	0.7	0.2	15.8	0.1	12.93	100
138-140-14	7.3	5	4.3	65.8	0.7	0.5	0.8	0.2	15.5	0.1	12.27	100
138-140-15	7	5.1	4.5	65	0.7	0.5	0.9	0.2	16	0.1	12.13	100
138-140-16	7.1	5	4.8	66.5	0.5	0.3	0.6	0.3	14.8	0	12.05	100
138-140-17	7.3	5.1	4.4	65	0.7	0.4	0.8	0.3	16	0.1	12.43	100
138-140-18	7.4	4.8	5	67.2	0.5	0.2	0.5	0.2	14.2	0	12.2	100
138-140-19	7.4	5	5.3	65.4	0.7	0.4	0.6	0.2	15.1	0.1	12.35	100
138-140-20	7	5	4.6	64.7	0.6	0.4	1	0.2	16.4	0.1	12.02	100
149-150-2	7	5.1	4.7	66.5	0.6	0.4	0.7	0.2	14.9	0.1	12.1	100
149-150-3	7.2	5	3.9	65.8	0.6	0.4	0.8	0.2	15.9	0.1	12.21	100
149-150-4	7.5	4.9	4.8	66.6	0.5	0.3	0.5	0.3	14.6	0	12.44	100
149-150-5	7.3	5	4.8	66.2	0.6	0.3	0.6	0.3	14.9	0	12.25	100
149-150-6	7.6	4.9	5	65.7	0.5	0.3	0.6	0.2	15.1	0	12.53	100
149-150-7	7.3	5.3	4.4	65	0.7	0.5	0.8	0.2	15.9	0.1	12.55	100
149-150-8	7.4	5.1	3.9	66.3	0.6	0.4	0.7	0.2	15.4	0.1	12.47	100
149-150-12	7.2	5.1	3.4	66	0.6	0.4	0.8	0.1	16.1	0.1	12.31	100
149-150-13	7.3	5.1	4.5	65	0.7	0.4	0.8	0.2	16	0.1	12.39	100
149-150-16	7	4.9	4.8	66	0.6	0.4	0.7	0.3	15.1	0.1	11.97	100
149-150-17	7.3	5.1	4.4	65.2	0.7	0.4	0.8	0.2	15.9	0.1	12.39	100
149-150-18	7.4	4.9	4.8	65.8	0.6	0.3	0.7	0.2	15.2	0.1	12.38	100
149-150-19	7.2	5	4.5	66.3	0.6	0.4	0.7	0.2	15	0.1	12.23	100
149-150-20	7.1	5	4.3	65.4	0.6	0.4	0.9	0.2	16	0.1	12.11	100
149-150-1	6	3.5	7.2	58.7	1.8	2	4.1	0.3	16.2	0.2	9.41	100
158-160-1	7.2	5	5.1	65.7	0.5	0.3	0.7	0.2	15.2	0	12.23	100
158-160-2	7.2	4.8	5.3	65.5	0.5	0.3	0.9	0.2	15.2	0	12.07	100
158-160-3	7.3	4.9	5.1	67.1	0.4	0.2	0.4	0.2	14.4	0	12.19	100

158-160-4	7.2	5	4.5	65	0.7	0.4	0.8	0.3	16.1	0.1	12.16	100
158-160-5	7.3	4.8	4.9	66.3	0.5	0.3	0.6	0.2	15	0.1	12.06	100
158-160-6	7.3	5	4.4	65.3	0.7	0.5	0.8	0.2	15.8	0.1	12.28	100
158-160-7	7.4	4.9	4.6	65.5	0.7	0.4	0.7	0.2	15.6	0.1	12.33	100
158-160-8	7.8	4.8	5.8	65.2	0.6	0.4	0.5	0.2	14.7	0.1	12.58	100
158-160-9	7	4.9	4.8	66.8	0.5	0.3	0.6	0.2	14.7	0.1	11.93	100
158-160-10	7.5	5	4.7	66.1	0.6	0.3	0.6	0.2	14.8	0.1	12.5	100
158-160-11	7.4	5	4.8	66	0.6	0.3	0.6	0.2	15	0	12.43	100
158-160-12	7.2	4.8	4.5	65.8	0.6	0.4	0.7	0.2	15.6	0.1	12.03	100
158-160-13	7.7	4.6	6.7	66.5	0.5	0.3	0.5	0.4	12.8	0	12.35	100
158-160-14	7.6	5.1	4.6	64.2	0.7	0.4	0.8	0.1	16.3	0.1	12.78	100
158-160-15	7.5	4.9	5	65.8	0.5	0.3	0.6	0.2	15	0.1	12.4	100
158-160-16	7.6	5.2	4.7	63.9	0.6	0.4	0.8	0.2	16.6	0.1	12.79	100
158-160-18	7.5	4.8	5.2	65.5	0.8	0.3	0.6	0.3	15	0.1	12.23	100
158-160-19	7.1	4.8	5.2	65.2	0.5	0.3	1	0.2	15.5	0.1	11.93	100
158-160-20	7.5	5	4.8	65.6	0.6	0.3	0.7	0.3	15.2	0	12.46	100
165-167-1	7.4	5	4.5	64.8	0.7	0.5	0.8	0.2	16.1	0.1	12.38	100
165-167-2	7.6	4.9	4.8	65.7	0.6	0.3	0.6	0.2	15.3	0	12.51	100
165-167-3	7.5	4.9	4.6	65.8	0.6	0.3	0.6	0.2	15.4	0.1	12.32	100
165-167-4	7.4	5.1	4.5	64.7	0.6	0.5	0.8	0.2	16	0.1	12.49	100
165-167-5	7.1	5	4.8	66.3	0.6	0.3	0.6	0.2	15.1	0	12.14	100
165-167-6	7.1	5.1	4.4	65.1	0.6	0.4	0.8	0.3	16	0.1	12.22	100
165-167-7	7.6	4.9	4.9	65.6	0.6	0.4	0.6	0.2	15.1	0.1	12.48	100
165-167-8	7.6	5	4.7	65.8	0.6	0.4	0.6	0.1	15.2	0.1	12.58	100
165-167-9	7.3	4.9	4.5	66.1	0.6	0.3	0.6	0.2	15.3	0.1	12.24	100
165-167-10	7.5	4.9	4.7	66	0.6	0.4	0.6	0.2	15.1	0.1	12.34	100
165-167-11	7.4	4.9	4.7	66.1	0.5	0.4	0.6	0.3	15	0.1	12.3	100
165-167-12	7.2	5	4.8	65.8	0.6	0.4	0.6	0.2	15.3	0.1	12.23	100
165-167-13	7.1	5.1	5.1	65.8	0.6	0.4	0.6	0.2	15	0.1	12.19	100
165-167-14	7.4	4.9	4.8	65.5	0.6	0.4	0.7	0.2	15.4	0.1	12.38	100
165-167-15	7.2	4.9	4.8	66	0.6	0.3	0.6	0.2	15.3	0	12.13	100
168-170-1	7.1	5	4.4	65	0.7	0.5	0.9	0.2	16	0.2	12.16	100
168-170-2	6.8	5.1	4.7	66.7	0.6	0.3	0.6	0.2	14.9	0	11.88	100
168-170-3	7.9	5.1	4.9	64.6	0.6	0.4	0.7	0.2	15.7	0	12.95	100
168-170-4	7.4	4.9	4.7	66.1	0.6	0.4	0.7	0.3	15	0	12.29	100
168-170-5	8	5	4.9	64.3	0.6	0.4	0.6	0.4	15.8	0	13.06	100
168-170-7	7.4	5	4.8	65.9	0.5	0.4	0.6	0.2	15.1	0.1	12.38	100
168-170-8	7.7	4.8	4.9	65.4	0.5	0.4	1	0.2	14.6	0.4	12.53	100
168-170-10	8.1	4.8	4.6	65.5	0.6	0.4	0.6	0.2	15.3	0	12.88	100
168-170-11	7.2	5	5.2	66.1	0.6	0.4	0.6	0.3	14.7	0	12.17	100
168-170-12	7.6	5	5.1	65.6	0.6	0.4	0.6	0.2	15	0	12.54	100
168-170-13	7.4	4.9	4.7	66.2	0.5	0.3	0.6	0.3	14.9	0.1	12.31	100
168-170-14	7.6	4.9	4.7	65.4	0.6	0.4	0.7	0.2	15.4	0	12.55	100
168-170-16	7.3	5.1	4.4	64.9	0.7	0.4	0.8	0.1	16.1	0.1	12.34	100
168-170-17	7.3	5	5	65.5	0.6	0.4	0.7	0.2	15.4	0.1	12.22	100

168-170-18	7.5	4.8	4.7	65.8	0.5	0.3	0.6	0.3	15.3	0.1	12.36	100
168-170-19	7.3	4.9	4.7	65.5	0.6	0.3	0.7	0.2	15.6	0.1	12.25	100
168-170-20	7.2	4.9	4	65.9	0.6	0.4	0.8	0.1	16	0.1	12.1	100
168-170-15	2.8	2.8	11.5	46.4	3.9	6.8	11.8	0.1	15.4	0.3	5.69	100
261-263-1	7.2	4.8	4.7	66	0.5	0.3	0.6	0.2	15.6	0	12.01	100
261-263-2	7.5	5	5	65.5	0.6	0.3	0.7	0.2	15.2	0.1	12.46	100
261-263-3	7.2	4.9	4.5	65.4	0.6	0.4	0.8	0.2	15.9	0	12.08	100
261-263-4	7.4	4.9	4.6	66.2	0.6	0.3	0.6	0.2	15.1	0.1	12.3	100
261-263-5	7.7	4.9	4.7	65.5	0.6	0.4	0.6	0.3	15.2	0.1	12.56	100
261-263-6	7.1	5	4.2	65.4	0.7	0.5	0.9	0	16.1	0.1	12.08	100
261-263-7	7.3	5	4.9	66.2	0.6	0.4	0.6	0.3	14.8	0	12.3	100
261-263-8	7.1	4.9	4.4	65.5	0.6	0.4	0.8	0.2	15.9	0.1	12.05	100
261-263-9	7.4	5	4.8	65.6	0.6	0.4	0.7	0.2	15.3	0.1	12.38	100
261-263-10	7.6	4.9	4.9	65.8	0.6	0.4	0.6	0.3	14.9	0.1	12.54	100
261-263-11	7.6	4.9	4.8	66.1	0.5	0.3	0.7	0.2	15	0	12.43	100
261-263-12	7.4	4.9	4.7	65.5	0.5	0.4	0.7	0.2	15.5	0.1	12.36	100
261-263-13	7.5	5	4.5	64.9	0.6	0.4	0.8	0.2	15.9	0.1	12.52	100
261-263-14	7.5	4.9	5.8	64.8	0.5	0.2	0.9	0.2	15.1	0	12.4	100
261-263-15	7.6	4.8	4.8	65.8	0.6	0.3	0.6	0.3	15.2	0.1	12.39	100
261-263-16	7.5	4.9	4.8	65.8	0.5	0.3	0.7	0.3	15.1	0.1	12.45	100
261-263-17	7.6	4.7	5.9	66.2	0.6	0.4	0.6	0.3	13.6	0.1	12.34	100
261-263-18	7.2	5	4.2	65.4	0.7	0.4	0.9	0.2	15.9	0.1	12.16	100
261-263-19	7.2	5	4.4	65.2	0.7	0.5	0.9	0.2	15.8	0.1	12.14	100
261-263-20	7.1	4.9	4.7	66.8	0.5	0.3	0.7	0.2	14.7	0	11.94	100
280-282-1	7.4	4.9	4.8	66.2	0.6	0.3	0.6	0.2	15	0	12.28	100
280-282-2	7.4	4.8	4.9	66.1	0.6	0.3	0.6	0.3	15	0	12.21	100
280-282-5	7.5	4.9	4.9	65.9	0.6	0.3	0.7	0.3	15	0.1	12.34	100
280-282-6	7.4	4.9	4.7	65.8	0.6	0.4	0.8	0.2	15.2	0	12.28	100
280-282-7	7.4	4.8	4.9	65.8	0.6	0.3	0.6	0.2	15.2	0.1	12.21	100
280-282-8	7.4	5	4.8	65.8	0.5	0.3	0.6	0.2	15.2	0.1	12.42	100
280-282-9	7.7	4.9	4.9	65.5	0.5	0.4	0.6	0.2	15.2	0.1	12.62	100
280-282-10	7.3	4.8	4.7	66.4	0.5	0.4	0.7	0.2	14.9	0.1	12.16	100
280-282-11	7.6	5	4.5	65.5	0.6	0.4	0.6	0.2	15.5	0.1	12.54	100
280-282-12	7.4	5	4.7	65.5	0.6	0.4	0.7	0.2	15.3	0.1	12.45	100
280-282-13	7.5	5	5	65	0.6	0.3	0.6	0.3	15.4	0.1	12.55	100
280-282-14	7.3	5	4.6	66.1	0.6	0.4	0.6	0.2	15.1	0.1	12.3	100
280-282-15	7.7	5	4.7	65.3	0.6	0.4	0.7	0.2	15.4	0.1	12.68	100
280-282-16	7.6	4.8	5.6	65.9	0.5	0.4	0.5	0.1	14.4	0.1	12.46	100
280-282-18	7.6	4.9	5.4	66.3	0.5	0.3	0.5	0.3	14.2	0	12.47	100
280-282-19	7.8	4.8	6.4	65.8	0.6	0.3	0.6	0.2	13.4	0	12.63	100
280-282-20	7.4	5	4.7	65.6	0.6	0.3	0.6	0.2	15.5	0.1	12.4	100
280-282-17	3.7	1.2	12.5	47	4.1	5.4	10.7	0.1	14.7	0.6	4.83	100
286-288-1	7.4	5.1	4.6	65.9	0.6	0.3	0.6	0.3	15	0.1	12.48	100
286-288-2	7.1	5.1	4.9	65.7	0.6	0.4	0.8	0.2	15.2	0.1	12.2	100
286-288-3	7.4	5	5	65.6	0.6	0.4	0.7	0.2	15.1	0	12.39	100

286-288-5	7.2	5.1	4.9	65.5	0.6	0.4	0.7	0.2	15.3	0.1	12.35	100
286-288-6	7.6	5	4.8	65.4	0.6	0.4	0.7	0.3	15.2	0.1	12.59	100
286-288-7	7.5	4.9	4.8	65.3	0.6	0.4	0.7	0.2	15.4	0.1	12.44	100
286-288-8	7.4	5	4.7	64.2	0.7	0.4	0.8	0.2	16.5	0.1	12.39	100
286-288-9	7	5	4.7	66.1	0.6	0.4	0.6	0.3	15.3	0.1	12.03	100
286-288-10	7.2	4.9	4.6	65.8	0.6	0.4	0.6	0.2	15.6	0.1	12.13	100
286-288-11	7	5	4.4	66	0.6	0.3	0.7	0.2	15.7	0	12.05	100
286-288-12	7.6	4.9	5.3	64.5	0.6	0.3	0.6	0.2	15.7	0.1	12.59	100
286-288-16	7.3	4.9	4.3	65.1	0.7	0.5	0.8	0.3	16	0.1	12.22	100
286-288-17	7.9	5.1	5	64.2	0.6	0.4	0.7	0.3	15.7	0.1	13.01	100
286-288-18	7.3	5	4.6	66.1	0.6	0.4	0.6	0.2	15.2	0	12.27	100
286-288-19	7.9	4.7	6.9	65.3	0.5	0.3	0.5	0.3	13.5	0	12.64	100
286-288-20	7.4	4.9	4.9	66.1	0.5	0.4	0.7	0.2	14.8	0.1	12.3	100
286-288-4	3.4	1.1	10.7	46.8	3.8	6.4	12.1	0.1	15.1	0.5	4.46	100
286-288-14	4.2	1.4	12.8	48.3	3.9	4.9	9.1	0.2	14.2	1.1	5.65	100
286-288-15	3.9	1.3	13.3	47.7	3.9	4.8	9.8	0.2	14.5	0.4	5.27	100
292-294-1	7.61	5.01	4.8	65.87	0.55	0.36	0.65	0.28	14.81	0.04	12.62	100
292-294-2	7.65	4.97	4.86	66.02	0.57	0.34	0.64	0.2	14.68	0.08	12.61	100
292-294-3	7.51	4.9	4.67	66.07	0.54	0.36	0.64	0.22	15.09	0.02	12.41	100
292-294-4	7.49	4.98	4.68	65.88	0.54	0.32	0.66	0.2	15.21	0.05	12.47	100
292-294-5	7.13	5.03	4.81	66.21	0.59	0.37	0.58	0.27	14.96	0.04	12.16	100
292-294-6	7.21	5.15	4.52	66.2	0.56	0.3	0.64	0.24	15.06	0.13	12.36	100
292-294-7	7.41	4.96	4.81	66.31	0.55	0.35	0.62	0.22	14.7	0.06	12.38	100
292-294-8	7.47	4.96	4.87	66.17	0.55	0.32	0.57	0.19	14.88	0.03	12.43	100
292-294-10	7.2	5.06	4.56	66.28	0.59	0.33	0.66	0.21	15.04	0.07	12.27	100
292-294-11	7.49	4.97	4.9	66.08	0.56	0.34	0.59	0.22	14.78	0.08	12.45	100
292-294-12	7.49	5.03	4.74	65.98	0.55	0.37	0.63	0.17	15	0.02	12.52	100
292-294-19	7.69	5.02	5.21	65.17	0.6	0.36	0.64	0.24	15.04	0.04	12.71	100
292-294-20	7.63	4.99	4.94	65.15	0.57	0.36	0.62	0.27	15.35	0.09	12.63	100
292-294-18	5.22	2.38	10.48	53.26	2.82	3.37	6.38	0.21	14.9	0.98	7.61	100
312-314-1	7.73	5.06	4.84	64.98	0.65	0.38	0.68	0.25	15.38	0.03	12.79	100
312-314-3	7.42	5.09	4.97	65.61	0.57	0.32	0.64	0.23	15.08	0.06	12.52	100
312-314-4	7.58	4.96	5.01	65.79	0.55	0.35	0.6	0.26	14.86	0.05	12.54	100
312-314-5	7.54	5.1	4.78	65.44	0.59	0.38	0.68	0.27	15.16	0.07	12.63	100
312-314-6	7.43	5.04	4.38	65.14	0.69	0.43	0.8	0.22	15.75	0.13	12.47	100
312-314-7	7.62	4.96	4.76	65.95	0.54	0.32	0.64	0.25	14.93	0.04	12.58	100
312-314-8	7.58	5.05	4.89	65.7	0.55	0.4	0.67	0.25	14.86	0.05	12.62	100
312-314-10	7.39	4.95	4.83	65.86	0.52	0.39	0.65	0.24	15.08	0.08	12.34	100
312-314-11	7.95	4.72	6.98	66.12	0.63	0.41	0.47	0.33	12.35	0.06	12.66	100
312-314-12	7.52	4.97	4.97	65.77	0.59	0.31	0.62	0.24	14.97	0.04	12.48	100
312-314-14	7.43	4.92	4.9	66.14	0.55	0.33	0.61	0.28	14.77	0.06	12.35	100
312-314-15	7.55	5.01	4.57	65.89	0.56	0.39	0.71	0.22	15.04	0.04	12.56	100
312-314-16	7.49	4.98	4.79	66.03	0.59	0.37	0.67	0.26	14.76	0.07	12.47	100
312-314-17	7.41	5	4.7	66.03	0.53	0.37	0.69	0.23	14.97	0.09	12.41	100
312-314-18	7.6	4.97	4.92	66.09	0.55	0.32	0.7	0.24	14.58	0.04	12.57	100

312-314-19	7.63	5	4.56	65.9	0.57	0.4	0.67	0.18	15.03	0.06	12.63	100
312-314-20	7.73	4.87	4.99	65.55	0.54	0.37	0.67	0.26	14.95	0.06	12.6	100
312-314-2	3.53	1.15	11.01	46.9	3.04	6.58	12.18	0.16	15.08	0.36	4.68	100
332-342-3	6.96	4.94	5.08	65	0.56	0.28	1	0.23	15.87	0.08	11.9	100
332-342-4	7.52	4.98	4.86	66	0.54	0.36	0.64	0.2	14.84	0.06	12.51	100
332-342-5	7.28	4.94	4.73	66.16	0.62	0.32	0.62	0.18	15.08	0.09	12.22	100
332-342-6	7.14	4.84	4.64	66.62	0.58	0.35	0.7	0.24	14.86	0.02	11.99	100
332-342-9	6.6	5.21	4.36	66.77	0.47	0.41	0.68	0.19	15.27	0.03	11.81	100
332-342-10	7.4	4.92	4.95	65.81	0.53	0.35	0.62	0.29	15.13	0.01	12.32	100
332-342-12	7.3	5.03	4.7	66.12	0.62	0.37	0.61	0.23	14.96	0.06	12.33	100
332-342-13	7.37	5.16	4.58	64.92	0.65	0.49	0.86	0.17	15.69	0.09	12.54	100
332-342-14	7.65	4.65	4.58	65.74	0.53	0.33	0.7	0.2	15.55	0.07	12.3	100
332-342-15	7.59	4.94	4.62	65.78	0.58	0.38	0.67	0.21	15.17	0.07	12.53	100
332-342-16	7.35	5.1	4.77	66.32	0.56	0.36	0.66	0.2	14.67	0.01	12.45	100
332-342-17	7.89	4.68	4.56	65.68	0.53	0.37	0.66	0.21	15.41	0.01	12.57	100
332-342-18	7.55	4.93	5.04	65.99	0.57	0.36	0.68	0.22	14.64	0.03	12.48	100
332-342-19	7.65	5.12	5	65.56	0.59	0.36	0.69	0.24	14.74	0.05	12.77	100
332-342-20	7.61	5.18	4.47	66.13	0.6	0.37	0.6	0.16	14.89	0.01	12.79	100
332-342-23	7.3	4.91	4.76	66.48	0.53	0.33	0.64	0.21	14.77	0.07	12.22	100
332-342-24	7.19	5.01	4.49	65.67	0.61	0.41	0.76	0.22	15.57	0.07	12.2	100
332-342-25	7.27	4.92	4.67	66.51	0.56	0.34	0.64	0.14	14.86	0.08	12.19	100
332-342-26	7.17	4.87	4.72	66.34	0.54	0.38	0.64	0.26	15.04	0.04	12.04	100
332-342-27	7.45	4.9	4.72	66.2	0.57	0.35	0.64	0.21	14.93	0.03	12.35	100
332-342-28	7.54	4.88	5.03	66.08	0.55	0.35	0.59	0.23	14.68	0.07	12.42	100
332-342-29	7.32	4.9	4.72	66.39	0.57	0.35	0.58	0.27	14.81	0.07	12.22	100
332-342-30	7.22	5.12	4.98	66.17	0.57	0.37	0.65	0.16	14.69	0.07	12.34	100
332-342-7	4.09	1.49	13.05	48.6	4.18	4.37	9.2	0.19	14.14	0.68	5.57	100
332-342-11	4.12	1.56	11.13	49.96	3.31	4.79	9.28	0.27	14.87	0.71	5.67	100
332-342-22	4.49	1.48	12.87	47.27	3.92	4.69	9.49	0.28	14.32	1.17	5.98	100

Appendix 4.3 Morphometric measurements of volcanic grains

Sample no	area	perimeter	major axis	minor axis	aspect ratio	normalized perimeter
	(mm ²)	(mm)	(mm)	(mm)		
1215-184 (bsf)						
1	0.099	1.310	0.527	0.239	2.205	1.174
2	0.046	0.873	0.261	0.222	1.176	1.148
3	0.031	0.750	0.230	0.172	1.337	1.202
4	0.040	0.831	0.279	0.181	1.541	1.172
5	0.059	1.005	0.329	0.228	1.443	1.167
6	0.033	0.764	0.265	0.158	1.677	1.186
7	0.040	0.813	0.260	0.196	1.327	1.147
8	0.024	0.670	0.196	0.158	1.241	1.220
9	0.014	0.538	0.146	0.124	1.177	1.283
10	0.014	0.488	0.149	0.121	1.231	1.163
11	0.072	1.121	0.370	0.249	1.486	1.179
12	0.023	0.646	0.184	0.157	1.172	1.202
13	0.024	0.670	0.189	0.161	1.174	1.220
14	0.022	0.633	0.216	0.132	1.636	1.204
15	0.014	0.509	0.147	0.123	1.195	1.214
16	0.042	0.830	0.261	0.206	1.267	1.142
17	0.349	2.680	0.780	0.570	1.368	1.280
18	0.032	0.739	0.233	0.173	1.347	1.165
19	0.058	1.006	0.325	0.226	1.438	1.178
20	0.099	1.274	0.410	0.307	1.336	1.142
21	0.072	1.116	0.379	0.242	1.566	1.173
22	0.074	1.041	0.329	0.288	1.142	1.080
23	0.020	0.616	0.188	0.135	1.393	1.229
24	0.027	0.662	0.210	0.163	1.288	1.137
25	0.029	0.729	0.228	0.164	1.390	1.208
26	0.069	1.221	0.373	0.236	1.581	1.311
27	0.043	0.951	0.283	0.193	1.466	1.294
28	0.125	1.465	0.419	0.380	1.103	1.169
29	0.042	0.841	0.263	0.204	1.289	1.158
30	0.074	1.153	0.373	0.253	1.474	1.196
31	0.052	1.136	0.405	0.165	2.455	1.405
32	0.085	1.308	0.405	0.266	1.523	1.266
33	0.022	0.594	0.177	0.158	1.120	1.130
34	0.008	0.367	0.132	0.075	1.760	1.157
35	0.006	0.323	0.122	0.058	2.103	1.176
36	0.011	0.424	0.137	0.098	1.398	1.140
37	0.014	0.481	0.162	0.113	1.434	1.147
38	0.061	1.062	0.352	0.220	1.600	1.213
39	0.113	1.367	0.433	0.331	1.308	1.147
40	0.053	1.075	0.319	0.213	1.498	1.317
41	0.034	0.811	0.262	0.164	1.598	1.241

42	0.014	0.487	0.173	0.101	1.713	1.161
43	0.019	0.606	0.188	0.132	1.424	1.240
44	0.032	0.726	0.257	0.157	1.637	1.145
45	0.011	0.491	0.140	0.101	1.386	1.321
ave	0.050	0.871	0.277	0.194	1.454	1.199
standard deviation	0.054	0.401	0.125	0.088	0.276	0.063
1215-214 (bsf)						
1	0.099	1.310	0.527	0.239	2.205	1.174
2	0.387	2.947	0.875	0.563	1.554	1.336
3	0.399	3.788	1.179	0.431	2.735	1.692
4	0.137	1.611	0.479	0.365	1.312	1.228
5	0.170	1.847	0.660	0.327	2.018	1.264
6	1.042	4.791	1.578	0.840	1.879	1.324
7	0.176	2.078	0.507	0.442	1.147	1.397
8	0.062	1.018	0.294	0.270	1.089	1.153
9	0.081	1.278	0.395	0.262	1.508	1.267
10	0.070	1.120	0.345	0.257	1.342	1.194
11	0.277	2.612	0.658	0.536	1.228	1.400
12	0.181	1.859	0.540	0.427	1.265	1.233
13	0.082	1.237	0.361	0.287	1.258	1.219
14	0.040	0.817	0.259	0.196	1.321	1.152
15	0.070	1.105	0.343	0.261	1.314	1.178
16	0.084	1.400	0.437	0.246	1.776	1.363
17	0.149	1.601	0.536	0.354	1.514	1.170
18	0.060	1.164	0.329	0.233	1.412	1.341
19	0.104	1.319	0.391	0.338	1.157	1.154
20	0.083	1.237	0.385	0.273	1.410	1.211
21	0.079	1.338	0.361	0.280	1.289	1.343
22	0.141	1.534	0.485	0.370	1.311	1.152
23	0.054	1.066	0.328	0.209	1.569	1.294
24	0.068	1.316	0.326	0.264	1.235	1.424
25	0.015	0.482	0.161	0.116	1.388	1.110
26	0.172	1.994	0.797	0.275	2.898	1.356
27	0.190	1.859	0.520	0.466	1.116	1.203
28	0.239	2.155	0.638	0.476	1.340	1.243
29	0.108	1.319	0.409	0.337	1.214	1.132
30	0.054	1.031	0.302	0.228	1.325	1.252
average	0.162	1.674	0.514	0.339	1.504	1.265
standard deviation	0.190	0.887	0.288	0.141	0.442	0.120
1215-222 (bsf)						
1	0.164	1.950	0.569	0.366	1.555	1.358
2	0.048	1.016	0.359	0.171	2.099	1.308
3	0.062	1.090	0.382	0.207	1.845	1.235
4	0.042	0.856	0.265	0.204	1.299	1.178
5	0.090	1.462	0.389	0.294	1.323	1.375
6	0.056	0.969	0.343	0.207	1.657	1.155

7	0.030	0.785	0.263	0.145	1.814	1.279
8	0.031	0.740	0.239	0.166	1.440	1.186
9	0.020	0.581	0.193	0.130	1.485	1.159
10	0.027	0.706	0.209	0.167	1.251	1.212
11	0.020	0.608	0.186	0.136	1.368	1.213
13	0.105	1.558	0.500	0.267	1.873	1.356
14	0.044	1.005	0.295	0.188	1.569	1.352
15	0.036	0.885	0.272	0.168	1.619	1.316
16	0.025	0.686	0.205	0.155	1.323	1.224
17	0.075	1.197	0.450	0.211	2.133	1.233
18	0.017	0.526	0.181	0.122	1.484	1.138
19	0.032	0.792	0.281	0.143	1.965	1.249
20	0.030	0.777	0.255	0.151	1.689	1.265
21	0.028	0.663	0.227	0.156	1.455	1.118
22	0.146	1.630	0.534	0.347	1.539	1.203
25	0.041	0.820	0.253	0.208	1.216	1.142
26	0.038	0.821	0.294	0.166	1.771	1.188
27	0.034	0.803	0.234	0.187	1.251	1.228
28	0.053	0.997	0.317	0.212	1.495	1.222
29	0.023	0.673	0.220	0.130	1.692	1.252
30	0.025	0.636	0.195	0.164	1.189	1.135
31	0.136	1.719	0.553	0.313	1.767	1.315
32	0.073	1.120	0.353	0.262	1.347	1.169
33	0.106	1.412	0.424	0.318	1.333	1.223
34	0.078	1.279	0.413	0.240	1.721	1.292
35	0.092	1.261	0.352	0.333	1.057	1.173
36	0.056	1.032	0.275	0.257	1.070	1.230
37	0.053	1.103	0.340	0.199	1.709	1.352
38	0.032	0.824	0.281	0.147	1.912	1.299
39	0.037	0.820	0.232	0.201	1.154	1.203
40	0.124	1.501	0.498	0.318	1.566	1.202
41	0.044	0.922	0.255	0.219	1.164	1.240
42	0.046	0.830	0.260	0.223	1.166	1.092
43	0.030	0.702	0.243	0.158	1.538	1.143
44	0.045	0.874	0.297	0.195	1.523	1.162
45	0.031	0.787	0.258	0.155	1.665	1.261
46	0.075	1.141	0.345	0.276	1.250	1.175
47	0.046	0.909	0.309	0.191	1.618	1.196
48	0.031	0.813	0.239	0.166	1.440	1.303
49	0.016	0.591	0.157	0.130	1.208	1.318
50	0.019	0.621	0.183	0.129	1.419	1.271
average	0.056	0.975	0.305	0.214	1.437	1.218
standard deviation	0.036	0.329	0.104	0.065	0.266	0.071
1219-12 (bsf)						
1	0.086	1.161	0.392	0.279	1.405	1.117
2	0.023	0.647	0.181	0.164	1.104	1.203

3	0.054	0.934	0.340	0.203	1.675	1.134
4	0.026	0.649	0.228	0.144	1.583	1.135
5	0.015	0.512	0.159	0.122	1.303	1.179
6	0.017	0.587	0.210	0.100	2.100	1.270
7	0.011	0.420	0.169	0.084	2.012	1.130
8	0.009	0.381	0.143	0.080	1.788	1.133
9	0.018	0.519	0.171	0.131	1.305	1.091
10	0.009	0.358	0.117	0.095	1.232	1.065
11	0.014	0.490	0.165	0.109	1.514	1.168
12	0.024	0.622	0.214	0.143	1.497	1.133
13	0.018	0.584	0.190	0.122	1.557	1.228
14	0.007	0.319	0.094	0.089	1.056	1.076
15	0.013	0.480	0.146	0.116	1.259	1.188
16	0.008	0.354	0.117	0.086	1.360	1.116
17	0.021	0.682	0.175	0.154	1.136	1.328
18	0.194	1.745	0.537	0.460	1.167	1.118
19	0.041	0.812	0.267	0.196	1.362	1.131
20	0.152	1.715	0.514	0.377	1.363	1.241
21	0.067	1.064	0.329	0.261	1.261	1.160
22	0.056	0.953	0.320	0.223	1.435	1.136
23	0.111	1.412	0.397	0.356	1.115	1.196
24	0.029	0.689	0.200	0.184	1.087	1.141
25	0.024	0.609	0.202	0.149	1.356	1.109
26	0.016	0.568	0.168	0.118	1.424	1.267
27	0.015	0.530	0.163	0.118	1.381	1.221
28	0.021	0.627	0.226	0.118	1.915	1.221
29	0.088	1.237	0.401	0.279	1.437	1.176
30	0.073	1.230	0.378	0.244	1.549	1.284
average	0.042	0.763	0.244	0.177	1.425	1.050
standard deviation	0.045	0.388	0.117	0.096	0.266	0.065
1219-27 (bsf)						
1	0.073	1.373	0.381	0.244	1.561	1.434
2	0.005	0.324	0.107	0.063	1.698	1.293
3	0.006	0.295	0.102	0.069	1.478	1.074
4	0.003	0.224	0.079	0.055	1.436	1.154
5	0.004	0.253	0.079	0.065	1.215	1.128
6	0.015	0.482	0.152	0.122	1.246	1.110
7	0.002	0.199	0.077	0.037	2.081	1.255
8	0.003	0.209	0.081	0.044	1.841	1.076
9	0.021	0.576	0.221	0.123	1.797	1.121
10	0.011	0.421	0.141	0.098	1.439	1.132
11	0.020	0.574	0.224	0.116	1.931	1.145
12	0.006	0.310	0.113	0.067	1.687	1.129
13	0.061	1.183	0.340	0.228	1.491	1.351
14	0.021	0.594	0.211	0.128	1.648	1.156
15	0.005	0.269	0.080	0.075	1.067	1.073

16	0.006	0.323	0.110	0.068	1.618	1.176
17	0.004	0.267	0.091	0.055	1.655	1.191
18	0.010	0.407	0.123	0.103	1.194	1.148
19	0.009	0.388	0.119	0.094	1.266	1.154
20	0.008	0.339	0.123	0.079	1.557	1.069
21	0.004	0.267	0.082	0.068	1.206	1.191
22	0.009	0.390	0.128	0.086	1.488	1.160
23	0.020	0.590	0.228	0.111	2.054	1.177
24	0.007	0.339	0.114	0.078	1.462	1.143
25	0.003	0.230	0.077	0.052	1.481	1.185
26	0.005	0.301	0.102	0.067	1.522	1.201
27	0.002	0.167	0.051	0.045	1.133	1.053
28	0.003	0.221	0.074	0.060	1.233	1.138
29	0.006	0.307	0.108	0.065	1.662	1.118
30	0.018	0.540	0.185	0.126	1.468	1.135
31	0.001	0.134	0.041	0.035	1.171	1.195
32	0.180	2.084	0.840	0.272	3.088	1.386
33	0.014	0.459	0.160	0.113	1.416	1.094
34	0.014	0.476	0.158	0.111	1.423	1.135
35	0.016	0.552	0.208	0.097	2.144	1.231
36	0.007	0.312	0.101	0.083	1.217	1.052
37	0.011	0.427	0.165	0.082	2.012	1.148
38	0.016	0.542	0.193	0.104	1.856	1.209
39	0.006	0.303	0.102	0.069	1.478	1.103
average	0.016	0.453	0.156	0.094	1.575	1.165
standard deviation	0.030	0.361	0.134	0.052	0.373	0.085
1219-53 (bsf)						
1	12.365	15.139	4.197	3.751	1.119	1.214
2	46.802	28.181	9.558	6.235	1.533	1.162
3	12.135	15.503	4.537	3.405	1.332	1.255
4	14.875	16.238	5.120	3.699	1.384	1.188
5	8.640	11.576	3.633	3.028	1.200	1.111
6	7.916	11.728	3.716	2.712	1.370	1.176
7	20.138	18.132	6.079	4.218	1.441	1.140
8	12.023	13.730	4.371	3.503	1.248	1.117
9	4.396	8.569	2.418	2.315	1.044	1.153
10	10.306	13.646	4.614	2.844	1.622	1.199
11	5.969	10.630	3.115	2.440	1.277	1.227
12	11.373	13.921	4.478	3.233	1.385	1.164
13	20.457	17.919	5.439	4.789	1.136	1.118
14	21.795	19.944	6.929	4.005	1.730	1.205
15	43.008	27.839	8.226	6.657	1.236	1.197
16	22.531	20.207	5.592	5.130	1.090	1.201
17	9.128	12.821	4.008	2.900	1.382	1.197
18	21.522	19.497	6.566	4.173	1.573	1.186
19	18.676	17.623	5.103	4.660	1.095	1.150

20	7.348	11.029	3.346	2.796	1.197	1.148
21	6.879	10.182	2.999	2.920	1.027	1.095
22	4.409	8.845	2.869	1.957	1.466	1.188
23	7.801	10.784	3.503	2.835	1.236	1.089
24	5.969	10.630	3.115	2.440	1.277	1.227
25	5.973	9.781	3.083	2.467	1.250	1.129
average	14.497	14.964	4.665	3.564	1.306	1.170
standard deviation	10.868	5.286	1.749	1.198	0.184	0.044
1219-58 (bsf)						
1	2.002	6.940	1.851	1.377	1.344	1.384
2	6.440	12.787	3.890	2.108	1.845	1.421
3	2.435	6.871	1.966	1.577	1.247	1.242
4	4.342	9.335	2.420	2.285	1.059	1.264
5	1.106	4.444	1.349	1.044	1.292	1.192
6	1.144	5.178	1.322	1.101	1.201	1.366
7	2.235	6.400	1.840	1.546	1.190	1.208
8	1.215	4.674	1.395	1.109	1.258	1.196
9	2.641	7.746	1.882	1.787	1.053	1.345
10	4.582	9.168	2.909	2.006	1.450	1.208
11	2.060	6.314	1.721	1.525	1.129	1.241
12	1.271	4.917	1.522	1.064	1.430	1.230
13	1.774	5.843	1.894	1.192	1.589	1.238
14	23.598	21.233	6.345	4.735	1.340	1.233
15	2.146	6.178	2.088	1.308	1.596	1.190
16	9.348	13.545	4.175	2.851	1.464	1.250
17	2.209	6.596	2.240	1.255	1.785	1.252
18	3.919	8.357	2.599	1.920	1.354	1.191
19	5.103	10.155	2.928	2.219	1.320	1.268
20	3.463	7.930	2.460	1.792	1.373	1.202
21	5.102	9.368	2.919	2.226	1.311	1.170
22	6.475	11.821	3.549	2.323	1.528	1.310
23	0.793	4.440	1.135	0.890	1.275	1.407
24	5.485	10.448	3.250	2.149	1.512	1.258
25	2.649	8.238	2.312	1.459	1.585	1.428
26	2.139	6.723	2.341	1.163	2.013	1.297
27	2.221	6.323	1.997	1.416	1.410	1.197
28	0.730	3.781	1.182	0.787	1.502	1.248
29	14.625	17.317	4.508	4.131	1.091	1.277
30	2.741	7.378	2.218	1.574	1.409	1.257
31	1.353	4.988	1.329	1.296	1.025	1.210
32	3.518	7.440	2.232	2.007	1.112	1.119
33	2.198	6.779	2.397	1.167	2.054	1.290
34	2.144	6.299	1.872	1.459	1.283	1.214
35	6.778	10.877	3.217	2.683	1.199	1.179
36	3.016	7.824	2.490	1.542	1.615	1.271
37	2.516	6.699	2.198	1.457	1.509	1.191

38	3.215	6.937	2.542	1.610	1.579	1.091
39	6.858	12.459	3.189	2.738	1.165	1.342
40	1.972	5.718	1.681	1.494	1.125	1.149
41	2.623	6.290	1.854	1.801	1.029	1.096
42	6.967	11.237	4.201	2.112	1.989	1.201
average	4.027	8.190	2.462	1.793	1.396	1.246
standard deviation	4.075	3.500	1.039	0.783	0.265	0.080
1219-61 (bsf)						
1	2.593	7.110	1.987	1.662	1.196	1.246
2	4.047	8.148	2.566	2.008	1.278	1.143
3	8.963	12.671	3.833	2.978	1.287	1.194
4	2.644	7.384	1.875	1.795	1.045	1.281
5	2.781	6.882	2.147	1.649	1.302	1.164
6	2.261	6.579	1.900	1.515	1.254	1.234
7	2.105	5.767	1.746	1.535	1.137	1.121
8	4.354	8.695	3.034	1.828	1.660	1.175
9	2.461	6.282	1.909	1.641	1.163	1.130
10	4.480	8.838	2.719	2.098	1.296	1.178
11	4.301	8.162	2.639	2.075	1.272	1.110
12	1.016	4.227	1.400	0.924	1.515	1.183
13	6.477	11.188	3.296	2.502	1.317	1.240
14	4.090	8.401	2.616	1.991	1.314	1.172
15	14.672	16.828	4.870	3.836	1.270	1.239
16	4.142	9.404	2.434	2.166	1.124	1.303
17	7.703	11.923	3.394	2.890	1.174	1.212
18	9.035	13.303	3.650	3.151	1.158	1.248
19	5.113	10.003	2.680	2.429	1.103	1.248
20	1.548	4.883	1.514	1.302	1.163	1.107
21	4.961	9.281	3.030	2.084	1.454	1.175
22	8.978	12.272	3.622	3.156	1.148	1.155
23	1.219	5.197	1.488	1.043	1.427	1.328
24	3.646	8.690	2.455	1.891	1.298	1.284
25	3.877	8.527	2.474	1.996	1.239	1.222
26	4.541	9.661	2.554	2.264	1.128	1.279
27	3.855	7.867	2.403	2.042	1.177	1.130
28	4.547	8.801	2.491	2.324	1.072	1.164
29	6.054	10.227	3.078	2.504	1.229	1.173
30	9.951	14.970	4.063	3.119	1.303	1.339
31	2.547	6.803	1.915	1.694	1.130	1.202
32	3.666	7.451	2.442	1.911	1.278	1.098
33	4.396	8.260	2.905	1.927	1.508	1.111
34	1.463	4.921	1.611	1.156	1.394	1.148
35	2.322	6.958	1.970	1.501	1.312	1.288
36	1.290	4.624	1.589	1.033	1.538	1.148
37	1.917	5.440	1.862	1.311	1.420	1.108
38	8.315	10.906	3.602	2.939	1.226	1.067

39	1.438	4.821	1.764	1.038	1.699	1.134
40	3.253	7.132	2.428	1.706	1.423	1.115
41	2.297	6.172	1.843	1.587	1.161	1.149
42	0.942	3.808	1.246	0.962	1.295	1.107
43	1.446	4.796	1.535	1.200	1.279	1.125
44	2.856	6.602	2.308	1.576	1.464	1.102
45	5.820	9.427	3.113	2.381	1.307	1.102
46	1.485	4.938	1.550	1.220	1.270	1.143
47	1.369	4.507	1.497	1.164	1.286	1.087
48	3.987	7.635	2.389	2.125	1.124	1.079
49	1.221	4.263	1.385	1.122	1.234	1.088
50	3.795	7.589	2.505	1.929	1.299	1.099
average	4.045	7.984	2.427	1.918	1.283	1.174
standard deviation	2.791	2.869	0.795	0.666	0.143	0.071
1219-132 (bsf)						
1	0.020	0.626	0.187	0.134	1.396	1.249
2	0.013	0.478	0.141	0.117	1.205	1.183
3	0.026	0.711	0.243	0.136	1.787	1.244
4	0.004	0.257	0.081	0.064	1.266	1.146
5	0.006	0.369	0.103	0.079	1.304	1.344
6	0.014	0.527	0.162	0.113	1.434	1.256
7	0.005	0.451	0.106	0.056	1.893	1.799
8	0.015	0.532	0.176	0.105	1.676	1.225
9	0.004	0.251	0.080	0.059	1.356	1.120
10	0.013	0.502	0.163	0.098	1.663	1.242
11	0.008	0.373	0.140	0.074	1.892	1.176
12	0.006	0.335	0.126	0.057	2.211	1.220
13	0.035	0.857	0.222	0.203	1.094	1.292
14	0.025	0.639	0.199	0.162	1.228	1.140
15	0.018	0.656	0.246	0.094	2.617	1.379
16	0.011	0.446	0.132	0.105	1.257	1.200
17	0.010	0.414	0.134	0.092	1.457	1.168
18	0.009	0.403	0.141	0.078	1.808	1.198
19	0.017	0.661	0.186	0.113	1.646	1.430
20	0.013	0.572	0.140	0.115	1.217	1.415
21	0.061	1.270	0.349	0.222	1.572	1.451
22	0.019	0.709	0.183	0.129	1.419	1.451
23	0.035	0.960	0.244	0.185	1.319	1.448
24	0.016	0.576	0.179	0.115	1.557	1.285
25	0.011	0.446	0.154	0.091	1.692	1.200
26	0.006	0.317	0.098	0.077	1.273	1.154
27	0.008	0.387	0.146	0.071	2.056	1.221
28	0.034	0.918	0.233	0.188	1.239	1.404
29	0.008	0.390	0.125	0.080	1.563	1.230
30	0.007	0.377	0.128	0.066	1.939	1.271
31	0.004	0.273	0.071	0.063	1.127	1.218

32	0.011	0.444	0.145	0.099	1.465	1.194
33	0.015	0.511	0.173	0.107	1.617	1.177
34	0.030	0.755	0.241	0.156	1.545	1.230
35	0.033	0.797	0.214	0.198	1.081	1.238
36	0.012	0.469	0.153	0.103	1.485	1.208
37	0.018	0.666	0.175	0.133	1.316	1.400
38	0.032	0.742	0.231	0.177	1.305	1.170
39	0.026	0.770	0.268	0.123	2.179	1.347
40	0.041	0.822	0.249	0.210	1.186	1.145
41	0.009	0.392	0.143	0.080	1.788	1.166
42	0.027	0.749	0.260	0.131	1.985	1.286
43	0.017	0.590	0.163	0.133	1.226	1.277
44	0.005	0.287	0.086	0.076	1.132	1.145
45	0.014	0.537	0.166	0.108	1.537	1.280
46	0.009	0.510	0.133	0.085	1.565	1.517
47	0.005	0.305	0.089	0.078	1.141	1.217
48	0.039	0.967	0.253	0.195	1.297	1.381
49	0.011	0.461	0.154	0.087	1.770	1.240
50	0.022	0.725	0.237	0.118	2.008	1.379
51	0.009	0.462	0.134	0.081	1.654	1.374
52	0.053	1.474	0.385	0.177	2.175	1.806
53	0.021	1.039	0.259	0.102	2.539	2.023
54	0.013	0.624	0.170	0.098	1.735	1.544
55	0.006	0.469	0.126	0.062	2.032	1.708
56	0.011	0.707	0.148	0.097	1.526	1.902
average	0.017	0.589	0.175	0.113	1.579	1.323
standard deviation	0.013	0.247	0.065	0.044	0.361	0.197
1219-172 (bsf)						
1	0.328	3.366	0.954	0.438	2.178	1.658
2	0.095	1.202	0.374	0.325	1.151	1.100
3	0.095	1.269	0.391	0.310	1.261	1.161
4	0.008	0.361	0.112	0.086	1.302	1.139
5	0.010	0.493	0.184	0.073	2.521	1.391
6	0.088	1.238	0.362	0.310	1.168	1.177
7	0.143	1.892	0.460	0.396	1.162	1.411
8	0.159	1.881	0.493	0.411	1.200	1.331
9	0.084	1.335	0.521	0.206	2.529	1.299
10	0.196	1.964	0.645	0.386	1.671	1.251
11	0.106	1.392	0.453	0.298	1.520	1.206
12	0.097	1.386	0.556	0.222	2.505	1.255
13	0.034	0.817	0.278	0.155	1.794	1.250
14	0.009	0.390	0.144	0.082	1.756	1.160
15	0.135	1.526	0.524	0.327	1.602	1.172
16	0.016	0.508	0.166	0.121	1.372	1.133
17	0.011	0.450	0.140	0.100	1.400	1.210
18	0.203	2.088	0.573	0.450	1.273	1.307

19	0.015	0.496	0.186	0.099	1.879	1.142
20	0.006	0.354	0.122	0.067	1.821	1.289
21	0.482	3.219	1.074	0.571	1.881	1.308
22	0.387	2.687	0.828	0.595	1.392	1.218
23	0.338	2.526	0.784	0.549	1.428	1.226
24	0.098	1.318	0.414	0.301	1.375	1.188
25	0.074	1.123	0.341	0.277	1.231	1.165
26	0.010	0.434	0.155	0.080	1.938	1.224
27	0.184	1.917	0.703	0.332	2.117	1.261
28	0.103	1.425	0.391	0.335	1.167	1.253
29	0.008	0.343	0.113	0.087	1.299	1.082
30	0.004	0.266	0.085	0.062	1.371	1.186
31	0.067	1.221	0.389	0.220	1.768	1.331
32	0.118	1.582	0.414	0.362	1.144	1.299
33	0.012	0.443	0.143	0.103	1.388	1.141
34	0.276	2.864	0.736	0.478	1.540	1.538
35	0.065	1.076	0.322	0.258	1.248	1.191
36	0.021	0.619	0.181	0.147	1.231	1.205
37	0.006	0.315	0.108	0.071	1.521	1.147
38	0.196	2.474	0.614	0.407	1.509	1.576
39	0.172	2.037	0.563	0.390	1.444	1.386
40	0.094	1.409	0.372	0.323	1.152	1.296
41	0.061	1.600	0.373	0.210	1.776	1.827
42	0.038	0.967	0.275	0.176	1.563	1.399
43	0.012	0.513	0.139	0.107	1.299	1.321
44	0.021	0.700	0.218	0.122	1.787	1.363
45	0.017	0.650	0.187	0.116	1.612	1.406
46	0.026	0.736	0.225	0.145	1.552	1.288
47	0.045	0.977	0.254	0.225	1.129	1.299
48	0.023	0.645	0.207	0.141	1.468	1.200
49	0.006	0.359	0.131	0.059	2.220	1.307
50	0.010	0.515	0.137	0.095	1.442	1.453
average	0.096	1.227	0.370	0.244	1.561	1.283
standard deviation	0.109	0.811	0.239	0.150	0.372	0.144
1226-34 (bsf)						
1	0.437	4.222	0.849	0.656	1.294	1.802
2	0.017	0.602	0.155	0.138	1.123	1.302
3	0.027	0.854	0.238	0.143	1.664	1.466
4	0.020	0.640	0.210	0.123	1.707	1.277
5	0.030	0.847	0.307	0.126	2.437	1.379
6	0.021	0.659	0.237	0.110	2.155	1.283
7	0.012	0.456	0.143	0.103	1.388	1.174
8	0.030	0.837	0.255	0.152	1.678	1.363
9	0.014	0.472	0.154	0.112	1.375	1.125
10	0.021	0.646	0.250	0.105	2.381	1.258
11	0.019	0.644	0.166	0.148	1.122	1.318

12	0.007	0.344	0.126	0.066	1.909	1.160
13	0.011	0.453	0.136	0.099	1.374	1.218
14	0.007	0.330	0.108	0.080	1.350	1.113
15	0.030	0.719	0.210	0.181	1.160	1.171
16	0.030	0.686	0.231	0.163	1.417	1.117
17	0.032	0.734	0.237	0.174	1.362	1.157
18	0.025	0.708	0.194	0.162	1.198	1.263
19	0.011	0.489	0.160	0.085	1.882	1.315
20	0.026	0.674	0.188	0.173	1.087	1.179
21	0.103	1.611	0.408	0.320	1.275	1.416
22	0.057	1.214	0.341	0.214	1.593	1.434
23	0.016	0.510	0.143	0.139	1.029	1.137
24	0.007	0.327	0.108	0.083	1.301	1.103
25	0.015	0.708	0.205	0.091	2.253	1.631
26	0.012	0.431	0.141	0.105	1.343	1.110
27	0.058	1.186	0.405	0.184	2.201	1.389
28	0.089	1.342	0.400	0.285	1.404	1.269
29	0.021	0.680	0.238	0.114	2.088	1.324
30	0.090	1.344	0.433	0.264	1.640	1.264
31	0.018	0.565	0.175	0.135	1.296	1.188
32	0.024	0.651	0.187	0.161	1.161	1.185
33	0.011	0.482	0.172	0.078	2.205	1.296
34	0.247	2.823	0.661	0.475	1.392	1.602
35	0.017	0.589	0.200	0.108	1.852	1.274
36	0.245	2.416	0.594	0.525	1.131	1.377
37	0.029	0.842	0.260	0.143	1.818	1.395
38	0.014	0.532	0.177	0.102	1.735	1.268
39	0.443	3.469	0.803	0.703	1.142	1.470
40	0.027	0.688	0.240	0.145	1.655	1.181
41	0.040	0.941	0.286	0.178	1.607	1.327
42	0.340	3.470	0.852	0.508	1.677	1.679
43	0.031	0.934	0.356	0.110	3.236	1.496
44	0.024	0.709	0.191	0.159	1.201	1.291
45	0.110	1.885	0.385	0.363	1.061	1.603
46	0.021	0.640	0.184	0.149	1.235	1.246
47	0.027	0.716	0.244	0.143	1.706	1.229
48	0.024	0.731	0.269	0.115	2.339	1.331
49	0.017	0.549	0.155	0.136	1.140	1.188
50	0.047	1.358	0.334	0.181	1.845	1.767
average	0.061	1.007	0.282	0.190	1.593	1.318
standard deviation	0.101	0.852	0.181	0.144	0.458	0.170
1226-90 (bsf)						
1	0.023	0.667	0.180	0.165	1.091	1.241
2	0.009	0.481	0.127	0.092	1.380	1.430
3	0.059	1.189	0.388	0.195	1.990	1.381
4	0.032	1.007	0.230	0.179	1.285	1.588

5	0.021	0.728	0.218	0.126	1.730	1.417
6	0.012	0.581	0.155	0.095	1.632	1.496
7	0.008	0.379	0.119	0.090	1.322	1.195
8	0.018	0.744	0.220	0.103	2.136	1.564
9	0.016	0.669	0.168	0.121	1.388	1.492
10	0.007	0.410	0.121	0.073	1.658	1.382
11	0.022	0.753	0.182	0.151	1.205	1.432
12	0.023	0.722	0.197	0.148	1.331	1.343
13	0.019	0.772	0.212	0.114	1.860	1.580
14	0.021	0.965	0.167	0.160	1.044	1.879
15	0.026	0.974	0.222	0.148	1.500	1.704
16	0.038	0.901	0.318	0.152	2.092	1.304
17	0.010	0.458	0.130	0.102	1.275	1.292
18	0.027	0.990	0.239	0.142	1.683	1.700
19	0.040	1.153	0.295	0.175	1.686	1.626
20	0.024	0.834	0.218	0.143	1.524	1.519
21	0.024	0.749	0.223	0.140	1.593	1.364
22	0.019	0.640	0.156	0.153	1.020	1.310
23	0.011	0.461	0.128	0.111	1.153	1.240
24	0.010	0.531	0.139	0.095	1.463	1.498
25	0.019	0.707	0.211	0.116	1.819	1.447
26	0.022	0.824	0.230	0.120	1.917	1.567
27	0.131	1.783	0.471	0.354	1.331	1.390
28	0.047	1.190	0.317	0.189	1.677	1.548
29	0.111	1.611	0.475	0.297	1.599	1.364
30	0.084	1.368	0.344	0.312	1.103	1.332
31	0.047	1.039	0.266	0.226	1.177	1.352
32	0.045	1.035	0.263	0.216	1.218	1.376
33	0.012	0.567	0.135	0.114	1.184	1.460
34	0.013	0.521	0.131	0.122	1.074	1.289
35	0.041	1.241	0.255	0.205	1.244	1.729
36	0.023	0.930	0.203	0.146	1.390	1.730
37	0.038	1.123	0.266	0.182	1.462	1.625
38	0.016	0.577	0.173	0.116	1.491	1.287
39	0.012	0.525	0.166	0.092	1.804	1.352
40	0.052	1.489	0.348	0.192	1.813	1.842
41	0.011	0.484	0.164	0.085	1.929	1.302
42	0.101	2.049	0.462	0.279	1.656	1.819
43	0.054	1.127	0.293	0.236	1.242	1.368
44	0.020	0.706	0.181	0.142	1.275	1.408
45	0.015	0.554	0.187	0.105	1.781	1.276
46	0.115	1.714	0.466	0.315	1.479	1.426
47	0.031	0.799	0.228	0.171	1.333	1.280
48	0.067	1.510	0.341	0.250	1.364	1.646
49	0.008	0.371	0.110	0.095	1.158	1.170
50	0.018	0.680	0.188	0.119	1.580	1.430

51	0.048	0.914	0.292	0.211	1.384	1.177
52	0.019	0.983	0.186	0.127	1.465	2.012
53	0.007	0.327	0.108	0.079	1.367	1.103
54	0.010	0.582	0.139	0.088	1.580	1.642
55	0.009	0.447	0.130	0.089	1.461	1.329
average	0.032	0.864	0.227	0.156	1.480	1.456
standard deviation	0.029	0.388	0.096	0.066	0.276	0.193
1226-101 (bsf)						
1	0.138	1.811	0.521	0.338	1.541	1.375
2	0.160	1.719	0.484	0.421	1.150	1.212
3	0.096	1.506	0.377	0.325	1.160	1.371
4	0.166	1.885	0.486	0.435	1.117	1.305
5	0.103	1.591	0.477	0.276	1.728	1.398
6	0.045	1.035	0.303	0.189	1.603	1.376
7	0.535	3.373	1.013	0.673	1.505	1.301
8	0.111	1.533	0.498	0.283	1.760	1.298
9	0.060	1.182	0.323	0.236	1.369	1.361
10	0.061	1.385	0.371	0.211	1.758	1.582
11	0.122	1.884	0.445	0.348	1.279	1.522
12	0.064	1.380	0.407	0.202	2.015	1.539
13	0.077	1.240	0.366	0.268	1.366	1.261
14	0.036	0.801	0.262	0.174	1.506	1.191
15	0.147	2.004	0.486	0.384	1.266	1.474
16	0.026	0.766	0.216	0.155	1.394	1.340
17	0.021	0.633	0.190	0.138	1.377	1.232
18	0.020	0.626	0.229	0.111	2.063	1.249
19	0.134	1.709	0.418	0.408	1.025	1.317
20	0.105	1.636	0.576	0.232	2.483	1.424
21	0.075	1.136	0.334	0.287	1.164	1.170
22	0.084	1.266	0.397	0.269	1.476	1.232
23	0.135	1.873	0.483	0.356	1.357	1.438
24	0.096	1.617	0.414	0.296	1.399	1.472
25	0.165	2.068	0.546	0.384	1.422	1.436
26	0.098	1.758	0.440	0.283	1.555	1.584
27	0.030	0.692	0.212	0.177	1.198	1.127
28	0.139	1.729	0.447	0.397	1.126	1.308
29	0.086	1.251	0.391	0.279	1.401	1.203
30	0.068	1.285	0.379	0.229	1.655	1.390
average	0.107	1.479	0.416	0.292	1.474	1.350
standard deviation	0.092	0.550	0.152	0.114	0.317	0.122
1226-117 (bsf)						
1	0.224	2.100	0.665	0.429	1.550	1.252
2	0.083	1.127	0.398	0.264	1.508	1.104
3	0.213	2.074	0.612	0.444	1.378	1.268
4	0.631	3.640	1.015	0.792	1.282	1.293
5	0.206	2.032	0.638	0.410	1.556	1.263

6	0.305	2.399	0.727	0.535	1.359	1.225
7	0.216	2.032	0.609	0.451	1.350	1.233
8	0.179	1.784	0.571	0.399	1.431	1.189
9	0.117	1.401	0.440	0.340	1.294	1.155
10	0.166	1.692	0.593	0.356	1.666	1.171
11	0.448	2.986	0.987	0.578	1.708	1.258
12	0.126	1.998	0.516	0.311	1.659	1.588
13	0.119	2.199	0.400	0.378	1.058	1.798
14	0.242	2.331	0.723	0.426	1.697	1.337
15	0.069	1.074	0.320	0.273	1.172	1.153
16	0.430	3.285	0.761	0.720	1.057	1.413
17	0.044	1.030	0.300	0.188	1.596	1.385
18	0.041	0.863	0.255	0.206	1.238	1.202
19	0.167	1.908	0.499	0.427	1.169	1.317
20	0.417	3.085	0.816	0.650	1.255	1.348
21	0.107	1.423	0.425	0.319	1.332	1.227
22	0.038	1.008	0.253	0.192	1.318	1.459
23	0.117	1.621	0.522	0.285	1.832	1.337
24	0.106	1.504	0.447	0.302	1.480	1.303
25	0.068	1.409	0.472	0.183	2.579	1.524
26	0.765	3.719	1.138	0.856	1.329	1.199
27	0.361	3.215	0.890	0.516	1.725	1.509
28	0.559	3.818	0.900	0.791	1.138	1.441
29	0.161	1.787	0.557	0.368	1.514	1.256
30	0.209	1.994	0.551	0.482	1.143	1.230
31	0.016	0.628	0.213	0.098	2.173	1.401
32	0.021	0.641	0.182	0.146	1.247	1.248
33	0.035	1.049	0.246	0.179	1.374	1.582
34	0.172	1.845	0.532	0.413	1.288	1.255
35	0.180	1.950	0.596	0.385	1.548	1.297
36	0.049	1.056	0.299	0.209	1.431	1.346
37	0.026	0.702	0.217	0.153	1.418	1.228
38	0.160	1.878	0.486	0.418	1.163	1.324
39	0.061	1.246	0.315	0.247	1.275	1.423
40	0.063	1.293	0.386	0.207	1.865	1.453
average	0.193	1.871	0.537	0.383	1.454	1.325
standard deviation	0.175	0.857	0.236	0.187	0.300	0.140
1226-127 (bsf)						
1	0.229	2.770	0.690	0.424	1.627	1.633
2	0.092	1.303	0.382	0.307	1.244	1.212
3	0.358	3.120	0.831	0.549	1.514	1.471
4	0.153	1.591	0.469	0.415	1.130	1.147
5	0.439	3.598	1.011	0.553	1.828	1.532
6	0.326	2.471	0.742	0.559	1.327	1.221
7	0.273	2.391	0.684	0.509	1.344	1.291
8	0.294	3.040	0.728	0.514	1.416	1.582

9	0.358	3.223	0.825	0.553	1.492	1.520
10	0.640	4.231	1.277	0.638	2.002	1.492
11	0.650	4.401	1.090	0.759	1.436	1.540
12	0.499	3.500	0.974	0.653	1.492	1.398
13	0.646	4.237	1.283	0.642	1.998	1.487
14	0.179	2.112	0.620	0.367	1.689	1.408
15	0.483	3.383	0.870	0.707	1.231	1.373
16	0.527	3.793	1.100	0.610	1.803	1.474
17	0.946	5.707	1.400	0.860	1.628	1.655
18	0.112	1.560	0.398	0.357	1.115	1.315
19	0.187	1.917	0.598	0.397	1.506	1.251
20	0.153	1.952	0.539	0.361	1.493	1.408
21	0.142	1.660	0.451	0.400	1.128	1.243
22	0.079	1.426	0.400	0.252	1.587	1.431
23	0.094	1.630	0.523	0.229	2.284	1.500
24	0.121	1.923	0.440	0.351	1.254	1.559
25	0.156	2.282	0.607	0.327	1.856	1.630
26	0.167	2.143	0.519	0.409	1.269	1.479
27	0.136	2.461	0.540	0.322	1.677	1.883
28	0.623	3.869	0.915	0.866	1.057	1.383
29	0.199	2.326	0.637	0.398	1.601	1.471
30	0.049	1.259	0.331	0.189	1.751	1.604
31	0.075	1.569	0.349	0.272	1.283	1.616
32	0.234	2.809	0.698	0.426	1.638	1.638
33	0.129	1.740	0.445	0.370	1.203	1.367
34	0.279	2.559	0.697	0.509	1.369	1.367
35	0.322	2.537	0.735	0.558	1.317	1.261
36	0.447	3.650	1.024	0.556	1.842	1.540
37	0.156	1.691	0.483	0.410	1.178	1.208
38	0.210	2.110	0.687	0.389	1.766	1.299
39	0.210	2.085	0.528	0.507	1.041	1.283
average	0.292	2.616	0.706	0.474	1.498	1.440
standard deviation	0.206	1.022	0.275	0.162	0.293	0.158
1226-138 (bsf)						
1	2.305	6.374	2.114	1.389	1.522	1.184
2	1.541	5.498	1.520	1.291	1.177	1.249
3	1.005	4.388	1.220	1.049	1.163	1.235
4	0.581	3.360	1.135	0.652	1.741	1.244
5	2.401	6.891	2.056	1.486	1.384	1.255
6	0.933	4.431	1.122	1.059	1.059	1.294
7	1.094	4.630	1.388	1.003	1.384	1.249
8	0.822	4.052	1.168	0.896	1.304	1.261
9	1.653	5.539	1.883	1.118	1.684	1.215
10	0.654	3.887	1.109	0.751	1.477	1.356
11	0.047	0.942	0.287	0.207	1.386	1.226
12	0.008	0.457	0.136	0.079	1.722	1.441

13	0.661	3.478	0.972	0.866	1.122	1.207
14	1.229	4.546	1.398	1.119	1.249	1.157
15	1.062	4.678	1.249	1.082	1.154	1.281
16	1.062	4.678	1.249	1.082	1.154	1.281
17	0.110	1.685	0.395	0.355	1.113	1.433
18	0.040	0.844	0.265	0.191	1.387	1.190
19	0.040	0.844	0.265	0.191	1.387	1.190
20	0.028	1.011	0.204	0.176	1.159	1.704
21	0.018	0.654	0.166	0.137	1.212	1.375
22	0.016	0.630	0.179	0.114	1.570	1.405
23	0.006	0.371	0.124	0.058	2.138	1.351
24	5.478	9.587	3.000	2.325	1.290	1.155
25	1.231	4.581	1.385	1.132	1.223	1.165
26	0.859	3.937	1.271	0.861	1.476	1.198
27	0.887	4.106	1.306	0.864	1.512	1.230
28	1.483	5.487	1.896	0.996	1.904	1.271
29	1.297	5.872	1.734	0.952	1.821	1.454
30	0.523	3.104	1.050	0.635	1.654	1.211
average	0.969	3.685	1.108	0.804	1.418	1.282
standard deviation	1.082	2.261	0.713	0.519	0.267	0.117
1226-151 (bsf)						
1	0.019	0.845	0.230	0.103	2.233	1.729
2	0.017	0.599	0.178	0.122	1.459	1.296
3	0.008	0.422	0.107	0.099	1.081	1.331
4	0.008	0.414	0.114	0.088	1.295	1.306
5	0.021	0.765	0.191	0.138	1.384	1.489
6	0.020	0.833	0.207	0.126	1.643	1.662
7	0.011	0.471	0.167	0.086	1.942	1.267
8	0.016	0.540	0.168	0.123	1.366	1.204
9	0.015	0.549	0.185	0.103	1.796	1.265
10	0.007	0.382	0.107	0.085	1.259	1.288
11	0.008	0.378	0.104	0.097	1.072	1.192
12	0.007	0.384	0.106	0.085	1.247	1.295
13	0.006	0.351	0.093	0.078	1.192	1.278
14	0.012	0.467	0.164	0.094	1.745	1.203
15	0.006	0.317	0.111	0.068	1.632	1.154
16	0.009	0.433	0.134	0.087	1.540	1.288
17	0.012	0.471	0.162	0.091	1.780	1.213
18	0.004	0.292	0.086	0.057	1.509	1.302
19	0.015	0.578	0.172	0.113	1.522	1.331
20	0.003	0.237	0.070	0.057	1.228	1.221
21	0.007	0.410	0.130	0.066	1.970	1.382
22	0.011	0.518	0.153	0.095	1.611	1.393
23	0.009	0.399	0.109	0.106	1.028	1.186
24	0.016	0.620	0.151	0.135	1.119	1.383
25	0.003	0.223	0.073	0.049	1.490	1.149

26	0.005	0.275	0.090	0.067	1.343	1.097
27	0.009	0.432	0.148	0.078	1.897	1.285
28	0.002	0.204	0.065	0.047	1.383	1.287
29	0.002	0.189	0.061	0.047	1.298	1.192
30	0.003	0.230	0.068	0.058	1.172	1.185
31	0.010	0.451	0.141	0.090	1.567	1.272
32	0.007	0.382	0.134	0.070	1.914	1.288
33	0.012	0.540	0.164	0.097	1.691	1.391
34	0.008	0.377	0.122	0.086	1.419	1.189
35	0.008	0.367	0.121	0.083	1.458	1.157
36	0.010	0.442	0.126	0.097	1.299	1.247
37	0.013	0.539	0.172	0.096	1.792	1.334
38	0.006	0.312	0.107	0.066	1.621	1.136
39	0.019	0.581	0.181	0.132	1.371	1.189
40	0.009	0.427	0.139	0.081	1.716	1.270
41	0.005	0.286	0.095	0.066	1.439	1.141
42	0.013	0.526	0.176	0.097	1.814	1.301
43	0.016	0.537	0.178	0.112	1.589	1.198
44	0.023	0.703	0.206	0.145	1.421	1.308
45	0.007	0.375	0.126	0.068	1.853	1.264
46	0.012	0.557	0.139	0.109	1.275	1.434
47	0.007	0.363	0.119	0.072	1.653	1.224
48	0.017	0.578	0.159	0.133	1.195	1.251
49	0.021	0.718	0.215	0.124	1.734	1.398
50	0.005	0.299	0.104	0.063	1.651	1.193
average	0.010	0.452	0.137	0.091	1.514	1.281
standard deviation	0.005	0.155	0.042	0.025	0.270	0.119
1226-159 (bsf)						
1	0.022	0.679	0.193	0.146	1.322	1.291
2	0.011	0.443	0.136	0.103	1.320	1.192
3	0.009	0.421	0.115	0.098	1.173	1.252
4	0.011	0.454	0.123	0.111	1.108	1.221
5	0.007	0.382	0.122	0.077	1.584	1.288
6	0.011	0.544	0.153	0.090	1.700	1.463
7	0.005	0.292	0.087	0.072	1.208	1.165
8	0.029	0.843	0.251	0.149	1.685	1.396
9	0.019	0.973	0.252	0.095	2.653	1.991
10	0.017	0.655	0.192	0.110	1.745	1.417
11	0.026	0.918	0.298	0.110	2.709	1.606
12	0.034	0.936	0.259	0.167	1.551	1.432
13	0.004	0.275	0.097	0.056	1.732	1.227
14	0.009	0.439	0.127	0.092	1.380	1.305
15	0.014	0.733	0.189	0.091	2.077	1.748
16	0.023	0.713	0.214	0.136	1.574	1.326
17	0.010	0.412	0.119	0.103	1.155	1.162
18	0.019	0.666	0.196	0.125	1.568	1.363

19	0.015	0.657	0.257	0.073	3.521	1.513
20	0.007	0.373	0.136	0.063	2.159	1.258
21	0.117	1.500	0.454	0.327	1.388	1.237
22	0.050	1.081	0.331	0.191	1.733	1.364
23	0.029	0.723	0.225	0.163	1.380	1.198
24	0.056	0.998	0.288	0.248	1.161	1.190
25	0.028	0.729	0.207	0.170	1.218	1.229
26	0.009	0.409	0.115	0.099	1.162	1.216
27	0.029	0.886	0.325	0.116	2.802	1.468
28	0.024	0.686	0.212	0.145	1.462	1.249
29	0.006	0.328	0.095	0.077	1.234	1.195
30	0.006	0.316	0.090	0.083	1.084	1.151
31	0.012	0.506	0.175	0.088	1.989	1.303
32	0.027	0.796	0.249	0.138	1.804	1.367
33	0.014	0.627	0.189	0.096	1.969	1.495
34	0.014	0.485	0.158	0.109	1.450	1.156
35	0.007	0.369	0.125	0.072	1.736	1.244
36	0.011	0.426	0.120	0.112	1.071	1.146
37	0.023	0.627	0.176	0.164	1.073	1.166
38	0.033	1.033	0.322	0.131	2.458	1.604
39	0.030	1.036	0.244	0.159	1.535	1.687
40	0.010	0.561	0.158	0.077	2.052	1.583
41	0.008	0.481	0.147	0.067	2.194	1.517
42	0.005	0.323	0.097	0.070	1.386	1.289
43	0.020	0.590	0.177	0.145	1.221	1.177
44	0.013	0.526	0.198	0.083	2.386	1.301
45	0.008	0.376	0.119	0.084	1.417	1.186
46	0.061	1.074	0.305	0.254	1.201	1.227
47	0.010	0.412	0.137	0.092	1.489	1.162
48	0.012	0.557	0.166	0.094	1.766	1.434
49	0.004	0.258	0.085	0.061	1.393	1.151
50	0.016	0.656	0.198	0.102	1.941	1.463
average	0.020	0.624	0.188	0.118	1.662	1.335
standard deviation	0.019	0.265	0.079	0.053	0.522	0.180
1226-171 (bsf)						
1	0.056	1.136	0.355	0.201	1.766	1.354
2	0.060	1.099	0.354	0.216	1.639	1.266
3	0.051	1.235	0.329	0.199	1.653	1.543
4	0.089	1.419	0.411	0.276	1.489	1.342
5	0.060	1.128	0.355	0.216	1.644	1.299
6	0.042	0.860	0.244	0.217	1.124	1.184
7	0.061	1.142	0.351	0.221	1.588	1.304
8	0.046	1.211	0.283	0.208	1.361	1.593
9	0.090	1.363	0.455	0.252	1.806	1.282
10	0.034	0.743	0.235	0.186	1.263	1.137
11	0.041	0.911	0.291	0.181	1.608	1.269

12	0.036	0.987	0.291	0.158	1.842	1.467
13	0.058	1.373	0.322	0.228	1.412	1.608
14	0.024	0.726	0.198	0.156	1.269	1.322
15	0.042	0.962	0.269	0.200	1.345	1.324
16	0.037	0.980	0.254	0.185	1.373	1.437
17	0.048	1.053	0.313	0.195	1.605	1.356
18	0.038	1.016	0.258	0.188	1.372	1.470
19	0.058	1.019	0.324	0.228	1.421	1.194
20	0.043	0.967	0.295	0.185	1.595	1.315
21	0.039	1.232	0.272	0.182	1.495	1.760
22	0.090	1.349	0.414	0.278	1.489	1.268
23	0.055	1.008	0.318	0.221	1.439	1.212
24	0.024	0.715	0.197	0.156	1.263	1.302
25	0.042	0.968	0.269	0.200	1.345	1.332
26	0.135	1.624	0.448	0.384	1.167	1.247
27	0.045	1.398	0.343	0.167	2.054	1.859
28	0.035	1.328	0.443	0.100	4.430	2.002
29	0.058	1.424	0.324	0.227	1.427	1.668
30	0.036	0.988	0.292	0.159	1.836	1.469
31	0.042	0.936	0.291	0.183	1.590	1.288
32	0.044	1.208	0.333	0.167	1.994	1.625
33	0.056	1.264	0.372	0.192	1.938	1.507
34	0.038	1.010	0.293	0.166	1.765	1.462
35	0.050	1.411	0.347	0.184	1.886	1.780
36	0.034	0.953	0.336	0.127	2.646	1.458
37	0.144	1.701	0.506	0.363	1.394	1.264
38	0.045	1.014	0.352	0.162	2.173	1.348
39	0.034	0.856	0.280	0.153	1.830	1.310
40	0.061	1.062	0.321	0.244	1.316	1.213
41	0.088	1.515	0.365	0.306	1.193	1.441
42	0.033	0.926	0.282	0.151	1.868	1.438
43	0.017	0.611	0.176	0.120	1.467	1.322
44	0.028	0.799	0.242	0.149	1.624	1.347
45	0.078	1.313	0.398	0.248	1.605	1.326
46	0.183	2.109	0.700	0.334	2.096	1.391
47	0.023	0.818	0.213	0.135	1.578	1.522
48	0.035	0.843	0.241	0.183	1.317	1.271
49	0.076	1.418	0.352	0.275	1.280	1.451
50	0.039	0.941	0.296	0.166	1.783	1.344
average	0.054	1.121	0.324	0.204	1.649	1.406
standard deviation	0.031	0.285	0.088	0.058	0.499	0.179
1226-174 (bsf)						
1	0.019	0.661	0.191	0.126	1.516	1.353
2	0.013	0.526	0.153	0.106	1.443	1.301
3	0.009	0.418	0.128	0.088	1.455	1.243
4	0.012	0.503	0.146	0.105	1.390	1.295

5	0.007	0.402	0.123	0.076	1.618	1.355
6	0.011	0.539	0.191	0.073	2.616	1.450
7	0.005	0.308	0.099	0.068	1.456	1.229
8	0.007	0.337	0.109	0.077	1.416	1.136
9	0.009	0.488	0.134	0.090	1.489	1.451
10	0.010	0.552	0.158	0.082	1.927	1.557
11	0.006	0.328	0.113	0.067	1.687	1.195
12	0.006	0.336	0.104	0.073	1.425	1.224
13	0.014	0.670	0.162	0.109	1.486	1.597
14	0.006	0.344	0.114	0.068	1.676	1.253
15	0.009	0.444	0.123	0.095	1.295	1.320
16	0.008	0.376	0.136	0.072	1.889	1.186
17	0.009	0.406	0.140	0.081	1.728	1.207
18	0.003	0.216	0.064	0.050	1.280	1.112
19	0.007	0.406	0.103	0.091	1.132	1.369
20	0.021	0.670	0.173	0.153	1.131	1.304
21	0.010	0.521	0.156	0.085	1.835	1.470
22	0.004	0.261	0.072	0.069	1.043	1.164
23	0.004	0.258	0.082	0.058	1.414	1.151
24	0.003	0.221	0.074	0.045	1.644	1.138
25	0.012	0.619	0.208	0.076	2.737	1.594
26	0.006	0.321	0.105	0.072	1.458	1.169
27	0.004	0.252	0.084	0.058	1.448	1.124
28	0.012	0.570	0.171	0.092	1.859	1.468
29	0.002	0.270	0.091	0.035	2.600	1.703
30	0.003	0.260	0.071	0.061	1.164	1.339
31	0.003	0.239	0.090	0.040	2.250	1.231
32	0.005	0.323	0.096	0.066	1.455	1.289
33	0.004	0.251	0.088	0.054	1.630	1.120
34	0.012	0.671	0.167	0.089	1.876	1.728
35	0.004	0.306	0.088	0.063	1.397	1.365
36	0.004	0.276	0.097	0.057	1.702	1.231
37	0.015	0.662	0.173	0.110	1.573	1.525
38	0.008	0.393	0.138	0.078	1.769	1.239
39	0.006	0.387	0.101	0.070	1.443	1.409
40	0.004	0.276	0.099	0.051	1.941	1.231
41	0.004	0.271	0.097	0.058	1.672	1.209
42	0.003	0.227	0.079	0.049	1.612	1.169
43	0.008	0.427	0.115	0.091	1.264	1.347
44	0.007	0.384	0.102	0.092	1.109	1.295
45	0.007	0.454	0.130	0.071	1.831	1.531
46	0.020	0.682	0.214	0.121	1.769	1.360
47	0.008	0.453	0.134	0.072	1.861	1.429
48	0.007	0.440	0.144	0.065	2.215	1.484
49	0.009	0.466	0.158	0.069	2.290	1.386
50	0.020	0.772	0.208	0.122	1.705	1.540

51	0.005	0.363	0.124	0.046	2.696	1.448
52	0.011	0.445	0.130	0.103	1.262	1.197
53	0.006	0.356	0.111	0.065	1.708	1.296
54	0.024	0.847	0.207	0.146	1.418	1.542
55	0.012	0.494	0.155	0.096	1.615	1.272
56	0.010	0.484	0.147	0.087	1.690	1.365
57	0.009	0.433	0.110	0.101	1.089	1.288
58	0.023	0.836	0.206	0.140	1.471	1.555
59	0.007	0.345	0.112	0.074	1.514	1.163
60	0.007	0.397	0.121	0.077	1.571	1.339
average	0.009	0.431	0.129	0.080	1.644	1.334
standard deviation	0.005	0.157	0.039	0.025	0.385	0.152
1226-188 (bsf)						
1	0.149	2.771	0.759	0.250	3.036	2.025
2	0.096	1.432	0.456	0.267	1.708	1.304
3	0.056	1.064	0.340	0.209	1.627	1.268
4	0.030	0.731	0.233	0.164	1.421	1.191
5	0.029	0.854	0.244	0.152	1.605	1.415
6	0.059	1.156	0.378	0.197	1.919	1.343
7	0.036	1.073	0.318	0.145	2.193	1.595
8	0.076	1.446	0.423	0.229	1.847	1.480
9	0.016	0.628	0.181	0.112	1.616	1.401
10	0.077	1.363	0.378	0.260	1.454	1.386
11	0.034	0.894	0.283	0.151	1.874	1.368
12	0.022	0.666	0.181	0.157	1.153	1.267
13	0.043	1.109	0.259	0.210	1.233	1.509
14	0.052	1.099	0.325	0.204	1.593	1.360
15	0.031	0.936	0.296	0.134	2.209	1.500
16	0.078	1.458	0.338	0.295	1.146	1.473
17	0.085	1.507	0.390	0.279	1.398	1.458
18	0.080	1.302	0.491	0.207	2.372	1.299
19	0.037	0.860	0.266	0.179	1.486	1.261
20	0.070	1.444	0.369	0.243	1.519	1.540
21	0.021	0.640	0.219	0.124	1.766	1.246
22	0.034	1.091	0.281	0.156	1.801	1.669
23	0.019	0.645	0.200	0.120	1.667	1.320
24	0.021	0.643	0.181	0.150	1.207	1.252
25	0.030	0.862	0.256	0.152	1.684	1.404
26	0.033	0.858	0.217	0.194	1.119	1.332
27	0.018	0.602	0.159	0.144	1.104	1.266
28	0.041	1.210	0.316	0.164	1.927	1.686
29	0.024	0.815	0.235	0.130	1.808	1.484
30	0.044	1.026	0.286	0.195	1.467	1.380
31	0.136	2.094	0.583	0.296	1.970	1.602
32	0.399	3.674	0.897	0.566	1.585	1.641
33	0.028	0.843	0.209	0.172	1.215	1.421

34	0.015	0.534	0.186	0.101	1.842	1.230
35	0.021	0.817	0.195	0.135	1.444	1.590
36	0.197	2.404	0.609	0.412	1.478	1.528
37	0.044	1.148	0.291	0.194	1.500	1.544
38	0.112	1.953	0.400	0.355	1.127	1.646
39	0.016	0.668	0.174	0.119	1.462	1.490
40	0.051	1.046	0.382	0.171	2.234	1.307
41	0.094	1.419	0.427	0.279	1.530	1.306
42	0.021	0.756	0.248	0.109	2.275	1.472
43	0.037	1.049	0.289	0.164	1.762	1.538
44	0.023	0.787	0.187	0.155	1.206	1.464
45	0.043	1.065	0.292	0.189	1.545	1.449
46	0.026	0.901	0.185	0.181	1.022	1.576
47	0.017	0.618	0.170	0.126	1.349	1.337
48	0.183	2.216	0.491	0.474	1.036	1.461
49	0.012	0.422	0.143	0.103	1.388	1.087
50	0.088	1.403	0.496	0.226	2.195	1.334
51	0.052	0.981	0.302	0.218	1.385	1.214
52	0.078	1.407	0.460	0.215	2.140	1.421
53	0.037	0.916	0.270	0.175	1.543	1.343
54	0.048	0.943	0.276	0.224	1.232	1.214
55	0.073	1.221	0.352	0.265	1.328	1.275
56	0.027	0.711	0.227	0.152	1.493	1.221
57	0.041	1.046	0.297	0.175	1.697	1.457
58	0.021	0.657	0.217	0.126	1.722	1.279
59	0.032	0.757	0.259	0.156	1.660	1.194
60	0.079	1.491	0.425	0.235	1.809	1.496
61	0.023	0.855	0.206	0.145	1.421	1.590
62	0.030	0.980	0.280	0.138	2.029	1.596
63	0.108	1.641	0.440	0.313	1.406	1.409
64	0.058	1.199	0.360	0.206	1.748	1.404
65	0.048	1.191	0.259	0.239	1.084	1.534
average	0.058	1.138	0.319	0.201	1.613	1.418
standard deviation	0.058	0.553	0.140	0.085	0.378	0.157
1230-63 (bsf)						
1	0.353	2.604	0.949	0.473	2.006	1.236
2	0.833	3.967	1.187	0.894	1.328	1.226
3	0.342	2.530	0.761	0.571	1.333	1.220
4	0.166	1.850	0.663	0.318	2.085	1.281
5	0.403	2.669	0.765	0.670	1.142	1.186
6	0.364	2.681	0.965	0.480	2.010	1.254
7	0.249	2.072	0.657	0.483	1.360	1.171
8	0.365	2.630	0.892	0.521	1.712	1.228
9	0.724	3.663	1.183	0.780	1.517	1.214
10	0.232	2.179	0.635	0.466	1.363	1.276
11	0.155	1.713	0.508	0.388	1.309	1.227

12	0.166	1.962	0.653	0.323	2.022	1.358
13	0.347	3.188	1.069	0.414	2.582	1.527
14	0.374	2.638	0.853	0.558	1.529	1.217
15	0.316	2.393	0.688	0.584	1.178	1.201
16	0.339	2.302	0.779	0.554	1.406	1.115
17	0.465	2.740	0.966	0.612	1.578	1.133
18	0.277	2.057	0.656	0.539	1.217	1.103
19	0.239	1.969	0.697	0.436	1.599	1.136
20	0.675	3.405	1.176	0.730	1.611	1.169
21	0.332	2.629	0.759	0.557	1.363	1.287
22	0.617	3.341	0.951	0.826	1.151	1.200
23	0.394	2.963	0.848	0.592	1.432	1.332
24	0.718	3.552	1.029	0.888	1.159	1.183
25	0.652	3.434	1.034	0.803	1.288	1.200
26	0.168	1.949	0.593	0.362	1.638	1.341
27	0.612	3.313	0.950	0.820	1.159	1.195
28	0.525	3.340	0.948	0.705	1.345	1.300
30	0.054	1.025	0.296	0.235	1.260	1.244
average	0.395	2.647	0.831	0.572	1.506	1.233
standard deviation	0.199	0.688	0.213	0.178	0.346	0.085
1230-138 (bsf)						
1	2.866	9.507	2.456	1.486	1.653	1.584
2	0.638	3.983	1.143	0.710	1.610	1.407
3	0.132	1.945	0.517	0.325	1.591	1.510
4	1.767	5.219	1.589	1.416	1.122	1.108
5	0.092	1.201	0.421	0.279	1.509	1.117
6	0.304	2.213	0.679	0.570	1.191	1.132
7	0.145	1.571	0.460	0.401	1.147	1.164
8	0.169	1.596	0.531	0.406	1.308	1.095
9	0.343	2.376	0.733	0.596	1.230	1.144
10	0.222	1.922	0.593	0.476	1.246	1.151
11	0.228	1.887	0.584	0.497	1.175	1.115
12	0.342	2.539	0.834	0.522	1.598	1.225
13	0.251	1.997	0.648	0.492	1.317	1.124
14	1.276	5.674	1.418	1.146	1.237	1.417
15	0.184	2.740	0.858	0.273	3.143	1.802
16	0.069	1.336	0.380	0.231	1.645	1.435
17	0.095	1.639	0.498	0.243	2.049	1.500
18	0.640	3.375	1.068	0.762	1.402	1.190
19	0.329	2.743	0.810	0.518	1.564	1.349
20	0.062	1.299	0.366	0.217	1.687	1.472
21	0.069	1.342	0.414	0.214	1.935	1.441
22	0.226	3.540	0.722	0.398	1.814	2.101
23	0.127	1.738	0.493	0.328	1.503	1.376
24	0.810	4.579	1.188	0.868	1.369	1.435
25	0.130	1.571	0.471	0.351	1.342	1.229

26	0.086	1.632	0.358	0.304	1.178	1.570
27	0.085	1.564	0.448	0.242	1.851	1.513
28	0.115	1.367	0.440	0.333	1.321	1.137
29	0.111	1.290	0.424	0.333	1.273	1.092
30	1.064	5.024	1.434	0.945	1.517	1.374
31	0.103	1.448	0.465	0.282	1.649	1.273
32	0.076	1.145	0.353	0.272	1.298	1.172
33	0.080	1.556	0.414	0.246	1.683	1.552
average	0.401	2.562	0.734	0.506	1.520	1.343
standard deviation	0.590	1.773	0.459	0.332	0.379	0.229
1230-158 (bsf)						
1	0.130	1.928	0.579	0.286	2.024	1.508
2	0.068	1.345	0.349	0.248	1.407	1.455
3	0.017	0.649	0.151	0.141	1.071	1.404
4	0.173	1.826	0.586	0.376	1.559	1.238
5	0.273	2.138	0.707	0.492	1.437	1.154
6	0.126	1.565	0.611	0.263	2.323	1.244
7	0.102	1.412	0.465	0.280	1.661	1.247
8	0.081	1.303	0.441	0.235	1.877	1.292
9	0.028	0.741	0.247	0.142	1.739	1.249
10	0.114	1.493	0.566	0.257	2.202	1.247
11	0.217	1.884	0.572	0.483	1.184	1.141
12	0.233	2.527	0.762	0.389	1.959	1.477
13	0.074	1.882	0.545	0.173	3.150	1.952
14	0.201	1.964	0.690	0.371	1.860	1.236
15	0.344	2.692	0.781	0.562	1.390	1.295
16	0.070	1.217	0.322	0.275	1.171	1.298
17	0.038	1.044	0.283	0.171	1.655	1.511
18	0.069	1.129	0.345	0.254	1.358	1.212
19	0.105	1.388	0.442	0.303	1.459	1.208
20	0.413	2.952	0.916	0.574	1.596	1.296
21	0.132	1.716	0.561	0.300	1.870	1.332
22	0.121	2.165	0.633	0.244	2.594	1.756
23	0.026	0.665	0.229	0.147	1.558	1.163
24	0.014	0.542	0.146	0.118	1.237	1.292
25	0.012	0.480	0.140	0.108	1.296	1.236
26	0.126	2.672	0.723	0.222	3.257	2.123
27	0.136	1.930	0.764	0.227	3.366	1.476
28	0.033	0.846	0.307	0.138	2.225	1.314
29	0.006	0.350	0.111	0.065	1.708	1.275
30	0.022	0.855	0.277	0.100	2.770	1.626
31	0.529	3.539	0.974	0.691	1.410	1.373
32	0.099	2.180	0.767	0.164	4.677	1.954
33	0.157	2.141	0.857	0.233	3.678	1.524
34	0.061	1.300	0.463	0.166	2.789	1.485
35	0.029	0.724	0.196	0.189	1.037	1.199

36	0.135	1.753	0.570	0.301	1.894	1.346
37	0.177	1.996	0.524	0.431	1.216	1.338
38	0.123	1.491	0.456	0.344	1.326	1.199
39	0.070	1.491	0.395	0.225	1.756	1.590
40	0.201	2.042	0.693	0.370	1.873	1.285
41	0.140	1.594	0.534	0.335	1.594	1.202
42	0.069	1.106	0.346	0.255	1.357	1.188
43	0.033	0.755	0.254	0.164	1.549	1.172
44	0.009	0.421	0.147	0.078	1.885	1.252
45	0.006	0.330	0.121	0.062	1.952	1.202
average	0.119	1.515	0.479	0.266	1.910	1.368
standard deviation	0.109	0.738	0.232	0.141	0.760	0.222
1230-297 (bsf)						
1	0.012	0.570	0.153	0.099	1.545	1.468
2	0.011	0.429	0.154	0.088	1.750	1.154
3	0.012	0.473	0.164	0.092	1.783	1.218
4	0.006	0.351	0.133	0.062	2.145	1.278
5	0.018	0.724	0.191	0.119	1.605	1.522
6	0.005	0.295	0.092	0.074	1.243	1.177
7	0.007	0.405	0.128	0.073	1.753	1.366
8	0.007	0.350	0.137	0.063	2.175	1.180
9	0.008	0.370	0.117	0.090	1.300	1.167
10	0.010	0.399	0.134	0.095	1.411	1.126
11	0.053	0.965	0.356	0.190	1.874	1.182
12	0.006	0.325	0.119	0.065	1.831	1.184
13	0.010	0.388	0.130	0.095	1.368	1.095
14	0.004	0.248	0.094	0.056	1.679	1.106
15	0.004	0.251	0.087	0.062	1.403	1.120
16	0.006	0.325	0.118	0.065	1.815	1.184
17	0.005	0.275	0.085	0.073	1.164	1.097
18	0.005	0.270	0.080	0.074	1.081	1.077
19	0.004	0.245	0.087	0.055	1.582	1.093
20	0.005	0.265	0.091	0.070	1.300	1.057
21	0.010	0.418	0.144	0.092	1.565	1.179
22	0.007	0.320	0.093	0.090	1.033	1.079
23	0.004	0.282	0.098	0.054	1.815	1.258
24	0.006	0.301	0.096	0.081	1.185	1.096
25	0.010	0.410	0.129	0.101	1.277	1.157
26	0.009	0.377	0.114	0.098	1.163	1.121
27	0.002	0.190	0.064	0.038	1.684	1.198
28	0.009	0.394	0.130	0.089	1.461	1.172
29	0.007	0.378	0.118	0.078	1.513	1.274
30	0.007	0.327	0.101	0.091	1.110	1.103
31	0.010	0.400	0.128	0.095	1.347	1.128
32	0.003	0.239	0.076	0.058	1.310	1.231
33	0.003	0.224	0.077	0.045	1.711	1.154

34	0.008	0.343	0.118	0.086	1.372	1.082
35	0.010	0.409	0.144	0.085	1.694	1.154
36	0.013	0.469	0.170	0.094	1.809	1.160
37	0.012	0.462	0.138	0.107	1.290	1.190
38	0.006	0.326	0.127	0.058	2.190	1.187
39	0.008	0.340	0.117	0.082	1.427	1.072
40	0.010	0.398	0.155	0.078	1.987	1.123
41	0.045	0.909	0.329	0.176	1.869	1.209
42	0.015	0.473	0.154	0.125	1.232	1.089
43	0.011	0.487	0.172	0.083	2.072	1.310
44	0.012	0.471	0.163	0.096	1.698	1.213
45	0.007	0.343	0.128	0.066	1.939	1.156
46	0.011	0.441	0.162	0.083	1.952	1.186
47	0.012	0.572	0.142	0.107	1.327	1.473
48	0.005	0.307	0.092	0.068	1.353	1.225
49	0.006	0.293	0.105	0.069	1.522	1.067
50	0.013	0.456	0.158	0.101	1.564	1.128
51	0.039	0.883	0.306	0.164	1.866	1.261
52	0.038	0.845	0.276	0.177	1.559	1.223
53	0.107	1.641	0.457	0.299	1.528	1.415
54	0.053	1.018	0.301	0.223	1.350	1.247
55	0.026	0.674	0.229	0.146	1.568	1.179
56	0.026	0.729	0.255	0.130	1.962	1.275
57	0.041	0.864	0.290	0.179	1.620	1.204
58	0.039	0.929	0.293	0.171	1.713	1.327
59	0.052	1.114	0.365	0.182	2.005	1.378
60	0.022	0.620	0.217	0.128	1.695	1.179
61	0.016	0.550	0.208	0.099	2.101	1.227
62	0.036	0.841	0.274	0.169	1.621	1.250
63	0.038	0.927	0.308	0.158	1.949	1.341
64	0.036	1.050	0.261	0.176	1.483	1.561
65	0.020	0.605	0.183	0.141	1.298	1.207
average	0.017	0.507	0.166	0.104	1.594	1.205
stv	0.018	0.277	0.084	0.048	0.294	0.111
1230-312 (bsf)						
1	0.011	0.431	0.154	0.094	1.638	1.159
2	0.031	0.744	0.268	0.145	1.848	1.192
3	0.005	0.285	0.096	0.070	1.371	1.137
4	0.006	0.328	0.099	0.081	1.222	1.195
5	0.012	0.461	0.127	0.125	1.016	1.187
6	0.012	0.469	0.132	0.117	1.128	1.208
7	0.015	0.507	0.181	0.103	1.757	1.168
8	0.011	0.410	0.121	0.114	1.061	1.103
9	0.063	0.991	0.338	0.238	1.420	1.114
10	0.002	0.188	0.062	0.045	1.378	1.186
11	0.012	0.429	0.138	0.113	1.221	1.105

12	0.006	0.307	0.102	0.078	1.308	1.118
13	0.062	0.975	0.297	0.266	1.117	1.105
14	0.028	0.682	0.222	0.162	1.370	1.150
15	0.006	0.308	0.100	0.082	1.220	1.122
16	0.039	0.850	0.253	0.194	1.304	1.214
17	0.029	0.810	0.245	0.149	1.644	1.342
18	0.051	1.023	0.261	0.250	1.044	1.278
19	0.003	0.230	0.083	0.053	1.566	1.185
20	0.016	0.623	0.173	0.119	1.454	1.389
21	0.004	0.257	0.086	0.063	1.365	1.146
22	0.013	0.491	0.142	0.114	1.246	1.215
23	0.064	1.030	0.363	0.224	1.621	1.149
24	0.023	0.606	0.201	0.147	1.367	1.127
25	0.021	0.600	0.212	0.127	1.669	1.168
26	0.025	0.623	0.209	0.152	1.375	1.112
27	0.045	0.810	0.264	0.216	1.222	1.077
28	0.020	0.599	0.179	0.144	1.243	1.195
29	0.019	0.576	0.185	0.128	1.445	1.179
30	0.002	0.197	0.065	0.046	1.413	1.243
average	0.022	0.561	0.179	0.132	1.369	1.175
standard deviation	0.019	0.254	0.081	0.061	0.213	0.069
1230-332 (bsf)						
1	0.063	1.192	0.479	0.168	2.851	1.340
2	0.020	0.551	0.160	0.157	1.019	1.099
3	0.064	1.107	0.375	0.218	1.720	1.234
4	0.041	0.940	0.329	0.157	2.096	1.310
5	0.025	0.673	0.263	0.123	2.138	1.201
6	0.017	0.528	0.180	0.119	1.513	1.142
7	0.017	0.507	0.174	0.128	1.359	1.097
8	0.068	1.219	0.465	0.185	2.514	1.319
9	0.097	1.228	0.406	0.306	1.327	1.112
10	0.018	0.543	0.169	0.139	1.216	1.142
11	0.015	0.525	0.187	0.100	1.870	1.209
12	0.045	0.956	0.329	0.174	1.891	1.271
13	0.013	0.440	0.145	0.110	1.318	1.089
14	0.028	0.706	0.273	0.131	2.084	1.190
15	0.095	1.193	0.400	0.303	1.320	1.092
16	0.024	0.606	0.207	0.145	1.428	1.103
17	0.018	0.539	0.162	0.142	1.141	1.133
18	0.047	0.961	0.328	0.181	1.812	1.250
19	0.516	3.071	1.129	0.582	1.940	1.206
20	0.154	1.918	0.529	0.370	1.430	1.379
21	0.684	3.484	1.079	0.807	1.337	1.188
22	0.283	2.117	0.604	0.597	1.012	1.123
23	0.335	2.603	0.881	0.485	1.816	1.269
24	0.155	1.836	0.660	0.300	2.200	1.316

25	0.318	2.433	0.772	0.525	1.470	1.217
26	0.522	3.058	1.148	0.579	1.983	1.194
27	0.162	1.817	0.608	0.340	1.788	1.273
28	0.544	3.346	1.160	0.597	1.943	1.280
29	0.327	2.471	0.783	0.532	1.472	1.219
30	0.287	2.188	0.609	0.601	1.013	1.152
31	0.129	1.782	0.722	0.227	3.181	1.400
32	0.690	4.378	1.462	0.601	2.433	1.487
average	0.040	0.801	0.280	0.166	1.701	1.185
stv	0.207	1.060	0.358	0.204	0.528	0.100
1215-184 (bsf)						
1	0.099	1.310	0.527	0.239	2.205	1.174
2	0.046	0.873	0.261	0.222	1.176	1.148
3	0.031	0.750	0.230	0.172	1.337	1.202
4	0.040	0.831	0.279	0.181	1.541	1.172
5	0.059	1.005	0.329	0.228	1.443	1.167
6	0.033	0.764	0.265	0.158	1.677	1.186
7	0.040	0.813	0.260	0.196	1.327	1.147
8	0.024	0.670	0.196	0.158	1.241	1.220
9	0.014	0.538	0.146	0.124	1.177	1.283
10	0.014	0.488	0.149	0.121	1.231	1.163
11	0.072	1.121	0.370	0.249	1.486	1.179
12	0.023	0.646	0.184	0.157	1.172	1.202
13	0.024	0.670	0.189	0.161	1.174	1.220
14	0.022	0.633	0.216	0.132	1.636	1.204
15	0.014	0.509	0.147	0.123	1.195	1.214
16	0.042	0.830	0.261	0.206	1.267	1.142
17	0.349	2.680	0.780	0.570	1.368	1.280
18	0.032	0.739	0.233	0.173	1.347	1.165
19	0.058	1.006	0.325	0.226	1.438	1.178
20	0.099	1.274	0.410	0.307	1.336	1.142
21	0.072	1.116	0.379	0.242	1.566	1.173
22	0.074	1.041	0.329	0.288	1.142	1.080
23	0.020	0.616	0.188	0.135	1.393	1.229
24	0.027	0.662	0.210	0.163	1.288	1.137
25	0.029	0.729	0.228	0.164	1.390	1.208
26	0.069	1.221	0.373	0.236	1.581	1.311
27	0.043	0.951	0.283	0.193	1.466	1.294
28	0.125	1.465	0.419	0.380	1.103	1.169
29	0.042	0.841	0.263	0.204	1.289	1.158
30	0.074	1.153	0.373	0.253	1.474	1.196
31	0.052	1.136	0.405	0.165	2.455	1.405
32	0.085	1.308	0.405	0.266	1.523	1.266
33	0.022	0.594	0.177	0.158	1.120	1.130
34	0.008	0.367	0.132	0.075	1.760	1.157
35	0.006	0.323	0.122	0.058	2.103	1.176

36	0.011	0.424	0.137	0.098	1.398	1.140
37	0.014	0.481	0.162	0.113	1.434	1.147
38	0.061	1.062	0.352	0.220	1.600	1.213
39	0.113	1.367	0.433	0.331	1.308	1.147
40	0.053	1.075	0.319	0.213	1.498	1.317
41	0.034	0.811	0.262	0.164	1.598	1.241
42	0.014	0.487	0.173	0.101	1.713	1.161
43	0.019	0.606	0.188	0.132	1.424	1.240
44	0.032	0.726	0.257	0.157	1.637	1.145
45	0.011	0.491	0.140	0.101	1.386	1.321
average	0.050	0.871	0.277	0.194	1.454	1.199
standard deviation	0.054	0.401	0.125	0.088	0.276	0.063
1215-214 (bsf)						
1	0.099	1.310	0.527	0.239	2.205	1.174
2	0.387	2.947	0.875	0.563	1.554	1.336
3	0.399	3.788	1.179	0.431	2.735	1.692
4	0.137	1.611	0.479	0.365	1.312	1.228
5	0.170	1.847	0.660	0.327	2.018	1.264
6	1.042	4.791	1.578	0.840	1.879	1.324
7	0.176	2.078	0.507	0.442	1.147	1.397
8	0.062	1.018	0.294	0.270	1.089	1.153
9	0.081	1.278	0.395	0.262	1.508	1.267
10	0.070	1.120	0.345	0.257	1.342	1.194
11	0.277	2.612	0.658	0.536	1.228	1.400
12	0.181	1.859	0.540	0.427	1.265	1.233
13	0.082	1.237	0.361	0.287	1.258	1.219
14	0.040	0.817	0.259	0.196	1.321	1.152
15	0.070	1.105	0.343	0.261	1.314	1.178
16	0.084	1.400	0.437	0.246	1.776	1.363
17	0.149	1.601	0.536	0.354	1.514	1.170
18	0.060	1.164	0.329	0.233	1.412	1.341
19	0.104	1.319	0.391	0.338	1.157	1.154
20	0.083	1.237	0.385	0.273	1.410	1.211
21	0.079	1.338	0.361	0.280	1.289	1.343
22	0.141	1.534	0.485	0.370	1.311	1.152
23	0.054	1.066	0.328	0.209	1.569	1.294
24	0.068	1.316	0.326	0.264	1.235	1.424
25	0.015	0.482	0.161	0.116	1.388	1.110
26	0.172	1.994	0.797	0.275	2.898	1.356
27	0.190	1.859	0.520	0.466	1.116	1.203
28	0.239	2.155	0.638	0.476	1.340	1.243
29	0.108	1.319	0.409	0.337	1.214	1.132
30	0.054	1.031	0.302	0.228	1.325	1.252
average	0.162	1.674	0.514	0.339	1.504	1.265
standard deviation	0.190	0.887	0.288	0.141	0.442	0.120
1215-222 (bsf)						

1	0.164	1.950	0.569	0.366	1.555	1.358
2	0.048	1.016	0.359	0.171	2.099	1.308
3	0.062	1.090	0.382	0.207	1.845	1.235
4	0.042	0.856	0.265	0.204	1.299	1.178
5	0.090	1.462	0.389	0.294	1.323	1.375
6	0.056	0.969	0.343	0.207	1.657	1.155
7	0.030	0.785	0.263	0.145	1.814	1.279
8	0.031	0.740	0.239	0.166	1.440	1.186
9	0.020	0.581	0.193	0.130	1.485	1.159
10	0.027	0.706	0.209	0.167	1.251	1.212
11	0.020	0.608	0.186	0.136	1.368	1.213
13	0.105	1.558	0.500	0.267	1.873	1.356
14	0.044	1.005	0.295	0.188	1.569	1.352
15	0.036	0.885	0.272	0.168	1.619	1.316
16	0.025	0.686	0.205	0.155	1.323	1.224
17	0.075	1.197	0.450	0.211	2.133	1.233
18	0.017	0.526	0.181	0.122	1.484	1.138
19	0.032	0.792	0.281	0.143	1.965	1.249
20	0.030	0.777	0.255	0.151	1.689	1.265
21	0.028	0.663	0.227	0.156	1.455	1.118
22	0.146	1.630	0.534	0.347	1.539	1.203
25	0.041	0.820	0.253	0.208	1.216	1.142
26	0.038	0.821	0.294	0.166	1.771	1.188
27	0.034	0.803	0.234	0.187	1.251	1.228
28	0.053	0.997	0.317	0.212	1.495	1.222
29	0.023	0.673	0.220	0.130	1.692	1.252
30	0.025	0.636	0.195	0.164	1.189	1.135
31	0.136	1.719	0.553	0.313	1.767	1.315
32	0.073	1.120	0.353	0.262	1.347	1.169
33	0.106	1.412	0.424	0.318	1.333	1.223
34	0.078	1.279	0.413	0.240	1.721	1.292
35	0.092	1.261	0.352	0.333	1.057	1.173
36	0.056	1.032	0.275	0.257	1.070	1.230
37	0.053	1.103	0.340	0.199	1.709	1.352
38	0.032	0.824	0.281	0.147	1.912	1.299
39	0.037	0.820	0.232	0.201	1.154	1.203
40	0.124	1.501	0.498	0.318	1.566	1.202
41	0.044	0.922	0.255	0.219	1.164	1.240
42	0.046	0.830	0.260	0.223	1.166	1.092
43	0.030	0.702	0.243	0.158	1.538	1.143
44	0.045	0.874	0.297	0.195	1.523	1.162
45	0.031	0.787	0.258	0.155	1.665	1.261
46	0.075	1.141	0.345	0.276	1.250	1.175
47	0.046	0.909	0.309	0.191	1.618	1.196
48	0.031	0.813	0.239	0.166	1.440	1.303
49	0.016	0.591	0.157	0.130	1.208	1.318

50	0.019	0.621	0.183	0.129	1.419	1.271
average	0.056	0.975	0.305	0.214	1.437	1.218
standard deviation	0.036	0.329	0.104	0.065	0.266	0.071

Appendix 4.4 Total organic carbon, total nitrogen, and carbon isotopes

core number and position	total organic carbon	TOC/TN	delta13C
(cm bsf)	(wt %)		(‰)
F1			
1226-162	0.15	10.76	-23.42
1226-167	0.21	11.50	-24.08
F2a (fine particles)			
1226-44	0.14	9.15	-21.75
1226-75	0.29	11.30	-23.41
1226-142	0.23	10.25	-22.20
1226-172	0.11	13.11	-25.08
F2a (coarse particles)			
1215-179	0.11	9.87	-22.79
1215-210	0.15	10.11	-23.18
1219-172	0.12	9.57	-23.52
1226-50	0.04	7.14	-24.39
1226-180	0.08	12.07	-25.13
1230-297	0.05	7.80	-24.19
1230-312	0.05	7.62	-18.98
1230-332	0.07	12.24	-23.71
F2b (fine particles)			
1219-16	0.08	7.53	-21.52
1219-46	0.06	7.17	-22.91
1219-312	0.04	6.70	-23.61
1226-90	0.05	9.25	-27.41
1226-151	0.05		
1230-48	0.06	8.36	-23.91
F2b (coarse particles)			
1219-58	0.02		
1219-61	0.05	7.25	-23.05
1226-34	0.05	8.76	-25.08
1226-101	0.05		
1226-117	0.05		
1226-134	0.03		
1226-138	0.03		
1226-159	0.04		
1226-171	0.05		
1226-174	0.05		
1226-18	0.04		
1230-56	0.05	8.13	-26.02
1230-63	0.04	6.16	-25.73
1230-138	0.03		
1230-158	0.03		

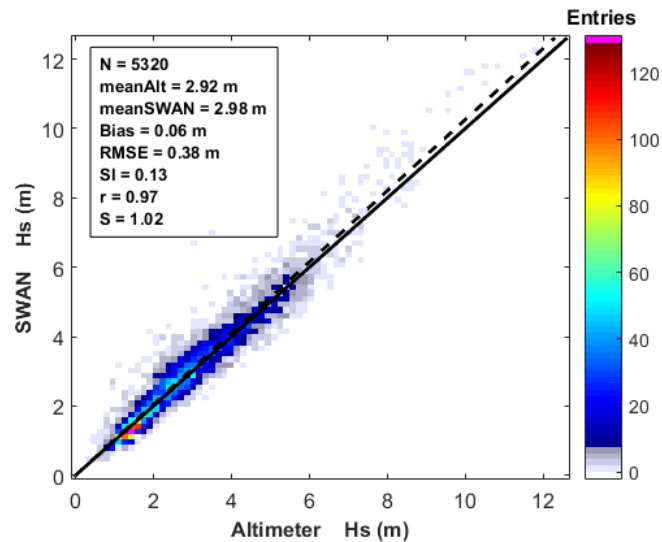
Appendix 5.1 Validation of wave property simulation

The characteristics of the waves around the Azores Archipelago were simulated with a wave modelling system based on the last version of the SWAN model (41.31A), implemented in the North Atlantic area and then in the target area. Simulations were performed from 1 January 2013 to 31 December 2014. To validate the SWAN model results in the Azores Archipelago, comparisons with altimeter measurements were made for 6 months (from September 2013 to February 2014). In this period various extreme events affected Europe.

The H_s fields simulated by SWAN model in the Azores Archipelago were interpolated in space and time using the triangulation-based linear interpolation method (Rusu and Guedes Soares, 2015), to collocate with the altimeter data L3 product (version v2.0.6) processed in the framework of Climate Change Initiative for Sea State (CCI-SS) project, (Dodet et al., 2020). Further, statistical analyses to assess the quality of the simulated H_s were performed. The computed statistical parameters are bias, root mean square error (RMSE), scatter index (SI), and correlation coefficient (r), defined with the following relationships:

$$\begin{aligned} \text{Bias} &= \frac{\sum_{i=1}^N (Y_i - X_i)}{N} & \text{RMSE} &= \sqrt{\frac{\sum_{i=1}^N (X_i - Y_i)^2}{N}}; \\ \text{SI} &= \frac{\text{RMSE}}{\tilde{X}}; & r &= \frac{\sum_{i=1}^N (X_i - \tilde{X})(Y_i - \tilde{Y})}{\left(\sum_{i=1}^N (X_i - \tilde{X})^2 \sum_{i=1}^N (Y_i - \tilde{Y})^2 \right)^{\frac{1}{2}}} \end{aligned} \quad (1)$$

with X_i being denoted the measured values (altimeter measurements), while Y_i represents the simulated values (SWAN results), and N is the number of pairs of data observations/simulations. The symmetric slope (S) was also evaluated, that is the coefficient of the regression line through the origin (model against measured data). This parameter shows when an over-estimation of the measurements occurs ($S > 1$) or on the contrary an under-estimation ($S < 1$).



Scatter diagram of H_s simulated by SWAN vs. altimeter measurements from September 2013 to February 2014.

References

- Dodet, G.; Piolle, J.-F.; Quilfen, Y.; Abdalla, S.; Accensi, M.; Ardhuin, F.; Ash, E.; Bidlot, J.-R.; Gommenginger, C.; Marechal, G.; et al., 2020. The Sea State CCI Dataset v1: Towards a Sea State Climate Data Record Based on Satellite Observations. *Earth Syst. Sci. Data* 12, 1929–1951, doi:10.5194/essd-12-1929-2020.
- Rusu, L., Guedes Soares, C., 2015. Impact of assimilating altimeter data on wave predictions in the western Iberian coast, *Ocean Modelling* 96, 126-135.

Appendix 5.2 Computed wave-induced stresses and the used parameters

Appendix 5.2.1 Characteristics of surface samples and computed threshold stresses of sediment

Sample ID	Latitude (°)	Longitude (°)	Depth (m)	Grain size Mode (m)	CaCO ₃ (%)	Threshold stresses of sediment motion (N/m ²)
			<i>z</i>	<i>D</i>		τ_{cr}
FAPI3_072	38.65538	-28.70825	85	0.001717	6.1	0.950
FAPI3_071	38.65175	-28.70820	65	0.001636	6.1	0.889
FAPI3_070	38.64660	-28.67942	73	0.002412	7.1	1.517
FAPI3_073	38.64517	-28.74408	65	0.000986	3.1	0.475
FAPI3_074	38.63728	-28.74165	40	0.000454	3.1	0.247
FAPI3_068	38.63472	-28.65470	60	0.000361	5.1	0.219
FAPI3_075	38.63215	-28.73740	18	0.000525	0.0	0.270
FAPI3_076	38.62823	-28.76147	58	0.000279	3.1	0.197
FAPI3_067	38.62713	-28.65437	21	0.000339	5.1	0.213
FAPI3_077	38.62203	-28.76075	40	0.000356	3.1	0.218
FAPI3_078	38.61693	-28.75952	19	0.000444	0.0	0.244
FAPI3_066	38.61668	-28.60758	81	0.001329	10.2	0.677
FAPI3_P07	38.61272	-28.75002	20	0.000707	0.0	0.341
FAPI3_065	38.61032	-28.60885	60	0.00132	5.1	0.672
FAPI3_P06	38.58877	-28.60386	20	0.000785	0.0	0.375
FAPI3_063	38.58810	-28.57970	61	0.001214	3.1	0.605
FAPI3_064	38.58760	-28.59660	20	0.000277	8.2	0.197
FAPI3_060	38.58008	-28.59900	20	0.000253	10.2	0.191
FAPI3_061	38.58005	-28.58977	39	0.000325	12.2	0.210
FAPI3_062	38.57952	-28.58145	59	0.00057	10.2	0.287
FAPI3_006	38.57178	-28.41695	79	0.002071	14.3	1.227
FAPI3_P04	38.56808	-28.60512	20	0.000779	0.0	0.372
FAPI3_007	38.56670	-28.39983	70	0.000959	6.1	0.460
FAPI3_058	38.56348	-28.59948	21	0.000279	5.1	0.197
FAPI3_059	38.56342	-28.59173	41	0.000415	22.4	0.235
FAPI3_079	38.56228	-28.77038	19	0.000415	0.0	0.235
FAPI3_008	38.55928	-28.36713	76	0.001385	4.1	0.714
FAPI3_080	38.55927	-28.77385	40	0.000747	0.0	0.358
FAPI3_002	38.55887	-28.53457	50.2	0.000551	59.2	0.280
FAPI3_P05	38.55773	-28.61024	20	0.000629	4.1	0.309
FAPI3_009	38.55738	-28.35702	85	0.000314	4.1	0.207
FAPI3_P02	38.55571	-28.61000	20	0.0005	0.0	0.262
FAPI3_081	38.55473	-28.77432	57	0.00105	4.1	0.509
FAPI3_010	38.55220	-28.35137	68	0.000973	16.3	0.467
FAPI3_011	38.54788	-28.34225	63	0.000877	4.1	0.418
FAPI3_P03	38.54265	-28.61992	20	0.000454	3.1	0.247
FAPI3_012	38.54052	-28.33308	45	0.000328	6.1	0.210
FAPI3_083	38.53860	-28.75772	28	0.000441	3.1	0.243
FAPI3_094	38.53795	-28.61532	20	0.000264	4.1	0.193
FAPI3_082	38.53758	-28.76448	58	0.001266	4.1	0.637
FAPI3_093	38.53390	-28.60887	40	0.000354	22.4	0.217
FAPI3_004	38.52593	-28.56233	68.7	0.000457	57.1	0.248
FAPI3_P01	38.52518	-28.62600	20	0.000444	21.4	0.244
FAPI3_003	38.52463	-28.54867	25	0.000228	36.7	0.184
FAPI3_P08	38.52315	-28.67071	20	0.001959	0.0	1.137
FAPI3_092	38.52222	-28.61980	24	0.000287	10.2	0.199
FAPI3_005	38.52040	-28.60898	44	0.000529	29.0	0.272
FAPI3_090	38.52015	-28.64220	20	0.000299	8.2	0.203
FAPI3_015	38.51725	-28.28943	76	0.000221	8.2	0.182
FAPI3_087	38.51670	-28.69183	37	0.000379	12.2	0.224

FAPI3_084	38.51622	-28.74123	62	0.001569	10.2	0.841
FAPI3_014	38.51413	-28.29158	41.8	0.000117	12.2	0.150
FAPI3_091	38.51357	-28.64172	60	0.000363	16.3	0.220
FAPI3_089	38.51312	-28.67590	62	0.000732	22.4	0.351
FAPI3_085	38.51085	-28.72625	63	0.001366	12.2	0.702
FAPI3_013	38.50975	-28.29228	22	0.000137	7.1	0.157
FAPI3_017	38.50548	-28.26602	74	0.000363	12.2	0.220
FAPI3_016	38.50337	-28.26737	55	0.000514	14.3	0.267
FAPI3_019	38.49567	-28.23222	61	0.000129	16.3	0.154
FAPI3_024	38.49187	-28.21643	65	0.000406	4.1	0.232
FAPI3_018	38.49125	-28.23230	23	0.000152	5.1	0.162
FAPI3_023	38.48868	-28.21610	40	0.000563	5.1	0.284
FAPI3_022	38.47075	-28.18408	58	0.000332	44.9	0.211
FAPI3_021	38.46938	-28.18375	43	0.000253	32.7	0.191
FAPI3_020	38.46597	-28.18480	24	0.000154	20.4	0.163
FAPI3_057	38.45660	-28.13328	58	0.000578	12.2	0.290
FAPI3_056	38.45552	-28.13462	45	0.000727	22.4	0.349
FAPI3_055	38.45497	-28.11502	43	0.000574	3.1	0.288
FAPI3_054	38.45388	-28.10092	58	0.000356	8.2	0.218
FAPI3_053	38.45293	-28.07572	57	0.000351	6.1	0.217
FAPI3_052	38.44952	-28.07578	33	0.000342	5.1	0.214
FAPI3_051	38.43647	-28.03642	59	0.000202	32.7	0.177
FAPI3_050	38.43353	-28.03648	52	0.000189	44.9	0.174
FAPI3_035	38.40670	-28.16688	27	0.001266	4.1	0.637
FAPI3_038	38.40645	-28.14805	28	0.001558	14.3	0.834
FAPI3_033	38.40613	-28.18098	29	0.000966	28.6	0.464
FAPI3_025	38.40540	-28.26700	30	0.000164	14.3	0.166
FAPI3_039	38.40518	-28.16658	70	0.000841	5.1	0.401
FAPI3_044	38.40258	-28.05787	41	0.000323	36.7	0.209
FAPI3_040	38.40162	-28.11905	42	0.000774	6.1	0.370
FAPI3_026	38.40117	-28.26658	47	0.000678	8.2	0.329
FAPI3_042	38.40103	-28.10552	23	0.001853	8.2	1.054
FAPI3_027	38.40077	-28.26533	38	0.000664	7.1	0.323
FAPI3_043	38.39987	-28.10872	39	0.000818	7.1	0.390
FAPI3_041	38.39943	-28.10762	49	0.000369	6.1	0.222
FAPI3_031	38.39012	-28.20730	28	0.000493	6.1	0.260
FAPI3_030	38.38727	-28.20765	37	0.000497	8.2	0.261
FAPI3_029	38.38407	-28.22317	39	0.000993	9.2	0.478

Appendix 5.2.2 Wave properties and computed wave-induced stresses on sediment

Sample ID	2001 peak wave period (s)	2001 95 th significant wave height (m)	2013-2014 peak wave period (s)	2013-2014 95 th significant wave height (m)	2001 wave induced bed shear stress (N/m ²)	2013-2014 wave induced bed shear stress (N/m ²)	2001 stress ratio	2013-2014 stress ratio
	<i>T</i>	<i>H_s</i>	<i>T</i>	<i>H_s</i>	τ_w	τ_w		
FAPI3_072	5.952	2.491	9.760	4.056	0.00002	0.11302	0.00002	0.11901
FAPI3_071	11.133	6.754	10.916	3.775	1.52827	0.59632	1.71822	0.67043
FAPI3_070	11.000	4.610	11.300	2.902	0.69409	0.39736	0.45763	0.26199
FAPI3_073	11.167	6.818	11.444	3.853	1.20538	0.56793	2.54025	1.19686
FAPI3_074	11.079	6.846	12.366	3.732	2.45968	1.16342	9.95877	4.71046
FAPI3_068	11.333	5.920	11.370	3.399	0.76391	0.33957	3.48240	1.54800
FAPI3_075	6.447	3.500	10.918	3.758	1.59432	3.32701	5.89439	12.30034
FAPI3_076	11.244	6.698	10.106	3.953	0.85466	0.26148	4.33136	1.32519
FAPI3_067	14.756	2.019	11.440	2.903	0.92107	1.53771	4.31811	7.20904
FAPI3_077	12.411	6.684	10.190	3.912	2.43905	0.80308	11.18977	3.68434
FAPI3_078	11.955	6.229	12.156	3.472	6.18194	2.60822	25.32994	10.68695
FAPI3_066	9.968	5.894	9.953	3.172	0.25964	0.10264	0.38325	0.15151
FAPI3_P07	7.514	4.814	10.520	3.369	3.41032	2.88414	10.01363	8.46864
FAPI3_065	9.984	5.816	11.567	1.812	0.87542	0.27702	1.30359	0.41251
FAPI3_P06	12.711	2.515	10.390	2.023	2.07000	1.42261	5.52555	3.79745

FAPI3_063	9.816	4.257	8.804	2.795	0.45668	0.12430	0.75441	0.20535
FAPI3_064	10.446	3.397	8.701	2.189	1.78865	0.81355	9.08800	4.13358
FAPI3_060	13.767	2.753	10.631	2.051	1.31811	0.81518	6.91617	4.27729
FAPI3_061	9.253	3.339	10.548	2.039	0.49655	0.33096	2.36973	1.57946
FAPI3_062	8.824	3.557	8.344	2.503	0.14173	0.05561	0.49442	0.19400
FAPI3_006	10.890	5.750	9.627	3.477	0.63132	0.12897	0.51432	0.10507
FAPI3_P04	10.435	4.462	10.628	2.045	4.57899	1.45515	12.30377	3.90999
FAPI3_007	10.860	5.774	9.610	3.537	0.65078	0.15502	1.41397	0.33683
FAPI3_058	9.940	5.915	8.264	1.926	3.72423	0.58345	18.87415	2.95691
FAPI3_059	9.827	6.754	7.558	2.056	1.68401	0.09181	7.16753	0.39077
FAPI3_079	8.196	5.790	9.882	2.487	4.27611	1.44087	18.20015	6.13268
FAPI3_008	10.615	5.238	9.496	3.224	0.44744	0.10179	0.62624	0.14247
FAPI3_080	8.237	5.863	8.467	2.569	1.03944	0.34758	2.90362	0.97094
FAPI3_002	9.648	7.033	8.866	2.991	1.12743	0.21326	4.03168	0.76263
FAPI3_P05	7.590	2.150	10.534	1.017	0.99215	0.46102	3.21505	1.49393
FAPI3_009	10.761	4.912	9.573	3.406	0.12943	0.03047	0.62660	0.14753
FAPI3_P02	7.590	2.150	10.534	1.017	0.88088	0.40932	3.36183	1.56213
FAPI3_081	8.251	5.903	8.382	3.046	0.29507	0.12521	0.57955	0.24592
FAPI3_010	11.189	4.394	10.950	2.803	0.54946	0.25732	1.17583	0.55066
FAPI3_011	10.806	5.012	10.931	2.990	0.69217	0.33769	1.65494	0.80739
FAPI3_P03	16.011	0.993	13.733	1.056	0.38850	0.43209	1.57297	1.74943
FAPI3_012	11.578	3.724	11.166	2.684	0.73061	0.42003	3.47660	1.99871
FAPI3_083	8.191	5.771	9.613	2.444	2.06539	0.79830	8.49601	3.28380
FAPI3_094	8.497	1.660	8.695	1.198	0.51250	0.32482	2.65012	1.67966
FAPI3_082	8.256	5.871	8.457	3.201	0.29746	0.14612	0.46673	0.22926
FAPI3_093	6.328	2.530	6.452	1.881	0.03126	0.02431	0.14387	0.11186
FAPI3_004	9.630	7.030	7.778	2.519	0.32076	0.01044	1.29345	0.04209
FAPI3_P01	6.083	1.185	13.970	0.856	0.18062	0.31312	0.74006	1.28296
FAPI3_003	9.634	7.041	7.885	2.419	3.27978	0.47585	17.82071	2.58551
FAPI3_P08	8.461	2.654	7.176	2.014	2.89380	1.44547	2.54515	1.27132
FAPI3_092	10.959	1.261	8.630	1.360	0.34228	0.29830	1.71675	1.49615
FAPI3_005	6.651	2.887	6.388	2.092	0.04351	0.01783	0.16011	0.06560
FAPI3_090	8.242	3.051	8.848	2.070	1.29431	0.79323	6.38870	3.91538
FAPI3_015	10.437	4.238	9.523	2.659	0.11370	0.03012	0.62478	0.16548
FAPI3_087	8.618	1.881	10.165	1.578	0.20847	0.25307	0.92877	1.12744
FAPI3_084	7.992	5.353	10.712	2.634	0.15250	0.36639	0.18126	0.43548
FAPI3_014	10.274	3.829	9.596	2.418	0.40342	0.16942	2.69234	1.13066
FAPI3_091	7.643	4.200	6.707	2.625	0.03897	0.00407	0.17709	0.01850
FAPI3_089	8.456	5.080	6.790	2.637	0.15644	0.00539	0.44537	0.01535
FAPI3_085	8.622	5.049	7.762	3.282	0.23170	0.04677	0.33012	0.06663
FAPI3_013	11.622	3.521	11.023	1.999	1.21515	0.51508	7.72153	3.27301
FAPI3_017	10.248	4.116	9.924	2.489	0.14063	0.05423	0.63904	0.24641
FAPI3_016	15.000	2.250	10.951	2.367	0.44170	0.26558	1.65570	0.99552
FAPI3_019	10.412	4.291	9.101	2.534	0.19139	0.04207	1.23946	0.27246
FAPI3_024	10.163	4.361	8.972	2.672	0.25540	0.05618	1.09898	0.24175
FAPI3_018	11.222	3.093	10.746	1.733	0.99027	0.41081	6.09914	2.53021
FAPI3_023	10.061	3.870	9.013	2.361	0.97301	0.33860	3.42854	1.19310
FAPI3_022	9.512	3.762	8.726	2.186	0.19723	0.05198	0.93298	0.24591
FAPI3_021	9.131	2.738	8.404	1.380	0.23787	0.05992	1.24813	0.31441
FAPI3_020	15.000	1.200	15.200	0.892	0.24796	0.15978	1.52089	0.98005
FAPI3_057	9.404	4.090	10.082	2.085	0.27965	0.14655	0.96573	0.50609
FAPI3_056	10.342	3.525	9.981	1.753	0.79466	0.25515	2.27651	0.73095
FAPI3_055	10.042	3.869	10.053	2.366	0.82905	0.40159	2.87761	1.39392
FAPI3_054	9.916	3.993	9.972	2.438	0.27581	0.13647	1.26536	0.62610
FAPI3_053	10.011	3.725	9.714	2.197	0.27355	0.10864	1.26288	0.50156
FAPI3_052	10.202	3.560	9.684	2.276	0.99929	0.47026	4.67064	2.19797
FAPI3_051	8.148	3.072	7.300	2.120	0.03604	0.00710	0.20375	0.04016
FAPI3_050	7.019	2.280	6.350	1.788	0.01126	0.00239	0.06488	0.01375
FAPI3_035	6.793	2.999	7.545	1.005	0.76479	0.23040	1.20000	0.36151
FAPI3_038	8.231	3.100	6.683	2.215	1.60738	0.44208	1.92817	0.53030
FAPI3_033	8.135	1.900	6.583	1.706	0.54098	0.18907	1.16653	0.40770
FAPI3_025	8.538	2.715	8.933	2.336	0.38417	0.34268	2.31289	2.06309
FAPI3_039	6.828	3.102	8.603	1.311	0.00286	0.01375	0.00714	0.03429
FAPI3_044	7.630	3.917	7.889	1.472	0.22225	0.06359	1.06372	0.30434

FAPI3_040	7.382	3.591	6.822	2.222	0.22301	0.05909	0.60319	0.15981
FAPI3_026	8.342	4.564	7.478	2.733	0.40555	0.08987	1.23437	0.27355
FAPI3_042	6.828	3.102	8.354	2.055	1.63355	1.48392	1.55048	1.40846
FAPI3_027	9.165	4.162	7.488	2.630	1.03430	0.21723	3.20369	0.67287
FAPI3_043	8.432	3.621	6.870	2.449	0.64412	0.10848	1.65146	0.27814
FAPI3_041	8.370	3.669	6.437	2.459	0.18465	0.00994	0.83361	0.04486
FAPI3_031	13.040	1.000	7.765	1.436	0.28816	0.23887	1.10944	0.91969
FAPI3_030	6.702	2.419	6.595	1.780	0.08767	0.04906	0.33605	0.18806
FAPI3_029	6.897	2.380	6.250	2.028	0.11855	0.03966	0.24792	0.08294

Appendix 6.1 Geochemical composition of full glass data for core 1230 at depth 180-250 cm. (The file of generated geochemical data is to be freely obtained from the supplementary information in the future open-access article)

Sample positions-ID	Na ₂ O	K ₂ O	FeO	SiO ₂	TiO ₂	MgO	CaO	MnO	Al ₂ O ₃	P ₂ O ₅	TAS	Total
(cm bsf)	(%)	(%)	(%)	(%)	(%)	(%)	(%)	(%)	(%)	(%)	(%)	(%)
1230												
178-180-3	7.25	5.00	4.76	65.97	0.54	0.35	0.65	0.25	15.16	0.07	12.24	100
178-180-4	7.26	5.05	4.64	66.19	0.53	0.31	0.63	0.20	15.15	0.04	12.31	100
178-180-5	6.72	4.98	4.70	66.61	0.63	0.35	0.60	0.23	15.13	0.06	11.70	100
178-180-6	7.03	5.13	4.32	65.67	0.69	0.46	0.79	0.23	15.59	0.09	12.16	100
178-180-7	6.85	4.97	4.54	66.76	0.52	0.36	0.61	0.22	15.10	0.08	11.82	100
178-180-12	7.23	5.12	4.64	65.90	0.62	0.41	0.65	0.19	15.16	0.07	12.36	100
178-180-13	7.27	4.90	4.63	66.10	0.56	0.37	0.63	0.30	15.23	0.01	12.17	100
178-180-14	7.46	4.89	4.55	66.43	0.61	0.35	0.58	0.18	14.86	0.09	12.36	100
178-180-15	7.27	4.94	4.70	66.25	0.51	0.33	0.59	0.31	15.06	0.05	12.21	100
185-186-1	7.17	4.91	4.88	66.26	0.57	0.34	0.61	0.19	15.04	0.02	12.08	100
185-186-2	7.32	4.86	4.62	66.16	0.70	0.33	0.62	0.22	15.07	0.09	12.18	100
185-186-5	7.48	4.98	4.54	65.89	0.63	0.35	0.63	0.18	15.23	0.07	12.46	100
185-186-6	7.25	5.00	4.37	65.96	0.56	0.36	0.71	0.25	15.47	0.07	12.25	100
185-186-7	7.51	5.00	4.19	64.97	0.69	0.50	0.84	0.20	15.96	0.13	12.51	100
185-186-8	7.12	4.79	5.06	65.53	0.60	0.32	0.89	0.20	15.40	0.10	11.90	100
185-186-9	6.91	4.94	4.75	66.64	0.57	0.34	0.63	0.18	15.00	0.04	11.86	100
185-186-10	7.48	4.90	4.54	66.07	0.72	0.34	0.64	0.20	15.12	0.00	12.37	100
185-186-12	6.59	4.78	4.66	67.02	0.63	0.33	0.58	0.24	15.11	0.07	11.36	100
185-186-14	6.92	4.84	4.94	66.71	0.56	0.31	0.61	0.23	14.87	0.00	11.77	100
185-186-15	7.42	4.98	4.55	65.92	0.64	0.34	0.57	0.30	15.23	0.04	12.41	100
198-200-1	6.98	4.91	4.73	66.44	0.53	0.40	0.60	0.22	15.08	0.11	11.89	100
198-200-2	7.20	4.93	4.69	66.39	0.51	0.38	0.61	0.25	14.96	0.09	12.13	100
198-200-3	7.31	4.90	4.95	65.93	0.59	0.35	0.63	0.24	15.05	0.05	12.21	100
198-200-5	7.40	4.85	4.77	64.79	0.82	0.56	0.80	0.27	15.56	0.17	12.25	100
198-200-7	7.14	5.02	4.19	65.66	0.63	0.44	0.80	0.17	15.84	0.11	12.17	100
198-200-8	6.79	4.95	4.89	66.85	0.57	0.30	0.60	0.19	14.82	0.04	11.74	100
198-200-9	7.11	5.05	4.28	65.52	0.69	0.43	0.76	0.18	15.86	0.13	12.16	100
198-200-11	7.17	4.98	4.65	66.42	0.56	0.31	0.59	0.21	15.04	0.05	12.16	100
198-200-12	7.29	4.99	4.71	66.14	0.58	0.38	0.68	0.19	15.03	0.01	12.28	100
198-200-14	7.08	4.97	4.72	66.34	0.63	0.38	0.65	0.22	14.95	0.06	12.06	100
198-200-15	7.32	4.98	4.70	65.85	0.56	0.36	0.58	0.23	15.41	0.02	12.29	100
198-200-4	3.66	1.14	10.53	49.00	3.53	6.00	10.73	0.14	14.76	0.51	4.80	100
238-240-2	7.16	4.86	4.75	66.08	0.62	0.32	0.61	0.22	15.31	0.06	12.02	100
238-240-3	7.08	4.92	4.66	66.45	0.59	0.34	0.56	0.29	15.03	0.07	12.00	100
238-240-4	7.04	4.93	5.34	66.87	0.42	0.21	0.61	0.22	14.34	0.01	11.97	100
238-240-5	7.39	4.96	4.62	66.15	0.58	0.30	0.66	0.27	15.03	0.03	12.35	100
238-240-6	7.28	4.95	4.74	66.30	0.56	0.33	0.56	0.24	14.95	0.09	12.23	100
238-240-7	7.06	4.98	4.79	66.16	0.57	0.33	0.62	0.22	15.20	0.06	12.04	100

238-240-8	7.27	5.00	4.67	66.35	0.53	0.33	0.59	0.20	15.05	0.02	12.27	100
238-240-9	7.14	4.98	4.62	66.50	0.61	0.34	0.65	0.23	14.86	0.06	12.12	100
238-240-10	6.80	4.84	4.76	66.26	0.66	0.40	0.64	0.26	15.33	0.06	11.64	100
238-240-11	7.22	4.85	4.66	66.44	0.51	0.31	0.68	0.25	15.05	0.02	12.08	100
238-240-14	7.16	4.84	4.71	65.88	0.51	0.35	0.96	0.21	15.31	0.06	12.01	100
218-220-1	4.47	1.61	10.40	50.42	3.11	4.63	8.68	0.29	15.57	0.81	6.08	100
238-240-13	4.18	1.56	10.46	50.44	3.17	4.44	9.05	0.19	15.71	0.80	5.74	100
218-220-1	7.21	4.90	4.73	66.30	0.60	0.29	0.60	0.20	15.14	0.03	12.11	100
218-220-2	7.03	5.03	4.71	66.16	0.51	0.31	0.61	0.28	15.31	0.05	12.06	100
218-220-3	7.30	4.95	4.56	66.14	0.57	0.35	0.61	0.23	15.18	0.10	12.25	100
218-220-4	7.13	4.96	4.48	66.24	0.56	0.37	0.59	0.25	15.33	0.08	12.08	100
218-220-6	7.02	4.90	4.76	66.37	0.55	0.29	0.58	0.25	15.19	0.10	11.92	100
218-220-7	7.17	5.06	4.73	66.15	0.50	0.38	0.61	0.28	15.07	0.05	12.23	100
218-220-8	7.37	4.99	4.36	65.39	0.57	0.44	0.68	0.14	15.99	0.06	12.36	100
218-220-9	7.25	4.98	4.71	65.72	0.62	0.33	0.63	0.21	15.47	0.07	12.23	100
218-220-10	7.23	5.10	4.73	65.81	0.54	0.31	0.66	0.25	15.31	0.07	12.33	100
218-220-11	7.39	4.88	4.78	65.96	0.58	0.35	0.63	0.29	15.09	0.06	12.27	100
218-220-12	7.15	4.96	4.76	66.27	0.54	0.29	0.60	0.25	15.11	0.07	12.11	100
218-220-13	7.46	4.69	6.81	66.60	0.59	0.31	0.48	0.30	12.64	0.11	12.15	100
218-220-14	6.95	4.96	4.28	65.15	0.70	0.51	0.88	0.19	16.29	0.09	11.92	100
248-250-1	7.39	4.90	4.84	66.07	0.56	0.33	0.55	0.20	15.11	0.05	12.29	100
248-250-3	7.06	5.09	4.74	66.01	0.57	0.35	0.64	0.32	15.16	0.06	12.15	100
248-250-4	6.98	4.92	4.79	66.47	0.64	0.31	0.54	0.21	15.09	0.05	11.90	100
248-250-5	7.06	5.13	4.14	65.42	0.63	0.42	0.84	0.21	16.01	0.14	12.19	100
248-250-6	7.42	4.85	4.66	66.73	0.46	0.25	0.47	0.27	14.88	0.02	12.26	100
248-250-7	7.56	4.94	4.61	65.85	0.55	0.29	0.56	0.23	15.34	0.06	12.50	100
248-250-8	6.87	5.11	4.44	65.42	0.55	0.42	0.77	0.19	16.11	0.13	11.97	100
248-250-9	7.17	4.94	4.79	65.83	0.56	0.31	0.63	0.27	15.41	0.08	12.11	100
248-250-10	6.99	5.04	4.80	66.00	0.57	0.29	0.61	0.18	15.48	0.04	12.02	100
248-250-11	7.22	4.96	4.63	66.41	0.62	0.30	0.65	0.23	14.87	0.11	12.17	100
248-250-12	7.19	4.94	4.24	65.12	0.69	0.39	0.78	0.24	16.29	0.11	12.13	100
248-250-13	7.70	4.79	5.87	65.59	0.50	0.28	0.53	0.26	14.42	0.06	12.49	100
248-250-14	7.12	5.03	4.41	65.62	0.70	0.39	0.72	0.16	15.74	0.11	12.14	100
248-250-15	7.72	4.77	5.52	66.48	0.50	0.27	0.47	0.34	13.89	0.04	12.49	100
248-250-2	4.36	1.52	12.33	48.84	4.34	4.46	8.90	0.22	13.89	1.12	5.89	100